A journey with a fish : exploring zebrafish as a model to study host-pathogen interaction

Valerio Laghi

Université Paris Cité

Université Paris Cité
Frontières de l'Innovation en Recherche et Éducation, ED474
Polarité cellulaire, Migration et Cancer (PCMC), Institut Pasteur

A journey with a fish: Exploring zebrafish as a model to study host-pathogen interaction

Par Valerio LAGHI

Thèse de doctorat d'Immunologie et Infectiologie

Dirigée par **Emma Colucci**
Et par **Jean-Pierre Levraud**

Présentée et soutenue **publiquement** le 23/11/2023

Devant un jury composé de :

Mme Annemarie Meijer	PR Leiden University	Rapportrice
M. Cyril Favard	IR HC CNRS Université Montpellier	Rapporteur
Mme. Joana Duarte Da Rocha Pereira	APR Ku Leuven	Examinatrice
M. Gerard Eberl	PR UPC	Examinateur
Mme. Muriel Mambrini	PR UPC	Invité
Mme Emma Colucci	CR UPC	Directrice
M. Jean-Pierre Levraud	DR Université Paris Saclay	Co-Directeur

Contents

FIGURE INDEX

RESUMÉ SUBSTANTIEL

Le poisson zèbre (Danio Rerio) est un petit poisson appartenant à la famille des cyprinidés et déjà largement utilisé pour la recherche associée au développement, à la régénération et à la toxicologie. L'année dernière, le poisson zèbre a démontré son potentiel dans la recherche sur les interactions hôte-pathogène. Ce modèle de poisson présente un degré élevé de transparence et un temps de génération rapide. Ces deux caractéristiques sont fondamentales pour le criblage à haut contenu et l'observation directe de la dissémination des pathogènes dans des larves vivantes entières. En outre, le système immunitaire inné du poisson zèbre est composé de leucocytes (c'est-à-dire de macrophages et de neutrophiles), et sa signalisation est baséee sur des cytokines dont linterféron, conservant ainsi un degré élevé de similitudes avec l'homme. Une autre caractéristique importante du poisson zèbre est la possibilité de manipuler facilement sa génétique grâce à des systèmes tels que le morpholino, la transposase Tol2 et CRISPR. Cela nous a permis de générer des lignées de poissons zèbres transgéniques afin de réguler l'expression de gènes cibles ou d'associer des fluorophores spécifiques (par exemple GFP et mCherry) à des protéines.

Dans cette thèse, nous allons confronter ce modèle à différents pathogènes (virus Sindbis, SARS-COV2 et Legionella pneumophila) afin de mettre en lumière les aspects positifs et négatifs de l'expérimentation sur le poisson zèbre tout en répondant à des questions biologiques importantes et en développant de nouveaux outils/approches expérimentaux.

Le virus Sindbis (SINV) est un alphavirus à ARN positif simple brin transmis par des arthropodes (principalement des moustiques) et capable d'infecter l'homme. Cet arbovirus est largement utilisé comme modèle d'encéphalite virale, mais, malgré des études approfondies sur des souris, les mécanismes d'invasion du cerveau et de réponse immunitaire restent encore largement à élucider.

En utilisant les outils générés par Gabriella Passoni dans le laboratoire, nous nous sommes concentrés sur : 1) identifier la voie d'invasion du cerveau exploitée par le SINV, 2) le rôle du système interféron dans le contrôle de l'infection, et 3) explorer la possibilité d'utiliser ce projet pour développer des modèles mathématiques capables de faire la lumière sur des paramètres difficilement mesurables par l'expérimentation in vivo.

En utilisant des constructions virales exprimant des rapporteurs fluorescents, nous avons suivi la propagation du SINV de la périphérie au cerveau. Nous avons montré que le SINV préfère infecter les fibres musculaires au cours de la première vague réplicative, où il génère une infection avec une propagation de cellule à cellule multidirectionnelle et transitoire. Grâce au criblage à haut contenu et à l'imagerie à haute résolution, nous avons identifié la population cellulaire impliquée dans la progression de l'infection et nous avons multiplexé les données d'imagerie avec la mesure de l'expression génétique de l'immunité antivirale du poisson-zèbre. Nous avons identifié dans les ganglions rachidiens (DRG) la principale porte d'accès au SNC utilisée par le SINV pour atteindre le cerveau. Grâce aux techniques utilisées, il a été possible d'observer directement la propagation de l'infection dans les populations du SNC. Outre les DRG, SINV s'est avéré capable d'infecter les interneurones et les motoneurones, en exploitant le réseau dense d'interconnexions axonales entre les neurones. Les résultats ont montré la présence de trois systèmes différents de propagation axonale ou de cellule à cellule utilisés par le SINV pour envahir le SNC, ce qui laisse entrevoir la possibilité d'un rôle de réservoir viral pour la moelle épinière. Nous avons associé ces résultats à une nouvelle perspective sur l'activité de l'interféron. En utilisant des techniques expérimentales pour minimiser la réponse de l'interféron à l'infection, nous avons montré que l'interféron de type I joue un rôle essentiel dans le contrôle de l'infection périphérique et de sa résolution. Les données obtenues ont été traitées et traduites en un modèle mathématique d'équations capable de simuler l'évolution de l'infection dans et hors du SNC, tant en l'absence qu'en présence d'une réponse interféron. Ce modèle nous a permis d'obtenir des informations qu'il n'est normalement pas facile de mesurer expérimentalement in vivo. Par exemple, nous avons identifié le principal mécanisme de contrôle de l'infection par l'interféron et la quantité théorique de virions infectieux générés par chaque cellule infectée et productive. Pour atteindre ces résultats, de nouvelles approches et technologies ont été développées. Par exemple, de nouveaux protocoles d'anesthésie combinatoire permettent de réduire la toxicité des procédures d'imagerie de longue durée et de réduire la variabilité associée. En outre, pour maximiser l'efficacité expérimentale et réduire le nombre d'échantillons requis, de nouveaux flux de travail expérimentaux ont été créés pour multiplexer les protocoles d'imagerie à haut contenu et d'analyse de l'expression génique, associés au développement de nouveaux supports physiques pour la microscopie et de logiciels pour l'analyse d'images.

Le SARS-Cov2 est un virus à ARN monocaténaire positif enveloppé qui fait partie de la famille très diversifiée des coronavirus (CoVs). Pendant la pandémie, pour répondre au besoin pressant d'un modèle animal capable de répondre rapidement aux questions biologiques posées par ce virus, nous avons exploré la possibilité d'utiliser des larves de poisson zèbre. Pour réaliser des expériences sur ce pathogène, nous avons créé un nouveau protocole d'infection et d'expérimentation du poisson zèbre dans des laboratoires de niveau de biosécurité 3. Dans un premier temps, nous avons testé différents critères d'injection, tels que la position et la concentration, afin de déterminer la combinaison optimale. Pour tenter de quantifier la présence de la transcription virale associée à la protéine N, nous avons utilisé la qRT-PCR sur les brins positifs et négatifs de l'ARN viral. Nous avons testé plusieurs souches différentes, ce qui a entraîné l'absence d'infection et de réplication dans la plupart des sites. En concentrant nos efforts sur la vessie natatoire, un organe aérien souvent utilisé comme modèle pour l'infection des poumons, nous avons réussi à infecter systématiquement la partie caudale de cet organe. Les larves infectées dans la vessie natatoire présentent des résultats positifs à la fois par marquage par immunohistochimie et par qRT-PCR de l'ARN viral antisens. Cette dernière montre que le cycle de réplication du SARS-COV2 dans la vessie natatoire s'arrête après la production d'ARN viral antisens, ne parvenant pas à achever la réplication du virus. Malheureusement, cela indique une réplication virale avortée du SARS-COV2, qui réussit à infecter les cellules de la vessie natatoire, mais ne parvient pas à s'y multiplier et à infecter le reste de la larve. Nous avons étudié l'importance du récepteur ACE2 dans cette infection. Nous avons partiellement humanisé les larves en utilisant des plasmides contenant des constructions ACE2 humaines associées au rapporteur mCherry. Nous avons d'abord testé cette construction sur des cellules, observant une augmentation de 100 fois de l'infection, puis nous avons injecté cette construction sous le contrôle d'un promoteur ubiquitiné dans le poisson zèbre, obtenant un modèle d'expression mosaïque. Chez les larves, l'expression de l'ACE2 humain n'a pas augmenté le taux d'infection.

Enfin, nous avons généré une nouvelle lignée de poisson zèbre transgénique qui bloque l'expression des interférons phi1, phi2 et phi3, bloquant ainsi complètement la réponse à l'interféron. Là encore, le taux d'infection du SARS-COV2 chez les larves de poisson zèbre n'a pas augmenté, ce qui démontre que la réplication avortée dans ce modèle est due à d'autres facteurs intracellulaires.

En outre, de nouvelles avancées dans les techniques d'humanisation du poisson zèbre ont été réalisées ces dernières années, ce qui laisse présager une meilleure manipulation génétique de ce modèle.

Bien que le poisson zèbre de type sauvage ne se soit pas révélé être un modèle prêt à l'emploi pour l'infection par SARS-CoV2, ce projet nous a permis de définir les bases d'une recherche plus approfondie visant à identifier la cause de la réplication avortée, car elle pourrait être utilisée pour de futures applications thérapeutiques.

Un autre agent pathogène humain présenté dans cette thèse est Legionella pneumophila. *L. pneumophila* est une bactérie gram-négative, non sporogène, non capsulante et aérobie. *L. pneumophila* est à l'origine de la maladie du légionnaire (LD) et fait partie de la famille des Legionellaceae. Cette bactérie est très dangereuse dans la société moderne, car elle est extrêmement résistante et préfère se reproduire dans des endroits humides, tels que les systèmes de ventilation ou d'eau. En fait, ce pathogène est beaucoup plus présent dans les environnements urbains que dans les environnements ruraux.

Nous avons caractérisé la dynamique d'infection de Legionella chez les larves de poisson zèbre. Nous avons d'abord identifié les voies d'infection militantes pour le poisson zèbre et quantifié l'activité des leucocytes dans la lutte contre cette infection. Les résultats ont montré que la réponse immunitaire à l'infection par Legionella est médiée par les macrophages. En outre, nous avons observé la dynamique de la dissémination de ce pathogène dans le corps du poisson zèbre. Grâce à cela, nous avons découvert une nouvelle dynamique d'infection du vitellus, jamais observée auparavant chez Legionella. Le vitellus est un organe essentiel au développement et à la survie du poisson zèbre. Cet organe est organisé en une seule macrocellule et est séparé par plusieurs barrières du reste du corps du poisson-zèbre, avec lequel il échange constamment des nutriments. En fait, jusqu'à environ 6 jours après la fécondation, le vitellus est la réserve de nutriments du poisson-zèbre. En fait, le vitellus est imperméable au passage des leucocytes en son sein et peut représenter un tissu de fuite pour l'agent pathogène. Myd88 est une protéine adaptatrice de la réponse immunitaire médiée par les récepteurs Toll-like (TLR). Chez la souris, la présence de cette protéine est essentielle pour l'activation précoce du système immunitaire en cas d'infection par la légionelle, en activant l'inflammation et en recrutant des leucocytes. Chez l'homme, en revanche, Myd88 n'a pas de rôle essentiel.

En nous appuyant sur les similitudes du système immunitaire de l'homme et du poisson zèbre, nous avons utilisé une lignée de poisson zèbre avec une expression knock-out de Myd88, observant que même chez le poisson zèbre, cette protéine n'est pas essentielle, comme chez l'homme. De plus, nous avons constaté que ce type d'infection dépend de la présence du système de sécrétion T4SS. En utilisant des souches bactériennes mutantes pour des gènes associés à la virulence et à l'évasion du système immunitaire, seules les bactéries dépourvues du système de sécrétion T4SS étaient incapables de pénétrer dans le vitellus et étaient éliminées par le système immunitaire en peu de temps. Des études récentes émettent l'hypothèse d'un rôle du T4SS dans la transformation et le métabolisme des nutriments, en particulier des acides gras, dont le jaune d'œuf regorge. Ainsi, l'infection du vitellus que nous démontrons dans cet article pourrait être associée non seulement à l'évasion du système immunitaire, mais aussi à l'utilisation optimale de nutriments plus complexes.

Dans l'ensemble, cette thèse a confirmé le rôle du poisson zèbre en tant que modèle ré-émergent pour les interactions entre l'hôte et le pathogène. Nous avons répondu à des questions biologiques importantes, tout en produisant de nouveaux moyens d'étudier efficacement les interactions hôte-pathogène et de définir des stratégies à long terme pour ce type d'expérimentation.

RESUMÉ COURT

Titre :
Un voyage avec un poisson : Explorer le poisson zèbre comme modèle pour étudier les interactions hôte-pathogène

Résumé :
Le poisson zèbre est de plus en plus utilisé comme organisme modèle pour l'étude des interactions hôte-pathogène. Cela est dû à un certain nombre d'avantages, notamment son degré élevé de transparence, son temps de génération rapide et son système immunitaire conservé. Dans cette thèse, nous avons utilisé le poisson zèbre pour étudier l'infection par trois pathogènes différents : le virus Sindbis (SINV), le SARS-CoV-2 et Legionella pneumophila.

Nous avons d'abord étudié la voie d'invasion du cerveau exploitée par le SINV. En utilisant des virus marqués par fluorescence, nous avons pu suivre la progression de l'infection de la périphérie au cerveau. Nous avons identifié les ganglions des racines dorsales comme la porte d'entrée vers le SNC utilisée par le SINV pour atteindre le cerveau. Nous avons également constaté que le SINV utilise trois systèmes de propagation axonal ou cellule à cellule différents pour envahir le SNC.

Nous avons ensuite exploré l'utilisation du poisson zèbre comme modèle d'infection par le SARS-CoV-2. Nous avons développé un nouveau protocole d'infection et d'expérimentation du poisson zèbre dans des laboratoires de biosécurité de niveau 3. Nous avons testé plusieurs souches différentes de SARS-CoV-2 et avons pu infecter la partie caudale de la vessie natatoire de manière cohérente. Cependant, l'infection a entraîné une réplication virale abortive et aucune propagation ultérieure. Nous avons étudié le rôle du récepteur ACE2 dans cette infection et généré un modèle de poisson zèbre humanisé pour cette protéine, mais cela n'a pas changé le résultat.

Enfin, nous avons utilisé le poisson zèbre pour étudier l'infection par *Legionella pneumophila*. Nous avons caractérisé la dynamique d'infection de Legionella chez les larves de poisson zèbre et observé une dynamique particulière d'infection du jaune. Nous avons constaté que la réponse immunitaire à l'infection par Legionella est médiée par les macrophages. Nous avons également utilisé une lignée de poisson zèbre avec une expression knock-out de Mydd88 pour établir une corrélation avec la réponse immunitaire humaine et nous avons confirmé que, contrairement aux souris, le poisson zèbre présente le même phénotype. Enfin, nous avons identifié une nouvelle caractéristique de l'infection par Legionella chez le poisson zèbre, à savoir que la bactérie peut infecter le jaune de manière dépendante du T4SS pour échapper à la clairance par les leucocytes et absorber les nutriments.

Dans l'ensemble, cette thèse démontre le potentiel du poisson zèbre en tant qu'organisme modèle pour l'étude des interactions hôte-pathogène. Nous avons répondu à des questions biologiques importantes tout en développant de nouveaux outils et approches pour ce type de recherche.

Mots clefs : Zebrafish, Danio rerio, système immunitaire, virus Sindbis, SARS-CoV-2, Legionella pneumophila, virus, bactérie, leucocytes, macrophages, neutrophiles, neurones, système nerveux central, infection, interféron, système de sécrétion de type IV

Summary

In the latest year, Zebrafish (Danio rerio) demonstrated its potential in host-pathogen interaction research. This fish model has a high degree of transparency and a fast generation time, both these characteristics are fundamental for high-content screening and direct observation of pathogens dissemination in whole live larvae. Furthermore, the zebrafish innate immune system is comprised of leucocytes (i.e., macrophages and neutrophils), and it is interferon-based, conserving a high degree of similarities with humans.

In this thesis, we will challenge this model with different pathogens (Sindbis virus, SARS-COV2, and Legionella pneumophila) to highlight light positive and negative sides of zebrafish experimentation while answering important biological questions and developing new experimental tools/approaches.

Sindbis virus (SINV) is a single-stranded positive RNA alphavirus transmitted by arthropods (mostly mosquitos) and able to infect humans. This arbovirus is largely used as a model for viral encephalitis, but, despite extensive studies on mice, the mechanisms of brain invasion and immune response are still largely to be elucidated. Using tolls generated by Gabriella Passoni in the lab, we focused on: 1) identifying the route of brain invasion exploited by SINV, 2) the role of the interferon system in controlling infection, and 3) exploring the possibility of using this project to develop mathematical models able to shed light on parameters not easily measurable by in vivo experimentation.

Using viral construct expressing fluorescent reporters we followed the propagation of SINV from the periphery to the brain. Through high-content screening and high-resolution imaging, we identified the cellular population involved in the progression of the infection and multiplexed the imaging data with genetic expression measurement of zebrafish antiviral immunity. We identified in dorsal Root Ganglia (DRG) the gateway to access the CNS used by SINV to reach the brain. Furthermore, results showed the presence of three different axonal or cell-to-cell propagation systems used by SINV to invade the CNS, hinting at the possibility of a role viral reservoir for the spinal cord. We coupled these findings with a new perspective on the activity of interferon in controlling the infection outside the CNS and used the data obtained to recapitulate the dynamics observed in a mathematical model.

SARS-Cov2 is an enveloped positive single-strand RNA virus part of the highly diverse coronaviruses (CoVs) family. During the pandemic, to answer the pressing need for an animal model able to answer rapidly the biological question created by this virus, we explored the possible use of zebrafish larvae. To perform experiments on this pathogen we created a novel protocol for zebrafish infection and experimentation in biosafety level 3 laboratories. We tested several different strains resulting in a lack of infection and replication in most of the sites. Upon concentrating our effort on the swim bladder, an organ often used as a model for bladder and lung infection, we manage to infect consistently the caudal part of this organ. Unfortunately, this infection resulted in an abortive viral replication and no further propagation of SARS-Cov2. We investigated the relevance of the ACE2 receptor in this infection, generating a humanized zebrafish model for this protein, but it didn't change the outcome. Although wild-type zebrafish didn't prove a ready-to-use model, in this project we still defined the basis for further investigation aimed at pinpointing the cause of the abortive replication, as it may be used for future therapeutic applications.

Lastly, we used *Legionella pneumophila* as a pathogen; a gram-negative, non-sporogenous, non-capsule forming, and aerobic bacteria. Legionella pneumophila is the cause of Legionnaires disease (LD), and it is part of the Legionellaceae family. We characterized the infection dynamics of Legionella in zebrafish larvae, observing a peculiar dynamic of yolk infection. Results showed that the immune response to *Legionella* infection is macrophage-mediated. Furthermore, we used a zebrafish line with knock-out Mydd88 expression to correlate with human immune response and confirmed that contrary to mice, zebrafish show the same phenotype. Lastly, we identified a new feature of Legionella in zebrafish infection, that can infect the yolk in a T4SS-dependent way to escape clearance by leucocytes and be able to absorb nutrients.

Altogether, in this thesis, we confirmed the role of zebrafish as a re-emerging model for host-pathogen interactions. We answered important biological questions while producing new means to proficiently investigate the host-pathogen interactions and define long-term strategies for this type of experimentation.

Short Summary

Title :
A journey with a fish: Exploring zebrafish as a model to study host-pathogen interaction.

Abstract :
Zebrafish are increasingly being used as a model organism to study host-pathogen interactions. This is due to a number of advantages, including their high degree of transparency, fast generation time, and conserved immune system. In this thesis, we used zebrafish to study infection with three different pathogens: Sindbis virus (SINV), SARS-CoV-2, and Legionella pneumophila.

We first investigated the route of brain invasion exploited by SINV. Using fluorescently labeled viruses, we were able to track the progression of infection from the periphery to the brain. We identified dorsal root ganglia as the gateway to the CNS used by SINV to reach the brain. We also found that SINV uses three different axonal or cell-to-cell propagation systems to invade the CNS.

We then explored the use of zebrafish as a model for SARS-CoV-2 infection. We developed a novel protocol for zebrafish infection and experimentation in biosafety level 3 laboratories. We tested several different strains of SARS-CoV-2 and were able to infect the caudal part of the swim bladder in a consistent manner. However, infection resulted in abortive viral replication and no further propagation. We investigated the role of the ACE2 receptor in this infection and generated a humanized zebrafish model for this protein, but this did not change the outcome.

Finally, we used zebrafish to study *Legionella pneumophila* infection. We characterized the infection dynamics of *Legionella* in zebrafish larvae and observed a peculiar dynamic of yolk infection. We found that the immune response to Legionella infection is macrophage mediated. We also used a zebrafish line with knock-out Mydd88 expression to correlate with the human immune response and confirmed that, contrary to mice, zebrafish show the same phenotype. Lastly, we identified a new feature of Legionella infection in zebrafish, that the bacteria can infect the yolk in a T4SS-dependent way to escape clearance by leucocytes and absorb nutrients.

Overall, this thesis demonstrates the potential of zebrafish as a model organism for studying host-pathogen interactions. We answered important biological questions while also developing new tools and approaches for this type of research.

Keywords : Zebrafish, Danio rerio, Immune system, Sindbis, SARS-COV2, Legionella, virus, bacteria, leucocytes, macrophages, neutrophils, neurons, CNS, infection, interferon, T4SS

List of Abbreviations

eGFP	Enhanced Green Fluorescent Protein
ABC	ATP-binding Cassette
ACE2	Angiotensin-converting Enzyme 2
AGM	Aorta-gonad-mesonephros
ALM	Anterior Lateral Mesoderm
ALPK1	Alpha Kinase 1
APCs	Antigen Presenting Cells
ARG2	Arginase Type2
ATP	Adenosine Triphosphate
BBB	Blood-Brain Barrier
BSL3	Bio-Safety Level 3
CARD	Caspase Recruitment Domain
CCL2	Chemokine Ligand 2
CCR2	Chemokine Receptor 2
CD	Connecting Domain
cDNA	Complementary DNA
CH	Central Helix
CHT	Caudal Hematopoietic Tissue
CLRs	C-type Lectins
CMs	Convoluted Membranes
CNS	Central Nervous System
CoV	Coronavirus
COVID-19	Cornavirus Disease 19
COX2	Cyclooxygenase-2
CP	Capsid Protein
CRISPR	Clustered Regularly Interspaced Short Palindromic Repeats

CSF	Colony-Stimulating Factor
CSF1R	Colony-Stimulating Factor 1 Receptor
CT	Cytoplasmic Tail
CXCL	C-X-C motif Ligand
CXCR	C-X-C motif Receptor
DAMPs	Damage-associated Molecular Patterns
DMSs	Double-membrane Spherules
DMVs	Double-membrane Vesicles
DRG	Dorsal Root Ganglia
EMPs	Erythromyeloid Progenitor Cells
ENU	Ethyl Nitrosourea
ER	Endoplasmic Reticulum
ERGIC	ER-Golgi Intermediate Compartments
FP	Fusion Peptide
GBPs	Guanylate-binding Proteins
gRNA	Genomic RNA
HCoV	Human Coronavirus
HCS	Hematopoietic Stem Cells
HIF1	Hypoxia-inducible Factor 1
hpi	Hour Post-Inoculation
hpf	Hour Post-Fertilization
HSCs	Hematopoietic Stem Cells
ICM	Intermediate Cellular Mass
IFN	Interferon
IFNAR	Interferon-α/β Receptor
Ig	Immunoglobulin
IL	Interleukin
iNOS	Induced NO-synthase

IP3	Inositol Triphosphate
IRF	Interferon Regulatory Factor
IRGs	Immunity-related GTPases
ISG	IFN Stimulated Gene
LAP	LC3- associated Phagocytosis
LCV	Legionella-containing Vacuole
LPS	Lipopolysaccharides
LRR	Leucine-rich Repeat Motifs
LRT	Low Respiratory Tract
LUT	Look Up Table
MAVS	Mitochondrial antiviral-signaling Protein
MERS-CoV	Middle East Respiratory Syndrome Coronavirus
MHC	Major Histocompatibility Complex
MOMP	Major Outer Membrane Protein
mRNA	Messenger RNA
NAM	Neurogenic Associated Microglia
NAS	Network-attached Storage Units
NC	Nucleocapsid
NET	Neutrophil Extracellular Traps
NLR	Nod-like Receptors
NOS2	Nitric Oxide Synthase 2
NRP1	Neuropilin1
NSP	Nonstructural Protein
NTD	N-terminal Domain
OM	Outer Membrane
ORF	Open Reading Frame
PAL	Peptidoglycan-associated Lipoprotein
PAMP	Pathogen-associated Molecular Pattern

PBI	Posterior Blood Island
PRR	Pattern Recognition Receptor
qRT-PCR	Quantitative Real-time PCR
RBM	Receptor Binding Motif
RdRP	RNA-dependent RNA-polymerase
RIG-I	Retinoic acid-inducible Gene I
RLR	RIG-I-like Receptors
ROS	Reactive Oxygen Species
RTC	Replication and Transcription Complex
SAM	Synaptic-region Associated Microglia
SARS	Severe Acute Respiratory Syndrome
SINV	Sindbis Virus
SLRs	Sequestosome1-like Receptors
SR	Scavenger Receptors
T1/4SS	Type I/IV Secretion System
TFs	Transcription Factors
TLR	Toll-like Receptors
TM	Transmembrane Domain
TME	Tumor Microenvironment
TNF	Tumor Necrosis Factor
TRSs	Transcription Regulatory Sequences
TSD	Teleost-specific Genome Duplication
VAPs	Viral Adhesion Proteins
WEEV	Western Equine Encephalitis Virus Complex
WT	Wild Type

A journey with a fish: Exploring Zebrafish as a Model to Study host-pathogen Interaction

Chapter 1: Introduction

1.1 General introduction to zebrafish

Danio rerio, commonly known as the zebrafish, is a cyprinid fish that was first described by Francis Hamilton in 1822, in his analysis of all the aquatic species normally living in the Ganges River, India (Hamilton and Hamilton, 1822). Hamilton noted that the fish was "beautiful," with "several blue and silver stripes on each side," which led to its colloquial name. The scientific name of the zebrafish has undergone several changes, but the most recent and accepted name is *Danio rerio*. This little fish can be found in most of the Indian subcontinent (Figure 1) including Pakistan, Bangladesh, Nepal, and Bhutan (Parichy, 2015a). Although Hamilton found this fish in the Ganges, its natural habitat is slow-paced streams, stagnant pools, and rice paddies. The water in these habitats can be clear or muddy, and it is often rich in vegetation. This vegetation helps to camouflage the zebrafish from predators.

Zebrafish are adaptable fish and can survive in a wide range of physical conditions in the wild. They can live in water with temperatures ranging from 12 to 39 degrees Celsius, they can tolerate pH levels from 5.9 to 9.8 (Arunachalam et al., 2013; Spence et al., 2006), and they can also survive in water with low salinity levels. This adaptability makes zebrafish well-suited for use in research. In stable laboratory conditions, zebrafish require more stringent conditions to remain healthy.

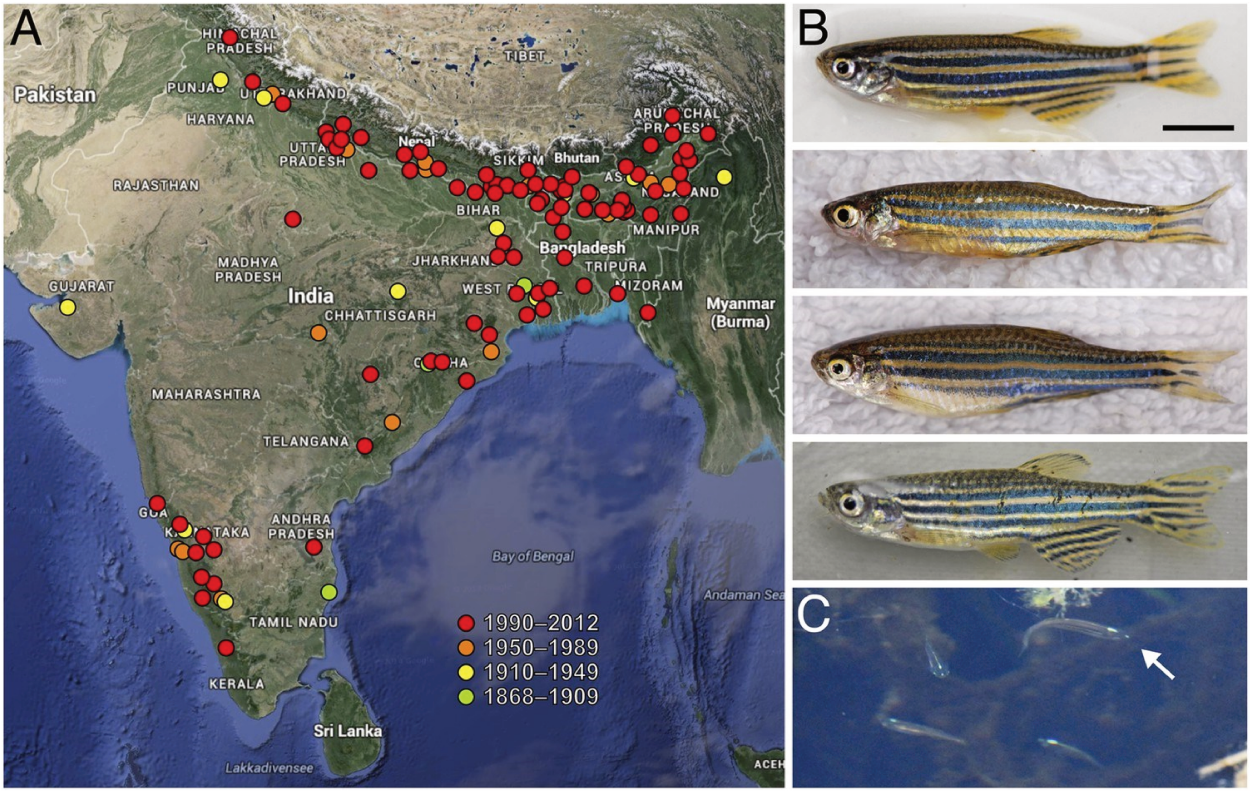

Figure 1: Zebrafish and their geographic range.

A) Historic and more recent sites where zebrafish have been reported in India, Nepal, Bangladesh, and possibly Myanmar (Spence et al., 2006; Engeszer et al., 2007b; Spence et al., 2008; Whiteley et al., 2011; Arunachalam et al., 2013). B) Zebrafish from several populations in northeastern India (Engeszer et al., 2007b). The upper two fish are males and the lower two fish are females; males tend to have a slightly yellow cast ventrally. C) A group of zebrafish (a single fish is highlighted with the arrow) in a stream-side pool in Meghalaya, India, north of Bangladesh. Scale bar: 5 mm B). ***Source (Parichy, 2015b)***

Zebrafish are omnivores, eating insects, small zooplankton, and vegetal material (Engeszer et al., 2007; McClure et al., 2006). In captivity, zebrafish alimentations are standardized depending on the developmental stage. In the first larval stages zebrafish use the nutrients contained in the yolks to sustain themselves, but around 6-7 days post fertilization the yolk is depleted (Charles B. Kimmel et al., 1995). Until 30-40 days post fertilization, when the fish are considered juveniles, the larvae are fed with rotifers and paramecia, to mimic the zooplankton normally eaten by zebrafish in nature. At the juvenile sage, the alimentation switches to the pellet, whose size progressively increases with zebrafish aging. The basic composition of these pellets is standardized, but it may partially change between different producers, normally it is good practice to integrate this diet with live food. As nutritional supplements, often used brine shrimps, daphnia, and bloodworms, although daphnia is preferred as they are easy to cultivate and control in laboratories (Ramsay et al., 2009). The debate on the optimal nutrition for zebrafish in captivity is still open, as it is widely accepted that it still needs optimization, as zebrafish have a variegated and active diet in nature. Indeed, further optimization can further improve the resilience of zebrafish in captivity, increasing resistance to pathogens and stress (Kent et al., 2009; Tsang et al., 2020).

Both lab and wild zebrafish have a highly developed sociality, tending to form shoals to protect themselves from predators (Engeszer et al., 2004; Mahabir et al., 2013; Peichel, 2004). Zebrafish develop and transmit to their progeny their “social imprinting”, demonstrating a high variability depending on the pool of zebrafish observed, regardless of their isolation in the wild or in the lab (Martins and Bhat, 2014; Oswald et al., 2012; Robison and Rowland, 2011).

Even during mating, a stereotyped process, an intricate hierarchical relationship between males and females can form, affecting embryo production (Paull et al., 2010; Spence et al., 2007). The female chooses the male, partially depending on the mating ritual (the male quivering and pushing the female), and drives him to the oviposition sites (Paull et al., 2010; Spence et al., 2007). To add to this variability, in nature zebrafish procreate every monsoon season, laying thousands of eggs, but in the laboratory this process can be monthly, if not weekly, affecting the efficiency of embryo generations.

Furthermore, the insensibility of the handler to the fine social and environmental parameters in zebrafish husbandry generates a relevant variability in oviposition and fecundity of the fishes and affects, the time, magnitude, and quality of embryos (Abdollahpour et al., 2020; Adatto et al., 2022, 2011).

The life expectancy of zebrafish is fairly long as it can survive 3 years on average in the wild and over 5 years in laboratory conditions, whereas, at around 3-4 years starts to show muscle degeneration, cataracts, and other indicators of senescence (Gerhard et al., 2002; Kishi et al., 2009).

Due to zebrafish inhabiting small ponds, pools, and paddies, it is possible to find many different species in the sub-family *Danioninae*, which besides zebrafish include species with high variability in size and pigmentation. We can go from the big *Danio dangila* (~13 cm) to the small *Danionella* (~1 cm) (Parichy, 2015a).

While many species of this sub-family are yet to be identified, we can ask ourselves the reason why *Danio rerio* was chosen as a model for research. The less exciting and realistic answer is that George Streisinger, pioneer of zebrafish uses for experimentation, selected this minnow mainly because was readily available, easy to use, and transparent enough, propelling the creation of facilities in Oregon, Tubingen, and Boston (Grunwald and Eisen, 2002a; Kinth et al., 2013; Ruzicka et al., 2015).

Interestingly this opens the possibility of investigating other members of the species to find more adapted models depending on the field of research itself.

The history of the use of zebrafish in the laboratory is fragmented and characterized by the development of tools for this fairly new animal model.

In 1960 zebrafish started to be used as a model for embryological studies, as it offered the possibility to directly observe embryo development. The first decade of use of zebrafish was characterized by a rapid turnover in the husbandry approaches, until in 1981 George Streisinger and colleagues published a paper to standardize this process (Streisinger et al., 1981).

Another big revolution, then further solidified the role of zebrafish as a transversal animal model, is the advent of large-scale mutagenesis tools to induce mutation and perform phenotypical studies.

For example, the use of ethyl nitrosourea (ENU) Driever since the early ’90s (Driever et al., 1996; Nüsslein-Volhard, 2012). Soon after, Kawakami published the first paper on the tol2 transposable element (Kawakami et al., 1998). In 2004 Kawakami showed how the Tol2 transgenesis system can be used to stably integrate exogenous DNA into the zebrafish genome (Kawakami, 2004). This has become the most popular method to generate transgenic lines by simply injecting the system into the embryos at the 1-cell stage.

Another genetic tool worth mentioning is the morpholino, patented in 1985 by James Summerton as a “method for inhibiting gene expression”. This tool demonstrated its efficacy in zebrafish in 2000, becoming one of the most used tools to knock down gene expression in zebrafish (Nasevicius and Ekker, 2000).

Finally, in 2001, the Wellcome Trust Sanger Institute used Tubingen/AB larvae to start sequencing the genome of zebrafish. Efforts bore fruit in 2013 with the publication of the Zv9 assembly containing the 1.412 gigabases of the zebrafish genome (Howe et al., 2013). At the time of writing this text, the most updated zebrafish genome assembly was the GRCz11.

While, in early 2000, many already envisioned the use of zebrafish as a model for immunology, toxicology, and pharmacology (Berman et al., 2005; Briggs, 2002; Vascotto et al., 2011), the role of zebrafish in the pure developmental and embryogenesis field solidified (Grunwald and Eisen, 2002b).

Nonetheless, the tireless work of researchers opened the possibility of using zebrafish as a model to study cancer, human genetic diseases, neurological disorders (Fontana et al., 2018; Sakai et al., 2018; Saleem and Kannan, 2018), and cardiovascular disease (Bakkers, 2011; González-Rosa, 2022; Wilkinson et al., 2014).

In the field of immunology, the work of many prominent scientists was pivotal in establishing zebrafish as a model for host-pathogen interaction and immunological research.

One of the pioneers in the characterization of the immune system of zebrafish is Philippe Herbomel, who leaped forward to the live imaging of zebrafish and discovered the primitive macrophages of zebrafish (Herbomel et al., 1999).

Besides the relevant work on innate immunity, he published several papers on host-immune response with Lalita Ramakrishnan, Jean-Pierre Levraud, and Emma Colucci-Guyon (Colucci-Guyon et al., 2011; Davis et al., 2002; Levraud et al., 2009).

Other researchers that need to be acknowledged for their work are Annemarie H. Meijer for her work on inflammation (Meijer et al., 2008), Philip Crosier for the work on hematopoiesis associated with immunity (Kalev-Zylinska et al., 2002), Herman P. Spaink for the work on zebrafish response to infection (Meijer et al., 2004), Anne Huttenlocher for her work on the role of innate immunity in regeneration (De Oliveira et al., 2016) and Stephen A Renshaw for the work on zebrafish-pathogen interaction (Henry et al., 2013).

Indeed, many other researchers should be put under the spotlight due to their work on zebrafish immunology, and they took over the responsibility of growing this field with their work and passion.

Thanks to their work zebrafish are now again under the spotlight as a model that can be adopted to further investigate the immune system and the host response to infection and to be used to screen drugs, potentially opening new doors in this field and providing a powerful tool for researchers.

Chapter 2: Zebrafish Immune System

In the latest years, the attention to the field of host-pathogen research increased, due to the high number of re-emerging viruses and increasingly resistant bacteria. This allowed researchers working on zebrafish to show the potentiality of this model and its immune system.

The first question that arises discussing an alternative model immune system is how far it is from the human immune system. Many different reviews tried to give a clear idea of the distance or closeness of zebrafish or humans (Meeker and Trede, 2008; Traver et al., 2003), but giving a definite answer is not biologically possible.

Zebrafish conserve many similarities in terms of tissue and organ structure and presence. For example, the central nervous system, liver, heart, intestine, and muscle are already used to model several types of diseases (Teame et al., 2019; X. Wang et al., 2021) (Figure 2).

From the genomic stand, we can observe that at least 70% of the human genome has one or more direct orthologues, and reciprocally, 69% of zebrafish genes have at least one orthologue. Among the human orthologues, around 47% have a one-to-one relationship with zebrafish orthologues, and, the remaining ones, either exhibit one-to-many or many-to-one relationships (Langheinrich, 2003).

When looking at OMIM (Online Mendelian Inheritance in Man) and GWAS (genome-wide association studies) respectively 82% and 76% of human genes associated with the genetic disease have orthologues in zebrafish, indicating that zebrafish have a relevant potential as a model to study genetic human diseases (Howe et al., 2013).

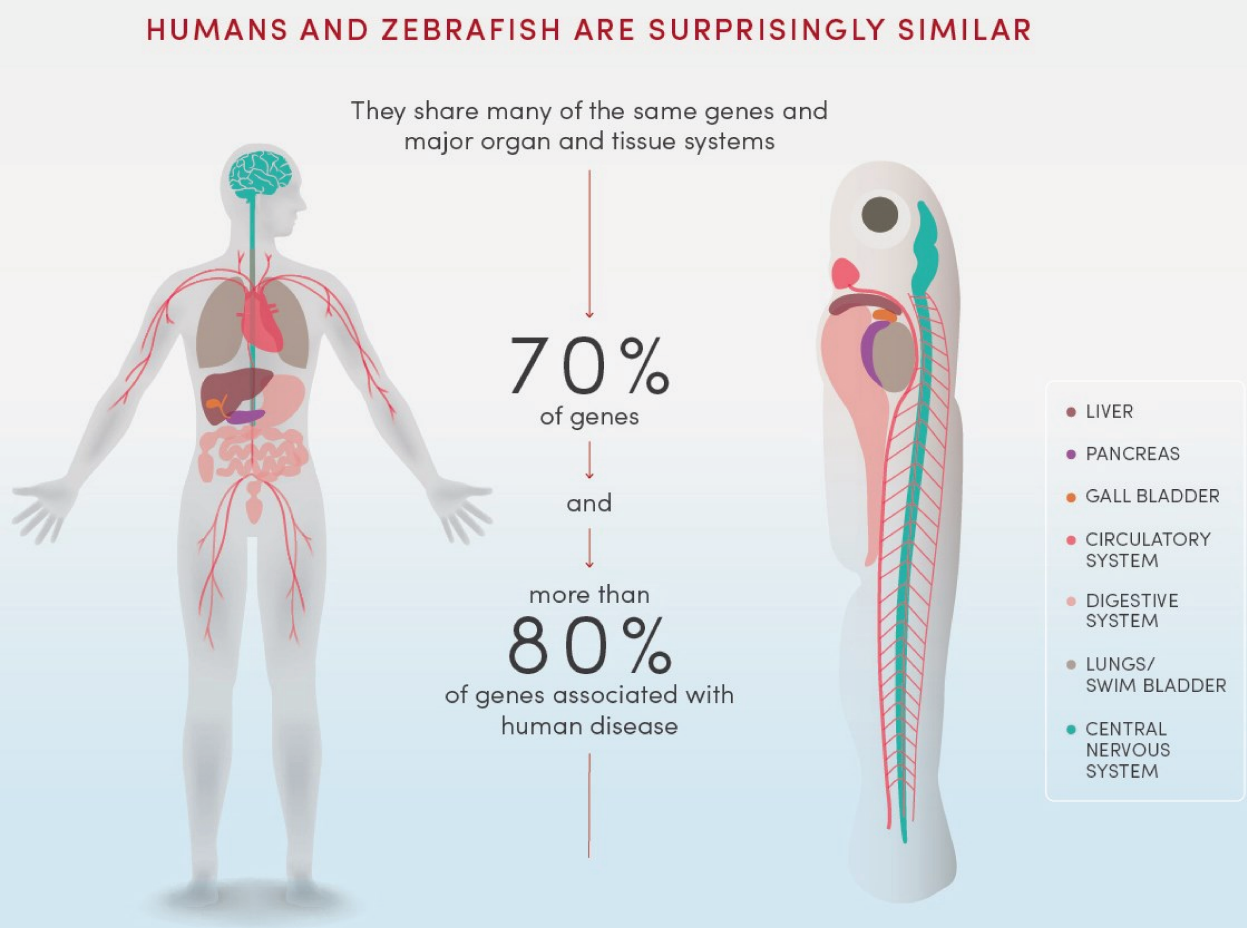

Figure 2: Similarities between Zebrafish and Human.

Schematic of corresponding organs between Zebrafish and Humans. ***Source https://www.research.utah.edu/animal-research/faqs/.***

Despite these similarities, the genome of zebrafish still underwent a massive duplication due to an event known as an event known as teleost-specific genome duplication (TSD), believe to have taken place around 350 million years ago in the evolutionary line of teleost (Bell et al., 2020; Kassahn et al., 2009; Yoder et al., 2002). It is hypothized that this duplication may have resulted in an advantage for teleost, duplicating the rapidly evolving elements of the immune system, such as interferon-associated genes, and enlarging the pool of antipathogenic tools available to the fish (J.-P. Levraud et al., 2019).

Similarly to other vertebrates, zebrafish develops its immune system in successive waves of hematopoiesis (Figure 3).

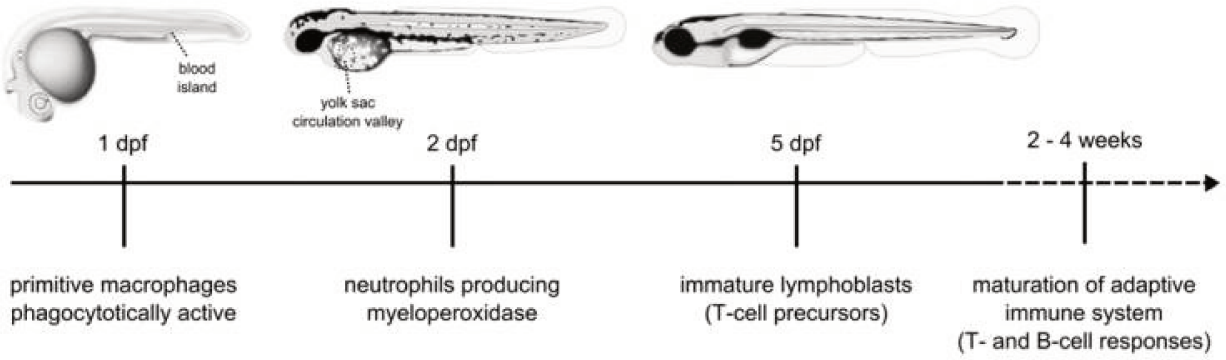

Figure 3: Zebrafish immune system development.

Schematic overview of the development of the zebrafish immune system. Commonly used sites for systemic bacterial infection of embryos by microinjection are the blood island and the yolk sac circulation valley at 1-3 dpf. ***Source(H. Meijer and P. Spaink, 2011).***

Between 12- and 24-hour post-fertilization, zebrafish innate immune system is solely based on primitive macrophages' phagocytotic activity. These first macrophages emerge from the Rostral Blood Island of the yolk sac (Murayama et al., 2006) and progressively invade all tissues following the M-CSF receptor/*fms*/*csf1r* genes pathway. Those that reach the brain differentiate in microglia (Herbomel et al., 2001; Oosterhof et al., 2018).

Between 25 and 48 hours post-fertilization, a transient wave of hematopoiesis starts in the posterior blood island, generating erythromyeloid progenitor cells (EMPs) that are multipotent hematopoietic progenitor cells, that will further differentiate in macrophages, neutrophils, and erythrocytes (Bertrand et al., 2010; Lam et al., 2004). In the aorta-gonad-mesonephros (AGM), a definitive wave of hematopoiesis takes place and hematopoietic stem cells (HCS) migrate toward the zebrafish tail and form the caudal hematopoietic tissue (CHT), analog of mammalian fetal liver (Kissa and Herbomel, 2010). In the CHT, these cells expand and differentiate in myeloperoxidases producing neutrophils and macrophages, maturing the innate immune system (Le Guyader et al., 2008) (Figure 4).

An ulterior migration from the CHT starts around 5dpf with the movement of HSCs towards the thymus and pronephros, where the latter further develop in kidney marrow in adult fish, considered equivalent to mammalian bone marrow (Murayama et al., 2006).

While at 2dpf, the innate immune system is already in place, it takes around 2-3 weeks for the adaptative immune system to appear. This allows us to perform studies on the pure innate immune system response to stimuli and pathogens.

During these successive waves, many human homologous genes are expressed in zebrafish, such as *gata1a, scl, and lmo2* in the erythroid lineage and *pu.1* in the myeloid lineage. The RUNX, ETs, and C/EBP family are highly conserved and, for example, the fate towards myeloid versus erythroid commitment is finely tuned by the Spi1 (also known as Pu.1) and Gata1, similarly to humans. Focusing on the markers for macrophages and neutrophils, it is widely used respectively mfap4 or *csf1r* gene (M-CSF receptor) for macrophages and *mpx gene* (myeloperoxidase) for neutrophils. Unfortunately, both largely overlap with other genes making it difficult to perfectly separate different leucocitary families, especially in the first 24hpf (Zakrzewska et al., 2010).

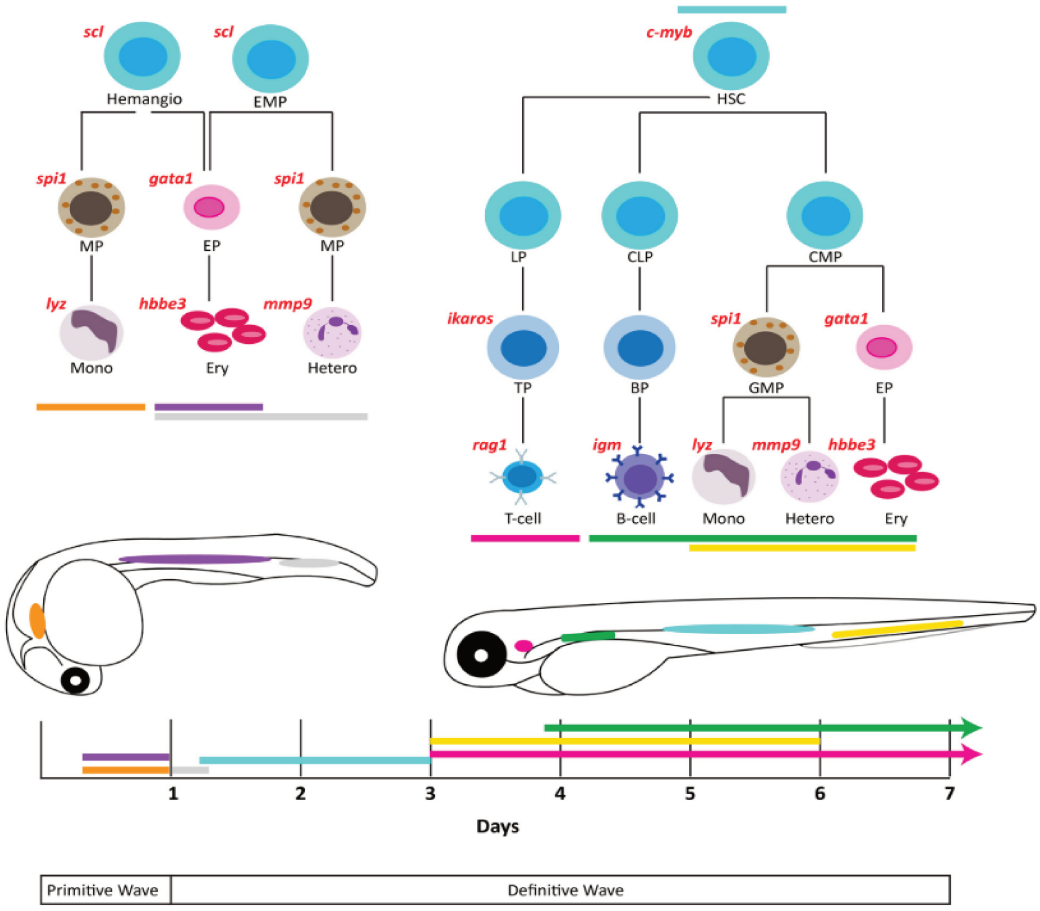

Figure 4: Zebrafish hematopoiesis and its key regulators.

Schematic representation of hematopoiesis in zebrafish. The primitive wave commences in two locations, the anterior lateral mesoderm (ALM) (orange), which gives rise to primitive monocytes, and the intermediate cellular mass (ICM) (violet), which generates mostly primitive erythrocytes before 24 hpf. A transient 'intermediate' wave occurs in the posterior blood island (PBI) where both erythrocytes and heterophils are formed (grey). Definitive hematopoietic stem cells (HSCs) are initially formed by budding from the hemogenic endothelium on the ventral wall of dorsal aorta (blue). A subset of these HSCs migrate to the caudal hematopoietic tissue (CHT) (yellow) to produce several cell lineages, and also the thymus (purple), where T lymphocyte production occurs. Finally, HSCs seed the developing kidney (green), the final site of definitive hematopoiesis where erythroid, myeloid, and B lymphocyte production occurs. The lineage-specific transcription factors that serve to regulate this process are in red. Abbreviations: BP: B cell progenitor, CLP: common lymphoid progenitor, CMP: common myeloid progenitor, EP: erythroid progenitor, Ery: erythrocyte, GMP: granulocyte-monocyte progenitor, Hemangio: hemangioblast, Hetero: heterophil, HSC: hematopoietic stem cell, Mono: monocyte, TP: T cell progenitor. ***Source (Rasighaemi et al., 2015).***

2.1 Zebrafish adaptative immune system

I this thesis we will focus on the innate immune system of zebrafish, but for the sake of completeness we decided to provide an complementary introduction to zebrafish adaptative immune system; to better encompass the potential of this model. The adaptative system starts to develop during the innate immune system maturation, through increased expression of *rag1, rag2, ikaros,* and *lck* (used as a reporter for primitive thymus) (Langenau et al., 2007; Willett et al., 2001). In parallel with the start of the kidney definitive hematopoiesis wave, the first primitive T-cells start to develop in the thymus and at 8dpf start to circulate. At around 20dpf the B-progenitor cells appear in the posterior cardinal vein and dorsal aorta (Page et al., 2013). The adaptive immune system can be considered mature in zebrafish at 3 weeks post-fertilization (Novoa and Figueras, 2012). Furthermore, zebrafish lack lymph nodes, but between 3 and 5 dpf develops a lymphatic system (Küchler et al., 2006). Its origins are still not fully clear, but it is potentially formed by LEC cells originating from the thoracic duct (Yaniv et al., 2006). The main lymphoid organs are the kidney marrow, and thymus in juvenile larvae, and the spleen in adult fish and, in the latter, we have the majority of APCs (antigen-presenting cells) interaction with lymphocytes (Renshaw and Trede, 2012).

Indeed, even though the interactions between the innate immune system and adaptive immune system are conserved in zebrafish, its cells express both MHC I and MHC II (Fischer et al., 2013).

Similarly to humans, the thymus of zebrafish shrinks with age and its role in T-cell development leaves space to mature T-cells migration in the kidney marrow of adult fish (Renshaw and Trede, 2012; Traver et al., 2003). The lag in the development of an adaptive immune system is prevalently correlated to B-cell development, as before 3 weeks post-fertilization, they are not fully mature yet (Lam et al., 2004). In zebrafish, the immunoglobulins classes are only 3 (IgD, IgM, and IgZ), but the overall similarity with humans still allows for the use of this model (Zimmerman et al., 2011). Furthermore, while Page et al. well characterized through direct observation B-cell population in zebrafish (Page et al., 2013), Liu et al. showed that contrary to humans, in zebrafish doesn't exist pre-B cell stage (Liu et al., 2017; Michelle D Peñaranda et al., 2019). Yet, zebrafish B-cells still need to be further explored.

Zebrafish T-cells were largely investigated as this model was used to characterize tumor microenvironment response (TME).

Using Ginbuna carp and rainbow trout, it was identified in teleost and cyprinid the presence of CD8 and CD4 lymphocyte populations, which corresponds to CD8+ cytotoxic cells and CD4 + Th or Tregs cells (Takizawa et al., 2011; Yamaguchi et al., 2019). Furthermore, in the CD8+, named CD8 α+ in trout, it was detected the expression of perforin and granulysin associated with perforin-mediated cytotoxic activity. In salmon with intestinal tumors, these cells were found to infiltrate the TME (Bjørgen et al., 2019) and, in Japanese flounder, express Fas ligand (Toda et al., 2011; Yamaguchi et al., 2019). Furthermore, in salmon was identified a clear antiviral role for this lymphocyte population (Somamoto et al., 2014).

Besides CD8+ lymphocytes, zebrafish have CD4+ lymphocytes, that in teleosts are *cd4-like* paralogs *cd4-1* and *cd4-2* (Yoon et al., 2015). These 2 genes differ in the Ig domain structure, with cd4-1 exhibiting four Ig domains like mammalian and cd4-2 having fewer Ig domains (Castro et al., 2011; Takizawa et al., 2016). Cd4-1 express Th1, Th2, and Th17-associated transcription factors and cytokines upon pathogens infection, confirming that in teleost this function is well conserved (Maisey et al., 2016; Takizawa et al., 2016; Yoon et al., 2015).

In zebrafish, both Th1 and Th2 are conserved. Using viral infection and bacterial infection in zebrafish it was observed the expression of T-bet, the transcription factor expressed by Th1, and higher expression of IFN γ (Igawa et al., 2006; Mitra et al., 2010).

In both cases, this activation is associated with IL-2 and IL22 increased expression, suggesting that the role of CD4+ Th1 in zebrafish is conserved, although yet to be better understood (Takizawa et al., 2016).

In teleosts, Th2 is better characterized than Th1 as a transgenic zebrafish line exists to monitor Cd4-1+ cells in different compartments, and in salmon was confirmed, that as in humans, Th2+ cells in the gills express *il-4/13b* and *gata3* (Dee et al., 2016; Takizawa et al., 2011). Interestingly, there are relevant similarities between zebrafish and humans in regards to CD4+ Th2, as we can observe the same degree of heterogeneity in relationship with a subset of Th2+ cells and the impairing of TIM-1 and TIM-4 sharply decrease the CD4+ T cells activation in zebrafish and increases proliferation of CD4+ Th2 subtype (Xu et al., 2016).

Alongside these subsets, a Th17 and Tregs subset were identified in zebrafish. The ROR transcription factor family, associated with Th17 differentiation is present in zebrafish (Flores et al., 2007; Monte et al., 2012). In the zebrafish spleen, upon LPS (lipopolysaccharide) stimulation and attenuated bacterial pathogen vaccination, we can observe expression of Il-17 (in particular the form Il-17A), Il-22 and ROR γt, all markers of Th17 (Gunimaladevi et al., 2006; Zhang et al., 2013). Large numbers of Th17-like cells can be found in the gut, in association with autoimmune and inflammatory diseases (Coronado et al., 2019).

Always in the zebrafish gut, we can find CD4+ Tregs with a clear immunosuppressive role expressing the *foxp3a* gene (Kasheta et al., 2017; Quintana et al., 2010). Different zebrafish reporters and knock-downs for this gene were produced to study the Treg-like cells and further investigate their role in tissue regeneration (Dee et al., 2016; Kasheta et al., 2017). Many of these cells were seen migrating to injured organs and damaged areas to aid in tissue regeneration, whereas Treg ablation impaired this process (Hui et al., 2017).

Lastly, recent studies show that zebrafish have a γδ T cells-like population, that can recognize antigens regardless of the MHC, and have a cytotoxic activity, as in humans (Miao et al., 2021). The evidence for the presence of this cell population is related to the presence of conserved elements in the zebrafish genome assembly and the isolation by flow cytometry of T cells exhibiting the CD4-/CD8+ surface markers and patterns/morphology scatter of human γδ T cells (Seelye et al., 2016; F. Wan et al., 2017). As in humans, these cells are mainly located in the gut (Picchietti et al., 2011).

2.2 Zebrafish's innate immune system

As we introduced before, zebrafish's innate immune system is comprised of well-conserved leucocytes.

After the first wave of primitive macrophages, already able to phagocyte pathogens, the mature innate immune system of zebrafish, established as early as 3 days post fertilization, is mainly comprised of neutrophils, macrophages, and microglia.

Starting from neutrophils, they are the first line of defense in zebrafish, but besides being able to phagocyte pathogens and cellular debris, they have many other functionalities. From secreting cytokines, growth factors, and lipid signaling molecules, to orchestrate the behavior of immune cells in the microenvironment.

Starting from 12 hours post-fertilization, the Pu.1-expressing myeloid cells are identified. During the primitive hematopoiesis wave these cells migrate over the yolk and differentiate in primitive macrophages at 20hpf, from primitive macrophages further differentiation in neutrophils takes place at around 30 hours post fertilization (Harvie and Huttenlocher, 2015). Starting with the definitive (or multilineage) hematopoiesis wave (24hpf) subsequent population of cells migrate and differentiate in the CHT, ultimately becoming the precursors of neutrophils, that will appear at 48hpf (Henry et al., 2013). Besides the neutrophils emerging from the CHT, a part of the global neutrophils population in zebrafish larvae is represented by randomly migrating neutrophils in the head mesenchyme. Starting from 4dpf, the kidney marrow will mature becoming the definitive site of hematopoiesis. From 3 days post-fertilization, the neutrophils can emit a burst of ROS and perform NETosis, the ejection of decondensed chromatin, histones, and antimicrobial proteins to trap microbes and kill them (Rosowski et al., 2018). Furthermore, the role of neutrophils in regeneration is essential and they can reverse migrate from the wounded area to continue their activity. More recent findings demonstrated that neutrophils play an important role in controlling invasive infection in late-stage infection by *Aspergillus fumigatus, Cryptococcus neoformans,* and mycobacterium (Davis et al., 2016; Rosowski et al., 2018; Yang et al., 2012).

Reducing neutrophil activity in late-stage infection by mucosal candidiasis in zebrafish, through inhibition of CxCr2, allows for easier tissue invasion and increases the host-death ratio (Gratacap et al., 2017). Interestingly, while the role of neutrophils in contrasting cancer is usually more known, recent studies show that neutrophils, in the $Kras^{+}$ astrocytes tumor line of zebrafish, can increase the proliferation of cancer cells (Antonio et al., 2015; Giese et al., 2019; Powell et al., 2018)w. The main marker of neutrophils is myeloperoxidase *(mpx)* and *lysozyme (lyz)*.

While neutrophils require minimal PU.1 expression, macrophages require higher and constant PU.1 expression. As we said at 20 hpf we have the first wave of primitive macrophages, able to proliferate and perform phagocytosis. Phagocytic activity is relevant both for the removal of apoptotic cell debris and to eliminate microbes. Indeed, neutrophils are more apt in clearing surface-associated bacteria, while macrophages can eliminate blood-circulating microbes. As previously explained, successive hematopoietic waves progressively substitute the embryonic macrophages with tissue-resident macrophages and kidney marrow macrophages. Macrophages, like neutrophils, are involved in microbes control during infection. Depending on the pathogen, neutrophils may be more relevant in clearing the surface bacteria, but in others, the role of macrophages is more fundamental. For example, infections by *Salmonella* and *C. neoformans* (high-virulence H99 strain) are controlled by macrophages, as their depletion increases the magnitude of the infection and host death ratio (Masud et al., 2019; Tenor et al., 2015). In *C. neoformans* the fungal pathogen can replicate in the macrophages, but they are needed to control the infection (Bojarczuk et al., 2016). Instead, in zebrafish infection with a less virulent strain of *C. neoformans*, macrophages act as a proliferative niche for the pathogens, that can replicate in the macrophages themselves (Davis et al., 2016). This was observed also for *Burkholderia cenocepacia* and *Talomyces marneffei* infections (Mesureur et al., 2017; Rosowski et al., 2018). Interestingly, infection by a faster-growing strain of *A. fumigatus* not only demonstrated the role of a proliferative niche of macrophages but the role of protection from neutrophils' phagocytic activity (Ellett et al., 2018).

Another fundamental role of macrophages is relative to regeneration. Damaging vessels in zebrafish highlighted how macrophages mediated vascular repair (Liu et al., 2016).

Macrophages wrap around damaged vessels in the injured site and, stimulate the regeneration process by priming the microenvironment and performing vessel pruning at later stages (Britto et al., 2018; Gurevich et al., 2018; Liu et al., 2016).

Even in the presence of nerve injury, there is evidence regarding the importance of recruited macrophages in the damaged area, as they are necessary to speed up the regeneration process (Carrillo et al., 2016; Tsarouchas et al., 2018).

Like neutrophils, macrophages can modulate the immune environment, and this is associated with the ill-named process of macrophage polarization either toward pro-inflammatory or anti-inflammatory phenotype (Tsarouchas et al., 2018). Upon injury or infection resident macrophages and neutrophils start to release cytokines and other paracrine factors to induce inflammation and, migrating macrophages that arrive in a second wave, sustain this inflammatory state until resolution of the problem, whereupon these macrophages switch to anti-inflammatory/pro-regenerative paracrine signaling (Tsarouchas et al., 2018; Villalta et al., 2008). This staple inflammatory scenario is well-conserved in zebrafish. Upon damage, macrophages start to express *il1b* and *tnfa* genes to spin up inflammation and induce proliferation in the blastemal cells, and recruit more leukocytes (Loynes et al., 2018; Nguyen-Chi et al., 2017). Furthermore, macrophages regulate neutrophils' local activation, avoiding further damage induced by the neutrophils themselves (Tsarouchas et al., 2018).

Another important leukocyte population is represented by the highly heterogenic microglia. Microglia originates from either rostral blood island and aortic gonad mesonephros (AGM) or exclusively AGM. The *ccl34b.1*$^{+}$ ameboid microglia originating from precursors from both sides is prevalent in developing brains, it migrates to the midline optic tectum exhibiting enhanced phagocytose capacity against bacteria and an important role in brain development. The *ccl34b.1*$^{-}$ population has a more ramified and complex morphology, acting more as a “sentinel” in the adult brain and can switch back to ameboid upon DAMPs or PAMPs stimuli (Ferrero et al., 2018; Lyons and Talbot, 2015; Wu et al., 2020; Xu et al., 2015). Interestingly, the brain population of microglia can be divided into neurogenic associated microglia (NAM), located in the OT and expressing *ccl34b.1*, *ctsa* and *ctsb*, and synaptic-region associated microglia (SAM), located in the hindbrain and expressing *c1qa* and *c1qc* (Silva et al., 2021).

Due to the high heterogeneity of the microglia-like populations, the marker used to visualize microglia is often *mpeg1*, but this marked is expressed in macrophages too, leaving the discrimination of the two leukocyte populations to the sole anatomic position of the cells.

To solve this problem a large effort in RNA transcriptomic is being done to identify a specific set of markers for microglia, but at the moment is possible to partially distinguish the microglia from other population using Apoeb (also expressed in other brain cells), P2ry12 and 4C4 (Butovsky et al., 2013; Mazzolini et al., 2020; Oosterhof et al., 2017).

Notably, already exists several different zebrafish transgenic lines labeling leukocytes (Figure 5) and the list is continuously expanding.

	Transgenic line(s)	Experimental use
Myeloid-progenitors	*Tg(spi1:EGFP)^{pA301}*	Cell labeling (whole cell)
	Tg(zpu.1:EGFP)^{df5}	
Neutrophils	*Tg(mpx:EGFP)^{i114}*	Cell labeling (whole cell)
	Tg(zMPO:GFP)	
	Tg(mpx:Dendra2)	Cell tracking (photoconversion)
	Tg(mpx:Gal4)^{i222};UAS-E1b:Kaede)^{s1999t}	
	Tg(lyz:GAL4.VP16)^{i252}; (UAS-E1b:Kaede)^{s1999t}	
	Tg(mpx:EGFPCAAX)^{gl27}	Cell labeling (cell membrane)
	Tg(lyz:EGFP)^{nz115}; Tg(lyz:DsRED2)^{nz50}	Cell labeling (whole cell)
Macrophages	*Tg(mpeg1:EGFP)^{gl22}*	Cell labeling (whole cell)
	Tg(mpeg1:mCherry)^{gl23}	
	Tg(mpeg1: mCherryCAAX)^{sh378}	Cell labeling (cell membrane)
	Tg(mpeg1: mCherry-F)^{ump2}	Cell labeling (cell membrane)
	Tg(mpeg1:Dendra2)	Cell tracking (photoconversion)
	Tg(csf1ra:GFP)^{sh377}	Cell labeling (whole cell)
	Tg(mpeg1:tdTomato-CAAX)^{xt3}	Cell labeling (cell membrane)
	Tg(mfap4:mTurquoise2)^{xt27}	Cell labeling (whole cell)
	Tg(mfap4:tdTomato)^{xt12}	
	Tg(mfap4:tdTomato-CAAX)^{xt6}	Cell labeling (cell membrane)
	Tg(mfap4:dLanYFP:CAAX)^{xt11}	
Eosinophils	*Tg(gata2^{high}:eGFP)*	Cell labeling (whole cell)

Figure 5: Examples of transgenic lines routinely used to visualize phagocytes in larval zebrafish.

Table of main transgenic zebrafish reporters adapted from ***(Linnerz and Hall, 2020).***

2.3 Zebrafish PRRs

The activation of the immune system upon viral infection is PAMP-dependent (pathogen-associated molecular patterns. These are elements of pathogens that, often evolutionary conserved, can be detected by PRRs (pattern recognition receptors) and activate the immune response. PRRs can directly sense pathogens when they form DAMPs (danger-associated molecular patterns). For example, double-strand RNA, normally not present in cells, but produced by RNA viruses during the replication, can be sensed by intracellular PRRs and start the immune response. PRRs can be located on the cell surface, on the endosome membrane, or in the cytoplasm, and depending on the position, they elicit a different response (Figure 6).

As PRRs, we can find Toll-like receptors (TLR), Nod-like receptors (NLR), RIG-I-like receptors (RLR), Scavenger receptors, and C-Type lectins.

TLRs are the most studied family of PRRS and in humans encompass a family of 10 proteins. In general, TLRs are glycoproteins with an extracellular ligand-binding domain with leucine-rich repeat motifs (LRR) and an intracellular domain called TIR (Toll/Interleukine1 receptor homology domain). Virtually, in mammals most cells can express TLRs in response to infection, but the cells normally expressing TLRs are macrophages, dendritic cells, and B lymphocytes. Each form of TLR is specialized in detecting a specific pathogen. For example, TLR4 recognizes Gram-negative bacteria via LPS, TLR2 Gram-positive bacteria via LTA and TLR5 recognizes the flagellin apparatus. Some TLRs can detect viruses, such as TLR3 which detects dsRNA, TLR7/8 detects single-strand viral RNA, and TLR9 unmethylated CpG DNA in both viruses and bacteria. Orthologs of TLRs have been identified in zebrafish and due to gene duplication, there are TLRs with two or more counterparts (i.e., for TLR4 there are *tlr4ba/tlr4bb*). Of all the TLRs in zebrafish, only a few identified the ligand. Nonetheless, the ligand specificity of TLR2, TLR3, and TLR5 is well conserved. Besides these orthologues, there are some fish-specific TLRs, like TLR22, that have shown sensibility to dsRNA and PolyI:C.

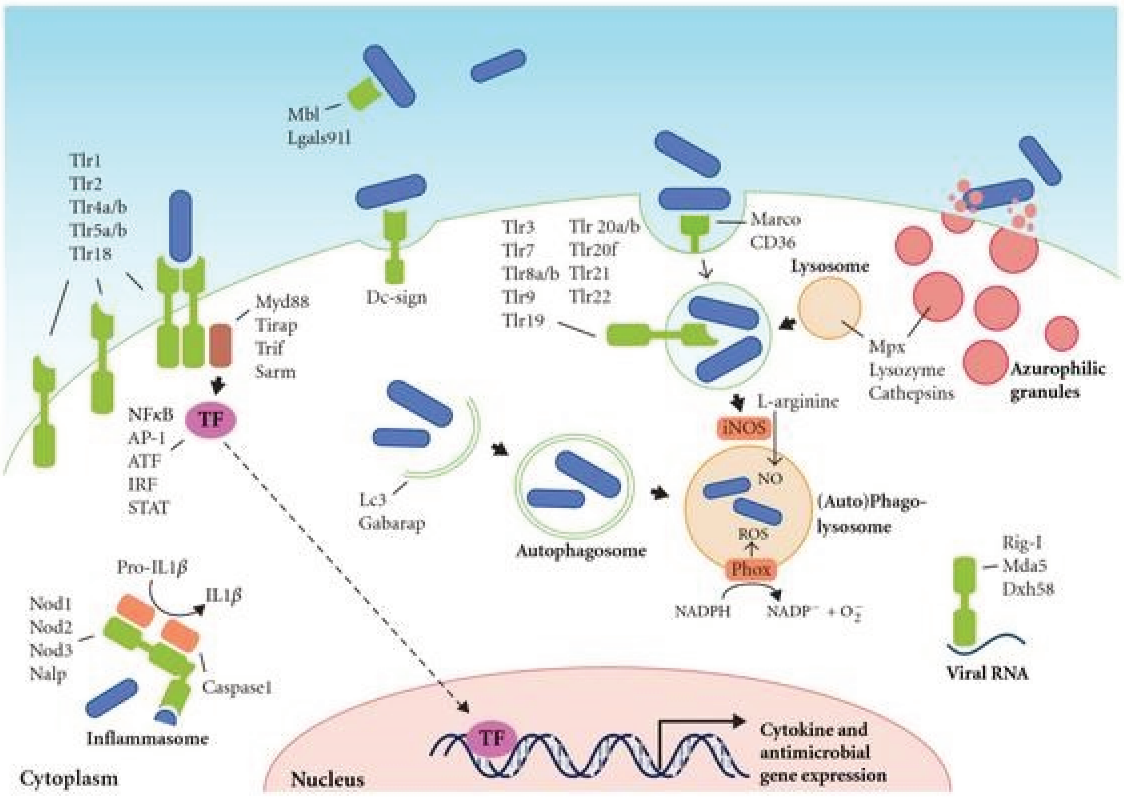

Figure 6: Pattern recognition receptors and effector mechanisms of the innate immune system.

The localization of Tlrs on the cell surface or on endosomes is hypothetical and based on the known or proposed functions of their homologs in other fish or mammals. The ability of PRRs (depicted in green) to recognize PAMPs present on various types of microorganisms, like bacteria, viruses, and fungi, has been simplified here by depicting microorganisms as rod-like bacteria (in blue). PAMP recognition by PRRs leads to activation of transcription factors (TFs), which translocate to the nucleus and initiate transcription of cytokine genes, antimicrobial genes, and other immune-related genes. Defense mechanisms such as autophagy, ROS and NO production, and degranulation can be immediately activated upon microbial recognition, without de novo gene transcription. ***Source (Van Der Vaart et al., 2012).***

Downstream, the adaptors identified in zebrafish are Myd88, Mal/Tirap, Trif/Ticam1, and Sarm.

NLRs are intracellular receptors with conserved structure and their family comprises 23 proteins in humans. They have a C-terminal ligand binding domain and an N-terminal interaction domain like CARD (caspase recruitment domain), PYD (pyrin domain), or BIR (baculovirus inhibitor repeat) domain. In mammals, NOD1 recognizes Gram-negative bacteria and NOD2 both Gram types of bacteria, but both can recognize other type of pathogens too. In zebrafish NOD1, NOD2, and NOD3 are conserved, and their antibacterial role was confirmed with *Salmonella enterica*. Furthermore, there is a subfamily of NLRs specific to teleosts and a subfamily resembling NALPs; associated with inflammasome oligomerization.

Another anti-viral PRR is the RLRs. They are cytosolic PRRs able to sense a broad range of viral RNA and activate the interferon (IFN) cascade. As in humans, the zebrafish RLRs family is comprised of 3 proteins: RIG-I, MDA5, and DXH58. The structure of these proteins in zebrafish is different and whilst in humans RIG-I has two CARDs domains, in zebrafish we have a single CARD domain. IPS-1/MAVS is the mitochondrial adaptor of RLR in zebrafish, which induces the expression of ISGs (interferon-stimulated genes).

Upon activation, MAVS associates with TRAF3 (tumor necrosis factor (TNF) receptor-associated factor) and via phosphorylation of IRF3/7 (IFN regulatory factor) activates TBK1 (Tank binding kinase 1), which leads to the production of type I IFN and subsequent ISGs.

Scavenger receptors (SR) are the least studied in zebrafish. This family of surface receptors is highly heterogenous and mainly expressed by macrophages, dendritic cells, mast cells, and in a subset of endothelial/epithelial cell types. This family is normally associated with the uptake of LDL (low-density lipoproteins), but it can act as PRRs for LPS, LTA, microbial surface protein, yeast, and CpG DNA. Upon activation, the scavenger receptors increase phagocytotic activity and cooperate with TLRs receptors to activate cytokine release. In zebrafish, the SRs MARCO (macrophages receptor with collagenous structure), able to sense for example *Streptococcus pneumoniae,* and CD36, able to sense LTA and possibly Hepatitis C virus, are conserved. MARCO is used as a marker for adult macrophages and *cd36* expression was upregulated in zebrafish infected with hemorrhagic septicemia rhabdovirus and downregulated in *Mycobacterium marinum* infection.

Lastly, only a few C-type Lectins (CLRs) have been described in zebrafish. For example, the CLRs MBL (mannose-binding lectin) is present in zebrafish and plays a role in *Listonella anguillarum* resistance. DC-SIGN homolog in zebrafish has been proposed as a receptor for tissue infection by *Aeromona anguillarum*. Other CLRs specific as NK cells receptor and myeloid cell receptors were individuated but are yet to be characterized.

2.4 Zebrafish Interferon response to viral infection

The following is an extract from: ***"IFN-Stimulated Genes in Zebrafish and Humans Define an Ancient Arsenal of Antiviral Immunity"*** (J.-P. Levraud et al., 2019)**.** *I had the fantastic opportunity to contribute to this paper and you can find the full text in the Annex 2.*

Interferon response is the hallmark of antiviral response in vertebrates, marking a largely conserved system that evolved from the RNA interference system of plants (Figure 7) (Guo et al., 2018; Jean-Pierre Levraud et al., 2019). The interferon system is the first line of defense against viral infection, and interferons (IFNs) are class II helical cytokines. Their main function is to relay the detection of viruses in a paracrine fashion, inducing the expression of many interferon-stimulated genes (ISGs). The proteins associated with ISGs prime the micro- and macro-environment, making them resilient to viral infection. (Schoggins and Rice, 2011).

Mammalian IFNs have been classified as type I (α, β, ω, ε, and κ), type II (γ), and type III (λ) IFNs. Only type I and III IFNs have a marked antiviral role, while type II IFNγ is an adaptive immunity regulatory cytokine that is mostly expressed upon intracellular bacterial infection.

In zebrafish, thanks to the increasing quality of the genome assembly and functional studies, four interferon genes (IFNφ 1-4) have been identified. These genes conserve a degree of structural similarity to mammalian type I IFNs. However, the debate on the subclassing and nomenclature of zebrafish IFNs is still open, as convergent evolution in functionality is not associated with structure homology. In general, the IFNφ genes can be divided into type I IFN 1/4, using the IFN receptors CRFB 1/5, and type II IFN 2/3, using the IFN receptors CRFB 2/5 (Figure 8) (Gan et al., 2020).

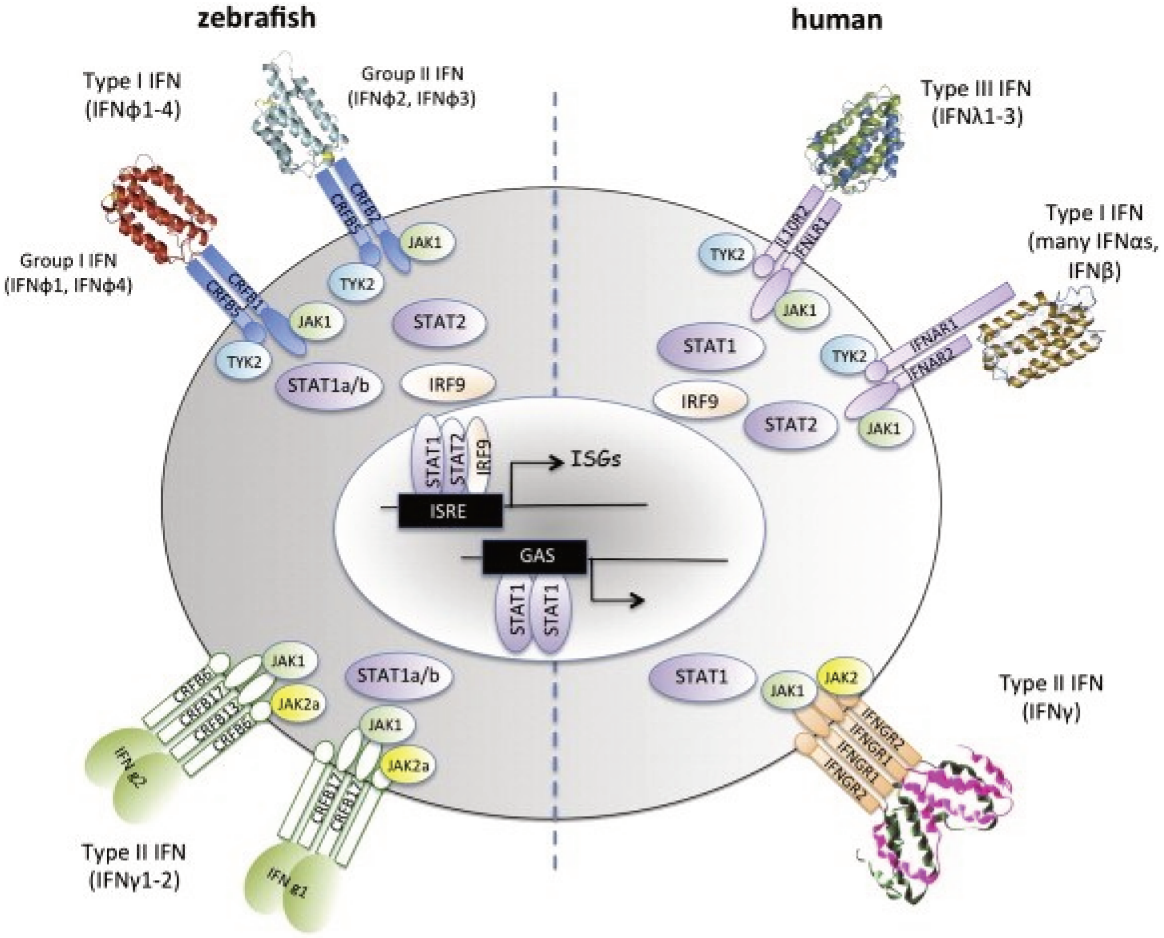

Figure 7: Schematic representation of zebrafish IFNs and their receptors.

Tridimensional representations of IFNs are from the Protein Data Bank (accession numbers: 3PIV, zebrafish IFNφ1; 3PIW, zebrafish IFNφ2; 3HHC, human IFNλ3; 1AU1, human IFNβ; 1HIG, human IFNγ). ***Source (Christelle Langevin et al., 2013).***

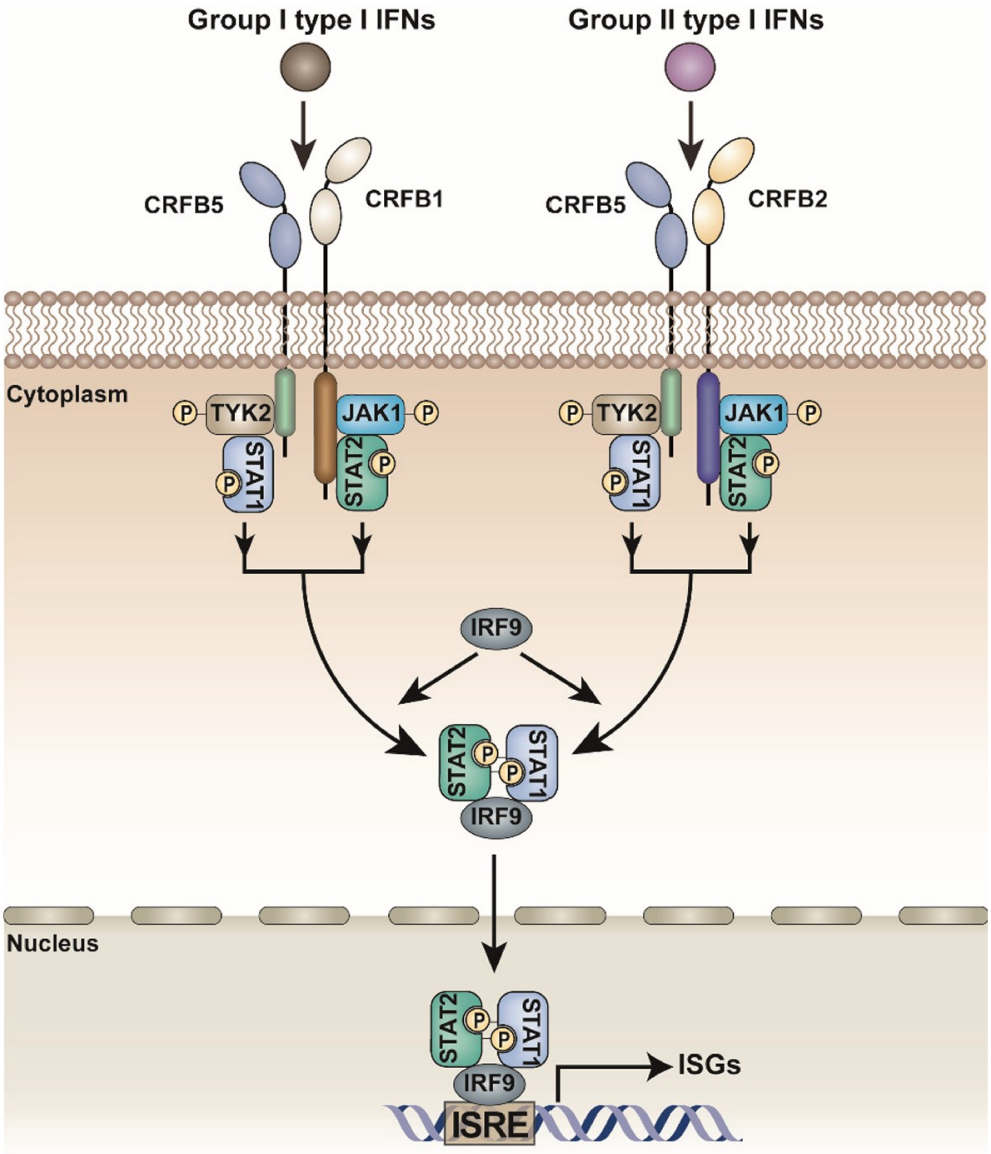

Figure 8: Signaling and ligand-receptor models for type I IFNs in fish.

The two groups of type I IFNs, two cysteine-containing group I and four cysteines-containing group II IFNs, bind to receptor complexes with a common short cytoplasmic receptor chain CRFB5, but two distinct long cytoplasmic receptor chains, CRFB1 and CRFB2. The interaction between type I IFNs and their receptors triggers the recruitment and activation of TYK2 and JAK1. Subsequently, these activated kinases promote the phosphorylation of STAT1 and STAT2, which are dimerized and assembled with IRF9 to form a complex called ISGF3. This trimolecular complex translocates to the nucleus and binds to ISREs, thus activating the transcription of ISGs. ***Source (Gan et al., 2020).***

Downstream, many components of the pathway components are conserved with 1 to 1 or 1 to 2 orthologues between zebrafish and humans. In mammals, upon IFN binding to its receptor (IFNAR), JAK1 and TYK2 are recruited to IFNAR and induce the phosphorylation of STAT1 and STAT2. The phosphorylated STAT1 and STAT2 oligomerize and recruit IRF9, forming the IFN-stimulated gene factor 3 complex (ISGF3), that induces the transcription of ISGs. In zebrafish, we can find the kinases JAK1, TYK2, STAT2, and IRF9, while for STAT1 we have two paralogues, *stat1a* and *stat1b*.(Stein et al., 2007).

Further regulators of ISG expression are IRF1, IRF3, and IRF7. These three factors can bind and activate type I IFN, increasing the expression of interferons and ISGs (Gan et al., 2020). Furthermore, these 3 IRFs can hetero- or -homo dimerize to recruit MyD88, further regulating the type I interferon response involving more intracellular pathways (Li et al., 2016; Wickramaarachchi et al., 2014).

Levraud et al. 2019 demonstrated that even by inducing only a response IFN φ1-dependent, 200 out of the 361 zebrafish ISGs have human homologs and most of the homologs are ISGs (J.-P. Levraud et al., 2019). This means that there are still ISGs for whom we have yet to understand their functionality. Nonetheless, we can identify in MX, ISG15, TRIM5, RSAD2/VIPERIN/VIG1, and PKR the main ISGs induced by the interferon upon viral infection (Gan et al., 2020; C. Langevin et al., 2013). Besides disrupting the viral infection, some ISGs have ancillary roles in controlling either positively (RSAD2 and MAVS) or negatively (SOCS1/2) the IFN signaling itself (Chen et al., 2015; Nie et al., 2014; L. Zhang et al., 2016). Furthermore, the induction of ISGs, regardless of the meaning of their acronym, is not exclusively interferon dependent. For example, MX and RSAD2 can be directly expressed upon sensing viral infection by other cellular sensors (Altmann et al., 2004; Li et al., 2016).

Besides type I interferon, in zebrafish two different genes for type II interferon, commonly called interferon gamma, have been found. The nomenclature of these two genes is yet to be standardized and not much is known about the role of these interferons (Igawa et al., 2006). While in mammals there is a single IFNγ receptor, in zebrafish there are two. IFNGR1-1/crfb13 preferentially binds IFNγ1 and IFNGR1-2/crfb17 binds IFNγ2 (H. Meijer and P. Spaink, 2011).

Not much is known about the function of IFNγ, but structural and functional studies showed that STAT1, STAT2, and STAT3 are still pivotal in the downstream pathway of IFNGR, hinting that the signal transduction is conserved between humans and zebrafish (Gan et al., 2020). Type II interferon is tissue- (Grayfer and Belosevic, 2009) and developmental-staged dependent, as it is mainly expressed in adults, but conserves an antiviral and pro-inflammatory role (López-Muñoz et al., 2011).

Type II interferon plays a role in antibacterial response too: infection by the bacterium *Yersinia ruckeri* in fish under or over-expressing IFNγ showed that its regulation is necessary for controlling the infection and level of inflammation (Aggad et al., 2010; Sieger et al., 2009).

Taken together, all the information points towards a regulatory role of interferon response, immune system, and inflammation for IFNγ in zebrafish, similar to the regulatory role in humans.

Proof that the zebrafish immune system is still mostly unexplored is the recent discovery of a new interferon, called IFNυ. This interferon shares structural and genetic similarities with other already known interferons, and the first experiments with grass carp reovirus (GCRV) attributed an important role in the ISGs-based antiviral response (Chen et al., 2022). This interferon may play a role in adaptive immunity too, as it was recently shown that IFNυ is significantly expressed in B cells in response to SVCV infection (Hu et al., 2023).

For both IFNγ and IFNυ, more research is needed to further characterize their role in zebrafish. However, their existence reinforces the potential of using zebrafish as a model for host-pathogen studies.

2.5 Zebrafish antibacterial response

Bacterial infection of zebrafish larvae started as a tool to study this model organism's immune system, but the incredible results obtained pushed the researchers to exploit this model in a holistic host-pathogen manner. Many different bacteria were tested during the past decade to define which ones could use zebrafish as a model organism.

As introduced before, the response to infection starts with the detection of PAMPs by PRRs. Although we tried to provide an extensive list of PRRs and their role, as we saw with the IFNs, in zebrafish there is still work that needs to be done to fully characterize all the PRRs available. An example is the recent discovery of an intracellular LPS sensor called ALPK1. Briefly, this kinase results able to directly bind ADP-heptose, one of the sugars in the core regions of LPSs, and activate independently through phosphorylation of TIFA/TRAF6 dimers, that forms oligomerized complex called TIFAsomes, able to induce an inflammatory response (García-Weber et al., 2018; García-Weber and Arrieumerlou, 2020).

Due to the high heterogeneity of downstream pathways activated, resulting from the intrinsic complexity and variability of pathogenic bacteria, in the following paragraph, we will focus on introducing the antibacterial effectors in innate immunity.

First and foremost, we can find the secreted peptides and lipid mediators of the innate immune system. These lipid mediators are cytokines, interleukins, chemokines, IFNs, and small secreted proteins, that, altogether can prime and polarize the micro- and macro-environments in the different phases of infection response and resolution (Commins et al., 2010). Cytokines are a family of peptides involved in a multitude of biological functions. To summarize their function, they are produced by cells to “communicate” with themselves (autocrine), close cells (paracrine), or at long distances (endocrine). This communication is as relevant as hormone production and their dysregulation during infection can induce a “cytokine storm” (Figure 8), a loss of control with overproduction of proinflammatory factors, and ultimately increase tissue damage like in Covid-19 (Darif et al., 2021). Pathologically speaking, cytokines are involved in many different diseases (i.e., autoimmune disease, cancer, and infection) (Liu et al., 2021; Propper and Balkwill, 2022).

Cytokines are produced by many different cells, but the main ones are the cells of the immune system (i.e., macrophages, neutrophils, and monocyte) and epithelial and endothelial cells (Kany et al., 2019).

The hallmarks of inflammation in mammals are TNF-α, IL1β, IL6, IL8, and IL2, while IL10 has an anti-inflammatory, pro-regenerative role. Interestingly, all these mediators are synthesized as precursors (Bottiglione et al., 2020). Upon activation of the immune response, they are cleaved and activated as a secretory faction to steer the environment.

In zebrafish, many of these factors and their receptors are conserved, although, due to gene duplication, we can find many more peptides to still characterize (Figure 9). Indeed, IL1β, IL8 and IL10 have been well studied and it was confirmed that their receptors, CXCR1/2 and IL10R1 respectively, are well conserved (Huising et al., 2004; Oehlers et al., 2010; van der Aa et al., 2010; Varela et al., 2012). TNF-α is another well-characterized protein, as different studies confirmed its role in zebrafish and the receptor structure (Campos-Sánchez and Esteban, 2021; Duan et al., 2021). Work on *Mycobacterium marinum* suggests that TNF plays a proinflammatory role, well counterbalanced by lipoxins' anti-inflammatory role, during infection; similarly, to IL12 and IL10 balance. A pivotal role of TNF-α is the recruitment of leucocytes at the site of infection (Roca et al., 2008; Tobin et al., 2010).

Cytokine	Percentage of identity amino acid sequence corresponding to human cytokine	Sequence number reference (Genbank; Entry Uniprot)	
		Zebrafish	Human
IL-1β	24.24%	NP_998009.2; E6N152	AAM88883.1; P01584
IL-4	19.62%	CAL48253.2; D1YSM1	AAH70123.1; P05112
IL-6	18.44%	NP_001248378.1; H9A0J9	AAK48987.1; P05231
IL-8/Cxcl8	33%	XP_009305130.1; A0A0G2KYH9	AAH13615.1; P10145
IL-10	29.12%	AAI63038.1; Q5EFQ8	AAA80104.1; P22301
IL-11α	21.55%	CAI61346.1; Q494Q5	AAH12506.1; P20809
IL-11β	19.09%	CAI61347.1; Q494Q4	AAH12506.1; P20809
IL-12α (IL-12 p35)	17.84%	BAD26596.1; Q6F3R0	AAK84425.1; P29459
IL-12β (IL-12 p40)	24%	AAI64577.1; Q0V941	AAG32620.1; P29460;
IL-13	17.58%	BAG50536.1; B3IWZ9	AAH96139.1; P35225
IL-15	22%	AAI62843.1; Q15KG7	AAI00964.1; P40933
IL-17_5	31.36%	AAI15082.1; Q5TKT0	AAH67505.1; Q16552
IL-17_3	25.24%	BAD72788.1; Q5TKT2	AAH69152.1; Q9P0M4
IL-17_4	52.53%	AAI62897.1; Q5TKT1	AAH36243.1; Q8TAD2
IL-21	16.46%	ABM46913.1; A1YYP5	AAH69124.1; Q9HBE4
IL-22	15.35%	BAD72867.1; Q5TLE4	AAK62468.1; Q9GZX6
IL-23 p19	18.90%	CBM41294.1; L0N860	AAQ89442.1; Q9NPF7
IL-26	17.03%	AAI63119.1; Q5TLE5	AAH66270.1; Q9NPH9
IL-34	24.23%	BAM75187.1; L8AZT5	AAH29804.1; Q6ZMJ4
IFN type I	22.63%	AAM95448.1; Q8AY12	EAW58611.1; P01563
IFN-β	22.63%	BAD20663.1; Q75S22	EAW97180.1; P01579
TNF-α	25.93%	AAR06286.1; Q6T9C7	CAA26669.1; P01375
TNF-β	25.40%	AAR06286.1; Q1JQ40	CAA26670.1; P01374
CSF1a	17.29%	CAP58787.1; A9JRD6	AAH21117.1; P09603
CSF1b	12.06%	CAP58788.1; B0UYR0	AAH21117.1; P09603
CSF3a	19.01%	CAQ64749.1; B8ZHI7	AAK62469.1; P09919
CSF3b	22.58%	ABX57823.1; B5L332	AAK62469.1; P09919
TGF-β1	42.21%	AAI62366.1; Q7ZZU7	AAH22242.1; P01137
TGF-β2	78.50%	AAQ18012.1; Q7SZV4	AAH99635.1; P61812
TGF-β3	73.36%	AAW66727.1; Q66I23	AAC79727.1; P10600

[a] Percentages obtained by alignment using UniProt Proteome [121].

Figure 9: Amino acid sequence identity between the zebrafish cytokine and the corresponding human cytokine.

Table of inflammation hallmark cytokines conserved between zebrafish and human. ***Source(Zanandrea et al., 2020)***.

Lastly, as introduced before, IFNs may play a role in bacterial infection too, although it still needs to be better investigated.

If the Cytokines are the messengers and the guides of the immune system, leucocytes are the effectors of these messages. We have already introduced before neutrophils and macrophages. Both are attracted by chemokines (a class of cytokines) and partially activated by the cytokines while producing more to keep the dynamic shift of the environment toward pro- or anti-inflammatory polarization.

Neutrophils are sensitive to a wide array of stimuli, as they express more than 30 different receptors, that can modulate their recruitment and programming (Futosi et al., 2013). Their recruitment can be triggered by a wide range of chemotactic signals, including danger signals (ATP, H_2O_2, NO (nitric oxide), HMGB1), cytokines (IL8, IL1β, TNFα), and other chemokines (Leiba et al., 2023).

Upon recruitment, neutrophils can activate phagocytosis, apoptosis, NETosis, degranulation, and Ros production.

Neutrophils are highly proficient in phagocytosis and once arrive in the infected area, they start to phagocyte bacteria and cellular debris. In comparison to macrophages, their phagocytosis is more active and "vacuum" rapidly the surface of tissues. Although the efficiency of this process is high, bacteria evolved systems to elude or take advantage of it. Once bacteria are phagocytosed, they are subjected to different autophagic processes, like xenophagy, LC3/SLR membrane repair process, Antimicrobial peptide delivery, and LC3- associated phagocytosis (LAP) (Figure 10) (Muñoz-Sánchez et al., 2020a). To understand the variability associated with the phagocytosis process and bacterial biology, we can use the LAP as an example. This type of phagocytosis is beneficial for the *Salmonella typhimurium* host response, but the same mechanism is detrimental for *Staphylococcus aureus,* which is responsible for delivering this bacteria to a replication niche (Muñoz-Sánchez et al., 2020b).

As explained before, neutrophils can perform NETosis, where through the ejection of chromatin and granular protein can form a physical and chemical structure that physically traps and kills bacteria. This process can be vital or suicidal (Burgener and Schroder, 2020). In the suicidal NETosis, neutrophils start to overproduce myeloperoxidases and Ros, while the GaderminD-p30 complex initiates a cascade that induces cytoplasmic degranulation, histone deactivation and creates pores on the nuclear and cellular membrane (Hakkim et al., 2010; Kambara et al., 2018; Sollberger et al., 2018). Upon the pore formation, the NET shoots out of the exploding cells, together with the granules, ROS, and myeloperoxidases (Li et al., 2010; Metzler et al., 2014). Vital NETosis can be canonical or noncanonical, depending on the sensing pathways stimulated. In canonical vital NETosis, the neutrophils are stimulated by bacteria, bacterial product, and TLR4-activated platelets, while in the noncanonical happens by cytosolic LPS sensing. Both these pathways are caspase and Gasdermin D dependent, but the neutrophils can survive the NETosis and keep operating normally (Byrd et al., 2013; Chen et al., 2018; T. Wan et al., 2017). In zebrafish, this system is conserved and dependent on caspy2-Gasdermin Eb, two paralogs mammalians of caspase and gasdermin, and it is activated during infections from bacteria like *Edwardsiella piscida* (Chen et al., 2021). The role of NETosis in zebrafish was confirmed for *S. aurus, Shigella flexneri, S. typhimium, Escherichia coli,* and *Candida albicans* (Pijanowski et al., 2013).

Degranulation is associated with NETosis and it is induced by the same signals (Figure 11). Granulopoyesis is conserved between mammals and zebrafish (Bennett et al., 2001). The main content of granules is antimicrobial peptides (i.e., cathepsin G and lactoferrin), neutrophil elastase (NE), MMP-9, myeloperoxidase, and ROS (Pijanowski et al., 2013).

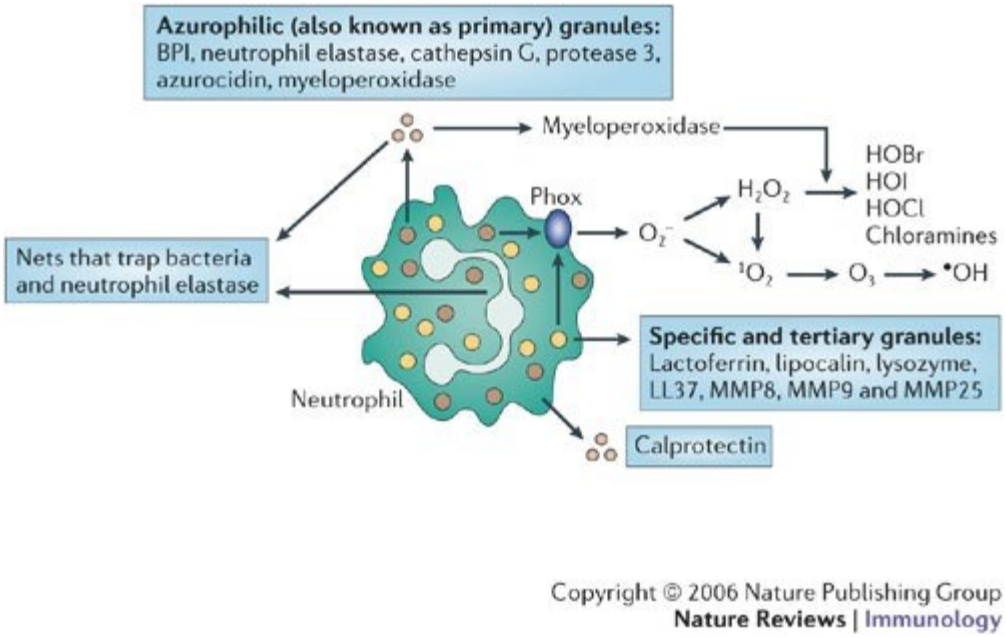

Figure 10: Neutrophils deliver multiple anti-microbial molecules.

Microbicidal products arise from most compartments of the neutrophil: azurophilic granules (also known as primary granules), specific granules (also known as secondary granules) and tertiary granules, plasma and phagosomal membranes, the nucleus and the cytosol. BPI, bactericidal permeability increasing protein; H2O2, hydrogen peroxide; HOBr, hypobromous acid; HOCl, hypochlorous acid; HOI, hypoiodous acid; MMP, matrix metalloproteinase; 1O2, singlet oxygen; O2−, superoxide; O3, ozone; OH, hydroxyl radical; phox, phagocyte oxidase. ***Source (Nathan, 2006).***

Associated with both NETosis and degranulation, there is ROS production, through oxidative burst, highly reactive oxygen species, such as H_2O_2, are produced. In zebrafish, P2y receptors are activated by ATP released by damaged cells, inducing the activation of PlC and subsequently the production of IP3 and Ca^{2+} release from the endoplasmic reticulum. Ca^{2+} activates Duox1, which promotes H_2O_2 production. Part of the H_2O_2 produced is released during the infection (along with other oxygen-reactive species), while cytoplasmatic H_2O_2 activates NF-kb, Erk, and Jnk. This activates the transcriptional factor Jun and Fos, expressing proinflammatory genes such as *cxcl8* (IL8*)* (Martínez-Navarro et al., 2020). Furthermore, H_2O_2 and IL8 are powerful chemoattractants and activators of neutrophils themselves (Figure 11), eliciting the proinflammatory polarization of the environment (De Oliveira et al., 2016; Martínez-Navarro et al., 2020).

The neutrophil's activity must be regulated to stop the release of granules and ROS upon infection resolution. Different signals contribute to the shifting of the environment towards pro-regenerative, but oxygen plays again a major role for neutrophils. The depletion of oxygen in the infected area particularly stress neutrophils, induces the stabilization of hypoxia-inducible factor 1 (HIF1). This factor determines the destiny of neutrophils after the release of the granules and ROS. At the end of the infection, a consistent fraction of neutrophils is dead due to apoptosis, and its debris gets removed by other leucocytes, but, upon stabilization of HIF1, a considerable fraction of neutrophils can reverse migrate, surviving and leaving the infected area (Nathan, 2006; Schild et al., 2020). Furthermore, while IL8 is a powerful chemoattractant, it is known that at higher concentrations *in vitro,* it has the opposite effect. Data demonstrates that increases in IL8 can induce internalization of surface receptors on neutrophils, impairing further activation and recruitment (Buckley et al., 2006). Furthermore, as macrophages increase in the area, they can reduce neutrophil activation by redox and src kinases signaling, promoting reverse migration (Tauzin et al., 2014).

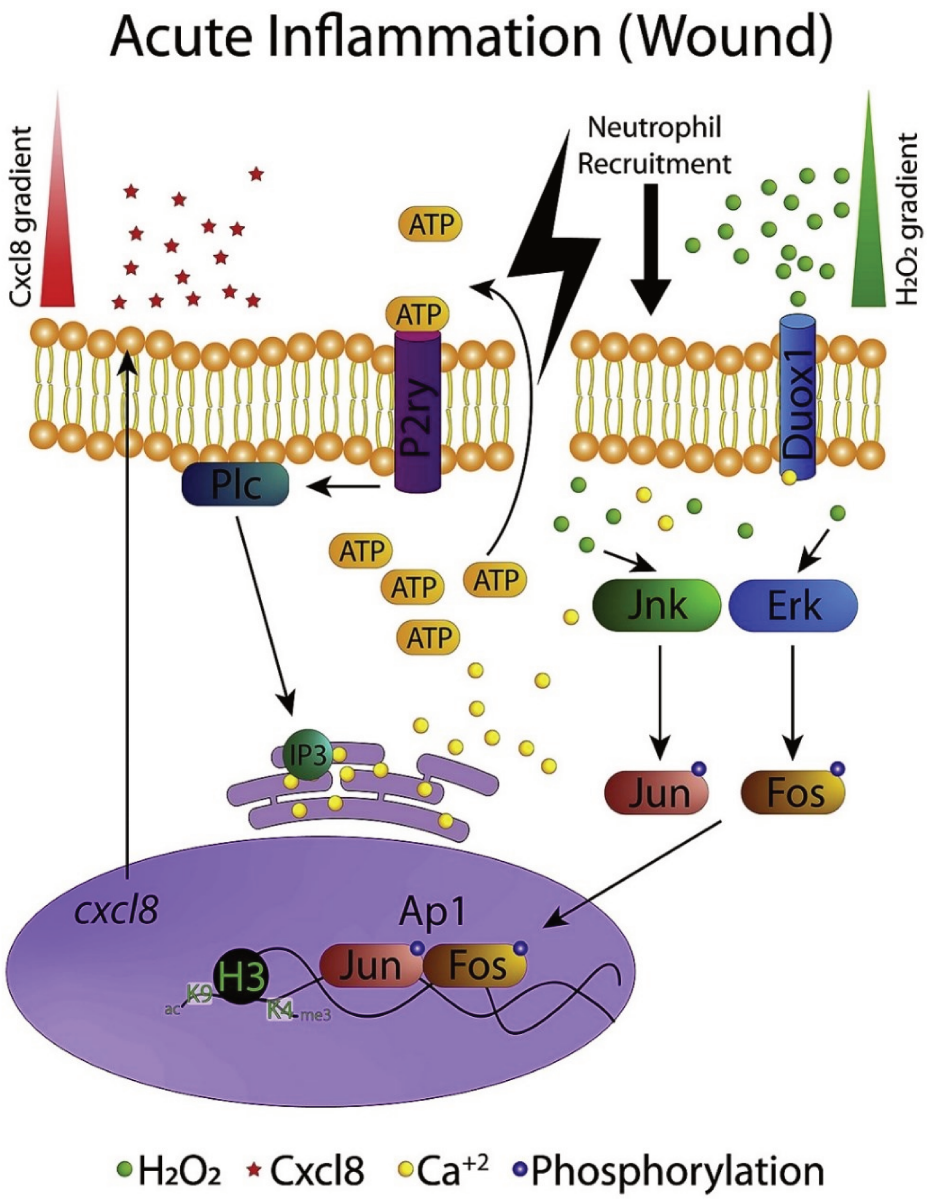

Figure 11:Proposed models showing the role of H2O2 in acute inflammation in zebrafish.

ATP released from damaged cells activates purinergic P2y receptors, which promotes the activation of Plc, the production of IP3 and Ca2+ release from the endoplasmic reticulum. Cytosolic Ca2+ activates Duox1, which produces H2O2 that then activates NF-κB, Jnk and Erk, promoting the phosphorylation of Jun and Fos and the expression of target pro-inflammatory genes, including cxcl8. The mechanism of how these molecules is activated by H2O2 is still unknown. Additionally, H2O2 is also able to modulate cxcl8 expression via covalent chromatin modifications, such as acetylation of H3K9 and trimethylation of H3K4. Newly synthesized Cxcl8 is then secreted to the extracellular matrix, forms a gradient, and together with H2O2 gradient, induces Cxcr2-and Lyn-mediated neutrophil recruitment. ***Source (Martínez-Navarro et al., 2020).***

Interestingly, pathogens can alter the recruitment and pro-reverse migration pathway to affect neutrophil activity and escape the immune system in the first stage of infection (Abtin et al., 2013; Gonzalez et al., 2015; Spinner et al., 2016).

While neutrophils are the first leukocytes to be recruited upon infection, they work in tandem with resident macrophages, that reside in different tissues to "guard" them, and subsequently recruited macrophages (Hall et al., 2009; Lazarov et al., 2023; Yu et al., 2017). A simplification of this system tries to order the leucocyte response in successive waves, with resident macrophages activating first, neutrophils wave following, and macrophages slowly replacing neutrophils during infection (Novais et al., 2009; Silva, 2010; Silva and Correia-Neves, 2012). The same can be said regarding the role of macrophages during infection and damage, which can polarize towards pro-inflammatory (M1) or pro-regenerative (M2) programming (Nguyen-Chi et al., 2015a; Rougeot et al., 2019; Wiegertjes et al., 2016).

Focusing again on macrophages, these cells are pivotal in the innate immune response. Like neutrophils, they have a strong phagocytotic activity, are activated upon PAMPs and DAMPs sensing (Kapellos et al., 2016; Petrovski et al., 2007), and are recruited through the CCL2/CCR2 and CXCL11aa/CXCR3.2 axes (Sommer et al., 2021, 2020). Once internalized in the phagosomes, the majority of the pathogens are eliminated by lumen acidification, nutrient restriction, and release in the phagolysosome lumen of antimicrobial agents and ROS(Kinchen and Ravichandran, 2008; Slauch, 2011). Not all pathogens are eliminated by this system, and many can survive (i.e., *Mycobacterium tuberculosis* and *S. typhimurium*) (Aderem and Underhill, 2003; Flannagan et al., 2012; Ray et al., 2009).

Furthermore, some pathogens can breach the phagolysosome and invade the cytosol (i.e. *Listeria monocytogenes*) (Ray et al., 2009). Due to this, even in macrophages, there is a highly conserved autophagy system, based on the detection of ubiquitinated substrates (i.e. bacterial membranes), non-self antigen containing phagosomes (IRGs and GBPs mediated or NLRs detection) (Yoshida et al., 2017). In all cases, the activation of these mechanisms contributes strongly to macrophage polarization toward pro-inflammatory phenotype.

The ability of macrophages to change their nature depending on the situation of the environment is bound to their great genetic plasticity, which allows them to assume a variety of different gene expression patterns (Stout and Suttles, 2004).

While we will often refer to M1 and M2 to address the two extremes of macrophage expression profiles for the sake of simplicity, we are aware that there is a broad spectrum of macrophage activation (Xue et al., 2014). This is even more true when we look at the different "shades" of phenotypical commitment of macrophages *in vivo* (Ginhoux et al., 2016; Nguyen-Chi et al., 2015b).

The molecular markers of M1 and M2 macrophages are conserved and the most important are nitric oxide synthase 2 (NOS2), IFNg, TNFa, IL1b, MHC class I and II, IL13, IL4, ARG2, and IL10 (Figure 12) (Leiba et al., 2023).

In zebrafish, different signals that can elicit activation or polarization of M1 macrophages are conserved. Besides the different DAMPs and PAMPS, calcium can trigger M1 macrophage activation and ROS sustains M1 polarization through NF-kB and Lyn. Furthermore, HIF1a activates COX2, which induces the production of PGE2, resulting in the upregulation of TNFα and IL1β. Upon activation, M1 increases substantially the production of ROS and No, with the latter produced by upregulation of induced No-synthase (iNOS). This is associated with the release of a wide range of signals and increased phagocytotic activity and upregulation of MHC molecules.

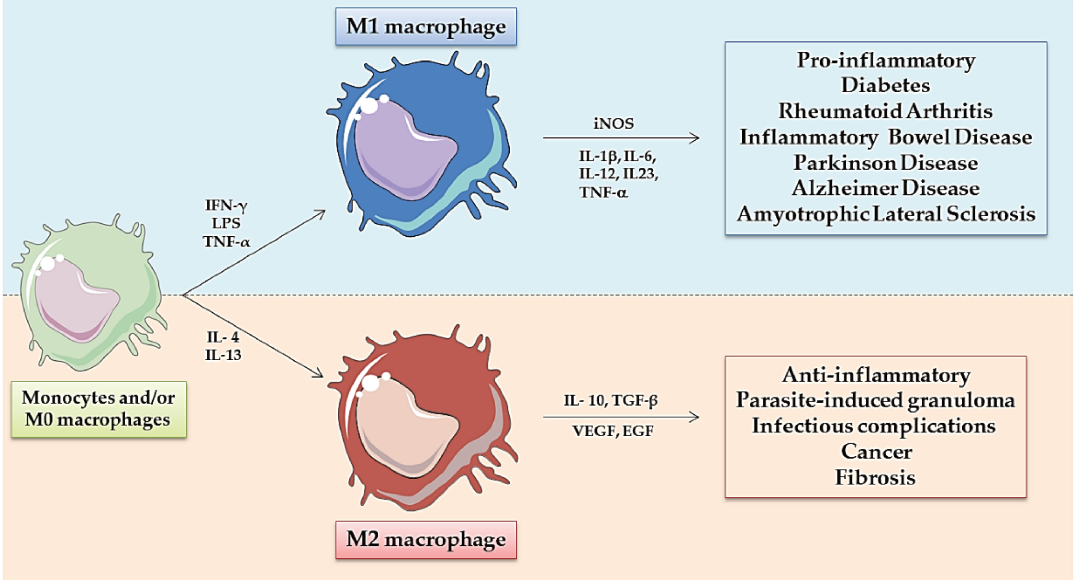

Figure 12: Macrophages polarization and its role.

Macrophages originate from monocytes or tissue-resident macrophages. In response to different microenvironmental stimuli macrophages polarize towards an M1-like or M2-like phenotype, and the excessive accumulation of macrophages with a particular phenotype has been correlated with a poor prognosis in some diseases (on the right). ***Source (Lazarov et al., 2023).***

Instead, M2 macrophages are poorly characterized in zebrafish, as the marker of this range of subpopulations is poorly conserved and, in general, less studied. In general, the M2 macrophage denomination represents a group of different phenotypes with a minor IL12 and a major IL10 expression (Mosser and Edwards, 2008). Cumulatively, their role is to “clean” the affected area from remaining debris and regulate tissue regeneration and remodeling (Leiba et al., 2023). Recently, it was discovered that the Wilms Tumor 1b (WT1b) factor can be found in a high level of expression in macrophages subpopulations that accumulate in regenerating tissue, suggesting that this factor may be one of the markers of M2 macrophages (Sanz-Morejón et al., 2019). Furthermore, Denans et al. used single-cell RNAseq to try to differentiate the different macrophagic populations and their expression profile in zebrafish. Interestingly they observed that the glucocorticoid (GR) pathway is activated in parallel with the induction of anti-inflammatory markers and negative regulation of ROS. During the first hour post-injury, IL10 pathway expression increases, and at 3 hours post-injury there is upregulation of IL4 and polyamine signaling, which are markers of anti-inflammatory macrophages (Denans et al., 2022). Nonetheless, further studies are needed to better define the anti-inflammatory macrophage populations, especially in post-infection environments.

Chapter 3:
Zebrafish as a model for host-pathogen studies: advantages and constraints

When performing host-pathogen studies, the careful choice of an animal model is necessary to obtain useful data that can enrich the puzzle of information already available on both the host response and the pathogen.

When mammal models are used, a mix of different approaches are used that span from intravital imaging to the more classic tissue biopsy to infer the data necessary. Using these methods, the result obtained is tiled corresponding to different organs' susceptibility to pathogens, the host's local response, and the global clinical signs of the infection. After that it is the work of researchers to patch together these tiles to have a global view of the host-pathogen interactions. Furthermore, this process is time-consuming, requires a high number of specimens and communal effort.

This is where arises a gap that can be filled by other models, and zebrafish is one of these. As we explained, the immune system of zebrafish is close enough to mammalians to be usable as a model. Furthermore, zebrafish husbandry is cheaper and offers the possibility to have hundreds of samples for a week when working on larvae.

Indeed, the use of larvae offers three great advantages: 1) we can observe and manipulate the host immunity, 2) a small size (1 mm length for 500 µm thickness) that can be used for high-content studies, and 3) a fully transparent system (David M. Tobin et al., 2012; Torraca and Mostowy, 2018).

The transparency of zebrafish, mixed with the facility in genetic manipulation, offer the possibility to generate reporter organism to directly observe pathogen dissemination and immune system response in a whole live organism. This means that it is possible to extrapolate kinetical data and identify tissue interactions, the cell population involved in the infection, and the interaction between the cells of the immune system and the pathogen.

This less invasive system can be leveraged to perform direct observations not possible on other animal models and it is a clear advantage of zebrafish (Figure 13).

Limitations of In Vitro Phagocyte Challenge	Advantages of Larval Zebrafish Model
Purification of immune cells can perturb function	Purification unnecessary
Media does not recapitulate tissue-specific in vivo nutrients	In vivo nutrients
No soluble factors (e.g., opsonins, cytokines) from other cell types	Normal soluble components
No contact activation or inhibition by other cell types	Normal tissue environment
No effect of extracellular matrix interactions	Normal extracellular environment
Cannot monitor dissemination of infection	Tissue-to-tissue dissemination can be imaged
Limitations of In Vivo Mouse Infection	**Advantages of Larval Zebrafish Model**
Too large to examine infection host-wide at high resolution	Possible to image entire live fish
Opaque skin and organs limit fluorescent imaging below ~100 μm	Fish larvae are transparent
Elimination of macrophage function pleiotropic	Temporary macrophage ablation feasible
Very limited high-resolution, non-invasive imaging of pathogen or immune morphology	High-resolution, non-invasive imaging facile throughout the host

doi:10.1371/journal.ppat.1002349.t001

Figure 13: Advantages of embryonic zebrafish model for study of innate immune-pathogen interaction. *Source* (David M. Tobin et al., 2012)**.**

Nevertheless, it is possible to multiplex the imaging data with RNA expression patterns by RT-qPCR, to spatially associate gene expression to specific patterns of infection and host response.

Furthermore, the relatively easier genetic manipulability of zebrafish allows for specific cell population depletion, gene expression manipulation (knock-down, knock-in, or over-expression), and humanization.

All of this translates into the possibility to perform high-content screening of the whole population's trend of host-pathogen interaction without the need to piece tiles of a puzzle, but directly observe all the dynamics *in vivo* (Carvalho et al., 2011).

Indeed, as with all animal models, zebrafish are still far from the perfect model.

One of this model's biggest limits is the tools available, while the massive investment and attention to mammals' experimentation (first and foremost mice) resulted in the creation and optimization of tools for experimentation; for zebrafish, as an alternative model, the investment was, and still is, marginal, resulting in fewer tools available for experimentation. For example, the number of antibodies available for zebrafish is a fraction of the one for mice, and the same can be said for other tools.

Nonetheless, in the latest year, the interest in zebrafish as a model is increasing and new tools appear on the market by the day (Figure 14).

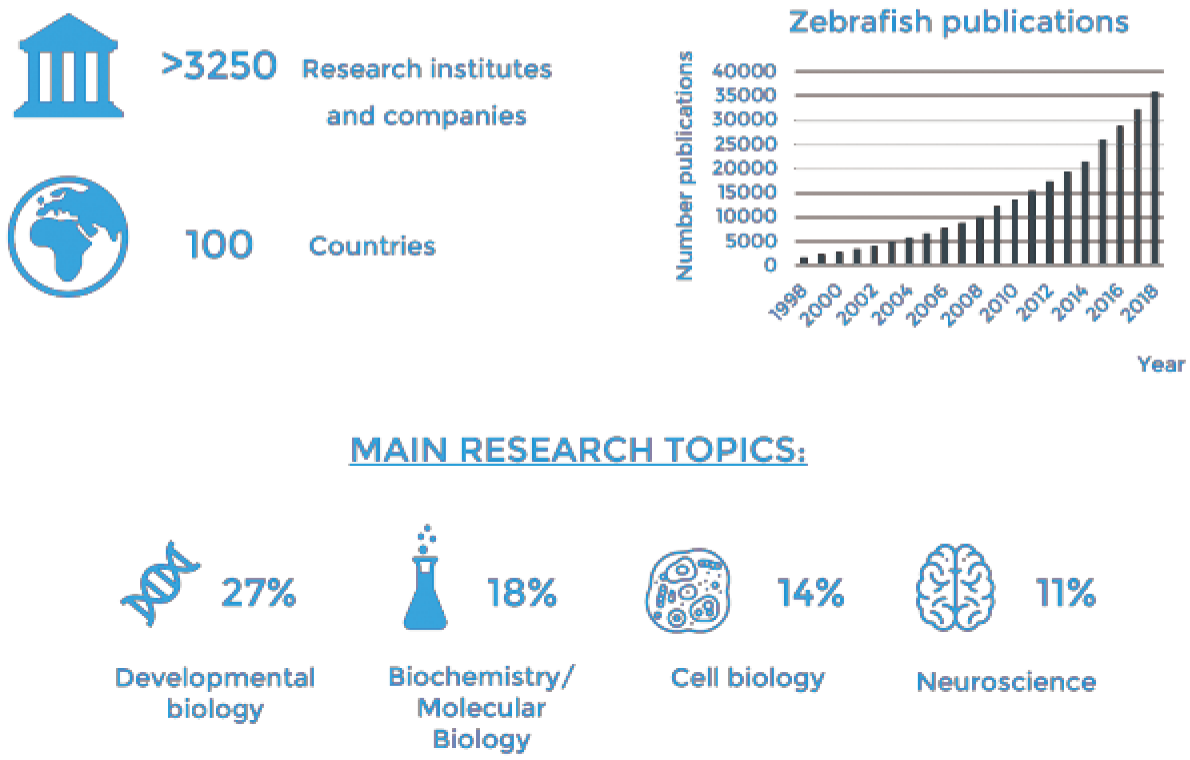

Figure 14: Research done in zebrafish.

There are more than 3250 institutions working with zebrafish around the world, in more than 100 countries. The number of publications using zebrafish has increased over the years, being the main topics: developmental biology, biochemistry, cell biology and neuroscience. ***Source (https://bionomous.ch/articles/what-are-zebrafish/).***

Another important limitation of zebrafish is that it is an aquatic model and, inevitably, some organs reflect these anatomical differences from mammals. For example, we lack a true pulmonary system. Indeed, the swim bladder can act both as a model for bladder disease (for example is amply used for *C. albicans* studies) and partially as a model for lung (Chao et al., 2010; Y. Zhang et al., 2016).

Furthermore, zebrafish larvae rear between 24°C and 33°C. This range of temperatures makes zebrafish an ill model for pathogens that need a temperature of 37°C to maintain their biology. Recently, it was demonstrated that elevating the water oxygenation to 150% air saturation (hyperoxia), makes larvae more resilient to higher temperatures, pushing the limit for their rearing to 36-37°C (Andreassen et al., 2022). Although this result is exciting, there is still the need to conduct more studies and selective breeding to effectively have zebrafish strains more tolerant to higher temperatures.

Lastly, as we explained, the adaptive immune system fully develops solely in juvenile fish, while zebrafish larvae have only an innate immune system. For some types of host-pathogen studies, this could be a limitation, as it would give only partial feedback on the host's immune response to pathogens. Indeed, in other cases can represent an advantage if the purpose is to study only innate immunity response.

Nevertheless, the use of zebrafish in host-pathogen studies is expanding and recently, researchers are embarking on the development of adult zebrafish as models for more complex host-pathogen studies (White and Patton, 2023). In the history of use of zebrafish larvae as a model for host-pathogen studies (López Hernández et al., 2015; Sullivan et al., 2021), this model gave important contributions. For example, the work of Lalita Ramakrishnan on tuberculosis and zebrafish demonstrated that zebrafish could recapitulate mechanisms observed in humans and primates, that are not replicated in other mammal models (Ramakrishnan, 2013).

To conclude, zebrafish represents an alternative model that can complement more established mammal and primate models to enrich the possibilities of researchers that conduct host-pathogen studies, offering possibilities not offered by other models.

Chapter 4: Aim of the work

The red line binding together the papers presented in this thesis is the exploration of zebrafish larvae as a model for host-pathogen interaction, using either human viruses or bacteria. An important aspect of this exploration is the development and testing of new approaches and techniques to unveil the potential of this alternative animal model.

I focused on the transparency of zebrafish, already a well-established advantage to develop new physical systems and strategies to maintain fragile infected fish under intensive imaging and combined this to extrapolate as much data as possible regarding the kinetics associated with the pathogen dissemination and host response. Multiplexing the data obtained with the genetic expression patterns, it was possible to effectively recapitulate the holistic dynamics associated with host-pathogen interactions. A further step forward was the “test” application of simple mathematical modeling to encompass the data obtained and demonstrate both the validity of zebrafish as a model for infection, able to recapitulate population dynamics and infer hidden information that could not be easily obtained experimentally.

Indeed, I wanted to demonstrate that this model could be used to either observe cellular level immune system-pathogen interactions *in vivo* or obtain a large amount of multiplexable global dynamics data with a low variability; perfect for future application in the training of AI systems for *in silico* experiments.

To do this I created a new physical system to stabilize environmental conditions during live imaging of parallel samples, while lowering anesthetic toxicity, by combinatorial anesthesia, and physical burden by special mounting. The large amount of data obtained pushed me to develop a coherent data management system and image analysis pipelines. Regarding the latter, I adopted the same philosophy of the paper in the Annex 1, creating a modular pipeline focused on a solid and adaptable approach that accounts for a certain degree of error as a tradeoff in the simplicity of use and variability of input. The idea is to create tools that can be accessible for everyone over minimal self-training and would not turn in abandonware.

Finally, all of this was under the umbrella of relevant biological questions aimed at unraveling the dynamics of pathogens and host response in a holistic way in a live organism, observing which tissue is affected, in which way, and how the immune system behaves differently in these compartments.

In conclusion, as stated at the beginning of the paragraph, in each paper I dwelt on both the role of zebrafish as a model and the important biological questions I was posed and developed the first, to answer the questions and further investigate the biological mechanism highlighted using zebrafish.

Some of the biological questions you will encounter in the following articles are: How does Sindbis virus propagate in zebrafish larvae? Zebrafish can be used as an animal model for SARS-COV2 and *Legionella*? How does zebrafish innate immune system counter these infections?

ARTICLES

Spatial dynamics of peripheral and central nervous system infection by an interferon-inducing neuroinvasive virus

Chapter1: Introduction

1.1 Sindbis virus

One of the most widely spread viruses in Eurasia and Africa is the Sindbis virus (SINV), a zoonotic alphavirus of the *Togaviridae* family. This virus is part of the arthritogenic alphavirus, that can induce chronic arthritis in humans, like the Chikungunya virus and Ross River virus. From the phylogenetic point of view, SINV is an "Old World" virus (accordingly to geographical placement) and belongs to the Western Equine Encephalitis virus complex (WEEV). Notably, SINV is the only Encephalitic alphavirus of the WEEV complex outside America (Adouchief et al., 2016a).

SINV is an enveloped spherical ssRNA-positive virus, of 70 nm in diameter. The capsid is formed by 240 monomers and assumes an icosahedral shape, while the lipid-based envelope is host cell-derived and covered with 80 trimeric spikes consisting of three heterodimers of E1 and E2 glycoproteins. The genome size is 11.7kB and has two open reading frames, generating separate mRNA replicons for 2 types of proteins: 4 nonstructural (NSP1-4) and 5 structural (C, E1, E2, E3 and 6K) (Figure 15) (Strauss et al., 1984; James H Strauss and Strauss, 1994).

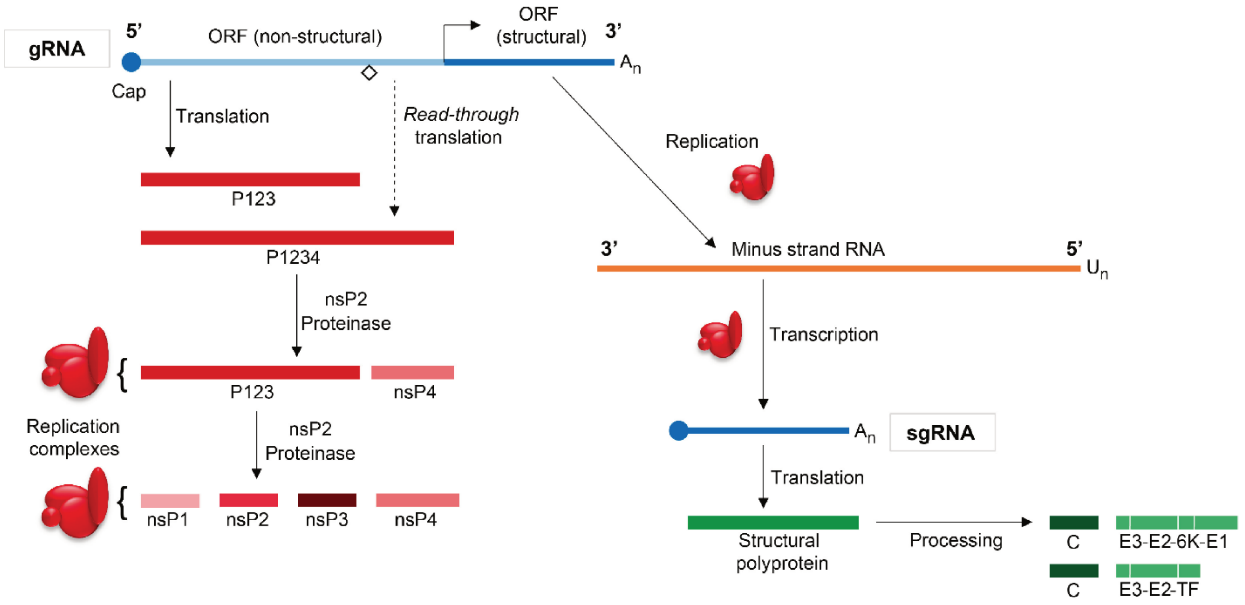

Figure 15: Schematic representation of the synthesis of SINV non-structural and structural proteins.

SINV has two different mRNAs that are translated at different times during infection. SINV genomic RNA (gRNA) codes both for non-structural proteins (nsPs) and structural proteins. The first two thirds of the SINV genome is translated to nsP1–nsP4, which are required for transcription and replication of SINV RNA; the remaining one-third of the genome codes for the viral structural proteins. This subgenomic mRNA (sgRNA) is transcribed from an internal promoter in the minus strand RNA derived from the replication of the gRNA, and is translated to a polyprotein that will be processed to C (capsid)-E3-E2-6K-E1. ORF: open reading frame. ***Source (Carrasco et al., 2018).***

SINV is internalized by clathrin-mediated endocytosis and upon low-ph-mediated fusion the capsid is released in the cytoplasm. After capsid disassembly, the first replication of non-structural polyproteins (nsPS) takes place using the 5' ORF. The structural proteins are produced a second time from the subgenomic 26S unit using the 3' ORF. The USPS forms a replication complex with host proteins and viral RNA. nsP1 has guanine-7-methyltransferase and guanylyl transferase activities, necessary for the capping and methylation of the synthesized genome. nsP2 has on the N-terminal domain helicase and triphosphatase and C-terminal domain protease activity. nsP3 acts as a phosphatase too and, lastly, nsP4 has RNA-dependent RNA-polymerase (RdRP) activity. The nsPs forms a replication complex with host proteins and viral RNA to synthesize full-length minus strand, which will be utilized as a template to produce copies of positive strands RNA and sub-genomic RNA. The structural proteins are transferred as pre-cleaving polyproteins to the Golgi, where furin cleaves the E2-E3 bond. The E1-2-3 heterotrimers interact with the C protein on the plasma membrane, forming an envelope-like structure around the forming nucleocapsid. The emerging capsid pulls with them the newly host-derived envelope, budding from the cells (Figure 16) (Carrasco et al., 2018; Leung et al., 2011).

The viral adhesion proteins (VAPs) and their cell surface receptor are still now well characterized, with scientists proposing laminin and heparan sulfate as two co-receptors for this virus (Adouchief et al., 2016a). Nonetheless, VAPs that could give cell specificity to SINV were suggested in the past years. For example, slc11a2/Nramp2 iron transporter is necessary for infection in drosophila and U2OS (isolated from bone sarcoma) cells, but its role has yet to be confirm on more complex systems(Rose et al., 2011).

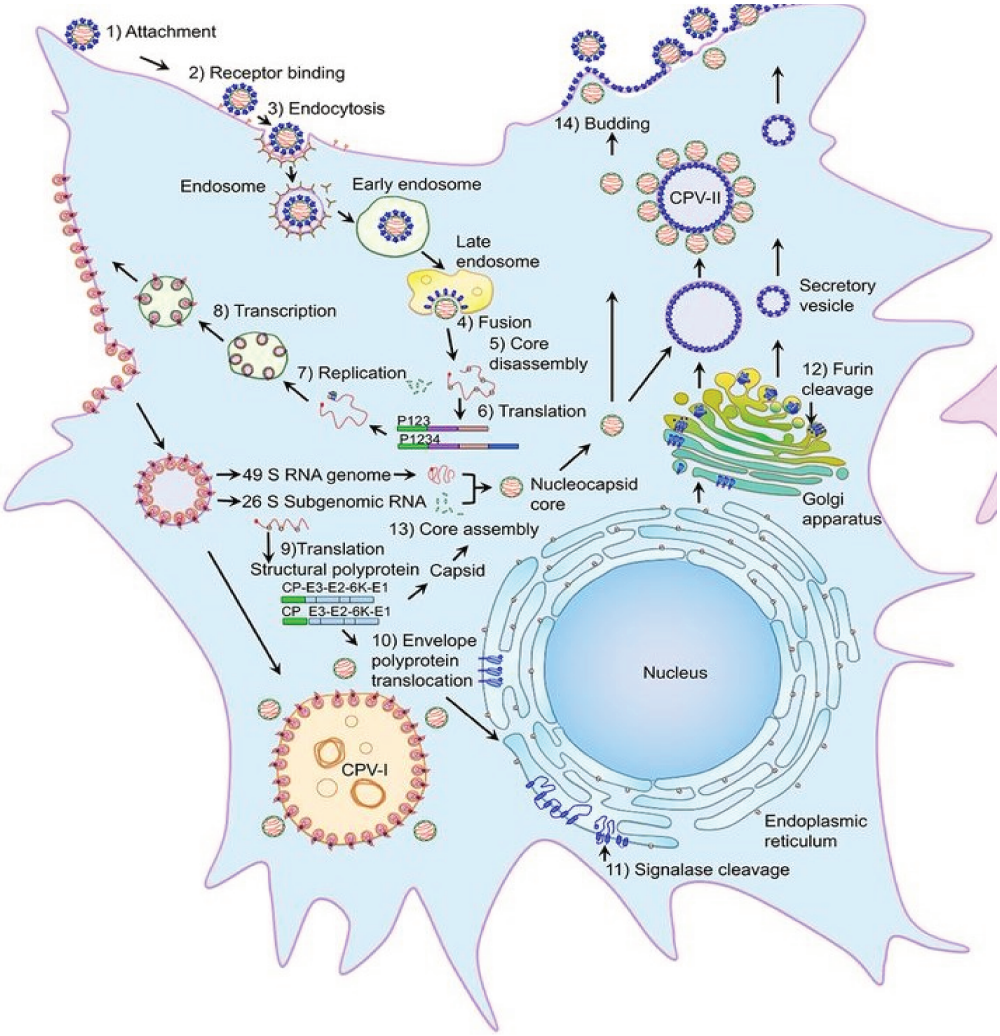

Figure 16: Models of the alphavirus life cycle and the virus-induced structures in mammalian cells.

Following attachment and receptor binding (steps 1 and 2), SINV is internalized by clathrin-mediated endocytosis (step 3). Low-pH-mediated fusion (step 4) in the late endosome releases nucleocapsid (NC), and after disassembly (step 5), nonstructural polyproteins are translated (step 6) from viral mRNA. Replication proteins and host proteins along with the viral RNA form replication complexes (step 7) that replicate and transcribe (step 8) viral RNA and induce spherule structures on endosomal and plasma membranes. Internalization of replication spherules from the plasma membrane via vesicles and subsequent fusion of these vesicles with lysosomes generate CPV-I structures. Structural polyprotein translated from the subgenomic RNA (step 9) is processed into capsid protein (CP), and envelope polyproteins that are translocated (step 10) to the ER, processed by signalase (step 11) and glycosylated and transported through the Golgi complex, where fuin cleavage removes E3 from E2 (step 12) to the PM via the secretory pathway. CP binds genome RNA to form NC (step 13) that binds the glycoprotein spikes on the PM and virus buds from PM (step 14). CPV-II structures that contain glycoprotein spikes and attached NCs originate from the Golgi complex and accumulate in the cells at the late stage of infection. ***Source (Jose et al., 2017).***

The zoonotic cycle of SINV use mosquitos as vector and birds as amplifying hosts, but this virus can infect humans, small marsupials, hamsters and frogs, making its control almost impossible (Al-Khalifa et al., 2007; Bell-Sakyi et al., 2016; Hubálek, 2008; Kostiukov et al., 1981; KOZUCH et al., 1978; Lundström, 1999).

The vector used by SINV is mainly mosquitos from *Culex spp.* and *Aedes spp.,* but recently, in Germany, this virus was isolated in *Anopheles maculipennis* (Ziegler et al., 2019). The wide range of vectors and migratory birds that can be infected allows for the rapid spread of SINV in different continents and global warming is pushing this virus in the rest of Europe (Figure 17). The last outbreak of SINV was in Finland in 1995 with the isolation of more than 1500 patients.

SINV is largely used as a model for viral encephalitis in mice (Sherman' And and Griffin', 1990), but its pathogenesis is still largely not known. Nevertheless, the clinical symptoms in adult humans are characterized. After a mosquito bites the first symptoms appear in four days, with an acute phase resolving in an average of 2 weeks and a hospitalization rate of 6% (Sane et al., 2011). Viremia in SINV infection is low with less than 103 RNA copies/ml, in comparison to 10E9-10E10 RNA copies/ml for chikungunya (Adouchief et al., 2016a).

The acute symptoms include itching rash, fatigue, fever, and headache, with a low percentage of cases with nausea, lymphadenopathy, and dizziness. After a few days, musculoskeletal symptoms start to appear, consisting mainly of joint symptoms (considered hallmarks of SINV disease) and myalgia (considered more common of arthralgia) (Adouchief et al., 2016a; Espmark and Niklasson, 1984). In rare cases, it is possible to observe hemorrhagic fever and viral meningitis, with the latter being more prominent in younger patients (Guard et al., 1982; Laine et al., 2000; Meno et al., 2022).

Myalgia remains a long-lasting symptom up to more than 6 months after infection and the duration of this symptom depends on muscle regeneration. SINV can infect myotubes, myoblast, and connective tissue, inducing tissue necrosis. Interestingly, even after the resolution of muscle infection, the antibody titer remains high for months after the infection, hinting at the possibility of a yet-to-identify viral reservoir in the body (Gylfe et al., 2018; Sane et al., 2012).

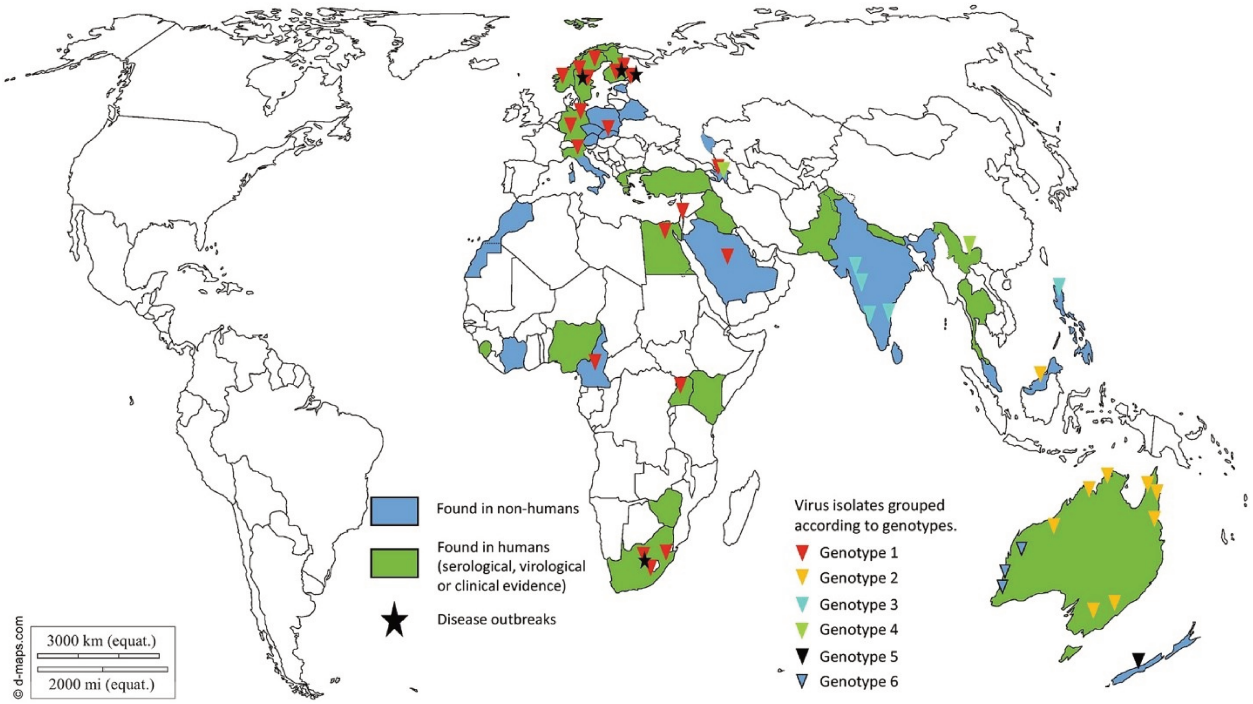

Figure 17: Geographical distribution of SINV.

Regions with serological, virological or clinical evidence of human infections are marked in green. Regions with signs of SINV in non-humans (mosquitoes, birds, etc) are marked in blue. Black stars indicate regions with known disease outbreaks because of SINV infection. Colored triangles indicate virus isolates belonging to genotypes 1 to 6 shown in red, orange, cyan, green, black and blue, respectively. ***Source*** (Adouchief et al., 2016a)**.**

1.2 Introduction to zebrafish CNS

To have a clearer understanding of the following paper, it is necessary to briefly introduce zebrafish larvae' central nervous system (CNS).

Zebrafish CNS comprises the brain and the spinal cord.

Zebrafish brain is very similar in structure to that of other vertebrates and it is divided into 5 regions: telencephalon, diencephalon, mesencephalon, metencephalon, and myelencephalon. Anatomically, the brain can be divided into the forebrain (telencephalon and diencephalon), midbrain (mesencephalon), and hindbrain (metencephalon and myelencephalon) (Figure 18) (Mueller et al., 2016).

In order, the general function of each region is:

- Telencephalon, connected in the anterior part to the olfactory bulb. This region controls vision, olfaction, memory, feeding, and reproductive behavior.
- Diencephalon, composed of epithalamus, thalamus, and hypothalamus. The complete role of this region has yet to be discovered, but in general, it oversees sensory inputs. In comparison to mammals, this region lacks some characteristics in zebrafish, such as a connection to the isocortex (Mueller et al., 2016).
- Mesencephalon, on the dorsal-exterior part there is the optic tectum, further divided into two parallel structures. The optic tectum oversees, vision, as it is connected to the optic nerves originating from each eye. In the ventral-interior part of the mesencephalon, there is the tegmentum.
- Cerebellum, also known as the metencephalon, oversees the movement, coordinating proprioceptive and balance stimuli.
- Myelencephalon, the most caudal part of the brain, from where originates the medulla oblongata, which connects to the spinal cord which is responsible for the autonomic nervous system function (respiration, cardiac and reflexes function).

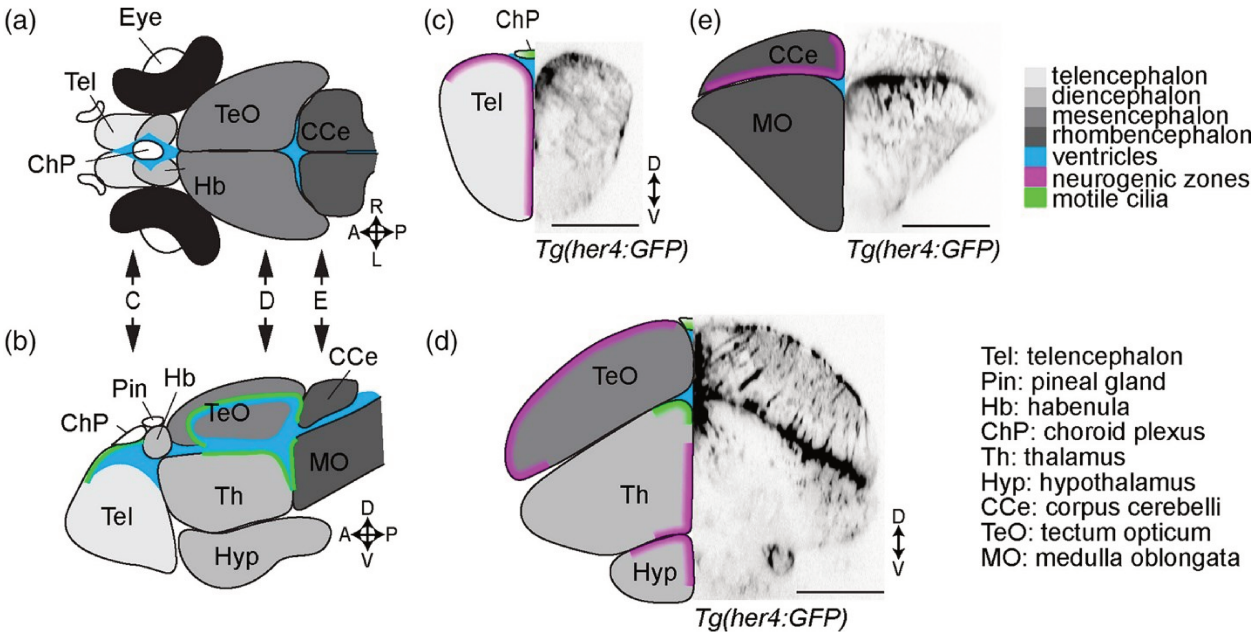

Figure 18: Anatomy of the larval zebrafish brain.

Schematic representation of a 4–5-day-old larval zebrafish brain seen from dorsal (a), lateral (b), or transverse (c–e) views. Brain areas are represented in different shades of grey, ventricles in blue, neurogenic zones in magenta and motile cilia generating CSF flow in green. (c–e) Transverse sections through the telencephalon (c), di−/mesencephalon (d), and rhombencephalon (e) as indicated in panels (a) and (b) show the various brain regions and the distribution of Tg(her4:GFP) positive radial glia (Yeo, Kim, Kim, Huh, & Chitnis, 2007) obtained by confocal microscopy. Note the radial organization of radial glia with their nuclei located along the ventricles and processes reaching the pial surface. A: anterior, P: posterior, D: dorsal, V: ventral, R: right, L: left. Scale bar: 100 µm. ***Source (Jurisch-Yaksi et al., 2020).***

It is important to briefly explain that the brain is protected by a barrier of continuous capillaries and specialized endothelial cells, which takes the name of the blood-brain barrier (BBB). At 3 days post fertilization, the BBB can block high molecular weight dyes over 900 Da; effectively blocking out many pathogens too (Quiñonez-Silvero et al., 2020).

The anatomical structure of the larval zebrafish spinal cord is a meticulously organized framework that underlines its essential role in motor coordination and sensory processing. At the cellular level, the spinal cord is made up of various distinct populations of neurons and glial cells, each contributing to complex neural circuitry (Figure 19). The neurons of the spinal cord are organized into functional domains called segments, which correspond to different regions of the body. These segments are further divided into dorsal, intermediate, and ventral regions, each housing specific neuronal populations responsible for sensory relays, inter-neuronal communication, and motor output. Within segments of the zebrafish spinal cord, highlight the presence of diverse excitatory and inhibitory interneurons, motor neurons, and sensory projection neurons (Cigliola et al., 2020; Goulding, 2009; Lewis and Eisen, 2003; Pedroni and Ampatzis, 2019):

- In the dorsal region we can find sensory neurons that branch on the long somatosensory axons that go from the tip of the tail to the hindbrain, transporting sensory information to the brain.
- In the intermediate region, some interneurons form interspinal circuits necessary to coordinate movement and process sensory reflexes.
- In the ventral region, there are motoneurons and axons transmitting signals from the brain to the periphery.

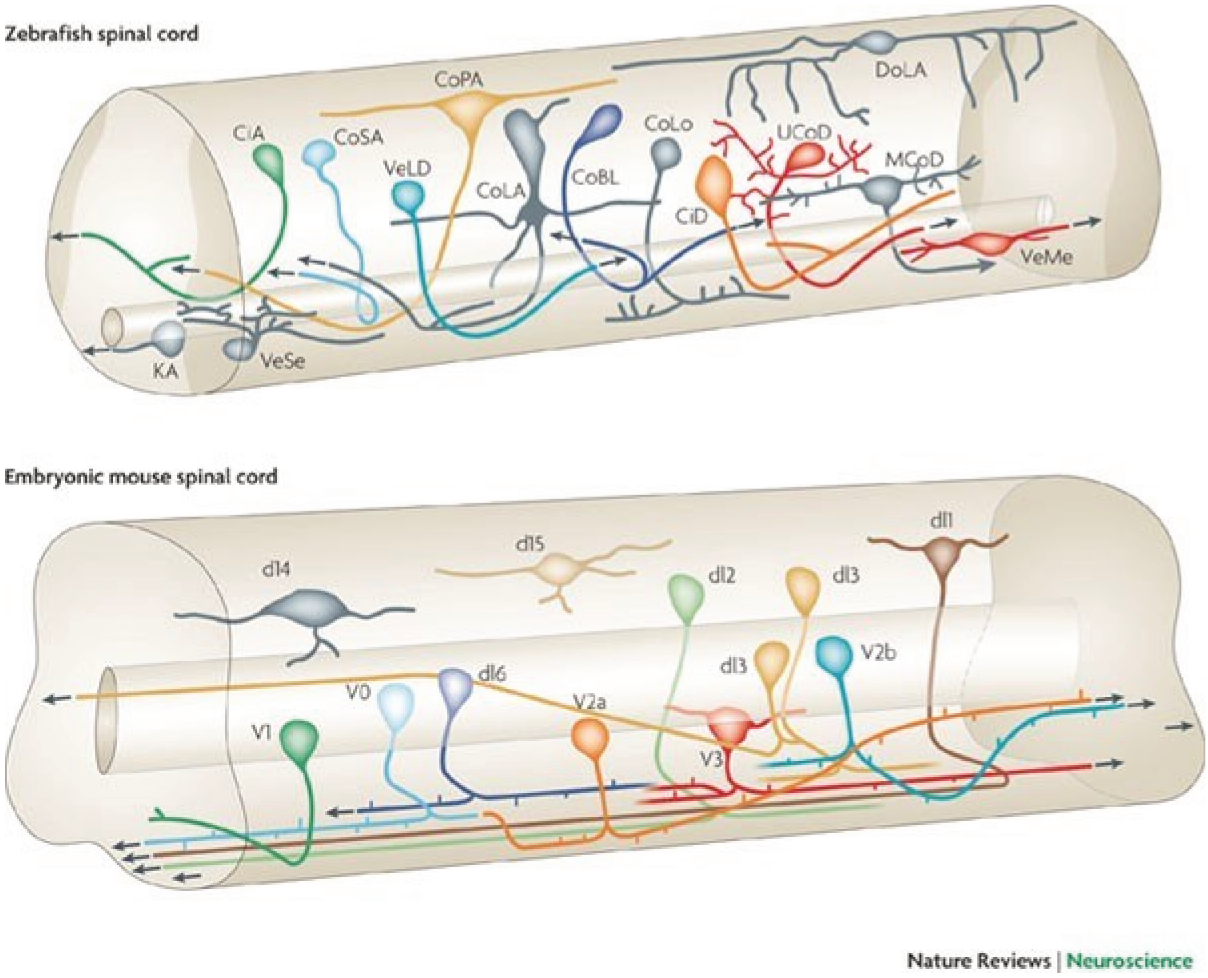

Figure 19: Identified spinal interneurons in the embryonic mouse and zebrafish spinal cord.

Similar neuronal cell types are present in the embryonic spinal cords of aquatic and terrestrial vertebrates. The putative zebrafish homologues of V0, V1, V2 and V3 locomotor interneurons are indicated by the same colour. These include V0 and CoSA neurons (light blue), V1 and CiA neurons (dark green), V2a and CiD neurons (orange), V2b and VeLD neurons (turquoise), and V3, UCoD and VeMe neurons (red). ***Source (Goulding, 2009).***

In addition, the indispensable contribution of glial cells, including astrocytes and oligodendrocytes, to neuronal support, myelination, and synaptic plasticity has been explored (Ackerman and Monk, 2016; Kyritsis et al., 2012). In particular, radial glia plays an important role in brain neurogenesis, modulating neuronal activity and brain homeostasis; functionally overlapping with mammals astrocytes(Jurisch-Yaksi et al., 2020). An important neuronal structure associated with the spinal cord is the dorsal root ganglion, these external sensory neuronal bodies are adjacent to the spinal cord and innervate the musculature of each somite, relaying the sensory stimuli inside the spinal cord. In the spinal cord, the branch and form synapses with interneurons and the dorsal long axon bundles (Figure 20) (An et al., 2002; Honjo et al., 2008; Kaslin and Ganz, 2020; Kelly Kuan et al., 2004).

This complex cellular composition, coupled with the precise organization of spinal cord segments, forms the basis of the intricate neural circuits that orchestrate locomotion, reflexes, and sensory integration in larvae.

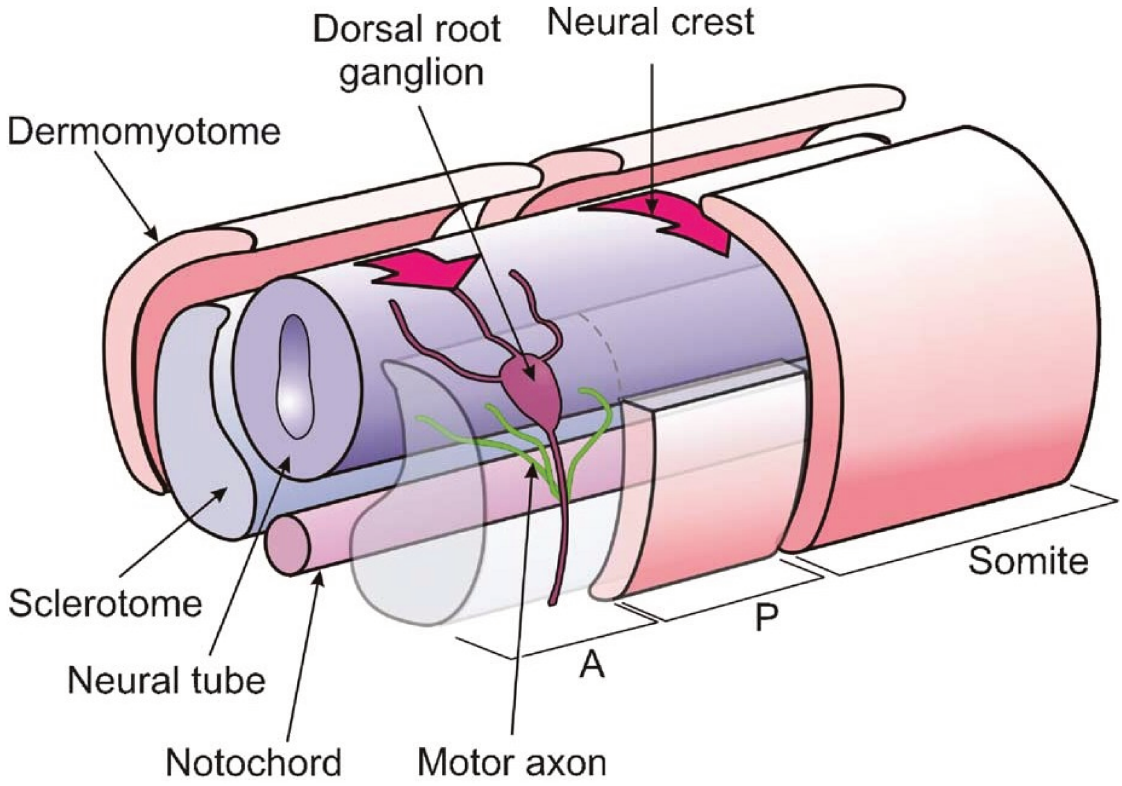

Figure 20: The anatomy of spinal nerve segmentation.

The spatial relationship between the early elements of the developing PNS (migrating neural crest cells and outgrowing motor and sensory axons) and the somite derivatives (dermomyotome and sclerotome) are shown. Most of the dermomyotome is removed from one somite, showing the sclerotome subdivided into anterior (A) and posterior (P) halves, as indicated; the dashed line shows the A/P boundary within the sclerotome (von Ebner's fissure). Neural crest cells and spinal axons grow, and the crest-derived dorsal root ganglion coalesces, within the anterior half- sclerotome. ***Source (Kelly Kuan et al., 2004).***

Chapter 2: Article

CONTENTS

Spatial dynamics of peripheral and central nervous system infection by an interferon-inducing neuroinvasive virus

Valerio Laghi[1], Laurent Boucontet[1], Hannah Wiggett[2], Payel Banerjee[3], Matthieu Simion[3], Ludovico Maggi[1], Sorana Ciura[4], Jérémie Guedj[5], Emma Colucci-Guyon[1]*, Jean-Pierre Levraud[1,2,3]*

1 - Institut Pasteur, Unité Macrophages et Développement, Centre National de la Recherche Scientifique (CNRS), Université Paris-Cité, 75015 Paris, France

2 - Université Paris-Saclay, CNRS UMR9197, Institut Pasteur, Université Paris-Cité, Institut des Neurosciences Paris-Saclay, 91400 Saclay, France

3 - TEFOR-Paris Saclay, Université Paris-Saclay, CNRS UAR2010, 91400 Saclay, France

4 - Université Paris Descartes Hôpital Necker-Enfants Malades, Institut Imagine, 75015 Paris, France

5 - Université de Paris, IAME, INSERM, 75018 Paris, France.

Address correspondence to : Jean-Pierre Levraud, jean-pierre.levraud@pasteur.fr

* E. C.-G. and J.-P. L. contributed equally to this work

Running title : imaging and modelling a neuroinvasive viral infection in zebrafish

Abstract (150 to 200 words)

Organ-to-organ dissemination of viruses is a critical feature of host-virus interactions. In particular, neuroinvasive viruses are able to enter the central nervous systems (CNS), which may result in death or permanent neurological impairment. The complex mechanisms underpinning this spread are poorly understood, as they depend on a variety of parameters, including initial site of entry, route of access to the CNS, and immune responses. To better understand these phenomena, we analyzed the spatial dynamics of Sindbis virus (SINV) dissemination in transparent zebrafish larvae. Using fluorescent reporter viruses, we observed that SINV readily invaded the CNS after inoculation at various peripheral sites. While peripheral infection was transient, CNS infection was persistent and more variable. From the tail muscle, the virus used dorsal root ganglia (DRG) sensory neurons as a gateway to the spinal cord and further propagation to the brain. Within the CNS, viral dissemination resulted both from long-distance axonal transport and short distance shedding. SINV infection induced a strong and rapid type I interferon (IFN) response with a key protective role, systemic in the periphery but localized in the CNS. A mathematical model was built on this quantitative imaging foundation, that provided additional insight on strong differences in IFN responsiveness between periphery and CNS.

Introduction

Invasion of the central nervous system (CNS) is one of the worst possible events during the course of a viral infection (Swanson and McGavern, 2015). This remains relatively rare because the CNS is protected by specialized barriers, notably the blood-brain barrier (BBB); but when it occurs, both the direct viral cytopathic effect and the inflammatory response induced may cause serious damage, often resulting in death or permanent neurological impairment (Venkatesan, 2015).

The complex interplay between the virus and the host response has been studied in a variety of animal models, but their dynamics remain poorly understood, largely because of the difficulty of following these events in the CNS. Mathematical modeling has provided insight in viral infection dynamics, typically relying on repeated blood sampling.

The larva of the zebrafish Danio rerio has recently emerged as a powerful model to study host-pathogen interactions. Its small size and transparency are key advantages; by full-body intravital imaging, using pathogens encoding fluorescent reporter genes, it is possible to follow their organ-to-organ dissemination in real time and at high resolution (David M Tobin et al., 2012). Here, we took advantage of these properties to understand the propagation of a neuroinvasive virus in vivo.

Sindbis virus (SINV) is a single-strand positive RNA virus belonging to genus *Alphavirus*, transmitted by mosquitoes to its natural bird hosts but also sometimes to mammals including humans. While SINV causes only mild symptoms in humans (Adouchief et al., 2016b), other members of this genus include major human pathogens such as chikungunya virus (CHIKV) (J H Strauss and Strauss, 1994a). Several members of this group, such as Eastern Equine Encephalitis Virus and Venezuelan Equine Encephalitis Virus are known to cause fatal encephalitis in humans. While CHIKV was mostly reputed to cause arthralgia and myalgia, the massive breakthrough that occurred in La Reunion Island revealed that it was also encephalitogenic, particularly in newborns (Das et al., 2010). SINV is used to study viral encephalitis in mice; it is generally injected directly in the brain, but in can propagate from the periphery to the CNS in newborns, particularly with strains adapted by multiple intracerebral passages (Lustig et al., 1988). More generally, SINV is well known to infect neurons and it may be used as a tool to label neurons and trace neural circuits (Furuta et al., 2001).

We have previously established that SINV was neuroinvasive in zebrafish larvae, relying on axonal transport, but not on BBB infection or opening, or on macrophage-mediated entry, to gain access to the CNS after peripheral inoculation (Passoni et al., 2017). SINV induced a rapid and strong type I interferon (IFN) response in zebrafish larvae after intravenous (IV) infection; knocking down IFN receptors revealed that this response was protective, preventing rapid death of infected larvae (Boucontet et al., 2018). Nevertheless, we observed that in wild-type larvae, SINV infection persisted or kept progressing in the CNS, in contrast to periphery where it appeared to be transient. Remarkably similar kinetics of IFN induction, and comparable persistence specifically in the CNS, had also been observed in zebrafish infected with CHIKV (Palha et al., 2013), despite a different CNS entry route (Passoni et al., 2017). This lead us to hypothesize that localization of IFN responses may play a key role in organ-specific persistence of CHIKV (Levraud et al., 2014).

To address these issues, we decided to perform detailed and quantitative analyses of SINV propagation from periphery to CNS. Because IV injection result in variable infection patterns, presumably due to stochastic initial infection of a few cells among a very large target pool in the whole body, we tested other injection routes which also systematically resulted in CNS entry, but with a more predictable pattern. Focusing on intramuscular (IM) injections in caudal somites, we observed that infection of peripheral cells was transient, while CNS infection was progressive and more variable. We identified sensory neurons in dorsal root ganglia (DRG) as a major entry way to the spinal cord and observed short- and long-range propagation modes within the CNS. Knocking down IFN receptors resulted in much stronger infection, most notably in periphery where transiency was lost, but also in the CNS. Mathematical modeling indicated that strong differences in IFN responsiveness must exist between periphery and CNS to account for these observations, which was consistent with imaging of IFN reporter zebrafish larvae. This study paves the way for a deeper understanding of the mechanisms at play in pathogen- and host response- mediated neurological damage during viral encephalitis.

Results

Organ to organ propagation of SINV

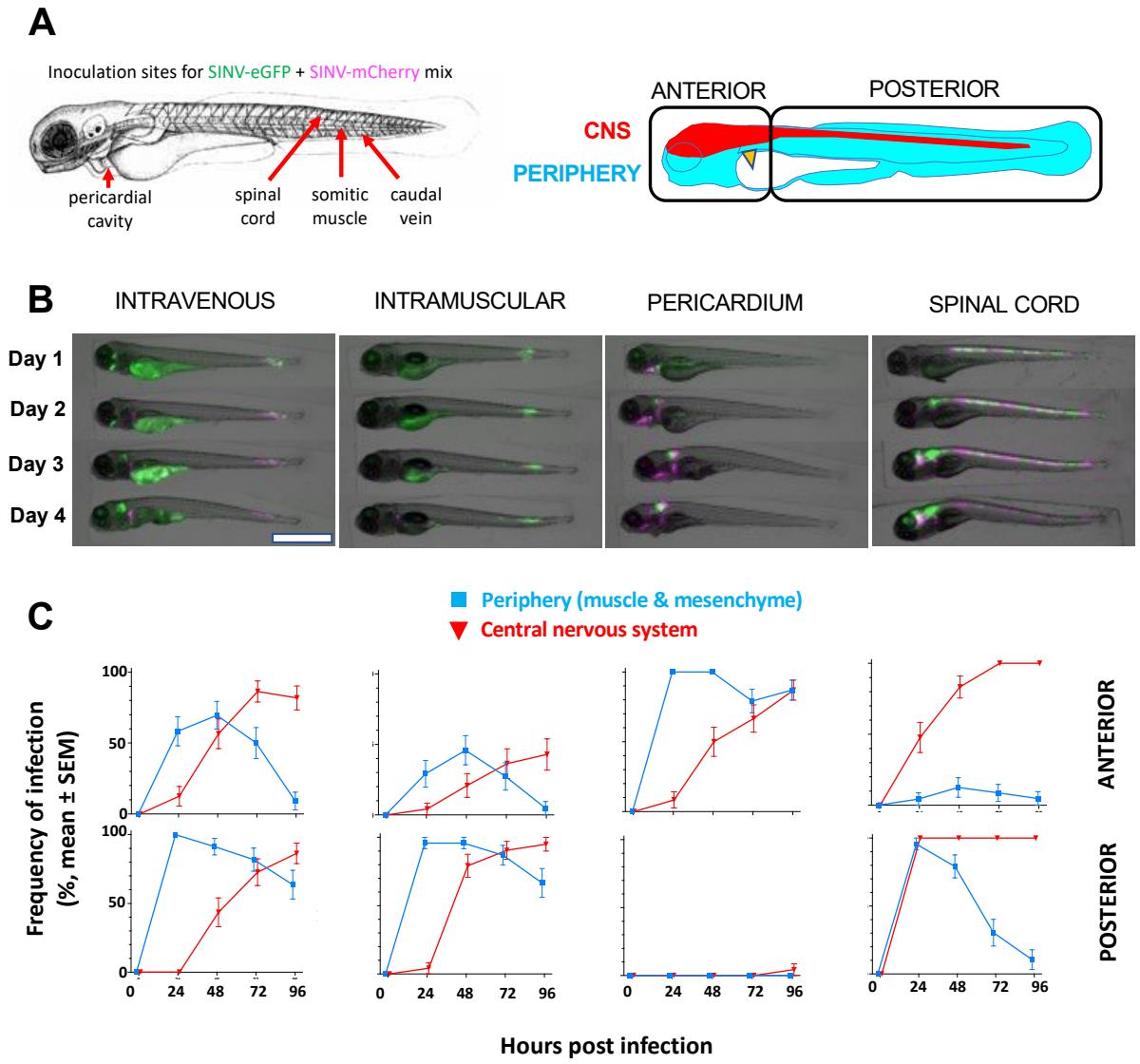

Figure 1: Dynamics of infection associated to different routes of injection.
A) *Scheme of 3dpf zebrafish larva showing routes of injection (LEFT) and compartmentalization of larva for quantification of viral presence frequency patterns inside (red) or outside (cyan) the CNS in anterior or posterior part of the larva (RIGHT). "PC" Pericardial Cavity, "IM" Intramuscular, "IV" Intravenous and "SC" Spinal Cord.* ***B)*** *Representative images of larvae injected in different sites with a mix of SinV:GFP (green) and SinV:mCherry (magenta) strains, and followed for 4 days upon injection.* ***C)*** *Quantification of viral presence frequency patterns relative to different routes of injection divided by anterior (head)/posterior (tail) area and periphery (cyan)/CNS (red) compartments (n=24; 2 independent experiments). Scale bar 1mm.*

To establish a global picture of SINV dissemination in zebrafish larvae, we compared different routes of virus inoculation. We co-injected two viruses encoding eGFP or mCherry with an otherwise identical backbone derived from the pTE3'2J SINV clone, previously established to be a of relatively low virulence in zebrafish (Boucontet et al., 2018; Passoni et al., 2017). The concomitant injection of two colors was used to highlight eventual presence of hierarchical propagation patterns. The virus mix was injected to 3 days post fertilization larvae (dpf), either intravenously (IV), intramuscularly (IM), inside the pericardial cavity, or in the spinal cord (Figure 1A). Intracerebral injection was also attempted but not pursued because of rapid mortality. For each route of injection type, two dozen larvae were followed, split over two independent experiments conducted on different weeks. Fluorescence images of infected larvae were taken daily up to 4 days post injection (dpi) using a widefield microscope at low magnification (Figure 1B), allowing to follow each injected larva over time during the infection.

Images were scored blindly to determine infected organs with either the eGFP or the mCherry virus (Figure 1 - source data 1). To verify that the two viruses are equally infectious, we compared the localization of mCherry and eGFP foci. We did not notice an obvious bias except in the proximal kidney tubule, which we know result from reuptake of fluorescent proteins from the renal filtrate, which are then directed to acidified endosomes in tubule cells (Eshbach and Weisz, 2017) where eGFP but not mCherry fluorescence is quenched; we also routinely observe a comparable signal in uninfected mCherry-expressing transgenic larvae. Thus, this difference in the kidney does not result from infection. We used Fisher's exact test to compare the frequencies of infection by the GFP and mCherry virus in 5 areas for the 4 injection sites and 4 time points (i.e., 80 comparisons) (Figure 1 – supplement 1). We found only 3 cases where the test indicated significantly different frequencies ($p<0.05$); with 80 tests performed, this is what is expected from random fluctuations. Therefore, as expected, the two viral clones display similar tropism and infection dynamics.

		JFG	SCA	FG	Br	Sp	n=	
d1	green	12	21	4	3	0	24	INTRAVENOUS
	red	7	21	1	0	0		
d2	green	13	20	10	11	5	23	
	red	11	18	5	9	7		
d3	green	10	16	8	15	9	22	
	red	7	17	3	11	14		
d4	green	0	7	4	16	*9*	22	
	red	2	12	3	13	*17*		

		JFG	SCA	FG	Br	Sp	n=	
d1	green	24	0	2	2	0	24	PERICARDIUM
	red	21	0	1	0	0		
d2	green	24	0	3	6	0	24	
	red	24	0	4	7	0		
d3	green	*8*	0	2	11	0	24	
	red	*18*	0	4	11	0		
d4	green	*6*	0	1	13	1	23	
	red	*20*	0	4	13	0		

		JFG	SCA	FG	Br	Sp	n=	
d1	green	4	23	1	0	0	24	INTRAMUSCULAR
	red	5	19	0	1	1		
d2	green	7	23	1	2	16	24	
	red	7	21	2	4	12		
d3	green	6	17	3	2	17	22	
	red	2	14	1	7	15		
d4	green	1	10	2	5	17	21	
	red	1	10	1	7	15		

		JFG	SCA	FG	Br	Sp	n=	
d1	green	0	20	0	11	23	23	SPINAL CORD
	red	1	15	0	8	23		
d2	green	0	17	1	18	24	24	
	red	3	12	2	15	24		
d3	green	0	7	0	21	23	23	
	red	2	3	0	22	23		
d4	green	0	2	1	19	21	21	
	red	1	0	0	20	20		

x	blue background (plain)
y	no significant difference
x	yellow background (italics)
y	significant difference

Fisher's exact test

JFG	Jaw, Gill, Facial muscles
SCA	Somites, caudal hematopoietic tissue, dorsal anastomotic zone
FG	facial ganglia
Br	brain
Sp	spinal cord

Figure 1 – supplement 1.

Comparison of frequencies of infection by SINV-GFP and SINV-mCherry in five compartments, at different timepoints, in wild type larvae injected with a mix of 30 PFU SINV:GFP and SINV:mCherry by intravenous, intramuscular, pericardium or spinal cord inoculation. Differences in frequencies were considered to be statistically different for $p<0.05$ using Fisher's exact test.

To compare the infection patterns over time and inoculation route, we tabulated the frequency of infection of 36 different body areas areas, deduced from our low-resolution images (Figure 1 – source data 2) and performed principal component analysis (PCA) of this dataset (Figure 1 – supplement 2A). The two independent replicate groups at a given injection site behaved similarly, indicating that our procedure was reproducible. Spinal cord injected animals were quite separate from other samples. Interestingly, all groups showed a similar trend towards a higher PC1 coordinate value with time, with peripherally injected animals progressively getting closer to spinal cord injected animals. Accordingly, the sites with the highest positive weights in PC1 were the brain and spinal cord regions (Figure 1 – supplement 2B). Thus, this evolution in the PCA plane over time essentially reflects the progressive invasion of the central nervous system by this neuroinvasive virus.

Bloodstream injection (Figure 1B, first row) yielded the broadest pattern of early infection. Tail muscle was often infected, undoubtedly because of the needle having to pass through somite to reach the main tail blood vessels. This is reflected by the close trajectories of IV and IM groups on the PCA graph (Figure 1 – supplement 1B). Positive organs distant from the injection site, and thus likely infected by bloodborne virus, included the liver, jaw, gills, heart, peripheral nerve ganglia, and the conspicuous syncytial yolk cell. Infection of these distant sites was quite variable from larva to larva. Consistent with our initial description of the SINV model in zebrafish (Passoni et al., 2017), infection propagated later to the central nervous system, where it lasted, unlike peripheral infection which was mostly transient. We plotted the frequencies of infection of significant areas of peripheral tissue and CNS in the anterior and posterior regions (Fig 1C) and this trend is observed in both regions.

Intramuscular injections (Figure 1B, second row) resulted in a more localized pattern. Early injection was typically restricted to the injected somite, then propagated to the closest somites (but rarely beyond) and often to nearby fin mesenchyme. Spinal cord infection almost systematically ensued, first at the position slightly anterior to the injected somite, then propagating both anteriorly and posteriorly. Occasional infections were observed in the anterior regions (Figure 1C) presumably because of some leakage of the inoculum into the blood when injecting IM.

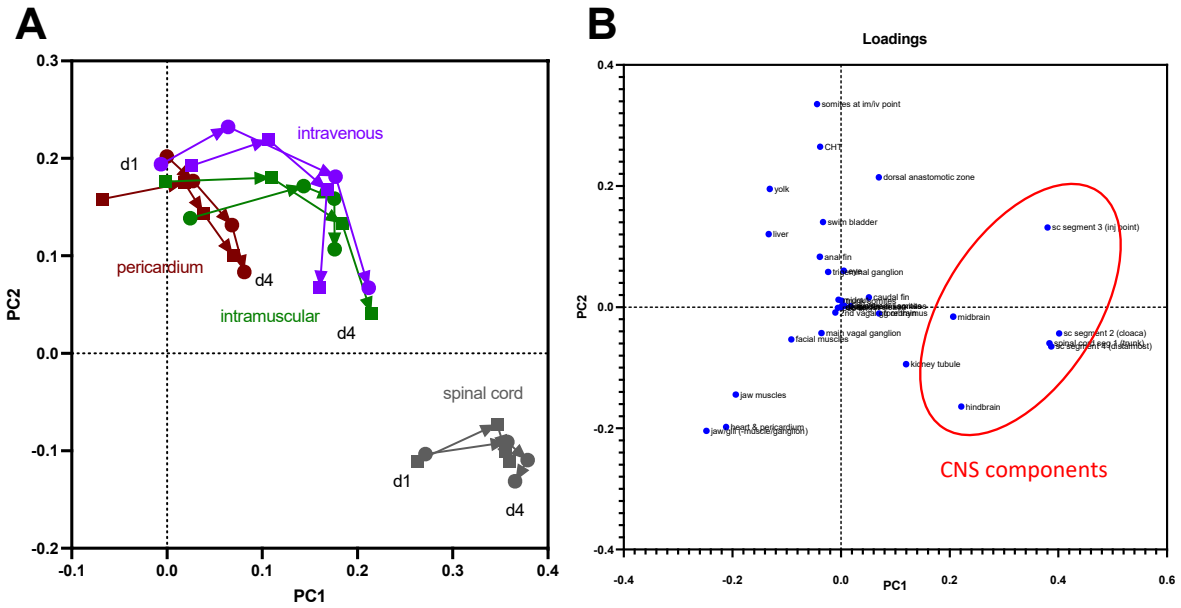

Figure 1 – supplement 2.

A) *Principal component analysis of the frequency table of infection, comparing the different injection sites and the different time points (d1 and d4 correspond to day 1 and 4 post inoculation; arrows show time progression for a given group of larvae; intermediate days not shown for clarity) . The two independently injected groups for each site were treated separately to assess reproducibility.* ***B)*** *table of weights (loadings) of each body region in the PCA analysis. The red oval contains CNS regions.*

Pericardial cavity injections (Figure 1B, third row) also resulted in a reproducible pattern. Heart, gill, and jaw mesenchyme were infected early, as well as mandibular muscles. Infection then propagated to the hindbrain. Remarkably, infection was never observed in the posterior region (Figure 1C).

Spinal cord injections (Figure 1B, fourth row) resulted in early infection of entire segments of the spinal cord, which then propagated to the rest of the spinal cord, hindbrain, and rest of the brain. Some tail muscle infection was also observed at early times; we interpret this as a primary event because the needle had to pass through muscle to reach the spinal cord. By contrast, almost no infection of anterior peripheral regions was observed (Figure 1C).

A striking mutual exclusion of the eGFP and mCherry positive cell patches was observed in spinal cord injected larvae (Figure 1B). On closer examination, it was also systematically observed at other sites with all injections. The only cell for which we observed unquestionable co-infection by SINV-GFP and SINV-mCherry was the syncitial yolk cell (in 6/24 IV-injected and 5/24 IM-injected larvae).

Infections near the injection site almost always included both eGFP and mCherry positive cells; by contrast, infected patches appearing at a distant site (except yolk) were typically single-colored, indicating initial seeding by a single virion.

A bottleneck effect was also observed for neuro invasion events: among 20 IM-injected larvae with clear dual color initial muscle infection, 12 later displayed dual-color and 7 single-color invasion of the spinal cord; while among 24 pericardium-injected larvae with dual color infection of the jaw/gill area, 7 later had a dual-color infected brain and 15 a single-color infected brain. Assuming that multiple instances of BBB crossing occur independently from each other, we can calculate using Poisson's law (Figure 1 – supplement 3) that there are ~3 events of successful CNS entry (range, 1.7 to 4.4) after IM injection and ~2 such events (range, 1.2 to 2.6) after pericardial injection.

In the tail, infection of caudal muscles preceded invasion of spinal cord, while anteriorly, infection of facial/jaw muscles preceded hindbrain invasion , which was consistent with the axonal transport of SINV we had established previously (Passoni et al., 2017). For the rest of the study, we decided to focus on IM tail injections because of its clear pattern of muscle to spinal cord propagation, relative thinness of the infected region facilitating imaging, and relevance for entry route of this mosquito-transmitted virus.

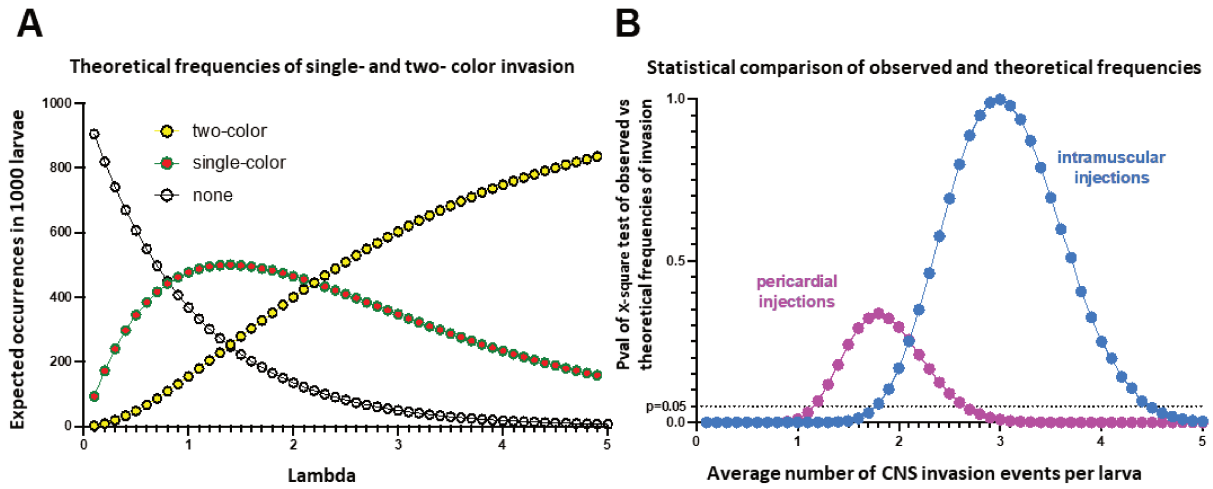

231

232 **Figure 1 – supplement 3**

233 ***A)*** *The number of separate events that resulted in successful invasion of the CNS by SINV was*
234 *estimated under the assumption that these events were random and independent of each other.*
235 *According to Poisson's distribution, if a random event happens in average λ times per trial over a*
236 *large number of trials, then the probability of that event not happening at all for any single trial is*
237 $e^{-\lambda}$*. Considering that the GFP and mCherry viruses are equally invasive, if CNS invasion occurs*
238 *in average λ times per larva, then it will occur λ/2 times for one given color, and absence of*
239 *invasion by that color has a probability of* $e^{-\lambda/2}$ *per larva. Thus, the probability of no invasion at*
240 *all is* $e^{-\lambda}$*, that of invasion with any single color would be* $2*(e^{-\lambda} - e^{-\lambda/2})$*, and that of two-color*
241 *invasion is* $1 - e^{-\lambda} - 2(e^{-\lambda} - e^{-\lambda/2})$*. We deduced from these probabilities the expected occurrences of*
242 *two-color invasion, single-color invasion, and lack of invasion for a large number of larvae*
243 *(n=1000) with a range of values of λ from 0.1 to 5 (with 0.1 increments).* ***B)*** We then compared
244 these frequencies with our observational data using χ-square tests. The range of likely values of λ
245 was that for which the observational and theoretical values were not statistically different (p>0.05).

246

247

248

249

Sensory and motor neurons contribute to spinal cord invasion

In our earlier work (Passoni 2017), we had already noted that infection of muscle fibers was followed by infection of neurons that innervate this somite. Here, we analyzed these events in greater detail by inoculating SINV-mCherry to Tg(*elavl3*:GFP) (also known as *HuC*:GFP) reporter zebrafish, labelling all neurons, or Tg(*vsx2*:GFP) (also known as *axl1*:GFP), labelling many interneurons. Time-lapse imaging by confocal microscopy detected the first infected cells at ~7 hours post-injection (6.86±0.38 hours, mean±SD, n=7 larvae). During the first 24 hours, infection progressed in the periphery (Figure 2A; movie S1); infected cells prominently included muscle fibers but also numerous stromal cells between myotomes (in myoseptum and myocommata), in the caudal hematopoietic areas, in the conjunctive tissue dorsal to the somites (Figure 2A, top row, movie S1), and sometimes in fin mesenchyme (Figure 2B, movie S2).

During the second day pi, infection largely stalled in the periphery (Figure 2A, bottom row; movie S3). Interestingly, movement of bright mCherry specks was often observed, suggesting that fragments of dead infected cells had been phagocytosed by a wandering leukocyte (movie S3). By contrast, infection started to be detectable in the spinal cord. When a neuron got infected, we first observed fluorescence in its soma, and labelling of its axon a few hours later, as expected for a soluble fluorescent protein produced in the soma. The first visibly virus-fluorescent axons invariably innervated the infected muscle area, suggesting that this axon had carried the virus to the spinal cord a few hours earlier (Figures 2B, C).

The somitic muscle is innervated by motor and by sensory neurons. To identify which neuron subtype was infected first, we performed time-lapse imaging of the infection using the motoneuron reporter line Tg(*mnx1*:GFP) infected with SINV-mCherry. We could identify the first neurons becoming infected, first by their soma becoming mCherry-positive and a few hours later by their axons being labelled. Figure 2C and movie S4 show infection of neuron that became just visible at 24 hpi, at the start of the timelapse. Three hours later, its axon was visibly labelled; as expected, it innervated the infected ventral trunk area. This axon ran close but distinct from that of the GFP+ motor neurons, and 3D reconstruction (movie S5) indicated that the soma of this axon was located lateral to the spinal cord, in a dorsal root ganglion (DRG). Thus, in this case, the first infected neuron was a sensory DRG neuron.

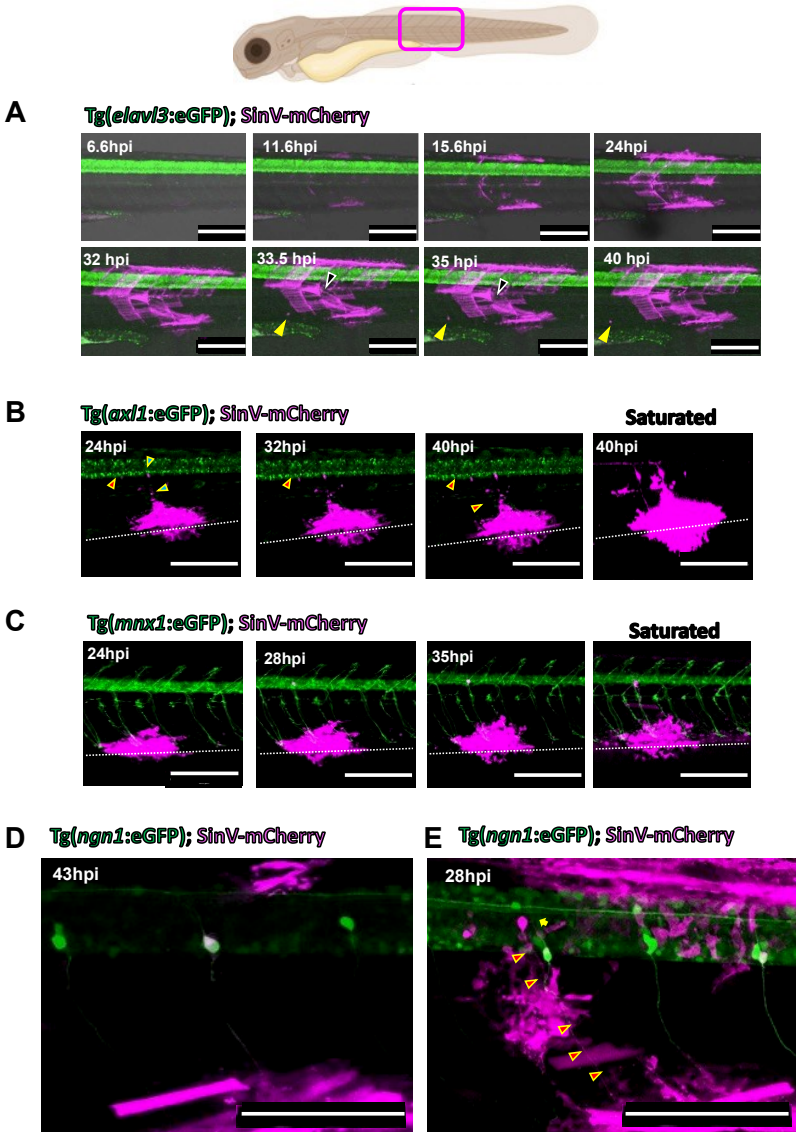

Figure 2: Timelapse imaging after IM inoculation of SINV, showing infection of the somite and identification of the first infected neurons.

Confocal in vivo imaging of zebrafish larvae expressing GFP transgenes (green) infected IM with SINV:mCherry (magenta), maximal projections. ***A)*** *Selected time-points from timelapse of Tg(elav3:GFP) larvae showing somite infection developing during the first and second days. Note that top and bottom rows correspond to two different larvae. Yellow arrowheads point to a wandering leucocyte containing fluorescent material. Black arrow points to a dying muscle fiber.* ***B)*** *Selected time-points from in vivo timelapse of a Tg(axl1:GFP) larva showing infected neurons innervating the infected zone in the ventral somite. Green-filled arrowheads point to an infected neuron with its axon already labelled by mCherry at start of timelapse; red-filled arrowhead point to another neuron with its axon becoming visibly labelled only later. The dotted line indicates the boundary between the trunk and the ventral fin.* ***C)*** *Selected time-points from in vivo timelapse of an infected Tg(mnx1:GFP) larva, revealing that the first infected neuron is not a motoneuron as its axon is not labelled by GFP.* ***D,E)*** *Confocal images of infected Tg(ngn1:GFP), showing infection of a DRG sensory neuron (D) and of a motor neuron (E). Scale Bar, 200µm in A-C, 100µm in D-E.*

To directly visualize infection of sensory DRG neurons, we inoculated SINV-mCherry into Tg(*ngn1*:GFP) fish, in which these cells are strongly labelled. We confirmed that a DRG sensory neuron often became infected before spinal neurons (Figure 2D; movie S6). In at least one case, however, when starting the time-lapse at 25 hpi, the most heavily infected neuron was clearly a motoneuron (Figure 2E), movie S7); a DRG sensory neuron was also infected, but its axon, unlike the axon of the infected motoneuron, was not mCherry-positive, indicating it had been infected later. Thus, both sensory and motor neurons may be the first infected neuron mediating SINV entry to the CNS.

Overall, our data suggest that CNS entry may be slightly more frequent via sensory neurons than via motoneurons; indeed, from our timelapse movie series, we observed that, at 24 hpi, one or more DRG neuron was already infected in 6 out of 8 fish, while one or more motoneuron was infected in 4 out of 8 fish. Considering that our statistical analysis from 2-color virus IM injections revealed 3 independent CNS entry events on average, entry in the spinal cord may be mediated by both muscle-innervating neuronal subtypes in a given fish.

Short- and long-range dissemination of SINV within the spinal cord

We then examined how the infection propagates inside the CNS. We hypothesized that the virus could propagate either to its direct neighbors after budding from the soma or to distant cells using axon-mediated travel. Our high-resolution time-lapses revealed both short- and long-distance dissemination in the spinal cord. In one case (Figure 3A, Movie S8) starting at 24 hpi we initially see an infected motoneuron (magenta arrow) and, 50µm rostrally, three infected neurons close to each other (green arrow). In a few hours, we can detect a group of newly infected neurons surrounding this latter cluster (yellow arrows), as well as an isolated neuron 100µm upstream (cyan arrow), with a few immediate neighbours becoming fluorescent later (blue arrow). By 38hpi, axons that connect the long-distance clusters became visibly fluorescent. Secondarily infected neurons were observed in all zones of the spinal cord without an obvious preference and included some *axl1*+ interneurons (not shown).

This axon-mediated propagation could span very long distances, as seen on fig 3B, where we see the appearance of infected cells in the hindbrain between 82 and 96hpi, more than one millimeter away from the entry site in the spinal cord. Such a propagation to the brain was however not systematic; the larva shown in 3C, injected on the same day as the one in 3B, had a stronger and locally increasing spinal cord infection, but it did not propagate to the brain.

Long spinal axons labelled by the virus reporter could be detected either in the dorsal or the ventral spine (Figure 3D), suggesting that long distance propagation is mediated either by sensory or motor pathways.

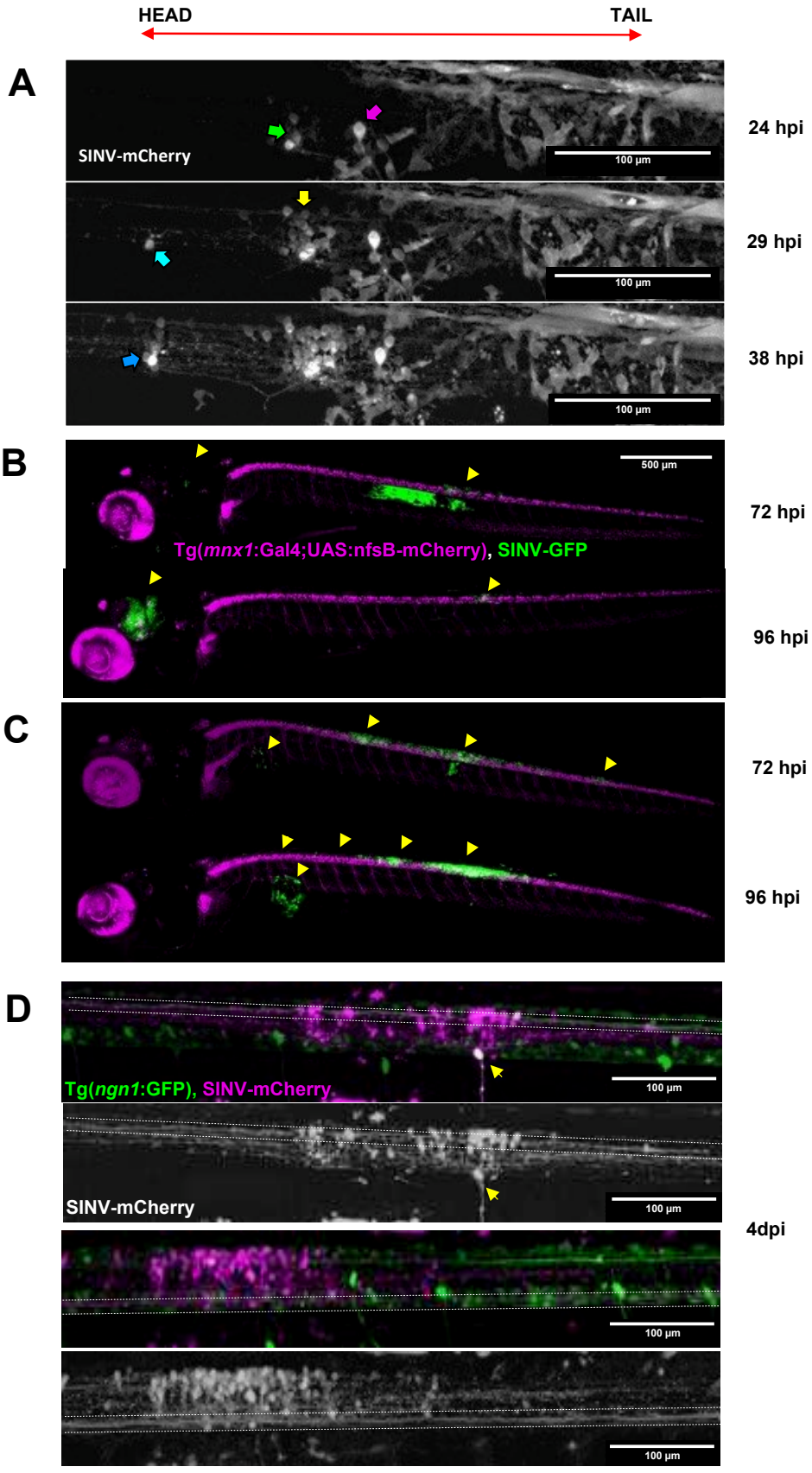
HEAD
TAIL
A
SINV-mCherry
100 µm
24 hpi
100 µm
29 hpi
100 µm
38 hpi
B
500 µm
Tg(mnx1:Gal4;UAS:nfsB-mCherry), SINV-GFP
72 hpi
96 hpi
C
72 hpi
96 hpi
D
Tg(ngn1:GFP), SINV-mCherry
100 µm
SINV-mCherry
100 µm
4dpi
100 µm
100 µm

336

Figure 3: Propagation of SINV within the CNS.

A*) Progression of SINV infection in the spinal cord, confocal timelapse (40x objective) Tg(ngn1:GFP) (GFP not shown, see movie S7 for uncropped two-color images) infected IM with SinV: mcherry, mCherry shown in grayscales. Neurons already infected at onset of the timelapse are shown with a magenta arrow (motoneuron) and green arrow (three neurons inside the cord). As infection progresses, a distant rostral neuron becomes infected (cyan arrow), while more neurons also become infected in the close vicinity of previous ones (yellow and blue arrows).* ***B,C)*** *Time points from confocal acquisition (10x objective) of Tg(mnx1:gal4; UAS:nfsB-mCherry), in magenta, infected with SinV:GFP (green). Arrows indicates infected cells: B) Long distance dissemination of SinV in absence of intermediate clusters between first point of entry in the spinal cord and brain secondary infection C) Short distance dissemination of SinV by clustering from primary point of entry in the spinal cord and secondary cluster in direction of the brain.* ***D)*** *Confocal images (40x objective) of infected long somatosensory axons connecting brain and periphery of Tg(ngn1:GFP) infected Intramuscularly with 30 PFU SinV:mCherry (magenta). Arrows indicates infected DRGs and dotted line delimit respectively dorsal somatosensory long axons (Top) and ventral somatosensory long axons (Bottom). Black and white images shows only the SinV:mCherry channel. Between dotted lines: infection of dorsal (top) and ventral (bottom) long somatosensory axon bundle. Yellow arrow: infected DRG.. Scale bar highlight as they ar not visible on the panels*

Death of infected sensory neurons

Although we imaged hundreds of infected neurons in our time-lapse experiments, their death was rarely observed and, because of considerable interindividual variability it was not possible to infer a post-infection survival time. Death of infected DRG sensory neurons was repeatedly seen, however (see below). In addition, since DRG neurons have a stereotypical distribution and are easy to count in the Tg(*ngn1*:GFP) transgenic fish, we observed that when we started imaging IM-injected fish at 48 hpi or later, some DRG neurons were typically already missing at the level of the initial injection (1.57±0.90 at 72 hpi, n=7). Thus, infected DRG sensory neurons probably survive infection for a shorter time than spinal neurons.

Interestingly, when an infected DRG neuron dies, its synaptic connections may survive it briefly. By timelapse imaging of Tg(*ngn1*:GFP) larva infected with SINV-mCherry, we observed a dorsal spinal axon decorated with double-labeled speckles, upstream and 120µm downstream of an infected DRG neuron. This is consistent with the typical size and T-shape of the spinal axon tract of DRG neurons (Bernhardt et al., 1990), and we interpret these speckles as synapses of this infected DRG neuron onto the ascending somatosensory tract. The abrupt death of the neuron coincided with the disappearance of the rostral-most speckle, and shortly followed by progressive loss of other speckles, with the 7 caudal-most ones disappearing synchronously about 1 hour after the soma (figure 3 - supplement 1; movie S9).

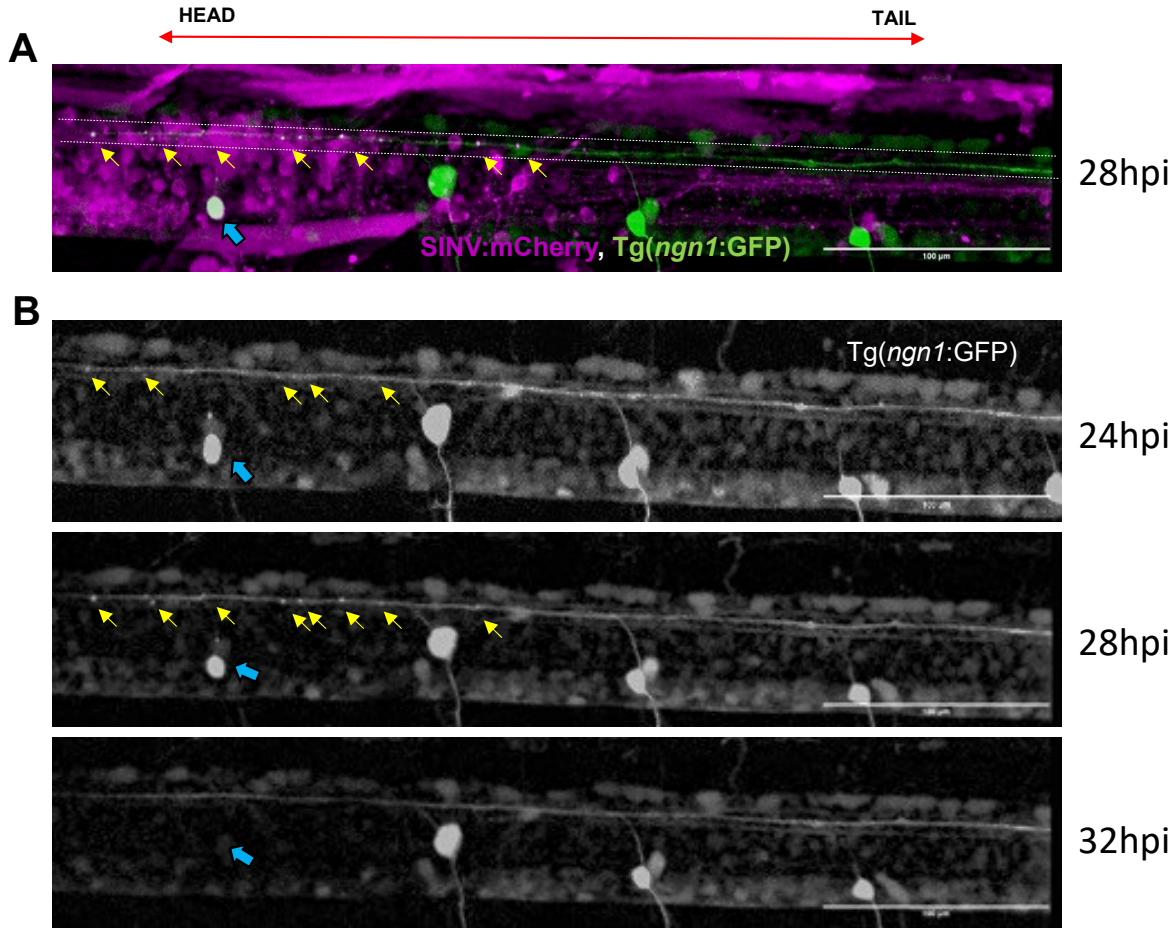

Figure 3 – supplement 1. ***Death of an infected DRG neuron.***

Confocal imaging (40x objective), maximal projection of Tg(ngn1:GFP) larvae infected IM with SINV:mCherry (magenta), derived from movie S9. ***A)*** *Superposition of the two channels, with long dorsal axons between dotted lines, yellow arrows indicating speckles and cyan arrow indicating infected DRG neuron.* ***B)*** *Selected time points of solely GFP channel. Long dorsal axons between dotted lines, yellow arrows indicating speckles and cyan arrow indicating infected.*

Entry via sensory neurons favours brain infection

To functionally test for the relative role of motor and sensory neurons in spinal cord invasion, we performed depletion experiments (Figure 4). DRG neurons were prevented from differentiating from neural crest by injecting in eggs an antisense morpholino targeting the *erbb3b* transcripts (Dooley et al., 2013) (Figure 4A-D). Motor neurons were transiently depleted by a chemogenetic approach, treating Tg(*mnx1*:gal4 ; *UAS*:nfsB-mCherry) larvae with metronidazole (MZ) prior to infection (Davison et al., 2007) (Figure 4E-H). After infection by SINV, spinal cord was invaded in all groups (Fig 4B,F), consistent with the notion that both sensory and motor neurons may carry the virus from periphery to CNS. One notable difference, however, was that propagation of the infection to the brain was rarer in DRG-depleted animals, while its frequency was unchanged in MN-depleted ones (Figure 4CG). Thus, the sensory neuron route appears to provide a privileged way to reach the hindbrain.

Unexpectedly, somite infection was more persistent in DRG-depleted, but not MN-depleted larvae (Figure 4D,H).

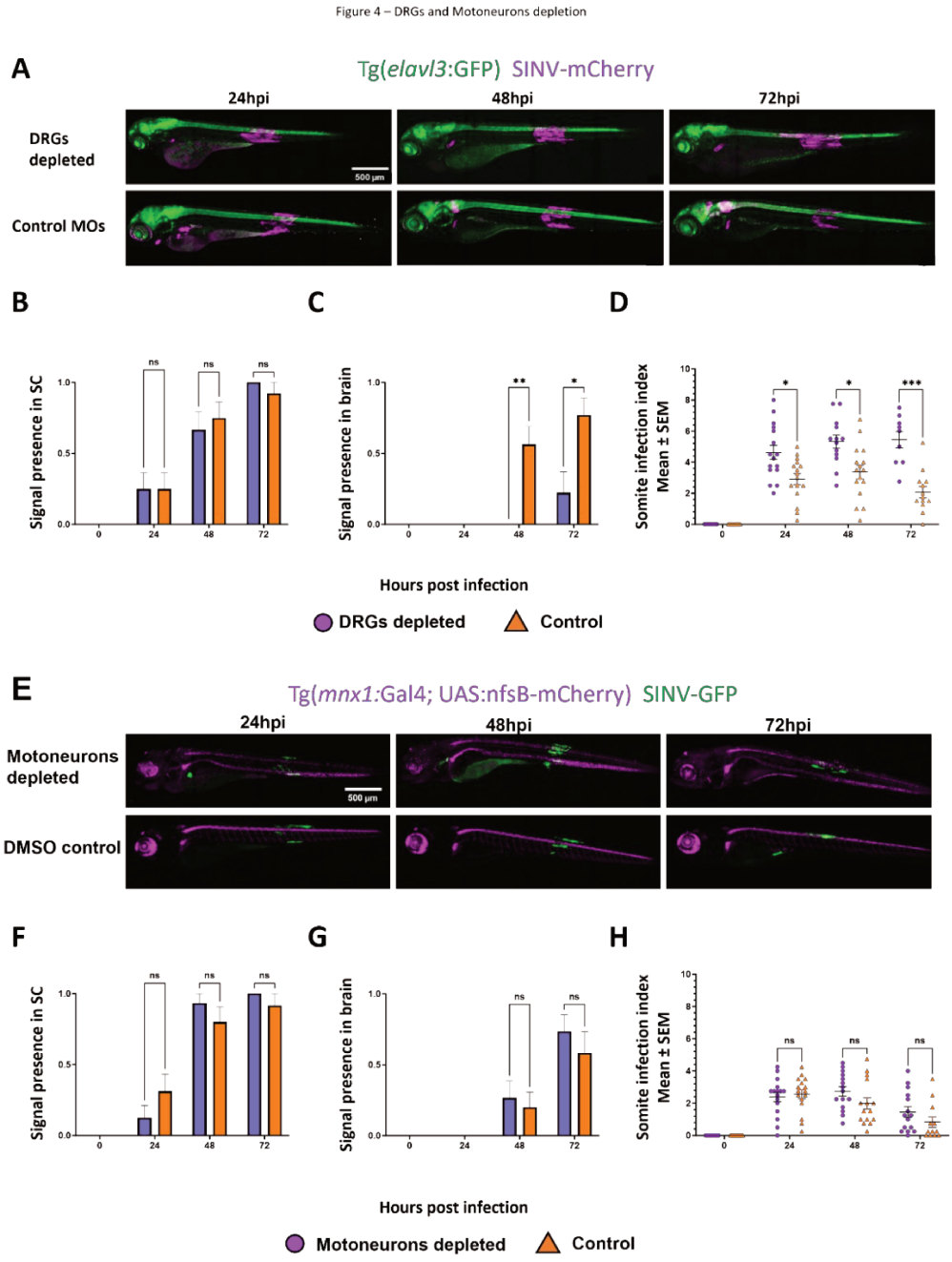

Figure 4: Impact of depletion of motor or sensory neurons on SINV infection.
A) *Maximum projection of confocal images of Tg(evlav3:GFP) (green) infected IM with SinV:mCherry (magenta) with DRG depleted by erbb3b morpholino treatment.* ***B-C)*** *Frequencies of spinal cord and of brain infection and* ***C)*** *Quantification of somite infection in DRG-depleted larvae followed over 3 days (n=16, 2 independent experiments).* ***D)*** *Maximum projection of confocal images of Tg(mnx:Gal4, UAS:nfsB-mCherry) IM with SINV:GFP with motoneurons depleted by metronidazole treatment.* ***F-G)*** *Frequencies of spinal cord and of brain infection and* ***H)*** *Quantification of somite infection in motoneuron-depleted larvae followed over 3 days (n=16, 2 independent experiments). (***P < 0.001; **P < 0.01; *P < 0.05; ns - not significant)*

SINV induces a strong IFN response, associated with transient peripheral infection

After this qualitative analysis, we performed quantitative measurements of infection dynamics after IM inoculation.

First we performed qRT-PCR on whole larval lysates to measure the expression of viral and host genes. Strong expression of viral transcripts was measured at 24 hpi, remained stable at 48 hpi; a stronger dispersion was observed at 72 hpi, with a ~10 fold decrease in most animals but no decrease in a few others (Figure 5A). A strong type I IFN response was induced, with a sustained *ifnphi1* induction (Figure 5B) but transient *ifnphi3* induction (Figure 5C). Accordingly, MXA, which as an ISG can be induced by both IFNϕ1 and IFNϕ3 (Aggad et al., 2009), was induced in a strong, sustained manner (Figure 5D).

After this whole-body analysis, to distinguish the dynamics of infection in periphery from CNS, we designed a semi-automatic 2D image analysis pipeline (Figure 5E; see methods). By segmenting the virus-encoded fluorescence signal from areas corresponding to CNS (spinal cord and brain) and periphery (rest of the body, excluding yolk and eyes), we quantified the extent of infection in these two compartments over time (Figure 5F). We verified that the data generated buy this image analysis pipeline fitted with qPCR-based quantification by infecting larvae for one to three days and imaging them before lysis and RNA extraction; the sum of periphery+CNS positive pixels was remarkably well correlated with SINV-E1 transcripts quantification in the whole larva (Figure 5 supplement 1).

As expected from our initial qualitative analysis (Figure 1), infection in periphery was quantitatively transient, with a peak of fluorescence around 36 hpi, while infection in the CNS started later and increased until 4 dpi, tha latest point analyzed. Interestingly, the variance of the signal in the periphery was relatively low during the whole time-course, while it greatly increased with time in the CNS. This reflects a strong heterogeneity in individual courses of infection of the CNS (Figure 5F), with some fish that appeared to control the infection while it exploded in other ones.

In conclusion, infection in the periphery is transient and consistent among individuals, with a peak at around 36 hpi; by contrast, CNS infection is progressive but also much more variable.

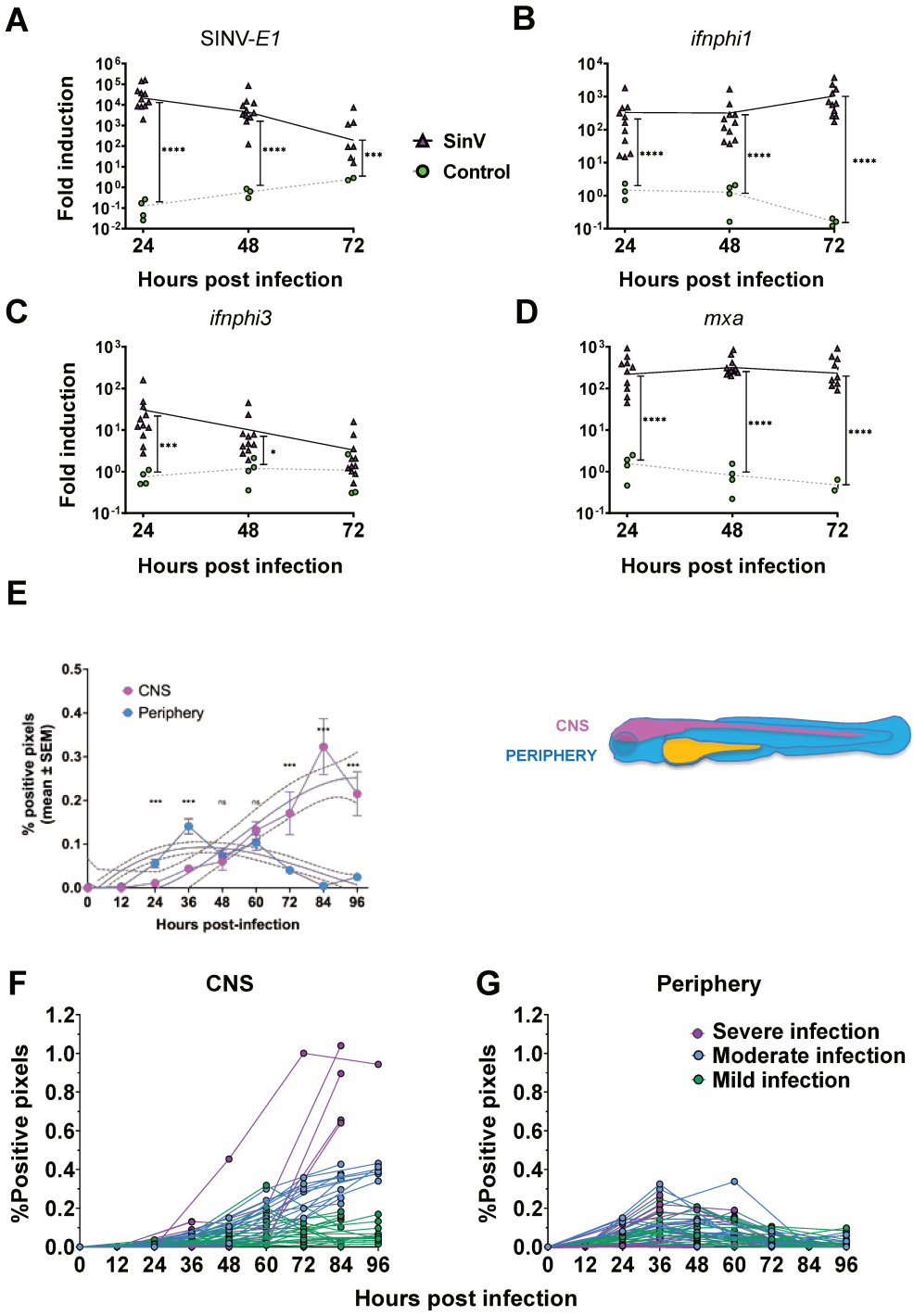

Figure 5: Kinetics of host response and SINV infection in wt larvae.

A-D) *Real time quantification of genes expression of SINV-E1, infphi1, ifnphi3 and mxa of WT zebrafish larvae infected with SINV-GFP or SINV-mCherry IM and sampled every 24 hours (n=12, 2 independent experiments pooled)* ***E-G)*** *Pixel quantification of SINV-GFP signal percentage in CNS (Magenta) or periphery (Cyan) in WT larvae imaged every 24 hours (n=48, 4 independent experiments). E: collated values with polynomial interpolation and 95% confidence interval; F and G: individual trajectories (***P < 0.001; **P < 0.01; *P < 0.05; not shown - not significant)*

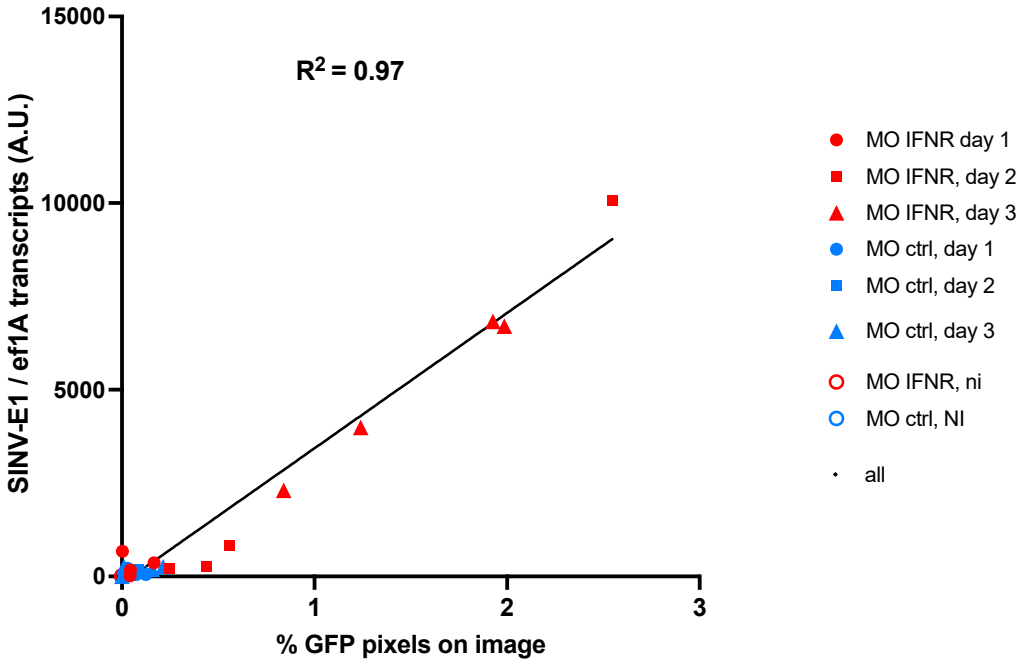

Figure 5 supplement 1. *Correlation of qRT-PCR and image quantification*

N=23 infected fish + 6 uninfected. Red color indicates IFNs KD larvae and blue color control morpholino injected larvae and different shape (round, square or triangle) represents different dpi. The Y axis is relative to RT-qPCR quantification of SINV-E1 gene and X axis is relative to image analysis quantification of percentage of positive area for SINV-GFP.

Type I IFN response is systemic in periphery but largely restricted to myeloid cells in CNS

To better understand this difference between peripheral and CNS compartments, we imaged IFN response reporter larvae infected with SINV. Tg(*MXA*:mCherry) inoculated with SINV-GFP displayed strongly elevated overall mCherry fluorescence (Figure 6A,B), with a 24h-delay relative to endogenous *MXA* expression (Figure 5D) as previously observed with other reporter transgenes (Palha et al., 2013). Virtual sectioning (Figure 6C) revealed that the *MXA*:mCherry transgene was highly induced in all gut, liver and skin. However, in the spinal cord, only a few positive cells are detected, always in the vicinity of infected neurons but distinct from them. Therefore, response to IFN is systemic in peripheral epithelia but seems to be restricted to a few cells in the spinal cord. Similarly, imaging of Tg(*ifnphi1*:mCherry) reporter fish revealed very few positive cells inside the spinal cord, despite a clear increase of mCherry positive leukocytes at the site of peripheral infection and, to a lesser extent in the entire body (Figure 6 supplement 1). Time-lapse imaging of scattered MXA or ifnphi1-reporter positive cells in the periphery or in the spinal cord revealed that positive cells were mobile (not shown). Thus, we imaged macrophage reporter fish Tg(*mfap4*:mCherry). While we could not detect microglia or macrophages inside the spinal cord of uninfected larvae, a few mCherry positive cells were observed in proximity to infected spinal cord areas. Using time-lapse, we even could image macrophages entering the spinal cord, with a directionality towards the infected segments (Movie S10, Figure 6D).

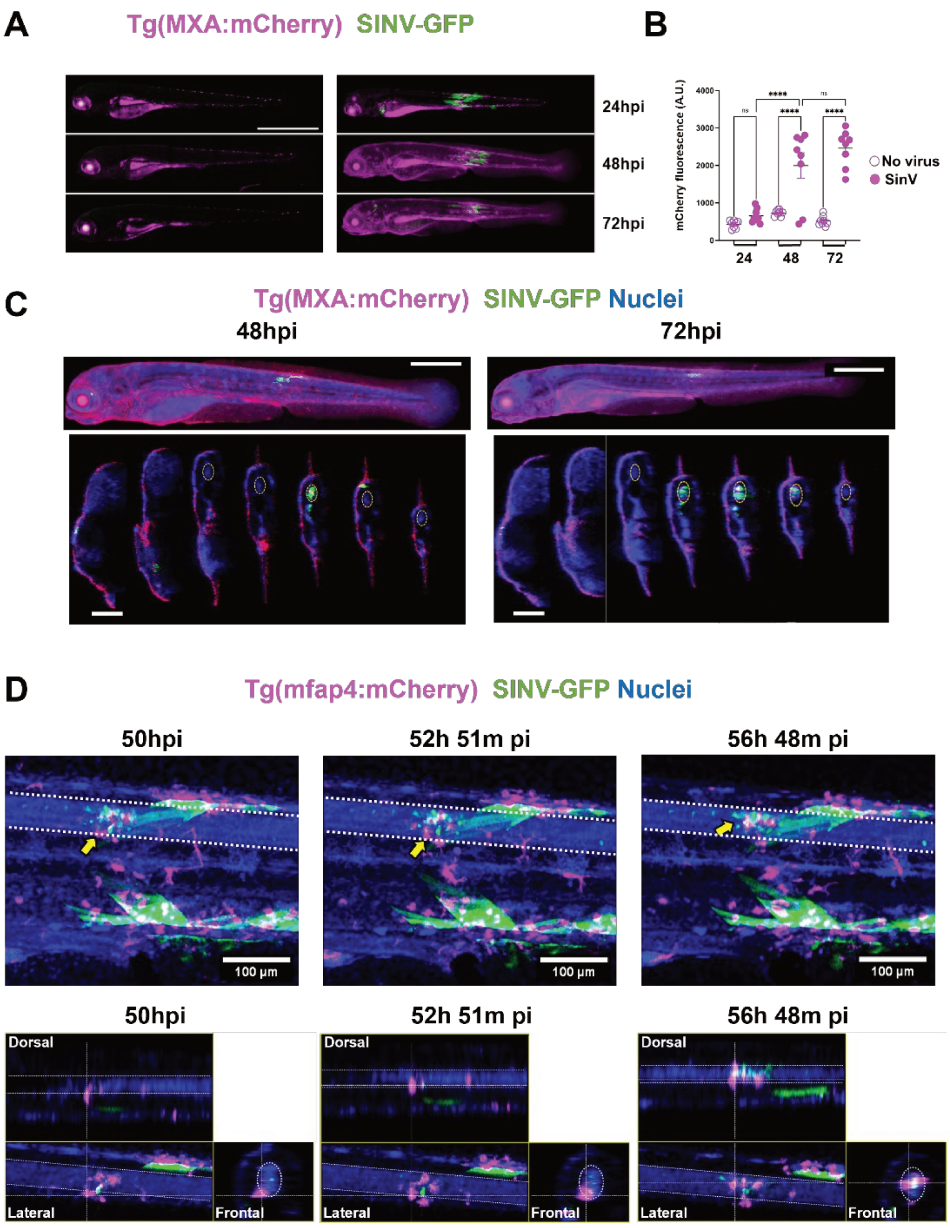

Figure 6. spatial features of IFN response during SINV infection.

A-C) *Tg(MXA:mCherry) (magenta) infected IM with SinV:GFP (green).* ***A****. Maximum projection of confocal images of representative individual larvae over time. Scale bar, 1mm* ***B)*** *Mean intensity measurement of mCherry signal over the whole larva (n=8 per group).* ***C)*** *Maximum projection of confocal images of a larva counterstained by NucRed live (blue) (top) and relative transverse sections (bottom). Spinal cord indicated by the dotted oval on sections. Scale bar, 500µm on top, 100µm on bottom.* ***D)*** *Maximum projection of confocal images of Tg(mfap4:mCherry) (magenta), with blue nuclei, infected IM with SinV:GFP (green) (top) and relative orthogonal projections (bottom). Spinal cord limits indicated by dotted lines.The yellow arrow points to a single macrophage entering the spinal cord (***P < 0.001; **P < 0.01; *P < 0.05; ns - not significant)*

In conclusion, while we observe a systemic type I response in the periphery, only very few IFN or ISG-positive cells were observed in the spinal cord in the vicinity of highly infected areas, and our data strongly suggest that these cells are macrophages attracted to the infection site.

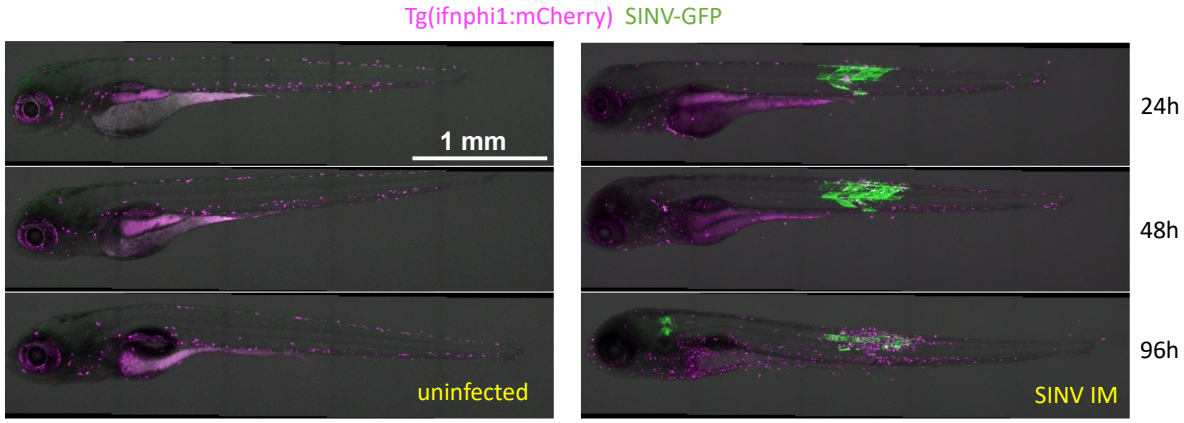

Figure 6 supplement 1. *IFNphi1 reporter cell imaging during SINV infection. Live confocal imaging of representative single larvae over time, maximal projections, merge of transmitted light and red and green fluorescence channels.*

Control of SINV infection by the type I IFN response

To delineate the role of this type I IFN response, we used morpholinos to transiently knock-down type I IFN receptors as previously established (Palha et al., 2013). IFN-R morphant larvae IM-injected with SINV displayed a more widespread and severe infection (Figure 7A; quantified below) with strong mortality (Figure 7B). Accordingly, qRT-PCR analysis revealed a higher viral burden (Figure 7C). IFN induction was stronger in IFN-R morphants, as expected from the higher viral burden (Figure 7D,E). MXA induction was lower at 24 hours (Figure 6F), as expected with IFN-R knockdown; at 48 and 72 hpi, it was similar to that of controls, still consistent with IFN-R knockdown when considering stronger type I IFN expression.

To quantify the impact of IFNR knockdown in CNS and periphery, we used our image analysis pipeline (Figure 5E). Infection was quantitatively stronger both in CNS and in peripheral compartments. In IFNR morphants, infection stabilizes but does not decrease in the periphery, while massive CNS infection systematically occurs (Figure 7G).

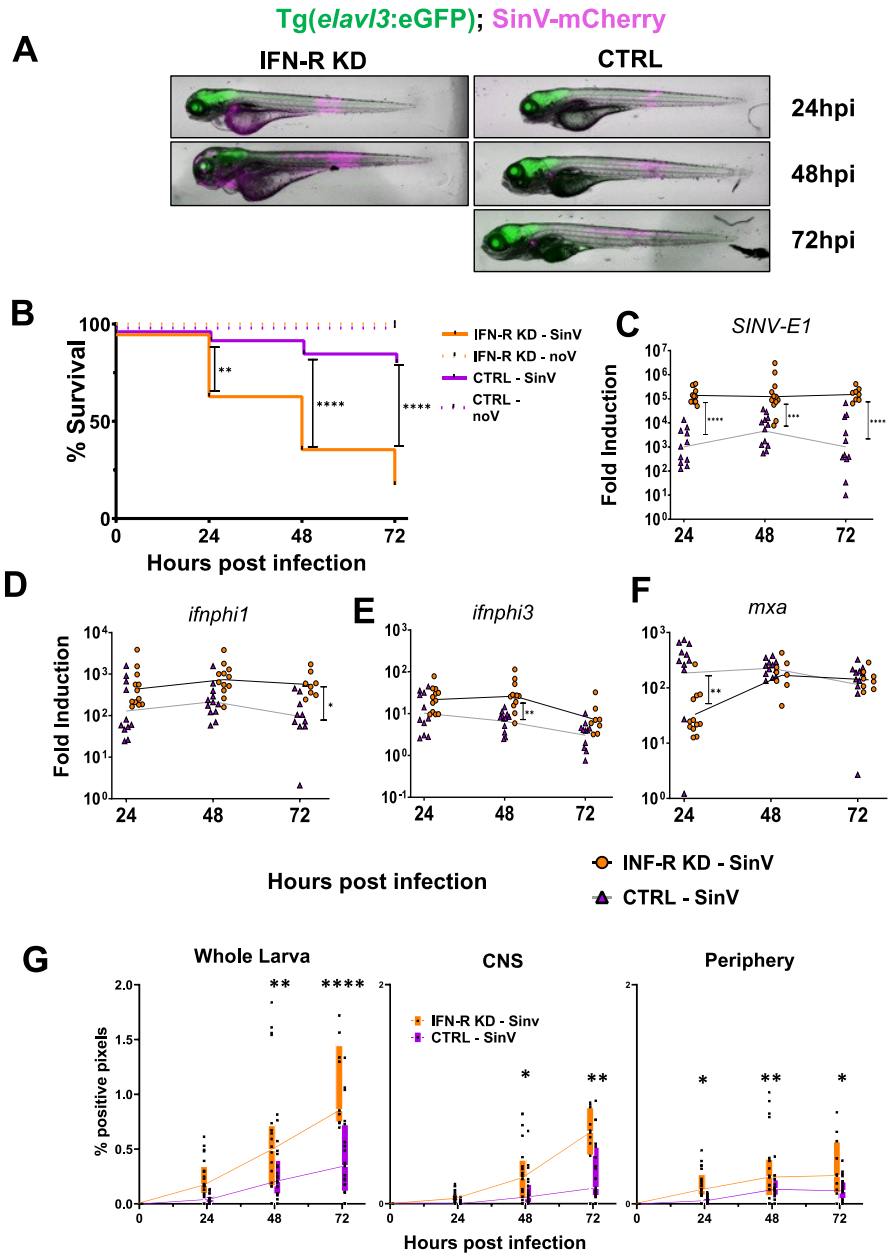

Figure 7: Analysis of kinetics and gene expression of INF knock-down larvae infected with SinV. ***A)*** *Top: Significative fluorescent images of Tg(elavl3:GFP) larvae infected with 30 PFU SinV:mCherry IM and injected either with IFNr or Control morpholino. The same larvae were followed each day. Bottom: Survival curve of Interferon Knock-down, wild type infected and not infected fish with 30 PFU SinV:mCherry IM. (n=44, 2 independent experiments)* ***B)*** *Real time quantification of gene expressions of SINV-E1, infphi1, infphi3 and mxa of zebrafish larvae infected with 30 PFU) SinV:mCherry IM, or uninfected (control) injected with either IFNr or Control morpholino and sampled every 24 hours from the same experimental pool. (n=12, 2 independent exp)* ***C)*** *Pixel quantification of SinV:mCherry signal percentage in whole body (Left), CNS (Center) or periphery (right) of IFN KD and WT larvae. Injection30 PFU IM. (n=21, 2 independent exp) (***P < 0.001; **P < 0.01; *P < 0.05; not shown - not significant)*

In our previous analysis of route of SINV entry to the CNS (Passoni et al., 2017), an important observation was that the endothelial cells were not infected by SINV, excluding BBB infection. We verified if endothelium infection occurred in IFNR morphants using Tg(Fli1:GFP) larvae infected with SINV-mCherry. After fixation and transparization, high-resolution imaging could exclude infection of endothelial cells even in strongly infected IFNR morphants (Figure 7 supplement 1, movie S11).

Thus, type I IFN responses play a key role in controlling SINV infection, both in periphery and in CNS. Route of CNS entry does not appear to be affected by this response, however.

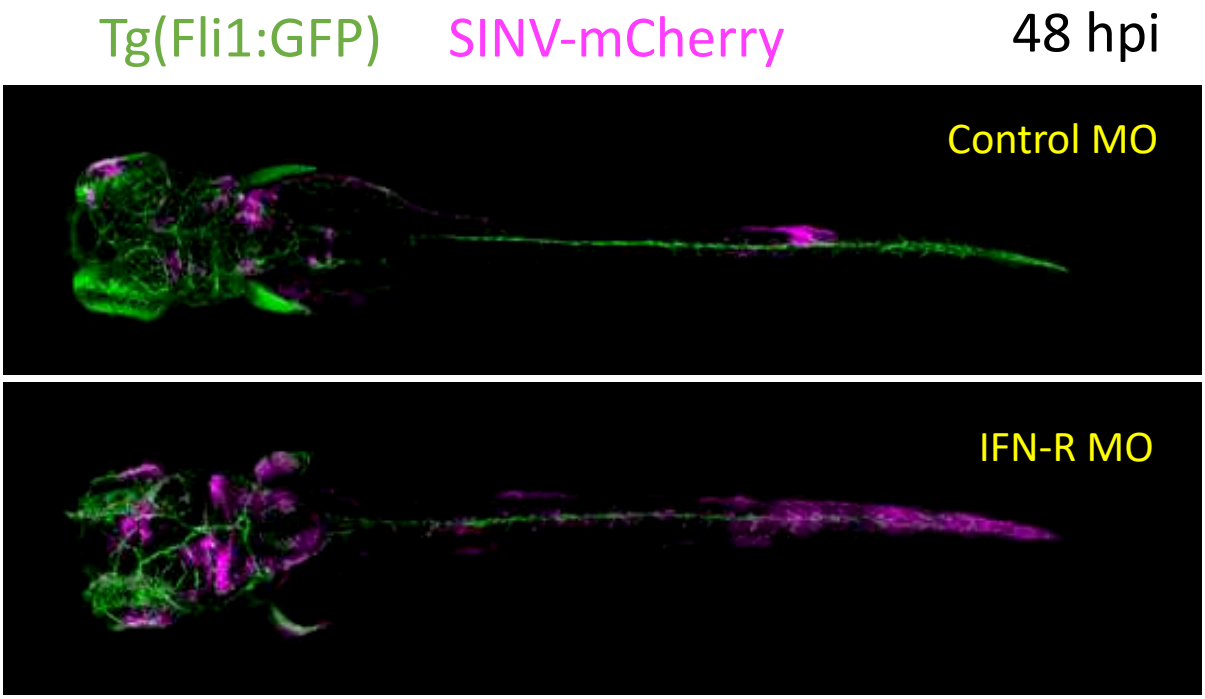

Figure 7 supplement 1. *High resolution confocal images of fixed larvae immunostained for GFP (green) and mCherry (magenta) to reveal vessels and virus-infected cells. Maximal projection. See Movie S11 for a rotating view.*

Mathematical modeling of the infection

To get insights into the in vivo dynamics of the infection in the whole animal, we generated a differential equation-based model, based on (Best et al., 2017), as detailed in Annex. The model considers two largely separate compartments, periphery and CNS. Briefly, each compartment includes three cellular subsets (Figure 8A): uninfected target cells, infected cells in eclipse phase (still functional and not yet producing virus), and productively infected cells entirely diverted into making new virions. Each compartment also has a pool of free virus and a pool of type I IFN. IFN induction pathways are highly conserved in zebrafish and mammals (Christelle Langevin et al., 2013). We considered two ways that IFN may be produced: via the Rig-I-like receptor (RLR) pathway, detecting of viral RNA in the cell cytosol of eclipse phase cells, or via the Toll-like receptor (TLR) pathway, detecting free virions. We also considered three ways that IFN may counteract the infection: by preventing virus from successfully entering a target, by preventing eclipse phase cells from entering productive state, and by accelerating the death of productively infected cells. Ignoring the effect of IFN amounted to modeling infection in IFNR-deficient larvae.

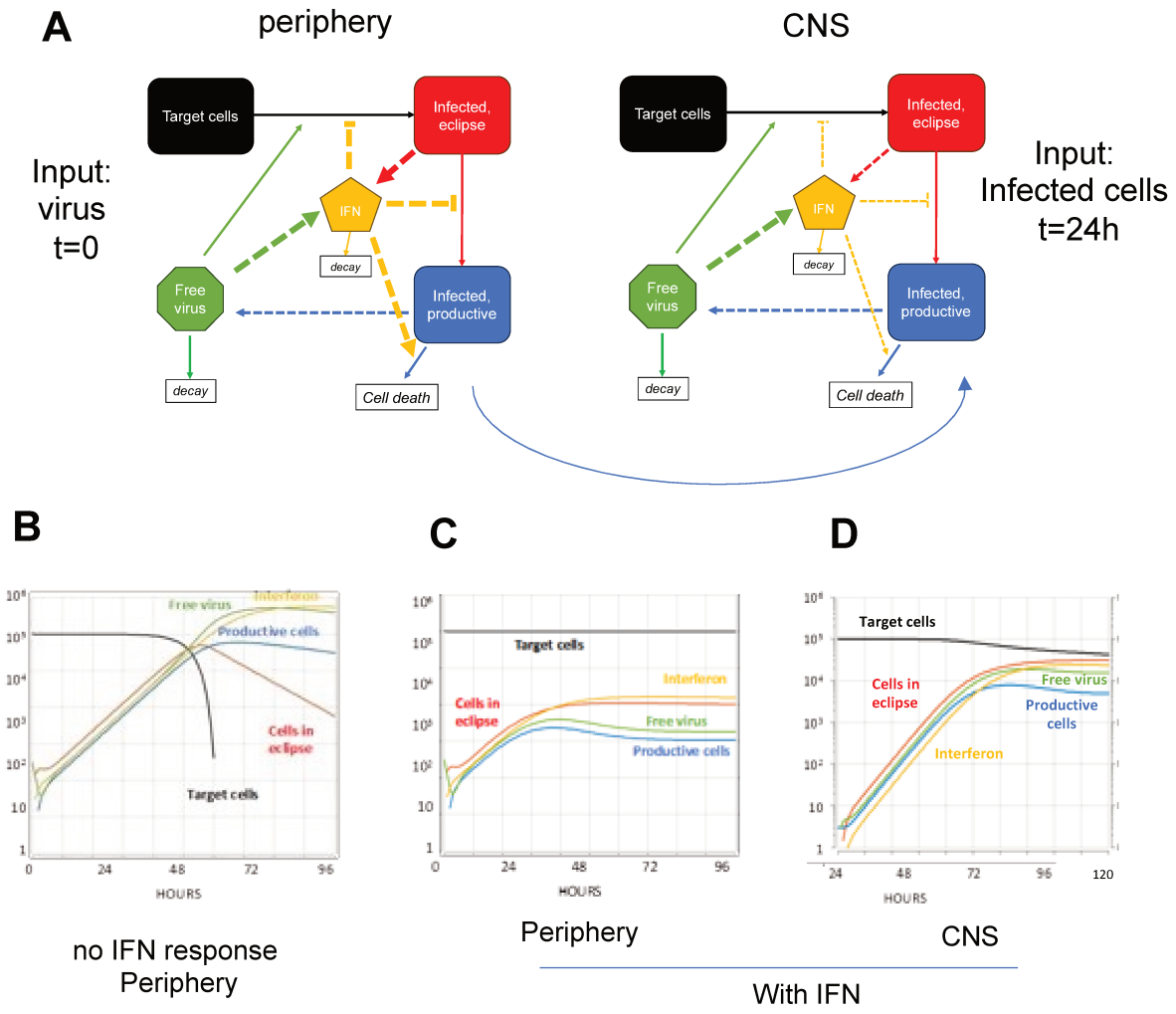

Figure 8: Modelling SINV infection in zebrafish larvae (see annex for details).
A) *organization of the model: periphery and CNS are ran as independent compartments, each with five variables: number of uninfected target cells, of infected cells in eclipse phase, and of productively infected cells; quantity of free infective virions; and concentration of type I IFNs.* ***B-D)*** *results of running the model after parameter fitting. B. Peripheral compartment if IFN has no effect (ie as in IFNR morphants).* ***C)*** *Peripheral compartment in wt larvae; D. CNS compartment in wt larvae.*

We fitted the parameters based on available literature and our own experimental data. To better translate our image quantification data into amount of infected cells, we performed flow cytometry (FC) to estimate the fraction of infected cells in larvae. Fluorescent reporters in our SINV strains are co-expressed with viral structural proteins, which are expressed during the late, productive stage of the infection (J H Strauss and Strauss, 1994a). Control and IFNR-morphant larvae were infected IM with SINV-GFP for one to three days, imaged, then dissociated to assess the fraction of GFP positive cells by FC. Imaging and FC results were well correlated (Figure 8 supplement 1), although not as well as imaging and qRT-PCR data (figure 5 supplement 1), possibly because dissociation efficiency is tissue-dependent, introducing biases. This, however, revealed that in the strongest infections, up to 20% of the cells may become GFP positive. Since not all larval cells are infectable by the virus (e.g, endothelial cells) we estimated that death would occur when half of target cells had become productively infected in the periphery.

One parameter that was difficult to assess was the rate of new virus production per infected cell. However, plausible values could be attributed to other parameters unrelated to IFN response. In IFNR-deficient larvae, rate of virus production determines when this threshold of 50% infected cells is reached. Considering that IFNR-deficient larvae typically die in two to three days from the infection, we could estimate the rate of new virus release by productively infected cells, which was surprisingly low: approximatively 1 virus per hour and per cell. The corresponding simulation is displayed on Figure 8B.

To fit the parameters of IFN response in periphery, we used the fact that in IFN-competent fish, infection peaks between 24 and 48 hpi (Figure 5G); our FC data suggest that at this time point, approximatively 1% of the cells should be productively infected. We found parameter values that reasonably recapitulated this peak and the following decay (Figure 8C). For this decay to occur, the RLR pathway was required, and IFN had to accelerate the death of infected cells (see annex).

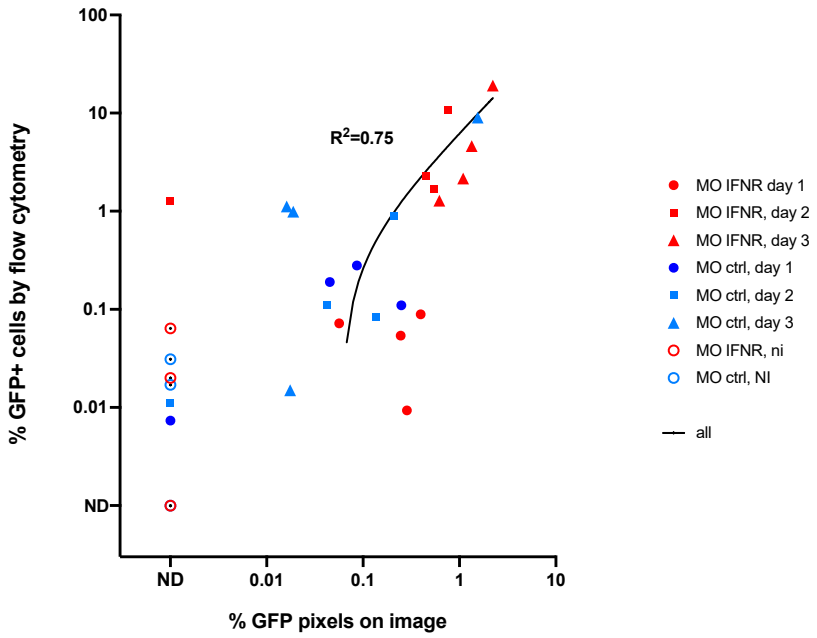

Figure 8 supplement 1. *Correlation of flow cytometry measurement and image-based quantification of the number of infected cells*
N=24 infected fish + 5 uninfected

These parameters result in a robust control of the infection, which is the situation observed in periphery. The situation in the CNS was different and parameters had to be adjusted to better reflect our results. We assumed that the BBB prevents the passage of IFN or free virions between the two compartments; the same overall model is therefore used for the CNS. Since we detected the first SINV-fluorescent neurons around 24 hpi and determined statistically an average of 3 independent CNS entry events, the CNS simulation starts with 3 productively infected cells, at a time corresponding to 24hpi.
Since death of infected neurons was rare, we reduced the parameter for CPE-induced death. Also, based on known properties of neurons (Viengkhou and Hofer, 2023) and our results with MXA and IFN reporter fish, we lowered the effectiveness of the RLR pathway. Our simulations still yielded a robust control if the infection. Finally, we reduced the impact of the IFN response on infected neurons and found that by making it 10 times less efficient than in the periphery, the infection would more or less stabilize close to the limit of overwhelming infection (Figure 8D). This would be as close as possible to the variable outcomes we observed, with CNS infection being sometimes controlled and sometimes not, in a model that is by essence deterministic.
In conclusion, despite its limitations, our model unveiled plausible values for two unknown parameters of SINV infection in zebrafish: productively infected cells release approximately only one infectious virion per hour, and the IFN response is is ten times less efficient in the CNS than it is in periphery.

Discussion

Taking advantage of the exquisite imaging assets of zebrafish larvae, we describe here in detail the spatial dynamics of a viral infection as it propagates from periphery to CNS in a whole vertebrate. Our previous work had established that SINV is neuroinvasive in zebrafish (Passoni et al., 2017). This had been performed using IV injection, yielding highly variable patterns of infection. Here, we compared several inoculation sites, and found that this variability can be reduced, although CNS invasion always occurred. When the virus was injected in the pericardial cavity, the infection was confined to the anterior half, with invasion of the hindbrain, probably via cranial ganglia. Upon IM injection in a caudal somite, peripheral infection remained localized to the tail, from where the virus invaded the spinal cord, and sometimes later spread to the brain. Subsequently, we focused on the outcome of IM injection, which reflected most closely natural SINV transmission by a mosquito bite. Furthermore, the thinness of the tail favored high-resolution imaging, and the relatively simple organization of the spinal cord facilitated the analysis of CNS entry and propagation.

After IM injection, SINV showed a strong tropism for muscle fibers and for stromal cells between somites or close to ventral or dorsal vessels (but not for endothelial cells themselves). This muscular tropism is relevant to the clinical features of SINV infection in humans, who sometimes develop long-lasting myalgia, associated with cycles of necrosis and regeneration in the patient muscles (Sane et al., 2012). Indeed, we observed rapid death of infected cells in zebrafish muscle, but not in a cyclical manner; in the time frame of our observations, peripheral infection appeared to be fully resolved. Although we did not analyze it in detail, muscle regeneration clearly occurred, not surprisingly considering the naturally potent regeneration abilities of zebrafish larvae. However, when IFN receptors were knocked down, the larvae lost the ability to control virus propagation in muscle, resulting in widespread areas of infection over multiple somites and subsequent extensive necrosis.

Spinal cord invasion always starts in the segment that innervates the infected somite, which is entirely consistent with CNS entry by axonal transport, as demonstrated previously (Passoni et al., 2017). As this could involve either motor or sensory neurons, we used time lapse imaging to determine which became infected first. We observed both situations – and since we have also established that 3 independent CNS entries occur per larvae, entry may occur by both sensory and motor neurons in the same larva. To establish the relative importance of both gateways, we performed depletion experiments. Spinal cord invasion still occurred after elimination of either sensory or motor neurons, confirming that both populations may constitute the entry route to the CNS. Still, some remarkable differences were observed after sensory or motor neuron depletion. Most strikingly, subsequent spread of SINV to the brain was suppressed when DRG sensory neurons were depleted. This would be expected if long-distance axonal propagation of SINV was more efficient by anterograde than by retrograde transport – a hypothesis that will be put to the test in the future. Surprisingly, DRG neuron depletion also had an impact on the periphery, resulting in more extensive somite infection. This suggests that DRG sensory neurons may somehow contribute to the antiviral response, possibly by playing an important immuno-sensing role.

However, DRG depletion was achieved by knocking down *erbb3b*, a transcription factor expressed in neural crest progenitors, preventing them to differentiate into sensory neurons or melanophores (Dooley et al., 2013), raising the possibility that another unknown neural crest-derived cell type may prevent virus spread.

High-resolution imaging clearly showed that most, if not all cells infected in the spinal cord were neurons; the other prominent cell type, radial glia, would have been readily identified by their typical morphology if they had become fluorescent upon infection. We observed two modalities of virus dissemination inside the CNS: axon-mediated long-distance transport (almost always in the anterior direction) and local cell-to-cell spread, most likely by virus shedding from neuronal soma. This resulted in the formation of progressively growing clusters. Cluster formation was particularly evident in larvae directly inoculated in the spinal cord with a mixture of SINV-GFP and SINV-mCherry, where stable territories of green and red fluorescent neurons became established without mixing. This remarkable virus exclusion phenomenon was actually observed everywhere, with the notable exception of the yolk. Superinfection exclusion has been well documented for SINV, requiring at most 1h after initial infection to be established (J H Strauss and Strauss, 1994b). Unlike other cells, the very large size of the yolk syncytial cell makes it likely that it could be infected by several virions simultaneously, and more time would also be required for exclusion signals to travel to travel to the entire cell.

This cluster growth played a clear role in progression of infection in the CNS, but axonal long-distance spread played a decisive role, at it seeded new distant clusters in the spinal cord and, more importantly, in the brain, starting with the hindbrain where the targets of spinal neurons reside. CNS infection was highly variable among individuals, with some larvae that managed to control the virus and others where a runaway infection occurred; apparition of new clusters in the anterior spine and in the brain was a major difference between the two groups. What is causing this initial difference is unclear but clearly of critical importance; as stated above, initial entry via sensory neurons, rather than motoneurons, is likely to be a major determinant.

SINV induces a strong type I IFN response in larvae. The dynamics of this response, as revealed by qRT-PCR in the whole larvae after IM inoculation, are very similar to those measured after IV infection of SINV (Boucontet et al., 2018) or of its relative CHIKV (Palha et al., 2013). The effect of knocking down IFN receptors was also similar, with a much stronger overall infection resulting in the death of most larvae within 2 to 3 days. We used reporter transgenes to assess the localization of IFN responses. ISG expression, as determined in Tg(MXA:mCherry) larvae, was highest in the gut and the skin; it was also high in leukocytes, particularly near to infected sites. Skin expression was remarkably uniform, being detected even in regions farthest from the infection, revealing a systemic IFN response in the periphery. This probably explains why SINV infection is efficiently controlled in the periphery, with a stereotypic transient infection. Interestingly, in IV-inoculated larvae, we observed at least one exception to this: when infection occurred in the swim bladder, it was highly persistent, which would be worth of future investigation. The situation in the CNS was very different, with MXA reporter expressing being restricted to a few mobile cells found only in already extensive clusters of infected neurons. It is very likely that these cells are macrophages attracted from the outside; indeed, we could document the entrance of macrophages into the spinal cord, with a clear directional tropism towards the infected clusters. What is attracting these macrophages would be an important question to address in the future.

To get deeper insights into the mechanisms by which the IFN response the infection in the periphery and in the CNS, we resorted to mathematical modeling. The parameters of our differential equation model were first determined for the peripheral compartment. After establishing various parameters based on literature or our literature data, we used simulations to fit the remaining ones. To match the survival time of IFN-R knockdown larvae, our model yielded an unexpected result for the rate of virus release by productively infected cells: about one infective virion per hour. This may appear very low since transmission electron microscopy of SINV-infected cells typically reveals many virions budding simultaneously at the plasma membrane; time-lapse imaging of tagged viruses detected several budding events per minute (Jose et al., 2015). However, it should be kept in mind that not all viral particles are infective virions; actually, comparisons of PFU titers and amount of viral genomes in typical BHK-produced SINV suspensions indicate than less than 1% of particles are infective (Poirier et al., 2015). Thus, this rate of 1 virion/infected cell/hour is not unrealistic; and it is sufficient to yield an explosive increase of the infection, if not counteracted by host immunity.

Our model allowed for various modalities of IFN production and impact of IFN on the infection. Testing these in turn did not allow to reach definitive conclusions, but indicated that the RLR detection pathway was important, and that IFN is probably accelerating the death of infected cells, as we hypothesized previously (Levraud et al., 2014). One notable difference in our simulations, when comparing the different possible impacts of IFN, was in the amount of cells in eclipse phase (see Annex). These are currently undetectable in our current and developing means to visualize them would be important to test key hypotheses regarding infection dynamics in vivo. The model also suggested that IFN were much less efficient on neurons than on peripheral cells. As far as we know this has not been compared directly, but it is well established that non-neuronal cells of the CNS (e.g. microglia or astrocytes) have a stronger response to IFN than neurons; furthermore, the repertoire of ISGs produced by neurons is relatively narrow (Viengkhou and Hofer, 2023). This can be understood as a tradeoff between the need to protect the CNS from viral infection and the deleterious impacts of neuroinflammation.

Our mathematical modeling has important limitations. First, our choice of parameters is sometimes arbitrary, if plausible, and will have to be refined in the future. The equations governing eclipse cells are clearly too simple, since in presence of a strong IFN response, our model induce eclipse cells to remain in this state forever; a return pathway to the target state, or to a transient refractory state, should be included in a more realistic – but more complex – model. Most important for the CNS component of our model, the localization IFN response is not taken in account. In all likelihood, local neuron-to-neuron spread of the virus is soon counteracted by the local IFN response; but when axonal transfer results in a new infection focus at a very distant site, this new area is probably completely unprotected for some time.

Nevertheless, the extensive of imaging data proved of high value to guide modelling and reveal novel features governing dissemination of viruses through the whole organisms, and particularly for the very important events of CNS invasion. It would be particularly relevant to adapt this approach to drug discovery, possibly with the help of artificial intelligence to better discover homologies between effective patterns and predicted drug effects.

Material and methods

Ethical Statement

Animal experiments described in the present study were conducted according to European Union guidelines for handling of laboratory animals and were approved by the Ethics Committee of Institut Pasteur.

Zebrafish lines

Zebrafish were handled as explained in (Laghi et al., 2022). Wild-type zebrafish (AB strain), initially obtained from ZIRC (Eugene, OR, USA), were raised in the aquatic facility of Institut Pasteur. After natural spawning, eggs were collected, treated for 5 min with 0.03% bleach, rinsed twice, and incubated at 28°C in Petri dishes in Volvic mineral water supplemented with 0.3 µg/ml methylene blue (Sigma-Aldrich, St. Louis, Missouri, USA). After 24 h, the water was supplemented with 200 µM phenylthiourea (PTU, Sigma-Aldrich) to prevent pigmentation of larvae. After this step, incubation was conducted at 24°C or 28°C depending on the desired developmental speed. Developmental stages given in the text correspond to the 28.5°C reference (C B Kimmel et al., 1995). At 3 dpf, immediately before infections, larvae that had not hatched spontaneously were manually dechorionated. Owing to silencing issues of some UAS-driven transgenes, breeders were carefully screened to select those whose progeny yielded full expression; correct fluorescence expression by larvae was checked before experiments. Sex of larvae is not yet determined at the time of experiments.

Organism	Line Name	Modification	Transgene name and reference	Reference
Danio rerio	Mnx1::Gal4	Transgenesis	Tg1(mnx1:GAL4) https://zfin.org/ZDB-TGCONSTRCT-160119-3	https://zfin.org/ZDB-TGCONSTRCT-160119-3
Danio rerio	axl1::eGFP	Transgenesis	Tg(foxa2:GFP) https://zfin.org/ZDB-GENE-980526-404	https://zfin.org/ZDB-GENE-980526-404
Danio rerio	IFN1::mCherry allele	Transgenesis	Tg(ifnphi1:mCherry) https://zfin.org/ZDB-TGCONSTRCT-120607-1	https://zfin.org/ZDB-TGCONSTRCT-120607-1
Danio rerio	HuC-GFP	Transgenesis	Tg(elavl3:EGFP) https://zfin.org/ZDB-TGCONSTRCT-070117-150	https://zfin.org/ZDB-TGCONSTRCT-070117-150
Danio rerio	Huc:Gal4	Transgenesis	Tg6(elavl3:GAL4-VP16) https://zfin.org/ZDB-ALT-161116-3	https://zfin.org/ZDB-ALT-161116-3
Danio rerio	Ml2Tg (hb9::eGFP)	Transgenesis	Tg(mnx1:GFP) https://zfin.org/ZDB-TGCONSTRCT-070117-40	ttps://zfin.org/ZDB-TGCONSTRCT-070117-40
Danio rerio	Sb1Tg (ngn1::eGFP)	Transgenesis	Tg(ngn1::eGFP) https://zfin.org/ZDB-GENE-990415-174	https://zfin.org/ZDB-GENE-990415-174
Danio rerio	MXA:mCherrry	Transgenesis	Tg(cryaa:DsRed,mxa:mCherryF)	http://zfin.org/ZDB-ALT-190116-3
Danio rerio	UAS:nfsB-mCherry	Transgenesis	UAS-E1B:NTR-mCherry c264; http://zfin.org/ZDB-FISH-150901-2592	http://zfin.org/ZDB-FISH-150901-2592

Viruses

Sindbis viruses were produced on BHK cells [originally obtained from American Type Culture Collection (ATCC), #CC-L10], according to (Hardwick and Levine, 2000). The SINV-GFP strain used here corresponds to the SINV-eGFP/2A strain described in (Boucontet et al., 2018), whose genome is based on athe bybrid TE12 strain backbone. The SINV-mCherry strain was generated on the same backbone, replacing the eGFP coding sequence with mCherry. Viruses were titered on Vero-E6 cells (ATCC #CRL-1586).

Injections

Injections and handling of larvae were performed as in (Passoni et al., 2017). Briefly, zebrafish larvae aged 70-72 hpf were inoculated by microinjection of ~30 PFU viral SINV particles (~1 nl of supernatant from infected BHK cells, diluted with PBS to ~$3x10^7$ PFU/ml). Before injection larvae were anesthetized with 0.2 mg/ml tricaine and positioned and oriented in the groove molded in 2% low melting agarose. Using a micromanipulator, the capillary was then inserted at the desired site and two pulses performed to inject approximately 1 nl. Larvae were then distributed in wells of culture plates with water containing PTU and kept at 28°C. For ethical reasons, all larvae used in the experiments were euthanized by anesthetic overdose at 7 dpi.

Lysis, RNA Extraction, and RT-qPCR of Larvae

RNA was extracted from individual larvae, which were first deeply anesthetized. After removal of almost all water and addition of RLT buffer (Qiagen), larvae were dissociated by 5 up- and-down-pipetting movements. Tubes may then be frozen at -20°C for a few days. Total RNA was then extracted with a RNeasy Mini Kit (Qiagen) without the DNase treatment step and a final elution with 30 µl of water.

RT was performed on 6 µl of eluted RNA using MMLV reverse transcriptase (Invitrogen, Carlsbad, CA, USA) with dT_{17} primer (for polyadenylated transcripts). cDNA was diluted with water to a final volume of 100 µl, of which 5 µl was used as a template for each qPCR assay.

Real-time qPCR was performed with an ABI7300 (Applied Biosystems, Foster City, CA, USA). Quantification was performed using a SYBR assay using the Takyon SYBR Blue MasterMix (Eurogentec, Seraing, Belgium) with primer pairs. These primers typically span exon boundaries to avoid amplification of contaminating genomic DNA. The *eef1a1l1* (also known as *ef1a*) was used as a housekeeping gene for normalization.

Morpholino and Plasmid Injection in Eggs

Morpholino antisense oligonucleotides (Gene Tools, Philomath, OR, USA) were injected (1 nl volume) in the cell or yolk of AB embryos at the one- to two-cell stage. crfb1 splice morpholino (2 ng, CGCCAAGATCATACCTGTAAAGTAA) was injected together with crfb2 splice morpholino (2 ng, CTATGAA TCCTCACCTAGGGTAAAC), knocking down all type I IFN receptors (Aggad et al., 2009). Erbb3b morpholino was used to prevent differentiation of DRG neurons and injected alone (2 ng, TGGGCTCGCAACTGGGTGGAAACAA) (Dooley et al., 2013). Control morphants were injected with 4 ng control morpholino, with no known target (GAAAGCATGGCATCTGGAT CATCGA).

Live Widefield Fluorescence Imaging

Live fluorescence imaging was performed as explained in (Laghi et al., 2022). SINV-GFP-infected larvae were imaged with an EVOS FL Auto microscope (Thermo Fisher Scientific, Waltham, MA, USA) using a 2× planachromatic objective (numerical aperture, 0.06), allowing capture of the entire larva in a field. Before imaging larvae were anesthetized with 0.2mg/ml tricaine and placed in individual wells of 24-well plate cell culture plate. Agarose 2% molds were used to properly set each larva in the same relative position. Transmitted light and fluorescence (GFP or Texas Red cube) images were taken. After imaging larvae were rinsed in water with 0.3 µg/ml methylene blue (Sigma-Aldrich, St. Louis, Missouri, USA) and transferred to individual wells of a 24-well plate cell culture plate in water with 200 µM phenylthiourea (PTU, Sigma-Aldrich) and stored in incubator at 28 C.

Live Confocal Imaging

Confocal imaging was performed as in (Viana et al., 2023). Injected larvae were mounted in lateral or ventral position in 35 mm glass-bottom-Dishes (Ibidi Cat#: 81158) or in glass bottom-8well-slides (Ibidi Cat#: 80827). Larvae were immobilized using a 1% low-melting-point agarose (Promega; Cat#: V2111) solution and covered with Volvic water containing 0.2mg/ml tricaine. A Leica SP8 confocal microscope equipped with two PMT and Hybrid detector, a 10X dry (PL Fluotar 10X dry:0.30), 20X IMM (HC PL APO CS2 20X/0.75), or a 40x water IMM (HC PL APO CS2 40X/1.10) objective, a X–Y motorized stage and with LAS-X software, was used to live image injected larvae. To generate images of the whole larvae, a mosaic of confocal z-stack of images was taken with the 10X or 40X objective using the Navigator tool of the LAS-X software. The acquisitions were performed either in conventional settings or resonant scanning, the latter being post processed with the Lightning tool of the LAS-X software to eliminate noise (deconvolution). After acquisition, larvae were washed and transferred in a new 24-well plate filled with 1 ml of fresh Volvic water per well, incubated at 28°C and imaged again under the same conditions over time.

Considering the image analysis strategy adopted and the need to adjust the acquisition setting to avoid over or under saturation of the sensor, the strategy adopted to set acquisition parameters always followed the same rule. Every single channel was brought up to saturation of true signal (ignoring saturation of noise from yolk or eye) and subsequently lowered enough to remove the saturation. At every timepoint this calibration is repeated on a batch of random samples and applied to the whole timepoint. In this way the whole range of emission is captured for every image, without affecting the integrity of the subsequent threshold-based analysis.

Image analysis

Image analysis was performed using FIJI software (Schindelin et al., 2012) and CellProfiler (Carpenter et al., 2006). Fluorescent images acquired through EVOS imaging were normalized (i.e., flip, crop and denoising) using a FIJI script (Script 1). After normalization a threshold check (biovoxxel toolbox plugin) was used to identify the best thresholding strategy for each channel, that resulted to be "Triangle dark" and "IsoData dark". Subsequently all the images were threshold using the same method (script 1). Both the binary masks and the normalized images were fed to Cell profiler pipeline (pipeline 1) to perform area filtering, segmentation, and measurement. All these operations were performed in batch. The final output obtained is a measurement of positive pixel area normalized to the constant area of the image, segmented in CNS and Periphery. Only the tg(INFphi1:mCherry) experiment was quantified from confocal images and for this all the operation were performed through CellProfiler software directly (pipeline2). In this case the threshold was performed directly in CellProfiler using "Otsu three class" method.

Statistical analysis

The difference between means was evaluated using analysis of variance (ANOVA) or two-tailed unpaired t-test. For multiple comparison Bonferroni's method was applied. Non-Gaussian data were analyzed with Kurskal-Walli's test followed by Dunn's Multiple comparison. For Normal distributions Kolmogorov-Smirnov test was used. $P<0.05$ was considered statistically significant (symbols: ***P<0.001; **P<0.01; *P<0.05). Survival data were plotted using the Kaplan-Meier estimator and log-rank tests were performed to assess differences between groups. Statistical analyses and PCA were performed using Prism software.

Model building

Model building was realized using Berkeley Madonna software. This software numerically solves ordinary differential equations and difference equation. All the details on the parameters used in this software are accessible in the Annex.

References

Abdollahpour H, Falahatkar B, Lawrence C. 2020. The effect of photoperiod on growth and spawning performance of zebrafish, Danio rerio. *Aquac Reports* **17**:100295. doi:10.1016/J.AQREP.2020.100295

Abtin A, Jain R, Mitchell AJ, Roediger B, Brzoska AJ, Tikoo S, Cheng Q, Ng LG, Cavanagh LL, Von Andrian UH, Hickey MJ, Firth N, Weninger W. 2013. Perivascular macrophages mediate neutrophil recruitment during bacterial skin infection. *Nat Immunol 2013 151* **15**:45–53. doi:10.1038/ni.2769

Ackerman SD, Monk KR. 2016. The scales and tales of myelination: using zebrafish and mouse to study myelinating glia. *Brain Res* **1641**:79–91. doi:10.1016/J.BRAINRES.2015.10.011

Adatto I, Lawrence C, Krug L, Zon LI. 2022. The effects of intensive feeding on reproductive performance in laboratory zebrafish (Danio rerio). *PLoS One* **17**:e0278302. doi:10.1371/JOURNAL.PONE.0278302

Adatto I, Lawrence C, Thompson M, Zon LI. 2011. A New System for the Rapid Collection of Large Numbers of Developmentally Staged Zebrafish Embryos. *PLoS One* **6**:e21715. doi:10.1371/JOURNAL.PONE.0021715

Aderem A, Underhill DM. 2003. MECHANISMS OF PHAGOCYTOSIS IN MACROPHAGES. *https://doi.org/101146/annurev.immunol171593* **17**:593–623. doi:10.1146/ANNUREV.IMMUNOL.17.1.593

Adouchief S, Smura T, Sane J, Vapalahti O, Kurkela S. 2016a. Sindbis virus as a human pathogen—epidemiology, clinical picture and pathogenesis. *Rev Med Virol* **26**:221–241. doi:10.1002/RMV.1876

Adouchief S, Smura T, Sane J, Vapalahti O, Kurkela S. 2016b. Sindbis virus as a human pathogen-epidemiology, clinical picture and pathogenesis. *Rev Med Virol* **26**:221–241. doi:10.1002/rmv.1876

Aggad D, Mazel M, Boudinot P, Mogensen KE, Hamming OJ, Hartmann R, Kotenko S, Herbomel P, Lutfalla G, Levraud J-P. 2009. The two groups of zebrafish virus-induced interferons signal via distinct receptors with specific and shared chains. *J Immunol* **183**:3924–3931. doi:10.4049/jimmunol.0901495

Aggad D, Stein C, Sieger D, Mazel M, Boudinot P, Herbomel P, Levraud J-P, Lutfalla G, Leptin M. 2010. In Vivo Analysis of Ifn-γ1 and Ifn-γ2 Signaling in Zebrafish. *J Immunol* **185**:6774–6782. doi:10.4049/JIMMUNOL.1000549

Al-Khalifa MS, Diab FM, Khalil GM. 2007. Man-threatening viruses isolated from ticks in Saudi Arabia. *Saudi Med J* **28**:1864–1867.

Altmann SM, Mellon MT, Johnson MC, Paw BH, Trede NS, Zon LI, Kim CH. 2004. Cloning and characterization of an Mx gene and its corresponding promoter from the zebrafish, Danio rerio. *Dev Comp Immunol* **28**:295–306. doi:10.1016/J.DCI.2003.09.001

Amraei R, Yin W, Napoleon MA, Suder EL, Berrigan J, Zhao Q, Olejnik J, Chandler KB, Xia C, Feldman J, Hauser BM, Caradonna TM, Schmidt AG, Gummuluru S, Mü E, Chitalia V, Costello CE, Rahimi N. 2021. CD209L/L-SIGN and CD209/DC-SIGN act as receptors for SARS-CoV-2. *ACS Publ* **7**:1156–1165. doi:10.1021/acscentsci.0c01537

An M, Luo R, Henion PD. 2002. Differentiation and maturation of zebrafish dorsal root and sympathetic ganglion neurons. *J Comp Neurol* **446**:267–275. doi:10.1002/CNE.10214

914 Andreassen AH, Hall P, Khatibzadeh P, Jutfelt F, Kermen F. 2022. Brain dysfunction during
915 warming is linked to oxygen limitation in larval zebrafish. *Proc Natl Acad Sci U S A*
916 **119**:e2207052119.
917 doi:10.1073/PNAS.2207052119/SUPPL_FILE/PNAS.2207052119.SM03.AVI
918 Antonio N, Bønnelykke-Behrndtz ML, Ward LC, Collin J, Christensen IJ, Steiniche T, Schmidt H,
919 Feng Y, Martin P. 2015. The wound inflammatory response exacerbates growth of pre-
920 neoplastic cells and progression to cancer. *EMBO J* **34**:2219–2236.
921 doi:10.15252/EMBJ.201490147
922 Artika IM, Dewantari AK, Wiyatno A. 2020. Molecular biology of coronaviruses: current
923 knowledge. *Heliyon* **6**:e04743. doi:10.1016/J.HELIYON.2020.E04743
924 Arunachalam M, Raja M, Vijayakumar C, Malaiammal P, Mayden RL. 2013. Natural history of
925 zebrafish (Danio rerio) in India. *Zebrafish* **10**:1–14.
926 doi:10.1089/ZEB.2012.0803/ASSET/IMAGES/LARGE/FIGURE6.JPEG
927 Bakkers J. 2011. Zebrafish as a model to study cardiac development and human cardiac disease.
928 *Cardiovasc Res* **91**:279–288. doi:10.1093/CVR/CVR098
929 Bell-Sakyi L, Weisheit S, Rückert C, Barry G, Fazakerley J, Fragkoudis R. 2016. Microscopic
930 Visualisation of Zoonotic Arbovirus Replication in Tick Cell and Organ Cultures Using Semliki
931 Forest Virus Reporter Systems. *Vet Sci* **3**. doi:10.3390/vetsci3040028
932 Bell EA, Cable J, Oliveira C, Richardson DS, Yant L, Taylor MI. 2020. Help or hindrance? The
933 evolutionary impact of whole-genome duplication on immunogenetic diversity and parasite
934 load. *Ecol Evol* **10**:13949–13956. doi:10.1002/ECE3.6987
935 Bennett CM, Kanki JP, Rhodes J, Liu TX, Paw BH, Kieran MW, Langenau DM, Delahaye-Brown A,
936 Zon LI, Fleming MD, Thomas Look A. 2001. Myelopoiesis in the zebrafish, Danio rerio. *Blood*
937 **98**:643–651. doi:10.1182/BLOOD.V98.3.643
938 Berman JN, Kanki JP, Look AT. 2005. Zebrafish as a model for myelopoiesis during embryogenesis.
939 *Exp Hematol* **33**:997–1006. doi:10.1016/J.EXPHEM.2005.06.010
940 Bernhardt RR, Chitnis AB, Lindamer L, Kuwada JY. 1990. Identification of spinal neurons in the
941 embryonic and larval zebrafish. *J Comp Neurol* **302**:603–616. doi:10.1002/cne.903020315
942 Bertrand JY, Cisson JL, Stachura DL, Traver D. 2010. Notch signaling distinguishes 2 waves of
943 definitive hematopoiesis in the zebrafish embryo. *Blood* **115**:2777–2783.
944 doi:10.1182/BLOOD-2009-09-244590
945 Best K, Guedj J, Madelain V, de Lamballerie X, Lim S-Y, Osuna CE, Whitney JB, Perelson AS. 2017.
946 Zika plasma viral dynamics in nonhuman primates provides insights into early infection and
947 antiviral strategies. *Proc Natl Acad Sci U S A* **114**:8847–8852. doi:10.1073/pnas.1704011114
948 Bjørgen H, Hellberg H, Løken OM, Gunnes G, Koppang EO, Dale OB. 2019. Tumor
949 microenvironment and stroma in intestinal adenocarcinomas and associated metastases in
950 Atlantic salmon broodfish (Salmo salar). *Vet Immunol Immunopathol* **214**.
951 doi:10.1016/J.VETIMM.2019.109891
952 Bojarczuk A, Miller KA, Hotham R, Lewis A, Ogryzko N V., Kamuyango AA, Frost H, Gibson RH,
953 Stillman E, May RC, Renshaw SA, Johnston SA. 2016. Cryptococcus neoformans Intracellular
954 Proliferation and Capsule Size Determines Early Macrophage Control of Infection. *Sci*
955 *Reports 2016 61* **6**:1–15. doi:10.1038/srep21489
956 Bottiglione F, Dee CT, Lea R, Zeef LAH, Badrock AP, Wane M, Bugeon L, Dallman MJ, Allen JE,
957 Hurlstone AFL. 2020. Zebrafish IL-4–like Cytokines and IL-10 Suppress Inflammation but Only

IL-10 Is Essential for Gill Homeostasis. *J Immunol* **205**:994–1008. doi:10.4049/JIMMUNOL.2000372

Boucontet L, Passoni G, Thiry V, Maggi L, Herbomel P, Levraud J-P, Colucci-Guyon E. 2018. A model of superinfection of virus-infected zebrafish larvae: Increased susceptibility to bacteria associated with neutrophil death. *Front Immunol* **9**:1084. doi:10.3389/fimmu.2018.01084

Brady M, Sundareshan V. 2017. Legionnaires' disease.

Brehm MA, Jouvet N, Greiner DL, Shultz LD. 2013. Humanized Mice for the Study of Infectious Diseases. *Curr Opin Immunol* **25**:428. doi:10.1016/J.COI.2013.05.012

Briggs JP. 2002. The zebrafish: a new model organism for integrative physiology. *https://doi.org/101152/ajpregu005892001* **282**. doi:10.1152/AJPREGU.00589.2001

Britto DD, Wyroba B, Chen W, Lockwood RA, Tran KB, Shepherd PR, Hall CJ, Crosier KE, Crosier PS, Astin JW. 2018. Macrophages enhance Vegfa-driven angiogenesis in an embryonic zebrafish tumour xenograft model. *DMM Dis Model Mech* **11**. doi:10.1242/DMM.035998/VIDEO-8

Buckley CD, Ross EA, McGettrick HM, Osborne CE, Haworth O, Schmutz C, Stone PCW, Salmon M, Matharu NM, Vohra RK, Nash GB, Rainger GE. 2006. Identification of a phenotypically and functionally distinct population of long-lived neutrophils in a model of reverse endothelial migration. *J Leukoc Biol* **79**:303–311. doi:10.1189/JLB.0905496

Burgener SS, Schroder K. 2020. Neutrophil Extracellular Traps in Host Defense. *Cold Spring Harb Perspect Biol* **12**:a037028. doi:10.1101/CSHPERSPECT.A037028

Burillo A, Pedro-Botet ML, Bouza E. 2017. Microbiology and Epidemiology of Legionnaire's Disease. *Infect Dis Clin* **31**:7–27. doi:10.1016/J.IDC.2016.10.002

Butovsky O, Jedrychowski MP, Moore CS, Cialic R, Lanser AJ, Gabriely G, Koeglsperger T, Dake B, Wu PM, Doykan CE, Fanek Z, Liu L, Chen Z, Rothstein JD, Ransohoff RM, Gygi SP, Antel JP, Weiner HL. 2013. Identification of a unique TGF-β–dependent molecular and functional signature in microglia. *Nat Neurosci 2013 171* **17**:131–143. doi:10.1038/nn.3599

Byrd AS, O'Brien XM, Johnson CM, Lavigne LM, Reichner JS. 2013. An Extracellular Matrix–Based Mechanism of Rapid Neutrophil Extracellular Trap Formation in Response to Candida albicans. *J Immunol* **190**:4136–4148. doi:10.4049/JIMMUNOL.1202671

Campos-Sánchez JC, Esteban MÁ. 2021. Review of inflammation in fish and value of the zebrafish model. *J Fish Dis* **44**:123–139. doi:10.1111/JFD.13310

Cantuti-Castelvetri L, Ojha R, Pedro LD, Djannatian M, Franz J, Kuivanen S, van der Meer F, Kallio K, Kaya T, Anastasina M, Smura T, Levanov L, Szirovicza L, Tobi A, Kallio-Kokko H, Österlund P, Joensuu M, Meunier FA, Butcher SJ, Winkler MS, Mollenhauer B, Helenius A, Gokce O, Teesalu T, Hepojoki J, Vapalahti O, Stadelmann C, Balistreri G, Simons M. 2020. Neuropilin-1 facilitates SARS-CoV-2 cell entry and infectivity. *Science (80-)* **370**. doi:10.1126/SCIENCE.ABD2985

Carpenter AE, Jones TR, Lamprecht MR, Clarke C, Kang IH, Friman O, Guertin DA, Chang JH, Lindquist RA, Moffat J, Golland P, Sabatini DM. 2006. CellProfiler: image analysis software for identifying and quantifying cell phenotypes. *Genome Biol* **7**:R100. doi:10.1186/gb-2006-7-10-r100

Carrasco L, Sanz MA, González-Almela E. 2018. The Regulation of Translation in Alphavirus-Infected Cells. *Viruses 2018, Vol 10, Page 70* **10**:70. doi:10.3390/V10020070

Carrillo SA, Anguita-Salinas C, Peña OA, Morales RA, Muñoz-Sánchez S, Muñoz-Montecinos C, Paredes-Zúñiga S, Tapia K, Allende ML. 2016. Macrophage Recruitment Contributes to Regeneration of Mechanosensory Hair Cells in the Zebrafish Lateral Line. *J Cell Biochem* **117**:1880–1889. doi:10.1002/JCB.25487

Carter KM, Woodley CM, Brown RS. 2011. A review of tricaine methanesulfonate for anesthesia of fish. *Rev Fish Biol Fish* **21**:51–59. doi:10.1007/s11160-010-9188-0

Carvalho R, de Sonneville J, Stockhammer OW, Savage NDL, Veneman WJ, Ottenhoff THM, Dirks RP, Meijer AH, Spaink HP. 2011. A High-Throughput Screen for Tuberculosis Progression. *PLoS One* **6**:e16779. doi:10.1371/JOURNAL.PONE.0016779

Casalino L, Gaieb Z, Goldsmith JA, Hjorth CK, Dommer AC, Harbison AM, Fogarty CA, Barros EP, Taylor BC, Mclellan JS, Fadda E, Amaro RE. 2020. Beyond Shielding: The Roles of Glycans in the SARS-CoV-2 Spike Protein. *ACS Cent Sci* **6**:1722–1734. doi:10.1021/ACSCENTSCI.0C01056

Castro R, Bernard D, Lefranc MP, Six A, Benmansour A, Boudinot P. 2011. T cell diversity and TcR repertoires in teleost fish. *Fish Shellfish Immunol* **31**:644–654. doi:10.1016/J.FSI.2010.08.016

Chao CC, Hsu PC, Jen CF, Chen IH, Wang Chieh Huei, Chan HC, Tsai PW, Tung KC, Wang Chian Huei, Lan CY, Chuang YJ. 2010. Zebrafish as a model host for Candida albicans infection. *Infect Immun* **78**:2512–2521. doi:10.1128/IAI.01293-09

Chen KW, Monteleone M, Boucher D, Sollberger G, Ramnath D, Condon ND, von Pein JB, Broz P, Sweet MJ, Schroder K. 2018. Noncanonical inflammasome signaling elicits gasdermin D–dependent neutrophil extracellular traps. *Sci Immunol* **3**:6676. doi:10.1126/SCIIMMUNOL.AAR6676/SUPPL_FILE/AAR6676_TABLE_S1.XLSX

Chen SN, Gan Z, Hou J, Yang YC, Huang L, Huang B, Wang S, Nie P. 2022. Identification and establishment of type IV interferon and the characterization of interferon-υ including its class II cytokine receptors IFN-υR1 and IL-10R2. *Nat Commun 2022 131* **13**:1–12. doi:10.1038/s41467-022-28645-6

Chen W, Zhao J, Mu D, Wang Z, Liu Q, Zhang Y, Yang D. 2021. Pyroptosis Mediates Neutrophil Extracellular Trap Formation during Bacterial Infection in Zebrafish. *J Immunol* **206**:1913–1922. doi:10.4049/JIMMUNOL.2001335

Chen WQ, Hu YW, Zou PF, Ren SS, Nie P, Chang MX. 2015. MAVS splicing variants contribute to the induction of interferon and interferon-stimulated genes mediated by RIG-I-like receptors. *Dev Comp Immunol* **49**:19–30. doi:10.1016/J.DCI.2014.10.017

Chen Y, Cai H, Pan J, Xiang N, Tien P, Ahola T, Guo D. 2009. Functional screen reveals SARS coronavirus nonstructural protein nsp14 as a novel cap N7 methyltransferase. *Proc Natl Acad Sci U S A* **106**:3484–3489. doi:10.1073/PNAS.0808790106

Chen Y, Su C, Ke M, Jin X, Xu L, Zhang Z, Wu A, Sun Y, Yang Z, Tien P, Ahola T, Liang Y, Liu X, Guo D. 2011. Biochemical and structural insights into the mechanisms of sars coronavirus RNA ribose 2′-O-methylation by nsp16/nsp10 protein complex. *PLoS Pathog* **7**. doi:10.1371/JOURNAL.PPAT.1002294

Chen Z, Mi L, Xu J, Yu J, Wang X, … JJ-TJ of, 2005 undefined. n.d. Function of HAb18G/CD147 in invasion of host cells by severe acute respiratory syndrome coronavirus. *Acad Chen, L Mi, J Xu, J Yu, X Wang, J Jiang, J Xing, P Shang, A Qian, Y Li, PX Shaw, J WangThe J Infect Dis 2005•academic.oup.com*.

Cheng E, Dorjsuren D, Lehman S, Larson CL, Titus SA, Sun H, Zakharov A, Rai G, Heinzen RA, Simeonov A, Machner MP. 2022. A comprehensive phenotypic screening strategy to identify modulators of cargo translocation by the bacterial Type IVB secretion system. *Am Soc MicrobiolE Cheng, D Dorjsuren, S Lehman, CL Larson, SA Titus, H Sun, A Zakharov, G RaiMbio, 2022•Am Soc Microbiol* **13**. doi:10.1128/mbio.00240-22

Cianciotto NP. 2013. Type II Secretion and Legionella Virulence 81–102. doi:10.1007/82_2013_339

Cigliola V, Becker CJ, Poss KD. 2020. Building bridges, not walls: Spinal cord regeneration in zebrafish. *DMM Dis Model Mech* **13**. doi:10.1242/DMM.044131/225225

Colucci-Guyon E, Tinevez JY, Renshaw SA, Herbomel P. 2011. Strategies of professional phagocytes in vivo: unlike macrophages, neutrophils engulf only surface-associated microbes. *J Cell Sci* **124**:3053–3059. doi:10.1242/JCS.082792

Commins SP, Borish L, Steinke JW. 2010. Immunologic messenger molecules: Cytokines, interferons, and chemokines. *J Allergy Clin Immunol* **125**:S53–S72. doi:10.1016/J.JACI.2009.07.008

Corman VM, Muth D, Niemeyer D, Drosten C. 2018. Hosts and Sources of Endemic Human Coronaviruses. *Adv Virus Res* **100**:163–188. doi:10.1016/BS.AIVIR.2018.01.001

Coronado M, Solis CJ, Hernandez PP, Feijóo CG. 2019. Soybean meal-induced intestinal inflammation in zebrafish is T cell-dependent and has a Th17 cytokine profile. *Front Immunol* **10**:610. doi:10.3389/FIMMU.2019.00610/FULL

D'Amico LA, Cooper MS. 2001. Morphogenetic domains in the yolk syncytial layer of axiating zebrafish embryos. *Dev Dyn* **222**:611–624. doi:10.1002/DVDY.1216

Daly JL, Simonetti B, Klein K, Chen KE, Williamson MK, Antón-Plágaro C, Shoemark DK, Simón-Gracia L, Bauer M, Hollandi R, Greber UF, Horvath P, Sessions RB, Helenius A, Hiscox JA, Teesalu T, Matthews DA, Davidson AD, Collins BM, Cullen PJ, Yamauchi Y. 2020. Neuropilin-1 is a host factor for SARS-CoV-2 infection. *Science (80-)* **370**:861–865. doi:10.1126/SCIENCE.ABD3072

Darif D, Hammi I, Kihel A, El Idrissi Saik I, Guessous F, Akarid K. 2021. The pro-inflammatory cytokines in COVID-19 pathogenesis: What goes wrong? *Microb Pathog* **153**:104799. doi:10.1016/J.MICPATH.2021.104799

Das T, Jaffar-Bandjee MC, Hoarau JJ, Krejbich Trotot P, Denizot M, Lee-Pat-Yuen G, Sahoo R, Guiraud P, Ramful D, Robin S, Alessandri JL, Gauzere BA, Gasque P. 2010. Chikungunya fever: CNS infection and pathologies of a re-emerging arbovirus. *Prog Neurobiol* **91**:121–9.

Dash PK, Gorantla S, Poluektova L, Hasan M, Waight E, Zhang C, Markovic M, Edagwa B, Machhi J, Olson KE, Wang X, Mosley RL, Kevadiya B, Gendelman HE. 2021. Humanized Mice for Infectious and Neurodegenerative disorders. *Retrovirology 2021 181* **18**:1–17. doi:10.1186/S12977-021-00557-1

Davis JM, Clay H, Lewis JL, Ghori N, Herbomel P, Ramakrishnan L. 2002. Real-time visualization of Mycobacterium-macrophage interactions leading to initiation of granuloma formation in zebrafish embryos. *Immunity* **17**:693–702. doi:10.1016/S1074-7613(02)00475-2

Davis JM, Huang M, Botts MR, Hull CM, Huttenlocher A. 2016. A zebrafish model of cryptococcal infection reveals roles for macrophages, endothelial cells, and neutrophils in the establishment and control of sustained fungemia. *Infect Immun* **84**:3047–3062. doi:10.1128/IAI.00506-16/SUPPL_FILE/ZII999091849SO1.PDF

Davison JM, Akitake CM, Goll MG, Rhee JM, Gosse N, Baier H, Halpern ME, Leach SD, Parsons MJ. 2007. Transactivation from Gal4-VP16 transgenic insertions for tissue-specific cell labeling and ablation in zebrafish. *Dev Biol* **304**:811–824. doi:10.1016/j.ydbio.2007.01.033

De Oliveira S, Rosowski EE, Huttenlocher A. 2016. Neutrophil migration in infection and wound repair: going forward in reverse. *Nat Rev Immunol 2016 166* **16**:378–391. doi:10.1038/nri.2016.49

Dee CT, Nagaraju RT, Athanasiadis EI, Gray C, Fernandez del Ama L, Johnston SA, Secombes CJ, Cvejic A, Hurlstone AFL. 2016. CD4-Transgenic Zebrafish Reveal Tissue-Resident Th2- and Regulatory T Cell–like Populations and Diverse Mononuclear Phagocytes. *J Immunol* **197**:3520–3530. doi:10.4049/JIMMUNOL.1600959/-/DCSUPPLEMENTAL

Denans N, Tran NTT, Swall ME, Diaz DC, Blanck J, Piotrowski T. 2022. An anti-inflammatory activation sequence governs macrophage transcriptional dynamics during tissue injury in zebrafish. *Nat Commun* **13**. doi:10.1038/S41467-022-33015-3

Di H, McIntyre AA, Brinton MA. 2018. New insights about the regulation of Nidovirus subgenomic mRNA synthesis. *Virology* **517**:38–43. doi:10.1016/j.virol.2018.01.026

Dooley CM, Mongera A, Walderich B, Nüsslein-Volhard C. 2013. On the embryonic origin of adult melanophores: the role of ErbB and Kit signalling in establishing melanophore stem cells in zebrafish. *Development* **140**:1003–1013. doi:10.1242/dev.087007

Driever W, Solnica-Krezel L, Schier AF, Neuhauss SCF, Malicki J, Stemple DL, Stainier DYR, Zwartkruis F, Abdelilah S, Rangini Z, Belak J, Boggs C. 1996. A genetic screen for mutations affecting embryogenesis in zebrafish. *Development* **123**:37–46. doi:10.1242/DEV.123.1.37

Duan Y, Wang Y, Li Z, Ma L, Wei X, Yang J, Xiao R, Xia C. 2021. The unique structure of the zebrafish TNF-α homotrimer. *Dev Comp Immunol* **122**:104129. doi:10.1016/J.DCI.2021.104129

Eckerle LD, Lu X, Sperry SM, Choi L, Denison MR. 2007. High fidelity of murine hepatitis virus replication is decreased in nsp14 exoribonuclease mutants. *Am Soc MicrobiolLD Eckerle, X Lu, SM Sperry, L Choi, MR DenisonJournal Virol 2007•Am Soc Microbiol* **81**:12135–12144. doi:10.1128/JVI.01296-07

Ellett F, Pazhakh V, Pase L, Benard EL, Weerasinghe H, Azabdaftari D, Alasmari S, Andrianopoulos A, Lieschke GJ. 2018. Macrophages protect Talaromyces marneffei conidia from myeloperoxidase-dependent neutrophil fungicidal activity during infection establishment in vivo. *PLOS Pathog* **14**:e1007063. doi:10.1371/JOURNAL.PPAT.1007063

Engeszer RE, Patterson LB, Rao AA, Parichy DM. 2007. Zebrafish in The Wild: A Review of Natural History And New Notes from The Field. *https://home.liebertpub.com/zeb* **4**:21–40. doi:10.1089/ZEB.2006.9997

Engeszer RE, Ryan MJ, Parichy DM. 2004. Learned social preference in zebrafish. *Curr Biol* **14**:881–884. doi:10.1016/J.CUB.2004.04.042

Eshbach ML, Weisz OA. 2017. Receptor-Mediated Endocytosis in the Proximal Tubule. *Annu Rev Physiol* **79**:425–448. doi:10.1146/annurev-physiol-022516-034234

Espmark A, Niklasson B. 1984. Ockelbo disease in Sweden: epidemiological, clinical, and virological data from the 1982 outbreak. *Am J Trop Med Hyg* **33**:1203–1211. doi:10.4269/AJTMH.1984.33.1203

Ferrero G, Mahony CB, Dupuis E, Yvernogeau L, Di Ruggiero E, Miserocchi M, Caron M, Robin C, Traver D, Bertrand JY, Wittamer V. 2018. Embryonic Microglia Derive from Primitive Macrophages and Are Replaced by cmyb-Dependent Definitive Microglia in Zebrafish. *Cell*

Rep **24**:130–141. doi:10.1016/j.celrep.2018.05.066
Fields BS, Benson RF, Besser RE. 2002. Legionella and legionnaires' disease: 25 Years of investigation. *Clin Microbiol Rev* **15**:506–526. doi:10.1128/CMR.15.3.506-526.2002
Fischer U, Koppang EO, Nakanishi T. 2013. Teleost T and NK cell immunity. *Fish Shellfish Immunol* **35**:197–206. doi:10.1016/J.FSI.2013.04.018
Flannagan RS, Jaumouillé V, Grinstein S. 2012. The Cell Biology of Phagocytosis. *https://doi.org/101146/annurev-pathol-011811-132445* **7**:61–98. doi:10.1146/ANNUREV-PATHOL-011811-132445
Fliermans CB, Soracco RJ, Pope DH. 1981. Measure of Legionella pneumophila activity in situ. *Curr Microbiol* **6**:89–94. doi:10.1007/BF01569010
Flores MV, Hall C, Jury A, Crosier K, Crosier P. 2007. The zebrafish retinoid-related orphan receptor (ror) gene family. *Gene Expr Patterns* **7**:535–543. doi:10.1016/J.MODGEP.2007.02.001
Fontana BD, Mezzomo NJ, Kalueff A V., Rosemberg DB. 2018. The developing utility of zebrafish models of neurological and neuropsychiatric disorders: A critical review. *Exp Neurol* **299**:157–171. doi:10.1016/J.EXPNEUROL.2017.10.004
Furuta T, Tomioka R, Taki K, Nakamura K, Tamamaki N, Kaneko T. 2001. In vivo transduction of central neurons using recombinant Sindbis virus: Golgi-like labeling of dendrites and axons with membrane-targeted fluorescent proteins. *J Histochem Cytochem Off J Histochem Soc* **49**:1497–1508. doi:10.1177/002215540104901203
Futosi K, Fodor S, Mócsai A. 2013. Neutrophil cell surface receptors and their intracellular signal transduction pathways. *Int Immunopharmacol* **17**:638–650. doi:10.1016/J.INTIMP.2013.06.034
Gan Z, Chen SN, Huang B, Zou J, Nie P. 2020. Fish type I and type II interferons: composition, receptor usage, production and function. *Rev Aquac* **12**:773–804. doi:10.1111/RAQ.12349
Gao Y, Yan L, Huang Y, Liu F, Zhao Y, Cao L, Science TW-, 2020 undefined. n.d. Structure of the RNA-dependent RNA polymerase from COVID-19 virus. *Sci Gao, L Yan, Y Huang, F Liu, Y Zhao, L Cao, T Wang, Q Sun, Z Ming, L Zhang, J GeScience, 2020•science.org*.
García-Weber D, Arrieumerlou C. 2020. ADP-heptose: a bacterial PAMP detected by the host sensor ALPK1. *Cell Mol Life Sci 2020 781* **78**:17–29. doi:10.1007/S00018-020-03577-W
García-Weber D, Dangeard A-S, Cornil J, Thai L, Rytter H, Zamyatina A, Mulard LA, Arrieumerlou C. 2018. ADP-heptose is a newly identified pathogen-associated molecular pattern of Shigella flexneri. *EMBO Rep* **19**:e46943. doi:10.15252/EMBR.201846943
Ge Z, Yuan P, Chen L, Chen J, Shen D, She Z, Lu Y. 2022. New Global Insights on the Regulation of the Biphasic Life Cycle and Virulence Via ClpP-Dependent Proteolysis in Legionella pneumophila. *Mol Cell Proteomics* **21**. doi:10.1016/J.MCPRO.2022.100233
Gerhard GS, Kauffman EJ, Wang X, Stewart R, Moore JL, Kasales CJ, Demidenko E, Cheng KC. 2002. Life spans and senescent phenotypes in two strains of Zebrafish (Danio rerio). *Exp Gerontol* **37**:1055–1068. doi:10.1016/S0531-5565(02)00088-8
Giese MA, Hind LE, Huttenlocher A. 2019. Neutrophil plasticity in the tumor microenvironment. *Blood* **133**:2159–2167. doi:10.1182/BLOOD-2018-11-844548
Ginhoux F, Guilliams M, Naik SH. 2016. Dendritic cell and macrophage nomenclature and classification. *Front Immunol* **7**. doi:10.3389/FIMMU.2016.00168
Gonçalves IG, Simões LC, Simões M. 2021. Legionella pneumophila. *Trends Microbiol* **29**:860–861.

doi:10.1016/j.tim.2021.04.005
González-Rosa JM. 2022. Zebrafish Models of Cardiac Disease: From Fortuitous Mutants to Precision Medicine. *Circ Res* **130**:1803–1826. doi:10.1161/CIRCRESAHA.122.320396
Gonzalez CD, Ledo C, Giai C, Garófalo A, Gómez MI. 2015. The Sbi Protein Contributes to Staphylococcus aureus Inflammatory Response during Systemic Infection. *PLoS One* **10**:e0131879. doi:10.1371/JOURNAL.PONE.0131879
Gorbalenya AE, Baker SC, Baric RS, de Groot RJ, Drosten C, Gulyaeva AA, Haagmans BL, Lauber C, Leontovich AM, Neuman BW, Penzar D, Perlman S, Poon LLM, Samborskiy D V., Sidorov IA, Sola I, Ziebuhr J. 2020. The species Severe acute respiratory syndrome-related coronavirus: classifying 2019-nCoV and naming it SARS-CoV-2. *Nat Microbiol 2020 54* **5**:536–544. doi:10.1038/s41564-020-0695-z
Goulding M. 2009. Circuits controlling vertebrate locomotion: moving in a new direction. *Nat Rev Neurosci 2009 107* **10**:507–518. doi:10.1038/nrn2608
Gratacap RL, Scherer AK, Seman BG, Wheeler RT. 2017. Control of mucosal candidiasis in the zebrafish swim bladder depends on neutrophils that block filament invasion and drive extracellular-trap production. *Infect Immun* **85**. doi:10.1128/IAI.00276-17/SUPPL_FILE/ZII999092113S1.PDF
Grayfer L, Belosevic M. 2009. Molecular characterization of novel interferon gamma receptor 1 isoforms in zebrafish (Danio rerio) and goldfish (Carassius auratus L.). *Mol Immunol* **46**:3050–3059. doi:10.1016/J.MOLIMM.2009.06.004
Grunwald DJ, Eisen JS. 2002a. Headwaters of the zebrafish — emergence of a new model vertebrate. *Nat Rev Genet 2002 39* **3**:717–724. doi:10.1038/nrg892
Grunwald DJ, Eisen JS. 2002b. Headwaters of the zebrafish — emergence of a new model vertebrate. *Nat Rev Genet 2002 39* **3**:717–724. doi:10.1038/nrg892
Guard RW, Mcauliffe MJ, Stallman ND, Bramston BA. 1982. Haemorrhagic manifestations with sindbis infection. Case report. *Pathology* **14**:89–90. doi:10.3109/00313028209069049
Gunimaladevi I, Savan R, Sakai M. 2006. Identification, cloning and characterization of interleukin-17 and its family from zebrafish. *Fish Shellfish Immunol* **21**:393–403. doi:10.1016/J.FSI.2006.01.004
Guo Z, Li Y, Ding SW. 2018. Small RNA-based antimicrobial immunity. *Nat Rev Immunol 2018 191* **19**:31–44. doi:10.1038/s41577-018-0071-x
Gurevich DB, Severn CE, Twomey C, Greenhough A, Cash J, Toye AM, Mellor H, Martin P. 2018. Live imaging of wound angiogenesis reveals macrophage orchestrated vessel sprouting and regression. *EMBO J* **37**:e97786. doi:10.15252/EMBJ.201797786
Gylfe Å, Ribers Å, Forsman O, Bucht G, Alenius GM, Wållberg-Jonsson S, Ahlm C, Evander M. 2018. Mosquitoborne Sindbis Virus Infection and Long-Term Illness. *Emerg Infect Dis* **24**:1141. doi:10.3201/EID2406.170892
H. Meijer A, P. Spaink H. 2011. Host-Pathogen Interactions Made Transparent with the Zebrafish Model. *Curr Drug Targets* **12**:1000. doi:10.2174/138945011795677809
Hakkim A, Fuchs TA, Martinez NE, Hess S, Prinz H, Zychlinsky A, Waldmann H. 2010. Activation of the Raf-MEK-ERK pathway is required for neutrophil extracellular trap formation. *Nat Chem Biol 2010 72* **7**:75–77. doi:10.1038/nchembio.496
Hall C, Flores MV, Crosier K, Crosier P. 2009. Live cell imaging of zebrafish leukocytes. *Methods Mol Biol* **546**:255–271. doi:10.1007/978-1-60327-977-2_16/FIGURES/5_16

Hamilton Francis, Hamilton Francis,. 1822. An account of the fishes found in the river Ganges and its branches. Edinburgh: Printed for A. Constable and company; [etc., etc.].

Hardwick JM, Levine B. 2000. Sindbis virus vector system for functional analysis of apoptosis regulators. *Methods Enzymol* **322**:492–508.

Harvie EA, Huttenlocher A. 2015. Neutrophils in host defense: new insights from zebrafish. *J Leukoc Biol* **98**:523–537. doi:10.1189/JLB.4MR1114-524R

Henry KM, Loynes CA, Whyte MKB, Renshaw SA. 2013. Zebrafish as a model for the study of neutrophil biology. *J Leukoc Biol* **94**:633–642. doi:10.1189/JLB.1112594

Herbomel P, Thisse B, Thisse C. 2001. Zebrafish early macrophages colonize cephalic mesenchyme and developing brain, retina, and epidermis through a M-CSF receptor-dependent invasive process. *Dev Biol* **238**:274–288. doi:10.1006/DBIO.2001.0393

Herbomel P, Thisse B, Thisse C. 1999. Ontogeny and behaviour of early macrophages in the zebrafish embryo. *Development* **126**:3735–3745. doi:10.1242/DEV.126.17.3735

High AS, Torosian SD, Rodgers FG. 1993. Cloning, nucleotide sequence and expression in Escherichia coli of a gene (ompM) encoding a 25 kDa major outer-membrane protein (MOMP) of Legionella pneumophila. *J Gen Microbiol* **139**:1715–1721. doi:10.1099/00221287-139-8-1715

Hindahl MS, Iglewski BH. 1984. Isolation and characterization of the Legionella pneumophila outer membrane. *J Bacteriol* **159**:107–113. doi:10.1128/JB.159.1.107-113.1984

Honjo Y, Kniss J, Eisen JS. 2008. Neuregulin-mediated ErbB3 signaling is required for formation of zebrafish dorsal root ganglion neurons. *Development* **135**:2615–2625. doi:10.1242/DEV.022178

Howe K, Clark MD, Torroja CF, Torrance J, Berthelot C, Muffato M, Collins JE, Humphray S, McLaren K, Matthews L, McLaren S, Sealy I, Caccamo M, Churcher C, Scott C, Barrett JC, Koch R, Rauch GJ, White S, Chow W, Kilian B, Quintais LT, Guerra-Assunção JA, Zhou Y, Gu Y, Yen J, Vogel JH, Eyre T, Redmond S, Banerjee R, Chi J, Fu B, Langley E, Maguire SF, Laird GK, Lloyd D, Kenyon E, Donaldson S, Sehra H, Almeida-King J, Loveland J, Trevanion S, Jones M, Quail M, Willey D, Hunt A, Burton J, Sims S, McLay K, Plumb B, Davis J, Clee C, Oliver K, Clark R, Riddle C, Eliott D, Threadgold G, Harden G, Ware D, Mortimer B, Kerry G, Heath P, Phillimore B, Tracey A, Corby N, Dunn M, Johnson C, Wood J, Clark S, Pelan S, Griffiths G, Smith M, Glithero R, Howden P, Barker N, Stevens C, Harley J, Holt K, Panagiotidis G, Lovell J, Beasley H, Henderson C, Gordon D, Auger K, Wright D, Collins J, Raisen C, Dyer L, Leung K, Robertson L, Ambridge K, Leongamornlert D, McGuire S, Gilderthorp R, Griffiths C, Manthravadi D, Nichol S, Barker G, Whitehead S, Kay M, Brown J, Murnane C, Gray E, Humphries M, Sycamore N, Barker D, Saunders D, Wallis J, Babbage A, Hammond S, Mashreghi-Mohammadi M, Barr L, Martin S, Wray P, Ellington A, Matthews N, Ellwood M, Woodmansey R, Clark G, Cooper J, Tromans A, Grafham D, Skuce C, Pandian R, Andrews R, Harrison E, Kimberley A, Garnett J, Fosker N, Hall R, Garner P, Kelly D, Bird C, Palmer S, Gehring I, Berger A, Dooley CM, Ersan-Ürün Z, Eser C, Geiger H, Geisler M, Karotki L, Kirn A, Konantz J, Konantz M, Oberländer M, Rudolph-Geiger S, Teucke M, Osoegawa K, Zhu B, Rapp A, Widaa S, Langford C, Yang F, Carter NP, Harrow J, Ning Z, Herrero J, Searle SMJ, Enright A, Geisler R, Plasterk RHA, Lee C, Westerfield M, De Jong PJ, Zon LI, Postlethwait JH, Nüsslein-Volhard C, Hubbard TJP, Crollius HR, Rogers J, Stemple DL. 2013. The zebrafish reference genome sequence and its relationship to the human genome. *Nat 2013 4967446* **496**:498–503.

doi:10.1038/nature12111
Hu C Bin, Wang J, Hong Y, Li H, Fan DD, Lin AF, Xiang LX, Shao JZ. 2023. Single-cell transcriptome profiling reveals diverse immune cell populations and their responses to viral infection in the spleen of zebrafish. *FASEB J* **37**:e22951. doi:10.1096/FJ.202201505RRRR
Huang Y, Yang C, Xu X feng, Xu W, Liu S wen. 2020. Structural and functional properties of SARS-CoV-2 spike protein: potential antivirus drug development for COVID-19. *Acta Pharmacol Sin 2020 419* **41**:1141–1149. doi:10.1038/s41401-020-0485-4
Hubálek Z. 2008. Mosquito-borne viruses in Europe. *Parasitol Res* **103**:29–43. doi:10.1007/S00436-008-1064-7/FIGURES/6
Hui SP, Sheng DZ, Sugimoto K, Gonzalez-Rajal A, Nakagawa S, Hesselson D, Kikuchi K. 2017. Zebrafish Regulatory T Cells Mediate Organ-Specific Regenerative Programs. *Dev Cell* **43**:659-672.e5. doi:10.1016/J.DEVCEL.2017.11.010
Huising MO, Stet RJM, Savelkoul HFJ, Verburg-Van Kemenade BML. 2004. The molecular evolution of the interleukin-1 family of cytokines; IL-18 in teleost fish. *Dev Comp Immunol* **28**:395–413. doi:10.1016/J.DCI.2003.09.005
Igawa D, Sakai M, Savan R. 2006. An unexpected discovery of two interferon gamma-like genes along with interleukin (IL)-22 and -26 from teleost: IL-22 and -26 genes have been described for the first time outside mammals. *Mol Immunol* **43**:999–1009. doi:10.1016/J.MOLIMM.2005.05.009
Iliadi V, Staykova J, Iliadis S, Konstantinidou I, Sivykh P, Romanidou G, Vardikov DF, Cassimos D, Konstantinidis TG. 2022. Legionella pneumophila: The Journey from the Environment to the Blood. *J Clin Med 2022, Vol 11, Page 6126* **11**:6126. doi:10.3390/JCM11206126
Irigoyen N, Firth AE, Jones JD, Chung BYW, Siddell SG, Brierley I. 2016. High-Resolution Analysis of Coronavirus Gene Expression by RNA Sequencing and Ribosome Profiling. *PLOS Pathog* **12**:e1005473. doi:10.1371/JOURNAL.PPAT.1005473
Isberg RR, O'Connor TJ, Heidtman M. 2008. The Legionella pneumophila replication vacuole: making a cosy niche inside host cells. *Nat Rev Microbiol 2008 71* **7**:13–24. doi:10.1038/nrmicro1967
Ivanov K, virology JZ-J of, 2004 undefined. 2004. Human coronavirus 229E nonstructural protein 13: characterization of duplex-unwinding, nucleoside triphosphatase, and RNA 5'-triphosphatase activities. *Am Soc MicrobiolKA Ivanov, J Zieb Virol 2004•Am Soc Microbiol* **78**:7833–7838. doi:10.1128/JVI.78.14.7833-7838.2004
Jackson CB, Farzan M, Chen B, Choe H. 2021. Mechanisms of SARS-CoV-2 entry into cells. *Nat Rev Mol Cell Biol 2021 231* **23**:3–20. doi:10.1038/s41580-021-00418-x
Jackson EB. 1952. Studies on two rickettsia-like agents probably isolated from guinea pigsBacteriol Proc. p. 119.
Jeffers SA, Tusell SM, Gillim-Ross L, Hemmila EM, Achenbach JE, Babcock GJ, Thomas WD, Thackray LB, Young MD, Mason RJ, Ambrosino DM, Wentworth DE, DeMartini JC, Holmes K V. 2004. CD209L (L-SIGN) is a receptor for severe acute respiratory syndrome coronavirus. *Proc Natl Acad Sci U S A* **101**:15748–15753. doi:10.1073/PNAS.0403812101
Jemielity S, Wang JJ, Chan YK, Ahmed AA, Li W, Monahan S, Bu X, Farzan M, Freeman GJ, Umetsu DT, DeKruyff RH, Choe H. 2013. TIM-family Proteins Promote Infection of Multiple Enveloped Viruses through Virion-associated Phosphatidylserine. *PLoS Pathog* **9**. doi:10.1371/JOURNAL.PPAT.1003232

Jose J, Tang J, Taylor AB, Baker TS, Kuhn RJ. 2015. Fluorescent Protein-Tagged Sindbis Virus E2 Glycoprotein Allows Single Particle Analysis of Virus Budding from Live Cells. *Viruses* **7**:6182–6199. doi:10.3390/v7122926

Jose J, Taylor AB, Kuhn RJ. 2017. Spatial and temporal analysis of alphavirus replication and assembly in mammalian and mosquito cells. *MBio* **8**. doi:10.1128/MBIO.02294-16/ASSET/CD8CAC71-6440-47ED-9F83-CF22DA513BFA/ASSETS/GRAPHIC/MBO0011731770009.JPEG

Journal J, Gholipour A, Moosavian M, Galehdari H, Makvandi M, Memari HR, Alvandi A. 2010. Cloning and periplasmic expression of peptidoglycan-associated lipoprotein (PAL) protein of Legionella pneumophila in Escherichia coli. *Jundishapur J Microbiol* **3**:1–9.

Jurisch-Yaksi N, Yaksi E, Kizil C. 2020. Radial glia in the zebrafish brain: Functional, structural, and physiological comparison with the mammalian glia. *Glia* **68**:2451–2470. doi:10.1002/GLIA.23849

Kalev-Zylinska ML, Horsfield JA, Flores MVC, Postlethwait JH, Vitas MR, Baas AM, Crosier PS, Crosier KE. 2002. Runx1 is required for zebrafish blood and vessel development and expression of a human RUNX1-CBF2T1 transgene advances a model for studies of leukemogenesis. *Development* **129**:2015–2030. doi:10.1242/DEV.129.8.2015

Kambara H, Liu F, Zhang X, Liu P, Bajrami B, Teng Y, Zhao L, Zhou S, Yu H, Zhou W, Silberstein LE, Cheng T, Han M, Xu Y, Luo HR. 2018. Gasdermin D Exerts Anti-inflammatory Effects by Promoting Neutrophil Death. *Cell Rep* **22**:2924–2936. doi:10.1016/J.CELREP.2018.02.067

Kamitani W, Narayanan K, Huang C, Lokugamage K, Ikegami T, Ito N, Kubo H, Makino S. 2006. Severe acute respiratory syndrome coronavirus nsp1 protein suppresses host gene expression by promoting host mRNA degradation. *Proc Natl Acad Sci U S A* **103**:12885–12890. doi:10.1073/PNAS.0603144103/SUPPL_FILE/03144FIG11.PDF

Kany S, Vollrath JT, Relja B. 2019. Cytokines in Inflammatory Disease. *Int J Mol Sci 2019, Vol 20, Page 6008* **20**:6008. doi:10.3390/IJMS20236008

Kapellos TS, Taylor L, Lee H, Cowley SA, James WS, Iqbal AJ, Greaves DR. 2016. A novel real time imaging platform to quantify macrophage phagocytosis. *Biochem Pharmacol* **116**:107–119. doi:10.1016/J.BCP.2016.07.011

Kasheta M, Painter CA, Moore FE, Lobbardi R, Bryll A, Freiman E, Stachura D, Rogers AB, Houvras Y, Langenau DM, Ceol CJ. 2017. Identification and characterization of T reg–like cells in zebrafish. *J Exp Med* **214**:3519. doi:10.1084/JEM.20162084

Kaslin J, Ganz J. 2020. Zebrafish Nervous Systems. *Zebrafish Biomed Res Biol Husbandry, Dis Res Appl* 181–189. doi:10.1016/B978-0-12-812431-4.00018-X

Kassahn KS, Dang VT, Wilkins SJ, Perkins AC, Ragan MA. 2009. Evolution of gene function and regulatory control after whole-genome duplication: Comparative analyses in vertebrates. *Genome Res* **19**:1404. doi:10.1101/GR.086827.108

Kawakami K. 2004. Transgenesis and Gene Trap Methods in Zebrafish by Using the Tol2 Transposable Element. *Methods Cell Biol* **77**:201–222. doi:10.1016/S0091-679X(04)77011-9

Kawakami K, Koga A, Hori H, Shima A. 1998. Excision of the Tol2 transposable element of the medaka fish, Oryzias latipes, in zebrafish, Danio rerio. *Gene* **225**:17–22. doi:10.1016/S0378-1119(98)00537-X

Kelly Kuan CY, Tannahill D, Cook GMW, Keynes RJ. 2004. Somite polarity and segmental patterning of the peripheral nervous system. *Mech Dev* **121**:1055–1068.

doi:10.1016/j.mod.2004.05.001
Kent ML, Feist SW, Harper C, Hoogstraten-Miller S, Law J Mac, Sánchez-Morgado JM, Tanguay RL, Sanders GE, Spitsbergen JM, Whipps CM. 2009. Recommendations for control of pathogens and infectious diseases in fish research facilities. *Comp Biochem Physiol Part C Toxicol Pharmacol* **149**:240–248. doi:10.1016/J.CBPC.2008.08.001
Kheawfu K, Pikulkaew S, Wellendorph P, Jørgensen L von G, Rades T, Müllertz A, Okonogi S. 2022. Elucidating Pathway and Anesthetic Mechanism of Action of Clove Oil Nanoformulations in Fish. *Pharmaceutics* **14**. doi:10.3390/PHARMACEUTICS14050919
Kim D, Lee J-Y, Yang J-S, Kim JW, Kim VN, Correspondence HC, Chang H. 2020. The architecture of SARS-CoV-2 transcriptome. *cell.comD Kim, JY Lee, JS Yang, JW Kim, VN Kim, H Chang 2020•cell.com* **181**:914-921.e10. doi:10.1016/j.cell.2020.04.011
Kimmel Charles B., Ballard WW, Kimmel SR, Ullmann B, Schilling TF. 1995. Stages of embryonic development of the zebrafish. *Dev Dyn* **203**:253–310. doi:10.1002/AJA.1002030302
Kimmel C B, Ballard WW, Kimmel SR, Ullmann B, Schilling TF. 1995. Stages of embryonic development of the zebrafish. *Dev Dyn* **203**:253–310. doi:10.1002/aja.1002030302
Kinchen JM, Ravichandran KS. 2008. Phagosome maturation: going through the acid test. *Nat Rev Mol Cell Biol 2008 910* **9**:781–795. doi:10.1038/nrm2515
Kinth P, Mahesh G, Panwar Y. 2013. Mapping of zebrafish research: A global outlook. *Zebrafish* **10**:510–517. doi:10.1089/ZEB.2012.0854/ASSET/IMAGES/LARGE/FIGURE2.JPEG
Kishi S, Slack BE, Uchiyama J, Zhdanova I V. 2009. Zebrafish as a Genetic Model in Biological and Behavioral Gerontology: Where Development Meets Aging in Vertebrates – A Mini-Review. *Gerontology* **55**:430. doi:10.1159/000228892
Kissa K, Herbomel P. 2010. Blood stem cells emerge from aortic endothelium by a novel type of cell transition. *Nat 2010 4647285* **464**:112–115. doi:10.1038/nature08761
Konishi T, Yamashiro T, Koide M, Nishizono A. 2006. Influence of temperature on growth of Legionella pneumophila biofilm determined by precise temperature gradient incubator. *J Biosci Bioeng* **101**:478–484. doi:10.1263/JBB.101.478
Kostiukov MA, Daniiarov O, Skvortsova TM, Kondrashina NG, Berezina LK. 1981. [Isolation of the Sindbis virus from Hyalomma anatolicum CL Kock 1844 ticks in Tadzhikistan]. *Med Parazitol (Mosk)* **50**:34–35.
KOZUCH O, M L, J N. 1978. ISOLATION OF SINDBIS VIRUS FROM THE FROG RANA RIDIBUNDA. *Isol SINDBIS VIRUS FROM FROG RANA RIDIBUNDA*.
Küchler AM, Gjini E, Peterson-Maduro J, Cancilla B, Wolburg H, Schulte-Merker S. 2006. Development of the zebrafish lymphatic system requires VEGFC signaling. *Curr Biol* **16**:1244–1248. doi:10.1016/J.CUB.2006.05.026
Kyritsis N, Kizil C, Zocher S, Kroehne V, Kaslin J, Freudenreich D, Iltzsche A, Brand M. 2012. Acute inflammation initiates the regenerative response in the adult zebrafish brain. *Science (80-)* **338**:1353–1356. doi:10.1126/SCIENCE.1228773/SUPPL_FILE/KYRITSIS.SM.PDF
Laghi V, Rezelj V, Boucontet L, Frétaud M, Da Costa B, Boudinot P, Salinas I, Lutfalla G, Vignuzzi M, Levraud JP. 2022. Exploring Zebrafish Larvae as a COVID-19 Model: Probable Abortive SARS-CoV-2 Replication in the Swim Bladder. *Front Cell Infect Microbiol* **12**. doi:10.3389/fcimb.2022.790851
Laine M, Luukkainen R, Jalava J, Ilonen J, Kuusistö P, Toivanen A. 2000. Prolonged arthritis associated with Sindbis-related (Pogosta) virus infection. *Rheumatology* **39**:1272–1274.

doi:10.1093/RHEUMATOLOGY/39.11.1272
Lam SH, Chua HL, Gong Z, Lam TJ, Sin YM. 2004. Development and maturation of the immune system in zebrafish, Danio rerio: a gene expression profiling, in situ hybridization and immunological study. *Dev Comp Immunol* **28**:9–28. doi:10.1016/S0145-305X(03)00103-4
Lamers MM, Haagmans BL. 2022. SARS-CoV-2 pathogenesis. *Nat Rev Microbiol 2022 205* **20**:270–284. doi:10.1038/s41579-022-00713-0
Langenau DM, Keefe MD, Storer NY, Guyon JR, Kutok JL, Le X, Goessling W, Neuberg DS, Kunkel LM, Zon LI. 2007. Effects of RAS on the genesis of embryonal rhabdomyosarcoma. *Genes Dev* **21**:1382–1395. doi:10.1101/GAD.1545007
Langevin Christelle, Aleksejeva E, Passoni G, Palha N, Levraud JP, Boudinot P. 2013. The Antiviral Innate Immune Response in Fish: Evolution and Conservation of the IFN System. *J Mol Biol* **425**:4904–4920. doi:10.1016/J.JMB.2013.09.033
Langevin C., van der Aa LM, Houel A, Torhy C, Briolat V, Lunazzi A, Harmache A, Bremont M, Levraud J-P, Boudinot P. 2013. Zebrafish ISG15 exerts a strong antiviral activity against RNA and DNA viruses and regulates the interferon response. *J Virol* **87**:10025–10036. doi:10.1128/JVI.01294-12
Langheinrich U. 2003. Zebrafish: A new model on the pharmaceutical catwalk. *BioEssays* **25**:904–912. doi:10.1002/BIES.10326
Lazarov T, Juarez-Carreño S, Cox N, Geissmann F. 2023. Physiology and diseases of tissue-resident macrophages. *Nat 2023 6187966* **618**:698–707. doi:10.1038/s41586-023-06002-x
Le Guyader D, Redd MJ, Colucci-Guyon E, Murayama E, Kissa K, Briolat V, Mordelet E, Zapata A, Shinomiya H, Herbomel P. 2008. Origins and unconventional behavior of neutrophils in developing zebrafish. *Blood* **111**:132–141. doi:10.1182/BLOOD-2007-06-095398
Leiba J, Özbilgiç R, Hernández L, Demou M, Lutfalla G, Yatime L, Nguyen-Chi M. 2023. Molecular Actors of Inflammation and Their Signaling Pathways: Mechanistic Insights from Zebrafish. *Biology (Basel)* **12**. doi:10.3390/BIOLOGY12020153
Leung JYS, Ng MML, Chu JJH. 2011. Replication of alphaviruses: A review on the entry process of alphaviruses into cells. *Adv Virol* **2011**. doi:10.1155/2011/249640
Levraud J.-P., Jouneau L, Briolat V, Laghi V, Boudinot P. 2019. IFN-stimulated genes in zebrafish and humans define an ancient arsenal of antiviral immunity. *J Immunol* **203**. doi:10.4049/jimmunol.1900804
Levraud Jean-Pierre, Jouneau L, Briolat V, Laghi V, Boudinot P. 2019. IFN-Stimulated Genes in Zebrafish and Humans Define an Ancient Arsenal of Antiviral Immunity. *J Immunol* **203**:3361–3373. doi:10.4049/JIMMUNOL.1900804
Levraud J-P, Palha N, Langevin C, Boudinot P. 2014. Through the looking glass: witnessing host-virus interplay in zebrafish. *Trends Microbiol* **22**:490–497. doi:10.1016/j.tim.2014.04.014
Levraud JP, Disson O, Kissa K, Bonne I, Cossart P, Herbomel P, Lecuit M. 2009. Real-time observation of Listeria monocytogenes-phagocyte interactions in living zebrafish larvae. *Infect Immun* **77**:3651–3660. doi:10.1128/IAI.00408-09/SUPPL_FILE/LEVRAUD_MOVIES3.MOV
Lewis KE, Eisen JS. 2003. From cells to circuits: development of the zebrafish spinal cord. *Prog Neurobiol* **69**:419–449. doi:10.1016/S0301-0082(03)00052-2
Li P, Li M, Lindberg MR, Kennett MJ, Xiong N, Wang Y. 2010. PAD4 is essential for antibacterial innate immunity mediated by neutrophil extracellular traps. *J Exp Med* **207**:1853–1862.

doi:10.1084/JEM.20100239
Li S, Lu LF, Wang ZX, Chen DD, Zhang YA. 2016. Fish IRF6 is a positive regulator of IFN expression and involved in both of the MyD88 and TBK1 pathways. *Fish Shellfish Immunol* **57**:262–268. doi:10.1016/J.FSI.2016.08.059
Li Y, Di Santo JP. 2019. Modeling Infectious Diseases in Mice with a "Humanized" Immune System. *Microbiol Spectr* **7**. doi:10.1128/MICROBIOLSPEC.BAI-0019-2019/ASSET/0826D6CF-82DB-4E5B-A3DB-CD340E0EC54A/ASSETS/GRAPHIC/BAI-0019-2019-FIG3.GIF
Li Z, Journal MB-B, 2021 undefined. 2021. Neuropilin-1 assists SARS-CoV-2 infection by stimulating the separation of Spike protein S1 and S2. *cell.comZ Li, M BuckBiophysical Journal, 2021•cell.com* **120**:2828–2837. doi:10.1016/j.bpj.2021.05.026
Linnerz T, Hall CJ. 2020. The Diverse Roles of Phagocytes During Bacterial and Fungal Infections and Sterile Inflammation: Lessons From Zebrafish. *Front Immunol* **11**:537369. doi:10.3389/FIMMU.2020.01094/BIBTEX
Liu C, Chu D, Kalantar-Zadeh K, George J, Young HA, Liu G. 2021. Cytokines: From Clinical Significance to Quantification. *Adv Sci* **8**:2004433. doi:10.1002/ADVS.202004433
Liu C, Wu C, Yang Q, Gao J, Li L, Yang D, Luo L. 2016. Macrophages Mediate the Repair of Brain Vascular Rupture through Direct Physical Adhesion and Mechanical Traction. *Immunity* **44**:1162–1176. doi:10.1016/j.immuni.2016.03.008
Liu X, Li Y-S, Shinton SA, Rhodes J, Tang L, Feng H, Jette CA, Look AT, Hayakawa K, Hardy RR. 2017. Zebrafish B Cell Development without a Pre–B Cell Stage, Revealed by CD79 Fluorescence Reporter Transgenes. *J Immunol* **199**:1706–1715. doi:10.4049/JIMMUNOL.1700552/-/DCSUPPLEMENTAL
Lockwood DC, Amin H, Costa TRD, Schroeder GN. 2022. The Legionella pneumophila Dot/Icm type IV secretion system and its effectors. *Microbiol (United Kingdom)* **168**. doi:10.1099/MIC.0.001187
López-Muñoz A, Sepulcre MP, Roca FJ, Figueras A, Meseguer J, Mulero V. 2011. Evolutionary conserved pro-inflammatory and antigen presentation functions of zebrafish IFNγ revealed by transcriptomic and functional analysis. *Mol Immunol* **48**:1073–1083. doi:10.1016/J.MOLIMM.2011.01.015
López Hernández Y, Yero D, Pinos-Rodríguez JM, Gibert I. 2015. Animals devoid of pulmonary system as infection models in the study of lung bacterial pathogens. *Front Microbiol* **6**:127206. doi:10.3389/FMICB.2015.00038/BIBTEX
Loynes CA, Lee JA, Robertson AL, Steel MJG, Ellett F, Feng Y, Levy BD, Whyte MKB, Renshaw SA. 2018. PGE2 production at sites of tissue injury promotes an anti-inflammatory neutrophil phenotype and determines the outcome of inflammation resolution in vivo. *Sci Adv* **4**. doi:10.1126/SCIADV.AAR8320/SUPPL_FILE/AAR8320_SM.PDF
Lundström JO. 1999. Mosquito-borne viruses in western Europe: a review. *J Vector Ecol* **24**:1–39.
Lundstrom K. 2001. Application of Alphavirus Vectors in Drug Discovery. *Anim Cell Technol From Target to Mark* 45–51. doi:10.1007/978-94-010-0369-8_11
Lustig S, Jackson AC, Hahn CS, Griffin DE, Strauss EG, Strauss JH. 1988. Molecular basis of Sindbis virus neurovirulence in mice. *J Virol* **62**:2329–2336. doi:10.1128/JVI.62.7.2329-2336.1988
Lyons DA, Talbot WS. 2015. Glial Cell Development and Function in Zebrafish. *Cold Spring Harb Perspect Biol* **7**:a020586. doi:10.1101/CSHPERSPECT.A020586
Mahabir S, Chatterjee D, Buske C, Gerlai R. 2013. Maturation of shoaling in two zebrafish strains:

a behavioral and neurochemical analysis. *Behav Brain Res* **247**:1–8. doi:10.1016/J.BBR.2013.03.013

Maisey K, Montero R, Corripio-Miyar Y, Toro-Ascuy D, Valenzuela B, Reyes-Cerpa S, Sandino AM, Zou J, Wang T, Secombes CJ, Imarai M. 2016. Isolation and Characterization of Salmonid CD4+ T Cells. *J Immunol* **196**:4150–4163. doi:10.4049/JIMMUNOL.1500439

Malone B, Urakova N, Snijder EJ, Campbell EA. 2021. Structures and functions of coronavirus replication–transcription complexes and their relevance for SARS-CoV-2 drug design. *Nat Rev Mol Cell Biol 2021 231* **23**:21–39. doi:10.1038/s41580-021-00432-z

Martínez-Navarro FJ, Martínez-Morcillo FJ, de Oliveira S, Candel S, Cabas I, García-Ayala A, Martínez-Menchón T, Corbalán-Vélez R, Mesa-del-Castillo P, Cayuela ML, Pérez-Oliva AB, García-Moreno D, Mulero V. 2020. Hydrogen peroxide in neutrophil inflammation: Lesson from the zebrafish. *Dev Comp Immunol* **105**:103583. doi:10.1016/J.DCI.2019.103583

Martins EP, Bhat A. 2014. Population-level personalities in zebrafish: Aggression-boldness across but not within populations. *Behav Ecol* **25**:368–373. doi:10.1093/BEHECO/ARU007

Masud S, Prajsnar TK, Torraca V, Lamers GEM, Benning M, Van Der Vaart M, Meijer AH. 2019. Macrophages target Salmonella by Lc3-associated phagocytosis in a systemic infection model. *Autophagy* **15**:796–812. doi:10.1080/15548627.2019.1569297/SUPPL_FILE/KAUP_A_1569297_SM3984.ZIP

Mazzolini J, Le Clerc S, Morisse G, Coulonges C, Kuil LE, van Ham TJ, Zagury JF, Sieger D. 2020. Gene expression profiling reveals a conserved microglia signature in larval zebrafish. *Glia* **68**:298–315. doi:10.1002/GLIA.23717

McClure MM, McIntyre PB, McCune AR. 2006. Notes on the natural diet and habitat of eight danionin fishes, including the zebrafish Danio rerio. *J Fish Biol* **69**:553–570. doi:10.1111/J.1095-8649.2006.01125.X

Meeker ND, Trede NS. 2008. Immunology and zebrafish: Spawning new models of human disease. *Dev Comp Immunol* **32**:745–757. doi:10.1016/J.DCI.2007.11.011

Meijer AH, Gabby Krens SF, Medina Rodriguez IA, He S, Bitter W, Snaar-Jagalska BE, Spaink HP. 2004. Expression analysis of the Toll-like receptor and TIR domain adaptor families of zebrafish. *Mol Immunol* **40**:773–783. doi:10.1016/J.MOLIMM.2003.10.003

Meijer AH, van der Sar AM, Cunha C, Lamers GEM, Laplante MA, Kikuta H, Bitter W, Becker TS, Spaink HP. 2008. Identification and real-time imaging of a myc-expressing neutrophil population involved in inflammation and mycobacterial granuloma formation in zebrafish. *Dev Comp Immunol* **32**:36–49. doi:10.1016/J.DCI.2007.04.003

Meno K, Yah C, Mendes A, Venter M. 2022. Incidence of Sindbis Virus in Hospitalized Patients With Acute Fevers of Unknown Cause in South Africa, 2019–2020. *Front Microbiol* **12**:798810. doi:10.3389/FMICB.2021.798810/BIBTEX

Mesureur J, Feliciano JR, Wagner N, Gomes MC, Zhang L, Blanco-Gonzalez M, van der Vaart M, O'Callaghan D, Meijer AH, Vergunst AC. 2017. Macrophages, but not neutrophils, are critical for proliferation of Burkholderia cenocepacia and ensuing host-damaging inflammation. *PLOS Pathog* **13**:e1006437. doi:10.1371/JOURNAL.PPAT.1006437

Metzler KD, Goosmann C, Lubojemska A, Zychlinsky A, Papayannopoulos V. 2014. Myeloperoxidase-containing complex regulates neutrophil elastase release and actin dynamics during NETosis. *Cell Rep* **8**:883–896. doi:10.1016/j.celrep.2014.06.044

Miao KZ, Kim GY, Meara GK, Qin X, Feng H. 2021. Tipping the Scales With Zebrafish to Understand

Adaptive Tumor Immunity. *Front Cell Dev Biol* **9**. doi:10.3389/FCELL.2021.660969
Michelle D Peñaranda M, Jensen I, Tollersrud LG, Bruun JA, Jørgensen JB. 2019. Profiling the Atlantic salmon IgM+ B cell surface proteome: Novel information on teleost fish B cell protein repertoire and identification of potential B cell markers. *Front Immunol* **10**:37. doi:10.3389/FIMMU.2019.00037/FULL
Mitra S, Alnabulsi A, Secombes CJ, Bird S. 2010. Identification and characterization of the transcription factors involved in T-cell development, t-bet, stat6 and foxp3, within the zebrafish, Danio rerio. *FEBS J* **277**:128–147. doi:10.1111/J.1742-4658.2009.07460.X
Molmeret M, Bitar DM, Han L, Kwaik YA. 2004. Cell biology of the intracellular infection by Legionella pneumophila. *Microbes Infect* **6**:129–139. doi:10.1016/J.MICINF.2003.11.004
Monte MM, Wang T, Costa MM, Harun NO, Secombes CJ. 2012. Cloning and expression analysis of two ROR-γ homologues (ROR-γa1 and ROR-γa2) in rainbow trout Oncorhynchus mykiss. *Fish Shellfish Immunol* **33**:365–374. doi:10.1016/J.FSI.2012.05.023
Moreira RA, Guzman H V., Boopathi S, Baker JL, Poma AB. 2020. Characterization of Structural and Energetic Differences between Conformations of the SARS-CoV-2 Spike Protein. *Mater 2020, Vol 13, Page 5362* **13**:5362. doi:10.3390/MA13235362
Mosser DM, Edwards JP. 2008. Exploring the full spectrum of macrophage activation. *Nat Rev Immunol* **8**:958–969. doi:10.1038/NRI2448
Mueller T, Wullimann MF, Mueller T, Wullimann MF. 2016. Chapter 1 – Vertebrate Central Nervous System Development: Introduction, Atlas of Early Zebrafish Brain Development.
Muñoz-Sánchez S, van der Vaart M, Meijer AH. 2020a. Autophagy and Lc3-Associated Phagocytosis in Zebrafish Models of Bacterial Infections. *Cells 2020, Vol 9, Page 2372* **9**:2372. doi:10.3390/CELLS9112372
Muñoz-Sánchez S, van der Vaart M, Meijer AH. 2020b. Autophagy and Lc3-Associated Phagocytosis in Zebrafish Models of Bacterial Infections. *Cells* **9**. doi:10.3390/CELLS9112372
Murayama E, Kissa K, Zapata A, Mordelet E, Briolat V, Lin HF, Handin RI, Herbomel P. 2006. Tracing hematopoietic precursor migration to successive hematopoietic organs during zebrafish development. *Immunity* **25**:963–975. doi:10.1016/J.IMMUNI.2006.10.015
Nasevicius A, Ekker SC. 2000. Effective targeted gene 'knockdown' in zebrafish. *Nat Genet 2000 262* **26**:216–220. doi:10.1038/79951
Nathan C. 2006. Neutrophils and immunity: challenges and opportunities. *Nat Rev Immunol 2006 63* **6**:173–182. doi:10.1038/nri1785
Nguyen-Chi M, Laplace-Builhé B, Travnickova J, Luz-Crawford P, Tejedor G, Lutfalla G, Kissa K, Jorgensen C, Djouad F. 2017. TNF signaling and macrophages govern fin regeneration in zebrafish larvae. *Cell Death Dis 2017 88* **8**:e2979–e2979. doi:10.1038/cddis.2017.374
Nguyen-Chi M, Laplace-Builhe B, Travnickova J, Luz-Crawford P, Tejedor G, Phan QT, Duroux-Richard I, Levraud JP, Kissa K, Lutfalla G, Jorgensen C, Djouad F. 2015a. Identification of polarized macrophage subsets in zebrafish. *Elife* **4**. doi:10.7554/ELIFE.07288
Nguyen-Chi M, Laplace-Builhe B, Travnickova J, Luz-Crawford P, Tejedor G, Phan QT, Duroux-Richard I, Levraud JP, Kissa K, Lutfalla G, Jorgensen C, Djouad F. 2015b. Identification of polarized macrophage subsets in zebrafish. *Elife* **4**. doi:10.7554/ELIFE.07288
Nie L, Xiong R, Zhang YS, Zhu L yun, Shao JZ, Xiang LX. 2014. Conserved inhibitory role of teleost SOCS-1s in IFN signaling pathways. *Dev Comp Immunol* **43**:23–29. doi:10.1016/J.DCI.2013.10.007

Nintasen R, … FU-M and, 2007 undefined. 2007. Enhancement of Legionella pneumophila Culture Isolation from Microenvironments by Macrophage Infectivity Potentiator (mip) Gene-Specific Nested Polymerase. *Wiley Online Libr Nintasen, F Utrarachkij, K Siripanichgon, A Bhumiratana, Y Suzuki, O SuthienkulMicrobiology Immunol 2007•Wiley Online Libr* **51**:777–785. doi:10.1111/j.1348-0421.2007.tb03967.x

Novais FO, Santiago RC, Báfica A, Khouri R, Afonso L, Borges VM, Brodskyn C, Barral-Netto M, Barral A, de Oliveira CI. 2009. Neutrophils and Macrophages Cooperate in Host Resistance against Leishmania braziliensis Infection. *J Immunol* **183**:8088–8098. doi:10.4049/JIMMUNOL.0803720

Novoa B, Figueras A. 2012. Zebrafish: model for the study of inflammation and the innate immune response to infectious diseases. *Adv Exp Med Biol* **946**:253–275. doi:10.1007/978-1-4614-0106-3_15

Nüsslein-Volhard C. 2012. The zebrafish issue of Development. *Development* **139**:4099–4103. doi:10.1242/DEV.085217

Oehlers SHB, Flores MV, Hall CJ, O'Toole R, Swift S, Crosier KE, Crosier PS. 2010. Expression of zebrafish cxcl8 (interleukin-8) and its receptors during development and in response to immune stimulation. *Dev Comp Immunol* **34**:352–359. doi:10.1016/J.DCI.2009.11.007

Oosterhof N, Holtman IR, Kuil LE, van der Linde HC, Boddeke EWGM, Eggen BJL, van Ham TJ. 2017. Identification of a conserved and acute neurodegeneration-specific microglial transcriptome in the zebrafish. *Glia* **65**:138–149. doi:10.1002/GLIA.23083

Oosterhof N, Kuil LE, van der Linde HC, Burm SM, Berdowski W, van Ijcken WFJ, van Swieten JC, Hol EM, Verheijen MHG, van Ham TJ. 2018. Colony-Stimulating Factor 1 Receptor (CSF1R) Regulates Microglia Density and Distribution, but Not Microglia Differentiation In Vivo. *Cell Rep* **24**:1203-1217.e6. doi:10.1016/J.CELREP.2018.06.113

Oswald ME, Drew RE, Racine M, Murdoch GK, Robison BD. 2012. Is Behavioral Variation along the Bold-Shy Continuum Associated with Variation in the Stress Axis in Zebrafish?*. *https://doi.org/101086/668203* **85**:717–728. doi:10.1086/668203

Page DM, Wittamer V, Bertrand JY, Lewis KL, Pratt DN, Delgado N, Schale SE, McGue C, Jacobsen BH, Doty A, Pao Y, Yang H, Chi NC, Magor BG, Traver D. 2013. An evolutionarily conserved program of B-cell development and activation in zebrafish. *Blood* **122**:e1. doi:10.1182/BLOOD-2012-12-471029

Palha N, Guivel-Benhassine F, Briolat V, Lutfalla G, Sourisseau M, Ellett F, Wang CH, Lieschke GJ, Herbomel P, Schwartz O, Levraud JP. 2013. Real-Time Whole-Body Visualization of Chikungunya Virus Infection and Host Interferon Response in Zebrafish. *PLoS Pathog* **9**:e1003619. doi:10.1371/journal.ppat.1003619

Papian S, Mohabati Mobarez A, khoramabadi N, Mehdi Abdol M, Talebi Bezmin Abadi A. 2020. Investigating the role of L. pnuemophila LPS derivatives in formation of specific cell-mediated immune responses against the pathogen. *Microb Pathog* **147**. doi:10.1016/J.MICPATH.2020.104396

Parichy DM. 2015a. The natural history of model organisms: Advancing biology through a deeper understanding of zebrafish ecology and evolution. *Elife* **2015**. doi:10.7554/eLife.05635.001

Parichy DM. 2015b. The natural history of model organisms: Advancing biology through a deeper understanding of zebrafish ecology and evolution. *Elife* **2015**.

Passoni G, Langevin C, Palha N, Mounce BC, Briolat V, Affaticati P, De Job E, Joly J-S, Vignuzzi M,

Saleh M-C, Herbomel P, Boudinot P, Levraud J-P. 2017. Imaging of viral neuroinvasion in the zebrafish reveals that Sindbis and chikungunya viruses favour different entry routes. *DMM Dis Model Mech* **10**:847–857. doi:10.1242/dmm.029231

Paull GC, Filby AL, Giddins HG, Coe TS, Hamilton PB, Tyler CR. 2010. Dominance Hierarchies in Zebrafish (Danio rerio) and Their Relationship with Reproductive Success. *https://home.liebertpub.com/zeb* **7**:109–117. doi:10.1089/ZEB.2009.0618

Pedroni A, Ampatzis K. 2019. Large-Scale Analysis of the Diversity and Complexity of the Adult Spinal Cord Neurotransmitter Typology. *iScience* **19**:1189–1201. doi:10.1016/J.ISCI.2019.09.010

Peichel CL. 2004. Social behavior: How do fish find their shoal mate? *Curr Biol* **14**. doi:10.1016/j.cub.2004.06.037

Perlman S, Netland J. 2009. Coronaviruses post-SARS: update on replication and pathogenesis. *Nat Rev Microbiol 2009 76* **7**:439–450. doi:10.1038/nrmicro2147

Petermann N, Hansen G, Schmidt CL, Hilgenfeld R. 2010. Structure of the GTPase and GDI domains of FeoB, the ferrous iron transporter of Legionella pneumophila. *FEBS Lett* **584**:733–738. doi:10.1016/J.FEBSLET.2009.12.045

Petrovski G, Zahuczky G, Májai G, Fésüs L. 2007. Phagocytosis of Cells Dying through Autophagy Evokes a Pro-Inflammatory Response in Macrophages. *https://doi.org/104161/auto4731* **3**:508–510. doi:10.4161/AUTO.4731

Piano M Del, Palombara P La, … RN-BD, 1984 U. 1984. The legionellosis. *Boll Ist Sieroter Milan*.

Picchietti S, Guerra L, Bertoni F, Randelli E, Belardinelli MC, Buonocore F, Fausto AM, Rombout JH, Scapigliati G, Abelli L. 2011. Intestinal T cells of Dicentrarchus labrax (L.): gene expression and functional studies. *Fish Shellfish Immunol* **30**:609–617. doi:10.1016/J.FSI.2010.12.006

Pijanowski L, Golbach L, Kolaczkowska E, Scheer M, Verburg-van Kemenade BML, Chadzinska M. 2013. Carp neutrophilic granulocytes form extracellular traps via ROS-dependent and independent pathways. *Fish Shellfish Immunol* **34**:1244–1252. doi:10.1016/J.FSI.2013.02.010

Poirier EZ, Mounce BC, Rozen-Gagnon K, Hooikaas PJ, Stapleford KA, Moratorio G, Vignuzzi M. 2015. Low-Fidelity Polymerases of Alphaviruses Recombine at Higher Rates To Overproduce Defective Interfering Particles. *J Virol* **90**:2446–2454. doi:10.1128/JVI.02921-15

Powell D, Lou M, Barros Becker F, Huttenlocher A. 2018. Cxcr1 mediates recruitment of neutrophils and supports proliferation of tumor-initiating astrocytes in vivo. *Sci Reports 2018 81* **8**:1–12. doi:10.1038/s41598-018-31675-0

Propper DJ, Balkwill FR. 2022. Harnessing cytokines and chemokines for cancer therapy. *Nat Rev Clin Oncol 2022 194* **19**:237–253. doi:10.1038/s41571-021-00588-9

Qin T, Zhou H, Ren H, Liu W. 2017. Distribution of secretion systems in the genus Legionella and its correlation with pathogenicity. *Front Microbiol* **8**. doi:10.3389/FMICB.2017.00388/FULL

Qualitative and Quantitative Evaluation of Two New Histogram Limiting Binarization Algorithms. n.d. https://www.cscjournals.org/library/manuscriptinfo.php?mc=IJIP-829

Quiñonez-Silvero C, Hübner K, Herzog W. 2020. Development of the brain vasculature and the blood-brain barrier in zebrafish. *Dev Biol* **457**:181–190. doi:10.1016/J.YDBIO.2019.03.005

Quintana FJ, Iglesias AH, Farez MF, Caccamo M, Burns EJ, Kassam N, Oukka M, Weiner HL. 2010. Adaptive Autoimmunity and Foxp3-Based Immunoregulation in Zebrafish. *PLoS One* **5**. doi:10.1371/JOURNAL.PONE.0009478

Raghuvamsi P V., Tulsian NK, Samsudin F, Qian X, Purushotorman K, Yue G, Kozma MM, Hwa WY, Lescar J, Bond PJ, Macary PA, Anand GS. 2021. Sars-cov-2 s protein:Ace2 interaction reveals novel allosteric targets. *Elife* **10**:1–47. doi:10.7554/ELIFE.63646

Ramakrishnan L. 2013. The Zebrafish Guide to Tuberculosis Immunity and Treatment. *Cold Spring Harb Symp Quant Biol* **78**:179–192. doi:10.1101/SQB.2013.78.023283

Ramsay JM, Watral V, Schreck CB, Kent ML. 2009. Husbandry stress exacerbates mycobacterial infections in adult zebrafish, Danio rerio (Hamilton). *J Fish Dis* **32**:931–941. doi:10.1111/J.1365-2761.2009.01074.X

Rasighaemi P, Basheer F, Liongue C, Ward AC. 2015. Zebrafish as a model for leukemia and other hematopoietic disorders. *J Hematol Oncol* **8**. doi:10.1186/S13045-015-0126-4

Ray K, Marteyn B, Sansonetti PJ, Tang CM. 2009. Life on the inside: the intracellular lifestyle of cytosolic bacteria. *Nat Rev Microbiol 2009 75* **7**:333–340. doi:10.1038/nrmicro2112

Renshaw SA, Trede NS. 2012. A model 450 million years in the making: zebrafish and vertebrate immunity. *Dis Model Mech* **5**:38–47. doi:10.1242/DMM.007138

Richard AS, Shim BS, Kwon YC, Zhang R, Otsuka Y, Schmitt K, Berri F, Diamond MS, Choe H. 2017. AXL-dependent infection of human fetal endothelial cells distinguishes Zika virus from other pathogenic flaviviruses. *Proc Natl Acad Sci U S A* **114**:2024–2029. doi:10.1073/PNAS.1620558114

Robison BD, Rowland W. 2011. A potential model system for studying the genetics of domestication: behavioral variation among wild and domesticated strains of zebra danio (Danio rerio). *https://doi.org/101139/f05-118* **62**:2046–2054. doi:10.1139/F05-118

Roca FJ, Mulero I, López-Muñoz A, Sepulcre MP, Renshaw SA, Meseguer J, Mulero V. 2008. Evolution of the Inflammatory Response in Vertebrates: Fish TNF-α Is a Powerful Activator of Endothelial Cells but Hardly Activates Phagocytes. *J Immunol* **181**:5071–5081. doi:10.4049/JIMMUNOL.181.7.5071

Rose PP, Hanna SL, Spiridigliozzi A, Wannissorn N, Beiting DP, Ross SR, Hardy RW, Bambina SA, Heise MT, Cherry S. 2011. Natural resistance-associated macrophage protein is a cellular receptor for Sindbis virus in both insect and mammalian hosts. *Cell Host Microbe* **10**:97–104. doi:10.1016/j.chom.2011.06.009

Rosowski EE, Raffa N, Knox BP, Golenberg N, Keller NP, Huttenlocher A. 2018. Macrophages inhibit Aspergillus fumigatus germination and neutrophil-mediated fungal killing. *PLOS Pathog* **14**:e1007229. doi:10.1371/JOURNAL.PPAT.1007229

Rougeot J, Torraca V, Zakrzewska A, Kanwal Z, Jansen HJ, Sommer F, Spaink HP, Meijer AH. 2019. RNAseq profiling of leukocyte populations in zebrafish larvae reveals a cxcl11 chemokine gene as a marker of macrophage polarization during mycobacterial infection. *Front Immunol* **10**:443723. doi:10.3389/FIMMU.2019.00832/BIBTEX

Ruzicka L, Bradford YM, Frazer K, Howe DG, Paddock H, Ramachandran S, Singer A, Toro S, Van Slyke CE, Eagle AE, Fashena D, Kalita P, Knight J, Mani P, Martin R, Moxon SAT, Pich C, Schaper K, Shao X, Westerfield M. 2015. ZFIN, The zebrafish model organism database: Updates and new directions. *genesis* **53**:498–509. doi:10.1002/DVG.22868

Sakai C, Ijaz S, Hoffman EJ. 2018. Zebrafish Models of Neurodevelopmental Disorders: Past, Present, and Future. *Front Mol Neurosci* **11**:396075. doi:10.3389/FNMOL.2018.00294/BIBTEX

Saleem S, Kannan RR. 2018. Zebrafish: an emerging real-time model system to study Alzheimer's

disease and neurospecific drug discovery. *Cell Death Discov 2018 41* **4**:1–13. doi:10.1038/s41420-018-0109-7

Sane J, Guedes S, Ollgren J, Kurkela S, Klemets P, Vapalahti O, Kela E, Lyytikäinen O, Nuorti JP. 2011. Epidemic Sindbis Virus Infection in Finland: A Population-Based Case-Control Study of Risk Factors. *J Infect Dis* **204**:459–466. doi:10.1093/INFDIS/JIR267

Sane J, Kurkela S, Desdouits M, Kalimo H, Mazalrey S, Lokki ML, Vaheri A, Helve T, Törnwall J, Huerre M, Butler-Browne G, Ceccaldi PE, Gessain A, Vapalahti O. 2012. Prolonged Myalgia in Sindbis Virus Infection: Case Description and In Vitro Infection of Myotubes and Myoblasts. *J Infect Dis* **206**:407–414. doi:10.1093/INFDIS/JIS358

Sanford JP. 1979. Legionnaires' Disease — The First Thousand Days. *N Engl J Med* **300**:654–656. doi:10.1056/NEJM197903223001205

Sanz-Morejón A, García-Redondo AB, Reuter H, Marques IJ, Bates T, Galardi-Castilla M, Große A, Manig S, Langa X, Ernst A, Piragyte I, Botos MA, González-Rosa JM, Ruiz-Ortega M, Briones AM, Salaices M, Englert C, Mercader N. 2019. Wilms Tumor 1b Expression Defines a Pro-regenerative Macrophage Subtype and Is Required for Organ Regeneration in the Zebrafish. *Cell Rep* **28**:1296-1306.e6. doi:10.1016/J.CELREP.2019.06.091

Sawicki SG, Sawicki DL. 1995. Coronaviruses use discontinuous extension for synthesis of subgenome-length negative strands. *Adv Exp Med Biol* **380**:499–506. doi:10.1007/978-1-4615-1899-0_79

Scherwitzl I, Opp S, Hurtado AM, Pampeno C, Loomis C, Kannan K, Yu M, Meruelo D. 2020. Sindbis Virus with Anti-OX40 Overcomes the Immunosuppressive Tumor Microenvironment of Low-Immunogenic Tumors. *Mol Ther - Oncolytics* **17**:431–447. doi:10.1016/j.omto.2020.04.012

Schild Y, Mohamed A, Wootton EJ, Lewis A, Elks PM. 2020. Hif-1alpha stabilisation is protective against infection in zebrafish comorbid models. *FEBS J* **287**:3925–3943. doi:10.1111/FEBS.15433

Schindelin J, Arganda-Carreras I, Frise E, Kaynig V, Longair M, Pietzsch T, Preibisch S, Rueden C, Saalfeld S, Schmid B, Tinevez J-Y, White DJ, Hartenstein V, Eliceiri K, Tomancak P, Cardona A. 2012. Fiji: an open-source platform for biological-image analysis. *Nat Methods* **9**:676–682. doi:10.1038/nmeth.2019

Schoggins JW, Rice CM. 2011. Interferon-stimulated genes and their antiviral effector functions. *Curr Opin Virol* **1**:519–525. doi:10.1016/J.COVIRO.2011.10.008

Schubert K, Karousis ED, Jomaa A, Scaiola A, Echeverria B, Gurzeler LA, Leibundgut M, Thiel V, Mühlemann O, Ban N. 2020. SARS-CoV-2 Nsp1 binds the ribosomal mRNA channel to inhibit translation. *Nat Struct Mol Biol 2020 2710* **27**:959–966. doi:10.1038/s41594-020-0511-8

Seelye SL, Chen PL, Deiss TC, Criscitiello MF. 2016. Genomic organization of the zebrafish (Danio rerio) T cell receptor alpha/delta locus and analysis of expressed products. *Immunogenetics* **68**:365–379. doi:10.1007/S00251-016-0904-3

Shen Y, Xu J, Zhi S, Wu W, Chen Y, Zhang Q, Zhou Y, Deng Z, Li W. 2022. MIP From Legionella pneumophila Influences the Phagocytosis and Chemotaxis of RAW264.7 Macrophages by Regulating the lncRNA GAS5/miR-21/SOCS6 Axis. *Front Cell Infect Microbiol* **12**. doi:10.3389/FCIMB.2022.810865/FULL

Sherman' And LA, Griffin' DE. 1990. Pathogenesis of encephalitis induced in newborn mice by virulent and avirulent strains of Sindbis virus. *J Virol* **64**:2041–2046. doi:10.1128/JVI.64.5.2041-2046.1990

1750 Shevchuk O, Jäger J, Steinert M. 2011. Virulence properties of the Legionella pneumophila cell
1751 envelope. *Front Microbiol* **2**. doi:10.3389/FMICB.2011.00074/FULL
1752 Shilts J, Crozier T, Greenwood E, reports PL-S, 2021 undefined. n.d. No evidence for
1753 basigin/CD147 as a direct SARS-CoV-2 spike binding receptor. *nature.comJ Shilts, TWM*
1754 *Crozier, EJD Greenwood, PJ Lehner, GJ WrightScientific reports, 2021•nature.com*.
1755 Sieger D, Stein C, Neifer D, Van Der Sar AM, Leptin M. 2009. The role of gamma interferon in
1756 innate immunity in the zebrafish embryo. *Dis Model Mech* **2**:571–581.
1757 doi:10.1242/DMM.003509
1758 Silva MT. 2010. Neutrophils and macrophages work in concert as inducers and effectors of
1759 adaptive immunity against extracellular and intracellular microbial pathogens. *J Leukoc Biol*
1760 **87**:805–813. doi:10.1189/JLB.1109767
1761 Silva MT, Correia-Neves M. 2012. Neutrophils and macrophages: The main partners of phagocyte
1762 cell systems. *Front Immunol* **3**:24656. doi:10.3389/FIMMU.2012.00174/BIBTEX
1763 Silva NJ, Dorman LC, Vainchtein ID, Horneck NC, Molofsky A V. 2021. In situ and transcriptomic
1764 identification of microglia in synapse-rich regions of the developing zebrafish brain. *Nat*
1765 *Commun 2021 121* **12**:1–12. doi:10.1038/s41467-021-26206-x
1766 Slauch JM. 2011. How does the oxidative burst of macrophages kill bacteria? Still an open
1767 question. *Mol Microbiol* **80**:580–583. doi:10.1111/J.1365-2958.2011.07612.X
1768 Sola I, Almazán F, Zúñiga S, Enjuanes L. 2015. Continuous and Discontinuous RNA Synthesis in
1769 Coronaviruses. *Annu Rev Virol* **2**:265–288. doi:10.1146/ANNUREV-VIROLOGY-100114-
1770 055218
1771 Sollberger G, Choidas A, Burn GL, Habenberger P, Lucrezia R Di, Kordes S, Menninger S, Eickhoff
1772 J, Nussbaumer P, Klebl B, Krüger R, Herzig A, Zychlinsky A. 2018. Gasdermin D plays a vital
1773 role in the generation of neutrophil extracellular traps. *Sci Immunol* **3**:6689.
1774 doi:10.1126/SCIIMMUNOL.AAR6689/SUPPL_FILE/AAR6689_TABLE_S1.XLSX
1775 Somamoto T, Koppang EO, Fischer U. 2014. Antiviral functions of CD8+ cytotoxic T cells in teleost
1776 fish. *Dev Comp Immunol* **43**:197–204. doi:10.1016/j.dci.2013.07.014
1777 Sommer F, Ortiz Zacarías N V., Heitman LH, Meijer AH. 2021. Inhibition of macrophage migration
1778 in zebrafish larvae demonstrates in vivo efficacy of human CCR2 inhibitors. *Dev Comp*
1779 *Immunol* **116**:103932. doi:10.1016/J.DCI.2020.103932
1780 Sommer F, Torraca V, Kamel SM, Lombardi A, Meijer AH. 2020. Frontline Science: Antagonism
1781 between regular and atypical Cxcr3 receptors regulates macrophage migration during
1782 infection and injury in zebrafish. *J Leukoc Biol* **107**:185–203. doi:10.1002/JLB.2HI0119-006R
1783 Spence R, Ashton R, Smith C. 2007. Oviposition decisions are mediated by spawning site quality
1784 in wild and domesticated zebrafish, Danio rerio. *Behaviour* **144**:953–966.
1785 doi:10.1163/156853907781492726
1786 Spence R, Fatema MK, Reichard M, Huq KA, Wahab MA, Ahmed ZF, Smith C. 2006. The
1787 distribution and habitat preferences of the zebrafish in Bangladesh. *J Fish Biol* **69**:1435–
1788 1448. doi:10.1111/J.1095-8649.2006.01206.X
1789 Spinner JL, Hasenkrug AM, Shannon JG, Kobayashi SD, Hinnebusch BJ. 2016. Role of the Yersinia
1790 YopJ protein in suppressing interleukin-8 secretion by human polymorphonuclear
1791 leukocytes. *Microbes Infect* **18**:21–29. doi:10.1016/J.MICINF.2015.08.015
1792 Spitz O, Erenburg IN, Beer T, Kanonenberg K, Holland IB, Schmitt L. 2019. Type I Secretion
1793 Systems—One Mechanism for All? *Microbiol Spectr* **7**. doi:10.1128/MICROBIOLSPEC.PSIB-

0003-2018
Stein C, Caccamo M, Laird G, Leptin M. 2007. Conservation and divergence of gene families encoding components of innate immune response systems in zebrafish. *Genome Biol* **8**:1–23. doi:10.1186/GB-2007-8-11-R251/FIGURES/16
Stout RD, Suttles J. 2004. Functional plasticity of macrophages: reversible adaptation to changing microenvironments. *J Leukoc Biol* **76**:509. doi:10.1189/JLB.0504272
Strauss EG, Rice CM, Strauss JH. 1984. Complete nucleotide sequence of the genomic RNA of Sindbis virus. *Virology* **133**:92–110. doi:10.1016/0042-6822(84)90428-8
Strauss James H, Strauss EG. 1994. The alphaviruses: gene expression, replication, and evolution. *Microbiol Rev* **58**:491–562. doi:10.1128/MR.58.3.491-562.1994
Strauss J H, Strauss EG. 1994a. The alphaviruses: gene expression, replication, and evolution. *Microbiol Rev* **58**:491–562.
Strauss J H, Strauss EG. 1994b. The alphaviruses: gene expression, replication, and evolution. *Microbiol Rev* **58**:491–562. doi:10.1128/mr.58.3.491-562.1994
Streisinger G, Walker C, Dower N, Knauber D, Singer F. 1981. Production of clones of homozygous diploid zebra fish (Brachydanio rerio). *Nat 1981 2915813* **291**:293–296. doi:10.1038/291293a0
Sullivan C, Soos BL, Millard PJ, Kim CH, King BL. 2021. Modeling Virus-Induced Inflammation in Zebrafish: A Balance Between Infection Control and Excessive Inflammation. *Front Immunol* **12**:636623. doi:10.3389/FIMMU.2021.636623/BIBTEX
Swanson PA, McGavern DB. 2015. Viral diseases of the central nervous system. *Curr Opin Virol* **11**:44–54. doi:10.1016/j.coviro.2014.12.009
Swinburne IA, Mosaliganti KR, Green AA, Megason SG. 2015. Improved Long-Term Imaging of Embryos with Genetically Encoded α-Bungarotoxin. *PLoS One* **10**:e0134005. doi:10.1371/journal.pone.0134005
Takizawa F, Dijkstra JM, Kotterba P, Korytář T, Kock H, Köllner B, Jaureguiberry B, Nakanishi T, Fischer U. 2011. The expression of CD8α discriminates distinct T cell subsets in teleost fish. *Dev Comp Immunol* **35**:752–763. doi:10.1016/J.DCI.2011.02.008
Takizawa F, Magadan S, Parra D, Xu Z, Korytář T, Boudinot P, Sunyer JO. 2016. Novel Teleost CD4-Bearing Cell Populations Provide Insights into the Evolutionary Origins and Primordial Roles of CD4+ Lymphocytes and CD4+ Macrophages. *J Immunol* **196**:4522–4535. doi:10.4049/JIMMUNOL.1600222
Tauzin S, Starnes TW, Becker FB, Lam P ying, Huttenlocher A. 2014. Redox and Src family kinase signaling control leukocyte wound attraction and neutrophil reverse migration. *J Cell Biol* **207**:589–598. doi:10.1083/JCB.201408090/VIDEO-8
Teame T, Zhang Z, Ran C, Zhang H, Yang Y, Ding Q, Xie M, Gao C, Ye Y, Duan M, Zhou Z. 2019. The use of zebrafish (Danio rerio) as biomedical models. *Anim Front Rev Mag Anim Agric* **9**:68. doi:10.1093/AF/VFZ020
Tenor JL, Oehlers SH, Yang JL, Tobin DM, Perfect JR. 2015. Live imaging of host-parasite interactions in a zebrafish infection model reveals cryptococcal determinants of virulence and central nervous system invasion. *MBio* **6**. doi:10.1128/MBIO.01425-15/ASSET/74CF9B49-9BBA-4434-9E00-FB20FA9B6865/ASSETS/GRAPHIC/MBO0051524760006.JPEG
Thoms M, Buschauer R, Ameismeier M, Koepke L, Denk T, Hirschenberger M, Kratzat H, Hayn M,

MacKens-Kiani T, Cheng J, Straub JH, Stürzel CM, Fröhlich T, Berninghausen O, Becker T, Kirchhoff F, Sparrer KMJ, Beckmann R. 2020. Structural basis for translational shutdown and immune evasion by the Nsp1 protein of SARS-CoV-2. *Science (80-)* **369**:1249–1256. doi:10.1126/SCIENCE.ABC8665/SUPPL_FILE/ABC8665_THOMS_SM.PDF

Tobin David M., May RC, Wheeler RT. 2012. Zebrafish: A See-Through Host and a Fluorescent Toolbox to Probe Host–Pathogen Interaction. *PLOS Pathog* **8**:e1002349. doi:10.1371/JOURNAL.PPAT.1002349

Tobin David M, May RC, Wheeler RT. 2012. Zebrafish: a see-through host and a fluorescent toolbox to probe host-pathogen interaction. *PLoS Pathog* **8**:e1002349. doi:10.1371/journal.ppat.1002349

Tobin DM, Vary JC, Ray JP, Walsh GS, Dunstan SJ, Bang ND, Hagge DA, Khadge S, King MC, Hawn TR, Moens CB, Ramakrishnan L. 2010. The lta4h Locus Modulates Susceptibility to Mycobacterial Infection in Zebrafish and Humans. *Cell* **140**:717–730. doi:10.1016/j.cell.2010.02.013

Toda H, Araki K, Moritomo T, Nakanishi T. 2011. Perforin-dependent cytotoxic mechanism in killing by CD8 positive T cells in ginbuna crucian carp, Carassius auratus langsdorfii. *Dev Comp Immunol* **35**:88–93. doi:10.1016/J.DCI.2010.08.010

Torraca V, Mostowy S. 2018. Zebrafish Infection: From Pathogenesis to Cell Biology. *Trends Cell Biol* **28**:143. doi:10.1016/J.TCB.2017.10.002

Traver D, Herbomel P, Patton EE, Murphey RD, Yoder JA, Litman GW, Catic A, Amemiya CT, Zon LI, Trede NS. 2003. The Zebrafish as a Model Organism to Study Development of the Immune System. *Adv Immunol* **81**:253–330. doi:10.1016/S0065-2776(03)81007-6

Tsang B, Gerlai RT, Ansari R. 2020. Maintenance and breeding of zebrafish, with some ethological and ecological considerations in mind. *Behav Neural Genet Zebrafish* 17–32. doi:10.1016/B978-0-12-817528-6.00002-4

Tsarouchas TM, Wehner D, Cavone L, Munir T, Keatinge M, Lambertus M, Underhill A, Barrett T, Kassapis E, Ogryzko N, Feng Y, van Ham TJ, Becker T, Becker CG. 2018. Dynamic control of proinflammatory cytokines Il-1β and Tnf-α by macrophages in zebrafish spinal cord regeneration. *Nat Commun* **9**:4670. doi:10.1038/s41467-018-07036-w

Tyson JY, Vargas P, Cianciotto NP. 2014. The novel Legionella pneumophila type II secretion substrate NttC contributes to infection of amoebae Hartmannella vermiformis and Willaertia magna. *Microbiol (United Kingdom)* **160**:2732–2744. doi:10.1099/MIC.0.082750-0

V'kovski P, Kratzel A, Steiner S, Stalder H, Thiel V. 2020. Coronavirus biology and replication: implications for SARS-CoV-2. *Nat Rev Microbiol 2020 193* **19**:155–170. doi:10.1038/s41579-020-00468-6

van der Aa LM, Chadzinska M, Tijhaar E, Boudinot P, Lidy verburg-Van kemenade BM. 2010. CXCL8 Chemokines in Teleost Fish: Two Lineages with Distinct Expression Profiles during Early Phases of Inflammation. *PLoS One* **5**:e12384. doi:10.1371/JOURNAL.PONE.0012384

Van Der Vaart M, Spaink HP, Meijer AH. 2012. Pathogen recognition and activation of the innate immune response in zebrafish. *Adv Hematol* **2012**. doi:10.1155/2012/159807

Varela M, Dios S, Novoa B, Figueras A. 2012. Characterisation, expression and ontogeny of interleukin-6 and its receptors in zebrafish (Danio rerio). *Dev Comp Immunol* **37**:97–106. doi:10.1016/J.DCI.2011.11.004

Vascotto SG, Beckham Y, Kelly GM. 2011. The zebrafish's swim to fame as an experimental model in biology. *https://doi.org/101139/o97-081* **75**:479–485. doi:10.1139/O97-081
Venkatesan A. 2015. Epidemiology and outcomes of acute encephalitis. *Curr Opin Neurol* **28**:277–282. doi:10.1097/WCO.0000000000000199
Viana F, Boucontet L, Laghi V, Schator D, Ibranosyan M, Jarraud S, Colucci-Guyon E, Buchrieser C. 2023. Hiding in the yolk: A unique feature of Legionella pneumophila infection of zebrafish. *PLoS Pathog* **19**:e1011375. doi:10.1371/journal.ppat.1011375
Viengkhou B, Hofer MJ. 2023. Breaking down the cellular responses to type I interferon neurotoxicity in the brain. *Front Immunol* **14**:1110593. doi:10.3389/fimmu.2023.1110593
Villalta SA, Nguyen HX, Deng B, Gotoh T, Tidball JG. 2008. Shifts in macrophage phenotypes and macrophage competition for arginine metabolism affect the severity of muscle pathology in muscular dystrophy. *Hum Mol Genet* **18**:482–496. doi:10.1093/hmg/ddn376
Virta VC, Cooper MS. 2011. Structural components and morphogenetic mechanics of the zebrafish yolk extension, a developmental module. *J Exp Zool Part B Mol Dev Evol* **316B**:76–92. doi:10.1002/JEZ.B.21381
Voleti V, Patel KB, Li W, Perez Campos C, Bharadwaj S, Yu H, Ford C, Casper MJ, Yan RW, Liang W, Wen C, Kimura KD, Targoff KL, Hillman EMC. 2019. Real-time volumetric microscopy of in vivo dynamics and large-scale samples with SCAPE 2.0. *Nat Methods 2019 1610* **16**:1054–1062. doi:10.1038/s41592-019-0579-4
Wan F, Hu C Bin, Ma JX, Gao K, Xiang LX, Shao JZ. 2017. Characterization of γδ T cells from zebrafish provides insights into their important role in adaptive humoral immunity. *Front Immunol* **7**:9. doi:10.3389/FIMMU.2016.00675/FULL
Wan T, Zhao Y, Fan F, Hu R, Jin X. 2017. Dexamethasone inhibits S. aureus-induced neutrophil extracellular pathogen-killing mechanism, possibly through toll-like receptor regulation. *Front Immunol* **8**:216336. doi:10.3389/FIMMU.2017.00060/BIBTEX
Wang Qihui, Zhang Y, Wu L, Niu S, Song C, Zhang Z, Lu G, Qiao C, Hu Y, Yuen KY, Wang Qisheng, Zhou H, Yan J, Qi J. 2020. Structural and Functional Basis of SARS-CoV-2 Entry by Using Human ACE2. *Cell* **181**:894-904.e9. doi:10.1016/J.CELL.2020.03.045
Wang X, Copmans D, de Witte PAM. 2021. Using Zebrafish as a Disease Model to Study Fibrotic Disease. *Int J Mol Sci 2021, Vol 22, Page 6404* **22**:6404. doi:10.3390/IJMS22126404
Wang Z, Ding Y, Satta S, Roustaei M, Fei P, Hsiai TK. 2021. A hybrid of light-field and light-sheet imaging to study myocardial function and intracardiac blood flow during zebrafish development. *PLOS Comput Biol* **17**:e1009175. doi:10.1371/JOURNAL.PCBI.1009175
White RM, Patton EE. 2023. Adult zebrafish as advanced models of human disease. *Dis Model Mech* **16**. doi:10.1242/DMM.050351/324979
Wickramaarachchi WDN, Wan Q, Lim BS, Jung HB, De Zoysa M, Park MA, Lee J, Whang I. 2014. Genomic characterization of interferon regulatory factor 5 from rock bream (Oplegnathus fasciatus) and its role in antiviral defense. *Fish Shellfish Immunol* **37**:256–267. doi:10.1016/J.FSI.2014.02.002
Wiegertjes GF, Wentzel AS, Spaink HP, Elks PM, Fink IR. 2016. Polarization of immune responses in fish: The 'macrophages first' point of view. *Mol Immunol* **69**:146–156. doi:10.1016/J.MOLIMM.2015.09.026
Wilkinson RN, Jopling C, Van Eeden FJM. 2014. Zebrafish as a Model of Cardiac Disease. *Prog Mol Biol Transl Sci* **124**:65–91. doi:10.1016/B978-0-12-386930-2.00004-5

Willett CE, Kawasaki H, Amemiya CT, Lin S, Steiner LA. 2001. Ikaros expression as a marker for lymphoid progenitors during zebrafish development. *Dev Dyn* **222**:694–698. doi:10.1002/DVDY.1223

Wu S, Nguyen LTM, Pan H, Hassan S, Dai Y, Xu J, Wen Z. 2020. Two phenotypically and functionally distinct microglial populations in adult zebrafish. *Sci Adv* **6**. doi:10.1126/SCIADV.ABD1160

Xiong C, Levis R, Shen P, Schlesinger S, Rice CM, Huang H V. 1989. Sindbis Virus: An Efficient, Broad Host Range Vector for Gene Expression in Animal Cells. *Science (80-)* **243**:1188–1191. doi:10.1126/SCIENCE.2922607

Xu J, Zhu L, He S, Wu Y, Jin W, Yu T, Qu JY, Wen Z. 2015. Temporal-Spatial Resolution Fate Mapping Reveals Distinct Origins for Embryonic and Adult Microglia in Zebrafish. *Dev Cell* **34**:632–641. doi:10.1016/j.devcel.2015.08.018

Xu X, Hu J, Ma J, Nie L, Shao T, Xiang L, Shao J. 2016. Essential Roles of TIM-1 and TIM-4 Homologs in Adaptive Humoral Immunity in a Zebrafish Model. *J Immunol* **196**:1686–1699. doi:10.4049/JIMMUNOL.1501736

Xue J, Schmidt S V., Sander J, Draffehn A, Krebs W, Quester I, DeNardo D, Gohel TD, Emde M, Schmidleithner L, Ganesan H, Nino-Castro A, Mallmann MR, Labzin L, Theis H, Kraut M, Beyer M, Latz E, Freeman TC, Ulas T, Schultze JL. 2014. Transcriptome-Based Network Analysis Reveals a Spectrum Model of Human Macrophage Activation. *Immunity* **40**:274. doi:10.1016/J.IMMUNI.2014.01.006

Yadav R, Chaudhary JK, Jain N, Chaudhary PK, Khanra S, Dhamija P, Sharma A, Kumar A, Handu S. 2021. Role of Structural and Non-Structural Proteins and Therapeutic Targets of SARS-CoV-2 for COVID-19. *Cells 2021, Vol 10, Page 821* **10**:821. doi:10.3390/CELLS10040821

Yamaguchi T, Takizawa F, Furihata M, Soto-Lampe V, Dijkstra JM, Fischer U. 2019. Teleost cytotoxic T cells. *Fish Shellfish Immunol* **95**:422–439. doi:10.1016/J.FSI.2019.10.041

Yang CT, Cambier CJ, Davis JM, Hall CJ, Crosier PS, Ramakrishnan L. 2012. Neutrophils exert protection in the early tuberculous granuloma by oxidative killing of mycobacteria phagocytosed from infected macrophages. *Cell Host Microbe* **12**:301–312. doi:10.1016/j.chom.2012.07.009

Yang Z-Y, Huang † Yue, Ganesh L, Leung † Kwanyee, Kong W-P, Schwartz O, Subbarao K, Nabel GJ. 2004. pH-dependent entry of severe acute respiratory syndrome coronavirus is mediated by the spike glycoprotein and enhanced by dendritic cell transfer through DC-SIGN. *Am Soc MicrobiolZY Yang, Y Huang, L Ganesh, K Leung, WP Kong, O Schwartz, K Subbarao, GJ NabelJournal Virol 2004•Am Soc Microbiol* **78**:5642–5650. doi:10.1128/JVI.78.11.5642-5650.2004

Yang Z, Chen Y, Zhang Q, Chen X, Deng Z. 2021. Research Article Major Outer Membrane Protein from Legionella pneumophila Inhibits Phagocytosis but Enhances Chemotaxis of RAW 264.7 Macrophages by. *J Immunol Res* **2021**. doi:10.1155/2021/9409777

Yaniv K, Isogai S, Castranova D, Dye L, Hitomi J, Weinstein BM. 2006. Live imaging of lymphatic development in the zebrafish. *Nat Med 2006 126* **12**:711–716. doi:10.1038/nm1427

Yoder JA, Nielsen ME, Amemiya CT, Litman GW. 2002. Zebrafish as an immunological model system. *Microbes Infect* **4**:1469–1478. doi:10.1016/S1286-4579(02)00029-1

Yoon S, Mitra S, Wyse C, Alnabulsi A, Zou J, Weerdenburg EM, Van Der Sar AM, Wang D, Secombes CJ, Bird S. 2015. First Demonstration of Antigen Induced Cytokine Expression by CD4-1+ Lymphocytes in a Poikilotherm: Studies in Zebrafish (Danio rerio). *PLoS One*

10:e0126378. doi:10.1371/JOURNAL.PONE.0126378
Yoshida N, Frickel EM, Mostowy S. 2017. Macrophage-microbe interactions: Lessons from the Zebrafish model. *Front Immunol* **8**:322709. doi:10.3389/FIMMU.2017.01703/BIBTEX
Yu T, Guo W, Tian Y, Xu J, Chen J, Li L, Wen Z. 2017. Distinct regulatory networks control the development of macrophages of different origins in zebrafish. *Blood* **129**:509–519. doi:10.1182/BLOOD-2016-07-727651
Zakrzewska A, Cui C, Stockhammer OW, Benard EL, Spaink HP, Meijer AH. 2010. Macrophage-specific gene functions in Spi1-directed innate immunity. *Blood* **116**:e1–e11. doi:10.1182/BLOOD-2010-01-262873
Zanandrea R, Bonan CD, Campos MM. 2020. Zebrafish as a model for inflammation and drug discovery. *Drug Discov Today* **25**:2201–2211. doi:10.1016/J.DRUDIS.2020.09.036
Zhang H, Fei C, Wu H, Yang M, Liu Q, Wang Q, Zhang Y. 2013. Transcriptome Profiling Reveals Th17-Like Immune Responses Induced in Zebrafish Bath-Vaccinated with a Live Attenuated Vibrio anguillarum. *PLoS One* **8**. doi:10.1371/JOURNAL.PONE.0073871
Zhang L, Chen WQ, Hu YW, Wu XM, Nie P, Chang MX. 2016. TBK1-like transcript negatively regulates the production of IFN and IFN-stimulated genes through RLRs-MAVS-TBK1 pathway. *Fish Shellfish Immunol* **54**:135–143. doi:10.1016/J.FSI.2016.04.002
Zhang Y, Liu H, Yao J, Huang Y, Qin S, Sun Z, Xu Y, Wan S, Cheng H, Li C, Zhang X, Ke Y. 2016. Manipulating the air-filled zebrafish swim bladder as a neutrophilic inflammation model for acute lung injury. *Cell Death Dis 2016 711* **7**:e2470–e2470. doi:10.1038/cddis.2016.365
Ziegler U, Fischer D, Eiden M, Reuschel M, Rinder M, Müller K, Schwehn R, Schmidt V, Groschup MH, Keller M. 2019. Sindbis virus- a wild bird associated zoonotic arbovirus circulates in Germany. *Vet Microbiol* **239**:108453. doi:10.1016/J.VETMIC.2019.108453
Zimmerman AM, Moustafa FM, Romanowski KE, Steiner LA. 2011. Zebrafish immunoglobulin IgD: unusual exon usage and quantitative expression profiles with IgM and IgZ/T heavy chain isotypes. *Mol Immunol* **48**:2220. doi:10.1016/J.MOLIMM.2011.06.441

Spatial dynamics of peripheral and central nervous system infection by an interferon-inducing neuroinvasive virus

Annex1: Construction of a mathematical model of SINV infection

We first built a single-compartment model of the infection, with the help of the Berkeley Madonna software (Figure 1). The model, essentially based on (Best et al., 2017), allows for a variety of actions of the interferon response, so they can be tested in turn.

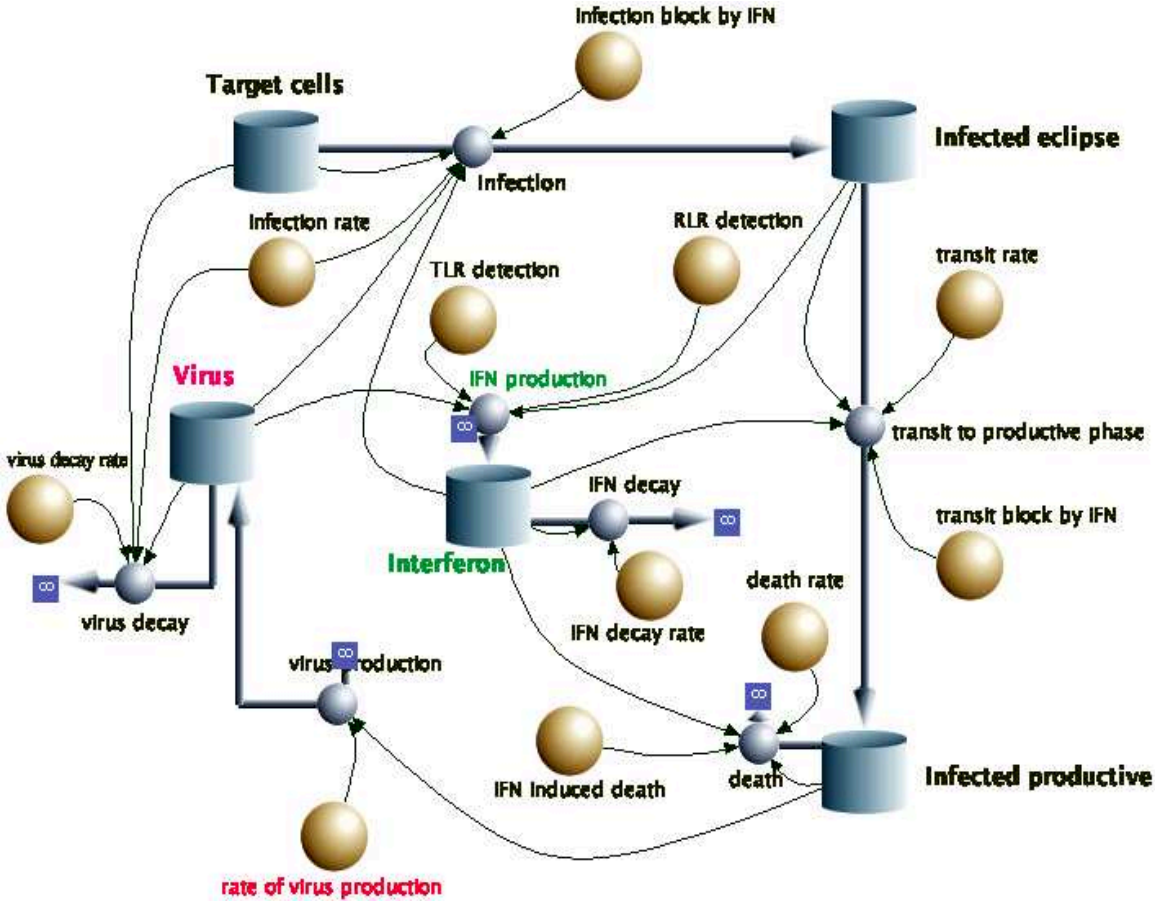

Annex1 Figure 1. Flowchart of the single-compartment model built with Berkeley Madonna. A simplified version of the model is shown in Figure 8A of the main article.

The model starts with a population of 10^5 target cells (T). In the presence of free virus, some of these cells get infected, entering first an eclipse phase (E) during which they do not produce the virus, before transiting to the productive phase of infection (P), where they start to release new infective virions at a fixed rate. We neglect the death or proliferation of target or eclipse cells, but the cytopathic effect causes the death of productively infected cells at a given rate.

Virions decay at a fixed rate and are also lost when infecting target cells. In the absence of a host response, this model is governed by the following equations:

$dT/dt = -bV(T/T_0)$ where **b** is the rate of infection (T_0 is the initial population)
$dE/dt = bV(T/T_0) - kE$ where **k** is the rate of transition from eclipse to productive
$dP/dt = kE - dP$ where **d** is the rate of cytopathic effect-induced death
$dV/dt = gP - cV - bV(T/T_0)$ where **g** is the rate of virion production per productively infected cells; and c is the rate of virus decay

By fluorescence microscopy, we detect the first wave of infected cells around 7 hours post inoculation; as the fluorescent reporter is co-expressed with structural genes, this corresponds to entry into a productive state. Therefore, we set the infection rate of target cells by free virus (**b**) at 0.5 per hour, implying a median time of 1 hour for a virus to cause a cell to enter the eclipse phase, and the transit rate from eclipse to productive state (k) at 0.1 per hour, implying a median duration of the eclipse phase of ~6 hours.
The death rate of productively infected cells (**d)** was set at 0.03 per hour, corresponding to a median survival time of ~24 hours for productively infected cells, a value consistent with our imaging data. The half-life of SINV in culture medium is 4 hours at 37°C (Purifoy et al., 1968); it should be a bit longer at 28°C, so we set virus decay rate (**c**) at 0.1 per hour (i.e. half-life of 6 hours).
After setting these parameters at plausible values, we were left with the more difficult task of estimating the rate of virus production per productively infected cell (**g**). However, we know that larvae lacking IFN response die from overwhelming infection between 48 and 72 hours after inoculation of ~30PFU of SINV (Figure 7 of main paper). We thus ran our model with an initial value of 30 for **V** and various values g (Figure 2). Except for extremely low values of g (<0.036) where infected cells may die before producing a new virus, this differential equation system ultimately leads to complete infection; we considered that larva death would occur when half the cells would have become productively infected or dead (e.g, $T+E<T_0$). To our surprise, this threshold was reached between 48 to 72 hours for values of **p** ranging from 0.6 and 1.5, much lower than we would have anticipated. Thus, according to our model and assumptions, productively infected cells release only one new infective viral particle every hour.

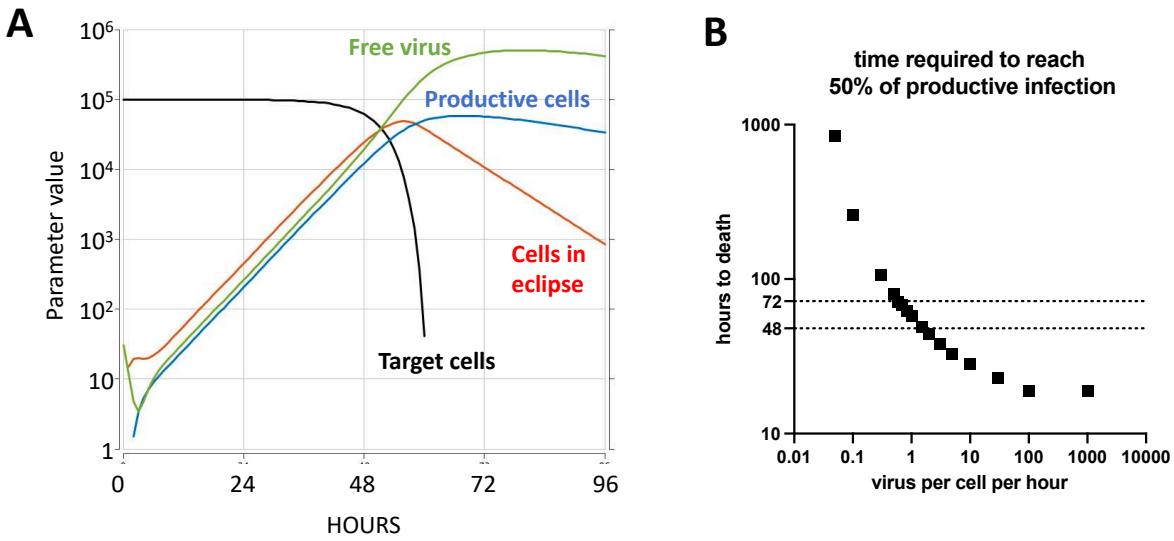

Annex 1 Figure 2. Results of running the model without an interferon response.
A) *simulation of model evolution with a virus production rate (g) set a 1 per infected cell per hour. Other parameters: b=0.5, d=0.03, k=0.1, c=0.1.).* ***B)*** *Effect of varying the value of g on the time required for half of the initial cell population to have died or entered the productive phase.*

We tested if this result was highly sensitive to the previous choice of parameters, by doubling and halving them one by one while keeping g=1. The highest sensitivity was observed for the rate of transit from eclipse to productive state **k** (Figure 3A). If this rate was halved (corresponding to a mean transition time of 14 hours), the threshold of 50% infected cells would be reached for values of g ranging from 1.3 to 4 (Figure 3B). Thus, even for this low value of transit meantime, the rate of infectious virus production would be no more than a few virions per hour for each productively infected cell**.**
For the rest of the modeling, we kept k=0.1 and g=1.

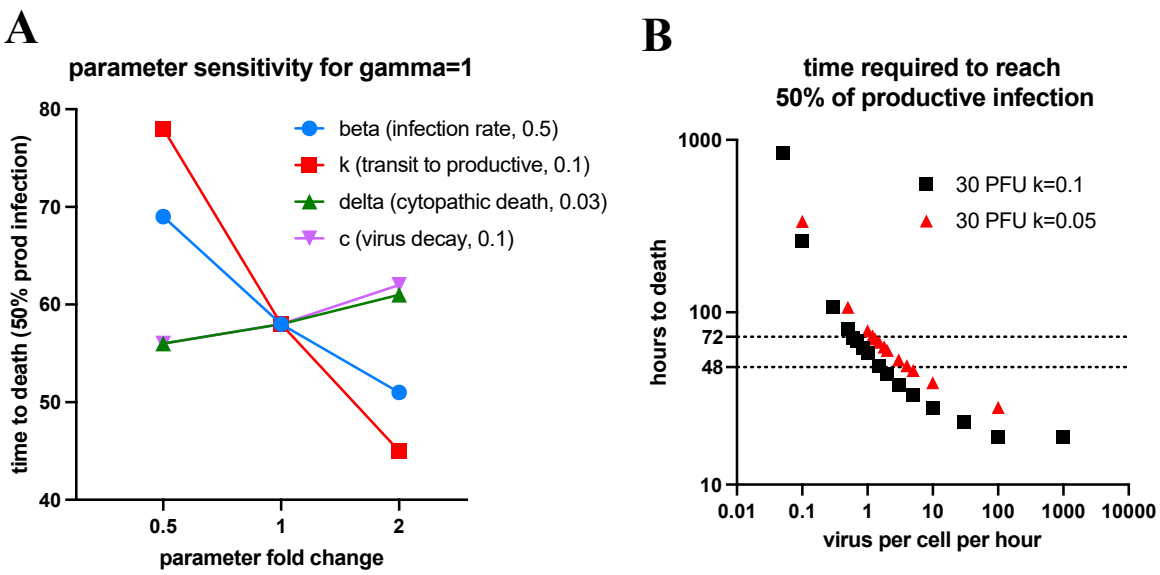

Annex1 Figure 3. Parameters sensitivity analysis.
A) *sensitivity of the model to the choice of initial parameters.* ***B)*** *effect of variation of the virus production rate for two different values of transit rate.*

We then incorporated the role of the interferon response, adding as a last variable the amount of free interferon (F), which starts at zero. We considered two detection pathways for the virus: either cytosolic viral RNA (RLR pathway) or extracellular/endosomal virions or fragments thereof (TLR pathway). RLR pathway would be activated in infected cells, but since SINV, like many viruses, shuts off host cell translation, we consider that no IFN would be released by productively infected cells; only cells in the eclipse phase would release IFN via this pathway. By contrast, we hypothesize virions would be detected by sentinel cells that do not get infected, as is the case for macrophages (Passoni et al., 2017). Thus, RLR production is proportional to the value of E and TLR production to the value of V. In addition, IFN decays at a constant rate, leading to this equation:

$dF/dT = rE + tV - hF$

r(ρ) is the rate of IFN release by eclipse phase cells
t(τ) is the rate of IFN released upon detection of virions
h is the rate of IFN decay

In humans, the half-life of recombinant IFNa has been measured at around 6 hours (Gutterman et al., 1982). We thus set h at 0.08 for a half-life of zebrafish IFN around 8 hours at 28°C.
We could not guesstimate values for r and t, but we expect that both pathways contribute to the IFN pool based on our findings where knock-down of the key RLR pathway adaptor MAVS reduced but did not abolish the IFN response of zebrafish larvae infected with the closely related chikungunya virus (Palha et al., 2013). Thus, we started by setting them at an equal value of 0.1 each (note that the value of the IFN unit is arbitrary – this choice will result in values of F of similar magnitude as V, which is convenient for the graphical representation).

If IFN is inactive, this results in an exponential increase of E, P, V, and F for two days, until all target cells have been infected.

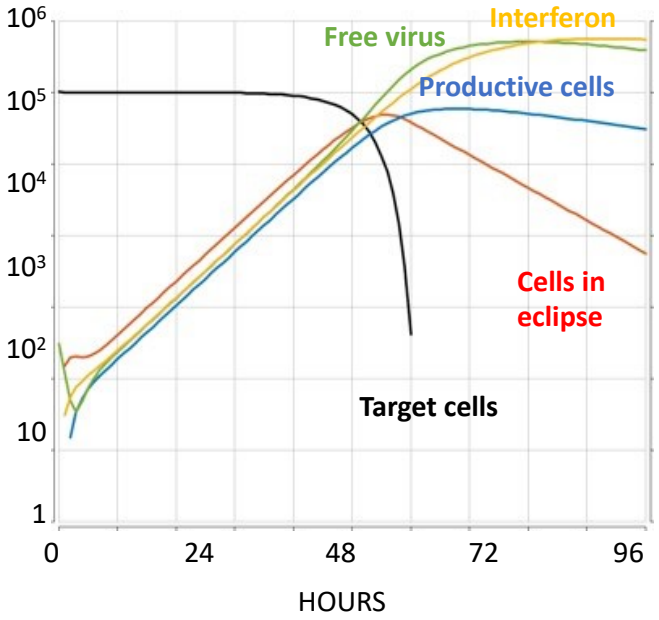

Annex 1 Figure 4. Result of running the model with IFN production, assuming IFN is inactive.
Parameters values: b=0.5, d=0.03, k=0.1, c=0.1, g=1, r=0.1, t=0.1, h=0.08, e = f = q = 0.

We then considered that IFN may counteract the infection via three mechanisms: preventing infection of target cells (if a virus attempts to infect a target cell but fails due to IFN response, it is still lost from the free virion pool), preventing the transit of eclipse cells into the productive state, and accelerating the death of productively infected cells (by any mechanism, such as direct effect of IFN on these cells or by activating killer immune cells). Following (Best et al., 2017), we assumed that IFN inhibited these events in a near-linear fashion, thus modifying our initial equations by adding the terms in bold below:

$dT/dt = (-bV(T/T_0))\mathbf{/(1+eF)}$
$dE/dt = bV(T/T_0)\mathbf{/(1+eF)} - kE\mathbf{/(1+fF)}$
$dP/dt = kE\mathbf{/(1+fF)} - dP\mathbf{*(1+qF)}$
$dV/dt = gP - cV - bV(T/T_0)$

e(ε) is the inhibition of infection by IFN
f(ϕ) is the inhibition of transit by IFN
q(θ) f is the induction of death by IFN

Our experimental results indicate that in IFN-competent larvae, the amount of productively infected cells in the periphery should peak at approximately 36 hours, then decline. We thus assessed the time and height of the peak values of P to fit the three unknown IFN-based inhibition parameters.
We first tested equal values for e f and q on the model (Figure 5A, B). Except at very low values (10^{-5} or less) for which all target cells got infected, adding this IFN response resulted in a stabilization (but not disappearance) of the infection after a peak, which was reached earlier if the IFN response was stronger.

The height of this peak was inversely proportional to the strength of the IFN response. The peak was reached at ~36 hours for e = f = q = 0.003, with 230 infected cells, a value that appears consistent with our microscopic observations.

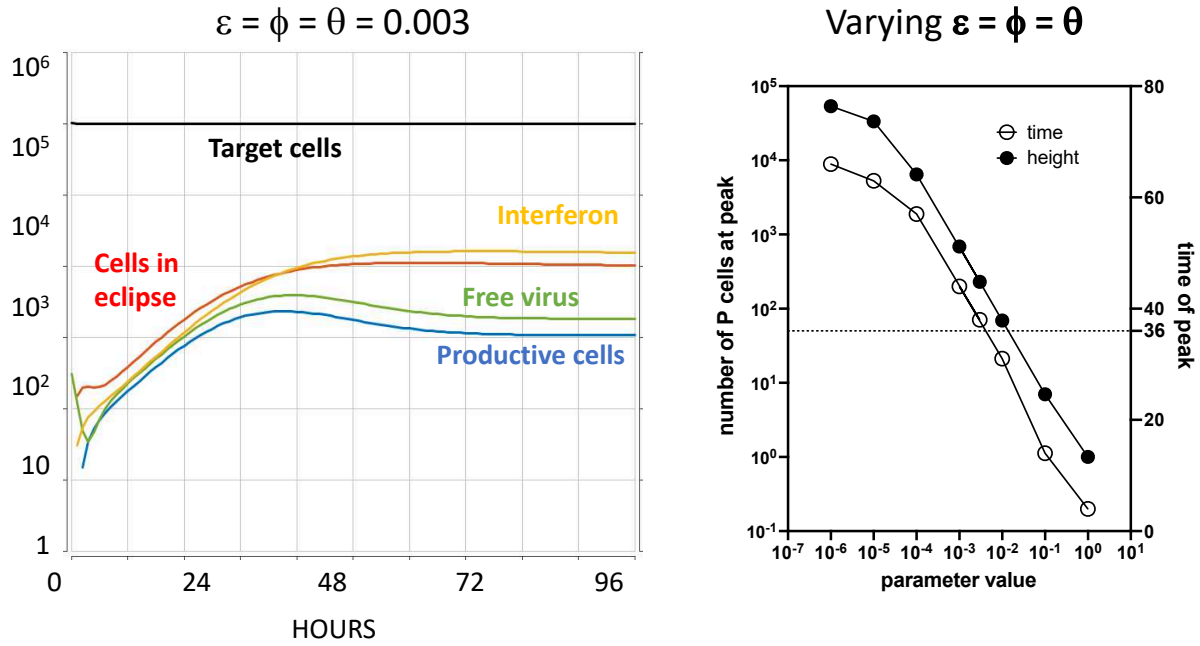

Annex 1 Figure 5. Initial fitting of the IFN inhibition values.
Parameter values for the simulation on the left: b=0.5, d=0.03, k=0.1, c=0.1, g=1, r=0.1, t=0.1, h=0.08, e = f = q = 0.03.

To determine the relative importance of these three modes of inhibition, we first canceled each of them in turn, keeping the other two at 0.03 (Figure 6). In simulations where the death of productive cells was not accelerated by IFN, no peak of infection is observed, only a plateau, this mode seems critical to reflect our experimental data. The importance of the other two modes is less clear. If transit is not blocked, the peak is attenuated; if infection is not blocked, a large population of eclipse cells is retained. In our model, not only was accelerated death necessary, but it was also sufficient; with a value q set at 0.01, our simulation reached a peak at 36 hours with dynamics globally similar to that shown in Fig 5A.

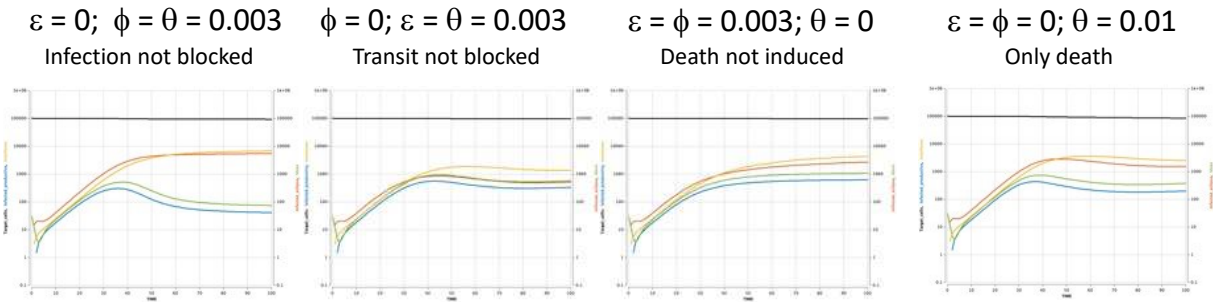

Annex 1 Figure 6. Testing the different pathways by which IFN may counteract the infection.
Other parameter values: b=0.5, d=0.03, k=0.1, c=0.1, g=1, r=0.1, t=0.1, h=0.08.

Finally, we tested the exclusion of the RLR or the TLR pathways for IFN induction. Keeping e = f = q = 0.003, we set either r or t to 0 (Figure 7). Interestingly, RLR detection alone resulted in a clear peak, while TLR detection only resulted in a plateau, indicating that RLR detection was critical while the TLR pathway may not play a major role.

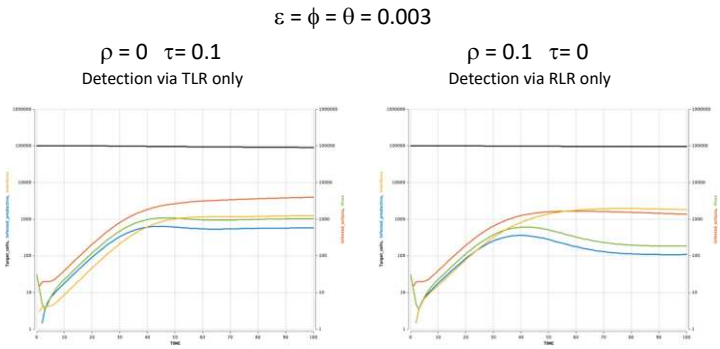

Figure 7. Testing the impact of the RLR and TLR pathways.
Other parameter values: b=0.5, d=0.03, k=0.1, c=0.1, g=1, e = f = q = 0.03.

Having established parameter values for which our model reflected relatively well SINV infection in the periphery, we turned to the CNS compartment.
Here we assume that the BBB prevents virion and IFN exchange between the periphery and CNS so that simulations are run independently in the two compartments. A few neurons initially get infected by axonal transport, and our experimental data indicate, on average, three independent events, with the first neurons expressing virus-encoded fluorescence around 24 hp. Thus, the simulation starts with no free virus, but 3 productively infected cells (in practice, this makes very little difference after the first three hours). Here, t=0 would correspond to 24 hp.
The model parameters for CNS could not be identical to those we determined in the periphery, as this would result in rapidly controlled infection. However, given the very large parameter space that could match the increased viral spread in the CNS, it was impossible to achieve unsupervised parameter fitting; we used arbitrary fitting guided by the literature and experimental data.
We considered that the following parameters should remain unchanged between periphery and CNS: rate of infection (b=0.5), rate of transit from eclipse to productive (k=0.1), rate of new virion production (g=1), rate of virus decay (c=0.1), rate of IFN decay (h=0.08).
Death of infected neurons was a rare event in our live imaging data (except for the very small population of DRG neurons). Accordingly, we reduced the cytopathic effect-induced death rate (d=0.01 instead of 0.03). This alone had little effect on the simulation.
Neurons are known to be poor IFN producers (Viengkhou and Hofer, 2023). For this reason, we strongly reduced the rate of IFN produced by eclipse cells via the RLR pathway (r=0.01 instead of 0.1). By contrast, since we observed ifnphi1-expressing leukocytes inside the infected CNS, the sentinel cell TLR pathway IFN source was unchanged (t=0.1).
This still resulted in a controlled infection but with a 3-fold increase in the maximal number of productively infected cells.

Finally, neurons are also known to have a narrow ISG response to IFNs (Viengkhou and Hofer, 2023). This is consistent with the lack of expression of the MXA:mCherry transgene that we observe in neurons. At this stage we do not know what pathways are affected at this stage, we first tested lowering equally all IFN impacts modeled here: blockade of infection, blockade of transition to productive phase, acceleration of death of infected cells. Reducing these effects resulted in a proportional increase in the peak number of productively infected cells. We observe a strong variability in the CNS of our experimental fish: some appear to control the infection, while others do not. This variance cannot be replicated in our mathematical model which is deterministic; however, parameters yielding an infection that is controlled only very close to the upper limit would reflect this, as small changes would result in this life-or-death outcome. This is attained when the three parameters that reflect IFN control (e, f, q) are reduced 10-fold (Figure 8A). We then tested the relative importance of these three parameters by setting each to zero in turn. The impact on the total number of productively infected cells (our observable value) was relatively modest, but dramatic differences were observed in the number of uninfected target cells and eclipse phase cells (Figure 8B).

In conclusion, although our simulations do not allow us to draw firm conclusions on the most appropriate values in the CNS, they suggest that IFNs are ~10 times less protective on neurons than on peripheral cells.

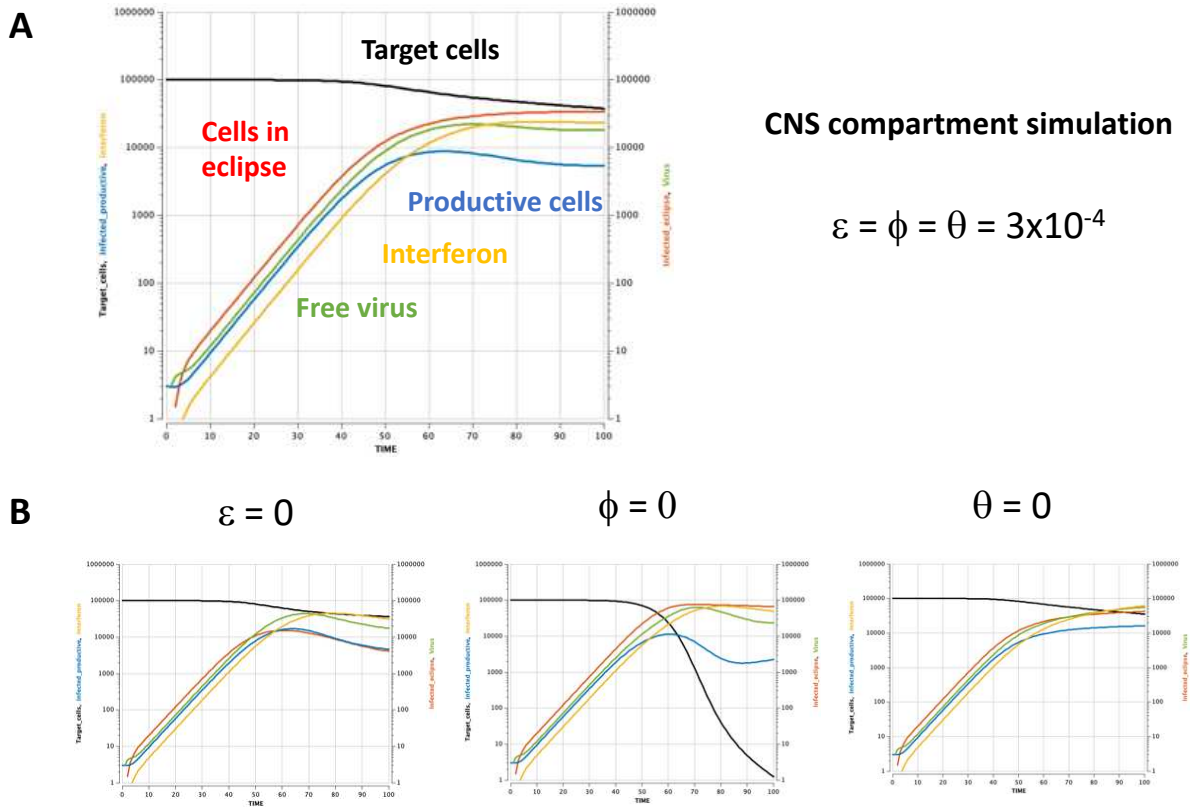

Figure 8. Adaptation of the model to the CNS compartment.
A) *simulation with all three IFN-impact parameters. Other parameter values: b=0.5, d=0.01, k=0.1, c=0.1, g=1, r=0.01, t=0.1, h=0.08.* ***B)*** *The model ran with one of the three IFN-impact parameters set to zero, while the other two are set at 3.10e-4. Other parameters as in A.*

References

Best, K., Guedj, J., Madelain, V., de Lamballerie, X., Lim, S.-Y., Osuna, C.E., Whitney, J.B., and Perelson, A.S. (2017). Zika plasma viral dynamics in nonhuman primates provides insights into early infection and antiviral strategies. Proc. Natl. Acad. Sci. U. S. A. *114*, 8847–8852.

Gutterman, J.U., Fine, S., Quesada, J., Horning, S.J., Levine, J.F., Alexanian, R., Bernhardt, L., Kramer, M., Spiegel, H., Colburn, W., et al. (1982). Recombinant leukocyte A interferon: pharmacokinetics, single-dose tolerance, and biologic effects in cancer patients. Ann. Intern. Med. *96*, 549–556.

Palha, N., Guivel-Benhassine, F., Briolat, V., Lutfalla, G., Sourisseau, M., Ellett, F., Wang, C.H., Lieschke, G.J., Herbomel, P., Schwartz, O., et al. (2013). Real-time whole-body Visualization of Chikungunya Virus Infection and Host Interferon Response in Zebrafish. PLoS Pathog. *9*, e1003619.

Passoni, G., Langevin, C., Palha, N., Mounce, B.C., Briolat, V., Affaticati, P., De Job, E., Joly, J.-S., Vignuzzi, M., Saleh, M.-C., et al. (2017). Imaging of viral neuroinvasion in the zebrafish reveals that Sindbis and chikungunya viruses favor different entry routes. DMM Dis. Model. Mech. *10*, 847–857.

Purifoy, D.J., Purifoy, J.A., and Sagik, B.P. (1968). A mathematical analysis of concomitant virus replication and heat inactivation. J. Virol. *2*, 275–280.

Viengkhou, B., and Hofer, M.J. (2023). Breaking down the cellular responses to type I interferon neurotoxicity in the brain. Front. Immunol. *14*, 1110593.

Chapter 3: Outlook

I consider this paper as the main paper from my PhD as I designed and performed all the experiments and analysis related.

Our paper investigated a wide range of questions, making it challenging to determine the best direction to take due to the technical obstacles involved. The data obtained generated several ramifications, making it difficult to narrow down our focus. Despite this, we ultimately decided to concentrate on three key questions: how the virus spreads in zebrafish larvae, how it infiltrates the CNS and brain, and whether mathematical modeling can provide additional insights.

We demonstrated that zebrafish can be used as an animal model to study SINV proficiently.

The SINV virus initially infects muscle cells and rapidly replicates, spreading cell-to-cell without a set directionality. This infection is transient in periphery and resolves between 2- and 3 days post-infection. Our research has shown that Dorsal Root Ganglia cells act as gateways for SINV, allowing it to invade the spinal cord and the brain. These sensory neurons innervate the muscle and can be infected by SINV, which uses the axons to enter the Spinal cord and infect the CNS. SINV can then spread from cell to cell, infecting interneurons and forming local clusters of infection, through short axonal transport, forming short distance clusters, and long axonal transport, using DRGs connection to long somatosensory axons to invade the brain. By contrast, motoneurons can be infected by SINV providing access to the brain, but do not provide a gateway for direct brain infection. Our study using fish with impaired interferon response demonstrated that interferon Type I φ1 and φ3 are highly expressed during SINV infection and are necessary to resolve the peripheral infection and protect the CNS. IFN φ1expression remains sustained during infection, while IFN φ3 expression declines over time.

Using mathematical modeling we simulated the infection of peripheral and CNS compartments in both wildtype and interferon receptor knock-down larvae, extrapolation values relative to the number of infective virions produce by infected cells, and the relevance of RLR pathways in the interferon response to infection.

These observations were achieved through diverse methods, including a novel approach that was developed to address the research problem. To investigate the virus propagation, a semi-high-content approach was employed in conjunction with semi-automatic image analysis, which enabled us to generate and use low-variance data for mathematical modeling. Additionally, a new multiwell multi-medium mounting system and combinatorial anesthetic were developed to facilitate high-resolution imaging of fragile infected zebrafish over long time lapses without compromising their physiology. The mathematical model yielded important insights that were not easily measurable by biological experimentation and were designed with a user-friendly approach, using software like Berkley Madonna with an accessible learning curve. The study demonstrates how zebrafish larvae can serve as a "researcher-friendly" animal model for mathematical modeling based on kinetical data.

From a personal stand, the behavior of the innate immune system during its passage from the periphery to the CNS is particularly intriguing. The data suggests that this passage is highly variable and involves a different immune response mechanic, not solely interferon driven. Interferon may play a protective role, but it is more likely a neuroimmune reflex elicited by sensory neurons that signal the infection in the CNS. This reflex could be responsible for the observed variability in CNS infection and different infection outcomes. Additionally, the similar phenotype between DRG deficient morphants and Interferon receptor morphants further supports this idea. Hypothetically, this system could work by blocking intracellular transport, activity, and apoptosis induction to hinder viral propagation without releasing granular contents that could worsen tissue damage. However, this hypothesis requires further validation through additional studies.

For this, we will perform single-cell RNAseq on infected cells in interferon morphants and compartments to find more information regarding the different actors of immune response to virus infection.

Exploring Zebrafish Larvae as a COVID-19 Model: Probable Abortive SARS-CoV-2 Replication in the Swim Bladder

Chapter 1: Introduction

1.1 Sars-CoV2

SARS-Cov2 is a virus part of the highly diverse coronaviruses (CoVs) family. The CoVs family is called *Coronaviridae* and can be further divided into the subfamily *Orthocoronavirinae,* and genera *alphacoronavirus, betacoranvirus, gammacoronavirus* and *deltacoravirus.* The alpha- and beta- coronavirus exclusively infect mammals and are respiratory and enteric viruses (Corman et al., 2018; Gorbalenya et al., 2020). Coronaviruses are not a novelty of the latest year, as strains such as HCoV-OC43, HCoV-229, HCoV-NL63, and HCoV-HKU1 have long been circulating in the population and are known as "common seasonal cold". The most pathogenic and dangerous CoVs are the middle east respiratory syndrome (MERS-CoV) and the severe acute respiratory syndrome (SARS-CoV) viruses. The last iteration of the evolution of this family is the SARS-Cov2, which we, unfortunately, got familiar with during the pandemic (Lamers and Haagmans, 2022).

These viruses can infect upper respiratory tracts and lungs in humans, inducing severe symptoms with high mortality. Specific antiviral drugs for SARS-Cov2 have been developed but used only as a backup therapy as their widespread use is expected to quickly lead to the selection of resistant variants.

SARS-COV2 is an enveloped positive single-strand RNA virus, with a genome of >30kb (Figure 21).

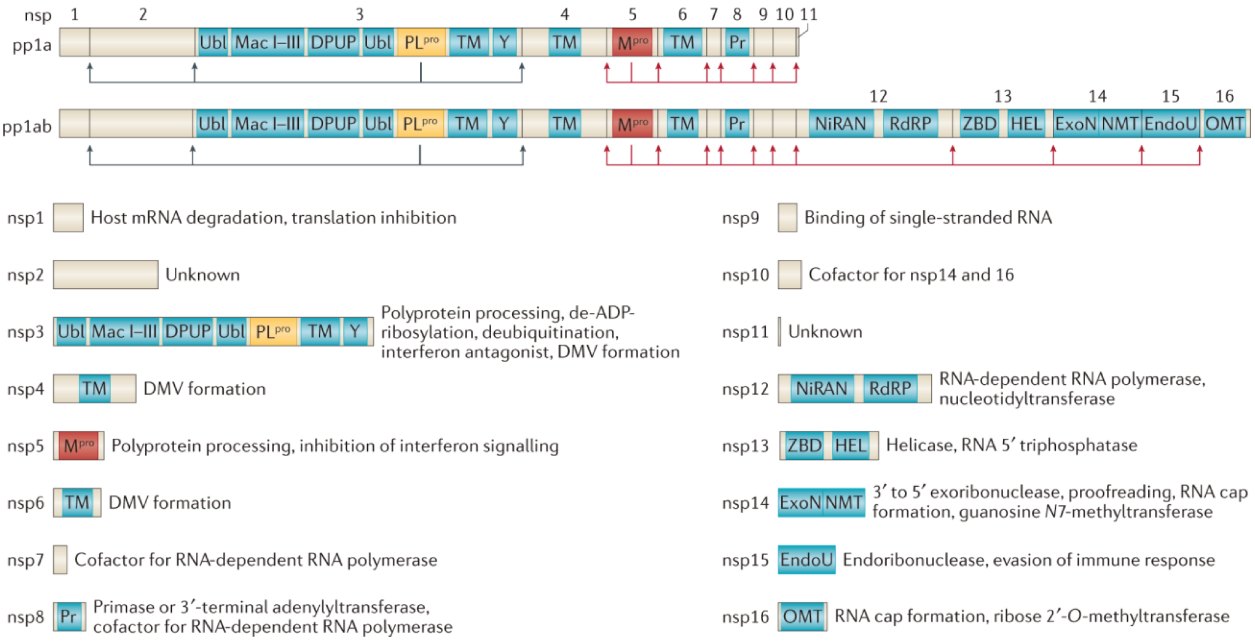

Figure 21: Coronavirus polyprotein processing and non-structural proteins.

Coronavirus polyprotein processing and domains of non-structural proteins (nsp) are illustrated for severe acute respiratory syndrome-related coronaviruses. Proteolytic cleavage of the polyproteins pp1a and pp1ab is facilitated by viral proteases residing in nsp3 (PLpro) and nsp5 (Mpro). PLpro proteolytically releases nsp1, nsp2, nsp3 and the amino terminus of nsp4 from the polyproteins pp1a and pp1ab (indicated by the blue arrows). Mpro proteolytically releases nsp5–16 and the carboxy terminus of nsp4 from the polyproteins pp1a and pp1ab (indicated by the red arrows)176. Conserved domains and known functions are schematically depicted for nsp1–16 (refs4,66,67,177). DMV, double-membrane vesicle; DPUP, Domain Preceding Ubl2 and PLpro; EndoU, endoribonuclease; ExoN, exoribonuclease; HEL, helicase; Mac I–III, macrodomains 1–3; Mpro, main protease; NiRAN, nidovirus RdRP-associated nucleotidyltransferase; NMT, guanosine N7-methyltransferase; OMT, ribose 2'-O-methyltransferase; PLpro, papain-like protease; Pr, primase or 3'-terminal adenylyl-transferase; RdRP, RNA-dependent RNA polymerase; TM, transmembrane domains; Ubl, ubiquitin-like domain; Y, Y and CoV-Y domain; ZBD, zinc-binding domain. ***Source (V'kovski et al., 2020).***

This large genome is flanked at 5' and 3' by untranslated regions, containing *cis*-acting RNA structures necessary for RNA synthesis. Two large open reading frames (ORF1a and ORF1b) are at the 5' ending, which occupy a large portion of this capped and polyadenylated ending. These two ORFs translate into 15-16 non-structural proteins (nsp), necessary for the formation of the viral replication and transcription complex (RTC). The RTC oversees RNA processing, RNA modification, and RNA proofreading, as the large genome needs to be replicated at full length to be incorporated in new viral particles. At the 3' there are interspersed ORFs for structural proteins and sub-genomic mRNAs (sg mRNAs) (Artika et al., 2020; Perlman and Netland, 2009).

Starting from ORF1a and ORF1b are produced two different polyproteins called pp1a and pp1b, which quantity is determined by -1 ribosomal frameshift efficiency (Irigoyen et al., 2016; Perlman and Netland, 2009). From pp1a, the nsp1-11 is released, and from pp1b the nsp12-16 (Gao et al., n.d.; Kamitani et al., 2006; Schubert et al., 2020; Thoms et al., 2020). Nsp3 and nsp5 are proteases that cleave the polyproteins. The nsp2-16 is part of the RTC, whereas nsp2-11 primes the cellular environments to accommodate the RTC, and nsp12-16 has enzymatic functions such as RNA synthesis, RNA modification, and RNA proofreading. Nsp12 is an RNA-dependent RNA polymerase (RdRP) and has nsp7 and nsp8 as cofactors. Nsp10 and nsp13 have 5'-triphosphatase activity, while nsp14 and nsp16 have N7-methyltransferase and 2'-O-methyltransferase activity, forming the capping machinery (Chen et al., 2011, 2009; Eckerle et al., 2007; Ivanov et al., 2004).

In SARS-Cov2, the positive single-strand RNA is firstly translated in a full-length negative sense copy, which acts as a template for more positive RNA. The new synthesized positive RNA copies act as amplification templates for nsps/RTCs production or get packed in new virions. A hallmark of coronavirus is the discontinuous viral transcription process, that produces nested sub-genomic RNAs. This mechanism is mediated by transcription regulatory sequences (TRSs) (Di et al., 2018; Sawicki and Sawicki, 1995). During the negative strand synthesis, the machinery can encounter the TRSs upstream of the ORFs in the 3' portion of the genome. When this happens, the machinery stops the synthesis of the filament and resumes it in a downstream leader TRS, close to the 5' end, skipping the synthesis of different portions of the viral genome and generating different sgRNA. This mechanism could be involved in SARS-COV2 rapid evolution, as non-canonical RNA fusion events were recorded in the past (Kim et al., 2020; Sola et al., 2015; V'kovski et al., 2020). A practical application of this mechanism is that, starting with purified RNA from an infected

sample, one can specifically generate cDNAs from the positive strand transcripts which are polyadenylated, using a (dT)15 primer, or from the negative strand transcripts using a TRS-specific primer. It is thus relatively simple to measure positive or negative viral RNA by qRT-PCR.

Besides, the nsp, SARS-Cov2 has several structural proteins (figure 22), that form a helically symmetrical nucleocapsid, composed of the +ssRNA and structural proteins.

- S protein (spike) gives the virus the "corona" aspect, forming a homotrimeric spike-like structure on the surface of the envelope. Each S protein has several domains, such as N-terminal (NTD), receptor binding motif (RBM), receptor binding domain (RBD, in the RBM), furin cleavage site, fusion peptide (FP), central helix (CH), connecting domain (CD), heptad repeat (HR1/2), transmembrane domain (TM) and cytoplasmic tail (CT). Each protein S folds to form three-dimensional structures containing exposing the S1/RBD domain, which recognizes and binds the ACE2 receptor on the host surface. This binding promotes conformational changes that expose the S2 subunit, containing the FP, CH, CD, and HR1/2. This allows for membrane fusion with the host cell and infection by SARS-COV2 (Casalino et al., 2020; Huang et al., 2020; Moreira et al., 2020; Yadav et al., 2021).
- M protein (membrane) is an O-linked glycoprotein of 30kDa, possessing three transmembrane domains. This protein associates with the nucleocapsid, facilitating the virus assembly and it is conserved in the family (Yadav et al., 2021).
- E protein (envelope) is a 12 kDa protein with a conserved structure. This protein is essential for pathogenesis, release, and virus assembly (Wang et al., 2020).
- N protein (nucleocapsid) forms a complex structure that binds to the +ssRNA packaging it in a beads-on-a-string fashion. Besides forming this helical nucleocapsid, it is involved in virion assembly and transcription efficiency (Yadav et al., 2021).

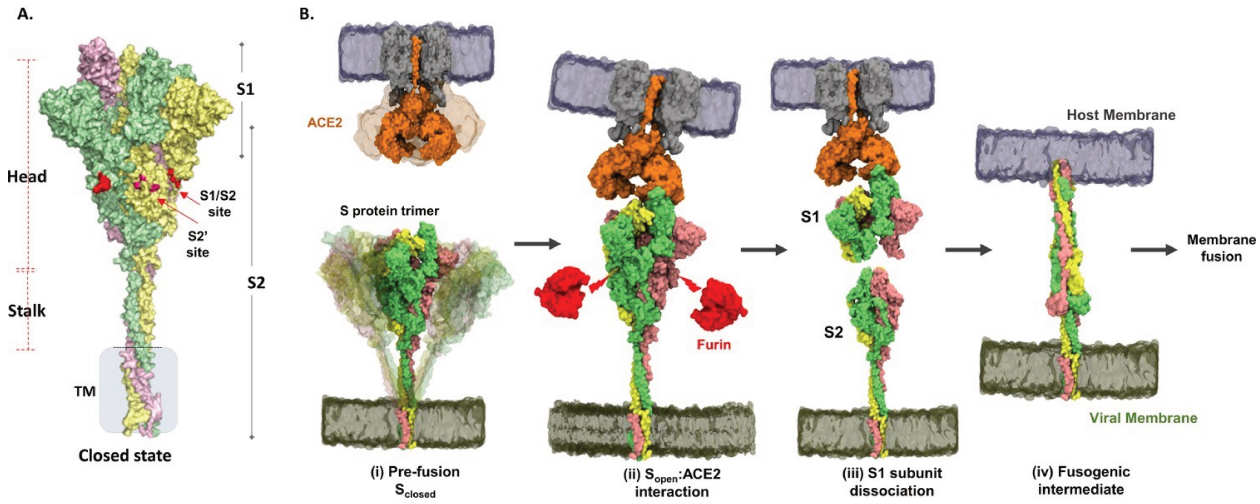

Figure 22: Structure and domain organization of trimeric spike (S) protein showing steps in the virus–host entry initiated by S recognition and binding to angiotensin-converting enzyme 2 (ACE2) receptor.

A) Prefusion S protein trimer in closed conformational state, with monomers shown in yellow, green, and pink. S protein construct (1–1245) used in this study showing head, stalk, and transmembrane (TM) segments as generated by integrative modeling. The S1/S2 and S20 cleavage sites are in red. Proteolytic processing (furin) of S protein generates S1 and S2 subunits. B) Schematic of viral entry into host cell mediated by S:ACE2 interactions: (i) Intrinsic dynamics of prefusion S protein trimer decorating SARS-CoV-2 and host ACE2 dimeric structure showing sweeping motions of S protein and ACE2 to facilitate S:ACE2 recognition. (ii) In the open conformation (Sopen), receptor binding domain adopts an 'up' orientation to recognize and bind the host membrane-bound ACE2 receptor (Protein Data Bank [PDB] ID: 1R42). ACE2 binding induces conformational changes promoting Furin (red) proteolysis at the S1/S2 cleavage site (red arrows), leading to dissociation of S1 and S2 subunits, the mechanism of which is unknown. *Furin here also denotes relevant related proteases. (iii) The residual ACE2-bound S1 subunit becomes stably bound to ACE2 and S2 subunits dissociate. (iv) Conformational changes in the separated S2 subunit promote formation of an extended helical fusogenic intermediate (PDB ID: 6M3W) for fusion into the host cell membrane, membrane fusion, and viral entry into the host cell.* ***Source (Raghuvamsi et al., 2021).***

In addition to ACE2 receptors, a broad range of entry cofactors were suggested in the past years, such as lectins (DC-SIGN and L-SIGN) (Amraei et al., 2021; Jeffers et al., 2004; Yang et al., 2004), phosphatidylserine receptors (TIM and TAM) (Jemielity et al., 2013; Richard et al., 2017) and transmembrane glycoproteins (CD147) (Chen et al., n.d.; Shilts et al., n.d.), but the most relevant for the following paper is neuropilin1 (NRP1) (Daly et al., 2020; Li et al., 2021). NRP1 is strongly expressed in respiratory endothelial cells and weakly expressed in ciliated cells (i.e., goblet cells); cell populations in organs with a high tropism for this virus (Cantuti-Castelvetri et al., 2020).

An important co-factor, necessary for the fusion is a type II transmembrane protein with protease activity called TMPRSS2. This protein is implicated in the infection process by both influenzas and SARS viruses and it is expressed in the gastrointestinal, respiratory, and urogenital epithelium. In these tissues, only goblet secretory cells, type II pneumocytes, and enterocytes express both ACE2 and TMPRSS2 in humans (Jackson et al., 2021).

After the fusion, the virus can enter by endosomal entry, with acidification and cathepsinL-mediated fusion, or directly by membrane fusion with the cell membrane (Jackson et al., 2021). In both cases, the capsid is released, and the following uncoating of viral RNA. As explained, this phase starts the gRNA translation with the production of nsp and the formation of the RTC complex. The infection induces the extensive remodeling of endoplasmic reticulum (ER) membranes, forming a complex structure of double-membrane vesicles (DMVs) and convoluted membranes (CMs) (Malone et al., 2021). These replicative organelles become viral factories where the RTC produces copies of +ssRNA and sg-mRNA. With the production of the structural proteins, a fraction of the new +ssRNA is used to form new nucleocapsids, while the S, M, and E proteins transmigrate to the ER-Golgi. These proteins transit through the ER-Golgi intermediate compartments (ERGIC) where their interaction with formed nucleocapsid forms the viral envelope by budding (Malone et al., 2021; V'kovski et al., 2020). The newly formed viral particles are then secreted by exocytosis (V'kovski et al., 2020) (Figure 23).

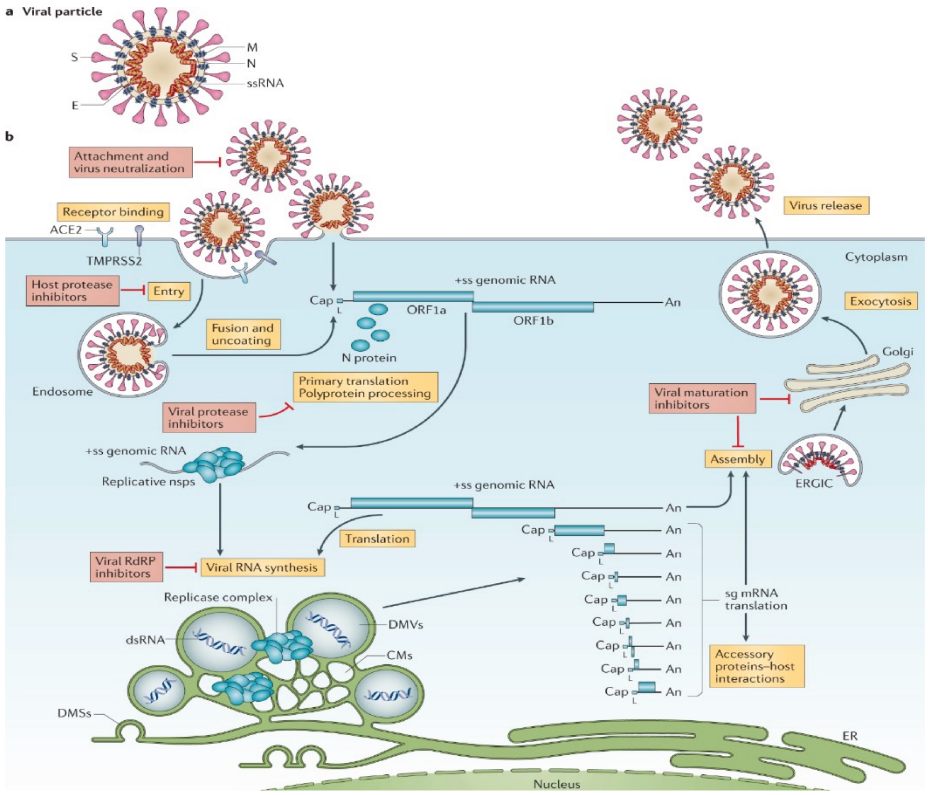

Figure 23: The coronavirus virion and life cycle.

The coronavirus virion consists of structural proteins, namely spike (S), envelope (E), membrane (M), nucleocapsid (N) and, for some betacoronaviruses, haemagglutinin-esterase (not shown). The positive-sense, single-stranded RNA genome (+ssRNA) is encapsidated by N, whereas M and E ensure its incorporation in the viral particle during the assembly process. S trimers protrude from the host-derived viral envelope and provide specificity for cellular entry receptors. B) Coronavirus particles bind to cellular attachment factors and specific S interactions with the cellular receptors (such as angiotensin-converting enzyme 2 (ACE2)), together with host factors (such as the cell surface serine protease TMPRSS2), promote viral uptake and fusion at the cellular or endosomal membrane. Following entry, the release and uncoating of the incoming genomic RNA subject it to the immediate translation of two large open reading frames, ORF1a and ORF1b. The resulting polyproteins pp1a and pp1ab are co-translationally and post-translationally processed into the individual non-structural proteins (nsps) that form the viral replication and transcription complex. Concordant with the expression of nsps, the biogenesis of viral replication organelles consisting of characteristic perinuclear double-membrane vesicles (DMVs), convoluted membranes (CMs) and small open double-membrane spherules (DMSs) create a protective microenvironment for viral genomic RNA replication and transcription of subgenomic mRNAs (sg mRNAs) comprising the characteristic nested set of coronavirus mRNAs. Translated structural proteins translocate into endoplasmic reticulum (ER) membranes and transit through the ER-to-Golgi intermediate compartment (ERGIC), where interaction with N-encapsidated, newly produced genomic RNA results in budding into the lumen of secretory vesicular compartments. Finally, virions are secreted from the infected cell by exocytosis. Key steps inhibited by compounds that are currently being validated and which represent attractive antiviral targets are highlighted in red. An, 3′ polyA sequence; cap, 5′ cap structure; dsRNA, double-stranded RNA; L, leader sequence; RdRP, RNA-dependent RNA polymerase. ***Source (V'kovski et al., 2020)***

Chapter 2: Article

frontiers in Cellular and Infection Microbiology

ORIGINAL RESEARCH
published: 11 March 2022
doi: 10.3389/fcimb.2022.790851

Exploring Zebrafish Larvae as a COVID-19 Model: Probable Abortive SARS-CoV-2 Replication in the Swim Bladder

Valerio Laghi[1], *Veronica Rezelj*[2], *Laurent Boucontet*[1], *Maxence Frétaud*[3], *Bruno Da Costa*[3], *Pierre Boudinot*[3], *Irene Salinas*[4], *Georges Lutfalla*[5], *Marco Vignuzzi*[2] *and Jean-Pierre Levraud*[1,6*]

[1] Institut Pasteur, Centre National de la Recherche Scientifique (CNRS) Unité mixte de Recherche (UMR) 3637, Unité Macrophages et Développement de l'Immunité, Paris, France, [2] Institut Pasteur, Unité Populations Virales et Pathogénèse, Institut Pasteur, Paris, France, [3] Université Paris-Saclay, Institut National pour la Recherche pour l'Agriculture, l'Alimentation et l'Environnement (INRAE), Université Versailles Saint-Quentin (UVSQ), Virologie et Immunologie Moléculaire (VIM), Jouy-en-Josas, France, [4] Department of Biology, University of New Mexico, Albuquerque, NM, United States, [5] Laboratory of Pathogen-Host Interactions (LPHI), Centre National de la Recherche Scientifique (CNRS), Université de Montpellier, Montpellier, France, [6] Université Paris-Saclay, Centre National de la Recherche Scientifique (CNRS), Institut Pasteur, Institut des Neurosciences Paris-Saclay, Gif-sur-Yvette, France

OPEN ACCESS

Edited by:
Vincenzo Torraca, University of Westminster, United Kingdom

Reviewed by:
*Stefan Oehlers, Agency for Science, Technology and Research (A*STAR), Singapore*
Con Sullivan, University of Maine at Augusta, United States

***Correspondence:**
Jean-Pierre Levraud
jean-pierre.levraud@pasteur.fr

Specialty section:
This article was submitted to Microbes and Innate Immunity, a section of the journal Frontiers in Cellular and Infection Microbiology

Received: *07 October 2021*
Accepted: *04 February 2022*
Published: *11 March 2022*

Citation:
Laghi V, Rezelj V, Boucontet L, Frétaud M, Da Costa B, Boudinot P, Salinas I, Lutfalla G, Vignuzzi M and Levraud J-P (2022) Exploring Zebrafish Larvae as a COVID-19 Model: Probable Abortive SARS-CoV-2 Replication in the Swim Bladder. Front. Cell. Infect. Microbiol. 12:790851. doi: 10.3389/fcimb.2022.790851

Animal models are essential to understanding COVID-19 pathophysiology and for preclinical assessment of drugs and other therapeutic or prophylactic interventions. We explored the small, cheap, and transparent zebrafish larva as a potential host for SARS-CoV-2. Bath exposure, as well as microinjection in the coelom, pericardium, brain ventricle, or bloodstream, resulted in a rapid decrease of SARS-CoV-2 RNA in wild-type larvae. However, when the virus was inoculated in the swim bladder, viral RNA stabilized after 24 h. By immunohistochemistry, epithelial cells containing SARS-CoV-2 nucleoprotein were observed in the swim bladder wall. Our data suggest an abortive infection of the swim bladder. In some animals, several variants of concern were also tested with no evidence of increased infectivity in our model. Low infectivity of SARS-CoV-2 in zebrafish larvae was not due to the host type I interferon response, as comparable viral loads were detected in type I interferon-deficient animals. A mosaic overexpression of human ACE2 was not sufficient to increase SARS-CoV-2 infectivity in zebrafish embryos or in fish cells *in vitro*. In conclusion, wild-type zebrafish larvae appear mostly non-permissive to SARS-CoV-2, except in the swim bladder, an aerial organ sharing similarities with the mammalian lung.

Keywords: SARS-CoV-2, zebrafish, animal model, swim bladder, type I interferon

INTRODUCTION

The COVID-19 pandemic has taken an enormous toll worldwide, in both human and economic losses. Although vaccination is finally under way, the SARS-CoV-2 virus is predicted to persist for years (Moore et al., 2021), and its variants represent an unpredictable threat. Thus, it will be necessary to continue the research efforts to understand its heterogeneous pathology and develop new drugs and vaccines.

Animal models play a central role during any pandemic since they are essential to analyzing pathology, transmission, and test vaccines and drugs. Besides non-human primates, other mammals such as Syrian hamsters and ferrets are naturally susceptible to SARS-CoV-2 (Muñoz-Fontela et al., 2020). Mice, the most widely used model for host–pathogen studies, require a transgene-mediated expression of human angiotensin-converting enzyme 2 (hACE2) to be infected (Lutz et al., 2020), although some recent variants replicate to a significant extent in wild-type mice (Montagutelli et al., 2021). All these models have several advantages and disadvantages. Non-human primates are very expensive, require large animal facilities, and are not conducive to large-scale experiments. hACE2 transgenic mice remain expensive and not readily available. As a result, expanding the repertoire of animal models for any disease is always beneficial and each model may shed light to unique aspects of the pathogen–host interaction. Here, we test if zebrafish larvae can be added to the list of suitable animal models for the study of COVID-19.

The zebrafish larva is an increasingly popular model to understand host–pathogen interactions (Torraca and Mostowy, 2018). Low cost of husbandry, high fecundity, and small size and transparency at early stages are among its main advantages. Thus, zebrafish larvae allow live imaging of pathogen dissemination at the whole organism to subcellular scales, and *in vivo* molecule screens in 96-well formats. Zebrafish is also a genetically tractable model, and thousands of mutant and reporter transgenic lines are available in fish facilities and repositories worldwide. Given that 80% of disease-associated genes of humans have a zebrafish ortholog (Howe et al., 2013), it is not surprising that zebrafish continue to be developed as models for human pathogens. Further, zebrafish is a bony vertebrate with an immune system that is also highly similar to ours. For instance, orthologs of the classical inflammatory cytokines (IL1β, TNFα, IL-6) as well as type I interferons (IFNs) are all found in zebrafish (Zou and Secombes, 2016). Interestingly, zebrafish adaptive immunity develops only at the juvenile stage, weeks after hatching (Lam et al., 2004), and the larva thus constitutes a system where innate immunity can be evaluated independently of adaptive responses. These assets make the zebrafish highly suitable to the study of host–virus interactions (Levraud et al., 2014).

Experimental infection has been established with various human viruses in zebrafish, including Herpes simplex virus 1 (Burgos et al., 2008), Chikungunya virus (CHIKV) (Palha et al., 2013), influenza A virus (IAV) (Gabor et al., 2014), and norovirus (Van Dycke et al., 2019). The upper temperature limit of proper zebrafish development, 33°C (Kimmel et al., 1995), may be an issue for some viruses; however, it corresponds to that of upper airways, and in fact SARS-CoV-2 replicates better at 33°C than at 37°C (V'kovski et al., 2021). The absence of lungs is another drawback to model a respiratory infection; however, teleost fish do possess an air-filled organ, the swim bladder, used for buoyancy regulation. Lungs of tetrapods and swim bladders of fish are evolutionarily related and share important structural homologies, such as surfactant coating (Cass et al., 2013). In support, inoculation of IAV in swim bladder resulted in localized infection (Gabor et al., 2014).

The zebrafish genome contains a unique, unambiguous ortholog of the gene encoding ACE2, the SARS-CoV-2 receptor; however, modest conservation of amino acids at the binding interface makes fish ACE2 proteins unlikely to bind the virus spike efficiently (Damas et al., 2020). Despite these *in silico* predictions, host susceptibility requires experimental validations, especially given that many other receptors and co-receptors for SARS-CoV-2 have been identified (Zamorano Cuervo and Grandvaux, 2020). In zebrafish larvae, based on single-cell transcriptomics, *ace2* is strongly expressed in a subtype of enterocytes (Postlethwait et al., 2021); the gut is also the organ with strongest *ace2* expression in humans.

There have been reports of the use of zebrafish to study COVID-19. We have recently reported pathological effects after exposure of zebrafish to recombinant SARS-CoV-2 spike protein, including accelerated heartbeat in larvae and severe olfactory damage causing transient hyposmia in adults after intranasal administration (Kraus et al., 2020). Injection of recombinant spike to adults has also been reported to induce adverse effects (Ventura Fernandes et al., 2020). Xenotransplantation of human lung cells in the swim bladder of adult zebrafish has been proposed to test the effect of an herbal drug on SARS-CoV-2 (Balkrishna et al., 2020). However, to date, no in-depth assessment of the ability of SARS-CoV-2 to replicate in zebrafish has been published.

Here we tested several tactics to infect zebrafish larvae with SARS-CoV-2, including bath exposure and microinjection in various organs or cavities. No evidence for production of new virions was obtained, but the distinct viral RNA dynamics obtained after swim bladder injection, together with immunohistochemical data, suggest that abortive infection occurred in that organ. Preventing type I IFN responses did not result in increased replication, consistent with the fact that SARS-CoV-2 inoculation did not result in strong IFN responses or induction of inflammatory cytokines.

RESULTS

SARS-CoV-2 Replicates in Zebrafish Larvae Only When Injected in the Swim Bladder

We first tested if an early strain of SARS-CoV-2 would replicate in wild-type zebrafish larvae after bath exposure. We exposed 4-day post-fertilization (dpf) larvae with inflated swim bladders (ensuring an open gut) as well as 2-dpf dechorionated embryos with suspension of either live or heat-inactivated virus added to water (8×10^4 PFU/ml). Larvae were then incubated at 32°C and observed regularly; no specific signs of distress were noted. After RNA extraction, the amount of polyadenylated SARS-CoV-2 *N* transcripts was measured by qRT-PCR. Although viral RNA was readily detectable after 6 h of exposure, it then declined and became undetectable after 48 h (**Figure 1**). Therefore, bath exposure failed to achieve infection.

We then turned to microinjection of larvae with SARS-CoV-2. Using a camera-fitted macroscope under a biosafety hood, a concentrated SARS-CoV-2 suspension was microinjected in

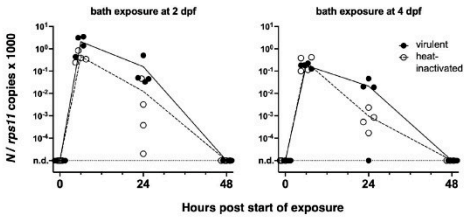

FIGURE 1 | Bath exposure of zebrafish larvae to SARS-CoV-2. Kinetics of qRT-PCR measurements of polyadenylated viral N copies; each point corresponds to an individual larva. n.d., not detected.

various sites of 3 dpf larvae (**Figure 2A**). Compared with our previous experience of microinjection using the eyepieces of a stereomicroscope, this was significantly harder, notably due to lack of stereovision. These challenging injection conditions resulted in variability during early attempts; this later improved greatly, and although success of intravenous (IV) injections remained difficult to ascertain, others, notably in the coelomic cavity, were achieved reliably and in a reasonable time frame. Injection of the syncytial yolk cell was relatively easy, but leakage was often observed after capillary withdrawal, in which case larvae were discarded. Injected larvae were immediately rinsed and transferred into individual wells of 24-well plates, which were then incubated at 32°C. Larvae were imaged daily; none of the typical disease signs that we noted during other viral infections (e.g., edemas, spine bending, necrotic spots, slow blood flow) (Palha et al., 2013) were observed.

At various time points, individual larvae were euthanized and RNA extracted. Sense transcripts of SARS-CoV-2, genomic or subgenomic, are polyadenylated (Kim et al., 2020) and were measured after reverse transcription with a poly(dT) primer. The initial inoculum, measured in larvae lysed ~30 min postinjection (pi), was readily detectable by qRT-PCR (**Table 1**). Absolute quantification by qRT-PCR, using certified commercial reagents, revealed an amount of polyadenylated SARS-CoV-2 *N* transcripts that was ~10^4-fold higher than the injected number of PFU (**Table 1**). Therefore, the overwhelming bulk of viral RNA injected in larvae must correspond to non-infectious molecules.

We then measured polyadenylated *N* copies over time. A decline was observed for all injection sites, with the notable exception of the yolk (**Figure 2B**). Amounts measured in yolk were highly variable at early time points, more than in other sites, probably due to leakage.

At this point, we wondered if this absence of replication may be due to a loss of infectivity of the virus in our microinjection conditions. We re-titered on Vero cells the leftover inoculum of one of our experiments, which had been left at room temperature for 1.5 h after thawing and addition of phenol red, and refrozen. The titer measured on Vero cells was 4.7×10^7 PFU/ml, i.e., a ~2.5-fold drop from the original titer of 1.13×10^8 PFU/ml. This was consistent with the drop expected from two rounds of freeze-thaw, suggesting that virus infectivity was not significantly decreased by our experimental conditions and confirming that we were injecting a significant amount of infectious particles.

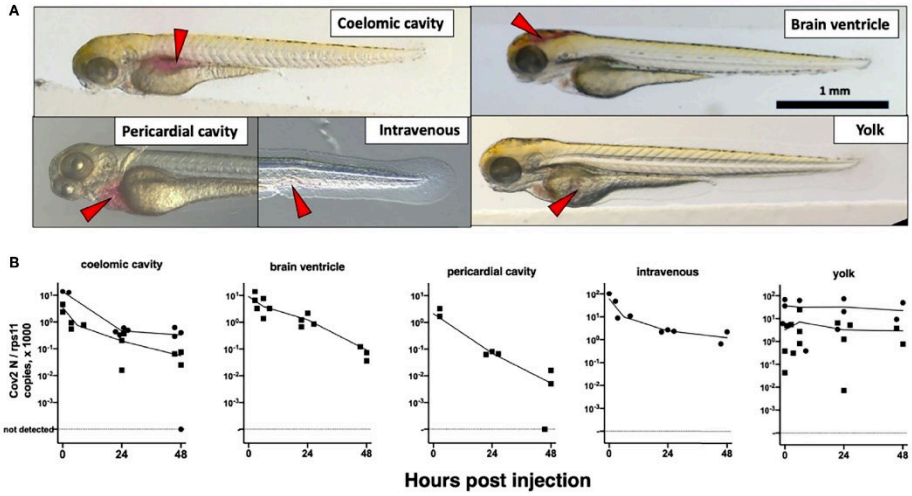

FIGURE 2 | Microinjection of SARS-CoV-2 to 3-dpf wild-type larvae. **(A)** Illustrations of the targeted sites. Images taken less than 1 min after injection of the phenol red-colored SARS-CoV-2 suspension. Red arrowheads point to the sites of microinjection. **(B)** Quantification of polyadenylated N transcripts over time, assessed by qRT-PCR; each symbol is an individual larva. Circles and squares correspond to injection of viral suspensions 1 and 2, as labeled on **Table 1**, respectively. Lines connect the means of values measured at each time point.

TABLE 1 | Initial sense N copy numbers.

	Viral suspension 1	Viral suspension 2
Titer (PFU/mL)	1.13×10^8	1.6×10^7
PFU in a 2-nl inoculum	205	29
Median *N* copies measured in a cDNA sample corresponding to 1/100th of larval extract	11,026	5,679
95% confidence interval	5,175–12,255	4,967–7,854
Number of samples	23	12
Ratio of median *N* copies to PFU	5,378	19,583

Quantification by RT-qPCR of polyadenylated viral N transcripts in zebrafish larvae microinjected with 2 nl of viral suspension (diluted 1.1-fold by addition of phenol red) in the coelomic cavity less than 1 h before lysis.

To determine if the relatively high amounts detected in yolk at late time points were due to viral replication, we reanalyzed these RNA samples by performing reverse transcription with a primer that hybridizes to the 5′ leader sequence of negative-strand subgenomic RNAs, a hallmark of active SARS-CoV-2 replication (Kim et al., 2020; Wölfel et al., 2020). Antisense transcripts are expected to be less abundant than sense transcripts in infected cells and absent from virions. Such transcripts were detected in the initial inoculum but in lower amounts than polyadenylated transcripts (median values of 1,042 and 191 copies for coelom-injected larvae with viral suspensions 1 and 2, respectively). In coelom-injected larvae, these antisense transcripts decreased and became undetectable at 48 h postinjection (hpi). By contrast, in yolk-injected larvae, levels were stable (**Figure S1A**). Therefore, both sense and antisense viral RNA molecules appeared to be protected from degradation in the yolk, and there was no clear evidence for viral replication. Notably, we did not observe yolk opacity in injected animals, a hallmark of yolk cell infection with other viruses such as CHIKV (Palha et al., 2013) and Sindbis virus (SINV) (**Figure S2**).

We then tested microinjection of SARS-CoV-2 in the swim bladder (SB), which inflates at 3.5–4 dpf (Parichy et al., 2009). We noticed that when the liquid was injected at the rostral end of the bladder, it was rapidly expelled *via* the pneumatic duct connecting the SB to the esophagus. By contrast, when liquid accumulated at the caudal end of the SB, if was well retained (**Figure 3A**). Therefore, injections were performed at 4 dpf by targeting the caudal half of the bladder; larvae with liquid injected at the rostral pole were discarded. As age-matched controls, we also injected 4-dpf larvae in the coelomic cavity, i.e., just next to, but outside of, the SB (**Figure 3A**).

Remarkably, in SB-infected larvae, after an initial decrease of viral transcripts during the first 24 h, their levels stabilized from 24 to 48 h; in contrast, the decline continued in coelom-injected larvae (**Figure 3B**). However, no disease signs were observed. We repeated the SB injection several times finding consistent results with a repeated trend of small re-increase from 24 to 48 h; extending the experiment by 1 day yielded comparable results at days 2 and 3 (**Figure 3C**). We also measured antisense transcripts in these larvae, observing the same trend (**Figure S1B**).

To perform statistical analysis with reasonable power, we normalized the results of each independent experiment to the mean of the values measured just after inoculation and then pooled the results by injection type. Because the dispersion increased considerably with time, we performed tests that allowed for unequal SDs when comparing time points. This analysis confirmed that after injection in the coelomic cavity, viral RNA amounts decline from 0 to 24 hpi and again from 24 to 48 hpi. By contrast, values measured in yolk were stable. In the SB, a very significant decrease is observed during the first 24 hpi,

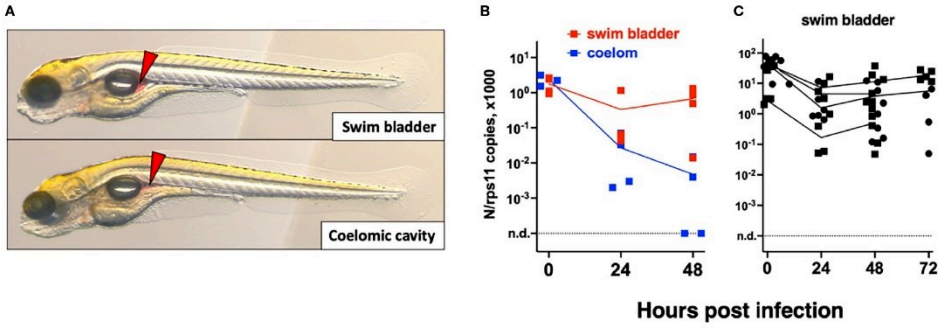

FIGURE 3 | Microinjection of SARS-CoV-2 to 4-dpf larvae. **(A)** Illustrations of injection in the posterior end of the swim bladder or in the coelomic cavity. **(B, C)** Quantification of polyadenylated N transcripts over time, assessed by qRT-PCR; each symbol is an individual larva. **(B)** Comparison of swim bladder (red) and coelom (blue) injection in a single experiment. **(C)** Four more swim bladder injection experiments. Lines connect the means of values measured at each time point. Circles and squares correspond to injection of viral suspensions 1 and 2, as labeled on **Table 1**.

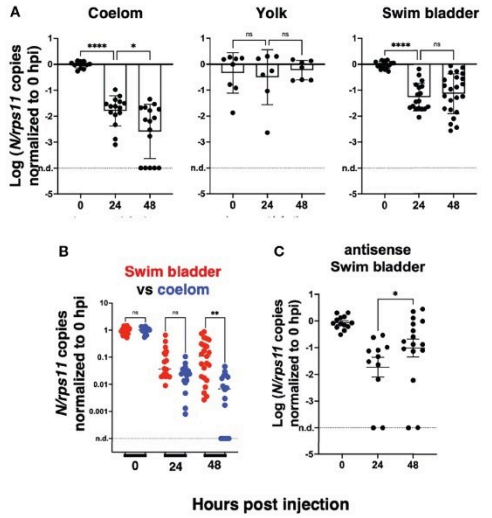

FIGURE 4 | Statistical analysis of viral transcript quantifications, after normalization to the means of values measured at 0 hpi for each experiment. **(A)** Comparison of SARS-CoV-2 RNA loads over time in each microinjection location; ANOVA analysis of log-transformed values, not assuming equal SDs (Brown–Forsythe test with Dunn's correction). Results pooled from four, two, and five experiments for coelom, yolk, and swim bladder injections, respectively. **(B)** Comparison of coelom and swim bladder injections at each time point; non-parametric multiple comparisons of non-transformed values (Kruskal–Wallis test with Dunn's correction). **(C)** Comparison of antisense transcripts in the swim bladder, log-transformed values, Mann–Whitney test, pooled from three experiments. ns, not significant; *p < 0.05; **p < 0.01; ****p < 0.0001.

while from 24 to 48 hpi, a non-significant re-increase of the means is observed (**Figure 4A**). Comparison between the coelom and the SB showed a significantly higher level of viral RNA in the latter at 48 (but not 24) hpi (**Figure 4B**). These results clearly establish that while continuous viral RNA degradation occurs in the coelomic cavity, different events take place in the SB, which can be interpreted in several ways. One possibility could be that after 24 h of rapid decay of viral RNAs in the SB, this degradative reaction stops. Alternatively, *de novo* production could be taking place as a consequence of successful or abortive infection, compensating for ongoing degradation but not at a sufficient level to result in a detectable increase. Since antisense RNA are the first viral RNA species produced during the viral cycle, we analyzed the pooled normalized qPCR measurements of the antisense viral transcripts and found a significant increase of these transcripts from 24 to 48 hpi (**Figure 4C**). This increase of antisense but stagnation of sense viral RNAs suggests that some cells of the SB were invaded by SARS-CoV-2 but that the viral replication cycle was incomplete, resulting in abortive infection.

To confirm infection by SARS-CoV-2 after SB injection, we used whole-mount immunohistochemistry (WIHC). We tested several commercial Abs against the SARS-CoV-2 nucleoprotein and selected a mouse Mab with minimal non-specific staining of naïve larvae, except for dots in the notochord that we routinely observe and which are due to the secondary antibody only (Levraud et al., 2009). As an anatomical reference, we also labeled glial fibrillary acidic protein (GFAP), to reveal glial cells and main nerves. In most virus-inoculated larvae at 2 dpi, a patchy signal for N could be clearly detected in the SBs which were partially collapsed due to the fixation and staining procedure (**Figures 5B–D**). 3D reconstruction (**Supplementary Video S1**) suggests that these signals correspond to a few infected cells in the bladder wall, generally located close to the rear pole. The signal was detected in 5/7 virus-injected larvae, and absent in 3/3 controls, but since this number was too low for statistical analysis, the experiment with repeated (without the GFAP stain) with a larger number of replicates (**Figure S3**) and at a higher resolution. A positive signal was detected in 11/14 samples, and only 1/14 among negative controls, with a highly significant statistical difference ($p = 0.0003$, Fisher's exact test), based on a blind assessment by a naïve observer. A 3D reconstruction of these samples confirmed localization of signal to the collapsed SB walls (**Supplementary Video S2**), and their relationship with nuclear staining, as visualized on confocal slices, was consistent with N protein in the cytoplasm of at least some cells (**Supplementary Video S3**). To ensure that the signal was detected inside cells of the SB wall, we counterstained these samples with the lipophilic stain DiI and reimaged them. When the anti-N-labeled structures were parallel to the imaging plane, numerous DiI-stained spheroids were observed to be scattered between the N-containing spots (**Figure 5E** and **Supplementary Video S4**). This is reminiscent of the formation of vesicular replication factories in SARS-CoV-2-infected cells (Eymieux et al., 2021), but because of the lower resolution in the Z-axis, overlying and underlying plasma membranes were ambiguous in these cases. However, by imaging bladder walls where they are perpendicular or strongly oblique to the imaging plane, it was possible to determine the relative positions of N-positive patches and plasma membranes. Some of these patches appeared to be affixed to the bladder wall without a membrane separating them from the lumen (**Figure 5F** and **Supplementary Video S4**); however, others were clearly surrounded by membranes (**Figures 5G–I** and **Supplementary Videos S4**, **S5**) and were therefore localized within the cytoplasm of swim bladder epithelial cells.

Variants of Concern Do Not Show Increased Infectivity in Wild-Type Larvae

We then tested a series of SARS-CoV-2 variants by SB inoculation. We obtained aliquotes from early passages after isolation of clinical strains, which had been titered at 3.10^7 PFU/ml or more and thus did not require further concentration. We tested the alpha variant (formerly known as UK variant, or B1.1.7), the beta variant (South African variant, B1.351), and the gamma variant (Brazilian variant, P1) as well as a representative of the G-clade which arose early during the pandemic. Non-diluted viral suspensions were injected as described above in the SB of 4-dpf larvae and were then monitored for 2 days; no clinical signs were observed. Viral replication was assessed by qRT-PCR. A global decline of polyadenylated N transcripts over time was observed with all variants (**Figure 6**).

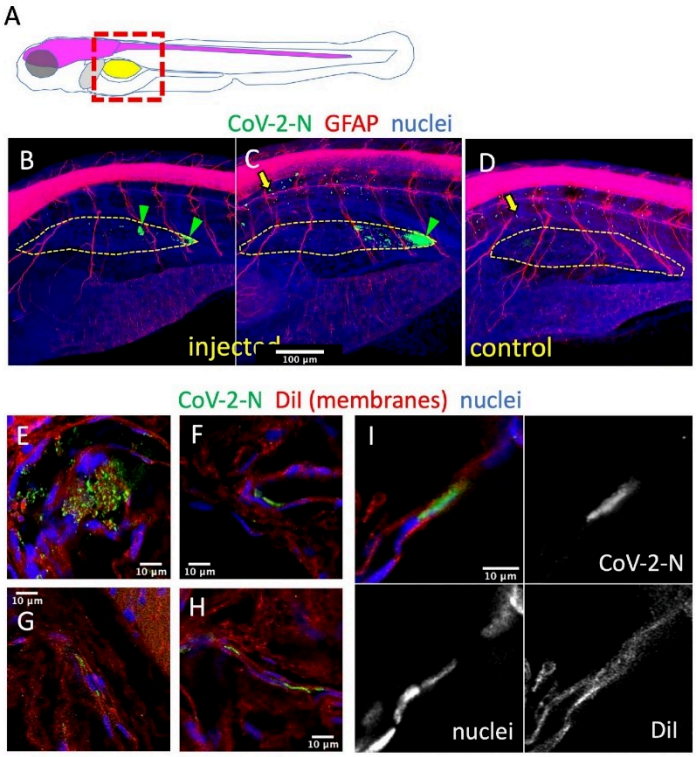

FIGURE 5 | Immunodetection of infected cells in the swim bladder. **(A)** Scheme of the imaged region: the swim bladder is shown in yellow, the brain and spinal cord in magenta, the liver in gray. **(B–F)** Confocal images of SARS-CoV-2-injected **(B, C, E–I)** or uninjected **(D)** larvae fixed at 2 dpi and subjected to whole-mount immunohistochemistry with an anti-CoV-2-N antibody (green), an anti-GFAP antibody (red in **B–D**) or membranes stained by DiI (red in **E–I**), and stained nuclei (blue). **(B–D)** Maximal projections. The approximate contours of the partially collapsed swim bladders are shown with a dotted yellow line. N-positive cells shown with green arrowheads. Yellow arrows point to non-specific punctate signal in the notochord. **(E–I)** Single confocal planes.

One unique larva injected with the gamma variant was found to contain slightly more N copies than the initial inoculum; therefore, the experiment was repeated for the gamma variant, and again, one larva did not show the same decline as others. Thus, results obtained with the gamma variant were comparable to those obtained with the initial strain, with a fraction of larvae in which some replication appeared to take place. No replication was found with the other strains, which also corresponded to lower inocula according to qPCR results. Overall, we saw no evidence for an increased infectivity of SARS-CoV-2 variants in zebrafish larvae.

A Defective Type I Interferon Response Does Not Increase SARS-CoV-2 Replication

Type I interferons (IFNs) are key antiviral cytokines in vertebrates, including teleost fish. We thus tested if SARS-CoV-2 may replicate in larvae with a crippled type I IFN response.

First, we used morpholino-mediated knockdown of the type I IFN receptor chains CRFB1 and CRFB2, known to make zebrafish larvae hypersusceptible to infection with CHIKV or SINV (Palha et al., 2013; Boucontet et al., 2018). After injection of SARS-CoV-2 in the coelom of 3-dpf larvae, decline of N transcripts was found to be similar in IFNR-knocked-down larvae than in controls (**Figure 7A**).

To ensure a long-lasting suppression of the IFN response, we used a newly generated mutant zebrafish line dubbed "triple ϕ," in which the three type I IFN genes *ifnphi1*, *ifnphi2*, and *ifnphi3*, tandemly located on chromosome 3, have been inactivated by CRISPR. Heterozygous triple ϕ mutants were viable and fertile; incrossing them yielded homozygous embryos at the expected Mendelian ratio of ~25%. Homozygous triple ϕ mutants could be raised up to juvenile stage, but, unlike their siblings, died in the 2 weeks following genotyping by fin clipping. To validate the phenotype of the mutants, we injected SINV-GFP to 3-dpf

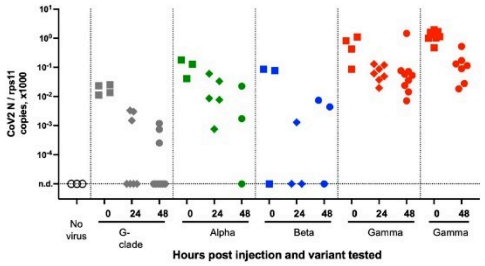

FIGURE 6 | Testing SARS-CoV-2 variants. qRT-PCR analysis of larvae at various times after injection of 2 nl of virus suspension in the swim bladder. Dotted lines separate independent experiments.

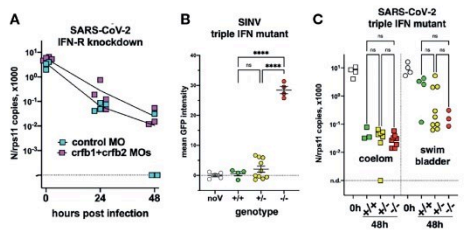

FIGURE 7 | Viral infection in IFN-defective larvae. **(A)** IFN-receptor (crfb1 and crfb2 genes) or control morphants infected at 3 dpf in the coelomic cavity; qRT-PCR. **(B, C)** Offspring from an incross of heterozygous triple IFN-mutants. **(B)** Larvae injected with SINV-GFP IV at 3 dpf, analyzed by fluorescence imaging at 48 hpi. **(C)** Larvae injected with SARS-CoV-2, either at 3 dpf in the coelom or at 4 dpf in the swim bladder; analyzed by qRT-PCR at 0 or 48 hpi. Statistical analysis by ordinary 1-way ANOVA in **(B)**, by Kruskal–Wallis test in **(C)**. ns, not significant; ****$p < 0.0001$.

larvae from a heterozygous incross. 48 h later, all larvae were alive although some showed strong signs of disease, including loss of reaction to touch, abnormal heartbeat, slow blood flow, edemas, and opacified yolk spots. All larvae were imaged with a fluorescence microscope to measure the extent of infection, then lysed individually and genotyped. The homozygous mutants displayed a considerably higher level of fluorescence (**Figure 7B**) and were also identified *a posteriori* as the sickest larvae, confirming that triple ϕ mutants are hypersusceptible to viral infection.

Larvae from triple ϕ heterozygous incrosses were thus injected with SARS-CoV-2, either in the coelomic cavity at 3 dpf or in the SB at 4 dpf. Larvae were lysed at 48 hpi, analyzed by qRT-PCR, and genotyped. Consistent with previous results, a 100-fold decrease of viral RNA was observed in coelom-injected larvae, while a weaker decrease was observed for SB injection, with a bimodal distribution suggesting that infection happened in about one-third of cases. In both situations, viral loads in homozygous triple ϕ mutants were not different from their wild-type siblings (**Figure 7C**). Thus, our results indicate that type I IFN responses are not responsible for the lack of replication of SARS-CoV-2 observed in wild-type zebrafish larvae.

Lack of Detectable Inflammatory Responses in SARS-CoV-2-Injected Larvae

We then tested if SARS-CoV-2 inoculation in the SB resulted in induction of a type I interferon response or inflammatory cytokines. For this, we performed qPCR on dT17-primed cDNAs from whole larvae. Based on our previous results (Levraud et al., 2019; Kraus et al., 2020), we tested the main type I interferon genes inducible in larvae, namely, *ifnphi1* and *ifnphi3*; the strongly IFN-inducible gene *MXA*; the classical inflammatory cytokines *il1b* and *tnfa*; cytokines that reflect induction of type 2 or type 3 responses, *il4* and *il17a/f3*, respectively; and chemokines *ccl19a.1* and *ccl20a.3*. Although individual experiments suggested significant induction of *ifnphi1* at 48 hpi or *il17a/f3* at 72 h, this could not be replicated; as shown on **Figure 8**, in which data from 4 independent experiments have been pooled, no significant change in expression of any of these genes can be observed compared to uninjected control larvae. Similar negative results were obtained with larvae injected at different sites (not shown).

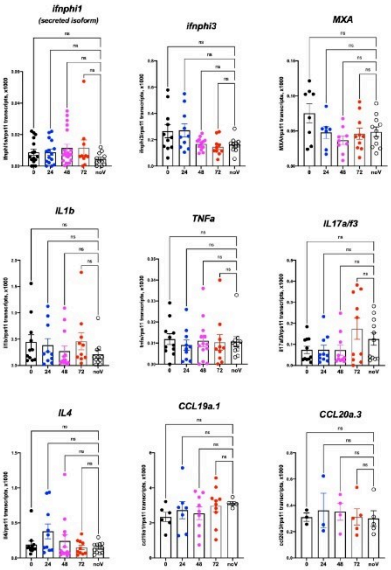

FIGURE 8 | Host response after SARS-CoV-2 injection in the swim bladder. qRT-PCR, pool of 4 independent experiments (except for ccl19a.1 and ccl20a.3, 3 and 2 experiments respectively). Numbers on the X-axis refer to hours postinjection; noV (for "no Virus"): pooled uninjected negative controls, age-matched to 24, 48, or 72 hpi. One-way ANOVA analysis. ns, not significant.

Although these results do not exclude a local response to SARS-CoV-2, they are in striking contrast with those we obtained previously in larvae infected with other pathogens such as SINV or *Shigella flexneri*, for which many of these genes were induced more than 100-fold (Boucontet et al., 2018). Since these experiments had been performed at 28°C, we verified that zebrafish larvae are also able to mount a strong type I response at 32°C (**Figure S4**).

Mosaic Overexpression of hACE2 Is Not Sufficient to Support SARS-CoV-2 Infection of 3-dpf Larvae or Fish Cells *In Vitro*

Finally, we tested if mosaic overexpression of human ACE2 in zebrafish larvae would increase their infectivity of SARS-CoV-2. We subcloned the *hace2* ORF in fusion with mCherryF under the control of the promoter of the ubiquitous ribosomal protein RPS26. In addition, the fragment is flanked by two inverted I-SceI meganuclease sites for higher transgenesis efficiency (Grabher et al., 2004). In order to be sure that the in-frame fusion of hACE2 with mCherry would not interfere with SARS-CoV-2 binding to its receptor and entry in the target cells, another construct was done by inserting a self-cleaving 2A peptide between hACE2 and mCherry ORFs. Both constructs were tested in BHK cells and increased by ~100-fold their infection by SARS-CoV-2 (**Figure 9A**). We optimized the injected dose of plasmid; 68 pg was the amount yielding the highest mCherry expression without increasing the proportion of misshapen embryos (**Figure 9B**). In 24-hpf embryos, many mCherry$^+$ cells, randomly distributed, were visible in these embryos under the fluorescence microscope. In swimming larvae, mCherry$^+$ cells were still clearly visible but in lower amounts (**Figure 9C**). To get a quantitative assessment of their frequency, we dissociated 4-dpf larvae and analyzed the suspension by flow cytometry, which indicated that ~0.5% of the cells were mCherry$^+$ (**Figure 9D**). Larvae were fixed and processed by immunohistochemistry, which confirmed ACE2 expression at the membrane of mCherry$^+$ cells (**Figure 9E**).

Zebrafish AB eggs were injected with the plasmid, and at 3 dpf, the 25% larvae displaying the highest mCherry expression and good morphology were selected. They were then microinjected

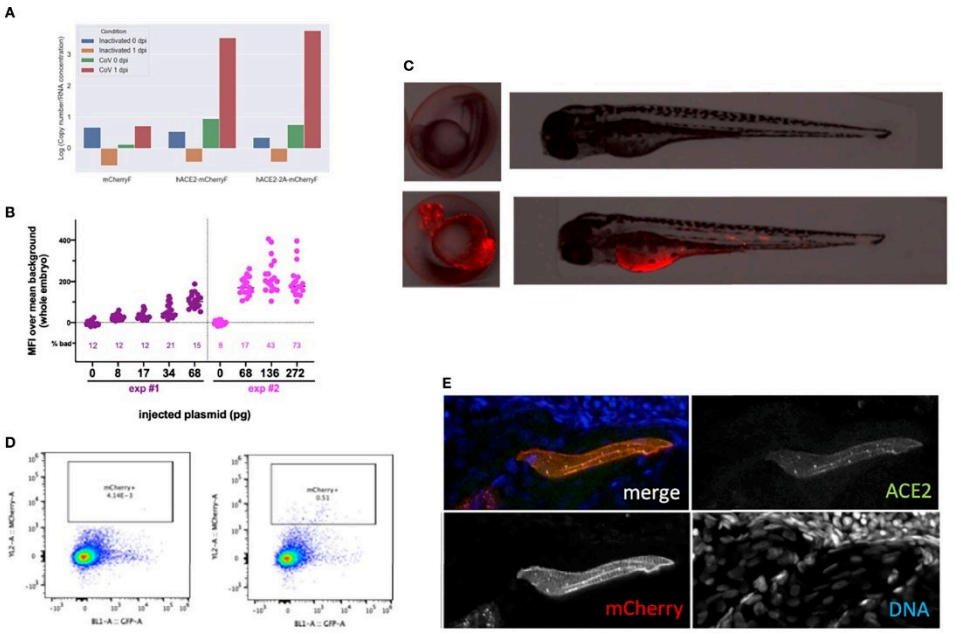

FIGURE 9 | Overexpression of hACE2-mCherry by plasmid injection at the 1-cell stage. **(A)** Verification of construct functionality by transfection in BHK cells. N mRNA levels measured 24 h after exposure of transfected cells with inactivated or with active SARS-CoV-2. **(B)** Optimization of the plasmid dose. Fluorescence intensity measured in 24-hpf embryos after injection at the 1-cell stage of the specified amount of the pz26hACE2-mCherryF plasmid together I-SceI, for the 25% embryos with the best expression in each group. The percentage of misshapen embryos in each group is indicated on the bottom of the graph. **(C)** representative image of a 24-hpf embryo (left) and a 3-dpf larva (right) after mock injection (top) or injection of 68 pg of pz26hACE2-mCherryF. **(D)** Representative flow cytometry analysis of cells dissociated from 4-dpf larvae, mock-injected (left) or injected with 68 pg of pz26hACE2-mCherryF (right). **(E)** Immunohistochemistry of a larva injected with 68 pg of pz26hACE2-2A-mCherryF, showing ACE2 detection of a mCherry-positive muscle fiber.

with SARS-CoV-2 in the coelom or the brain ventricle and processed as above. qRT-PCR analysis revealed that viral mRNA transcripts decreased just as it did in AB larvae (**Figure 10**). Thus, this approach did not increase the infectivity of SARS-CoV-2 in zebrafish larvae.

We finally tested if hACE2 overexpression by *in vitro* cultured fish cells made them susceptible to SARS-CoV-2, using the cyprinid cell line EPC. EPC cells were co-transfected with GFP and hACE2 expression plasmids; transfection efficiency and membrane hACE2 expression was verified by IHC (**Figures 11A, B**). These transfected cells were incubated with active or heat-killed SARS-CoV-2 at a MOI of 0.1 and then tested for viral replication by qRT-PCR on cell lysates. No difference was observed between GFP-only and GFP+hACE2-expressing cells (**Figure 11C**); furthermore, the amount of N transcripts fell dramatically from day 0 to day 2 (**Figure 11D**), showing that hACE2-expressing EPC cells were not able to support SARS-CoV-2 replication.

DISCUSSION

We report here our in-depth attempt to infect zebrafish larvae with SARS-CoV-2. Only larvae were tested because they present multiple practical advantages over adult fish: they can be rapidly generated in large quantities, can be incubated in multi-well plates, are highly amenable to imaging, and are subject to fewer ethical regulations; therefore, they would be most suitable to drug screening. Whether juvenile or adult zebrafish would be more susceptible to SARS-CoV-2 remains to be tested.

We used absolute qRT-PCR of viral transcripts to test for viral replication. Surprisingly high numbers were measured shortly after injection, as the concentrated viral suspensions we used contained a considerable amount of noninfectious viral molecules, including negative-strand species. In all likelihood, these molecules were released by infected Vero-E6 cells during the production of the virus stock, possibly by living cells as defective viral particles or in vesicles such as exosomes, or as free or membrane-bound RNA from dying cells. Whatever their origin, they complicate the detection of active viral replication, which has to generate enough molecules to exceed this background.

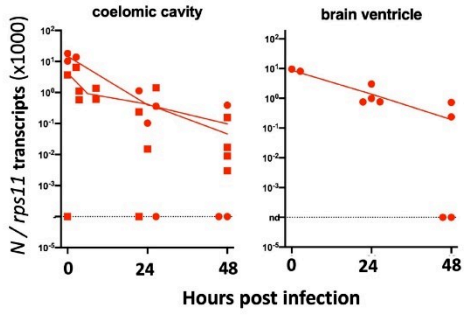

FIGURE 10 | Injection of 3-dpf hACE2-mCherry mosaic larvae. Quantification of sense N transcripts in individual hACE2-mCherry mosaic larvae injected in coelomic cavity (left; one experiment with hACE2-mCherry, one with hACE2-2A-mCherry) or brain ventricle (right; with hACE2-2A-mCherry) by qRT-PCR.

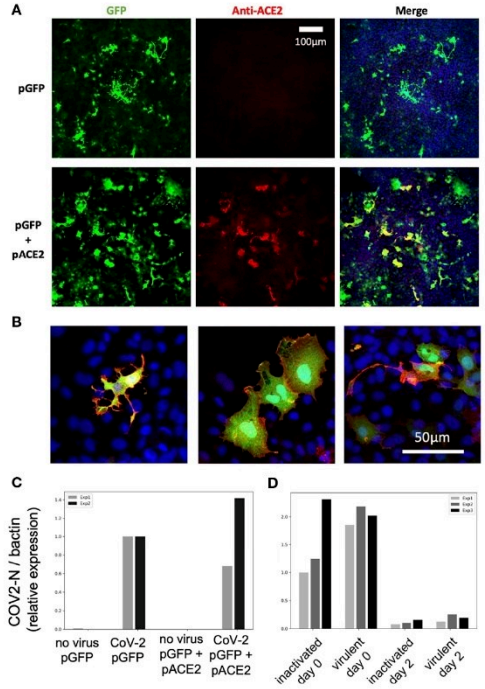

FIGURE 11 | SARS-CoV-2 does not replicate on EPC cells transfected with human ACE2. **(A, B)** Confocal microscopic images of EPC cells cultures 3 days after transfection. **(A)** Assessment of transfection efficiency at low magnification. **(B)** Demonstration of hACE2 expression at the membrane of cells transfected with both plasmids, high magnification, merge images of GFP, hACE2, and nuclei labels. **(C, D)** qRT-PCR measurement of N copies in cells. **(C)** Measurement at 2 days postexposure with virulent SARS-CoV-2, comparison of GFP and GFP+hACE2 overexpression. **(D)** Decline of RNA levels from day 0 to day 2 postexposure, and comparison of heat-inactivated and virulent virus.

In almost all of our tests, a rapid (10- to 100-fold) decrease of mRNA copies was observed during the first day, likely due to degradation of noninfectious RNA species. After a few hours of bath exposure, viral RNA was detected in doubly rinsed larvae; this did not require active fusion or viral particles as RNA was also detected after exposure to heat-inactivated virus and may have resulted from sticking of particles to skin surfaces or entry in the pharyngeal cavity. Two days after the starting of exposure, viral RNA was undetectable and thus the virus failed to achieve infection by bath, consistent with the results of Kraus et al. (2020).

Microinjection is the most common way to infect zebrafish larvae with viruses (Levraud et al., 2014). After microinjection of a few nanoliters in larvae, the inoculum was readily measurable; however, when injected in the coelom, the pericardium, the bloodstream, or the brain ventricle, viral RNA copy numbers then steadily declined, indicating unsuccessful infection. Two injection sites yielded different results: the yolk and the swim bladder. In the yolk, no RNA decrease was observed, suggesting that viral RNA molecules—perhaps owing to their coating with nucleoprotein and/or their localization in vesicles—were spared from degradation. Importantly, the yolk was unique among all tested sites as the one where injection is performed inside the cytosol of a cell (the yolk syncytial cell, not to be confused with the yolk sac) and not in the extracellular milieu. This does not necessarily prevent infection, as other viruses, such as CHIKV (Briolat et al., 2014) or human noroviruses (Van Dycke et al., 2019), have been shown to infect larvae after yolk injection. No signs of yolk infection (such as opacity observed with CHIKV and SINV) were observed, and no increase of viral mRNA was observed, so we believe that yolk injection did not result in active SARS-CoV-2 replication.

By contrast, injections in the SB resulted in a ~20-fold decrease of mRNA copies during the first day, followed by a stabilization of sense viral RNA levels and a modest re-increase of antisense RNAs; this was accompanied by progressive dispersion of data points. This suggests that abortive infection occurred in some but not all larvae after SB infection. Because of the considerable spread in measured copy numbers at 2 dpi, the re-increase is statistically borderline, but the bimodal distribution observed in the independent type I IFN mutant assay, and the comparisons with injections in the coelom support this interpretation. Importantly, this was reinforced by an independent immunohistochemistry assay as we observed, in a fraction of injected larvae, a few cells in the SB wall labeled by an antibody that detects the SARS-CoV-2 nucleoprotein. By staining membranes, we confirmed the presence of this protein in the cytosol of cells in the bladder wall. Nucleoprotein-rich patches were also interspersed with numerous vesicular structures suggesting formation of replication factories. Thus, we believe that a few cells of the bladder wall were successfully invaded by SARS-CoV-2, although there is no evidence that this resulted in the production of new infectious virions. It also remains unclear why infections succeed in only a fraction of SB-injected larvae. This could be due to a very low effective inoculum, but this seems unlikely since the success rate was not obviously higher with viral suspension 1 than suspension 2, despite a 7-fold higher titer.

Unfortunately, given the small re-increases of N copy number observed, it can be predicted that even if successful virus replication had occurred, the amount of infectious particles remained too small to be detectable by direct titrations from infected whole larvae. This is a clear limitation of our study that we hope can be solved when conditions allowing stronger replication are identified.

The stabilization of the amount of sense viral RNA in the SB could also be interpreted as persistence rather than *de novo* production. In fact, these two possibilities are non-exclusive; however, the fact the during the first 24 h, the number of viral mRNA strongly decreases, indicates that the SB environment is not hospitable and it is unlikely that degradative mechanisms become less active as the fish age, which is usually accompanied by stronger immune reactions. Could internalization of virions by cells of the SB protect them from this activity? If the SB epithelium was scavenging the luminal content, then a regular distribution of N across the SB would be expected; instead, the patchiness observed in IHC experiments is consistent with the infection of very few cells followed by *de novo* production of N by these cells.

What could be the mechanisms mediating virus clearing from the SB? This has not been studied in the context of viral infection, but in a model of filamentous candidiasis, the recruitment of neutrophils to the SB lumen and the subsequent extracellular trap production (Gratacap et al., 2017) and of inflammatory macrophages (Archambault et al., 2019) have been observed. A strong expression of a defensin gene specifically in the SB has also been reported (Oehlers et al., 2011). It seems also plausible that microbes trapped in mucus may be cleared from the SB *via* the pneumatic duct, although such a mechanism has not been described to our knowledge.

It is interesting that the organ found to be most permissive to infection in zebrafish larvae is homologous to the human lung which is the primary target of the virus. We do not know if SB epithelial cells express *ace2*. Unfortunately, there is no "swim bladder epithelium" subset in the scRNAseq zebrafish developmental atlas (Farnsworth et al., 2020), perhaps because these cells are too rare or difficult to isolate enzymatically. However, the SB derives from the gut, which is the only organ in which cells highly express *ace2* in the atlas (Postlethwait et al., 2020). One may speculate that, besides surface protein expression, biophysical parameters such as surfactant coating or pressure-mediated tension of the epithelium could contribute to infectivity.

Given the expression of *ace2* in zebrafish enterocytes, it would also have been interesting to microinject the virus in the gut lumen. We tried, unsuccessfully, in part because of the close apposition of the gut and the easily damaged yolk. It should be noted, however, that coelomic injections (the equivalent of intraperitoneal injections), comparatively easy to perform, deliver the virus in close proximity to the basal side of enterocytes but do not yield successful infection.

Not surprisingly, the SARS-CoV-2 virus has evolved during the pandemic with successful waves of variants of concern with mutated spike protein, predicted to modulate binding to hACE2 and antibody neutralization. In the normally non-permissive wild-type mouse model, it has been shown that the beta and gamma variants replicated to a significant extent (Montagutelli et al., 2021). We tested several variants, including those two, in the zebrafish swim bladder model but did not find increased infectivity compared to the reference strain.

To stay within the thermal range of both virus and host, we incubated SARS-CoV-2-injected larvae at 32°C. Because SARS-CoV-2 replicates better at 33°C than at 37°C in

mammalian cells (V'kovski et al., 2020) (and our own observations), this is unlikely to be the reason for the poor replication of the virus in larvae. We also verified that at this temperature, larvae are able to mount a type I IFN response against another virus, eliminating temperature stress as the explanation for the lack of inflammatory response of zebrafish larvae to SARS-CoV-2. This is more likely due to the small number of infected cells in our conditions and possibly also active inhibition of some innate immune pathways by the virus. Protocols resulting in stronger infection will be needed for studying SARS-CoV-2-induced inflammation in zebrafish larvae. This absence of measurable type I IFN response is consistent with the finding that IFN or IFN-R deficiency did not rescue virus infectivity. Thus, a limited compatibility between the virus and the host, rather than an intrinsic active resistance, seems the most likely explanation for our largely negative results.

The mosaic overexpression of hACE2 did not result in infectivity of 3-dpf larvae by SARS-CoV-2. We do not know if this was due to the relatively small number of cells expressing the transgene (<1%), to low expression or misfolding of the hACE2 protein, and/or to other causes. As an alternative strategy, we also tested injection of synthetic mRNA encoding hACE2-mCherryF; this resulted in clear ubiquitous mCherry expression at 24 hpf, but it became undetectable by 2 dpf (not shown). This suggests that the hACE2 protein and mRNA have a relatively short half-life in the zebrafish larval context. This issue may be solved by the establishment of stable transgenic zebrafish lines expressing hACE2. However, we also tested the effect of overexpression of hACE2 in the more stable context using the EPC cell line. EPCs are derived from a cyprinid fish and used routinely to test the pro- or antiviral activity of zebrafish genes by overexpression [e.g., (Langevin et al., 2013)]. However, the expression of hACE2 was not sufficient to allow replication of SARS-CoV-2 on these cells. The lack of replication may be due to the need for co-expression of the transmembrane serine protease TMPRSS2, which has been shown to greatly increase SARS-CoV-2 infectivity (Hoffmann et al., 2020). We also attempted to overexpress human TMPRSS2 in zebrafish embryos, by either plasmid or mRNA injection; unfortunately, this was found to be highly toxic, as it resulted in severe developmental anomalies that precluded injections.

Thus, it seems that fish cells are intrinsically unable to support full SARS-CoV-2 replication, which could be due to the lack of a required host cell component that the virus must interact with, or to intrinsic immunity linked to the expression of a restriction factor, or both. Given the dissimilarities between human and zebrafish ACE2 in the Spike-interaction region (Kraus et al., 2020), a good receptor is probably missing, but we have shown that hACE2 overexpression is not sufficient. One interesting clue to a possible restriction mechanism may lie with the aspect of cells containing nucleoprotein observed in the SB by IHC, which contain numerous lipidic vesicles reminiscent of replication factories, albeit larger and less regular than those observed in Vero cells (Eymieux et al., 2021). This suggests an improper interaction of viral and host cell components required to properly establish these double-membrane structures.

In conclusion, our experiments indicate that the zebrafish larva is largely not infectable by SARS-CoV-2, except when the virus is injected in the swim bladder, which appears to result in abortive infection in a subset of the animals. Further optimization of infection procedures, starting with the generation of transgenic zebrafish expression stably expressing human ACE2, and identification of mechanisms that prevent SARS-CoV-2 replication in fish cells, will be needed to unleash the full potential of the zebrafish larva in the fight against COVID-19.

METHODS

Ethical Statement

Animal experiments described in the present study were conducted according to European Union guidelines for handling of laboratory animals (http://ec.europa.eu/environment/chemicals/lab_animals/home_en.htm) and were approved by the Ethics Committee of Institut Pasteur.

Fish

Wild-type zebrafish (AB strain), initially obtained from ZIRC (Eugene, OR, USA), were raised in the aquatic facility of Institut Pasteur. After natural spawning, eggs were collected, treated for 5 min with 0.03% bleach, rinsed twice, and incubated at 28°C in Petri dishes in Volvic mineral water supplemented with 0.3 µg/ml methylene blue (Sigma-Aldrich, St. Louis, Missouri, USA). After 24 h, the water was supplemented with 200 µM phenylthiourea (PTU, Sigma-Aldrich) to prevent pigmentation of larvae. After this step, incubation was conducted at 24°C, 28°C, or 32°C depending on the desired developmental speed. Developmental stages given in the text correspond to the 28.5°C reference (Kimmel et al., 1995). Sex of larvae is not yet determined at the time of experiments.

Triple type I interferon CRISPR mutants have been generated by the AMAGEN transgenesis platform (Gif-sur-Yvette, France) by co-injection of CAS9 with two sgRNA targeting *ifnphi1* (target sequence, GCTCTGCGTCTACTTGCGAAtgg) and *ifnphi2* (target sequence, ATGTGCGCGAAAAAGAGTGCtgg) in one-cell eggs from homozygous ifnphi3$^{ip7/ip7}$-null mutants of the AB background (Maarifi et al., 2019). After growth to adulthood, a founder was identified that co-transmitted mutations in *ifnphi1* and *ifnphi2* in addition to the *ip7* mutation of *ifnphi3*. The *ip9* allele mutation in *ifnphi1* consists in a 7-base pair deletion in the first exon of the secreted isoform (GAATGGC, 75 bases downstream of the start ATG). The *ip10* allele in *ifnphi2* consists in a 19-bp deletion in the first exon (TGCGTTCTTATGTCCAGCA, 20 bases downstream of the start ATG). This founder was crossed with AB fish, and F1 fish triply heterozygous for mutations *ip7*, *ip9*, and *ip10* were selected to establish the "triple φ" mutant line. As expected, since *ifnphi1*, *ifnphi2*, and *ifnphi3* are closely located in tandem on a 35-kb region of zebrafish chromosome 3, the *ip7, ip9*, and *ip10* mutations were always found to co-segregate. Genotyping PCR primers are listed in **Table 2**.

Viruses

The main SARS-CoV-2 stock used (BetaCoV/France/IDF0372/2020 strain) was propagated twice in Vero-E6 cells and is a kind gift from the National Reference Centre for Respiratory Viruses at Institut Pasteur, Paris, headed by Dr Sylvie van der Werf; this strain was isolated from a human sample provided by Drs. Xavier Lescure and Yazdan Yazdanpanah from the Bichat Hospital, Paris. To generate concentrated virus, Vero-E6 cells were infected with virus at an MOI of 0.01 PFU/cell in DMEM/2% FBS and incubated for 72 h at 37°C, 5% CO_2. At this point, the cell culture supernatant was harvested, clarified, and concentrated using Amicon Ultra-15 Centrifugal units 30K (Merck Millipore, Burlington, MA, USA). Virus titers were quantified by plaque assay in Vero-E6.

The variant strains used were also supplied by the National Reference Centre for Respiratory Viruses at Institut Pasteur and were used directly without further propagation. The G-clade (BetaCoV/France/GE1973/2020; 3×10^7 PFU/ml), alpha (hCoV-19/France/IDF-IPP11324i/2020; 6.75×10^7 PFU/ml), beta (hCoV-19/France/PDL-IPP01065i/2021; 1.75×10^8 PFU/ml), and gamma (hCoV-19/French Guiana/IPP03772i/2021; 5.53×10^7 PFU/ml) variants were isolated from human samples provided respectively by Dr. Laurent Andreoletti, from Robert Debré Hospital, Reims, France; Dr. Foissaud, HIA Percy, France; Dr. Besson J. from Bioliance Laboratory, France; and Dr. Rousset, Institut Pasteur, Cayenne, French Guiana.

The SINV-GFP virus corresponds to the SINV-eGFP/2A strain described in Boucontet et al. (2018) and was used as a BHK cell supernatant at 2×10^7 PFU/ml. The eGFP sequence is inserted with self-cleaving sequences between the capsid and envelope genes of SINV.

Bath Exposure

Bath exposures were conducted in a 12-well plate with 4 larvae per well in 2 ml of water plus PTU. 2-dpf embryos were manually dechorionated previously. 10 µl of SARS-CoV-2 suspension 2 (either freshly thawed or heat-inactivated for 5 min at 70°C) was added to each well and gently mixed, then the plates were incubated at 32°C. After a given incubation time, larvae were deeply anesthetized with 0.4 mg/ml tricaine (MS222, Sigma-Aldrich), rinsed twice in 10 ml of water, transferred individually into tubes, and after removal of almost all water, lysed in 320 µl of RLT buffer (Qiagen, Hilden, Germany) supplemented with 1% β-mercaptoethanol (Sigma-Aldrich).

Microinjection

SARS-CoV-2 microinjections are carried out under a microbiological safety hood inside a BSL3 laboratory, in which a camera-fitted macroscope (DMS1000, Leica, Wetzlar, Germany) with a transilluminated base is installed, as in (Van Dycke et al., 2019). Borosilicate glass capillaries are loaded with a concentrated SARS-CoV-2 suspension previously colored by the addition of 10% (V/V) of 0.5% phenol red in PBS (Sigma), then connected to a FemtoJet 4i microinjector (Eppendorf, Framingham, MA, USA). Otherwise, the procedure was similar to the one detailed in Levraud et al. (2008). After breakage of the capillary tip, pressure was adjusted to obtain droplets with a diameter of ~0.13 mm. Larvae at the desired developmental stage were anesthetized with 0.2 mg/ml tricaine and positioned and oriented in the groove molded in agarose of an injection plate overlaid with water containing tricaine. Using a micromanipulator, the capillary was then inserted at the desired site and two pulses performed to inject approximately 2 nl. Proper injection is ascertained visually with the help of phenol red staining; otherwise, the larva is discarded. A picture of the injected larva is taken with the camera, and it is then rinsed by transfer inside a water-filled Petri dish and immediately transferred to its individual well in a 24-well plate, containing 1 ml of water with PTU. Larvae are then incubated at 32°C (actual temperatures measured inside the incubator ranged from 31.6°C to 33.2°C). At daily intervals, all larvae were anesthetized by addition of a drop of 4 mg/ml tricaine into each well and a snapshot was taken. A randomized subset of larvae was then transferred to tubes and individually lysed in 320 µl of RLT buffer + 1% β-mercaptoethanol. Water with tricaine was then removed from the remaining wells, replaced with 1 ml of freshwater with PTU, and the plate returned to the incubator.

SINV injections were performed in a BSL2 laboratory as described in Passoni et al. (2017).

Lysis, RNA Extraction, and RT-qPCR of Larvae

After addition of RLT buffer, larvae were dissociated by 5 up-and-down-pipetting movements. Tubes may then be frozen at -80°C for a few days. Before export from the BSL3 laboratory, RLT lysates were incubated at 70°C for 5 min to ensure complete virus inactivation (preliminary tests confirmed that this had a negligible impact on qRT-PCR results). Total RNA was then extracted with an RNeasy Mini Kit (Qiagen) without the DNase treatment step and a final elution with 30 µl of water.

RT was performed on 6 µl of eluted RNA using MMLV reverse transcriptase (Invitrogen, Carlsbad, CA, USA) with either a dT_{17} primer (for polyadenylated transcripts) or the SgleadSARSCoV2-F primer (for negative-strand viral transcripts) (Wölfel et al., 2020) (**Table 2**). cDNA was diluted with water to a final volume of 100 µl, of which 5 µl was used as a template for each qPCR assay.

Real-time qPCR was performed with an ABI7300 (Applied Biosystems, Foster City, CA, USA). Quantitation of sense or antisense viral *N* transcripts was performed by a TaqMan probe assay, using the primer–probe mix from the 2019-nCoV RUO kit (IDT, Coralville, IA, USA) with the iTaq Universal Probes One-Step kit (Bio-Rad, Hercules, CA, USA). The 2019-nCoV_N_Positive Control plasmid (IDT) was used as a standard for absolute quantification. Quantification of zebrafish transcripts was performed using a SYBR assay using the Takyon SYBR Blue MasterMix (Eurogentec, Seraing, Belgium) with primer pairs listed in **Table 2**. These primers typically span exon boundaries to avoid amplification of contaminating genomic DNA. For absolute quantification of the housekeeping gene *rps11*, a standard was produced by PCR using primers to amplify a fragment including the whole open-

TABLE 2 | Primers used in this study.

Genotyping primers		**5′–>3′ sequences**	
Gene (allele)	**ZFIN ID**	**Forward primer**	**Reverse primer**
ifnphi1 (wt)	ZDB-GENE-030721-3	CTCTGCGTCTACTTGCGAAT	CTCCAACCCAACAAGTCGC
ifnphi1 (ip9)		AGCTCTGCGTCTACTTGCTT	CTCCAACCCAACAAGTCGC
ifnphi2 (wt)	ZDB-GENE-071128-1	TCTTGGGGATTCATGTCTTCA	GCGAAAAAGAGTGCTGGACA
ifnphi2 (ip10)		TCTTGGGGATTCATGTCTTCA	GTGCGCGAAAAAGAGACGAA
ifnphi3 (wt)	ZDB-GENE-071128-2	AGAATGGACCTTCACCGTGT	CGCAGTCTCCAGAAGTGTAT
ifnphi3 (ip7)		ATTCCGTATAGGCATCTGATT	CGCAGTCTCCAGAAGTGTAT
RT primers			
(dT)17		TTTTTTTTTTTTTTTT	
sgLeadSARSCoV2-F		CGATCTCTTGTAGATCTGTTCTC	
qPCR primers			
rps11	ZDB-GENE-040426-2701	CGTGAAAGACTGTCTTCCGT	TCAACAACACAGAGGAGCCA
ifnphi1	ZDB-GENE-030721-3	TGAGAACTCAAATGTGGACCT	GTCCTCCACCTTTGACTTGT
ifnphi3	ZDB-GENE-071128-2	GAGGATCAGGTTACTGGTGT	GTTCATGATGCATGTGCTGTA
mxa	ZDB-GENE-030721-5	GACCGTCTCTGATGTGGTTA	GCATGCTTTAGACTCTGGCT
tnfa	ZDB-GENE-050317-1	TTCACGCTCCATAAGACCCA	CAGAGTTGTATCCACCTGTTA
il1b	ZDB-GENE-040702-2	GAGACAGACGGTGCTGTTTA	GTAAGACGGCACTGAATCCA
il4	ZDB-GENE-100204-1	GACAGGACACTACTCTAAGAA	CAGTTTCCAGTCCCGGTATA
il17a/f3	ZDB-GENE-041001-192	TCAAAGAAAGACAGCTTGGGT	AACAGAAGTTGTGTATGTCCAA
ccl19a.1	ZDB-GENE-060526-181	CCCACGTGATGCTGTAATATT	AGCGTCTCTCGATGAACCTT
ccl20a.3	ZDB-GENE-081022-193	AGCTGTGTCGTGTTGCAGAA	CCGTTTGTGTGGAATATGACA
b-actin (EPC cells)	*Pimephales promelas* gene	GATGACGCAGATCATGTTCGAG	CCGCAAGATTCCATACCAAGGAAGG
Construction primers			
rps11 standard	ZDB-GENE-040426-2701	CCCAGAGAAGCTATTGATGGC	TCACATCCCTGAAGCATGGG
hACE2NotStart3		TATAGCGGCCGCGGGGACGATGTCAAGCTCTTCCT	
ACE2EndNot3		TATAGCGGCCGCAAAAGGAGGTCTGAACATCA	
hAce2.2ANot		AATTGCGGCCGCAGGGCCCAGGGTTGGACTCGACGTCTCCCGCAAGCTTAAGAAGGTCAAAATTCAACAGCTGAGATCTAAAGGAGGTCTGAACATCAT	

reading frame, which was gel-purified and quantified by spectrophotometry. Ratios of other transcripts to *rps11* were estimated by the $2^{\Delta Ct}$ method.

Morpholino and Plasmid Injection in Eggs

Morpholino antisense oligonucleotides (Gene Tools, Philomath, OR, USA) were injected (1 nl volume) in the cell or yolk of AB embryos at the one- to two-cell stage as described (Levraud et al., 2008). crfb1 splice morpholino (2 ng, CGCCAAGATC ATACCTGTAAAGTAA) was injected together with crfb2 splice morpholino (2 ng, CTATGAA TCCTCACCTAGGGTAAAC), knocking down all type I IFN receptors (Aggad et al., 2009). Control morphants were injected with 4 ng control morpholino, with no known target (GAAAGCATGGCATCTGGAT CATCGA).

Expression plasmids, produced using an endotoxin-free kit (Macherey-Nagel, Düren, Germany), were co-injected with the I-SceI meganuclease (Grabher et al., 2004). Briefly, 12.5 µl of plasmid is mixed with 1.5 µl of CutSmart Buffer and 1 µl of I-SceI (New England Biolabs, Ipswich, MA, USA) and incubated at room temperature for 5 min before being put on ice until injection of 1 nl inside the cell of AB embryos at the one-cell stage.

Live Fluorescence Imaging

SINV-GFP-infected or hACE2-mCherry-expressing larvae were imaged with an EVOS FL Auto microscope (Thermo Fisher Scientific, Waltham, MA, USA) using a 2× planachromatic objective (numerical aperture, 0.06), allowing capture of the entire larva in a field. Transmitted light and fluorescence (GFP or Texas Red cube) images were taken. They were further processed (superposition of channels, rotation, crop, and fluorescence intensity measure) using Fiji. Mean background fluorescence of uninjected control animals was subtracted from the measured signal to obtain the specific fluorescence.

Flow Cytometry

Pools of 10 larvae were dissociated by a combination of mechanical trituration (repeated pipetting) and enzymatic treatment at 30°C, first with 200 µl of 0.25% Trypsin-EDTA (Gibco, Grand Island, NY, USA) for 10 min, and 10 more min after addition of 10% sheep serum, $CaCl_2$ to 2 µM, and 1 µl of 5 mM collagenase (C9891, Sigma). Cell suspensions were then washed with PBS 1×, pelleted, resuspended in PBS, and filtered on a 40-µm mesh. Dead cells were labeled with SYTOX AADvanced (Thermo Fisher). Cell suspensions were acquired on an Attune NxT flow cytometer (Thermo Fisher) with blue and yellow lasers, and data analyzed with FlowJo (Ashland, OR, USA).

Cell Culture

The *Epithelioma papulosum cyprini* cell line (EPC) was maintained in Leibovitz's 15 media (L-15, Gibco) supplemented with 10% fetal bovine serum (FBS, Gibco), 100 µg/l penicillin, and 100 µg/ml streptomycin. EPC cells were cultured at 32 °C without CO_2.

BHK-21 cells were maintained in DMEM (Gibco) supplemented with 5% FBS and 2 mM L-glutamine and maintained at 37°C with 5% CO_2.

Human ACE2-Expressing Constructs

The hACE2 ORF was amplified from clone IOH80645 (Thermo Fisher, GenBank NM_021804.2) using primers hACE2NotStart3 and hACE2EndNot3 (**Table 2**). The amplified PCR fragment was digested by NotI and inserted in the NotI site of the Tol2S263C:mC-F vector between the promoter of the zebrafish ubiquitous ribosomal protein RPS26 encoded by chromosome 3, and the mCherry ORF. In this construct, the RPS26 promoter drives the expression of a hACE2 protein fused at its C-term with farnesylated mCherry. In order for the ORF to drive the expression of two separated proteins (hACE2 and mCherry-F), primers hACE2NotStart3 and hAce2.2ANot were used to amplify the hACE2 ORF from the IOH80645 clone. The amplified fragment was digested by NotI and cloned in the NotI site of Tol2S263C:mC-F between the promoter of the zebrafish ubiquitous ribosomal protein RPS26 encoded by chromosome 3, and the mCherry ORF. Maps and sequences of plasmids are available at https://doi.org/10.5281/zenodo.4672028.

For *in vitro* transfection of EPC cells, plasmid pcDNA3.1-hACE2 (Addgene, Watertown, MA, USA, #1786) was directly used along plasmid pmEGFP-N1 (Chen and Reich, 2010).

Cell Transfection

EPC cells were electroporated with the Neon transfection system (Invitrogen). Briefly, EPC cells were trypsinized and resuspended in L15 media supplemented with FBS and antibiotics. Cells were counted and centrifuged at 2,000 rpm for 5 min. 0.8×10^6 cells per condition were resuspended in 80 µl of L15 without phenol red with 2.4 µg of each plasmid. Cells were electroporated using 10-µl neon tips with 1 pulse of 1,700 V during 20 ms. Electroporated cells were plated in a 6-well plate in L15 + FBS + antibiotics and incubated 3 days at 32°C before experiment.

BHK21 were transfected with Lipofectamine 2000 (Invitrogen). Briefly, cells at 80% confluence in 12-well plates were incubated with 750 ng of plasmid and 1 µl of Lipofectamine in Opti-MEM (Gibco). Transfection efficiency was checked at 1 day post-transfection.

Cell Infection and RT-qPCR

Transfected EPC cells were transferred to BSL3 laboratory for infection with SARS-CoV-2. Cells were rinsed with L15 media + FBS + antibiotics and incubated 5 min at 32°C. Cells were infected at MOI 0.1 with virus diluted in L15 media + FBS + antibiotics and incubated at 32°C during 1 h with agitation. After incubation, L15 media + 10% FBS + antibiotics was added and cells were incubated 2 days at 32°C or processed directly for RNA extraction.

Transfected BHK21 cells were transferred to BSL3 laboratory for infection with SARS-CoV-2. Cells were rinsed with DMEM + 5% FBS and incubated for 5 min at 37°C + 5% CO_2. Cells were infected with virus at MOI 0.1 diluted in DMEM + 5% FBS and incubated at

37°C + 5% CO_2 during 1 h with agitation. After incubation, DMEM + 5% FBS was added and cells were incubated 2 days at 32°C or processed directly for RNA extraction.

Before RNA extraction, culture medium was removed and cells were rinsed once with PBS. Extraction of total RNA was performed using TRI Reagent (Sigma) following the manufacturer's recommendations. Total RNA was resuspended in 100 µl of RNase-free water.

Reverse transcription was performed on 5 µl of RNA suspension using the QuantiTect Reverse Transcription Kit (Qiagen) with either the Qiagen RT Primer Mix or the SgleadSARSCoV2-F primer (for negative-strand viral transcripts) (Wölfel et al., 2020). cDNA was diluted with water to a final volume of 50 µl, of which 2.5 µl was used as a template for each qPCR assay.

Real-time qPCR was performed with a RealPlex 2 (Eppendorf). Quantitation of viral N transcripts was performed by a TaqMan probe assay, using the primer–probe mix from the 2019-nCoV RUO kit (IDT) with the iTaq Universal Probes kit (Bio-Rad). Quantitation of actin transcripts was performed by a SYBR Green assay, using primers specific for fathead minnow β-actin (**Table 2**) with iTaq Universal SYBR Green Supermix (Bio-Rad).

Immunohistochemistry

Whole-mount immunohistochemistry of larvae was performed essentially as described in Palha et al. (2013) and Santos et al. (2018). For COV2-N detection, additional treatment with glycine 0.3 M in PBST (30 min at RT) and heat-induced antigen retrieval (HIER) were performed. HIER treatment was performed in 150 mM Tris–HCl, pH 9.0, at 70°C for 15 min. Primary Ab antibodies used for this labeling were mouse anti-SARS-CoV-2 nucleoprotein (Sino Biological, Beijing, China, 40143-MM05, 1:100) and rabbit anti-GFAP (GeneTex, Irvine, CA, USA, GTX128741, 1:100). As secondary Ab antibodies used were goat anti-mouse F(ab)′2 Alexa Fluor 488 (Molecular Probes, Eugene, OR, USA, A11017, 1:300) and goat anti-rabbit Cy3 (Jackson Laboratories, Bar Harbor, ME, USA, 111-166-003, 1:300). Furthermore, to label the nuclei NucRed Live 647 (Thermo Fisher, R37106, 4 drops for mL for 45 min) was used. For hACE2 detection, staining was performed sequentially since both the primary Ab for ACE2 and the secondary Ab for mCherry were from goat. Primary staining for ACE2 (goat anti-ACE2, AF933, R&D Systems, Minneapolis, MN, USA, 4 µg/ml) was performed first, followed by its secondary staining (donkey anti-goat Ig Alexa 488, A100555, Invitrogen, 1:300), then primary staining for mCherry (rabbit anti-DsRed, 632393, Clontech, Mountain View, CA, USA, 1:300) and secondary staining (goat anti-rabbit Ig Cy3, 111-166-003, 1:300). Nuclei were labeled with 2 µg/ml Hoechst 33342 (Invitrogen). To label membranes, we used DilC18(3) (Thermo Fisher Scientific, D282) staining at 1 µM working solution for 24 h at 4°C, followed by 6 × 45-min washes in PBST.

Afterward, IHC larvae were conserved in 80% glycerol until acquisition. For acquisition of N-CoV-2, the larvae were mounted in 2% agarose in 80% glycerol singularly in a glass-bottom 8-well slide (ibidi, Gräfelfing, Germany, 80827). Images were acquired using an inverted confocal microscope Leica SP8 using a ×10 objective zoomed 1.25× (PL FLUOTAR ×10/0.30 DRY) and ×20 immersion objective (HC PL APO CS2 ×20/0.75 multi-IMM). For both magnification, the bidirectional resonant scanning method was used and images were deconvolved using Leica Lightning Plug-in. For acquisition of hACE2, images were acquired on an upright Leica SPE confocal microscope using a ×40 oil objective (numerical aperture, 1.15).

For IHC of *in vitro* transfected cells, EPC were cultured in a 6-well plate containing sterilized coverslips. At 3 days post-transfection, culture media were removed, and cells were rinsed with PBS once. Cells were fixed overnight at 4°C with 4% methanol-free formaldehyde (Sigma) in PBS. Formaldehyde was removed, and cells were rinsed twice with PBS and kept at 4°C in PBS + 0.05% sodium azide. Fixed cells were rinsed 3 times in PBS. Cells were then permeabilized and blocked with PBS + 0.3% Triton X-100 + 10% horse serum during 45 min at RT. Cells were stained for 1 h at RT with a goat polyclonal anti-human ACE2 (AF933, R&D Systems) diluted at 3 µg/ml in PBS + 0.3% Triton X-100 + 1% horse serum + 1% BSA + 0.01% sodium azide. Cells were then rinsed and stained during 1 h at RT with Alexa 647 anti-goat diluted at 1/500 in PBS + 0.3% Triton X-100 + 1% horse serum + 1% BSA + 0.01% sodium azide. After 3 rinses with PBS, cells were incubated for 1 h at RT with DAPI diluted at 2.5 µg/ml in PBS. After 3 rinses in PBS, coverslips were mounted on slides with Fluoromount-G (Thermo Fisher Scientific).

Transfection efficiency was checked at 3 days post-transfection using a Zeiss Axio Observer Z1 widefield microscope with a ×10/NA 0.25 objective. The phase and GFP channel were acquired on a field of view of 5. Confocal acquisition of immunostained EPC cells was performed on a Leica SP8 upright microscope using a ×25/NA 0.95 coverslip-corrected objective. Endogenous GFP and Alexa 647 were excited with 488 and 638 nm, respectively, and detected with PMT. Fiji was used to adjust the brightness and contrast of confocal images of immunostained EPC cells. Transfection efficiency was quantified using Fiji by manually counting total cells and GFP-expressing cells, respectively.

Statistical Analysis

Analyses were performed with GraphPad Prism. Methods used are indicated in Figure legends. Normality/log-normality tests of data distribution were performed to decide the most appropriate assays.

DATA AVAILABILITY STATEMENT

The raw data supporting the conclusions of this article will be made available by the authors, without undue reservation.

AUTHOR CONTRIBUTIONS

J-PL, PB, IS, and MV designed the study, which was coordinated by J-PL. VR generated the concentrated SARS-CoV-2 virus and

supervised early BSL3 work in IP. BdC supervised BSL3 work in INRAE. J-PL and VL performed 1-cell injections and SARS-CoV-2 microinjections in the BSL3 lab. VL performed SINV injections, WIHC, and fluorescence imaging. MF performed *in vitro* work. J-PL, LB, VL, and MF performed qRT-PCR assays. GL generated the overexpression plasmids. J-PL wrote the manuscript with input from all authors. All authors contributed to the article and approved the submitted version.

FUNDING

This work was supported by the "Urgence COVID-19" fundraising campaign of Institut Pasteur, a dedicated grant co-funded by Institut Pasteur and Institut du Cerveau-Paris Brain Institute, the "ZebraCorona" grant from the exceptional research program call of Université Paris-Saclay, the MUSE-University of Montpellier COVID program, the Agence Nationale de la Recherche (Grant ANR-16-CE20-0002-03 « fish-RNAvax »), and the "ImageInLife" Innovative Training Network funded by European Community's Horizon 2020 Marie-Curie Program under grant agreement no. 721537.

ACKNOWLEDGMENTS

We thank Frédéric Sohm and Joanne Edouard (AMAGEN, Gif-sur-Yvette) for the generation of the triple interferon mutants; our animal facility manager Yohann Rolin for ensuring fish health and fertility despite lockdowns; and numerous members of Institut Pasteur for sharing materials (Olivier Schwartz, Julian Buchrieser, Pierre Charneau, Viviana Scoca, Amandine Noirat, Nathalie Sauvonnet, Pierre Lafaye, Christophe Zimmer, Christian Weber), managing the BSL3 lab (Ferdinand Roesch, Florence Guivel-Benhassine, Thomas Vallet, Heloise Mary), occasional help in experiments (François Huetz, Björn Meyer, Doris-Lou Demy, Emi Murayama), and useful discussions (Emma Colucci-Guyon, Anne Schmidt, Philippe Herbomel). We thank Bertrand Collet and Lise Chaumont (INRAE, Jouy en Josas) for sharing the pmEGFP-N1 plasmid, helpful advice on transfection, and fathead minnow β-actin primers, and Pierre Affaticati (TEFOR Paris-Saclay) for sharing DiI and membrane staining protocol.

SUPPLEMENTARY MATERIAL

The Supplementary Material for this article can be found online at: https://www.frontiersin.org/articles/10.3389/fcimb.2022.790851/full#supplementary-material

Supplementary Video S1 | 3D reconstruction of a larva inoculated with SARS-CoV-2 in the swim bladder after immunodetection of CoV-2 nucleoprotein (green) and GFAP (red). Nuclei are shown in blue. Related to (left-most panel).

Supplementary Video S2 | 3D reconstruction of the swim bladder area of a larva inoculated with SARS-CoV-2 in the swim bladder after immunodetection of CoV-2 nucleoprotein (magenta) with nuclei are shown in cyan. Related to **Figure S3C** (10th panel).

Supplementary Video S3 | Confocal Z-stack of the same larva as in **Supplementary Video S2**. Yellow arrows point to some cells with intimate contact of the two labels strongly suggesting presence of the SARS-CoV-2 nucleoprotein inside the cell cytosol.

Supplementary Video S4 | Confocal Z-stacks of the swim bladder area of a larva inoculated with SARS-CoV-2 in the swim bladder after immunodetection of CoV-2 nucleoprotein (green) with membranes labelled by DiI (red) and nuclei shown in blue. Related to Panels E-H of **Figure 5**, showing 15 confocal planes.

Supplementary Video S5 | Confocal Z-stack of the swim bladder area of a larva inoculated with SARS-CoV-2 in the swim bladder after immunodetection of CoV-2 nucleoprotein (green) with membranes labelled by DiI (red) and nuclei shown in blue. Related to **Figure 5I**.

REFERENCES

Aggad, D., Mazel, M., Boudinot, P., Mogensen, K. E., Hamming, O. J., Hartmann, R., et al. (2009). The Two Groups of Zebrafish Virus-Induced Interferons Signal via Distinct Receptors With Specific and Shared Chains. *J. Immunol. (Baltimore Md. : 1950)* 183 (6), 3924–3931. doi: 10.4049/jimmunol.0901495

Archambault, L. S., Trzilova, D., Gonia, S., Gale, C., and Wheeler, R. T. (2019). Intravital Imaging Reveals Divergent Cytokine and Cellular Immune Responses to Candida Albicans and Candida Parapsilosis. *MBio* 10 (3), e00266-19. doi: 10.1128/mBio.00266-19

Balkrishna, A., Solleti, S. K., Verma, S., and Varshney, A. (2020). Application of Humanized Zebrafish Model in the Suppression of SARS-CoV-2 Spike Protein Induced Pathology by Tri-Herbal Medicine Coronil *via* Cytokine Modulation. *Molecules (Basel Switzerland)* 25 (21), 5091. doi: 10.3390/molecules25215091

Boucontet, L., Passoni, G., Thiry, V., Maggi, L., Herbomel, P., Levraud, J.-P., et al. (2018). A Model of Superinfection of Virus-Infected Zebrafish Larvae: Increased Susceptibility to Bacteria Associated With Neutrophil Death. *Front. Immunol.* 9, 1084. doi: 10.3389/fimmu.2018.01084

Briolat, V., Jouneau, L., Carvalho, R., Palha, N., Langevin, C., Herbomel, P., et al. (2014). Contrasted Innate Responses to Two Viruses in Zebrafish: Insights Into the Ancestral Repertoire of Vertebrate IFN-Stimulated Genes. *J. Immunol. (Baltimore Md. : 1950)* 192, 4328–4341. doi: 10.4049/jimmunol.1302611

Burgos, J. S., Ripoll-Gomez, J., Alfaro, J. M., Sastre, I., and Valdivieso, F. (2008). Zebrafish as a New Model for Herpes Simplex Virus Type 1 Infection. *Zebrafish* 5, 323–333. doi: 10.1089/zeb.2008.0552

Cass, A. N., Servetnick, M. D., and McCune, A. R. (2013). Expression of a Lung Developmental Cassette in the Adult and Developing Zebrafish Swimbladder. *Evol. Dev.* 15, 119–132. doi: 10.1111/ede.12022

Chen, H.-C., and Reich, N. C. (2010). Live Cell Imaging Reveals Continuous STAT6 Nuclear Trafficking. *J. Immunol. (Baltimore Md. : 1950)* 185 (1), 64–70. doi: 10.4049/jimmunol.0903323

Damas, J., Hughes, G. M., Keough, K. C., Painter, C. A., Persky, N. S., Corbo, M., et al. (2020). Broad Host Range of SARS-CoV-2 Predicted by Comparative and Structural Analysis of ACE2 in Vertebrates. *Proc. Natl. Acad. Sci. U.S.A.* 117 (36), 22311–22322. doi: 10.1073/pnas.2010146117

Eymieux, S., Rouillé, Y., Terrier, O., Seron, K., Blanchard, E., Rosa-Calatrava, M., et al. (2021). Ultrastructural Modifications Induced by SARS-CoV-2 in Vero Cells: A Kinetic Analysis of Viral Factory Formation, Viral Particle Morphogenesis and Virion Release. *Cell. Mol. Life Sciences : CMLS* 78 (7), 3565–3576. doi: 10.1007/s00018-020-03745-y

Farnsworth, D. R., Saunders, L. M., and Miller, A. C. (2020). A Single-Cell Transcriptome Atlas for Zebrafish Development. *Dev. Biol.* 459 (2), 100–108. doi: 10.1016/j.ydbio.2019.11.008

Gabor, K. A., Goody, M. F., Mowel, W. K., Breitbach, M. E., Gratacap, R. L., Witten, P. E., et al. (2014). Influenza A Virus Infection in Zebrafish

Recapitulates Mammalian Infection and Sensitivity to Anti-Influenza Drug Treatment. *DMM Dis. Models Mech.* 7, 1227–1237. doi: 10.1242/dmm.014746

Grabher, C., Joly, J.-S., and Wittbrodt, J. (2004). Highly Efficient Zebrafish Transgenesis Mediated by the Meganuclease I-SceI. *Methods Cell Biol.* 77, 381–401. doi: 10.1016/s0091-679x(04)77021-1

Gratacap, R. L., Scherer, A. K., Seman, B. G., and Wheeler, R. T. (2017). Control of Mucosal Candidiasis in the Zebrafish Swim Bladder Depends on Neutrophils That Block Filament Invasion and Drive Extracellular-Trap Production. *Infect. Immun.* 85 (9), e00276-17. doi: 10.1128/IAI.00276-17

Hoffmann, M., Kleine-Weber, H., Schroeder, S., Krüger, N., Herrler, T., Erichsen, S., et al. (2020). SARS-CoV-2 Cell Entry Depends on ACE2 and TMPRSS2 and Is Blocked by a Clinically Proven Protease Inhibitor. *Cell* 181, 271–280. doi: 10.1016/j.cell.2020.02.052

Howe, K., Clark, M. D., Torroja, C. F., Torrance, J., Berthelot, C., Muffato, M., et al. (2013). The Zebrafish Reference Genome Sequence and its Relationship to the Human Genome. *Nature* 496 (7446), 498–503. doi: 10.1038/nature12111

Kim, D., Lee, J.-Y., Yang, J.-S., Kim, J. W., Kim, V. N., and Chang, H. (2020). The Architecture of SARS-CoV-2 Transcriptome. *Cell* 181 (4), 914–921.e10. doi: 10.1016/j.cell.2020.04.011

Kimmel, C. B., Ballard, W. W., Kimmel, S. R., Ullmann, B., and Schilling, T. F. (1995). Stages of Embryonic Development of the Zebrafish. *Dev. Dynamics : Off. Publ. Am. Assoc. Anatomists* 203 (3), 253–310. doi: 10.1002/aja.1002030302

Kraus, A., Casadei, E., Huertas, M., Ye, C., Bradfute, S., Boudinot, P., et al. (2020). A Zebrafish Model for COVID-19 Recapitulates Olfactory and Cardiovascular Pathophysiologies Caused by SARS-CoV-2. *BioRxiv*, 2020.11.06.368191. doi: 10.1101/2020.11.06.368191. 2020.11.06.368191.

Lam, S. H., Chua, H. L., Gong, Z., Lam, T. J., and Sin, Y. M. (2004). Development and Maturation of the Immune System in Zebrafish, Danio Rerio: A Gene Expression Profiling, *in Situ* Hybridization and Immunological Study. *Dev. Comp. Immunol.* 28 (1), 9–28. doi: 10.1016/s0145-305x(03)00103-4

Langevin, C., van der Aa, L. M., Houel, A., Torhy, C., Briolat, V., Lunazzi, A., et al. (2013). Zebrafish ISG15 Exerts a Strong Antiviral Activity Against RNA and DNA Viruses and Regulates the Interferon Response. *J. Virol.* 87 (18), 10025–10036. doi: 10.1128/JVI.01294-12

Levraud, J.-P., Colucci-Guyon, E., Redd, M. J., Lutfalla, G., and Herbomel, P. (2008). *In Vivo* Analysis of Zebrafish Innate Immunity. *Methods Mol. Biol. (Clifton N.J.)* 415, 337–363. doi: 10.1007/978-1-59745-570-1_20

Levraud, J.-P., Disson, O., Kissa, K., Bonne, I., Cossart, P., Herbomel, P., et al. (2009). Real-Time Observation of Listeria Monocytogenes-Phagocyte Interactions in Living Zebrafish Larvae. *Infect. Immun.* 77 (9), 3651–3660. doi: 10.1128/IAI.00408-09

Levraud, J.-P., Jouneau, L., Briolat, V., Laghi, V., and Boudinot, P. (2019). Interferon-Stimulated Genes in Zebrafish and Human Define an Ancient Arsenal of Antiviral Immunity. *J. Immunol.* 203, 3361–3373. doi: 10.4049/jimmunol.1900804

Levraud, J.-P., Palha, N., Langevin, C., and Boudinot, P. (2014). Through the Looking Glass: Witnessing Host-Virus Interplay in Zebrafish. *Trends Microbiol.* 22, 490–497. doi: 10.1016/j.tim.2014.04.014

Lutz, C., Maher, L., Lee, C., and Kang, W. (2020). COVID-19 Preclinical Models: Human Angiotensin-Converting Enzyme 2 Transgenic Mice. *Hum. Genomics* 14, 20. doi: 10.1186/s40246-020-00272-6

Maarifi, G., Smith, N., Maillet, S., Moncorgé, O., Chamontin, C., Edouard, J., et al. (2019). TRIM8 Is Required for Virus-Induced IFN Response in Human Plasmacytoid Dendritic Cells. *Sci. Adv.* 5, eaax3511. doi: 10.1126/sciadv.aax3511

Montagutelli, X., Prot, M., Levillayer, L., Salazar, E. B., Jouvion, G., Conquet, L., et al. (2021). The B1.351 and P.1 Variants Extend SARS-CoV-2 Host Range to Mice. *BioRxiv*, 2021.03.18.436013. doi: 10.1101/2021.03.18.436013. 2021.03.18.436013.

Moore, S., Hill, E. M., Tildesley, M. J., Dyson, L., and Keeling, M. J. (2021). Vaccination and non-Pharmaceutical Interventions for COVID-19: A Mathematical Modelling Study. *Lancet Infect. Dis.* 21, 793–802. doi: 10.1016/S1473-3099(21)00143-2

Muñoz-Fontela, C., Dowling, W. E., Funnell, S. G. P., Gsell, P.-S., Riveros-Balta, A. X., Albrecht, R. A., et al. (2020). Animal Models for COVID-19. *Nature* 586 (7830), 509–515. doi: 10.1038/s41586-020-2787-6

Oehlers, S. H., Flores, M. V., Chen, T., Hall, C. J., Crosier, K. E., and Crosier, P. S. (2011). Topographical Distribution of Antimicrobial Genes in the Zebrafish Intestine. *Dev. Comp. Immunol.* 35 (3), 385–391. doi: 10.1016/j.dci.2010.11.008

Palha, N., Guivel-Benhassine, F., Briolat, V., Lutfalla, G., Sourisseau, M., Ellett, F., et al. (2013). Real-Time Whole-Body Visualization of Chikungunya Virus Infection and Host Interferon Response in Zebrafish. *PloS Pathog.* 9 (9), e1003619. doi: 10.1371/journal.ppat.1003619

Parichy, D. M., Elizondo, M. R., Mills, M. G., Gordon, T. N., and Engeszer, R. E. (2009). Normal Table of Postembryonic Zebrafish Development: Staging by Externally Visible Anatomy of the Living Fish. *Dev. Dynamics: Off. Publ. Am. Assoc. Anatomists* 238 (12), 2975–3015. doi: 10.1002/dvdy.22113

Passoni, G., Langevin, C., Palha, N., Mounce, B. C., Briolat, V., Affaticati, P., et al. (2017). Imaging of Viral Neuroinvasion in the Zebrafish Reveals That Sindbis and Chikungunya Viruses Favour Different Entry Routes. *DMM Dis. Models Mech.* 10 (7), 847–857. doi: 10.1242/dmm.029231

Postlethwait, J. H., Farnsworth, D. R., and Miller, A. C. (2020). An Intestinal Cell Type in Zebrafish Is the Nexus for the SARS-CoV-2 Receptor and the Renin-Angiotensin-Aldosterone System That Contributes to COVID-19 Comorbidities. *BioRxiv* 2, 2020.09.01.278366. doi: 10.1101/2020.09.01.278366. 2020.09.01.278366.

Postlethwait, J. H., Massaquoi, M. S., Farnsworth, D. R., Yan, Y.-L., Guillemin, K., and Miller, A. C. (2021). The SARS-CoV-2 Receptor and Other Key Components of the Renin-Angiotensin-Aldosterone System Related to COVID-19 Are Expressed in Enterocytes in Larval Zebrafish. *Biol. Open* 10 (3), bio058172. doi: 10.1242/bio.058172

Santos, D., Monteiro, S. M., and Luzio, A. (2018). General Whole-Mount Immunohistochemistry of Zebrafish (Danio Rerio) Embryos and Larvae Protocol. *Methods Mol. Biol. (Clifton N.J.)* 1797, 365–371. doi: 10.1007/978-1-4939-7883-0_19

Torraca, V., and Mostowy, S. (2018). Zebrafish Infection: From Pathogenesis to Cell Biology. *Trends Cell Biol.* 28 (2), 143–156. doi: 10.1016/j.tcb.2017.10.002

Van Dycke, J., Ny, A., Conceição-Neto, N., Maes, J., Hosmillo, M., Cuvry, A., et al. (2019). A Robust Human Norovirus Replication Model in Zebrafish Larvae. *PloS Pathog.* 15, e1008009. doi: 10.1371/journal.ppat.1008009

Ventura Fernandes, B. H., Feitosa, N. M., Barbosa, A. P., Bomfim, C. G., Garnique, A. M. B., Gomes, F. I. F., et al. (2020). Zebrafish Studies on the Vaccine Candidate to COVID-19, the Spike Protein: Production of Antibody and Adverse Reaction. *BioRxiv*, 2020.10.20.346262. doi: 10.1101/2020.10.20.346262. 2020.10.20.346262.

V'kovski, P., Gultom, M., Kelly, J., Steiner, S., Russeil, J., Mangeat, B., et al. (2020). Disparate Temperature-Dependent Virus – Host Dynamics for SARS-CoV-2 and SARS-CoV in the Human Respiratory Epithelium. *BioRxiv*, 2020.04.27.062315. doi: 10.1101/2020.04.27.062315. 2020.04.27.062315.

V'kovski, P., Gultom, M., Kelly, J. N., Steiner, S., Russeil, J., Mangeat, B., et al. (2021). Disparate Temperature-Dependent Virus-Host Dynamics for SARS-CoV-2 and SARS-CoV in The Human Respiratory Epithelium. *PloS Biol.* 19 (3), e3001158. doi: 10.1371/journal.pbio.3001158

Wölfel, R., Corman, V. M., Guggemos, W., Seilmaier, M., Zange, S., Müller, M. A., et al. (2020). Virological Assessment of Hospitalized Patients With COVID-2019. *Nature* 581 (7809), 465–469. doi: 10.1038/s41586-020-2196-x

Zamorano Cuervo, N., and Grandvaux, N. (2020). ACE2: Evidence of Role as Entry Receptor for SARS-CoV-2 and Implications in Comorbidities. *ELife* 9, e61390. doi: 10.7554/eLife.61390

Zou, J., and Secombes, C. J. (2016). The Function of Fish Cytokines. *Biology* 5 (2), 23. doi: 10.3390/biology5020023

Conflict of Interest: The authors declare that the research was conducted in the absence of any commercial or financial relationships that could be construed as a potential conflict of interest.

Publisher's Note: All claims expressed in this article are solely those of the authors and do not necessarily represent those of their affiliated organizations, or those of the publisher, the editors and the reviewers. Any product that may be evaluated in this article, or claim that may be made by its manufacturer, is not guaranteed or endorsed by the publisher.

Chapter 3: Outlook

In this project, I performed experiments in BSL3, imaging, image analysis, and part of the RT-qPCR. From the technical point of view, a large amount of time was dedicated to the creation and optimization of injection and handling protocols for zebrafish larvae in BSL3. We had to find new technical solutions, both physical and biological, to experiment with the safety rules without affecting zebrafish biology. Fundamental was the collaboration with Marco Vignuzzi lab and Veronica Rezelj to the realization of this work.

Although the project did not show a clear applicability for zebrafish as an animal model for SARS-CoV2, created protocols that can be adapted and used in other BSL3.

In the paper, we showed the presence of abortive infection of swim bladder cells, with only a partial replication of the virus taking place and no further infection of propagation. Due to the complexity of the tissue and the difficulties in handling SARS-CoV2-infected samples at the time, it was not possible to identify the cell population involved.

While the experiments did not induce a proper infection, the abortive infection of zebrafish can still be used to identify which proteins are missing and are responsible for complete virus replication. Identifying these proteins is of interest as they could be used as targets for specific antiviral drugs if conserved in humans.

Moreover, we attempted the expression of human ACE2 proteins in zebrafish, demonstrating that is possible, although not sufficient. The development of humanization protocols for zebrafish is important as it could be a powerful tool in further developing zebrafish as an animal model for human pathogens infection.

Indeed, now there are no clear protocols to humanize zebrafish to increase susceptibility to infection. Granted the easiness of genetic manipulability of zebrafish, without a clear vision of which proteins need to be humanized for each pathogen in zebrafish, the process of adaptation of this animal to different pathogens could be too slow and expensive. Nonetheless, from a different point of view, the humanization process itself can be a powerful tool to reconstruct intracellular pathways associated with proficient infection and results in the generation of a permissive zebrafish line.

Indeed, this latter approach is already used in mice with different degrees of success, showing that more than a problem of feasibility, the delay in the creation of humanization protocols for zebrafish is associated with a lack of commitment by the research community (Brehm et al., 2013; Dash et al., 2021; Li and Di Santo, 2019).

Hiding in the yolk: A unique feature of Legionella pneumophila infection of zebrafish

Chapter 1: Introduction

1.1 Legionella Pneumophila

Legionella is a gram-negative, non-sporogenous, non-capsule forming, and aerobic bacteria. *Legionella spp.* was initially isolated in 1947 and classified as a "rickettsia-like" bacteria. In 1977 its classification changed and was included in the same species and serogroup of the Philadelphia bacterium (Jackson, 1952). The classification as *Legionella pneumophila* followed the identification of this bacteria as a cause of Legionnaires disease (LD), including it in the Legionellaceae family (Piano et al., 1984). *L. pneumophila* has a degree of motility depending on the serogroup, is viable between 25 and 37 °C, and forms biofilm to protect itself (Konishi et al., 2006). Furthermore, this bacterium can infect humans by inhalation of infected organisms, and it is normally a risk factor for air cooling systems, spas, and other appliances that may vaporize/nebulize water (Figure 24) (Brady and Sundareshan, 2017; Sanford, 1979). Moreover, *Legionella* can also propagate by human-to-human contact (Novais et al., 2009).

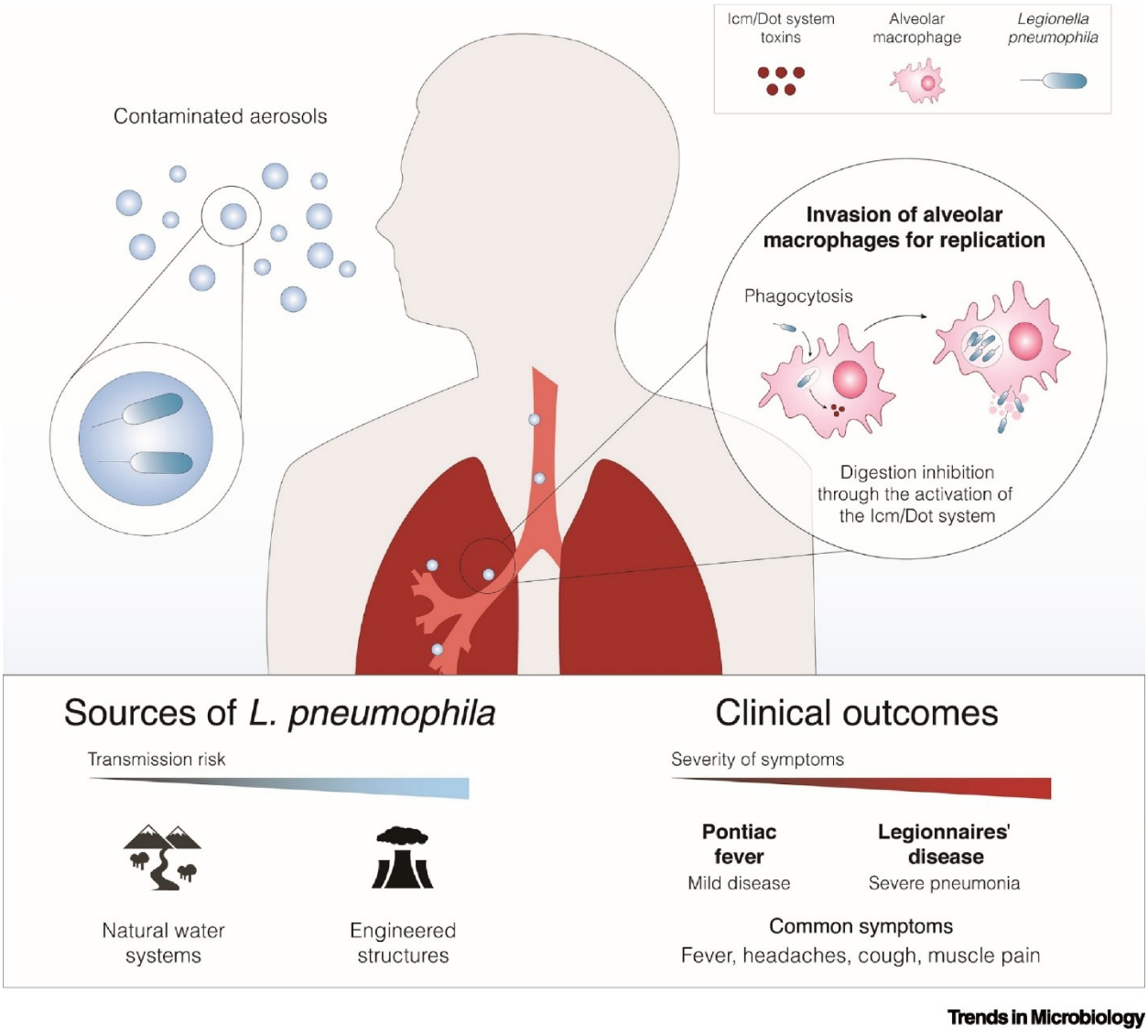

Figure 24: Overview of *Legionella pneumophila*.

L. pneumophila is a pathogenic bacterium that infects human preferentially via aerosol. The risk of contracting L. pneumophila increases in urban areas due to specific environmental conditions and the clinical outcome is potentially lethal. ***Source (Gonçalves et al., 2021).***

Although *Legionella* is considered an airborne disease of the low respiratory tract, this bacterium is ubiquitous and often present in aquatic environments. The formation of biofilm allows this bacterium to survive from 20 to 50 °C (Fields et al., 2002; Fliermans et al., 1981). Furthermore, it can exist as an intracellular parasite of protozoa, mold, and amebae. The prevention of *Legionella* biofilm formation in warm waters with enough nutrients is the only way to prevent this bacterium infection, especially in hospitals, where it is responsible for nosocomial infections (Burillo et al., 2017).

Like all Gram-negative bacteria, *Legionella* exhibits the classic membrane structure formed by the inner membrane, periplasmic space, and outer membrane (Figure 25).

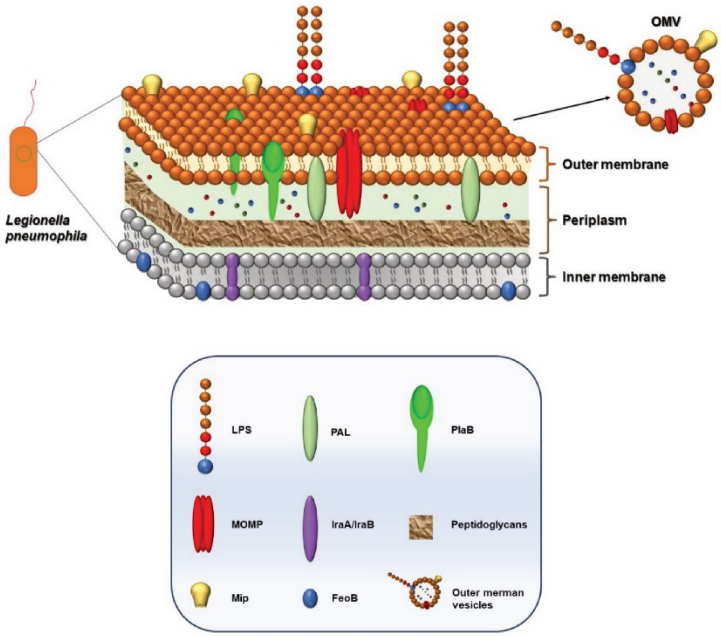

Figure 25: Virulence factors of Legionella spp.

Structure of Legionella pneumophila. The outer membrane (OM) is a lipid bilayer composed of phospholipids, lipoproteins, LPS, and proteins, some of which connect the outer membrane to peptidoglycan. In addition, the presence of surface-associated proteins on OM, macrophage infectivity potentiator (Mip) protein, and the major outer membrane protein (MOMP) play a critical role in LD outcome. ***Source (Iliadi et al., 2022).***

The inner membrane is composed of a bilayer of phospholipids containing proteins such as FeoB, IraA/IraB, phosphatidylethanolamine, and phosphatidylcholine (Hindahl and Iglewski, 1984). In particular, it has been shown that FeoB, a GTP-dependent iron transporter, and IraA/IraB, two methyltransferase proteins, play a role in the inactivation and replication of macrophages (Petermann et al., 2010) (Iliadi et al., 2022).

The periplasm is the space between the inner and the outer membrane and it contains many soluble enzymes and antigens, and the classic Gram-negative thin peptidoglycan that plays a fundamental role as a virulence factor and in the survival of *Legionella* in macrophages and amoeba. One of the most important antigens present in the periplasm is the peptidoglycan-associated lipoprotein (PAL), which is used as an alternative diagnostic test for *Legionella* since it is expelled in the urines of infected patients (Journal et al., 2010; Shevchuk et al., 2011).

The outer membrane is the most external layer, and it is formed by a bilayer of phospholipids, lipopolysaccharides (LPS), lipoproteins, and other structural proteins. Although the components of this membrane are still not well-characterized, researchers identified proteins such as PlaB, a phospholipase involved in the destruction of the host membrane and signaling pathways (Iliadi et al., 2022).

One of the several proteins present on the external surface of *Legionella* is the major outer membrane protein (MOMP), necessary for adhesion to host cells and interfering with the host's chemotactic activity (High et al., 1993). MOMP can also affect the expression of the host immune system factors like IL10, FOXO1, and NOD1 (Yang et al., 2021). Another important virulence factor in *Legionella* is the macrophage infectivity potentiator (Mip), which influences macrophages activity during the first stage of respiratory epithelium infection, increases chemotaxis, and inhibits the phagocytosis (Nintasen et al., 2007; Shen et al., 2022). Lastly, we can find the LPS, the main antigen of Gram-negative bacteria, involved in the adhesion of *Legionella* to the host cells (Papian et al., 2020).

L. pneumophila induces low respiratory tract (LRT) infection, which brings forth a pneumonia-like disease. This is possibly due to the ability of this bacterium to invade the tissue and the ability to use macrophages as a replication niche. To “prime” macrophages as a permissive environment for replication, *Legionella* uses secretory factors that affect almost all the aspects of the intracellular environment.

The most relevant of these factors is the Type IV secretion system (T4SS), encoded by *dot/icm* genes, that allows the formation of "specialized vacuoles" (*Legionella* containing vacuole, LCV) exploiting mitochondria, ER-derived membrane and other host proteins (Molmeret et al., 2004) (Figure 26). As LCV mature, this structure's resemblance to rough ER develops, with the studding of this membranous structure with ribosomes (Isberg et al., 2008). T4SS is responsible for a variety of fundamental activities, such as cell invasion, replication, apoptosis, and exit from host cells (Cheng et al., 2022; Ge et al., 2022; Lockwood et al., 2022). The *dot/icm* genes are involved in conjugation, micropinocytosis, phagocytosis, apoptosis of macrophages, and pore formation (Iliadi et al., 2022). This shows that T4SS is important for *Legionella* virulence during infection, nevertheless, in *L. pneumophila,* there are T2SS and T1SS. T2SS secretes more than 25 proteins and degradation enzymes, and also factors that affect host innate immunity and survival at low temperatures (Cianciotto, 2013; Tyson et al., 2014). Instead, T1SS consists of an ATP-binding cassette (ABC) transporter, that act as a membrane fusion protein, and secretes lipases, adhesins, and iron-scavenger proteins (Qin et al., 2017; Spitz et al., 2019).

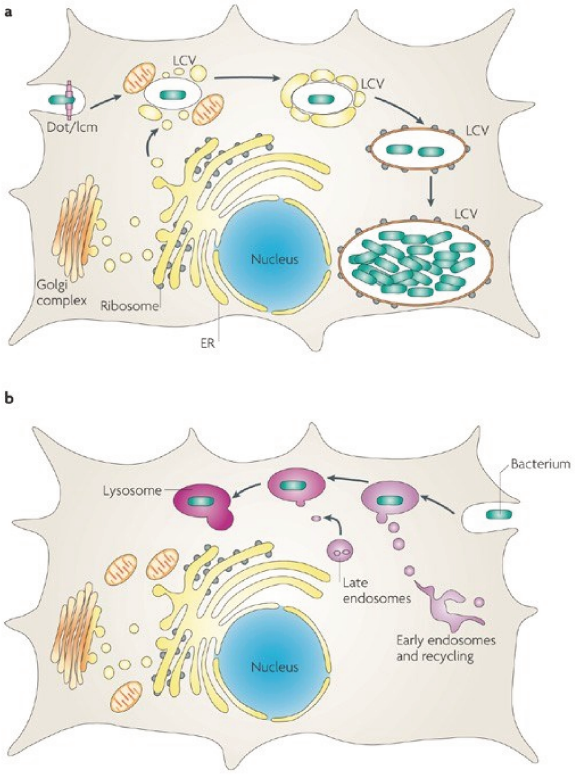

Figure 26: Legionella pneumophila modulates the trafficking of its vacuole to establish a replicative niche.

A) Formation of the replication vacuole. After uptake into target amoebae or macrophages, the Legionella-containing vacuole (LCV) evades transport to the lysosomal network and is sequestered in a compartment that is different from those observed for non-pathogens. Within minutes of uptake, vesicles derived from the endoplasmic reticulum (ER; yellow compartments) and mitochondria appear in close proximity to the LCV surface. The identity of the ER-derived vesicles is based on the presence of proteins that are known to be associated with the early secretory apparatus. The vesicles that surround the LCV appear to be docked and extend out onto the surface, and eventually, the membranes that surround the bacterium become similar to rough ER in appearance and become studded with ribosomes. Within this ER-like compartment, the bacterium replicates to high numbers and eventually lyses the host cell. B) Default pathway of trafficking a non-pathogen. After bacterial uptake, the membrane-bound compartment acquires the character of early endosomes and late endosomes before entering the lysosomal network. Dot/Icm, defect in organelle trafficking/intracellular multiplication. ***Source (Isberg et al., 2008).***

Chapter 2: Article

PLOS PATHOGENS

RESEARCH ARTICLE

Hiding in the yolk: A unique feature of *Legionella pneumophila* infection of zebrafish

Flávia Viana[1☯], Laurent Boucontet[2☯¤], Valerio Laghi[2¤], Daniel Schator[1,3], Marine Ibranosyan[4], Sophie Jarraud[4,5], Emma Colucci-Guyon[2☯¤*], Carmen Buchrieser[1☯*]

1 Institut Pasteur, Université Paris Cité, Université Paris Cité, Biologie des Bactéries Intracellulaires and CNRS UMR 6047, Paris, France, **2** Institut Pasteur, Université Paris Cité, Unité Macrophages et Développement de l'Immunité and CNRS UMR 3738, Paris, France, **3** Sorbonne Université, Collège doctoral, Paris, France, **4** National Reference Centre of *Legionella*, Institute of Infectious Agents, Hospices Civils de Lyon, Lyon, France, **5** Centre International de Recherche en Infectiologie, Université Lyon 1, UMR CNRS 5308, Inserm U1111, ENS de Lyon, Lyon, France

☯ These authors contributed equally to this work.
¤ Current address: Cell Polarity, Migration and Cancer Unit, Institut Pasteur, CNRS UMR3691, Université Paris Cité, Équipe Labellisée Ligue Contre le Cancer, Paris, France.
* emma.colucci@pasteur.fr (ECG); cbuch@pasteur.fr (CB)

Citation: Viana F, Boucontet L, Laghi V, Schator D, Ibranosyan M, Jarraud S, et al. (2023) Hiding in the yolk: A unique feature of *Legionella pneumophila* infection of zebrafish. PLoS Pathog 19(5): e1011375. https://doi.org/10.1371/journal.ppat.1011375

Editor: Matthew A. Mulvey, University of Utah, UNITED STATES

Received: December 7, 2022

Accepted: April 19, 2023

Published: May 8, 2023

Data Availability Statement: All relevant data are within the paper and its Supporting Information files. The movies related to the paper are available at https://zenodo.org/record/7410466.

Funding: Work in the CB laboratory is financed by the Fondation pour la Recherche Médicale (FRM) grant EQU201903007847 and the grant ANR-10-LABX-62-IBEID and ANR-22-CE15 0009 01 ZebraLegion. Work in ECG group is financed by ANR 17-CE15-0026 and 20-CE15-0024 and ANR-22-CE15 0009 01 ZebraLegion. Valerio Laghi is

Abstract

The zebrafish has become a powerful model organism to study host-pathogen interactions. Here, we developed a zebrafish model to dissect the innate immune response to *Legionella pneumophila* during infection. We show that *L. pneumophila* cause zebrafish larvae death in a dose dependent manner. Additionally, we show that macrophages are the first line of defence and cooperate with neutrophils to clear the infection. Immunocompromised humans have an increased propensity to develop pneumonia, similarly, when either macrophages or neutrophils are depleted, these "immunocompromised" larvae become lethally sensitive to *L. pneumophila*. Also, as observed in human infections, the adaptor signalling molecule Myd88 is not required to control disease in the larvae. Furthermore, proinflammatory cytokine genes *il1β* and *tnf-α* were upregulated during infection, recapitulating key immune responses seen in human infection. Strikingly, we uncovered a previously undescribed infection phenotype in zebrafish larvae, whereby bloodborne, wild type *L. pneumophila* invade and grow in the larval yolk region, a phenotype not observed with a type IV secretion system deficient mutant that cannot translocate effectors into its host cell. Thus, zebrafish larva represents an innovative *L. pneumophila* infection model that mimics important aspects of the human immune response to *L. pneumophila* infection and will allow the elucidation of mechanisms by which type IV secretion effectors allow *L. pneumophila* to cross host cell membranes and obtain nutrients from nutrient rich environments.

Author summary

L. pneumophila is an intracellular pathogen that has co-evolved with aquatic protozoa but can also infect humans to cause a severe pneumonia. *L. pneumophila* infections are

funded by ANR 20-CE15-0024. The funders, other than the authors, did not play any role in the study or in the preparation of the article or decision to publish.

Competing interests: The authors have declared that no competing interests exist.

increasingly recognized worldwide, with outbreaks affecting hundreds of people commonly reported. Although *Legionella* infection has been widely studied in various model organisms, key aspects of human disease and host response to infection are not well reflected in these organisms. Here we have established the zebrafish as a new model for *Legionella* infection and use cutting-edge intravital imaging to reveal the temporal dynamics of bacterial dissemination, and the interactions between bacteria and macrophages/neutrophils, within a whole-of-organism spatial context. We show that as in humans, macrophages are the main drivers of the host defense and "immunocompromised" fish are highly susceptible to infection. In addition, we identified a previously undescribed infection phenotype in which *Legionella* enter and replicate in the yolk region of zebrafish larvae, an aspect which ultimately drives the outcome of infection. The new zebrafish model should prove useful as a platform to study host and bacterial factors underlying *Legionella* infection.

Introduction

Legionella pneumophila, a gram negative, facultative intracellular bacterium inhabits natural, freshwater sources [1,2]. As an environmental aquatic microbe, *L. pneumophila* replicates intracellularly in aquatic protozoa [3]. Most interestingly, in contrast to other intracellular pathogens *L. pneumophila* is not adapted to a single host, but it exhibits a broad host range including Amoebozoa (amoebae), Percolozoa (excavates) and Ciliophora (ciliated protozoa) [3,4]. In the environment *L. pneumophila* can also be found within biofilms or it can survive in a planktonic form for a certain time [5]. As fresh water and engineered systems are connected, *L. pneumophila* can also contaminate artificial water systems. Protected within its protozoan hosts *L. pneumophila* survives water disinfectants and may infect humans *via* aerosols produced by different engineered structures and devices. The inhalation of *L. pneumophila* containing aerosols can cause a severe pneumonia, the so-called Legionnaires' disease [6]. However, not every infection leads to disease. Disease outcome is determined by virulence of the bacterial strain, the bacterial burden in the inhaled aerosols and most importantly by the host immune status. Host factors determining susceptibility include: age above 50, smoking and/or having chronic lung disease, being immunocompromised and genetic factors that alter the immune response [2,7,8].

Once the bacteria reach the lungs of susceptible individuals, they can infect alveolar macrophages and replicate therein. After being phagocytosed *L. pneumophila* avoids lysosomes and establishes an endoplasmic reticulum derived vacuole, named the *Legionella* containing vacuole (LCV) [9,10]. The LCV, a safe haven for bacterial replication, is established by utilizing the Dot/Icm type IV secretion system (T4SS) that injects over 330 proteins into the host cell [9–11]. These effector proteins manipulate a myriad of host pathways such as, recruiting vesicles derived from the endoplasmic reticulum to the LCV, supplying the bacteria with nutrients, restraining autophagy and supressing apoptosis and to subvert the host cell immune response [9–11]. A surprisingly high number of these effectors mimic host proteins and encode eukaryotic functions helping *L. pneumophila* to modulate numerous host pathways to its own benefit in remarkably diverse ways [11–13]

Intracellular replication of *L. pneumophila* and innate immune responses to this pathogen have been studied *in vitro* using both murine and human cell lines and *in vivo* using different animal models of infection. However, results obtained with these models cannot be easily extrapolated to what is observed in human disease. Studies in invertebrate models, such as *Galleria mellonella* and *Caenorhabditis elegans*, [14,15] require further validation in more developed

models as their immune system greatly differs from that of vertebrates. Mouse infection fails to recapitulate the human disease phenotype, as most inbred mice strains are naturally resistant to *L. pneumophila*. This natural resistance is due to the activation of the inflammasome through NAIP5/NLRC4, triggered by flagellin, as well as through an apoptosis-associated speck-like protein containing a CARD (ASC)-dependent pathway, resulting in the production of cytokines *via* an IL-1 autocrine loop [16]. Humans lack the NAIP5 allele present in murine cells [17]. The only mouse model able to support *Legionella* growth are A/J mice, as they have a hypermorphic *NAIP5* allele, however knock out mice are rarely available for A/J mice [18]. Very early after the discovery of *L. pneumophila*, a guinea pig model of Legionnaires' disease was developed, as the guinea pig is highly susceptible to *L. pneumophila* when infected through injection into the peritoneum [6] or when exposed to *L. pneumophila* containing aerosols [6]. Several studies thereafter have shown that the guinea pig infection model recalls human disease and allows to study the immune response to *L. pneumophila* infection [19,20]. However, the guinea pig model is rarely used due to the limited availability of specific immunological reagents for these animals and the demanding laboratory and husbandry requirements.

The above-mentioned models, including the widely used murine model, have limitations for studying *L. pneumophila* infection *in vivo*. Furthermore, exhibit discrepancies between results obtained in human cells, for example mouse macrophages restrict *L. pneumophila* growth *via* caspase 1 and caspase 7 activation, whereas human macrophages do not activate caspase 1 and 7 and thus allow growth of *L. pneumophila* [21,22]. Thus, we sought to develop a new, alternative model for *Legionella* infection. The zebrafish *(Danio rerio)* originally introduced as a model organism in developmental biology has emerged in recent years as a powerful non-mammalian model to study nearly every aspect of biology, including immune cell behaviour and host-pathogen interactions [23,24]. Zebrafish are evolutionary closer to humans than fruit flies and nematodes, easier to manipulate than mice and their immune system is remarkably similar to the one of mammals, making them an attractive laboratory model for immunology and infection biology [23,24]. Its popularity is also due to its small size and the natural translucency of its embryos and larvae, which makes it possible to follow leukocyte behaviour and infection onset at the level of the whole organism in real-time and high resolution [25]. Additionally, although adult organisms display a fully developed immune system with both active innate and adaptive branches, studies can also be conducted at the early stages of life (embryonic or larvae) when the organism solely relies on innate immunity, allowing the dissection of mechanisms arising from different immune responses [25–27]. Here we examined whether the zebrafish could be an alternative model for analysing host-pathogen interactions, in particular the innate immune response to *L. pneumophila* infection.

We show that *L. pneumophila* infection of zebrafish larvae recapitulate human disease onset, as infected wild-type larvae are generally able to clear the infection, but immunocompromised fish fail to do so. Both macrophages and neutrophils quickly interact and engulf injected *L. pneumophila*. Macrophage-depleted larvae show a dramatic increase of bacterial burden concomitant with host death, pointing to a crucial role of macrophages in controlling the infection. Interestingly, not all wild-type larvae are able to control the infection; a fraction showed high bacterial burden in the yolk region, a unique zebrafish infection phenotype.

Results

Legionella pneumophila infection induces mortality in zebrafish larvae in a dose dependent manner

To analyse whether *L. pneumophila* can cause disease in zebrafish larvae we microinjected larvae 72 hours post fertilisation (hpf) intravenously in the caudal vessels near the cloaca (Fig 1A),

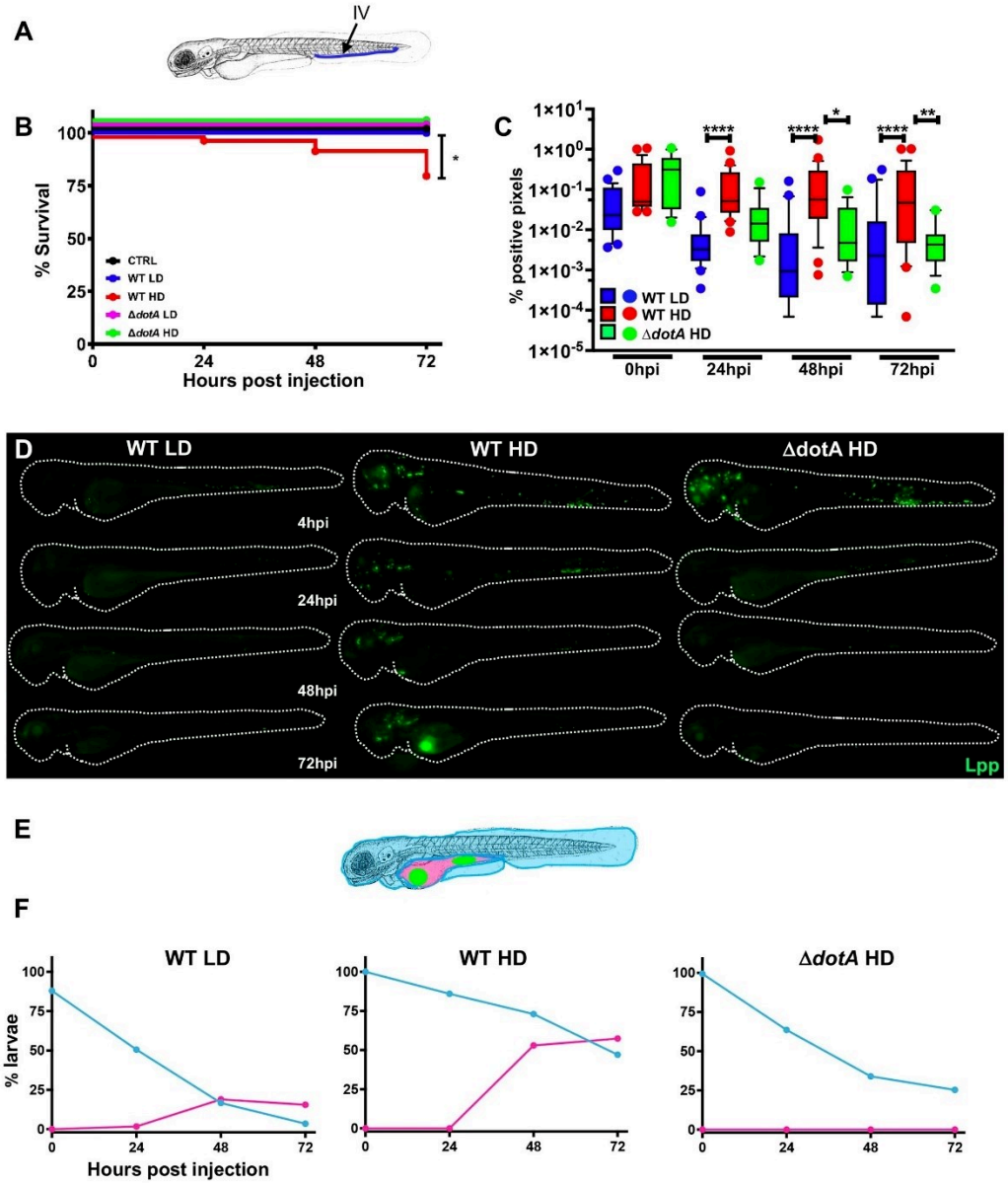

Fig 1. Zebrafish larvae are susceptible to intravenous *L. pneumophila* infection in a dose dependent manner. A) Scheme of the experimental set up of bacterial infection using zebrafish. A 72hpf zebrafish larva. Bacteria are injected in the bloodstream (iv) via the caudal vein (green arrow). The scheme of the zebrafish larvae has been adapted from [35] and has been previously modified from [87] **B)** Survival curves (three independent experiments pooled) of

zebrafish larvae injected with WT-GFP Low Dose (WT LD) (blue curve, n = 60) or High Dose (HD) (red curve, n = 60), or with Δ*dotA*-GFP Low Dose (Δ*dotA* LD) (green curve, n = 12) or High Dose (Δ*dotA* HD) (green curve, n = 36), and incubated at 28˚C. Control non-injected fish (CTRL, black curve; n = 72). $P < 0.05$ was considered statistically significant (symbols: **** $P < 0.0001$; ***$P < 0.001$; **$P < 0.01$; *$P < 0.05$. **C**) Bacterial burden evaluation by quantification of % of fluorescent pixel counts from images of individual injected larvae followed over time from 0 to 72 hpi. Each larva was imaged daily, and images were analysed with Fiji for bacterial burden quantification. Five experiments have been pooled, for a total of 28 larvae for WT LD and LD, 18 for Δ*dotA* HD. $P < 0.05$ was considered statistically significant (symbols: **** $P < 0.0001$; ***$P < 0.001$; **$P < 0.01$; *$P < 0.05$. No symbol on graphs means that not statistically differences were observed. **D**) Representative images of *L. pneumophila* dissemination, determined by live imaging using a fluorescence stereomicroscope, of zebrafish AB larvae infected with a LD or a HD of WT-GFP, or a HD of Δ*dotA*-GFP. Individual infected larvae were followed over time by live imaging at 4h, 24h, 48h, and 72h post injection. GFP fluorescence of the injected bacteria is shown. **E**) Scheme of a 72 hpi larva with body (light blue) and yolk (pink) region highlighted. Green dot in the yolk represents bacteria burden. The scheme of the zebrafish larvae has been adapted from [35] and has been previously modified from [87]. **F**) Quantification of bacterial dissemination over time. Larvae injected with LD, HD LD or Δ*dotA* HD were imaged over time, and then scored for the GFP + bacteria absolute presence for each larva over time. Larvae were scored as "infected" when they showed at least one small detectable GFP+ dot. Data obtained were plotted as % of larvae with bacteria in the body (tail, trunk, head; blue curve), or in the yolk (pink curve). 11 independent experiments have been plotted (representing a total of n = 69 WT LD; n = 58 WT HD; n = 54 Δ*dotA* HD infected larvae).

https://doi.org/10.1371/journal.ppat.1011375.g001

with 10^3 or 10^4 CFU of wild type (WT) *L. pneumophila* strain Paris expressing GFP (WT-GFP) or the type IV secretion system (T4SS) deficient isogenic mutant expressing GFP (Δ*dotA*-GFP). The infected larvae were kept at 28˚C and were monitored regularly until 72 hours post infection (hpi) to record survival or death using a stereomicroscope. Larvae infected with doses of up to $2x10^3$ CFU of WT-GFP (defined as low dose, LD) all survived (100% survival). In contrast, larvae infected intravenously with doses of 10^4 CFU (defined as high dose, HD) resulted in approximately 30% of death within 72 hpi (Fig 1B). Importantly, all larvae injected with HD of the Δ*dotA*-GFP strain survived for the entire time of observation (Fig 1B) indicating that the T4SS is crucial for replication in zebrafish larvae, as it is in other infection models and in humans.

The progression of the infection was followed by analysing the bacterial load at 0, 24, 48 and 72 hpi comparing three different methods. First, we quantified the pixel counts of GFP fluorescence of live larvae images (S1A Fig), secondly, we analysed the number of GFP expressing bacteria present in lysed infected larvae by flow cytometry (S1B Fig) and thirdly we plated serial dilutions of homogenates of euthanized larvae on BCYE medium (S1C Fig). The results obtained with the three methods showed a similar trend. However, as *Legionella* are slow growing microbes (at least three days to form colonies on plates), they are rapidly overgrown and outcompeted by the zebrafish-associated microbes, even when using selective *Legionella* agar plates, making counting colonies imprecise. We found that measuring the bacterial burden by Flow Cytometry is technically difficult at later time points, as the fish die due to the high bacterial burden and the bacteria are released from the degrading fish. Thus, the bacteria are removed during the washing steps. In contrast, pixel count values only increase when bacteria are alive and divide, thus increasing pixel counts are an excellent proxy for increasing numbers of bacteria and most accurately represent the bacterial load. Thus, we choose to monitor the *L. pneumophila* load of zebrafish larvae by fluorescent pixel counts on live injected larvae as the primary method. As shown in Fig 1C, where the bacterial burden was evaluated by fluorescent pixel counts on individual injected larvae followed over 72hpi, most larvae injected with LD of WT-GFP progressively control the bacteria by 24 hpi, with only few larvae showing an increase in bacterial numbers at 72hpi. Similarly, HD of Δ*dotA*-GFP were also progressively controlled by 24 hpi. In contrast, some zebrafish larvae injected with HD of WT-GFP were unable to eliminate the bacteria at 72 hpi, and the bacterial counts remained high (Fig 1C). These results were corroborated by FACS analysis on lysed larvae (S2A Fig). We also monitored infected larvae by fluorescence microscopy. Immediately upon injection (20 min to 2 hpi), bacteria were detectable as small foci, probably associated with professional phagocytes (Fig 1D). By 24 hpi, in both, larvae injected with LD of WT-GFP, as well as larvae injected with HD of the avirulent Δ*dotA*-GFP strain, the GFP signal declined becoming undetectable by 48 hpi, suggesting that the bacteria were progressively cleared. Despite

showing the same pattern at 24 hpi, larvae injected with HD of WT-GFP showed an increase in GFP signal at 48 hpi, suggesting that bacterial proliferation occurred in a fraction of the infected larvae. Interestingly, in these larvae, bacterial proliferation occurred mainly in the yolk region where the bacterial foci increased dramatically over time, with concomitant death of the infected larvae by 72 hpi (Fig 1D).

To gain insight into the progression of the infection of LD and HD of WT-GFP or HD of Δ*dotA*-GFP infected larvae, we analysed the bacterial presence in the yolk (pink, Fig 1E), a region where professional phagocytes are unable to enter, and in the rest of the body (tail + trunk + head; blue, Fig 1E), using fluorescence microscopy over time. A single small GFP dot (indicating few bacteria) present in the larvae was scored as positive for infection. We observed that about 60% of larvae injected with HD of WT-GFP and about 20% of larvae injected with LD WT-GFP showed yolk growth at 72 hpi. In contrast, larvae injected with HD of Δ*dotA*-GFP progressively cleared the bacteria, and bacteria were never observed growing in the yolk (Fig 1F). The presence of bacteria in the yolk was intriguing and prompted us to investigate whether this unique feature was dependent on the site of injection of bacteria in the larvae. Thus, we injected 72hpf zebrafish larvae with HD of WT-GFP in different closed cavities such as, the otic vesicle and the hind brain ventricle and compared: larvae survival, bacterial burden, and outcome of bacterial dissemination over time. Only blood stream injected bacteria were found to successfully replicate in zebrafish and establish a proliferative niche in the yolk. This suggests a role of the blood circulation in the capacity of *L. pneumophila* to reach the yolk region and to replicate there (S3A–S3C Fig).

Secondly, we tested if a natural route of uptake could cause infection in zebrafish. As in its usual habitat *L. pneumophila* lives in freshwater and replicates in protozoan hosts [28], it is possible that fish get infected in the environment by taking up infected amoeba. Indeed, amoebae are prey of zebrafish larvae. To test this hypothesis, we infected *A. castellanii* with *L pneumophila* and exposed 120 hpf zebrafish larvae (start of autonomous feeding) to *L. pneumophila* infected *L. pneumophila*-infected amoebae and evaluated bacterial survival (S4A Fig) and bacterial dissemination (S4B–S4D Fig) in the larvae over time. While zebrafish larvae engulfed the infected amoebae, as shown by the GFP signal detectable in the exposed larvae at 48 hours post bacterial exposure (S4C Fig), no permanent infection was established and the engulfed bacteria were evacuated with other faecal content without impact on larvae survival, suggesting that this might not be an important route of infection in the environment.

Collectively these results indicate that only bloodstream injected WT *L. pneumophila* induce a dose dependent death of zebrafish larvae. Larvae that were unable to control infection by 48 hpi, showed a unique infection phenotype, a high increase of the bacterial burden in the yolk region.

Legionella pneumophila replication in the yolk of zebrafish larvae is T4SS dependent

The replication of *L. pneumophila* in the yolk region of infected zebrafish larvae was strictly dependent on a functioning T4SS, as Δ*dotA*-GFP failed to reach the yolk. To investigate whether the secretion mutant can grow in the yolk cell when reaching it, we injected LD and HD of WT-GFP or of Δ*dotA*-GFP *L. pneumophila* directly into the yolk cell cytoplasm of 72 hpf zebrafish larvae (Fig 2A). Surprisingly, Δ*dotA*-GFP did not replicate in the yolk even when injected directly, although it persisted over 48 hpi (Figs 2B, 2C and S2B). When LD or HD of WT-GFP was directly injected into the yolk, a higher rate of bacterial proliferation and larvae death was observed compared to the bloodstream injection whereby 100% of the larvae dying have bacteria replicating in the yolk. (Figs 2B, 2C and S2B). These observations suggest that

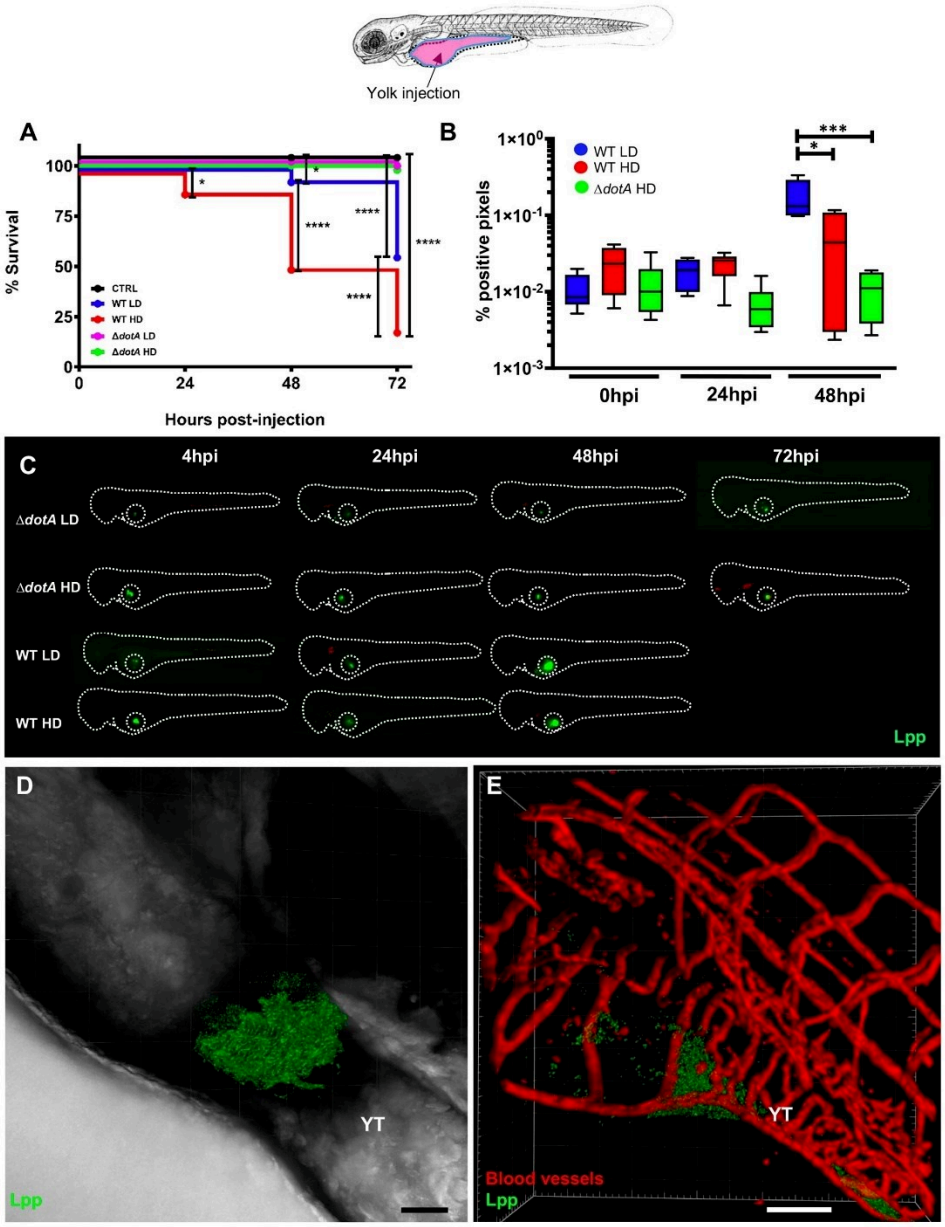
Yolk injection
A
% Survival
Hours post-injection
CTRL
WT LD
WT HD
ΔdotA LD
ΔdotA HD
B
% positive pixels
WT LD
WT HD
ΔdotA HD
0hpi
24hpi
48hpi
C
4hpi
24hpi
48hpi
72hpi
ΔdotA LD
ΔdotA HD
WT LD
WT HD
Lpp
D
YT
Lpp
E
YT
Blood vessels
Lpp

Fig 2. Bloodstream *L. pneumophila* establish a proliferative niche in the yolk causing a persistent local infection. A) Survival curves (two independent experiments pooled) of zebrafish larvae injected into the yolk with WT-GFP Low Dose (WT LD) (blue curve, n = 48) or High Dose (HD) (red curve, n = 48), or with Δ*dotA*-GFP Low Dose (Δ*dotA* LD) (magenta curve, n = 48) or High Dose (Δ*dotA* HD) (green curve, n = 48), and incubated at 28˚C. Non-injected fish (CTRL, black curve; n = 48). The scheme of the zebrafish larvae has been adapted from [35] and has been previously modified from [87]. **B)** Bacterial burden evaluation by quantification of % of fluorescent pixel counts on individual injected larvae followed over time by 0 to 48 hpi. Each larva was imaged daily, and images were analysed with Fiji for bacterial burden evaluation. One experiment plotted, 6 larvae per condition. $P < 0.05$ was considered statistically significant (symbols: **** $P < 0.0001$; *** $P < 0.001$; ** $P < 0.01$; * $P < 0.05$. No symbol on graphs means that not statistically differences were observed). **C)** Representative images of *L. pneumophila* localization, determined by live imaging using a fluorescence stereomicroscope, of zebrafish larvae infected with a LD or a HD of WT-GFP, or a LD or a HD of Δ*dotA*-GFP. Individual infected larvae were followed over time by live imaging at 4h, 24h, 48h, and 72 hpi. GFP fluorescence of the injected bacteria is shown. Dotted circle highlights GFP bacteria in the yolk. **D)** Representative maximum intensity projection of confocal acquisition of a 72 hpi zebrafish larva injected in the bloodstream with HD of WT-GFP, mounted laterally and live imaged using high resolution confocal fluorescence microscope, showing bacteria growing in the yolk and yolk tube (YT) region. The x-y-z raw data were post treated with the LEICA lighting application for reducing noise and processed with Imaris for 3D volume rendering. Related to S1 Movie. **E)** Imaris 3D reconstruction and volume rendering of the *L. pneumophila* growth (GFP labelling) in the yolk of *kdrl*:ras-mCherry (red vessels) infected larva at 72hpi, showed laterally. Overlay of GFP and mCherry is shown; BF is shown to help to visualize the yolk region and host anatomy. YT Related to S2 Movie. Scale bar = 50mm.

https://doi.org/10.1371/journal.ppat.1011375.g002

T4SS system is not only crucial for reaching the yolk region but likely that some of its effectors are necessary for the bacteria to obtain nutrients from the yolk environment to allow replication. To further analyse this hypothesis, we selected a mutant in the gene encoding a sphingosine-1 phosphate lyase, (WT, Δ*spl)* [29], as we reasoned that this enzyme might be implicated in degrading sphingolipids present in the yolk of zebrafish larvae and thereby might aid *L. pneumophila* to obtain nutrients. Injection of Δ*spl* in the yolk sac region, and analyses of larvae death as compared to WT-GFP or Δ*dotA*-GFP howed that survival of zebrafish larvae injected with the Δ*spl* was slightly but significantly higher than with WT injected larvae (S5A Fig), suggesting that the T4SS effector *Lp*Spl might be implicated in nutrient acquisition in the yolk environment.

Interestingly, the first isolation of *L. pneumophila* was achieved by inoculating the yolk region of embryonated eggs probably due to the richness in nutrients provided by the yolk [6]. Thus, we decided to investigate the infection phenotype of *L. pneumophila* WT-GFP and Δ*dotA-GFP* in the yolk sac further using as model embryonated chicken eggs (ECE). We inoculated ECE directly in the yolk region with WT-GFP and with the Δ*dotA* -GFP strain at a median quantity of 8.7 $\log_{10}$ CFU/mL for each and assessed mortality of the embryos daily (calculated form 4 independent experiments and 42 ECE in total). The survival curves were significantly different ($p<0.0001$). The total mortality during the 6-day observation period was significantly higher in WT-GFP infected eggs (95%) than in the Δ*dotA-GFP* infected eggs (18%) or PBS inoculated control eggs (24%) (S5C Fig). The highest mortality was observed at 1 and 2 days post infection in WT-GFP inoculated eggs with 79% mortality at day 2 *versus* 18% in Δ*dotA-GFP* or PBS inoculated eggs. Quantification of *L. pneumophila* in the yolk sac region at the day of mortality or at day 6 post infection revealed that the number of bacteria in the yolk sac of WT-infected ECE, was significantly higher than that in the yolk sac of those infected with the Δ*dotA*- GFP strain (8.5 $\log_{10}$ CFU/mL and 7.4 $\log_{10}$ CFU/mL, respectively, $p = 0.011$) (S5D Fig). Controls inoculated with PBS (n = 4) showed no *L. pneumophila* growth. Thus, like in zebrafish larvae only the WT strain can persist and replicate in the yolk region and of inducing mortality in the embryos, while the T4SS mutant strain persists but is not able to replicate and does not induce high embryo mortality. This result further supports the finding that the T4SS is crucial for obtaining nutrients which might be both, proteins and lipids [30].

Taken together, these results suggest that the *L. pneumophila* T4SS plays a crucial role for the bacteria to pass from the blood circulation into the yolk and that T4SS effectors play an important role to obtain nutrients for bacterial proliferation in the yolk.

Bloodstream *L. pneumophila* establishes a proliferative niche in the yolk region causing a persistent infection

To characterise the *L. pneumophila* foci identified in the yolk region of zebrafish larvae, we used high resolution fluorescence microscopy of HD of WT-GFP *L. pneumophila* injected in the bloodstream of 72hpf zebrafish larvae and analysed them at 72 hpi. This analysis confirmed that these bacterial structures localize in the yolk and or in the yolk tube region (Fig 2D, S1 Movie). *L. pneumophila* foci in the yolk region are highly complex aggregate-like structures of long filamentous bacteria. Moreover, upon injection of HD of WT-GFP in transgenic (Tg) zebrafish larvae Tg (*kdrl*::mCherry)^{is5} (blood vessels, fluorescently labelled red) larvae, we showed that the fast growing bacterial aggregates localize close to the blood vessels, mostly below and probably above the yolk cell. Single bacteria near the aggregates localized within the blood vessels, indicating that the bacteria can cross the endothelial barrier to reach the yolk region (Fig 2E, S2 Movie). To analyse macrophage and neutrophil interactions with the bacterial aggregates in the yolk region, we injected HD of WT-GFP in: Tg(*mfap4*::*mCherryF*) (herein referred as *mfap4*:mCherryF) (macrophages, fluorescently labelled red), or Tg(*Lyz*::*DsRed)*^{nz50} (herein referred as *lyz*:DsRed) (neutrophils, fluorescently labelled red). or Tg(*kdrl*::mCherry)^{is5} zebrafish larvae. At 72 hpi macrophages accumulated around the yolk region containing *L. pneumophila* but did not seem to be able to engulf the bacterial aggregates (Fig 3A, S3 Movie). Similarly, upon injection of HD of WT-GFP in *lyz*:DsRed larvae, at 72 hpi neutrophils accumulated around the growing bacterial aggregates, but seemed also unable to engulf them (Fig 3C, S4 Movie). Strikingly, quantification analyses showed that bacterial colonisation of the yolk of zebrafish larvae injected with the T4SS deficient Δ*dotA* mutant strain, never took place, suggesting that zebrafish susceptibility to *L. pneumophila* infection and yolk penetration depends on a functional T4SS system or the T4SS deficient Δ*dotA* mutant enters a viable but non culturable state (Fig 3D). It should be noted that the yolk is the only food source of the larvae during this developmental stage. The fast proliferation of the bacteria in the yolk region probably depletes its nutritional content, and replicating bacteria may also release toxic compounds, leading to larvae death.

To gain deeper insight into the exact anatomical localisation of the bacteria in the yolk region, we performed high resolution confocal time lapse acquisitions of HD of WT-GFP bloodstream injected larvae harbouring red macrophages between 48 and 72 hpi. We observed that *L. pneumophila* foci seem to localize both above but also below the plasmatic yolk membrane, suggesting that they can cross it, and that professional phagocytes remain above the growing bacterial aggregates failing to engulf them (Fig 3E, S5 Movie). Live imaging showed that both macrophages and neutrophils accumulated around bacteria proliferating in the yolk region. To investigate if professional phagocytes were recruited to the bacteria from other sites, or if only the population located on the yolk was involved, we quantified macrophages and neutrophils in the body and in the yolk of the whole larva over time, focusing on HD of WT-GFP infected larvae. We then separated the larvae with bacterial burden in the yolk from the total population of infected larvae, to specifically analyse the recruitment of professional leukocytes to the bacteria growing in the yolk. Following the same criteria as above, we quantified the bacterial burden of the infected larvae over time. This quantitative analysis showed that macrophages and neutrophils that accumulated where the bacteria are seen in the yolk by 48 hpi, were the ones located on the yolk surface, and that no professional phagocyte population was recruited from the other parts of the body (Figs 3F and S6). Moreover, this analysis confirmed that the bacterial burden increased in the yolk while decreasing in the body and it also revealed a transient decrease of professional phagocyte populations at 24h in infected larvae upon HD of WT-GFP injection (Fig 1E).

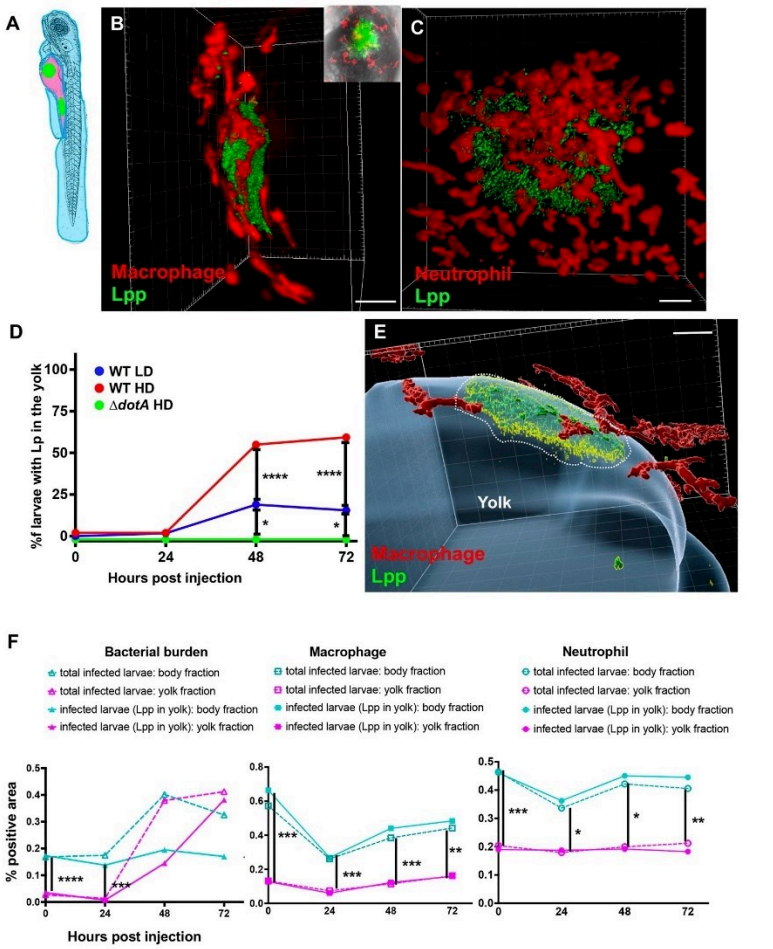

Fig 3. Characterization of the *L. pneumophila* foci growing in the yolk region of zebrafish larvae. A) Scheme of 72hpf with body (light blue) and yolk region (pink) highlighted; the yolk sustaining *L. pneumophila* growing has been indicated with green dots. The scheme of the zebrafish larvae has been adapted from [35] and has been previously modified from [87]. **B)** Imaris 3D reconstruction and volume rendering of the *L. pneumophila* growth in the yolk of 72 hpi *mfap4*: mCherry larva (red macrophages) injected in the bloodstream with HD of WT-GFP at 72hpf, shown laterally. Inset shows the maximum intensity projection of the *L. pneumophila* foci of the same larva mounted ventrally. Scale bar = 20mm. Related to S3 Movie. **C)** Imaris 3D reconstruction and volume rendering of the *L. pneumophila* growth in the yolk of *lyz*:DsRed (red neutrophils) infected larva at 72 hpi, showed laterally. Scale bar = 20mm. Related to S4 Movie. **D)** Quantification of bacterial burden in the yolk over time. Larvae injected with LD, HD WT, or Δ*dotA* HD were imaged over time, and then scored for the GFP + bacteria absolute presence in the yolk for each larva over time. Larvae were scored as "infected" when they showed at least one small detectable GFP + dot. Data obtained were plotted as % of larvae with bacteria in the in the yolk upon LD (blue curve), HD (red curve) WT or Δ*dotA* HD (green curve) injection over time. 11 independent experiments have been plotted (representing a total of n = 69 WT LD; n = 58 WT HD; n = 54 Δ*dotA* HD infected larvae) **E)** Time frame extracted from a 4D acquisition of *L. pneumophila* growth in the yolk between 48 and 72 hpi of *mfap4*: mCherry larva (red macrophages) injected in the bloodstream with HD of WT-GFP shown laterally. Imaris 4D reconstruction and volume rendering of the bacteria aggregate and interaction with macrophages. The yolk has been manually highlighted (in blue) with

Imaris. Scale bar: 10. Related to S5 Movie. **F)** Quantification of bacterial burden in the whole body, in the body or in the yolk region versus macrophage or neutrophil quantification in the body or in the yolk region in HD WT-GFP infected larvae followed over time. Two independent experiments plotted for each phagocyte type (total of 11 larvae for macrophage and 11 larvae for neutrophil quantification). Quantification of the fluorescence images (GFP bacteria and RFP leukocytes) was done using CellProfiler software. $P < 0.05$ was considered statistically significant (symbols: **** $P < 0.0001$; *** $P < 0.001$; ** $P < 0.01$; * $P < 0.05$). No symbol on graphs means that not statistically differences were observed.

https://doi.org/10.1371/journal.ppat.1011375.g003

Thus, blood-borne *L. pneumophila* can invade the yolk sac of zebrafish larvae, a previously undescribed phenotype of bacterial infection in this model. Once in the yolk, the bacteria replicate extensively, forming complex, organized, aggregate-like structures that cannot be removed by macrophages and neutrophils, thereby avoiding the host's immune control and clearance, and eventually causing the death of the larvae.

Infection of zebrafish larvae with high doses of *L. pneumophila* leads to macrophage and neutrophil death

In human infection, alveolar macrophages are the primary cell type infected by *L. pneumophila* supporting its intracellular replication. Following infection, neutrophils are recruited to the lung and are key players for controlling infection as they possess antimicrobial activity and kill *L. pneumophila* [31]. In this study, the recruitment of professional leukocytes to bacteria in the yolk following HD ofWT-GFP larvae infection revealed a decrease of professional phagocyte populations over time (Fig 3F). Thus, to analyse whether zebrafish infection mirrors human infection, we monitored the behaviour of zebrafish macrophages or neutrophils over time. The zebrafish larvae *mfap4*:mCherryF and *lyz*:DsRed were injected with LD or HD of WT-GFP or with high doses HD of Δ*dotA*-GFP. Infected live larvae were monitored using widefield fluorescence microscopy and the number of leukocytes per larva was assessed by counting fluorescent macrophages and neutrophils over time until 72 hpi. We observed that upon injection of HD of WT-GFP, the macrophage count decreased dramatically at 24 hpi and 48 hpi, but started to increase at 72 hpi (Fig 4A). Neutrophil counts gave similar results at 24 and 48 hpi upon injection of HD of WT bacteria, as there was a dramatic decrease observed in neutrophil numbers by 24 hpi. However, the neutrophil counts were still decreased at 72 hpi (Fig 5A). In contrast macrophage and neutrophil counts remained unaffected upon injection of equal amounts of the avirulent Δ*dotA*- GFP strain, with a slight increase of neutrophil numbers at 72 hpi, suggesting that phagocyte death is linked to a functional T4SS system (Figs 4A and 5).

Taken together, these results show that high dose *L. pneumophila* infection leads to a decrease in the number of professional phagocytes dependent on the T4SS, like what is seen during human infection by *L. pneumophila* or *Mycobacterium tuberculosis* [31,32]

Macrophages are the primary cells to phagocytise blood-borne *Legionella pneumophila* and neutrophils co-operate to decrease bacterial load

As macrophages and neutrophils are the phagocytes known to interact with *L. pneumophila* we analysed phagocyte-*L. pneumophila* interactions *in vivo* by injecting *mfap4*:mCherryF or *lyz*:DsRed 72hpf larvae with WT-GFP or Δ*dotA*-GFP and recorded phagocyte-*L. pneumophila* interactions using high resolution confocal microscopy. This showed that upon injection of LD WT-GFP, macrophages immediately contacted and engulfed blood-borne bacteria. Macrophages were continuously recruited to the site of injection and by 16 hpi the bacteria were mostly undetectable while macrophage numbers increased (Fig 4B top panel, S6 Movie). Macrophages that had engulfed a large amount of *L. pneumophila* stopped moving and rounded-

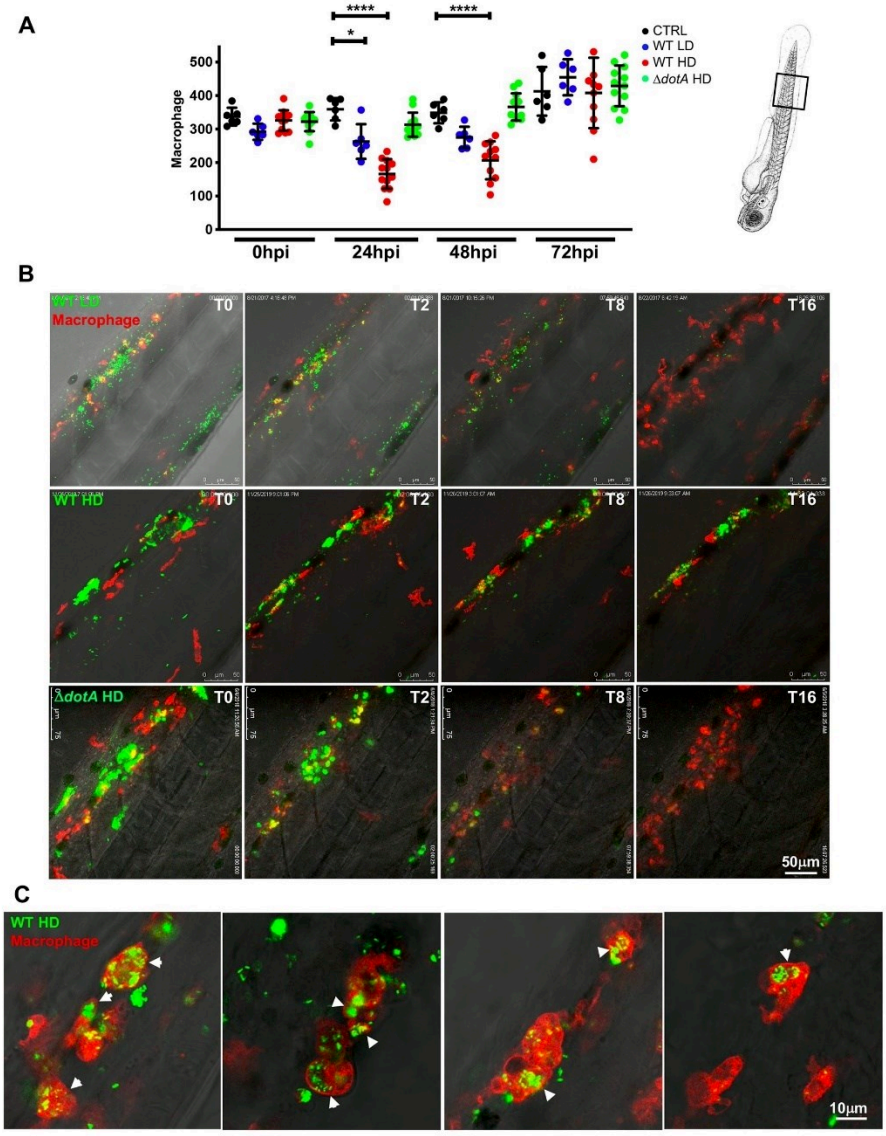

Fig 4. *L. pneumophila* high dose injection results in (systemic) macrophage and neutrophil death. A) Macrophage counts of control larvae (black symbols) or upon Low Dose (blue symbols) or High Dose of WT-GFP (red symbols), or High Dose (green symbols) of Δ*dotA* -GFP injection. The scheme of the zebrafish larvae has been adapted from [35] and has been previously modified from [87]. Macrophages were counted manually from images taken on live infected larvae over time from T0 to T72 hpi, using ImageJ software, and results were plotted using GraphPad Prism software. Mean±SEM are also shown (horizontal bars). Data plotted are from two pooled independent experiments (n = 12 larvae scored for each condition). $P < 0.05$ was considered statistically significant (symbols: **** $P < 0.0001$; *** $P < 0.001$; ** $P < 0.01$; * $P < 0.05$). No symbol on graphs means that not statistically differences were observed. **B)** Frames extracted from maximum intensity projection of *in vivo* time-lapse confocal fluorescence microscopy of 72hpf Tg(*mfap4*::*mCherryF*)

larvae injected in the bloodstream (iv) with a LD, HD (of WT-GFP or a HD of Δ*dotA*-GFP (upper panel) or Tg(*LysC*::*DsRed*)^{nz50} in the bloodstream with a LD, HD of WT-GFP or a HD of Δ*dotA*-GFP (lower panel) to follow macrophage bacteria interaction over time during the first 16 hpi. Overlay of green (*L. pneumophila*) and red (leucocytes) fluorescence of the caudal area of the larvae (region boxed in the scheme on the right of the panel) is shown. BF helps for anatomical region indication. Representative of n = 12 to 16 injected larvae for each condition. Scale bar: 50μm. See also related S6 Movie. **C)** macrophage *L pneumophila* interaction at 72 hpi captured at high resolution upon HD WT injection. Bacteria inside zebrafish macrophages suggesting the establishment of a replicative niche (arrows), as documented for cultured mammalian macrophages or amoebae. Representative of n = 15 scored infected larvae. Overlay of green (GFP bacteria), red (mCherry macrophages) and BF is shown. Scale bar = 10mm.

https://doi.org/10.1371/journal.ppat.1011375.g004

up. Similarly, the inhibition of the migration of phagocytes by *L. pneumophila* has been observed previously during infection of RAW 264.7 macrophages and the amoeba *Dictyostelium discoideum* and *Acanthamoeba castellanii*, [33,34]. In contrast, zebrafish injected with HD of WT-GFP were not able to restrict the bacterial growth by 16 hpi. Injection of HD of *L pneumophila* led to the formation of big bacterial aggregates, that were not easily engulfed and cleared by macrophages, as previously shown for bacterial aggregates proliferating in the yolk region (Fig 4B, second panel, S6 Movie). Remarkably, macrophages were very efficient in engulfing and rapidly clearing high doses and big bacterial aggregates of blood-borne Δ*dotA*-GFP bacteria. By 10 hpi most of the Δ*dotA* bacteria and bacterial aggregates had been engulfed and cleared as suggested by the diffuse GFP staining in phagocytes (Fig 4B, bottom panel, S6 Movie). However, upon infection with a HD of WT-GFP, bacteria were not completely cleared and at 72 hpi *L. pneumophila* were found in macrophages, suggesting that the bacteria are also replicating in macrophages of zebrafish larvae. Indeed, high resolution confocal microscopy showed that at 72 hpi, *L. pneumophila* are also found inside of macrophages in structures resembling replicative vacuoles (Fig 4C).

The analyses of *L. pneumophila*-neutrophil interactions showed that these cells engulfed the bacteria trapped in the mesenchyme around the site of injection, but they were less efficient at clearing blood-borne bacteria. This has also been previously observed for infection of zebrafish larvae with *Escherichia coli* or *Shigella flexneri* [26,35]. Indeed, upon injection with a HD of WT-GFP, neutrophils failed to restrict *L. pneumophila*, leading to massive death of infected neutrophils, they rounded up and lost their fluorescence (Fig 5B, second panel; S7 Movie; Fig 5C; S8 Movie). In sharp contrast, neutrophils very efficiently engulfed and cleared large amounts of Δ*dotA*-GFP aggregated and trapped in the mesenchyme (Fig 5B, lower panel, S7 Movie) as well as when fish were injected with LD of WT-GFP (Fig 5B upper panel, S7 Movie).

Altogether this shows that upon low dose bloodstream injection of *L. pneumophila*, macrophages and neutrophils efficiently cooperate to eliminate most of the injected bacteria within 20–24 hpi, with macrophages playing the primary role. However, *L. pneumophila* seems to persist upon high dose WT-GFP injection, and the observation of structures resembling large vacuoles containing *L pneumophila* at 72 hpi suggests that they can replicate in zebrafish macrophages. In contrast, neutrophils interact with *L. pneumophila* by quickly engulfing bacteria trapped in the mesenchyme near the site of injection but are less efficient in clearing blood-borne bacteria.

Macrophages are the first line defence restricting *L. pneumophila* infection

In humans, innate immune responses, based essentially on the activity of professional phagocytes and the induction of pro-inflammatory cytokine genes, are the key players to control and restrict *L. pneumophila* proliferation. Hence, human disease develops primarily in immunocompromised individuals [10]. To investigate whether the phagocytes of the innate immune system, macrophages and neutrophils, are also responsible for controlling *L. pneumophila* infection in zebrafish larvae, we selectively and transiently depleted macrophages or

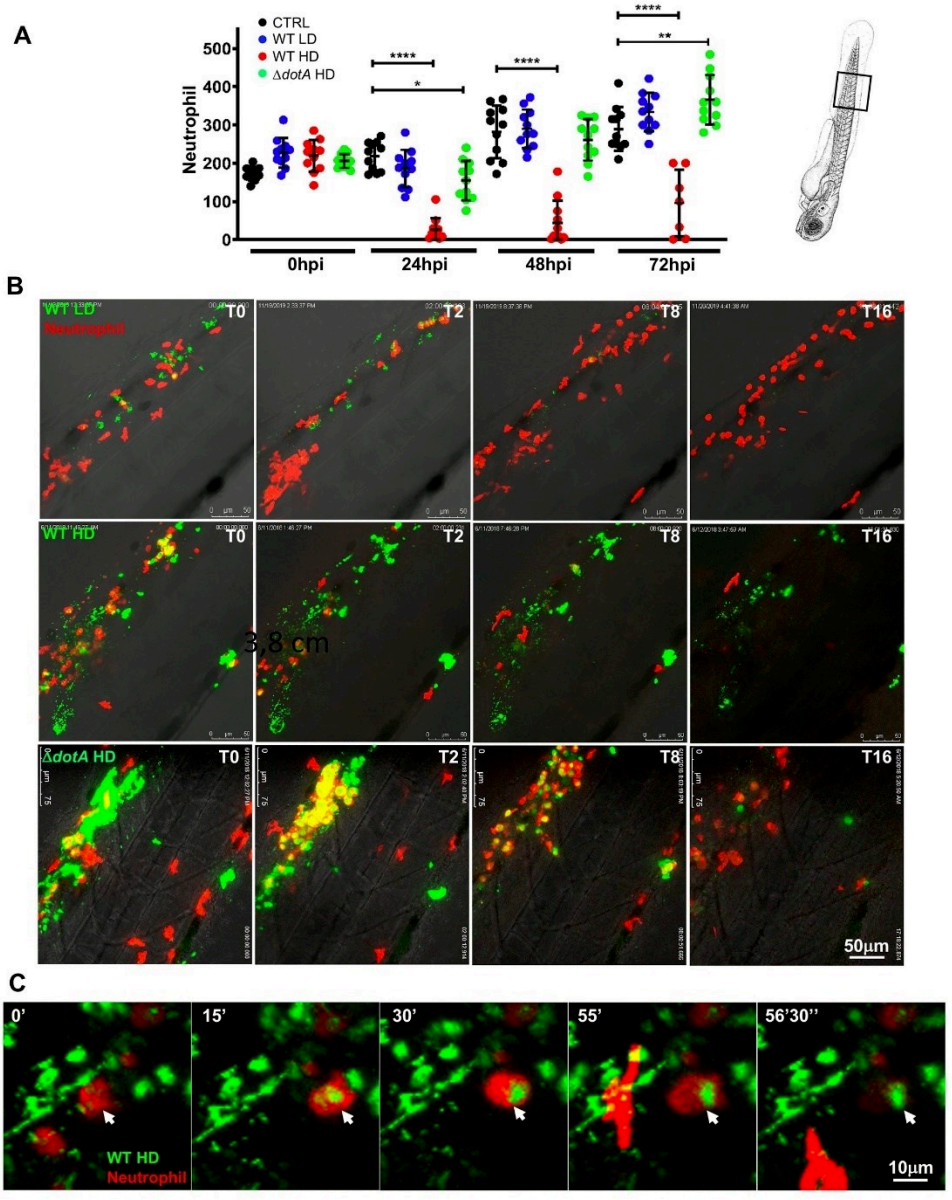

Fig 5. *L. pneumophila* interaction with neutrophils and neutrophil counts upon bloodstream injection of LD, HD WT GFP or HD ΔdotA *L. pneumophila*. A) Neutrophil counts from control larvae (CTRL, black symbols) or Low Dose or High Dose of WT-GFP (blue or red symbols), or High Dose of Δ*dotA*-GFP (green symbols) injected larvae. The scheme of the zebrafish larvae has been adapted from [35] and has been previously

modified from [87]. Data plotted in the same way as for macrophage counts in Fig 4. Two pooled independent experiments (n = 10 larvae scored for each condition). $P < 0.05$ was considered statistically significant (symbols: **** $P < 0.0001$; *** $P < 0.001$; ** $P < 0.01$; * $P < 0.05$). No symbol on graphs means that not statistically differences were observed. **B)** Frames extracted from maximum intensity projection of *in vivo* time-lapse confocal fluorescence microscopy of 72hpf Tg(*LysC::DsRed)*^{nz50} in the bloodstream (iv) with a LD, HD of WT-GFP or a HD of Δ*dotA*-GFP (lower panel) to follow neutrophil interaction with *L. pneumophila* immediately upon injection for 16 hpi. Images were taken from time lapse at different time points (0 hpi, 2 hpi, 4 hpi, 8 hpi and 16 hpi). Overlay of green (*L. pneumophila*) and red (neutrophils) fluorescence of the caudal area of the larvae (region boxed in the scheme on the right of the panel) is shown. Data representative of n = 12 to 16 larvae scored. Scale bar: 50μm. See also related S7 Movie. **C)** Details of a dying phagocytosing neutrophil, progressively rounding-up and loosing fluorescence upon HD WT injection. Arrowheads point to the dying phagocytosing neutrophils. Representatives of n = 14 larvae scored. Scale bar = 10mm. See also related S8 Movie.

https://doi.org/10.1371/journal.ppat.1011375.g005

neutrophils, and infected these "immunocompromised" larvae with *L. pneumophila*. Depletion of macrophages was achieved by knocking down the expression of s*pi1b*, a transcription factor involved in early myeloid progenitor formation. A low dose of s*pi1b* morpholino was reported to impact macrophages without affecting neutrophils [36]. We monitored the effect of low doses s*pi1b* morpholino injection on macrophage and neutrophil populations in double transgenic larvae with green neutrophils (*mpx*:GFP) and red macrophages (*mfap4*:mCherryF). The specific depletion of macrophages was confirmed by counting macrophages and neutrophils at 72hpf (S7A Fig).

We then infected macrophage depleted larvae (s*pi1b* knockdown) by intravenous injection of LD or HD of WT-GFP. Regardless of the infection dose, a dramatic decrease in larvae survival was observed, as even injection of low doses of WT-GFP resulted in the death of 30% of the larvae (Fig 6A). When injecting HD of WT-GFP nearly all the infected larvae died by 72 hpi, with the earliest deaths starting 48 hpi (Fig 6A). In contrast, s*pi1b* knockdown larvae injected with HD of Δ*dotA*-GFP did not show impaired survival (Fig 6A). The increased mortality correlated with an increased but not significantly different bacterial burden in the s*pi1b* knockdown larvae compared to control larvae (Figs 6B and S2C). Intravital imaging of infected s*pi1b* knock down larvae also showed that both LD and HD of WT-GFP failed to be cleared and that the bacteria established a replicative niche in the yolk, where they proliferated extensively (Fig 6C). This highlights, that macrophages are critical to restrict the onset of infection and *L. pneumophila* proliferation *in vivo*. Furthermore, these results also suggest that neutrophils, which are not depleted in s*pi1b* knockdown larvae, fail to control *L. pneumophila* infection in the absence of macrophages.

To analyse the role of neutrophils in controlling the infection, neutrophil development was disrupted by knocking down the G-CSF/GCSFR pathway using *csf3R* morpholino, previously reported to decrease up to 70% of the neutrophils present [37–39]. First, we monitored the efficiency of the *csf3R* morpholino knockdown in double transgenic larvae, and confirmed that 75% of the neutrophil population was depleted, while macrophage numbers were only slightly decreased (S7B Fig). When HD of Δ*dotA*-GFP was the bacterial burden remained unchanged, as observed in infections of macrophage-depleted larvae (Fig 6D and 6E). However, when neutrophil-depleted larvae were injected with HD of WT-GFP, larvae survival significantly decreased and bacterial burdens slightly increased by 48 hpi (Figs 6D, 6E and S2D). Intravital imaging revealed that those *csf3R* knockdown larvae that were unable to control *L. pneumophila* infection showed bacterial proliferation in the yolk comparable to WT larvae (Fig 6F).

These results show that both macrophages and neutrophils are required for restricting and controlling *L. pneumophila* infection in the zebrafish model, but macrophages play the main role. Although neutrophils contributed less to clear the bacteria upon bloodstream injection, neutrophils might impact the infection outcome through cytokine release that can modulate macrophage activity.

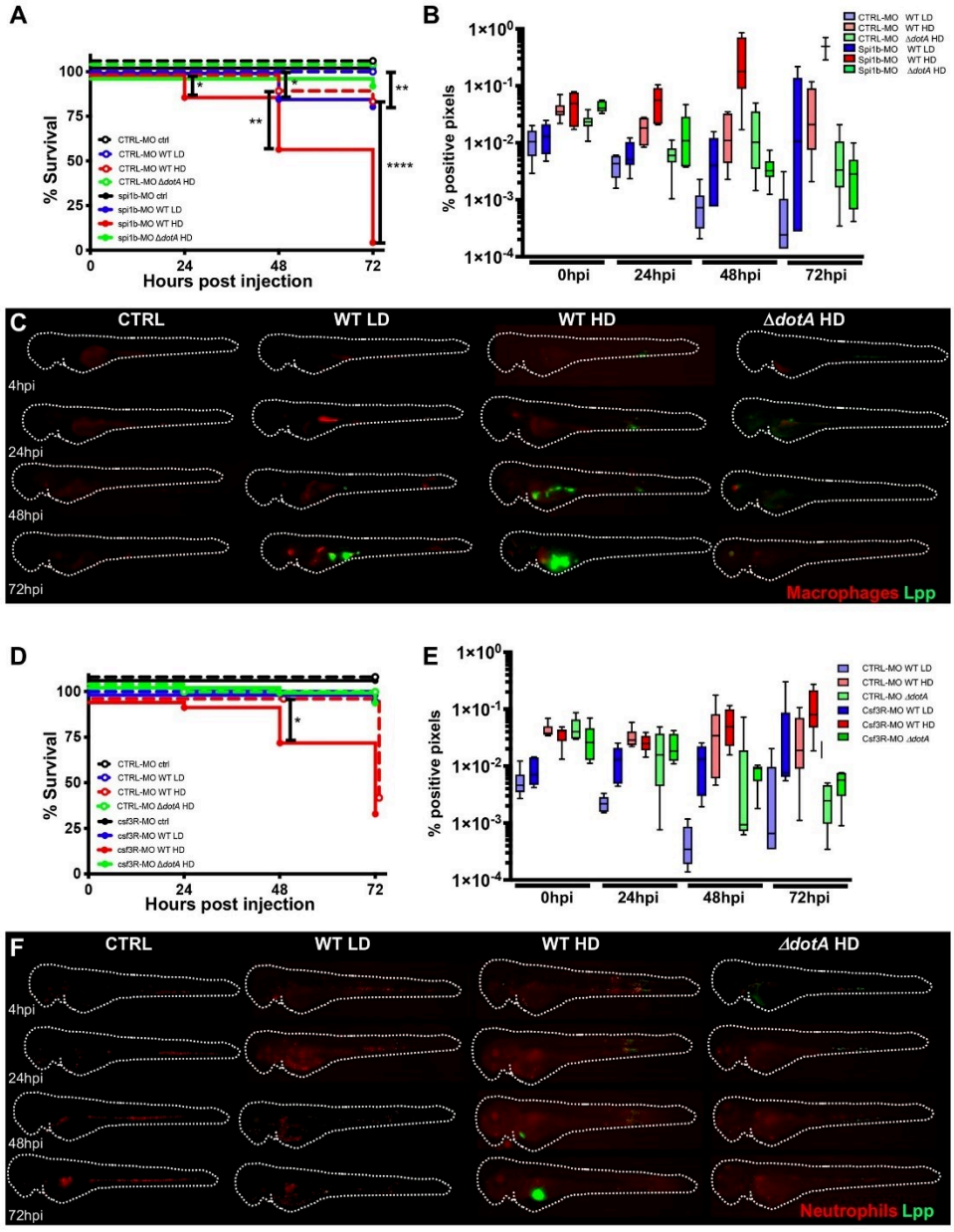
A
% Survival
Hours post injection
CTRL-MO ctrl
CTRL-MO WT LD
CTRL-MO WT HD
CTRL-MO ΔdotA HD
spi1b-MO ctrl
spi1b-MO WT LD
spi1b-MO WT HD
spi1b-MO ΔdotA HD
B
% positive pixels
0hpi
24hpi
48hpi
72hpi
CTRL-MO WT LD
CTRL-MO WT HD
CTRL-MO ΔdotA HD
Spi1b-MO WT LD
Spi1b-MO WT HD
Spi1b-MO ΔdotA HD
C
CTRL
WT LD
WT HD
ΔdotA HD
4hpi
24hpi
48hpi
72hpi
Macrophages Lpp
D
% Survival
Hours post injection
CTRL-MO ctrl
CTRL-MO WT LD
CTRL-MO WT HD
CTRL-MO ΔdotA HD
csf3R-MO ctrl
csf3R-MO WT LD
csf3R-MO WT HD
csf3R-MO ΔdotA HD
E
% positive pixels
0hpi
24hpi
48hpi
72hpi
CTRL-MO WT LD
CTRL-MO WT HD
CTRL-MO ΔdotA
Csf3R-MO WT LD
Csf3R-MO WT HD
Csf3R-MO ΔdotA
F
CTRL
WT LD
WT HD
ΔdotA HD
4hpi
24hpi
48hpi
72hpi
Neutrophils Lpp

Fig 6. Macrophages are crucial to restrict *Legionella pneumophila* dissemination. A) Survival curves of CTRL morphant zebrafish larvae injected with a Low Dose (LD) (blue dashed curve, n = 34 larvae) or a High Dose (HD) (red dashed curve, n = 34) of WT-GFP, or with a HD (green dashed curve, n = 24) of Δ*dotA* -GFP, and *spi1b* morphant zebrafish larvae injected with a LD (blue curve, n = 48) or a HD (red curve, n = 48) of WT-GFP, or with a High Dose (HD) (green curve, n = 48) of Δ*dotA* -GFP. Non-injected CTRL morphant fish (black dashed curve, n = 48), and *spi1b* morphant fish (black curves, n = 48) were used as control. Infected and control larvae were incubated at 28˚C. Data plotted are from two pooled independent experiments. **B)** and **E)** Bacterial burden evaluation by quantification of % of fluorescent pixel counts on individual injected larvae followed over time by 0 to 72 hpi. Each larva was imaged daily, and images were analysed with Fiji for bacterial burden evaluation. One experiment per phagocyte type plotted, 6 larvae for each condition. **D)** Survival curves of CTRL morphant zebrafish larvae injected with a LD (blue dashed curve, n = 36) or a HD (red dashed curve, n = 36) of WT-GFP, or with a HD (green dashed curve, n = 24) of Δ*dotA* -GFP, and *csf3r* morphant zebrafish larvae injected with a LD (blue curve, n = 24) or a HD (red curve, n = 36) of WT-GFP, or with a HD (green curve, n = 36) of Δ*dotA* -GFP. Non-injected CTRL morphant fish (black dashed curve, n = 48), and *csf3r* morphant fish (black curve, n = 36) were used as control. Data plotted are from two pooled independent experiments. Significant differences are highlighted with stars (see experimental procedure for statistical analysis) **C)** and **F)** Representative images of *L. pneumophila* dissemination, determined by live imaging using a fluorescence stereomicroscope, of Tg(*mfap4*::*mCherryF*) *spi1b* morphant larvae (**C**) and of Tg(*LysC*::*DsRed*)^{nz50} (**F**) *csf3r* morphant larvae non infected, or infected with a LD or a HD of WT-GFP, or a HD of Δ*dotA*-GFP. The same infected larvae were live imaged 4h, 24h, 48h, and 72h post *L. pneumophila* injection. Overlay of GFP and mCherry fluorescence is shown. $P < 0.05$ was considered statistically significant (symbols: **** $P < 0.0001$; ***$P < 0.001$; **$P < 0.01$; *$P < 0.05$). No symbol on graphs means that not statistically differences were observed.

https://doi.org/10.1371/journal.ppat.1011375.g006

Key pro-inflammatory cytokine genes are induced upon *L. pneumophila* infection of zebrafish larvae

Proinflammatory cytokines produced by infected and bystander cells during *L. pneumophila* infection of humans and mice play crucial roles in orchestrating host defences to control infection [40,41]. Infected cells produce IL-1α and IL-1β through a mechanism involving myeloid differentiation factor 88 (MyD88)-dependent translational bypass. In contrast, bystander cells produce: IL-6, TNF-α and IL-12 in an IL-1 receptor (IL-1R) dependant way [40,42]. To determine the pro-inflammatory responses of zebrafish larvae during *L. pneumophila* infection, we analysed *il1b*, *tnfa*, and *ifng1/2* (orthologues of mammalian *Ifng*) gene expression levels over time by qRT-PCR on RNA isolated from individual infected larvae. We found that infection of zebrafish larvae with LD or HD of WT-GFP induced a rapid (by 6 hpi) and robust induction of *il1b* and *tnfa* gene expression. In larvae injected with LD of WT-GFP the expression levels of *il1b* and *tnfa* started to decrease by 24 hpi, and gradually became undetectable at 72 hpi. In contrast, larvae injected with HD of WT-GFP, expression of *il1b* and *tnfa* did not decrease over time (Fig 7A and 7B) and a significant induction of *ifng1* was observed at 48 hpi (Fig 7C) but not of *ifng2* (Fig 7D). In parallel, we scored the bacterial burden of the infected larvae before the measurement of pro-inflammatory cytokine gene induction at each time point under the microscope, which consistently showed that larvae with increased *il1b* and *tnfa* induction also had high bacterial burdens in the yolk and were not controlling the infection (S8A FIg). These pro-inflammatory responses were T4SS dependent, as zebrafish larvae infected with HD of Δ*dotA*-GFP did not show significant induction of transcription of *tnfa*, *il1b* and *ing1/2* (Fig 7A-7D).

Collectively, these results reveal that key pro-inflammatory cytokines known to orchestrate the host response during *L. pneumophila* infection in humans, are also induced in zebrafish larvae, and that cytokine gene induction is sustained when uncontrolled *L. pneumophila* proliferation occurs.

The immune response of zebrafish larvae to L. pneumophila infection is independent of MyD88 signalling

In innate immunity, MyD88 plays a pivotal role in immune cell activation through Toll-like receptors (TLRs). MyD88-deficient mice are highly susceptible to *L. pneumophila* infection [43–46], however this is not the case when human macrophages are depleted of MyD88 [47]. Therefore, we sought to analyse which role MyD88 plays in zebrafish larvae during *L.*

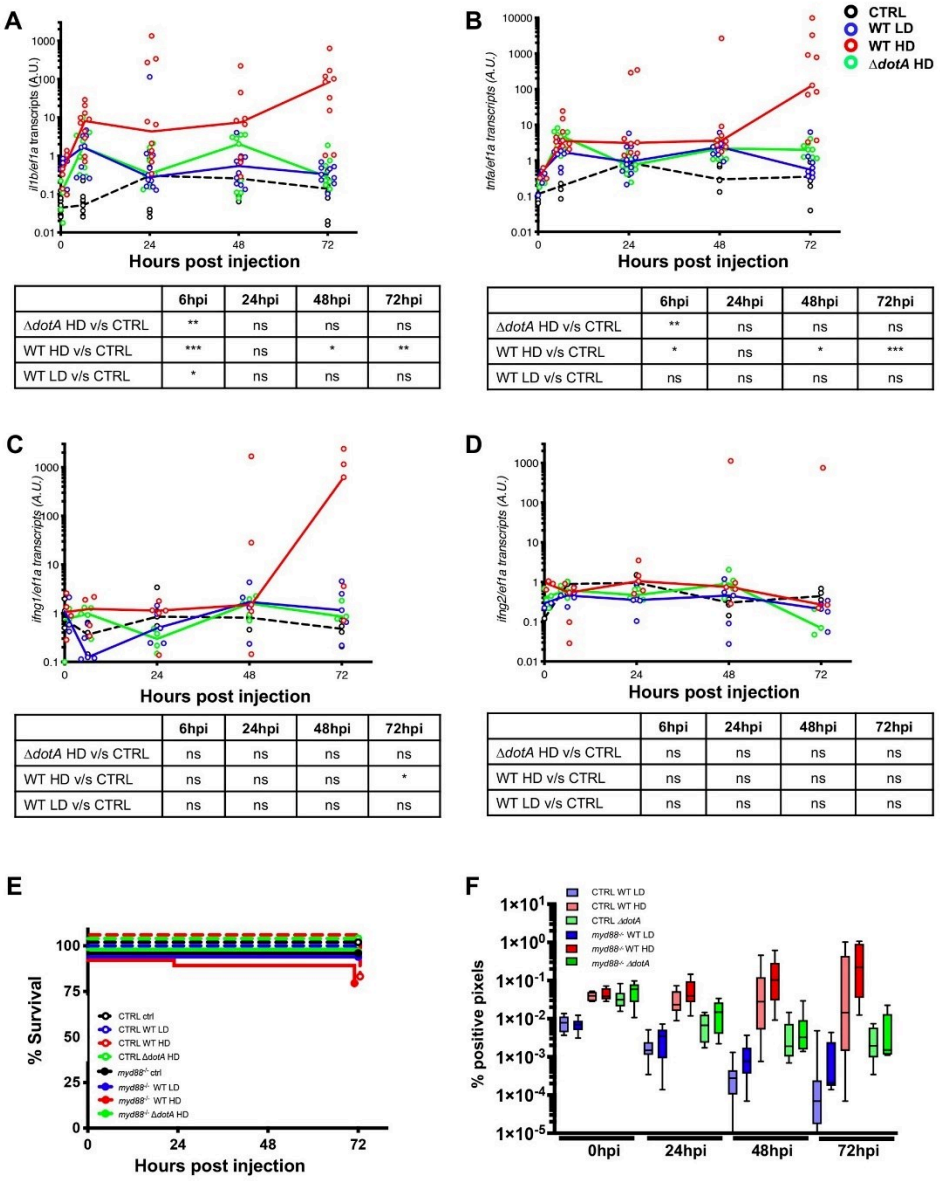

	6hpi	24hpi	48hpi	72hpi
Δ*dotA* HD v/s CTRL	**	ns	ns	ns
WT HD v/s CTRL	***	ns	*	**
WT LD v/s CTRL	*	ns	ns	ns

	6hpi	24hpi	48hpi	72hpi
Δ*dotA* HD v/s CTRL	**	ns	ns	ns
WT HD v/s CTRL	*	ns	*	***
WT LD v/s CTRL	ns	ns	ns	ns

	6hpi	24hpi	48hpi	72hpi
Δ*dotA* HD v/s CTRL	ns	ns	ns	ns
WT HD v/s CTRL	ns	ns	ns	*
WT LD v/s CTRL	ns	ns	ns	ns

	6hpi	24hpi	48hpi	72hpi
Δ*dotA* HD v/s CTRL	ns	ns	ns	ns
WT HD v/s CTRL	ns	ns	ns	ns
WT LD v/s CTRL	ns	ns	ns	ns

Fig 7. Cytokine gene induction upon *L. pneumophila* infection and zebrafish larva Immunity to *L. pneumophila* is independent from signalling through MyD88 or compensated by other signalling pathways. A-D) Cytokine gene (*il1b*, *tnfa*, *ifng1*, *ifng2*) induction was measured from non-injected larvae as control (CTRL, dashed black curves) and individual zebrafish larvae injected with a LD (blue curves) or a HD (red

curves) of WT-GFP, or a HD of Δ*dotA*-GFP (green curves). Data plotted are from 2 pooled experiments (n = 10 larvae for each condition) for *il1b* and *tnfa*, and from 1 experiment (n = 5 larvae for each condition) for *ifng1* and *ifng2*; individual values are shown, and curves correspond to the medians. Statistical analyses are shown in the table under each graph. **E)** Survival curves of CTRL zebrafish larvae injected with WT-GFP Low Dose (LD) (blue dashed curve) or High Dose (HD) (red dashed curve), or with Δ*dotA* -GFP HD (green dashed curve), and *myd88*^{hu3568} mutant zebrafish larvae injected with WT-GFP LD (blue curve) or HD (red curve), or with Δ*dotA* -GFP HD (green curve). Non-injected CTRL larvae (black dashed curves), and *myd88*^{hu3568} mutant larvae (black curves) were used as control. Infected and control larvae (n = 72 fish for *myd88*^{hu3568} mutant conditions and n = 57 fish for CTRL conditions) were incubated at 28˚C. Data plotted are from 3 pooled independent experiments. **F)** Bacterial burden evaluation by quantification of % of fluorescent pixel counts on individual injected larvae followed over time from 0 to 72 hpi. Each larva was imaged daily, and images were analysed with Fiji for bacterial burden evaluation. Two pooled experiments, 8 larvae for each condition. $P < 0.05$ was considered statistically significant (symbols: **** $P < 0.0001$; *** $P < 0.001$; ** $P < 0.01$; * $P < 0.05$). No symbol on graphs means that not statistically differences were observed.

https://doi.org/10.1371/journal.ppat.1011375.g007

pneumophila infection. We injected *myd88*-/- and WT larvae with LD or HD of WT-GFP, or with HD of Δ*dotA*-GFP and monitored larvae survival and bacterial burden over time as described in Fig 1. Our results show that susceptibility to infection of *myd88*-/- larvae injected with HD of WT-GFP was comparable to that of WT larvae, as only a very slight, but no significant increase of bacterial burden was observed in *myd88*-/- larvae by 24 hpi. When *myd88*-/- larvae or WT larvae were injected with Δ*dotA*-GFP, infection was not established and the bacterial burden decreased over time, indicating that bacteria were cleared (Figs 7E, 7F and S2E). To determine if pro-inflammatory responses were affected in the absence of MyD88 signalling, we analysed *il1b*, *tnfa* and *ing1/2* gene expression levels over time in WT and *myd88*-/- larvae. Our results showed that *il1b*, *tnfa* and *ing1/2* gene expression levels were comparable in the WT control and *myd88*-/- infected larvae for all tested conditions LD of WT-GFP and HD of Δ*dotA*-GFP (S8B and S8C Fig).

Taken together, our results suggest that MyD88 signalling is not required for the innate immune response against *L. pneumophila* infection in the zebrafish larvae, corroborating what has been observed in human cell infection models. However, we cannot exclude that MyD88 signalling may also be functionally compensated by other immune signalling pathways.

Discussion

In this study, we developed a zebrafish larva infection model for *L. pneumophila* and have analysed host pathogen interactions as well as the host innate immune response to infection. We have found that a successful infection of zebrafish larvae by *L. pneumophila* depends on: the infection site, the infection dose, the T4SS Dot/Icm and the innate immune response of the host, in particular on the action of macrophages and neutrophils. Wild type zebrafish larvae are susceptible to infection in a dose dependent manner, as larvae injected in the bloodstream with increasing doses of bacteria, developed an infection with bacterial dissemination and replication, concomitant with host death proportional to the initial injected bacterial load. However, the fact that only about 30% of the larvae displayed this phenotype, indicates that the innate immune defence of the larvae against *L. pneumophila* infection is relatively efficient. Thus, the establishment of infection in zebrafish larvae is determined not only by the infection dose but also by the capacity of the host immune system to quickly and efficiently fence off the infection.

Like in the zebrafish infection models for *Staphylococcus aureus* and *Shigella*, only blood borne *L. pneumophila* can proliferate and induce mortality in zebrafish larvae [48,49]. Once in the blood circulation, bacteria are engulfed and are eliminated by both macrophages and neutrophils in a dose-dependent manner. However, T4SS competent *L. pneumophila* are also able to reach the yolk region, cross the endothelium of the yolk vessels and enter the yolk sac region. Once there, *L. pneumophila* gains a significant advantage in the pathogen-host arms race and establishes a replicative niche where it proliferates extensively, forming complex,

aggregated bacterial structures, located below and above the yolk cell membrane, that professional phagocytes fail to clear. In the yolk sac region *L. pneumophila* is protected from professional phagocytes as they are unable to enter the yolk. Extensive proliferation of the bacteria eventually leads to host death, likely due to exhaustion of the nutrients present in the yolk, which are key in supporting the larvae development. Additionally, the bacteria may also release compounds toxic for the larvae. Interestingly, we have also observed that in few cases (less than 5%) the infected larvae were able to extrude the bacterial aggregates growing in the yolk and survived. This host defence mechanism has also been reported in a caudal fin model of *Mycobacterium marinum* infection, where infected zebrafish larvae extruded the bacteria-containing granuloma and during infection with *Aspergillus fumigatus* [50,51].

To our knowledge, the tropism, and the establishment of a replicative niche in the yolk upon pathogen injection in the bloodstream is a unique feature of *L. pneumophila*. Our results have shown that, when macrophages and neutrophils are depleted, blood-borne *L. pneumophila* can still reach the yolk cell. It seems that *L. pneumophila* can cross the venous endothelium of the yolk and reach the nutrient-rich content of the yolk cell. Interestingly, direct yolk cell injection revealed that only the WT but not the T4SS knockout strain is able to replicate and establish a persistent infection in the yolk, irrespective of the dose injected. This result points towards the involvement of the T4SS system and its secreted effectors in infection and replication but also nutrient uptake in the yolk environment. Yolk sac injection has already been used previously for the analyses of *Candida albicans* infection or the study of streptococcal infections, however in these cases the pathogens disseminated from the yolk sac into the animal [52,53], a phenotype not observed when *L. pneumophila* was injected in the yolk sac. The preference for the yolk sac as a replicative niche, was further analysed in embryonated chicken eggs. Again only WT *L. pneumophila* was able to replicate in the yolk region, not the T4SSS mutant (S5A–S5C Fig), demonstrating that the T4SS is necessary to establish the yolk as a replicative niche, perhaps *via* its roles in nutrient uptake. *L. pneumophila* is known to mainly use amino acids as carbon and energy sources for growth [54] and secreted T4SS effectors have been shown to aid in amino acid uptake [55]. However, fatty acids, glucose and/or glycerol also serve as carbon sources during the later stages of the life cycle of *L. pneumophila* [56,57], but effectors connected to the uptake of these nutrients have not yet been identified. The yolk cell is composed of a complex and dynamic mixture of different lipids on which the zebrafish larvae rely for nutrition throughout development in the early larva phase. Cholesterol and phosphatidylcholine are the main constituents until 120hpf. Triacylglycerol, phosphatidylinositol, phosphatidylethanolamine, diacyl-glycerol, cholesteryl esters and sphingomyelins are also present in significant concentrations [58]. *L. pneumophila* is known to secrete several effectors with lipolytic activity through its T4SS, which could be important for growth in a lipid rich environment like the yolk [59]. In a first attempt to identify one of these effectors, we analysed the growth of a *L. pneumophila* mutant for a gene encoding a sphingosine-1 phosphate lyase (*Lp*Spl) [29]. When compared to the WT strain after direct injection in the zebrafish larvae yolk sac, a small but significant difference in larvae mortality was observed for the Δ*spl* strain, suggesting that *Lp*Spl is one of several effectors that might participate in nutrient acquisition from lipids (S5A Fig). However, further analyses are needed to characterize the involvement of *Lp*Spl in nutrient acquisition during infection of the yolk region and to identify other effectors potentially implicated in this phenotype. Additionally, the T4SS might be implicated in counteracting host defence mechanisms as innate immune factors like immunoglobulins and complement have been described in the yolk of zebrafish embryos [60,61].

Studies of *Legionella* infection in humans, guinea pigs and mouse lungs have shown that *L. pneumophila* interacts closely with neutrophils and mononuclear phagocytes [62,63]. Professional phagocytes are the main replication niche for *L. pneumophila*, with monocytes and

macrophages and in particular alveolar macrophages, representing the main cells for replication in the lungs [64–67]. *In vivo* studies in mice have shown that upon lung infection with *L. pneumophila*: neutrophils, cDCs, monocytes, and monocyte-like cells are rapidly recruited to the infection site. Although all these cells seem to engulf the bacteria, *L. pneumophila* has only been shown to translocate effectors into neutrophils and alveolar macrophages. In zebrafish, macrophages appear during the first days of development, followed by neutrophils a day later, with both forming an efficient immune system that protects the developing fish [27,68–70]. Therefore, the zebrafish larva offers a unique possibility to interrogate the role of innate immune responses to infection [25]. Indeed, macrophage depleted larvae showed a dramatically increased susceptibility to *L. pneumophila* infection, as nearly 100% of larvae inoculated with HD of WT and 30% of larvae inoculated with LD of *L. pneumophila* WT died from the infection. Hence, macrophages are the first line of infection control against *L. pneumophila* and are essential for restricting and controlling blood-borne infections, similar to what has been observed for *Burkholderia cenocepacia or Staphylococcus aureus* zebrafish infection [71,72]. In contrast, when neutrophils were depleted, the innate immune response was less affected, suggesting that macrophages alone are not able to contain high burdens of *L. pneumophila* infection (Fig 6).

Human innate immune signalling relies strongly on activation of Toll-like receptors (TLRs) and respective adaptor molecules, all of which are highly conserved in the zebrafish [73,74]. One of these adaptors is MyD88, known as a central player in interleukin 1 receptor (IL-1R) and TLR signalling in humans and mammalian models [75]. MyD88 signalling is crucial for mice to combat *L. pneumophila* infection, as it triggers the early secretion of inflammatory cytokines, neutrophil recruitment, and the host immune response to the infection. Consequently, mice that lack MyD88 are highly susceptible to infection [42–45]. However, in MyD88 depleted human macrophages *L. pneumophila* replication is not different to replication in WT cells [76] Given the conservation between the zebrafish and the human immune system, we decided to use the zebrafish model to determine the role of MyD88 signalling. Gene expression analyses in zebrafish confirm that MyD88 has no influence on the control of the inflammatory response, as no statistically significant difference in the transcript levels of *il1b, tnfa, ifng1 or infg2* was observed, further suggesting that activation of the IL1R and certain TLR pathways are not crucial for *L. pneumophila* clearance in zebrafish larvae. Taken together, MyD88 signalling does not play a crucial role or may be redundant in the control of the innate immune response to *L. pneumophila* infection of zebrafish larvae, suggesting that zebrafish infection mirrors human infection better than the mouse model.

In the mouse model *L. pneumophila*-infected macrophages are not producing cytokines, such as tumour necrosis factor (TNF) and interleukin-12 (IL-12), which are necessary to control infection [40,77]. In contrast, infection of zebrafish larvae with LD of *L. pneumophila* WT leads to a short induction of *Il1b* transcript levels at 6 hpi before declining to control levels at later time points, suggesting that a short boost of IL-1β is sufficient to control LD of *L. pneumophila*. Furthermore, HD of WT *L. pneumophila* induced a rapid (by 6 hpi) and robust induction of *il1b* and *tnfa* gene expression. However, this high and long-term induction of IL-1β is not sufficient to warrant infection control, suggesting that the self-regulation of the immune response may be abrogated leading to a constant activation of IL-1β expression. It is even possible that IL-1β release is beneficial for *L. pneumophila* replication, as it was shown in human cells that it may indicate an activation of the metabolic state of the bystander cells. Indeed, as reported IL-1β induces a shift towards more metabolically active cells and increased cellular glucose uptake [78], which could aid *L. pneumophila* replication.

In conclusion, the zebrafish infection model for *L. pneumophila* mimics the immune response observed during human infection and recalls the essentiality of the T4SS for virulence

of this pathogen. The unique advantages of the zebrafish model provide exciting possibilities to further explore *L. pneumophila* host interactions and to interrogate at the molecular level the bacterial determinants and host factors involved in the dynamics of bacterial dissemination, the molecular basis of yolk region invasion and the interactions of the bacteria with macrophages and neutrophils.

Materials and methods

Ethics statement

Animal experiments were performed according to European Union guidelines for handling of laboratory animals (http://ec.europa.eu/environment/chemicals/lab_animals/home_en.htm) and were approved by the Institut Pasteur Animal Care and Use Committee and the French Ministry of Research (APAFIS#31827). The inoculation of embryonated chicken eggs is a standard procedure in diagnostics for multiplication and antigen production of *Legionella* and is not covered by the national law for animal experiments in France (Décret n˚ 2013–118 du 1er février 2013).

Zebrafish care and maintenance

Wild-type AB fish, initially obtained from the Zebrafish International Resource Center (Eugene, OR), Tg(*Lyz*::*DsRed*)^{nz50} [79], Tg*(mfap4*::*mCherryF*) (ump6Tg) [39] Tg(mpx:GFP)^{i114} [80], Tg(kdrl::mCherry)^{is5} [81] and *myd88*^{hu3568} mutant line (obtained from the Hubrecht Laboratory and the Sanger Institute Zebrafish Mutation Resource) [82], were raised in our facility. Eggs were obtained by natural spawning, bleached according to standard protocols, and kept in Petri dishes containing Volvic source water and, from 24 hours post fertilization (hpf) onwards 0.003% 1-phenyl-2-thiourea (PTU) (Sigma-Aldrich) was added to prevent pigmentation. Embryos were reared at 28˚C or 24˚C according to the desired speed of development; infected larvae were kept at 28˚C. Timings in the text refer to the developmental stage at the reference temperature of 28.5˚C. Larvae were anesthetized with 200μg/ml tricaine (Sigma-Aldrich) during the injection procedure as well as during *in vivo* imaging and processing for bacterial burden evaluation or cytokine expression studies.

Bacterial strains and growth conditions

Legionella pneumophila strain Paris carrying the pNT28 plasmid encoding for green fluorescent protein (constitutive GFP) [83], wild-type (WT-GFP) or Δ*dotA*-GFP were plated from -80˚C glycerol stocks on N-(2-acetamido)-2-aminoethanesulfonic acid (ACES)-buffered charcoal yeast-extract (BCYE) medium supplemented with 10 μg/ml of chloramphenicol and cultured for 3 days at 37˚C. Suspensions were prepared by resuspending bacteria in sterile 1x Phosphate Buffered Saline (PBS) and adjusting the OD 600 according to the desired bacterial concentrations for injection.

Morpholino injections

Morpholino antisense oligonucleotides (Gene Tools LLC, Philomath, OR, USA) were injected at the one to two cell stage as described [84]. A low dose (4ng) of *spi1b* (previously named pu1) translation blocking morpholino (GATATACTGATACTCCATTGGTGGT) [85] blocks macrophage development only but can also block neutrophil development when it is injected at a higher dose (20ng in 2nl). The csf3r translation blocking morpholino (GAACTGGCGGAT CTGTAAAGACAAA) (4ng) [37] was injected to block neutrophil development. Control

morphants were injected with 4ng control morpholino, with no known target (GAAAGC ATGGCATCTGGATCATCGA).

Amoebae infections

Acanthamoebae castellanii was infected with *L. pneumophila* wild type expressing GFP and then used to assess if zebrafish develop an infection when ingesting infected amoebae. *A. castellanii* was seeded in a flask with infection buffer (4 mM $MgSO_4$, 0.4 M $CaCl_2$, 0.1% sodium citrate dihydrate, 0.05 mM $Fe(NH_4)_2(SO_4)_2 \times 6H_2O$, 2.5 mM NaH_2PO_3, 2.5 mM K_2HPO_3), and after 1 hour of attachment the cells were infected with the bacteria at MOI 1. After one hour of infection, the amoebae were washed three times with PBS and fresh infection buffer was added. After 48 hours of infection, the amoebae were carefully washed, detached, and used for the bath immersion experiment.

Bath immersion

Experiments were performed using the AB or Tg(mfap4::mCherryF) zebrafish lines maintained at 28˚C under standard conditions in Volvic water. Bath immersion infections were done with 120hpf larvae that already had a developed swim bladder. Groups of 10 larvae were distributed into 6-well plates containing 4.0 ml/well of Volvic spring water and either 1ml of bacterial suspension, 1ml of *L. pneumophila*-containing amoebae, or 1ml of non-infected amoebae, all in PBS. The plates were incubated at 28˚C for 24 hours, and then larvae were individually distributed in an individual well in 24 wells culture plates and monitored by imaging using a fluorescence stereomicroscope.

Zebrafish injection

The volume of injected suspension was deduced from the diameter of the drop obtained after mock microinjection, as described in [84]. Bacteria were recovered by centrifugation, washed, resuspended at the desired concentration in PBS. 72h post-fertilization (hpf) anesthetized zebrafish larvae were microinjected iv or in closed cavities, or the yolk with 0.5-1nl of bacterial suspension at the desired dose (~10^3 bacteria/nl for Low Dose (LD) and ~10^4 bacteria/nl for High Dose (HD) as described [26,35]. Infected larvae were transferred into individual wells (containing 1ml of Volvic water + 0.003% PTU in 24-well culture plates), incubated at 28˚C and regularly observed under a stereomicroscope, twice a day over time up to 72 hpi.

Evaluation of the bacterial burden in infected larvae

The bacterial burden was measured routinely by counting the total number of fluorescent pixels corresponding to the GFP channel using the Metavue software 7.5.6.0. Briefly, images corresponding to the GFP channel were adjusted to a fixed threshold that allowed to abrogate the background of the autofluorescence of the yolk. The same threshold was used for all images. The histogram in the "Analyze" menu was used to obtain the number of black and white pixels. As shown in S1A Fig, the percentage of white pixels in each image corresponding to *L. pneumophila* was plotted using GraphPad Prism software. This method was chosen to routinely quantify bacterial burden as it allows to follow each infected larva over time (individual larvae were imaged with the fluorescence stereomicroscope daily using the same settings from 0 to 72 hpi).

Bacterial burden analyses by FACS

Injected zebrafish larvae were collected at 0, 24, 48 and 72 hpi and lysed. Each larva was placed in a 1.5 ml Eppendorf tube and anesthetized with tricaine (200μg/ml), washed with 1ml of sterile water and placed in 150 μl of sterile water. Larvae were then homogenized using a pestle motor mixer (Argos). Each sample was transferred to an individual well of a 96 well plate, counted on a MACSQuant VYB FACS (Miltenyi Biotec) and data analysed using FlowJo version 7.6.5. as shown in S1B Fig. For CFU enumeration, serial dilutions were plated on BCYE agar plates supplemented with10ug/ml chloramphenicol and the *Legionella* Selective Supplement GVPN (Sigma) added according to the manufacturer's instructions. Plates were incubated for 4–5 days at 37˚C and colonies with the appropriate morphology and colour were scored using the G-Box imaging system (Syngene) and enumerated using the Gene Tools software (Syngene) as shown in S1C Fig. Manual quantification was also performed to identify absolute absence or presence of bacteria in the different zebrafish compartments. Larvae with a single GFP dot (indicating the presence of few bacteria) were considered as infected. The resulting statistical presence map was used to follow the evolution of the infection and dissemination of *L. pneumophila* in zebrafish larvae over time (Fig 1E).

Inoculation and quantification of *L. pneumophila* strains in *in ovo* experiments

Fertilized chicken eggs purchased from a local producer (Saint-Maurice-sur-Dargoire, Rhône, France) were incubated at 35˚C in an egg incubator (Maino, Italy) to maintain normal embryonic development. Eggs were pathogen and antibiotic free. On day 0, 53 embryonated chicken eggs (ECE) were inoculated at 8 days of embryonation (DOE) with either *L. pneumophila* WT (n = 19 ECE in total corresponding to 9, 4, 3 and 3 tested in the experiments No.1, 2, 3 and 4 respectively), *L. pneumophila ΔdotA* (n = 17 ECE in total corresponding to 8, 4, 2 and 3 tested in the experiments No.1, 2, 3 and 4 respectively) or sterile PBS as control (n = 17 ECE in total corresponding to 7, 4, 3 and 3 tested in the experiments No.1, 2, 3 and 4 respectively). Two-day cultures of Lpp-WT and Lpp-Δ*dotA* on BCYE at 36˚C were suspended in PBS at a DO = 2.5 McFarland and 0.5 mL of suspensions or PBS (negative control) were inoculated in the yolk sac of ECE. *L. pneumophila* concentration in WT and Δ*dotA* suspensions before ECE injection was quantified at 9.0 $\log_{10}$ CFU/mL for each suspension, and considering the injected volume of 0.5 mL, the median amount of *L. pneumophila* in the yolk sac of ECE directly after injection was 8.7 $\log_{10}$ CFU. After inoculation, ECE were candled every 24 hours to assess embryo viability until day-6 post infection. Embryo that died the day of inoculation (D0) (n = 1, corresponding to one WT-infected and one *ΔdotA*-infected embryo) was discarded for *L. pneumophila* quantification as death was probably due to bad inoculation. Dead embryos were stored at 4˚C overnight prior to harvesting the yolk sacs. Remaining live embryos at 6-days post injection were euthanized by overnight refrigeration and the yolk sacs were collected. After measuring their volume, yolk sacs were homogenized using gentleMACS Octo Dissociator (Miltenyi Biotec, Germany) and 100 μL of serial dilutions at 10^{-2}, 10^{-4} and 10^{-6} were automatically plated using easySpiral automatic plater (Interscience, France) in triplicates on BCYE agar. *L. pneumophila* were quantified after 5 days-incubation using Scan 1200 Automatic HD colony counter (Interscience, France). Comparison of survival curves was performed using Log-rank (Mantel-Cox) test. $P < 0.05$ was considered statistically significant. *L. pneumophila* amounts in the yolk sac after death of ECE were estimated, considering both the measured UFC counts in yolk sac and the yolk sac volumes (median (interquartile range) [IQR] volume, 30 [28.7–31.2] mL). Comparison of *L. pneumophila* quantifications between

WT- and Δ*dotA*-infected embryos was done using Mann-Whitney test. $P < 0.05$ was considered statistically significant (symbols: **** $P < 0.0001$; *** $P < 0.001$; ** $P < 0.01$; * $P < 0.05$).

Live imaging, image processing and analysis

Quantification of total neutrophils and/or macrophages on living transgenic reporter larvae upon infection was performed as previously described [35]. Briefly, bright field, DsRed and GFP images of whole living anesthetized larvae were taken using a Leica Macrofluo Z16 APOA (zoom 16:1) equipped with a Leica PlanApo 2.0X lens, and a Photometrics CoolSNAP *HQ2* camera. Images were captured using Metavue software 7.5.6.0 (MDS Analytical Technologies). Then larvae were washed and transferred in a new 24 wells plate filled with 1ml of fresh Volvic water per well, incubated at 28˚C and imaged again under the same conditions the day after. Pictures were analysed, and Tg(*lyzC*::*DsRed*) neutrophils or Tg(*mfap4*::*mCherryF*) macrophages manually counted using the ImageJ software (V 1.52a). Counts shown in figures are numbers of cells per image. The quantification of fluorescence images was also done using CellProfiler Software (Broad Institute) using two semi-automatic batch pipelines. Both pipelines normalize the intensity, operate image pre-processing, and use thresholding to calculate the percentage of area positive for macrophage/neutrophils and bacteria, normalized on the whole image area. Both pipelines also take advantage of manual editing to increase identification accuracy and define the yolk area. The positive signal is then automatically masked to calculate the amount of signal in the body or yolk of each zebrafish for all the experiments and produce a.csv file used for subsequent statistical treatment (Figs 3F and S6). High resolution confocal live imaging of injected larvae was performed as previously described [86]. Briefly, injected larvae were positioned in lateral or ventral position in 35 mm glass-bottom-Dishes (Ibidi Cat#: 81158) or in glass bottom- 8well-slides (Ibidi Cat#: 80827). Larvae were immobilized using a 1% low-melting-point agarose (Promega; Cat#: V2111) solution and covered with Volvic water containing tricaine. A Leica SP8 confocal microscope equipped with two PMT and Hybrid detector, a 10X dry (PL Fluotar 10X dry:0.30), 20X IMM (HC PL APO CS2 20X/0.75), or a 40x water IMM (HC PL APO CS2 40X/1.10) objective, a X–Y motorized stage and with LAS-X software, was used to live image injected larvae. To generate images of the whole larvae, a mosaic of confocal z-stack of images was taken with the 10X or 20X objective using the Tile Scan tool of the LAS-X software and was stitched together using the Mosaic Merge tool of the LAS-X software. All samples were acquired using the same settings, allowing comparisons of independent experiments. The acquisitions were post processed with the Lightning tool of the LAS-X software to eliminate noise (deconvolution). After acquisition, larvae were washed and transferred in a new 24-well plate filled with 1 ml of fresh Volvic water per well, incubated at 28˚C and imaged again under the same conditions over time. A Leica SPE inverted confocal microscope and a 40x oil IMM objective (ACS APO 40 × 1.15 UV) was also used to live image larvae infected with *L. pneumophila* Δ*dotA*-GFP (Figs 4 and 5). The 3D or 4D files generated by the time-lapse acquisitions were processed, cropped, analysed, and annotated using the LAS-X and LAS-AF Leica software. Acquired Z-stacks were projected using maximum intensity projection and exported as AVI files. Frames were captured from the AVI files and handled with Miocrosoft PowerPoint (Microsoft Office 365) software to mount figures. AVI files were cropped and annotated using ImageJ software. Files generated with the LAS-X software were also processed and analysed with the Imaris software version9.5 (Bitplane, OXFORD Instruments) for 3D or 4D reconstruction, surfacing and volume rendering. For the 4D reconstruction of the yolk membrane, we used two factors to draw its position: 1) the shape of the bacteria, that forms a "ceiling "with a net edge 2) the Transmitted Light (bright field) to delimitate the yolk cell, and the putative localization of the yolk membrane. The

location of the yolk cell membrane is thus assumed by these parameters and has been manually annotated (S5 Movie) but cannot be formally established.

qRT-PCR to measure gene expression of cytokine encoding genes

RNA was extracted from individual larvae using the RNeasy Mini Kit (Qiagen). cDNA was obtained using M-MLV H- reverse-transcriptase (Promega) with a dT17 primer. Quantitative PCR was performed on an ABI7300 thermocycler (Applied Biosystems) using Takyon ROX SYBR 2X MasterMix (Eurogentec) in a final volume of 10 μl. Primers used: *ef1a (housekeeping gene used for normalization)*: GCTGATCGTTGGAGTCAACA and ACAGACTTGACCTC AGTGGT*; il1b*: GAGACAGACGGTGCTGTTTA and GTAAGACGGCACTGAATCCA*; tnfa*: TTCACGCTCCATAAGACCCA and CAGAGTTGTATCCACCTGTTA*; ifng-1-1*: ACCAGCTGAATTCTAAGCCAA and TTTTCGCCTTGACTGAGTGAA; *ifng-2*: GAAT CTTGAGGAAAGTGAGCA and TCGTTTTCCTTGATCGCCCA.

Statistical analysis

Normal distributions were analysed with the Kolmogorov–Smirnov and the Shapiro–Wilk tests. To evaluate difference between means of normally distributed data (for neutrophil and macrophage numbers), an analysis of variance followed by Bonferroni's multiple comparison tests was used. For bacterial burdens (CFU/FACS counts), values were Log10 transformed. For cytokine expression and bacterial burdens (evaluated by fluorescent pixel count, or FACS) non-Gaussian data were analysed with the Kruskal–Wallis test followed by Dunn's multiple comparison test. $P < 0.05$ was considered statistically significant (symbols: **** $P < 0.0001$; ***$P < 0.001$; **$P < 0.01$; *$P < 0.05$). No symbol on graphs means that not statistically differences were observed. Survival data were plotted using the Kaplan–Meier estimator and log-rank (Mantel–Cox) tests were performed to assess differences between groups. Statistical analyses were performed using GraphPad Prism software. Statistical analyses for *in ovo* experiments, were performed using GraphPrism version 9.4.

Supporting information

S1 Fig. Comparison of three methods to estimate the bacterial burden of infected zebrafish larvae at different points post infection. A) For bacterial burden measure by fluorescent pixel counts, the pictures corresponding to the GFP channel were analysed to quantify the percentage of fluorescent pixels using the ImageJ software. Individual larvae injected with WT-GFP Low Dose (LD) (blue symbols) or High Dose (HD) (red symbols) or infected with Δ*dotA*-GFP HD (green symbols) have been plotted and represented as box plot. Two independent experiments pooled, n = 10 larvae per condition). **B**) For FACS analyses, infected larvae were lysed and then GFP bacteria were counted on a MACSQuant VYB FACS (Miltenyi Biotec). One experiment plotted, n = 5 larvae per condition. **C**) CFUs were enumerated by plating serial dilutions of lysed infected larvae in BCYE agar supplemented with Chloramphenicol and *Legionella* Selective Supplement GVPN (Sigma). One experiment plotted, n = 5 larvae per condition. $P < 0.05$ was considered statistically significant (symbols: **** $P < 0.0001$; ***$P < 0.001$; **$P < 0.01$; *$P < 0.05$). No symbol on graphs means that not statistically differences were observed.
(TIF)

S2 Fig. Bacterial burden evaluation by FACS overtime on individual lysed larvae after *Legionella pneumophila* infection. For FACS analyses, individual infected larvae were lysed and then GFP bacteria were counted on a MACSQuant VYB FACS (Miltenyi Biotec). **A)**

Related to Fig 1C: 6 pooled experiments, n = 26 larvae for WT HD (28 for 72h), n = 26 larvae for WT LD (30 for 72h), n = 25 larvae for *ΔdotA* HD (26 for 72h) **B)** Related to Fig 2B: Fluorescent pixel count evaluation overtime upon yolk cell injection. One experiment is plotted. N = 6 larvae for WT HD, n = 6 larvae for WT LD, n = 5 larvae for *ΔdotA* HD**. C)** Related to Fig 6B: 2 pooled experiments, n = 8 Spi1b-MO larvae for WT HD, n = 8 Spi1b-MO larvae for WT LD, n = 5 Spi1b-MO larvae for *ΔdotA* HD, n = 5 control larvae for WT HD, n = 5 control larvae for WT LD and n = 5 control larvae for *ΔdotA* HD. **D)** Related to Fig 6E: 2 pooled experiments, n = 8 Csf3R-MO larvae for WT HD (10 for 72h), n = 8 Csf3R-MO larvae for WT LD (9 for 72h), n = 5 Csf3R-MO larvae for *ΔdotA* HD (4 for 0h), n = 6 control larvae for WT HD (8 for 72h), n = 6 control larvae for WT LD (9 for 72h) and n = 5 control larvae for *ΔdotA* HD (6 for 72h). **E)** Related to Fig 7B: 3 pooled experiments, n = 13 *myd88* larvae for WT HD, n = 13 *myd88* larvae for WT LD (12 for 0h), n = 13 *myd88* larvae for *ΔdotA* HD, n = 10 control larvae for WT HD, n = 10 control larvae for WT LD, n = 10 control larvae for *ΔdotA* HD. $P < 0.05$ was considered statistically significant (symbols: **** $P < 0.0001$; ***$P < 0.001$; **$P < 0.01$; *$P < 0.05$). No symbol on graphs means that not statistically differences were observed.
(TIF)

S3 Fig. *L. pneumophila* invades the yolk only upon bloodstream inoculation and only blood borne *L. pneumophila* WT proliferate in the yolk region of zebrafish larvae. A) Scheme of 72hpf larva indicating the sites of bacterial injection. The scheme of the zebrafish larvae has been adapted from [35] and has been previously modified from [87]. Site of injection are indicated by green dashed boxes. OV: otic vesicle; HBV: hind brain ventricle; IV: intravenous injection. **B.** Survival curves. 2 experiments pooled; n = 36 larvae for CTRL and OV, 31 for IV, and 33 for HBV injection. **C**) bacterial burden evaluated over time by fluorescent pixel counts. 1 experiment, 6 larvae per condition. **D.** Representative images of *L. pneumophila* dissemination, determined by live imaging using a fluorescence stereomicroscope, of zebrafish larvae infected with a HD WT-, in closed compartments (OV, HBV) or in the bloodstream (IV). Infected larvae were live imaged 4h, 24h, 48h, and 72h post *L. pneumophila* injection. Only GFP fluorescence is shown. Green autofluorescence of the lens eye (e) or of the gastrointestinal tract (g) is indicated on CTRL larvae. $P < 0.05$ was considered statistically significant (symbols: **** $P < 0.0001$; ***$P < 0.001$; **$P < 0.01$; *$P < 0.05$). No symbol on graphs means that not statistically differences were observed.
(TIF)

S4 Fig. Bath immersion of 120 hpf zebrafish larvae using *WT L pneumophila* infected *A castellanii*. A) Survival curves. **B)** % of larvae with GFP bacteria. A and B: 1 experiment, 30 larvae for WT Lpp-amoebae, 10 for WT Lpp and 10 for amoebae. **C)** Representative fluorescent imaging of larvae with GFP bacteria in the intestinal tract followed over time. The intestinal tractus is highlighted with white dotted lines. Arrowhead points to GFP bacteria being eliminated with the fecal content. D) representative closeup of GFP bacteria in the intestinal tract. $P < 0.05$ was considered statistically significant (symbols: **** $P < 0.0001$; ***$P < 0.001$; **$P < 0.01$; *$P < 0.05$). No symbol on graphs means that not statistically differences were observed.
(TIF)

S5 Fig. Δ*spl* mutant injected in the yolk and *L. pneumophila* WT but not the T4SS mutant proliferates in the yolk of zebrafish and the yolk of chicken eggs upon direct injection. A). 72hpf larva: the yolk cell is highlighted in blue and the yolk content in pink. The scheme of the zebrafish larvae has been adapted from [35] and has been previously modified from [87]. **B).** Survival curves of 72hpf larvae upon injection in the yolk of HD WT (red curve), Δ*dot*A

(green curve) or Δ*spi* mutant (violet curve) *L. pneumophila* strain. CTRL larvae (black curve). One experiment, 24 larvae for each condition. Significant differences are indicated with stars. C) Survival curves of embryonated chicken eggs (ECE) inoculated with WT strain (red, n = 19 ECE in total corresponding to 9, 4, 3 and 3 ECE tested in the experiments No. 1, 2, 3 and 4 respectively), Δ*dot*A strain (green, n = 17 ECE in total corresponding to 8, 4, 2 and 3 ECE tested in the experiments No.1, 2, 3 and 4 respectively) or PBS (black, n = 17 ECE in total corresponding to 7, 4, 3 and 3 ECE tested in the experiments No.1, 2, 3 and 4 respectively). Survival is expressed in percentage and time in days. Comparison of survival curves was performed using Logrank (Mantel-Cox) test. $P < 0.05$ was considered statistically significant. D, E) Quantification of *L. pneumophila* (expressed in log10 CFU) in the yolk sac of WT-infected embryos (n = 19 in total) and Δ*dotA* infected embryos (n = 17 in total), according to the day of mortality of the embryos (D1, D2, D3 and alive at D6 (euthanized) (D) or the experiments (n = 4) (E). The inoculum after infection was estimated by considering the *L. pneumophila* count in the inoculum (WT and Δ*dotA*) before injection and the volume of the yolk sac. Comparison of the quantifications of *L. pneumophila* WT- or Δ*dotA*-infected embryos was done using the Mann-Whitney test. Medians and interquartile range are represented. $P < 0.05$ was considered statistically significant (**** $P < 0.0001$; *** $P < 0.001$; ** $P < 0.01$; * $P < 0.05$).
(TIF)

S6 Fig. Quantification of bacterial burden in the whole body, in the body or in the yolk region versus macrophage or neutrophil quantification in the body or in the yolk region in HD WT-GFP infected larvae followed overtime. Two independent experiments plotted for each phagocyte type (total of 11 larvae for macrophage or 11 larvae for neutrophil quantification). Quantification of the fluorescent images (GFP bacteria and RFP leukocytes) was done using CellProfiler software (see Material and Methods for details about the pipeline). Bacterial burden quantification was done over the whole larva (red dot) or discriminating the body (light blue dot) form the yolk region (pink dot). Scheme of 72hpf with body (light blue) and yolk region (pink) highlighted; The scheme of the zebrafish larvae has been adapted from [35] and has been previously modified from [87]. The yolk sustaining *L. pneumophila* growing has been indicated with green dots. Quantification of macrophage or neutrophil located in body (light blue dot) or yolk (pink dot) over time. $P < 0.05$ was considered statistically significant (symbols: **** $P < 0.0001$; *** $P < 0.001$; ** $P < 0.01$; * $P < 0.05$). No symbol on graphs means that not statistically differences were observed.
(TIF)

S7 Fig. Macrophage and neutrophil depletion by morpholino: evaluation of the impact on the non-depleted leukocyte population. Comparison of the impact of *spi1b* morpholino injection that blocks macrophage development or csf3r morpholino injection that blocks neutrophil development were administered. Macrophages (red symbols) and neutrophils (green symbols) were counted in CTRL (open symbols) or morphant (full symbols) conditions. **A)** effect of spe1b morpholino on macrophages and neutrophils, showing that spe1b morpholino injection leads to the specific depletion of macrophages and not neutrophils. Related to Fig 4: 2 plotted experiments, n = 10 larvae per group. B) effect of Csf3R morpholino on macrophages and neutrophils, showing that Csf3R morpholino injection leads to the specific depletion neutrophils and slightly impairs the number of macrophages. Related to Fig 5: 2 plotted experiments, n = 10 larvae per group.
(TIF)

S8 Fig. A. Correlation between bacterial burden (evaluated by fluorescence on individual injected larvae before RNA extraction) and cytokine gene induction at 48 and 72 hpi upon

bloodstream injection LD, HD WT or HD Δ*dot*A *L pneumophila* strain. Control non injected, HD WT or HD Δ*dot*A injected larvae were scored under the fluorescent microscope for evaluating bacterial burden immediately before to be lysed and processed for RNA extraction. "-", "+" to "+++ "respectively indicate no or in, creasing bacterial burden. "-"and "+" symbols were also used to respectively indicate infected dead or live larvae. Related to Fig 7A-7D. **C-D) Cytokine gene (*il1b*, *tnfa*, *ifng1/2*) induction is independent from Myd88 signalling in *L pneumophila* HD WT infected zebrafish larvae**.Cytokine gene induction was measured from individual *myd88*^{hu3568} mutant larvae injected with a HD (red curves) of WT-GFP and non-injected fish (CTRL, black curves). The same colours are used for individual CTRL non injected (black dashed) or HD WT injected (red dashed) zebrafish curves. Data plotted are from one experiment (n = 5 larvae for each condition); individual values are shown, and curves correspond to the medians. There is no statistically significant difference between CTRL and *myd88*^{hu3568} mutant curves over time for all the conditions analysed. Related to Fig 7E and 7F.
(TIF)

S1 Movie. *L. pneumophila* growing in the yolk region at 72 hpi: localization in the yolk in AB wild type larva. AB wild type larva 72hpf was injected in the bloodstream with HD of *L. pneumophila* WT-GFP, and was analyzed using confocal high microscopy at 72 hpi, to study the behavior of the highly growing bacteria in the yolk region. The infected larva was mounted laterally and acquired using a 20X oil-immersion objective. The acquired Z-stack was deconvolved using Leica Lightening Plug-in and processed for 3D visualization and volume rendering, using IMARIS 9.6 (Bitplane). Note the complex, filamentous, highly aggregate structures (green) formed by the growing *Legionella* in the yolk region (visualized by the bright field).
(MP4)

S2 Movie. *L. pneumophila* growing in the yolk region at 72 hpi: interactions with blood vessels. *kdrl*:mCherry (red blood vessels) 72hpf larva was injected in the bloodstream with HD of *L. pneumophila* WT-GFP, and was analyzed with confocal high microscopy at 72 hpi, to study the behavior of the highly growing bacteria in the yolk region and their interactions with the yolk vasculature. The infected larva was mounted laterally and acquired using a 20X oil-immersion objective. The acquired Z-stack was deconvolved using Leica Lightening Plug-in and processed for 3D visualization and volume rendering, using IMARIS 9.6 (Bitplane). The interactions of the blood vessels (red cells) with the growing bacterial aggregates (green), and the yolk region (bright field) are shown at various magnifications (scale bar indicated on the movie) and various rotations angles to highlight the complex filamentous bacterial structures and their interactions with the blood vessels. Due to the peculiar yolk composition and thickness, it was impossible to acquire the fluorescence of the bacteria growing inside the yolk region distal to the objective, thus appearing as big dark spots.
(MP4)

S3 Movie. *L. pneumophila* growing in the yolk region at 72 hpi: interactions with macrophages. *Mfap4*: mCherry (red macrophages) 72hpf larva was injected in the bloodstream with HD of *L. pneumophila* WT-GFP, and was analyzed with confocal high microscopy at 72 hpi, to study the behavior of the bacteria growing in the yolk region and their interactions with macrophages. The infected larva was mounted ventrally and acquired using a 40X water-immersion objective. Only the yolk region containing the bacterial aggregates was imaged. The acquired Z-stack was deconvolved using Leica Lightening Plug-in and processed for 3D visualization and volume rendering, using IMARIS 9.6 (Bitplane). The interactions of macrophages (red cells) with the growing bacterial aggregates (green), and the yolk region (bright field) are

shown at various magnifications (scale bar indicated on the movie) and various rotation angles to highlight the complex filamentous bacterial structures and the recruited macrophages, that recognize the growing bacteria, but fail to penetrate the yolk content, and to engulf the bacterial aggregates. Due to the peculiar yolk composition and thickness, it was impossible to acquire the fluorescence of the bacteria growing inside the yolk distal to the objective, thus appearing as big dark spots.
(MP4)

S4 Movie. *L. pneumophila* growing in the yolk region at 72 hpi: interactions with neutrophils. *Lys*:DsRed (red neutrophils) 72hpf larva was injected in the bloodstream with HD of *L. pneumophila* WT-GFP, and was analyzed with confocal high microscopy at 72 hpi, to study the behavior of the bacteria growing in the yolk region and their interactions with neutrophils. The infected larva was mounted laterally and acquired using a 20X oil-immersion objective. The acquired Z-stack was deconvolved using Leica Lightening Plug-in and processed for 3D visualization and volume rendering, using IMARIS 9.6 (Bitplane). The interactions of neutrophils (red cells) with the growing bacterial aggregates (green), and the yolk region (bright field) are shown at various magnifications (scale bar indicated on the movie) and various rotations angles to highlight the complex filamentous bacterial structures and the recruited neutrophils, that recognize and sense the growing bacteria, migrate to them, but fail to penetrate the yolk content, and to engulf the big bacterial aggregates. Due to the peculiar yolk composition and thickness, it was impossible to acquire the fluorescence of the bacteria growing inside the yolk distal to the objective, thus appearing as big dark spots.
(MP4)

S5 Movie. *L. pneumophila* growing in the yolk region between 48 and 72 hpi: interactions with macrophages (related to Fig 3E). 4D, 40X objective, 6h time lapse between 48–72 hpi, 1microm optical sections, infected larva mounted ventral, bacteria growing in aggregate on the yolk. *Mfap4*: mCherry (red macrophages) 72hpf larva was injected in the bloodstream with HD of *L. pneumophila* WT-GFP, and was analyzed with confocal high microscopy between 48 and 72 hpi, to study the behavior of the bacteria growing in the yolk region, their spatial localization (above or below the yolk plasma membrane), and their interactions with macrophages overtime. The infected larva was mounted ventrally and acquired using a 40X water-immersion objective. Only the yolk region containing the bacterial aggregates was imaged. The acquired Z-stack was deconvolved using Leica Lightening Plug-in and processed for 4D visualization and volume rendering, using IMARIS 9.6 (Bitplane). Macrophage and bacteria surfacing automatically done, yolk region manually delimitated frame by frame with Imaris.
(MOV)

S6 Movie. Macrophage—*L. pneumophila* interactions (LD, HD). *Mfap4*: mCherry (red macrophages) 72hpf larvae were injected in the bloodstream with LD (left panel) or HD (middle panel) of *L. pneumophila* WT-GFP or with HD OF *L. pneumophila* Δ*dotA*-GFP (right panel), mounted laterally and acquired using high resolution confocal microscopy to analyze macrophages (red cells) bacteria (green) interactions immediately upon bacteria injection. The infected larvae were acquired over time from 20 min to approximately 16 hours post injection. Maximum projections of the acquired Z-stacks are shown. The 3D movies generated were combined using Image J software, to have them side by side, to compare the macrophage-bacteria interaction over time in the various conditions. Left panel: *mfap4*: mCherry (red macrophages) 72hpf larva injected in the bloodstream with LD wt GFP *Legionella* (green). Note that macrophages are recruited to the injected bacteria, engulf them, and the bacteria are cleared progressively from the bloodstream. Middle panel: *mfap4*: mCherry (red macrophages) 72hpf

larva injected in the bloodstream with HD wt GFP *Legionella* (green). Macrophages are recruited upon bacteria injection but failed to eliminate them over time; the phagocytosing macrophages round-up. Right panel: *mfap4*: mCherry (red macrophages) 72hpf larva injected in the bloodstream with HD GFP Δ*dotA Legionella* (green). Note that the recruited macrophages efficiently engulf and eliminate the injected bacteria, clearing them progressively from the blood and the mesenchyme near the point of injection.
(MP4)

S7 Movie. Neutrophil—*L. pneumophila* (LD, HD) interactions. (*Lys*: DsRed (red neutrophils) 72hpf larvae were injected in the bloodstream with LD (left panel) or HD (middle panel) *L. pneumophila* WT-GFP, or with HD of Δ*dotA*-GFP (right panel), mounted laterally and acquired using high resolution confocal microscopy to analyze neutrophil (red cells) bacteria (green) interactions immediately upon bacteria injection. The infected larvae were acquired over time from 20 min to approximately 16 hours post injection. Maximum projections of the acquired Z-stacks are shown. The 3D movies generated were combined using ImageJ software, to have them side by side, to compare neutrophil-bacteria interactions over time in the various conditions. Left panel: *Lys*: DsRed (red neutrophils) 72hpf larva injected in the bloodstream with LD of WT-GFP (green). Note that neutrophils are recruited to the injected bacteria, engulfing the bacteria trapped in the mesenchyme near the site of injection, cooperating with macrophages (DsRed–cells, GFP+ having engulfed large amount of GFP bacteria), clearing progressively the infection. Middle panel: *Lys*:DsRed (red neutrophils) 72hpf larva injected in the bloodstream with HD of WT-GFP (green). Neutrophils are massively recruited upon bacterial injection but failed to eliminate them over time; the phagocytosing neutrophils round-up and loose DsRed fluorescence, suggesting cell death. Right panel: *lys*:DsRed (red neutrophils) 72hpf larva injected in the bloodstream with HD of Δ*dotA*-GFP *L. pneumophila* (green). Note that the recruited neutrophils engulf and eliminate the injected bacteria, clearing them progressively from mesenchyme near the point of injection, efficiently cooperating with macrophages in controlling the infection.
(MP4)

S8 Movie. Dying phagocytosing neutrophils upon *L. pneumophila* HD injection (related to Fig 5). (*Lys*: DsRed (red neutrophils) 72hpf larvae were injected in the bloodstream with HD *L. pneumophila* WT-GFP, mounted laterally and acquired using high resolution confocal microscopy to analyze neutrophil (red cells) bacteria (green) interactions immediately upon bacteria injection. The infected larvae were acquired over time from 20 min to approximately 16 hours post injection. Time lapses every 1'30". Maximum projections of the acquired Z-stacks (2mm per optical section) are shown. 6 neutrophils were manually tracked with Fiji (1 to 6) and highlighted with open white circle overtime. Note that the tracked neutrophils having engulfed *L. pneumophila* progressively dyed, rounding up and losing their red fluorescence, while the green fluorescence of the GFP bacteria is still visible overtime.
(MP4)

Acknowledgments

We thank Pedro Escoll and Jean-Pierre Levraud for help and ideas in the initial set up of the project, Tobias Sahr and Philippe Herbomel for helpful discussions and scientific advice, Yohann Rolin for his excellent care of the fish, the Image analyses Hub at Institut Pasteur for the use of the IMARIS workstation and Jessica Martyn for critical reading of the manuscript.

Author Contributions

Conceptualization: Flávia Viana, Laurent Boucontet, Sophie Jarraud, Emma Colucci-Guyon, Carmen Buchrieser.

Formal analysis: Flávia Viana, Laurent Boucontet, Valerio Laghi, Sophie Jarraud, Emma Colucci-Guyon.

Funding acquisition: Emma Colucci-Guyon, Carmen Buchrieser.

Investigation: Flávia Viana, Laurent Boucontet, Valerio Laghi, Daniel Schator, Marine Ibranosyan, Emma Colucci-Guyon.

Methodology: Valerio Laghi.

Project administration: Emma Colucci-Guyon, Carmen Buchrieser.

Supervision: Emma Colucci-Guyon, Carmen Buchrieser.

Writing – original draft: Flávia Viana.

Writing – review & editing: Emma Colucci-Guyon, Carmen Buchrieser.

References

1. Fliermans CB. Ecology of Legionella: From Data to Knowledge with a Little Wisdom. Microb Ecol. 1996; 32(2):203–28. https://doi.org/10.1007/BF00185888 PMID: 8688009.
2. Cunha BA, Burillo A, Bouza E. Legionnaires' disease. Lancet. 2016; 387(10016):376–85. https://doi.org/10.1016/S0140-6736(15)60078-2 PMID: 26231463.
3. Rowbotham TJ. Preliminary report on the pathogenicity of *Legionella pneumophila* for freshwater and soil amoebae. J Clin Pathol. 1980; 33(12):1179–83.
4. Boamah DK, Zhou G, Ensminger AW, O'Connor TJ. From Many Hosts, One Accidental Pathogen: The Diverse Protozoan Hosts of *Legionella*. Frontiers in cellular and infection microbiology. 2017; 7:477. https://doi.org/10.3389/fcimb.2017.00477 PMID: 29250488; PubMed Central PMCID: PMC5714891.
5. Mampel J, Spirig T, Weber SS, Haagensen JA, Molin S, Hilbi H. Planktonic replication is essential for biofilm formation by *Legionella pneumophila* in a complex medium under static and dynamic flow conditions. Appl Environ Microbiol. 2006; 72(4):2885–95. https://doi.org/10.1128/AEM.72.4.2885–2895.2006 PMID: 16597995; PubMed Central PMCID: PMC1448985.
6. McDade JE, Shepard CC, Fraser DW, Tsai TR, Redus MA, Dowdle WR. Legionnaires' disease: isolation of a bacterium and demonstration of its role in other respiratory disease. N Engl J Med. 1977; 297 (22):1197–203. https://doi.org/10.1056/NEJM197712012972202 PMID: 335245
7. Lanternier F, Ader F, Pilmis B, Catherinot E, Jarraud S, Lortholary O. Legionnaire's Disease in Compromised Hosts. Infect Dis Clin North Am. 2017; 31(1):123–35. Epub 2017/02/06. https://doi.org/10.1016/j.idc.2016.10.014 PMID: 28159172.
8. Naujoks J, Lippmann J, Suttorp N, Opitz B. Innate sensing and cell-autonomous resistance pathways in *Legionella pneumophila* infection. Int J Med Microbiol. 2018; 308(1):161–7. Epub 2017/11/04. https://doi.org/10.1016/j.ijmm.2017.10.004 PMID: 29097162.
9. Isberg RR, O'Connor TJ, Heidtman M. The *Legionella pneumophila* replication vacuole: making a cosy niche inside host cells. Nat Rev Microbiol. 2009; 7(1):13–24. Epub 2008/11/18. nrmicro1967 [pii] https://doi.org/10.1038/nrmicro1967 PMID: 19011659.
10. Mondino S, Schmidt S, Rolando M, Escoll P, Gomez-Valero L, Buchrieser C. Legionnaires' Disease: State of the Art Knowledge of Pathogenesis Mechanisms of *Legionella*. Annu Rev Pathol. 2020; 15:439–66. Epub 2019/10/29. https://doi.org/10.1146/annurev-pathmechdis-012419-032742 PMID: 31657966.
11. Ensminger AW. *Legionella pneumophila*, armed to the hilt: justifying the largest arsenal of effectors in the bacterial world. Curr Opin Microbiol. 2016; 29:74–80. https://doi.org/10.1016/j.mib.2015.11.002 PMID: 26709975.
12. Cazalet C, Rusniok C, Bruggemann H, Zidane N, Magnier A, Ma L, et al. Evidence in the *Legionella pneumophila* genome for exploitation of host cell functions and high genome plasticity. Nat Genet. 2004; 36(11):1165–73.

13. Mondino S, Schmidt S, Buchrieser C. Molecular Mimicry: a Paradigm of Host-Microbe Coevolution Illustrated by Legionella. mBio. 2020; 11(5). Epub 2020/10/08. https://doi.org/10.1128/mBio.01201-20 PMID: 33024033.
14. Brassinga AK, Kinchen JM, Cupp ME, Day SR, Hoffman PS, Sifri CD. *Caenorhabditis* is a metazoan host for *Legionella*. Cell Microbiol. 2009; 12(3):343–61. Epub 2009/10/30. CMI1398 [pii] https://doi.org/10.1111/j.1462-5822.2009.01398.x. PMID: 19863556.
15. Harding CR, Schroeder GN, Reynolds S, Kosta A, Collins JW, Mousnier A, et al. *Legionella pneumophila* pathogenesis in the *Galleria mellonella* infection model. Infect Immun. 2012; 80(8):2780–90. https://doi.org/10.1128/IAI.00510-12 PMID: 22645286; PubMed Central PMCID: PMC3434583.
16. Brown AS, van Driel IR, Hartland EL. Mouse Models of Legionnaires' Disease. Curr Top Microbiol. 2014; 376:271–91. https://doi.org/10.1007/82_2013_349 WOS:000330592900014. PMID: 23918179
17. Lucena Lage S, Longo C, Migliari Branco L, Boccia da Costa T, de Lima Buzzo C, Ramalho Bortoluci K. Emerging Concepts about NAIP/NLRC4 Inflammasomes Frontiers in immunology. 2014;(5):309. https://doi.org/10.3389/fimmu.2014.00309 PMID: 25071770
18. Massis LM, Zamboni DS. Innate immunity to *Legionella pneumophila*. Front Microbiol. 2011; 2:109. Epub 2011/08/13. https://doi.org/10.3389/fmicb.2011.00109 PMID: 21833338.
19. Breiman RF, Horwitz MA. Guinea pigs sublethally infected with aerosolized *Legionella pneumophila* develop humoral and cell-mediated immune responses and are protected against lethal aerosol challenge. A model for studying host defense against lung infections caused by intracellular pathogens. J Exp Med. 1987; 165(3):799–811. https://doi.org/10.1084/jem.165.3.799 PMID: 3819647.
20. Weeratna R, Stamler DA, Edelstein PH, Ripley M, Marrie T, Hoskin D, et al. Human and guinea pig immune responses to Legionella pneumophila protein antigens OmpS and Hsp60. Infect Immun. 1994; 62(8):3454–62. https://doi.org/10.1128/iai.62.8.3454-3462.1994 PMID: 7913699.
21. Akhter A, Gavrilin MA, Frantz L, Washington S, Ditty C, Limoli D, et al. Caspase-7 activation by the Nlrc4/Ipaf inflammasome restricts *Legionella pneumophila* infection. PLoS Pathog. 2009; 5:e1000361. https://doi.org/10.1371/journal.ppat.1000361 PMID: 19343209
22. Santic M, Asare R, Doric M, Abu Kwaik Y. Host-dependent trigger of caspases and apoptosis by *Legionella pneumophila*. Infect Immun. 2007; 75(6):2903–13.
23. Masud S, Torraca V, Meijer AH. Modeling Infectious Diseases in the Context of a Developing Immune System. Curr Top Dev Biol. 2017; 124:277–329. https://doi.org/10.1016/bs.ctdb.2016.10.006 WOS:000406859900009. PMID: 28335862
24. Torraca V, Mostowy S. Zebrafish Infection: From Pathogenesis to Cell Biology. Trends in Cell Biology. 2018; 28(2):143–56. https://doi.org/10.1016/j.tcb.2017.10.002 WOS:000424633500006. PMID: 29173800
25. Gomes MC, Mostowy S. The Case for Modeling Human Infection in Zebrafish. Trends in Microbiology. 2020; 28(1):10–8. https://doi.org/10.1016/j.tim.2019.08.005 WOS:000503037700005. PMID: 31604611
26. Colucci-Guyon E, Tinevez JY, Renshaw SA, Herbomel P. Strategies of professional phagocytes in vivo: unlike macrophages, neutrophils engulf only surface-associated microbes. J Cell Sci. 2011; 124 (Pt 18):3053–9. Epub 2011/08/27. https://doi.org/10.1242/jcs.082792 PMID: 21868367.
27. Herbomel P, Thisse B, Thisse C. Ontogeny and behaviour of early macrophages in the zebrafish embryo. Development. 1999; 126(17):3735–45. Epub 1999/08/06. https://doi.org/10.1242/dev.126.17.3735 PMID: 10433904.
28. Hilbi H, Buchrieser C. Microbe Profile: *Legionella pneumophila*—a copycat eukaryote. Microbiology (Reading). 2022; 168(3). https://doi.org/10.1099/mic.0.001142 PMID: 35230931.
29. Rolando M, Escoll P, Nora T, Botti J, Boitez V, Bedia C, et al. *Legionella pneumophila* S1P-lyase targets host sphingolipid metabolism and restrains autophagy. Proc Natl Acad Sci U S A. 2016; 113(7):1901–6. https://doi.org/10.1073/pnas.1522067113 PMID: 26831115; PubMed Central PMCID: PMC4763766.
30. Riddle MR, Hu CK. Fish models for investigating nutritional regulation of embryonic development. Dev Biol. 2021; 476:101–11. Epub 20210326. https://doi.org/10.1016/j.ydbio.2021.03.012 PMID: 33831748.
31. Liu X, Shin S. Viewing *Legionella pneumophila* Pathogenesis through an Immunological Lens. J Mol Biol. 2019; 431(21):4321–44. Epub 2019/07/29. https://doi.org/10.1016/j.jmb.2019.07.028 PMID: 31351897.
32. Cohen SB, Gern BH, Delahaye JL, Adams KN, Plumlee CR, Winkler JK, et al. Alveolar Macrophages Provide an Early *Mycobacterium tuberculosis* Niche and Initiate Dissemination. Cell Host Microbe. 2018; 24(3):439–46 e4. Epub 2018/08/28. https://doi.org/10.1016/j.chom.2018.08.001 PMID: 30146391; PubMed Central PMCID: PMC6152889.

33. Mengue L, Richard FJ, Caubet Y, Rolland S, Hechard Y, Samba-Louaka A. *Legionella pneumophila* decreases velocity of Acanthamoeba castellanii. Exp Parasitol. 2017; 183:124–7. Epub 2017/08/06. https://doi.org/10.1016/j.exppara.2017.07.013 PMID: 28778742.

34. Simon S, Wagner MA, Rothmeier E, Muller-Taubenberger A, Hilbi H. Icm/Dot-dependent inhibition of phagocyte migration by *Legionella* is antagonized by a translocated Ran GTPase activator. Cell Microbiol. 2014; 16(7):977–92. https://doi.org/10.1111/cmi.12258 PMID: 24397557.

35. Mostowy S, Boucontet L, Mazon Moya MJ, Sirianni A, Boudinot P, Hollinshead M, et al. The zebrafish as a new model for the in vivo study of *Shigella flexneri* interaction with phagocytes and bacterial autophagy. PLoS Pathog. 2013; 9(9):e1003588. https://doi.org/10.1371/journal.ppat.1003588 PMID: 24039575; PubMed Central PMCID: PMC3764221.

36. Su F, Juarez MA, Cooke CL, Lapointe L, Shavit JA, Yamaoka JS, et al. Differential regulation of primitive myelopoiesis in the zebrafish by Spi-1/Pu.1 and C/ebp1. Zebrafish. 2007; 4(3):187–99. Epub 2007/11/29. https://doi.org/10.1089/zeb.2007.0505 PMID: 18041923.

37. Ellett F, Pase L, Hayman JW, Andrianopoulos A, Lieschke GJ. mpeg1 promoter transgenes direct macrophage-lineage expression in zebrafish. Blood. 2011; 117(4):e49–56. Epub 2010/11/19. https://doi.org/10.1182/blood-2010-10-314120 PMID: 21084707; PubMed Central PMCID: PMC3056479.

38. Palha N, Guivel-Benhassine F, Briolat V, Lutfalla G, Sourisseau M, Ellett F, et al. Real-time whole-body visualization of Chikungunya Virus infection and host interferon response in zebrafish. PLoS Pathog. 2013; 9(9):e1003619. Epub 2013/09/17. https://doi.org/10.1371/journal.ppat.1003619 PMID: 24039582; PubMed Central PMCID: PMC3764224.

39. Phan QT, Sipka T, Gonzalez C, Levraud JP, Lutfalla G, Mai NC. Neutrophils use superoxide to control bacterial infection at a distance. Plos Pathogens. 2018; 14(7). ARTN e1007157 https://doi.org/10.1371/journal.ppat.1007157 WOS:000440351300015. PMID: 30016370

40. Copenhaver AM, Casson CN, Nguyen HT, Duda MM, Shin S. IL-1R signaling enables bystander cells to overcome bacterial blockade of host protein synthesis. Proc Natl Acad Sci U S A. 2015; 112(24):7557–62. Epub 2015/06/03. https://doi.org/10.1073/pnas.1501289112 PMID: 26034289; PubMed Central PMCID: PMC4475993.

41. Friedman H, Yamamoto Y, Klein TW. *Legionella pneumophila* pathogenesis and immunity. Semin Pediatr Infect Dis. 2002; 13(4):273–9. Epub 2002/12/20. https://doi.org/10.1053/spid.2002.127206 PMID: 12491233.

42. Asrat S, de Jesus DA, Hempstead AD, Ramabhadran V, Isberg RR. Bacterial pathogen manipulation of host membrane trafficking. Annu Rev Cell Dev Biol. 2014; 30:79–109. https://doi.org/10.1146/annurev-cellbio-100913-013439 PMID: 25103867.

43. Archer KA, Alexopoulou L, Flavell RA, Roy CR. Multiple MyD88-dependent responses contribute to pulmonary clearance of *Legionella pneumophila*. Cell Microbiol. 2009; 11(1):21–36. Epub 2008/09/11. CMI1234 [pii] https://doi.org/10.1111/j.1462-5822.2008.01234.x PMID: 18782351.

44. Archer KA, Roy CR. MyD88-dependent responses involving toll-like receptor 2 are important for protection and clearance of *Legionella pneumophila* in a mouse model of Legionnaires' disease. Infect Immun. 2006; 74(6):3325–33. Epub 2006/05/23. https://doi.org/74/6/3325 [pii] PMID: 16714560; PubMed Central PMCID: PMC1479235.

45. Hawn TR, Smith KD, Aderem A, Skerrett SJ. Myeloid differentiation primary response gene (88)- and toll-like receptor 2-deficient mice are susceptible to infection with aerosolized *Legionella pneumophila*. J Infect Dis. 2006; 193(12):1693–702. Epub 2006/05/17. https://doi.org/10.1086/504525 PMID: 16703513.

46. Sporri R, Joller N, Albers U, Hilbi H, Oxenius A. MyD88-dependent IFN-gamma production by NK cells is key for control of *Legionella pneumophila* infection. J Immunol. 2006; 176(10):6162–71. Epub 2006/05/04. https://doi.org/176/10/6162 [pii]. PMID: 16670325.

47. Mascarenhas DP, Pereira MS, Manin GZ, Hori JI, Zamboni DS. Interleukin 1 receptor-driven neutrophil recruitment accounts to MyD88-dependent pulmonary clearance of legionella pneumophila infection in vivo. J Infect Dis. 2015; 211(2):322–30. Epub 20140807. https://doi.org/10.1093/infdis/jiu430 PMID: 25104770.

48. Li YJ, Hu B. Establishment of multi-site infection model in zebrafish larvae for studying Staphylococcus aureus infectious disease. J Genet Genomics. 2012; 39(9):521–34. Epub 20120823. https://doi.org/10.1016/j.jgg.2012.07.006 PMID: 23021551.

49. Mazon-Moya MJ, Willis AR, Torraca V, Boucontet L, Shenoy AR, Colucci-Guyon E, et al. Septins restrict inflammation and protect zebrafish larvae from Shigella infection. PLoS Pathog. 2017; 13(6):e1006467. Epub 2017/06/27. https://doi.org/10.1371/journal.ppat.1006467 PMID: 28650995; PubMed Central PMCID: PMC5507465.

50. Hosseini R, Lamers GE, Soltani HM, Meijer AH, Spaink HP, Schaaf MJ. Efferocytosis and extrusion of leukocytes determine the progression of early mycobacterial pathogenesis. J Cell Sci. 2016; 129 (18):3385–95. Epub 2016/07/30. https://doi.org/10.1242/jcs.135194 PMID: 27469488.

51. Rosowski EE, Raffa N, Knox BP, Golenberg N, Keller NP, Huttenlocher A. Macrophages inhibit *Aspergillus fumigatus* germination and neutrophil-mediated fungal killing. PLoS Pathog. 2018; 14(8): e1007229. Epub 20180802. https://doi.org/10.1371/journal.ppat.1007229 PMID: 30071103; PubMed Central PMCID: PMC6091969.

52. Saralahti A, Ramet M. Zebrafish and Streptococcal Infections. Scand J Immunol. 2015; 82(3):174–83. https://doi.org/10.1111/sji.12320 PMID: 26095827.

53. Scherer AK, Blair BA, Park J, Seman BG, Kelley JB, Wheeler RT. Redundant Trojan horse and endothelial-circulatory mechanisms for host-mediated spread of *Candida albicans* yeast. PLoS Pathog. 2020; 16(8):e1008414. Epub 20200810. https://doi.org/10.1371/journal.ppat.1008414 PMID: 32776983; PubMed Central PMCID: PMC7447064.

54. Tesh MJ, Miller RD. Amino acid requirements for *Legionella pneumophila* growth. J Clin Microbiol. 1981; 13(5):865–9.

55. Fonseca MV, Swanson MS. Nutrient salvaging and metabolism by the intracellular pathogen *Legionella pneumophila*. Frontiers in cellular and infection microbiology. 2014; 4:12. https://doi.org/10.3389/fcimb.2014.00012 PMID: 24575391; PubMed Central PMCID: PMC3920079.

56. Hauslein I, Manske C, Goebel W, Eisenreich W, Hilbi H. Pathway analysis using (13) C-glycerol and other carbon tracers reveals a bipartite metabolism of *Legionella pneumophila*. Mol Microbiol. 2016; 100(2):229–46. https://doi.org/10.1111/mmi.13313 PMID: 26691313.

57. Hauslein I, Sahr T, Escoll P, Klausner N, Eisenreich W, Buchrieser C. *Legionella pneumophila* CsrA regulates a metabolic switch from amino acid to glycerolipid metabolism. Open Biol. 2017; 7(11). https://doi.org/10.1098/rsob.170149 PMID: 29093212.

58. Fraher D, Sanigorski A, Mellett NA, Meikle PJ, Sinclair AJ, Gibert Y. Zebrafish Embryonic Lipidomic Analysis Reveals that the Yolk Cell Is Metabolically Active in Processing Lipid. Cell Rep. 2016; 14 (6):1317–29. Epub 2016/02/09. https://doi.org/10.1016/j.celrep.2016.01.016 PMID: 26854233.

59. Hiller M, Lang C, Michel W, Flieger A. Secreted phospholipases of the lung pathogen *Legionella pneumophila*. Int J Med Microbiol. 2017. https://doi.org/10.1016/j.ijmm.2017.10.002 PMID: 29108710.

60. Ji JF, Hu CB, Zhang N, Huang X, Shao T, Fan DD, et al. New Insights into IgZ as a Maternal Transfer Ig Contributing to the Early Defense of Fish against Pathogen Infection. J Immunol. 2021; 206(9):2001–14. Epub 20210415. https://doi.org/10.4049/jimmunol.2001197 PMID: 33858963.

61. Wang Z, Zhang S, Wang G, An Y. Complement activity in the egg cytosol of zebrafish Danio rerio: evidence for the defense role of maternal complement components. PLoS One. 2008; 3(1):e1463. Epub 20080123. https://doi.org/10.1371/journal.pone.0001463 PMID: 18213372; PubMed Central PMCID: PMC2194919.

62. Brieland J, Freeman P, Kunkel R, Chrisp C, Hurley M, Fantone J, et al. Replicative *Legionella pneumophila* lung infection in intratracheally inoculated A/J mice. A murine model of human Legionnaires' disease. Am J Pathol. 1994; 145(6):1537–46. Epub 1994/12/01. PMID: 7992856; PubMed Central PMCID: PMC1887509.

63. Glavin FL, Winn WC Jr., Craighead JE. Ultrastructure of lung in Legionnaires' disease. Observations of three biopsies done during the Vermont epidemic. Ann Intern Med. 1979; 90(4):555–9. Epub 1979/04/01. https://doi.org/10.7326/0003-4819-90-4-555 PMID: 434634

64. Horwitz MA. Formation of a novel phagosome by the Legionnaires' disease bacterium (*Legionella pneumophila*) in human monocytes. J Exp Med. 1983; 158(4):1319–31.

65. Horwitz MA, Silverstein SC. Legionnaires' disease bacterium (*Legionella pneumophila*) multiples intracellularly in human monocytes. J Clin Invest. 1980; 66(3):441–50. https://doi.org/10.1172/JCI109874 PMID: 7190579.

66. Jager J, Marwitz S, Tiefenau J, Rasch J, Shevchuk O, Kugler C, et al. Human lung tissue explants reveal novel interactions during *Legionella pneumophila* infections. Infect Immun. 2014; 82(1):275–85. Epub 2013/10/30. https://doi.org/10.1128/IAI.00703-13 PMID: 24166955; PubMed Central PMCID: PMC3911869.

67. Copenhaver AM, Casson CN, Nguyen HT, Fung TC, Duda MM, Roy CR, et al. Alveolar macrophages and neutrophils are the primary reservoirs for *Legionella pneumophila* and mediate cytosolic surveillance of type IV secretion. Infect Immun. 2014; 82(10):4325–36. Epub 2014/08/06. https://doi.org/10.1128/IAI.01891-14 PMID: 25092908; PubMed Central PMCID: PMC4187856.

68. Bennett CM, Kanki JP, Rhodes J, Liu TX, Paw BH, Kieran MW, et al. Myelopoiesis in the zebrafish, *Danio rerio*. Blood. 2001; 98(3):643–51. Epub 2001/07/27. https://doi.org/10.1182/blood.v98.3.643 PMID: 11468162.

69. Le Guyader D, Redd MJ, Colucci-Guyon E, Murayama E, Kissa K, Briolat V, et al. Origins and unconventional behavior of neutrophils in developing zebrafish. Blood. 2008; 111(1):132–41. Epub 2007/09/19. https://doi.org/10.1182/blood-2007-06-095398 PMID: 17875807.

70. Willett CE, Cortes A, Zuasti A, Zapata AG. Early hematopoiesis and developing lymphoid organs in the zebrafish. Dev Dyn. 1999; 214(4):323–36. Epub 1999/04/23. https://doi.org/10.1002/(SICI)1097-0177(199904)214:4<323::AID-AJA5>3.0.CO;2-3 PMID: 10213388.

71. Mesureur J, Feliciano JR, Wagner N, Gomes MC, Zhang L, Blanco-Gonzalez M, et al. Macrophages, but not neutrophils, are critical for proliferation of *Burkholderia cenocepacia* and ensuing host-damaging inflammation. PLoS Pathog. 2017; 13(6):e1006437. Epub 2017/06/27. https://doi.org/10.1371/journal.ppat.1006437 PMID: 28651010; PubMed Central PMCID: PMC5501683.

72. Prajsnar TK, Cunliffe VT, Foster SJ, Renshaw SA. A novel vertebrate model of *Staphylococcus aureus* infection reveals phagocyte-dependent resistance of zebrafish to non-host specialized pathogens. Cell Microbiol. 2008; 10(11):2312–25. Epub 2008/08/22. https://doi.org/10.1111/j.1462-5822.2008.01213.x PMID: 18715285.

73. Jault C, Pichon L, Chluba J. Toll-like receptor gene family and TIR-domain adapters in *Danio rerio*. Mol Immunol. 2004; 40(11):759–71. Epub 2003/12/23. https://doi.org/10.1016/j.molimm.2003.10.001 PMID: 14687933.

74. Meijer AH, Gabby Krens SF, Medina Rodriguez IA, He S, Bitter W, Ewa Snaar-Jagalska B, et al. Expression analysis of the Toll-like receptor and TIR domain adaptor families of zebrafish. Mol Immunol. 2004; 40(11):773–83. Epub 2003/12/23. https://doi.org/10.1016/j.molimm.2003.10.003 PMID: 14687934.

75. Akira S, Takeda K. Toll-like receptor signalling. Nat Rev Immunol. 2004; 4(7):499–511. Epub 2004/07/02. https://doi.org/10.1038/nri1391 PMID: 15229469.

76. Mallama CA, McCoy-Simandle K, Cianciotto NP. The Type II Secretion System of *Legionella pneumophila* Dampens the MyD88 and Toll-Like Receptor 2 Signaling Pathway in Infected Human Macrophages. Infect Immun. 2017; 85(4). Epub 2017/02/01. https://doi.org/10.1128/IAI.00897-16 PMID: 28138020; PubMed Central PMCID: PMC5364298.

77. Fontana MF, Banga S, Barry KC, Shen X, Tan Y, Luo ZQ, et al. Secreted bacterial effectors that inhibit host protein synthesis are critical for induction of the innate immune response to virulent *Legionella pneumophila*. PLoS Pathog. 2011; 7(2):e1001289.

78. Wik JA, Phung D, Kolan S, Haraldsen G, Skalhegg BS, Hol Fosse J. Inflammatory activation of endothelial cells increases glycolysis and oxygen consumption despite inhibiting cell proliferation. FEBS Open Bio. 2021; 11(6):1719–30. Epub 2021/05/13. https://doi.org/10.1002/2211-5463.13174 PMID: 33979025; PubMed Central PMCID: PMC8167874.

79. Hall C, Flores MV, Storm T, Crosier K, Crosier P. The zebrafish lysozyme C promoter drives myeloid-specific expression in transgenic fish. Bmc Dev Biol. 2007; 7. Artn 42 WOS:000246708100001. https://doi.org/10.1186/1471-213X-7-42 PMID: 17477879

80. Renshaw SA, Loynes CA, Trushell DM, Elworthy S, Ingham PW, Whyte MK. A transgenic zebrafish model of neutrophilic inflammation. Blood. 2006; 108(13):3976–8. Epub 2006/08/24. https://doi.org/10.1182/blood-2006-05-024075 PMID: 16926288.

81. van Leeuwen LM, Evans RJ, Jim KK, Verboom T, Fang X, Bojarczuk A, et al. A transgenic zebrafish model for the *in vivo* study of the blood and choroid plexus brain barriers using claudin 5. Biol Open. 2018; 7(2). Epub 2018/02/14. https://doi.org/10.1242/bio.030494 PMID: 29437557; PubMed Central PMCID: PMC5861362.

82. van der Vaart M, van Soest JJ, Spaink HP, Meijer AH. Functional analysis of a zebrafish myd88 mutant identifies key transcriptional components of the innate immune system. Dis Model Mech. 2013; 6(3):841–54. https://doi.org/10.1242/dmm.010843 WOS:000318847400030. PMID: 23471913

83. Tiaden A, Spirig T, Weber SS, Bruggemann H, Bosshard R, Buchrieser C, et al. The *Legionella pneumophila* response regulator LqsR promotes host cell interactions as an element of the virulence regulatory network controlled by RpoS and LetA. Cell Microbiol. 2007; 9(12):2903–20. Epub 2007/07/07. CMI1005 [pii] https://doi.org/10.1111/j.1462-5822.2007.01005.x PMID: 17614967.

84. Levraud JP, Colucci-Guyon E, Redd MJ, Lutfalla G, Herbomel P. In vivo analysis of zebrafish innate immunity. Methods Mol Biol. 2008; 415:337–63. https://doi.org/10.1007/978-1-59745-570-1_20 PMID: 18370164.

85. Brannon MK, Davis JM, Mathias JR, Hall CJ, Emerson JC, Crosier PS, et al. *Pseudomonas aeruginosa* Type III secretion system interacts with phagocytes to modulate systemic infection of zebrafish embryos. Cell Microbiol. 2009; 11(5):755–68. Epub 2009/02/12. https://doi.org/10.1111/j.1462-5822.2009.01288.x PMID: 19207728; PubMed Central PMCID: PMC2933946.

86. Colucci-Guyon E, Rifflet A, Saint-Auret S, da Costa A, Boucontet L, Laval T, et al. Spatiotemporal analysis of mycolactone distribution i*n vivo* reveals partial diffusion in the central nervous system. PLoS Negl

Trop Dis. 2020; 14(12):e0008878. Epub 2020/12/03. https://doi.org/10.1371/journal.pntd.0008878 PMID: 33264290; PubMed Central PMCID: PMC7710047.

87. Kimmel CB, Ballard WW, Kimmel SR, Ullmann B, Schilling TF. Stages of embryonic development of the zebrafish. Dev Dyn. 1995; 203(3):253–310. https://doi.org/10.1002/aja.1002030302 PMID: 8589427.

Chapter 3: Outlook

In this paper, I was involved in imaging, image reconstruction, image analysis, and partially in statistical analysis. The finalization was possible due to the collaboration with Carmen Buchreiser lab and Flavia Vania, which contribute was fundamental.

We effectively demonstrated that zebrafish larvae can be used as an animal model to study *L. pneumophila.* Upon infection by *Legionella,* we observed the depletion of professional phagocytes and the essential role of macrophages in controlling this infection. Moreover, we demonstrated that zebrafish and humans share similarities in the Myd88 mediated response as for both it is not relevant to control infection, in contrast with what was observed in mice. Furthermore, we identified the tissues affected by *Legionella* infection about the role of T4SS. In a consistent percentage of larvae, we observed the passage of *Legionella* from the blood circulation to the yolk. The yolk has a fundamental role as a nutrient reservoir in zebrafish larvae and it is a giant cell separated from the rest of the larva by a 3-layer membrane, which makes it impervious to leukocyte infiltration(D'Amico and Cooper, 2001; Virta and Cooper, 2011). T4SS-proficient *Legionella* can infect this compartment and proliferate in it, demonstrating that T4SS is necessary for both infection and nutrient uptake.

Moreover, by high-resolution imaging, we demonstrated that *Legionella,* once in the yolk, still produces factors that can elicit inflammation and leukocyte recruitment. As the yolk is impervious to leukocyte infiltration and is nutrient-rich, it can act both as immune escape tissue and replication niche for *Legionella.*

Lastly, we observed a parallelism between cytokines and inflammation factors between zebrafish and humans, with the expression of TNF□ and interleukins, missing in mouse infection.

Similar to the approach used in the SINV paper, I optimized the mounting conditions to perform long time-lapses on several samples to observe *Legionella* interaction with different tissues. Major optimization was done to perform ultrarapid acquisition with resonant scanning, which can scan bidirectionally at 8000Hz sacrificing some photon acquisition, and image post-processing to recover the image quality. Due to the size of the files (~300 gb per larvae), further optimization was performed to be able to reconstruct the images in 4D videos.

Moreover, was adopted a new image analysis method to quantify the relative number of bacteria and leucocytes, whether macrophages and/or neutrophils, in the periphery or the yolk of each larva.

Our project will move forward with Clarisse Leseigneur as the new post-doc to identify the soluble factor released by *Legionella* in the yolk and investigate the immune response to *Legionella* infection and its behavior in zebrafish.

IMAGING AND ZEBRAFISH

As we explained, one of the most useful advantages of zebrafish larvae is the transparency, which coupled with their reduced size, allows for unique imaging of a mid/large number of samples to observe in vivo cell/tissue/pathogen interactions.

A large number of my efforts went to the optimization of zebrafish imaging.

I streamlined the workflow and identified critical handling points:

- Anesthetic: normally tricaine is used, on fragile larvae imaged in small wells for >24h it generates toxicity, especially under evaporation which induces water acidification.
- Mounting: Normally larvae are mounted in 1% low melting agarose, but under long imaging, the physical constraints in growing larvae and edemas induced by pathogens, speed up death by tail-tip crooking and blood circulation block
- Imaging: 2 types of imaging were needed for the papers. The first is a high-content screening of whole larvae and the second is a low/mid-high resolution, high-speed imaging of whole larvae or single tiles.
- Data handling, post-processing, and image analysis: Due to the large size of images it is necessary to create specific data handling rules to store and work on the images (single experiment ~1.5 Tb). After the images need to be processed and analyzed conserving a user-friendly spirit to advantage the whole laboratory.

To resolve the first problem of anesthetic toxicity, I opted for combinatorial anesthesia, usually used in mammals. I focused on using the two widespread anesthetics for zebrafish, Tricaine, and Isoeugenol(Swinburne et al., 2015). Tricaine mesylate, also known as Tricaine methanesulfonate, is a widespread benzocaine-derived anesthetic for fish. This compound easily permeates the larvae, blocking neuronal depolarization by competitive binding of sodium channels (Carter et al., 2011). Isoeugenol is a compound extracted from clover and characterized by a distinctive clover smell. Isoeugenol is used as a common anesthetic even in humans as it inhibits the pain sensation by blocking GABA receptors (Kheawfu et al., 2022). In both cases, the anesthetic effect is exercised on nervous cells and does not block muscle depolarization.

Nonetheless, testing different combinations, I managed to reduce to the minimum the amount of anesthetic by combining these two compounds in a sodium-buffered solution to avoid tricaine induce acidification. As this solution is still not optimal, I am designing a chemically inducible transgenic line expressing bungarotoxin under the heavy chain myosin promoter control, to block the neuromuscular junction. Regardless, neither of these solutions can block completely twitching by involuntary muscle depolarization, so more tests are needed to find a combination that can block both neuronal signaling and muscle twitching. Nonetheless, when studying viruses like SINV, it is advisable to test different anesthetics to exclude competitive binding with the receptor class on the neuromuscular junction that may be used by the virus to enter the synapse.

For the mounting, the purpose was to set the x, y, z coordinates of each larva in the respective medium, while avoiding physical constraints. For this purpose, I designed several molds with different approximations of zebrafish larvae shapes. After identification of the best shape, the mold was used to shape phytagel 1% in each well simultaneously. Each larva can slip in the grove and, to avoid physical constraints, it is blocked by hydrogel or low melting agarose 0.6% gel at room temperature. This further eliminates the risk associated with encasing larvae in solidifying hot agarose. To stabilize the larvae, as the stage of our microscopes moves, we further added a thin sheet of agarose 1% on the top of the multilayer mounting.

Regarding imaging, although many new technologies are now available and optimized for zebrafish high-content screening on ultra-fast high-resolution imaging, I optimized the pre-existing microscopes available in the laboratory.

For mid/high content screening we used a simple EVOS flauto2 by thermofisher. This microscope is mainly used for cell cultures, so it is not optimized for zebrafish images. Coupling the mold system previously explained with a Fiji script to reconstruct and normalize each well, we managed to automate the acquisition process satisfactorily using 24 or 48 multiwells. All the images used for global dissemination in the SINV paper were generated with this method.

For low-content screening and high-resolution imaging, many new technologies such as Scape light sheet technology or hybrid widefield/confocal technology appeared in the latest year and focused a part of their effort on zebrafish larvae imaging (Voleti et al., 2019; Z. Wang et al., 2021). Nonetheless, these systems are still expensive and were not available at the time of experimentation.

For this purpose, I optimized the use of a Leica sp8 confocal equipped with resonant scanning and a moving stage. Resonant scanning technology is based on a fast-spinning mirror that can reach 8 kHz (normal confocal speed has a maximum average of 1.5 kHz). The fast-rotating mirror associated with bidirectional scanning allows fast imaging and reduces photobleaching. In contrast, this speed increases the number of lost photons and is subject to manual aligning of bidirectional scanning. Nonetheless, upon optimization of hardware and software settings (i.e., data transfer type, integration method, and bit depth) it was possible to balance phototoxicity, acquisition speed, and resolution. With this approach I was able to acquire large portions of zebrafish larvae, in the whole thickness, to observe leucocyte behaviors on an average of 8 zebrafish for experiments or acquire whole larvae confocal images of an average of ~12 larvae to increase resolution and being able to observe tissue dynamics.

Indeed, the optimization work of the confocal acquisition setting was an interesting part of the work as we were pushing the hardware and software of the machine to the limit, often discovering new bugs in the system that we reported to Leica directly.

Nevertheless, the data generated from such types of experimentation was increasingly large, with single experiments reaching easily the 2Tb size. This required a different approach to data handling, as Institut Pasteur data structures were not able to handle it.

I created a data mirroring system using two sinology network-attached storage units (NAS). The first was able to export with direct rapid connection large quantity of data at <5Gb/s and the second mirrors the data from the first NAS to conserve a security copy of raw data. With this solution, I was able to divide in shards the bigger files to operate on them.

For example, as I explained the resonant scanning image can be “noisy” as a large percentage of photons are lost. To solve this problem, I applied two layers of denoising and deconvolution. The first one uses the Leica addon directly during live acquisition, thanks to the speed of the first NAS, and the second, in post-processing uses the slower NAS.

Returning to the high-content screening, the challenge was the normalization of each larvae image and successive analysis. For the normalization, I designed a Fiji script to automatically denoise by Gaussian filter each image and subsequently record the original intensity. The script proceeds with tophat filtering and light correction. It stretches the LUT and re-crops the larvae.

As the intensity of the signal produced by the pathogen increases over time, it was impossible to set parameters of acquisition at the start of the experiment that would avoid sensor oversaturation. This means that was necessary to adjust the parameters each day, effectively eliminating the possibility of using integrated intensity for quantification. To solve this problem, I parametrized each acquisition on the saturation value of the sensor for the brightest larvae and reduced said value by 5%. In this way, I was able to be sure to acquire the totality of the intensity range without under or over-saturation. Subsequently, for analysis, I used thresholding instead of intensity.

Using the BioVoxxel toolbox I identify the best thresholding method and imported it into the Fiji script, thresholding each larvae in the same way ("Qualitative and Quantitative Evaluation of Two New Histogram Limiting Binarization Algorithms," n.d.). The binary images were imported in a cell profiler script, which segmented the positive area in objects and applied filters on the size, robustness, and circularity of the object. Finally, these objects were semi-automatically cleaned to remove specific signals and masked to divide the signal in each compartment. As we standardized the image dimension, the number of positive pixels was further divided by the number of pixels for each image. Instead, for neutrophils, for example, the same approach was used to directly control the number of cells.

The purpose of using this approach, as shown in Annex 1 was to create a user-friendly and robust method, that does not require a high degree of training and continuous support by a programmer, but, instead, can be used, optimized, and updated by less image analysis savvy biologists. Indeed, CellProfiler software is fully annotated, and it is a module based while it allows for the creation of Python personalized modules and Fiji scripts integration, it has a mild learning curve.

Instead, for the large image generated by high-resolution imaging, all the post-processing (i.e., normalization, denoising, edging) was conducted in Fiji. The 4D reconstruction was conducted on Imaris software. The surfacing and further post-processing were established on a random pool of images and automatically applied to all the experiments, while the contouring of compartments (i.e., the yolk for paper 3) was manual.

To conclude, besides the work on the biological question, I embarked on the optimization process of the laboratory workflow, with the ideal aim to perform data mining of kinetical data from the images generated and to improve experiment consistency. Unfortunately, the technologies to perform this type of inquiry are still limited.

For example, the variety of genetically encoded proteins is still limited as there are close to none near-infrared fluorescent proteins available for zebrafish larvae, forcing the multiplexing of close-spectrum fluorescent proteins that often yield unsatisfactory results *in vivo*.

At the moment of writing this thesis, I embarked on a collaboration to create an fully automatic platform able to perform the image screening and genetic screening I performed in the papers, aiming in the future to develop a system for data mining able to pour in a database the host-pathogen variables extracted from different zebrafish lines and pathogens. These data could be useful to train machine learning systems to identify homologies between patterns of already studied pathogens or new emerging pathogens and identify protein family targets for humanization or new immunological pathways.

GLOBAL CONCLUSIONS

"The red line binding together the papers presented in this thesis is the exploration of zebrafish larvae as a model for host-pathogen interaction, using either human viruses or bacteria. An important aspect of this exploration is the development and testing of new approaches and techniques to unveil the potential of this alternative animal model. "

Through a series of papers, I investigated the potential of zebrafish larvae as a model for studying host-pathogen interactions, with a focus on human pathogens. My work aimed to answer complex biological questions and develop new methodologies.

One of my key findings, detailed in the first paper, was the identification of the propagation route of the Sindbis virus in zebrafish larvae. This research revealed the role of the spinal cord as a viral reservoir and highlighted parallels between zebrafish and humans. For example, muscle infection in zebrafish was coherent with human myalgia (Sane et al., 2012). Additionally, the persistence of IgM in humans after the resolution of muscle infection hints at the presence of a "long SINV" replicative niche. Our findings suggested that the "long SINV" replicative niche in humans could be the equivalent of zebrafish spinal cord. These discoveries have important implications for the study of host-pathogen interactions and the development of new treatments and therapies.

Indeed, we demonstrated that this model can rapidly generate relatively consistent data of the whole statistical population, which are perfect for mathematical modeling. Factoring this, a topic I would like to explore in the future is the coupling between zebrafish experimentation and *in silico* simulation through machine learning, as it could further speed up research and prove a useful tool.

Moreover, we demonstrated that SINV can be used as a tool to discriminate the intricate network of connection in live zebrafish, to complement the already well-known use of SINV as a vector for gene therapies (Lundstrom, 2001; Scherwitzl et al., 2020; Xiong et al., 1989).

Following my purpose of exploring zebrafish potential and the urgent need to understand the infection caused by this emerging virus, I approached the project on SARS-CoV2. In this paper, we detail the possibility of using zebrafish as a model for this pathogen, a possible humanization of the ACE2 receptor, and further challenge the technical difficulties of zebrafish experimentation in BSL3.

Although the project did not yield marked positive results, it still defined the "go-no go" for this type of project and increasingly demonstrated the potential of investing in zebrafish humanization and research to create ad-hoc models for pathogens and/or identify key proteins in pathogen's intracellular pathways.

In the third paper, we positively explored the possibility of using zebrafish as an animal model for *L. pneumophila*, finding interesting parallelism between zebrafish and human infection, lacking in mice. Furthermore, we characterize a unique T4SS-dependent behavior of *Legionella* in zebrafish yolk. One of the technical challenges we solved in this paper is imaging. Due to the rapidity of leukocyte movement and the large area to image for a long time, I developed new sample preparation and data handling and quantification to effectively observe the interaction in 4D and measure the leukocyte recruitment.

To conclude, my perspectives are to keep investigating the zebrafish immune system to pathogen infection while in parallel developing new techniques aimed to maintain a physiologic environment (i.e., a chemically inducible line expressing bungarotoxin under heavy chain myosin), automatization (platform for automatic screening on microfluidic chips), machine learning based on zebrafish data and humanization protocols.

From the biological point of view, a topic I would like to explore is the priming of the microenvironment in the intersection between the periphery and CNS in the frame of single or double infection and subsequent tissue regeneration. To clarify this sentence, I want to focus on the neuro-immune reflex, and in detail on immunity carry-over from the periphery to CNS; investigating the mechanisms of immune sensing and associated elicitor pathways. I would like to keep a holistic vision of the process of infection, using both viruses and bacteria to identify the different pathways associated to immune sensing and further delve in co-infection scenarios, that are often overlooked for a matter of complexity. Indeed, this is the reason to focus on new techniques and tools. Moreover, I would like to investigate the presence of alternative forms of immunological memory and observe if it affects the regeneration post infection too.

Lastly, while investigating these topics, I would still characterize new mechanisms on pathogen side, as we did for *Legionella* and Sindbis virus papers.

I won’t hide the fact that these past years of work on viruses greatly expanded my interest in these pathogens, which in their relative “simplicity” are able to generate complex mechanisms with incredible efficiency. For this reason, in the future, I will always try to expand my knowledge of pathogens and build part of my career around them.

I am aware that these fields are wide and possibly dispersed and for this reason I would focus on the use of emerging pathogens and their treatments.

BIBLIOGRAPHY

Abdollahpour H, Falahatkar B, Lawrence C. 2020. The effect of photoperiod on growth and spawning performance of zebrafish, Danio rerio. *Aquac Reports* **17**:100295. doi:10.1016/J.AQREP.2020.100295

Abtin A, Jain R, Mitchell AJ, Roediger B, Brzoska AJ, Tikoo S, Cheng Q, Ng LG, Cavanagh LL, Von Andrian UH, Hickey MJ, Firth N, Weninger W. 2013. Perivascular macrophages mediate neutrophil recruitment during bacterial skin infection. *Nat Immunol 2013 151* **15**:45–53. doi:10.1038/ni.2769

Ackerman SD, Monk KR. 2016. The scales and tales of myelination: using zebrafish and mouse to study myelinating glia. *Brain Res* **1641**:79–91. doi:10.1016/J.BRAINRES.2015.10.011

Adatto I, Lawrence C, Krug L, Zon LI. 2022. The effects of intensive feeding on reproductive performance in laboratory zebrafish (Danio rerio). *PLoS One* **17**:e0278302. doi:10.1371/JOURNAL.PONE.0278302

Adatto I, Lawrence C, Thompson M, Zon LI. 2011. A New System for the Rapid Collection of Large Numbers of Developmentally Staged Zebrafish Embryos. *PLoS One* **6**:e21715. doi:10.1371/JOURNAL.PONE.0021715

Aderem A, Underhill DM. 2003. MECHANISMS OF PHAGOCYTOSIS IN MACROPHAGES. *https://doi.org/101146/annurev.immunol171593* **17**:593–623. doi:10.1146/ANNUREV.IMMUNOL.17.1.593

Adouchief S, Smura T, Sane J, Vapalahti O, Kurkela S. 2016a. Sindbis virus as a human pathogen—epidemiology, clinical picture and pathogenesis. *Rev Med Virol* **26**:221–241. doi:10.1002/RMV.1876

Adouchief S, Smura T, Sane J, Vapalahti O, Kurkela S. 2016b. Sindbis virus as a human pathogen-epidemiology, clinical picture and pathogenesis. *Rev Med Virol* **26**:221–241. doi:10.1002/rmv.1876

Aggad D, Mazel M, Boudinot P, Mogensen KE, Hamming OJ, Hartmann R, Kotenko S, Herbomel P, Lutfalla G, Levraud J-P. 2009. The two groups of zebrafish virus-induced interferons signal

via distinct receptors with specific and shared chains. *J Immunol* **183**:3924–3931. doi:10.4049/jimmunol.0901495

Aggad D, Stein C, Sieger D, Mazel M, Boudinot P, Herbomel P, Levraud J-P, Lutfalla G, Leptin M. 2010. In Vivo Analysis of Ifn-γ1 and Ifn-γ2 Signaling in Zebrafish. *J Immunol* **185**:6774–6782. doi:10.4049/JIMMUNOL.1000549

Al-Khalifa MS, Diab FM, Khalil GM. 2007. Man-threatening viruses isolated from ticks in Saudi Arabia. *Saudi Med J* **28**:1864–1867.

Altmann SM, Mellon MT, Johnson MC, Paw BH, Trede NS, Zon LI, Kim CH. 2004. Cloning and characterization of an Mx gene and its corresponding promoter from the zebrafish, Danio rerio. *Dev Comp Immunol* **28**:295–306. doi:10.1016/J.DCI.2003.09.001

Amraei R, Yin W, Napoleon MA, Suder EL, Berrigan J, Zhao Q, Olejnik J, Chandler KB, Xia C, Feldman J, Hauser BM, Caradonna TM, Schmidt AG, Gummuluru S, Mü E, Chitalia V, Costello CE, Rahimi N. 2021. CD209L/L-SIGN and CD209/DC-SIGN act as receptors for SARS-CoV-2. *ACS Publ* **7**:1156–1165. doi:10.1021/acscentsci.0c01537

An M, Luo R, Henion PD. 2002. Differentiation and maturation of zebrafish dorsal root and sympathetic ganglion neurons. *J Comp Neurol* **446**:267–275. doi:10.1002/CNE.10214

Andreassen AH, Hall P, Khatibzadeh P, Jutfelt F, Kermen F. 2022. Brain dysfunction during warming is linked to oxygen limitation in larval zebrafish. *Proc Natl Acad Sci U S A* **119**:e2207052119. doi:10.1073/PNAS.2207052119/SUPPL_FILE/PNAS.2207052119.SM03.AVI

Antonio N, Bønnelykke-Behrndtz ML, Ward LC, Collin J, Christensen IJ, Steiniche T, Schmidt H, Feng Y, Martin P. 2015. The wound inflammatory response exacerbates growth of pre-neoplastic cells and progression to cancer. *EMBO J* **34**:2219–2236. doi:10.15252/EMBJ.201490147

Artika IM, Dewantari AK, Wiyatno A. 2020. Molecular biology of coronaviruses: current knowledge. *Heliyon* **6**:e04743. doi:10.1016/J.HELIYON.2020.E04743

Arunachalam M, Raja M, Vijayakumar C, Malaiammal P, Mayden RL. 2013. Natural history of zebrafish (Danio rerio) in India. *Zebrafish* **10**:1–14.

doi:10.1089/ZEB.2012.0803/ASSET/IMAGES/LARGE/FIGURE6.JPEG

Bakkers J. 2011. Zebrafish as a model to study cardiac development and human cardiac disease. *Cardiovasc Res* **91**:279–288. doi:10.1093/CVR/CVR098

Bell-Sakyi L, Weisheit S, Rückert C, Barry G, Fazakerley J, Fragkoudis R. 2016. Microscopic Visualisation of Zoonotic Arbovirus Replication in Tick Cell and Organ Cultures Using Semliki Forest Virus Reporter Systems. *Vet Sci* **3**. doi:10.3390/vetsci3040028

Bell EA, Cable J, Oliveira C, Richardson DS, Yant L, Taylor MI. 2020. Help or hindrance? The evolutionary impact of whole-genome duplication on immunogenetic diversity and parasite load. *Ecol Evol* **10**:13949–13956. doi:10.1002/ECE3.6987

Bennett CM, Kanki JP, Rhodes J, Liu TX, Paw BH, Kieran MW, Langenau DM, Delahaye-Brown A, Zon LI, Fleming MD, Thomas Look A. 2001. Myelopoiesis in the zebrafish, Danio rerio. *Blood* **98**:643–651. doi:10.1182/BLOOD.V98.3.643

Berman JN, Kanki JP, Look AT. 2005. Zebrafish as a model for myelopoiesis during embryogenesis. *Exp Hematol* **33**:997–1006. doi:10.1016/J.EXPHEM.2005.06.010

Bernhardt RR, Chitnis AB, Lindamer L, Kuwada JY. 1990. Identification of spinal neurons in the embryonic and larval zebrafish. *J Comp Neurol* **302**:603–616. doi:10.1002/cne.903020315

Bertrand JY, Cisson JL, Stachura DL, Traver D. 2010. Notch signaling distinguishes 2 waves of definitive hematopoiesis in the zebrafish embryo. *Blood* **115**:2777–2783. doi:10.1182/BLOOD-2009-09-244590

Best K, Guedj J, Madelain V, de Lamballerie X, Lim S-Y, Osuna CE, Whitney JB, Perelson AS. 2017. Zika plasma viral dynamics in nonhuman primates provides insights into early infection and antiviral strategies. *Proc Natl Acad Sci U S A* **114**:8847–8852. doi:10.1073/pnas.1704011114

Bjørgen H, Hellberg H, Løken OM, Gunnes G, Koppang EO, Dale OB. 2019. Tumor microenvironment and stroma in intestinal adenocarcinomas and associated metastases in Atlantic salmon broodfish (Salmo salar). *Vet Immunol Immunopathol* **214**. doi:10.1016/J.VETIMM.2019.109891

Bojarczuk A, Miller KA, Hotham R, Lewis A, Ogryzko N V., Kamuyango AA, Frost H, Gibson RH, Stillman E, May RC, Renshaw SA, Johnston SA. 2016. Cryptococcus neoformans Intracellular Proliferation and Capsule Size Determines Early Macrophage Control of Infection. *Sci Reports 2016 61* **6**:1–15. doi:10.1038/srep21489

Bottiglione F, Dee CT, Lea R, Zeef LAH, Badrock AP, Wane M, Bugeon L, Dallman MJ, Allen JE, Hurlstone AFL. 2020. Zebrafish IL-4–like Cytokines and IL-10 Suppress Inflammation but Only IL-10 Is Essential for Gill Homeostasis. *J Immunol* **205**:994–1008. doi:10.4049/JIMMUNOL.2000372

Boucontet L, Passoni G, Thiry V, Maggi L, Herbomel P, Levraud J-P, Colucci-Guyon E. 2018. A model of superinfection of virus-infected zebrafish larvae: Increased susceptibility to bacteria associated with neutrophil death. *Front Immunol* **9**:1084. doi:10.3389/fimmu.2018.01084

Brady M, Sundareshan V. 2017. Legionnaires' disease.

Brehm MA, Jouvet N, Greiner DL, Shultz LD. 2013. Humanized Mice for the Study of Infectious Diseases. *Curr Opin Immunol* **25**:428. doi:10.1016/J.COI.2013.05.012

Briggs JP. 2002. The zebrafish: a new model organism for integrative physiology. *https://doi.org/101152/ajpregu005892001* **282**. doi:10.1152/AJPREGU.00589.2001

Britto DD, Wyroba B, Chen W, Lockwood RA, Tran KB, Shepherd PR, Hall CJ, Crosier KE, Crosier PS, Astin JW. 2018. Macrophages enhance Vegfa-driven angiogenesis in an embryonic zebrafish tumour xenograft model. *DMM Dis Model Mech* **11**. doi:10.1242/DMM.035998/VIDEO-8

Buckley CD, Ross EA, McGettrick HM, Osborne CE, Haworth O, Schmutz C, Stone PCW, Salmon M, Matharu NM, Vohra RK, Nash GB, Rainger GE. 2006. Identification of a phenotypically and functionally distinct population of long-lived neutrophils in a model of reverse endothelial migration. *J Leukoc Biol* **79**:303–311. doi:10.1189/JLB.0905496

Burgener SS, Schroder K. 2020. Neutrophil Extracellular Traps in Host Defense. *Cold Spring Harb Perspect Biol* **12**:a037028. doi:10.1101/CSHPERSPECT.A037028

Burillo A, Pedro-Botet ML, Bouza E. 2017. Microbiology and Epidemiology of Legionnaire's Disease. *Infect Dis Clin* **31**:7–27. doi:10.1016/J.IDC.2016.10.002

Butovsky O, Jedrychowski MP, Moore CS, Cialic R, Lanser AJ, Gabriely G, Koeglsperger T, Dake B, Wu PM, Doykan CE, Fanek Z, Liu L, Chen Z, Rothstein JD, Ransohoff RM, Gygi SP, Antel JP, Weiner HL. 2013. Identification of a unique TGF-β–dependent molecular and functional signature in microglia. *Nat Neurosci 2013 171* **17**:131–143. doi:10.1038/nn.3599

Byrd AS, O'Brien XM, Johnson CM, Lavigne LM, Reichner JS. 2013. An Extracellular Matrix–Based Mechanism of Rapid Neutrophil Extracellular Trap Formation in Response to Candida albicans. *J Immunol* **190**:4136–4148. doi:10.4049/JIMMUNOL.1202671

Campos-Sánchez JC, Esteban MÁ. 2021. Review of inflammation in fish and value of the zebrafish model. *J Fish Dis* **44**:123–139. doi:10.1111/JFD.13310

Cantuti-Castelvetri L, Ojha R, Pedro LD, Djannatian M, Franz J, Kuivanen S, van der Meer F, Kallio K, Kaya T, Anastasina M, Smura T, Levanov L, Szirovicza L, Tobi A, Kallio-Kokko H, Österlund P, Joensuu M, Meunier FA, Butcher SJ, Winkler MS, Mollenhauer B, Helenius A, Gokce O, Teesalu T, Hepojoki J, Vapalahti O, Stadelmann C, Balistreri G, Simons M. 2020. Neuropilin-1 facilitates SARS-CoV-2 cell entry and infectivity. *Science (80-)* **370**. doi:10.1126/SCIENCE.ABD2985

Carpenter AE, Jones TR, Lamprecht MR, Clarke C, Kang IH, Friman O, Guertin DA, Chang JH, Lindquist RA, Moffat J, Golland P, Sabatini DM. 2006. CellProfiler: image analysis software for identifying and quantifying cell phenotypes. *Genome Biol* **7**:R100. doi:10.1186/gb-2006-7-10-r100

Carrasco L, Sanz MA, González-Almela E. 2018. The Regulation of Translation in Alphavirus-Infected Cells. *Viruses 2018, Vol 10, Page 70* **10**:70. doi:10.3390/V10020070

Carrillo SA, Anguita-Salinas C, Peña OA, Morales RA, Muñoz-Sánchez S, Muñoz-Montecinos C, Paredes-Zúñiga S, Tapia K, Allende ML. 2016. Macrophage Recruitment Contributes to Regeneration of Mechanosensory Hair Cells in the Zebrafish Lateral Line. *J Cell Biochem* **117**:1880–1889. doi:10.1002/JCB.25487

Carter KM, Woodley CM, Brown RS. 2011. A review of tricaine methanesulfonate for anesthesia of fish. *Rev Fish Biol Fish* **21**:51–59. doi:10.1007/s11160-010-9188-0

Carvalho R, de Sonneville J, Stockhammer OW, Savage NDL, Veneman WJ, Ottenhoff THM,

Dirks RP, Meijer AH, Spaink HP. 2011. A High-Throughput Screen for Tuberculosis Progression. *PLoS One* **6**:e16779. doi:10.1371/JOURNAL.PONE.0016779

Casalino L, Gaieb Z, Goldsmith JA, Hjorth CK, Dommer AC, Harbison AM, Fogarty CA, Barros EP, Taylor BC, Mclellan JS, Fadda E, Amaro RE. 2020. Beyond Shielding: The Roles of Glycans in the SARS-CoV-2 Spike Protein. *ACS Cent Sci* **6**:1722–1734. doi:10.1021/ACSCENTSCI.0C01056

Castro R, Bernard D, Lefranc MP, Six A, Benmansour A, Boudinot P. 2011. T cell diversity and TcR repertoires in teleost fish. *Fish Shellfish Immunol* **31**:644–654. doi:10.1016/J.FSI.2010.08.016

Chao CC, Hsu PC, Jen CF, Chen IH, Wang Chieh Huei, Chan HC, Tsai PW, Tung KC, Wang Chian Huei, Lan CY, Chuang YJ. 2010. Zebrafish as a model host for Candida albicans infection. *Infect Immun* **78**:2512–2521. doi:10.1128/IAI.01293-09

Chen KW, Monteleone M, Boucher D, Sollberger G, Ramnath D, Condon ND, von Pein JB, Broz P, Sweet MJ, Schroder K. 2018. Noncanonical inflammasome signaling elicits gasdermin D–dependent neutrophil extracellular traps. *Sci Immunol* **3**:6676. doi:10.1126/SCIIMMUNOL.AAR6676/SUPPL_FILE/AAR6676_TABLE_S1.XLSX

Chen SN, Gan Z, Hou J, Yang YC, Huang L, Huang B, Wang S, Nie P. 2022. Identification and establishment of type IV interferon and the characterization of interferon-υ including its class II cytokine receptors IFN-υR1 and IL-10R2. *Nat Commun 2022 131* **13**:1–12. doi:10.1038/s41467-022-28645-6

Chen W, Zhao J, Mu D, Wang Z, Liu Q, Zhang Y, Yang D. 2021. Pyroptosis Mediates Neutrophil Extracellular Trap Formation during Bacterial Infection in Zebrafish. *J Immunol* **206**:1913–1922. doi:10.4049/JIMMUNOL.2001335

Chen WQ, Hu YW, Zou PF, Ren SS, Nie P, Chang MX. 2015. MAVS splicing variants contribute to the induction of interferon and interferon-stimulated genes mediated by RIG-I-like receptors. *Dev Comp Immunol* **49**:19–30. doi:10.1016/J.DCI.2014.10.017

Chen Y, Cai H, Pan J, Xiang N, Tien P, Ahola T, Guo D. 2009. Functional screen reveals SARS coronavirus nonstructural protein nsp14 as a novel cap N7 methyltransferase. *Proc Natl Acad*

Sci U S A **106**:3484–3489. doi:10.1073/PNAS.0808790106

Chen Y, Su C, Ke M, Jin X, Xu L, Zhang Z, Wu A, Sun Y, Yang Z, Tien P, Ahola T, Liang Y, Liu X, Guo D. 2011. Biochemical and structural insights into the mechanisms of sars coronavirus RNA ribose 2′-O-methylation by nsp16/nsp10 protein complex. *PLoS Pathog* **7**. doi:10.1371/JOURNAL.PPAT.1002294

Chen Z, Mi L, Xu J, Yu J, Wang X, … JJ-TJ of, 2005 undefined. n.d. Function of HAb18G/CD147 in invasion of host cells by severe acute respiratory syndrome coronavirus. *Acad Chen, L Mi, J Xu, J Yu, X Wang, J Jiang, J Xing, P Shang, A Qian, Y Li, PX Shaw, J WangThe J Infect Dis 2005•academic.oup.com*.

Cheng E, Dorjsuren D, Lehman S, Larson CL, Titus SA, Sun H, Zakharov A, Rai G, Heinzen RA, Simeonov A, Machner MP. 2022. A comprehensive phenotypic screening strategy to identify modulators of cargo translocation by the bacterial Type IVB secretion system. *Am Soc MicrobiolE Cheng, D Dorjsuren, S Lehman, CL Larson, SA Titus, H Sun, A Zakharov, G RaiMbio, 2022•Am Soc Microbiol* **13**. doi:10.1128/mbio.00240-22

Cianciotto NP. 2013. Type II Secretion and Legionella Virulence 81–102. doi:10.1007/82_2013_339

Cigliola V, Becker CJ, Poss KD. 2020. Building bridges, not walls: Spinal cord regeneration in zebrafish. *DMM Dis Model Mech* **13**. doi:10.1242/DMM.044131/225225

Colucci-Guyon E, Tinevez JY, Renshaw SA, Herbomel P. 2011. Strategies of professional phagocytes in vivo: unlike macrophages, neutrophils engulf only surface-associated microbes. *J Cell Sci* **124**:3053–3059. doi:10.1242/JCS.082792

Commins SP, Borish L, Steinke JW. 2010. Immunologic messenger molecules: Cytokines, interferons, and chemokines. *J Allergy Clin Immunol* **125**:S53–S72. doi:10.1016/J.JACI.2009.07.008

Corman VM, Muth D, Niemeyer D, Drosten C. 2018. Hosts and Sources of Endemic Human Coronaviruses. *Adv Virus Res* **100**:163–188. doi:10.1016/BS.AIVIR.2018.01.001

Coronado M, Solis CJ, Hernandez PP, Feijóo CG. 2019. Soybean meal-induced intestinal inflammation in zebrafish is T cell-dependent and has a Th17 cytokine profile. *Front Immunol*

10:610. doi:10.3389/FIMMU.2019.00610/FULL

D'Amico LA, Cooper MS. 2001. Morphogenetic domains in the yolk syncytial layer of axiating zebrafish embryos. *Dev Dyn* **222**:611–624. doi:10.1002/DVDY.1216

Daly JL, Simonetti B, Klein K, Chen KE, Williamson MK, Antón-Plágaro C, Shoemark DK, Simón-Gracia L, Bauer M, Hollandi R, Greber UF, Horvath P, Sessions RB, Helenius A, Hiscox JA, Teesalu T, Matthews DA, Davidson AD, Collins BM, Cullen PJ, Yamauchi Y. 2020. Neuropilin-1 is a host factor for SARS-CoV-2 infection. *Science (80-)* **370**:861–865. doi:10.1126/SCIENCE.ABD3072

Darif D, Hammi I, Kihel A, El Idrissi Saik I, Guessous F, Akarid K. 2021. The pro-inflammatory cytokines in COVID-19 pathogenesis: What goes wrong? *Microb Pathog* **153**:104799. doi:10.1016/J.MICPATH.2021.104799

Das T, Jaffar-Bandjee MC, Hoarau JJ, Krejbich Trotot P, Denizot M, Lee-Pat-Yuen G, Sahoo R, Guiraud P, Ramful D, Robin S, Alessandri JL, Gauzere BA, Gasque P. 2010. Chikungunya fever: CNS infection and pathologies of a re-emerging arbovirus. *Prog Neurobiol* **91**:121–9.

Dash PK, Gorantla S, Poluektova L, Hasan M, Waight E, Zhang C, Markovic M, Edagwa B, Machhi J, Olson KE, Wang X, Mosley RL, Kevadiya B, Gendelman HE. 2021. Humanized Mice for Infectious and Neurodegenerative disorders. *Retrovirology 2021 181* **18**:1–17. doi:10.1186/S12977-021-00557-1

Davis JM, Clay H, Lewis JL, Ghori N, Herbomel P, Ramakrishnan L. 2002. Real-time visualization of Mycobacterium-macrophage interactions leading to initiation of granuloma formation in zebrafish embryos. *Immunity* **17**:693–702. doi:10.1016/S1074-7613(02)00475-2

Davis JM, Huang M, Botts MR, Hull CM, Huttenlocher A. 2016. A zebrafish model of cryptococcal infection reveals roles for macrophages, endothelial cells, and neutrophils in the establishment and control of sustained fungemia. *Infect Immun* **84**:3047–3062. doi:10.1128/IAI.00506-16/SUPPL_FILE/ZII999091849SO1.PDF

Davison JM, Akitake CM, Goll MG, Rhee JM, Gosse N, Baier H, Halpern ME, Leach SD, Parsons MJ. 2007. Transactivation from Gal4-VP16 transgenic insertions for tissue-specific cell

labeling and ablation in zebrafish. *Dev Biol* **304**:811–824. doi:10.1016/j.ydbio.2007.01.033

De Oliveira S, Rosowski EE, Huttenlocher A. 2016. Neutrophil migration in infection and wound repair: going forward in reverse. *Nat Rev Immunol 2016 166* **16**:378–391. doi:10.1038/nri.2016.49

Dee CT, Nagaraju RT, Athanasiadis EI, Gray C, Fernandez del Ama L, Johnston SA, Secombes CJ, Cvejic A, Hurlstone AFL. 2016. CD4-Transgenic Zebrafish Reveal Tissue-Resident Th2- and Regulatory T Cell–like Populations and Diverse Mononuclear Phagocytes. *J Immunol* **197**:3520–3530. doi:10.4049/JIMMUNOL.1600959/-/DCSUPPLEMENTAL

Denans N, Tran NTT, Swall ME, Diaz DC, Blanck J, Piotrowski T. 2022. An anti-inflammatory activation sequence governs macrophage transcriptional dynamics during tissue injury in zebrafish. *Nat Commun* **13**. doi:10.1038/S41467-022-33015-3

Di H, McIntyre AA, Brinton MA. 2018. New insights about the regulation of Nidovirus subgenomic mRNA synthesis. *Virology* **517**:38–43. doi:10.1016/j.virol.2018.01.026

Dooley CM, Mongera A, Walderich B, Nüsslein-Volhard C. 2013. On the embryonic origin of adult melanophores: the role of ErbB and Kit signalling in establishing melanophore stem cells in zebrafish. *Development* **140**:1003–1013. doi:10.1242/dev.087007

Driever W, Solnica-Krezel L, Schier AF, Neuhauss SCF, Malicki J, Stemple DL, Stainier DYR, Zwartkruis F, Abdelilah S, Rangini Z, Belak J, Boggs C. 1996. A genetic screen for mutations affecting embryogenesis in zebrafish. *Development* **123**:37–46. doi:10.1242/DEV.123.1.37

Duan Y, Wang Y, Li Z, Ma L, Wei X, Yang J, Xiao R, Xia C. 2021. The unique structure of the zebrafish TNF-α homotrimer. *Dev Comp Immunol* **122**:104129. doi:10.1016/J.DCI.2021.104129

Eckerle LD, Lu X, Sperry SM, Choi L, Denison MR. 2007. High fidelity of murine hepatitis virus replication is decreased in nsp14 exoribonuclease mutants. *Am Soc MicrobiolLD Eckerle, X Lu, SM Sperry, L Choi, MR DenisonJournal Virol 2007•Am Soc Microbiol* **81**:12135–12144. doi:10.1128/JVI.01296-07

Ellett F, Pazhakh V, Pase L, Benard EL, Weerasinghe H, Azabdaftari D, Alasmari S, Andrianopoulos A, Lieschke GJ. 2018. Macrophages protect Talaromyces marneffei conidia

from myeloperoxidase-dependent neutrophil fungicidal activity during infection establishment in vivo. *PLOS Pathog* **14**:e1007063. doi:10.1371/JOURNAL.PPAT.1007063

Engeszer RE, Patterson LB, Rao AA, Parichy DM. 2007. Zebrafish in The Wild: A Review of Natural History And New Notes from The Field. *https://home.liebertpub.com/zeb* **4**:21–40. doi:10.1089/ZEB.2006.9997

Engeszer RE, Ryan MJ, Parichy DM. 2004. Learned social preference in zebrafish. *Curr Biol* **14**:881–884. doi:10.1016/J.CUB.2004.04.042

Eshbach ML, Weisz OA. 2017. Receptor-Mediated Endocytosis in the Proximal Tubule. *Annu Rev Physiol* **79**:425–448. doi:10.1146/annurev-physiol-022516-034234

Espmark A, Niklasson B. 1984. Ockelbo disease in Sweden: epidemiological, clinical, and virological data from the 1982 outbreak. *Am J Trop Med Hyg* **33**:1203–1211. doi:10.4269/AJTMH.1984.33.1203

Ferrero G, Mahony CB, Dupuis E, Yvernogeau L, Di Ruggiero E, Miserocchi M, Caron M, Robin C, Traver D, Bertrand JY, Wittamer V. 2018. Embryonic Microglia Derive from Primitive Macrophages and Are Replaced by cmyb-Dependent Definitive Microglia in Zebrafish. *Cell Rep* **24**:130–141. doi:10.1016/j.celrep.2018.05.066

Fields BS, Benson RF, Besser RE. 2002. Legionella and legionnaires' disease: 25 Years of investigation. *Clin Microbiol Rev* **15**:506–526. doi:10.1128/CMR.15.3.506-526.2002

Fischer U, Koppang EO, Nakanishi T. 2013. Teleost T and NK cell immunity. *Fish Shellfish Immunol* **35**:197–206. doi:10.1016/J.FSI.2013.04.018

Flannagan RS, Jaumouillé V, Grinstein S. 2012. The Cell Biology of Phagocytosis. *https://doi.org/101146/annurev-pathol-011811-132445* **7**:61–98. doi:10.1146/ANNUREV-PATHOL-011811-132445

Fliermans CB, Soracco RJ, Pope DH. 1981. Measure of Legionella pneumophila activity in situ. *Curr Microbiol* **6**:89–94. doi:10.1007/BF01569010

Flores MV, Hall C, Jury A, Crosier K, Crosier P. 2007. The zebrafish retinoid-related orphan receptor (ror) gene family. *Gene Expr Patterns* **7**:535–543.

doi:10.1016/J.MODGEP.2007.02.001

Fontana BD, Mezzomo NJ, Kalueff A V., Rosemberg DB. 2018. The developing utility of zebrafish models of neurological and neuropsychiatric disorders: A critical review. *Exp Neurol* **299**:157–171. doi:10.1016/J.EXPNEUROL.2017.10.004

Furuta T, Tomioka R, Taki K, Nakamura K, Tamamaki N, Kaneko T. 2001. In vivo transduction of central neurons using recombinant Sindbis virus: Golgi-like labeling of dendrites and axons with membrane-targeted fluorescent proteins. *J Histochem Cytochem Off J Histochem Soc* **49**:1497–1508. doi:10.1177/002215540104901203

Futosi K, Fodor S, Mócsai A. 2013. Neutrophil cell surface receptors and their intracellular signal transduction pathways. *Int Immunopharmacol* **17**:638–650. doi:10.1016/J.INTIMP.2013.06.034

Gan Z, Chen SN, Huang B, Zou J, Nie P. 2020. Fish type I and type II interferons: composition, receptor usage, production and function. *Rev Aquac* **12**:773–804. doi:10.1111/RAQ.12349

Gao Y, Yan L, Huang Y, Liu F, Zhao Y, Cao L, Science TW-, 2020 undefined. n.d. Structure of the RNA-dependent RNA polymerase from COVID-19 virus. *Sci Gao, L Yan, Y Huang, F Liu, Y Zhao, L Cao, T Wang, Q Sun, Z Ming, L Zhang, J GeScience, 2020•science.org*.

García-Weber D, Arrieumerlou C. 2020. ADP-heptose: a bacterial PAMP detected by the host sensor ALPK1. *Cell Mol Life Sci 2020 781* **78**:17–29. doi:10.1007/S00018-020-03577-W

García-Weber D, Dangeard A-S, Cornil J, Thai L, Rytter H, Zamyatina A, Mulard LA, Arrieumerlou C. 2018. ADP-heptose is a newly identified pathogen-associated molecular pattern of Shigella flexneri. *EMBO Rep* **19**:e46943. doi:10.15252/EMBR.201846943

Ge Z, Yuan P, Chen L, Chen J, Shen D, She Z, Lu Y. 2022. New Global Insights on the Regulation of the Biphasic Life Cycle and Virulence Via ClpP-Dependent Proteolysis in Legionella pneumophila. *Mol Cell Proteomics* **21**. doi:10.1016/J.MCPRO.2022.100233

Gerhard GS, Kauffman EJ, Wang X, Stewart R, Moore JL, Kasales CJ, Demidenko E, Cheng KC. 2002. Life spans and senescent phenotypes in two strains of Zebrafish (Danio rerio). *Exp Gerontol* **37**:1055–1068. doi:10.1016/S0531-5565(02)00088-8

Giese MA, Hind LE, Huttenlocher A. 2019. Neutrophil plasticity in the tumor microenvironment. *Blood* **133**:2159–2167. doi:10.1182/BLOOD-2018-11-844548

Ginhoux F, Guilliams M, Naik SH. 2016. Dendritic cell and macrophage nomenclature and classification. *Front Immunol* **7**. doi:10.3389/FIMMU.2016.00168

Gonçalves IG, Simões LC, Simões M. 2021. Legionella pneumophila. *Trends Microbiol* **29**:860–861. doi:10.1016/j.tim.2021.04.005

González-Rosa JM. 2022. Zebrafish Models of Cardiac Disease: From Fortuitous Mutants to Precision Medicine. *Circ Res* **130**:1803–1826. doi:10.1161/CIRCRESAHA.122.320396

Gonzalez CD, Ledo C, Giai C, Garófalo A, Gómez MI. 2015. The Sbi Protein Contributes to Staphylococcus aureus Inflammatory Response during Systemic Infection. *PLoS One* **10**:e0131879. doi:10.1371/JOURNAL.PONE.0131879

Gorbalenya AE, Baker SC, Baric RS, de Groot RJ, Drosten C, Gulyaeva AA, Haagmans BL, Lauber C, Leontovich AM, Neuman BW, Penzar D, Perlman S, Poon LLM, Samborskiy D V., Sidorov IA, Sola I, Ziebuhr J. 2020. The species Severe acute respiratory syndrome-related coronavirus: classifying 2019-nCoV and naming it SARS-CoV-2. *Nat Microbiol 2020 54* **5**:536–544. doi:10.1038/s41564-020-0695-z

Goulding M. 2009. Circuits controlling vertebrate locomotion: moving in a new direction. *Nat Rev Neurosci 2009 107* **10**:507–518. doi:10.1038/nrn2608

Gratacap RL, Scherer AK, Seman BG, Wheeler RT. 2017. Control of mucosal candidiasis in the zebrafish swim bladder depends on neutrophils that block filament invasion and drive extracellular-trap production. *Infect Immun* **85**. doi:10.1128/IAI.00276-17/SUPPL_FILE/ZII999092113S1.PDF

Grayfer L, Belosevic M. 2009. Molecular characterization of novel interferon gamma receptor 1 isoforms in zebrafish (Danio rerio) and goldfish (Carassius auratus L.). *Mol Immunol* **46**:3050–3059. doi:10.1016/J.MOLIMM.2009.06.004

Grunwald DJ, Eisen JS. 2002a. Headwaters of the zebrafish — emergence of a new model vertebrate. *Nat Rev Genet 2002 39* **3**:717–724. doi:10.1038/nrg892

Grunwald DJ, Eisen JS. 2002b. Headwaters of the zebrafish — emergence of a new model vertebrate. *Nat Rev Genet 2002 39* **3**:717–724. doi:10.1038/nrg892

Guard RW, Mcauliffe MJ, Stallman ND, Bramston BA. 1982. Haemorrhagic manifestations with sindbis infection. Case report. *Pathology* **14**:89–90. doi:10.3109/00313028209069049

Gunimaladevi I, Savan R, Sakai M. 2006. Identification, cloning and characterization of interleukin-17 and its family from zebrafish. *Fish Shellfish Immunol* **21**:393–403. doi:10.1016/J.FSI.2006.01.004

Guo Z, Li Y, Ding SW. 2018. Small RNA-based antimicrobial immunity. *Nat Rev Immunol 2018 191* **19**:31–44. doi:10.1038/s41577-018-0071-x

Gurevich DB, Severn CE, Twomey C, Greenhough A, Cash J, Toye AM, Mellor H, Martin P. 2018. Live imaging of wound angiogenesis reveals macrophage orchestrated vessel sprouting and regression. *EMBO J* **37**:e97786. doi:10.15252/EMBJ.201797786

Gylfe Å, Ribers Å, Forsman O, Bucht G, Alenius GM, Wållberg-Jonsson S, Ahlm C, Evander M. 2018. Mosquitoborne Sindbis Virus Infection and Long-Term Illness. *Emerg Infect Dis* **24**:1141. doi:10.3201/EID2406.170892

H. Meijer A, P. Spaink H. 2011. Host-Pathogen Interactions Made Transparent with the Zebrafish Model. *Curr Drug Targets* **12**:1000. doi:10.2174/138945011795677809

Hakkim A, Fuchs TA, Martinez NE, Hess S, Prinz H, Zychlinsky A, Waldmann H. 2010. Activation of the Raf-MEK-ERK pathway is required for neutrophil extracellular trap formation. *Nat Chem Biol 2010 72* **7**:75–77. doi:10.1038/nchembio.496

Hall C, Flores MV, Crosier K, Crosier P. 2009. Live cell imaging of zebrafish leukocytes. *Methods Mol Biol* **546**:255–271. doi:10.1007/978-1-60327-977-2_16/FIGURES/5_16

Hamilton Francis, Hamilton Francis,. 1822. An account of the fishes found in the river Ganges and its branches. Edinburgh: Printed for A. Constable and company; [etc., etc.].

Hardwick JM, Levine B. 2000. Sindbis virus vector system for functional analysis of apoptosis regulators. *Methods Enzymol* **322**:492–508.

Harvie EA, Huttenlocher A. 2015. Neutrophils in host defense: new insights from zebrafish. *J*

Leukoc Biol **98**:523–537. doi:10.1189/JLB.4MR1114-524R

Henry KM, Loynes CA, Whyte MKB, Renshaw SA. 2013. Zebrafish as a model for the study of neutrophil biology. *J Leukoc Biol* **94**:633–642. doi:10.1189/JLB.1112594

Herbomel P, Thisse B, Thisse C. 2001. Zebrafish early macrophages colonize cephalic mesenchyme and developing brain, retina, and epidermis through a M-CSF receptor-dependent invasive process. *Dev Biol* **238**:274–288. doi:10.1006/DBIO.2001.0393

Herbomel P, Thisse B, Thisse C. 1999. Ontogeny and behaviour of early macrophages in the zebrafish embryo. *Development* **126**:3735–3745. doi:10.1242/DEV.126.17.3735

High AS, Torosian SD, Rodgers FG. 1993. Cloning, nucleotide sequence and expression in Escherichia coli of a gene (ompM) encoding a 25 kDa major outer-membrane protein (MOMP) of Legionella pneumophila. *J Gen Microbiol* **139**:1715–1721. doi:10.1099/00221287-139-8-1715

Hindahl MS, Iglewski BH. 1984. Isolation and characterization of the Legionella pneumophila outer membrane. *J Bacteriol* **159**:107–113. doi:10.1128/JB.159.1.107-113.1984

Honjo Y, Kniss J, Eisen JS. 2008. Neuregulin-mediated ErbB3 signaling is required for formation of zebrafish dorsal root ganglion neurons. *Development* **135**:2615–2625. doi:10.1242/DEV.022178

Howe K, Clark MD, Torroja CF, Torrance J, Berthelot C, Muffato M, Collins JE, Humphray S, McLaren K, Matthews L, McLaren S, Sealy I, Caccamo M, Churcher C, Scott C, Barrett JC, Koch R, Rauch GJ, White S, Chow W, Kilian B, Quintais LT, Guerra-Assunção JA, Zhou Y, Gu Y, Yen J, Vogel JH, Eyre T, Redmond S, Banerjee R, Chi J, Fu B, Langley E, Maguire SF, Laird GK, Lloyd D, Kenyon E, Donaldson S, Sehra H, Almeida-King J, Loveland J, Trevanion S, Jones M, Quail M, Willey D, Hunt A, Burton J, Sims S, McLay K, Plumb B, Davis J, Clee C, Oliver K, Clark R, Riddle C, Eliott D, Threadgold G, Harden G, Ware D, Mortimer B, Kerry G, Heath P, Phillimore B, Tracey A, Corby N, Dunn M, Johnson C, Wood J, Clark S, Pelan S, Griffiths G, Smith M, Glithero R, Howden P, Barker N, Stevens C, Harley J, Holt K, Panagiotidis G, Lovell J, Beasley H, Henderson C, Gordon D, Auger K, Wright D, Collins J, Raisen C, Dyer L, Leung K, Robertson L, Ambridge K, Leongamornlert D,

McGuire S, Gilderthorp R, Griffiths C, Manthravadi D, Nichol S, Barker G, Whitehead S, Kay M, Brown J, Murnane C, Gray E, Humphries M, Sycamore N, Barker D, Saunders D, Wallis J, Babbage A, Hammond S, Mashreghi-Mohammadi M, Barr L, Martin S, Wray P, Ellington A, Matthews N, Ellwood M, Woodmansey R, Clark G, Cooper J, Tromans A, Grafham D, Skuce C, Pandian R, Andrews R, Harrison E, Kimberley A, Garnett J, Fosker N, Hall R, Garner P, Kelly D, Bird C, Palmer S, Gehring I, Berger A, Dooley CM, Ersan-Ürün Z, Eser C, Geiger H, Geisler M, Karotki L, Kirn A, Konantz J, Konantz M, Oberländer M, Rudolph-Geiger S, Teucke M, Osoegawa K, Zhu B, Rapp A, Widaa S, Langford C, Yang F, Carter NP, Harrow J, Ning Z, Herrero J, Searle SMJ, Enright A, Geisler R, Plasterk RHA, Lee C, Westerfield M, De Jong PJ, Zon LI, Postlethwait JH, Nüsslein-Volhard C, Hubbard TJP, Crollius HR, Rogers J, Stemple DL. 2013. The zebrafish reference genome sequence and its relationship to the human genome. *Nat 2013 4967446* **496**:498–503. doi:10.1038/nature12111

Hu C Bin, Wang J, Hong Y, Li H, Fan DD, Lin AF, Xiang LX, Shao JZ. 2023. Single-cell transcriptome profiling reveals diverse immune cell populations and their responses to viral infection in the spleen of zebrafish. *FASEB J* **37**:e22951. doi:10.1096/FJ.202201505RRRR

Huang Y, Yang C, Xu X feng, Xu W, Liu S wen. 2020. Structural and functional properties of SARS-CoV-2 spike protein: potential antivirus drug development for COVID-19. *Acta Pharmacol Sin 2020 419* **41**:1141–1149. doi:10.1038/s41401-020-0485-4

Hubálek Z. 2008. Mosquito-borne viruses in Europe. *Parasitol Res* **103**:29–43. doi:10.1007/S00436-008-1064-7/FIGURES/6

Hui SP, Sheng DZ, Sugimoto K, Gonzalez-Rajal A, Nakagawa S, Hesselson D, Kikuchi K. 2017. Zebrafish Regulatory T Cells Mediate Organ-Specific Regenerative Programs. *Dev Cell* **43**:659-672.e5. doi:10.1016/J.DEVCEL.2017.11.010

Huising MO, Stet RJM, Savelkoul HFJ, Verburg-Van Kemenade BML. 2004. The molecular evolution of the interleukin-1 family of cytokines; IL-18 in teleost fish. *Dev Comp Immunol* **28**:395–413. doi:10.1016/J.DCI.2003.09.005

Igawa D, Sakai M, Savan R. 2006. An unexpected discovery of two interferon gamma-like genes along with interleukin (IL)-22 and -26 from teleost: IL-22 and -26 genes have been described

for the first time outside mammals. *Mol Immunol* **43**:999–1009. doi:10.1016/J.MOLIMM.2005.05.009

Iliadi V, Staykova J, Iliadis S, Konstantinidou I, Sivykh P, Romanidou G, Vardikov DF, Cassimos D, Konstantinidis TG. 2022. Legionella pneumophila: The Journey from the Environment to the Blood. *J Clin Med 2022, Vol 11, Page 6126* **11**:6126. doi:10.3390/JCM11206126

Irigoyen N, Firth AE, Jones JD, Chung BYW, Siddell SG, Brierley I. 2016. High-Resolution Analysis of Coronavirus Gene Expression by RNA Sequencing and Ribosome Profiling. *PLOS Pathog* **12**:e1005473. doi:10.1371/JOURNAL.PPAT.1005473

Isberg RR, O'Connor TJ, Heidtman M. 2008. The Legionella pneumophila replication vacuole: making a cosy niche inside host cells. *Nat Rev Microbiol 2008 71* **7**:13–24. doi:10.1038/nrmicro1967

Ivanov K, virology JZ-J of, 2004 undefined. 2004. Human coronavirus 229E nonstructural protein 13: characterization of duplex-unwinding, nucleoside triphosphatase, and RNA 5′-triphosphatase activities. *Am Soc MicrobiolKA Ivanov, J Zieb Virol 2004•Am Soc Microbiol* **78**:7833–7838. doi:10.1128/JVI.78.14.7833-7838.2004

Jackson CB, Farzan M, Chen B, Choe H. 2021. Mechanisms of SARS-CoV-2 entry into cells. *Nat Rev Mol Cell Biol 2021 231* **23**:3–20. doi:10.1038/s41580-021-00418-x

Jackson EB. 1952. Studies on two rickettsia-like agents probably isolated from guinea pigsBacteriol Proc. p. 119.

Jeffers SA, Tusell SM, Gillim-Ross L, Hemmila EM, Achenbach JE, Babcock GJ, Thomas WD, Thackray LB, Young MD, Mason RJ, Ambrosino DM, Wentworth DE, DeMartini JC, Holmes K V. 2004. CD209L (L-SIGN) is a receptor for severe acute respiratory syndrome coronavirus. *Proc Natl Acad Sci U S A* **101**:15748–15753. doi:10.1073/PNAS.0403812101

Jemielity S, Wang JJ, Chan YK, Ahmed AA, Li W, Monahan S, Bu X, Farzan M, Freeman GJ, Umetsu DT, DeKruyff RH, Choe H. 2013. TIM-family Proteins Promote Infection of Multiple Enveloped Viruses through Virion-associated Phosphatidylserine. *PLoS Pathog* **9**. doi:10.1371/JOURNAL.PPAT.1003232

Jose J, Tang J, Taylor AB, Baker TS, Kuhn RJ. 2015. Fluorescent Protein-Tagged Sindbis Virus

E2 Glycoprotein Allows Single Particle Analysis of Virus Budding from Live Cells. *Viruses* **7**:6182–6199. doi:10.3390/v7122926

Jose J, Taylor AB, Kuhn RJ. 2017. Spatial and temporal analysis of alphavirus replication and assembly in mammalian and mosquito cells. *MBio* **8**. doi:10.1128/MBIO.02294-16/ASSET/CD8CAC71-6440-47ED-9F83-CF22DA513BFA/ASSETS/GRAPHIC/MBO0011731770009.JPEG

Journal J, Gholipour A, Moosavian M, Galehdari H, Makvandi M, Memari HR, Alvandi A. 2010. Cloning and periplasmic expression of peptidoglycan-associated lipoprotein (PAL) protein of Legionella pneumophila in Escherichia coli. *Jundishapur J Microbiol* **3**:1–9.

Jurisch-Yaksi N, Yaksi E, Kizil C. 2020. Radial glia in the zebrafish brain: Functional, structural, and physiological comparison with the mammalian glia. *Glia* **68**:2451–2470. doi:10.1002/GLIA.23849

Kalev-Zylinska ML, Horsfield JA, Flores MVC, Postlethwait JH, Vitas MR, Baas AM, Crosier PS, Crosier KE. 2002. Runx1 is required for zebrafish blood and vessel development and expression of a human RUNX1-CBF2T1 transgene advances a model for studies of leukemogenesis. *Development* **129**:2015–2030. doi:10.1242/DEV.129.8.2015

Kambara H, Liu F, Zhang X, Liu P, Bajrami B, Teng Y, Zhao L, Zhou S, Yu H, Zhou W, Silberstein LE, Cheng T, Han M, Xu Y, Luo HR. 2018. Gasdermin D Exerts Anti-inflammatory Effects by Promoting Neutrophil Death. *Cell Rep* **22**:2924–2936. doi:10.1016/J.CELREP.2018.02.067

Kamitani W, Narayanan K, Huang C, Lokugamage K, Ikegami T, Ito N, Kubo H, Makino S. 2006. Severe acute respiratory syndrome coronavirus nsp1 protein suppresses host gene expression by promoting host mRNA degradation. *Proc Natl Acad Sci U S A* **103**:12885–12890. doi:10.1073/PNAS.0603144103/SUPPL_FILE/03144FIG11.PDF

Kany S, Vollrath JT, Relja B. 2019. Cytokines in Inflammatory Disease. *Int J Mol Sci 2019, Vol 20, Page 6008* **20**:6008. doi:10.3390/IJMS20236008

Kapellos TS, Taylor L, Lee H, Cowley SA, James WS, Iqbal AJ, Greaves DR. 2016. A novel real time imaging platform to quantify macrophage phagocytosis. *Biochem Pharmacol* **116**:107–

119. doi:10.1016/J.BCP.2016.07.011

Kasheta M, Painter CA, Moore FE, Lobbardi R, Bryll A, Freiman E, Stachura D, Rogers AB, Houvras Y, Langenau DM, Ceol CJ. 2017. Identification and characterization of T reg–like cells in zebrafish. *J Exp Med* **214**:3519. doi:10.1084/JEM.20162084

Kaslin J, Ganz J. 2020. Zebrafish Nervous Systems. *Zebrafish Biomed Res Biol Husbandry, Dis Res Appl* 181–189. doi:10.1016/B978-0-12-812431-4.00018-X

Kassahn KS, Dang VT, Wilkins SJ, Perkins AC, Ragan MA. 2009. Evolution of gene function and regulatory control after whole-genome duplication: Comparative analyses in vertebrates. *Genome Res* **19**:1404. doi:10.1101/GR.086827.108

Kawakami K. 2004. Transgenesis and Gene Trap Methods in Zebrafish by Using the Tol2 Transposable Element. *Methods Cell Biol* **77**:201–222. doi:10.1016/S0091-679X(04)77011-9

Kawakami K, Koga A, Hori H, Shima A. 1998. Excision of the Tol2 transposable element of the medaka fish, Oryzias latipes, in zebrafish, Danio rerio. *Gene* **225**:17–22. doi:10.1016/S0378-1119(98)00537-X

Kelly Kuan CY, Tannahill D, Cook GMW, Keynes RJ. 2004. Somite polarity and segmental patterning of the peripheral nervous system. *Mech Dev* **121**:1055–1068. doi:10.1016/j.mod.2004.05.001

Kent ML, Feist SW, Harper C, Hoogstraten-Miller S, Law J Mac, Sánchez-Morgado JM, Tanguay RL, Sanders GE, Spitsbergen JM, Whipps CM. 2009. Recommendations for control of pathogens and infectious diseases in fish research facilities. *Comp Biochem Physiol Part C Toxicol Pharmacol* **149**:240–248. doi:10.1016/J.CBPC.2008.08.001

Kheawfu K, Pikulkaew S, Wellendorph P, Jørgensen L von G, Rades T, Müllertz A, Okonogi S. 2022. Elucidating Pathway and Anesthetic Mechanism of Action of Clove Oil Nanoformulations in Fish. *Pharmaceutics* **14**. doi:10.3390/PHARMACEUTICS14050919

Kim D, Lee J-Y, Yang J-S, Kim JW, Kim VN, Correspondence HC, Chang H. 2020. The architecture of SARS-CoV-2 transcriptome. *cell.comD Kim, JY Lee, JS Yang, JW Kim, VN Kim, H Chang 2020•cell.com* **181**:914-921.e10. doi:10.1016/j.cell.2020.04.011

Kimmel Charles B., Ballard WW, Kimmel SR, Ullmann B, Schilling TF. 1995. Stages of embryonic development of the zebrafish. *Dev Dyn* **203**:253–310. doi:10.1002/AJA.1002030302

Kimmel C B, Ballard WW, Kimmel SR, Ullmann B, Schilling TF. 1995. Stages of embryonic development of the zebrafish. *Dev Dyn* **203**:253–310. doi:10.1002/aja.1002030302

Kinchen JM, Ravichandran KS. 2008. Phagosome maturation: going through the acid test. *Nat Rev Mol Cell Biol 2008 910* **9**:781–795. doi:10.1038/nrm2515

Kinth P, Mahesh G, Panwar Y. 2013. Mapping of zebrafish research: A global outlook. *Zebrafish* **10**:510–517. doi:10.1089/ZEB.2012.0854/ASSET/IMAGES/LARGE/FIGURE2.JPEG

Kishi S, Slack BE, Uchiyama J, Zhdanova I V. 2009. Zebrafish as a Genetic Model in Biological and Behavioral Gerontology: Where Development Meets Aging in Vertebrates – A Mini-Review. *Gerontology* **55**:430. doi:10.1159/000228892

Kissa K, Herbomel P. 2010. Blood stem cells emerge from aortic endothelium by a novel type of cell transition. *Nat 2010 4647285* **464**:112–115. doi:10.1038/nature08761

Konishi T, Yamashiro T, Koide M, Nishizono A. 2006. Influence of temperature on growth of Legionella pneumophila biofilm determined by precise temperature gradient incubator. *J Biosci Bioeng* **101**:478–484. doi:10.1263/JBB.101.478

Kostiukov MA, Daniiarov O, Skvortsova TM, Kondrashina NG, Berezina LK. 1981. [Isolation of the Sindbis virus from Hyalomma anatolicum CL Kock 1844 ticks in Tadzhikistan]. *Med Parazitol (Mosk)* **50**:34–35.

KOZUCH O, M L, J N. 1978. ISOLATION OF SINDBIS VIRUS FROM THE FROG RANA RIDIBUNDA. *Isol SINDBIS VIRUS FROM FROG RANA RIDIBUNDA*.

Küchler AM, Gjini E, Peterson-Maduro J, Cancilla B, Wolburg H, Schulte-Merker S. 2006. Development of the zebrafish lymphatic system requires VEGFC signaling. *Curr Biol* **16**:1244–1248. doi:10.1016/J.CUB.2006.05.026

Kyritsis N, Kizil C, Zocher S, Kroehne V, Kaslin J, Freudenreich D, Iltzsche A, Brand M. 2012. Acute inflammation initiates the regenerative response in the adult zebrafish brain. *Science*

(80-) **338**:1353–1356. doi:10.1126/SCIENCE.1228773/SUPPL_FILE/KYRITSIS.SM.PDF

Laghi V, Rezelj V, Boucontet L, Frétaud M, Da Costa B, Boudinot P, Salinas I, Lutfalla G, Vignuzzi M, Levraud JP. 2022. Exploring Zebrafish Larvae as a COVID-19 Model: Probable Abortive SARS-CoV-2 Replication in the Swim Bladder. *Front Cell Infect Microbiol* **12**. doi:10.3389/fcimb.2022.790851

Laine M, Luukkainen R, Jalava J, Ilonen J, Kuusistö P, Toivanen A. 2000. Prolonged arthritis associated with Sindbis-related (Pogosta) virus infection. *Rheumatology* **39**:1272–1274. doi:10.1093/RHEUMATOLOGY/39.11.1272

Lam SH, Chua HL, Gong Z, Lam TJ, Sin YM. 2004. Development and maturation of the immune system in zebrafish, Danio rerio: a gene expression profiling, in situ hybridization and immunological study. *Dev Comp Immunol* **28**:9–28. doi:10.1016/S0145-305X(03)00103-4

Lamers MM, Haagmans BL. 2022. SARS-CoV-2 pathogenesis. *Nat Rev Microbiol 2022 205* **20**:270–284. doi:10.1038/s41579-022-00713-0

Langenau DM, Keefe MD, Storer NY, Guyon JR, Kutok JL, Le X, Goessling W, Neuberg DS, Kunkel LM, Zon LI. 2007. Effects of RAS on the genesis of embryonal rhabdomyosarcoma. *Genes Dev* **21**:1382–1395. doi:10.1101/GAD.1545007

Langevin Christelle, Aleksejeva E, Passoni G, Palha N, Levraud JP, Boudinot P. 2013. The Antiviral Innate Immune Response in Fish: Evolution and Conservation of the IFN System. *J Mol Biol* **425**:4904–4920. doi:10.1016/J.JMB.2013.09.033

Langevin C., van der Aa LM, Houel A, Torhy C, Briolat V, Lunazzi A, Harmache A, Bremont M, Levraud J-P, Boudinot P. 2013. Zebrafish ISG15 exerts a strong antiviral activity against RNA and DNA viruses and regulates the interferon response. *J Virol* **87**:10025–10036. doi:10.1128/JVI.01294-12

Langheinrich U. 2003. Zebrafish: A new model on the pharmaceutical catwalk. *BioEssays* **25**:904–912. doi:10.1002/BIES.10326

Lazarov T, Juarez-Carreño S, Cox N, Geissmann F. 2023. Physiology and diseases of tissue-resident macrophages. *Nat 2023 6187966* **618**:698–707. doi:10.1038/s41586-023-06002-x

Le Guyader D, Redd MJ, Colucci-Guyon E, Murayama E, Kissa K, Briolat V, Mordelet E, Zapata A, Shinomiya H, Herbomel P. 2008. Origins and unconventional behavior of neutrophils in developing zebrafish. *Blood* **111**:132–141. doi:10.1182/BLOOD-2007-06-095398

Leiba J, Özbilgiç R, Hernández L, Demou M, Lutfalla G, Yatime L, Nguyen-Chi M. 2023. Molecular Actors of Inflammation and Their Signaling Pathways: Mechanistic Insights from Zebrafish. *Biology (Basel)* **12**. doi:10.3390/BIOLOGY12020153

Leung JYS, Ng MML, Chu JJH. 2011. Replication of alphaviruses: A review on the entry process of alphaviruses into cells. *Adv Virol* **2011**. doi:10.1155/2011/249640

Levraud J.-P., Jouneau L, Briolat V, Laghi V, Boudinot P. 2019. IFN-stimulated genes in zebrafish and humans define an ancient arsenal of antiviral immunity. *J Immunol* **203**. doi:10.4049/jimmunol.1900804

Levraud Jean-Pierre, Jouneau L, Briolat V, Laghi V, Boudinot P. 2019. IFN-Stimulated Genes in Zebrafish and Humans Define an Ancient Arsenal of Antiviral Immunity. *J Immunol* **203**:3361–3373. doi:10.4049/JIMMUNOL.1900804

Levraud J-P, Palha N, Langevin C, Boudinot P. 2014. Through the looking glass: witnessing host-virus interplay in zebrafish. *Trends Microbiol* **22**:490–497. doi:10.1016/j.tim.2014.04.014

Levraud JP, Disson O, Kissa K, Bonne I, Cossart P, Herbomel P, Lecuit M. 2009. Real-time observation of Listeria monocytogenes-phagocyte interactions in living zebrafish larvae. *Infect Immun* **77**:3651–3660. doi:10.1128/IAI.00408-09/SUPPL_FILE/LEVRAUD_MOVIES3.MOV

Lewis KE, Eisen JS. 2003. From cells to circuits: development of the zebrafish spinal cord. *Prog Neurobiol* **69**:419–449. doi:10.1016/S0301-0082(03)00052-2

Li P, Li M, Lindberg MR, Kennett MJ, Xiong N, Wang Y. 2010. PAD4 is essential for antibacterial innate immunity mediated by neutrophil extracellular traps. *J Exp Med* **207**:1853–1862. doi:10.1084/JEM.20100239

Li S, Lu LF, Wang ZX, Chen DD, Zhang YA. 2016. Fish IRF6 is a positive regulator of IFN expression and involved in both of the MyD88 and TBK1 pathways. *Fish Shellfish Immunol* **57**:262–268. doi:10.1016/J.FSI.2016.08.059

Li Y, Di Santo JP. 2019. Modeling Infectious Diseases in Mice with a “Humanized” Immune System. *Microbiol Spectr* **7**. doi:10.1128/MICROBIOLSPEC.BAI-0019-2019/ASSET/0826D6CF-82DB-4E5B-A3DB-CD340E0EC54A/ASSETS/GRAPHIC/BAI-0019-2019-FIG3.GIF

Li Z, Journal MB-B, 2021 undefined. 2021. Neuropilin-1 assists SARS-CoV-2 infection by stimulating the separation of Spike protein S1 and S2. *cell.comZ Li, M BuckBiophysical Journal, 2021•cell.com* **120**:2828–2837. doi:10.1016/j.bpj.2021.05.026

Linnerz T, Hall CJ. 2020. The Diverse Roles of Phagocytes During Bacterial and Fungal Infections and Sterile Inflammation: Lessons From Zebrafish. *Front Immunol* **11**:537369. doi:10.3389/FIMMU.2020.01094/BIBTEX

Liu C, Chu D, Kalantar-Zadeh K, George J, Young HA, Liu G. 2021. Cytokines: From Clinical Significance to Quantification. *Adv Sci* **8**:2004433. doi:10.1002/ADVS.202004433

Liu C, Wu C, Yang Q, Gao J, Li L, Yang D, Luo L. 2016. Macrophages Mediate the Repair of Brain Vascular Rupture through Direct Physical Adhesion and Mechanical Traction. *Immunity* **44**:1162–1176. doi:10.1016/j.immuni.2016.03.008

Liu X, Li Y-S, Shinton SA, Rhodes J, Tang L, Feng H, Jette CA, Look AT, Hayakawa K, Hardy RR. 2017. Zebrafish B Cell Development without a Pre–B Cell Stage, Revealed by CD79 Fluorescence Reporter Transgenes. *J Immunol* **199**:1706–1715. doi:10.4049/JIMMUNOL.1700552/-/DCSUPPLEMENTAL

Lockwood DC, Amin H, Costa TRD, Schroeder GN. 2022. The Legionella pneumophila Dot/Icm type IV secretion system and its effectors. *Microbiol (United Kingdom)* **168**. doi:10.1099/MIC.0.001187

López-Muñoz A, Sepulcre MP, Roca FJ, Figueras A, Meseguer J, Mulero V. 2011. Evolutionary conserved pro-inflammatory and antigen presentation functions of zebrafish IFNγ revealed by transcriptomic and functional analysis. *Mol Immunol* **48**:1073–1083. doi:10.1016/J.MOLIMM.2011.01.015

López Hernández Y, Yero D, Pinos-Rodríguez JM, Gibert I. 2015. Animals devoid of pulmonary system as infection models in the study of lung bacterial pathogens. *Front Microbiol*

6:127206. doi:10.3389/FMICB.2015.00038/BIBTEX

Loynes CA, Lee JA, Robertson AL, Steel MJG, Ellett F, Feng Y, Levy BD, Whyte MKB, Renshaw SA. 2018. PGE2 production at sites of tissue injury promotes an anti-inflammatory neutrophil phenotype and determines the outcome of inflammation resolution in vivo. *Sci Adv* **4**. doi:10.1126/SCIADV.AAR8320/SUPPL_FILE/AAR8320_SM.PDF

Lundström JO. 1999. Mosquito-borne viruses in western Europe: a review. *J Vector Ecol* **24**:1–39.

Lundstrom K. 2001. Application of Alphavirus Vectors in Drug Discovery. *Anim Cell Technol From Target to Mark* 45–51. doi:10.1007/978-94-010-0369-8_11

Lustig S, Jackson AC, Hahn CS, Griffin DE, Strauss EG, Strauss JH. 1988. Molecular basis of Sindbis virus neurovirulence in mice. *J Virol* **62**:2329–2336. doi:10.1128/JVI.62.7.2329-2336.1988

Lyons DA, Talbot WS. 2015. Glial Cell Development and Function in Zebrafish. *Cold Spring Harb Perspect Biol* **7**:a020586. doi:10.1101/CSHPERSPECT.A020586

Mahabir S, Chatterjee D, Buske C, Gerlai R. 2013. Maturation of shoaling in two zebrafish strains: a behavioral and neurochemical analysis. *Behav Brain Res* **247**:1–8. doi:10.1016/J.BBR.2013.03.013

Maisey K, Montero R, Corripio-Miyar Y, Toro-Ascuy D, Valenzuela B, Reyes-Cerpa S, Sandino AM, Zou J, Wang T, Secombes CJ, Imarai M. 2016. Isolation and Characterization of Salmonid CD4+ T Cells. *J Immunol* **196**:4150–4163. doi:10.4049/JIMMUNOL.1500439

Malone B, Urakova N, Snijder EJ, Campbell EA. 2021. Structures and functions of coronavirus replication–transcription complexes and their relevance for SARS-CoV-2 drug design. *Nat Rev Mol Cell Biol 2021 231* **23**:21–39. doi:10.1038/s41580-021-00432-z

Martínez-Navarro FJ, Martínez-Morcillo FJ, de Oliveira S, Candel S, Cabas I, García-Ayala A, Martínez-Menchón T, Corbalán-Vélez R, Mesa-del-Castillo P, Cayuela ML, Pérez-Oliva AB, García-Moreno D, Mulero V. 2020. Hydrogen peroxide in neutrophil inflammation: Lesson from the zebrafish. *Dev Comp Immunol* **105**:103583. doi:10.1016/J.DCI.2019.103583

Martins EP, Bhat A. 2014. Population-level personalities in zebrafish: Aggression-boldness across but not within populations. *Behav Ecol* **25**:368–373. doi:10.1093/BEHECO/ARU007

Masud S, Prajsnar TK, Torraca V, Lamers GEM, Benning M, Van Der Vaart M, Meijer AH. 2019. Macrophages target Salmonella by Lc3-associated phagocytosis in a systemic infection model. *Autophagy* **15**:796–812. doi:10.1080/15548627.2019.1569297/SUPPL_FILE/KAUP_A_1569297_SM3984.ZIP

Mazzolini J, Le Clerc S, Morisse G, Coulonges C, Kuil LE, van Ham TJ, Zagury JF, Sieger D. 2020. Gene expression profiling reveals a conserved microglia signature in larval zebrafish. *Glia* **68**:298–315. doi:10.1002/GLIA.23717

McClure MM, McIntyre PB, McCune AR. 2006. Notes on the natural diet and habitat of eight danionin fishes, including the zebrafish Danio rerio. *J Fish Biol* **69**:553–570. doi:10.1111/J.1095-8649.2006.01125.X

Meeker ND, Trede NS. 2008. Immunology and zebrafish: Spawning new models of human disease. *Dev Comp Immunol* **32**:745–757. doi:10.1016/J.DCI.2007.11.011

Meijer AH, Gabby Krens SF, Medina Rodriguez IA, He S, Bitter W, Snaar-Jagalska BE, Spaink HP. 2004. Expression analysis of the Toll-like receptor and TIR domain adaptor families of zebrafish. *Mol Immunol* **40**:773–783. doi:10.1016/J.MOLIMM.2003.10.003

Meijer AH, van der Sar AM, Cunha C, Lamers GEM, Laplante MA, Kikuta H, Bitter W, Becker TS, Spaink HP. 2008. Identification and real-time imaging of a myc-expressing neutrophil population involved in inflammation and mycobacterial granuloma formation in zebrafish. *Dev Comp Immunol* **32**:36–49. doi:10.1016/J.DCI.2007.04.003

Meno K, Yah C, Mendes A, Venter M. 2022. Incidence of Sindbis Virus in Hospitalized Patients With Acute Fevers of Unknown Cause in South Africa, 2019–2020. *Front Microbiol* **12**:798810. doi:10.3389/FMICB.2021.798810/BIBTEX

Mesureur J, Feliciano JR, Wagner N, Gomes MC, Zhang L, Blanco-Gonzalez M, van der Vaart M, O'Callaghan D, Meijer AH, Vergunst AC. 2017. Macrophages, but not neutrophils, are critical for proliferation of Burkholderia cenocepacia and ensuing host-damaging inflammation. *PLOS Pathog* **13**:e1006437. doi:10.1371/JOURNAL.PPAT.1006437

Metzler KD, Goosmann C, Lubojemska A, Zychlinsky A, Papayannopoulos V. 2014. Myeloperoxidase-containing complex regulates neutrophil elastase release and actin dynamics during NETosis. *Cell Rep* **8**:883–896. doi:10.1016/j.celrep.2014.06.044

Miao KZ, Kim GY, Meara GK, Qin X, Feng H. 2021. Tipping the Scales With Zebrafish to Understand Adaptive Tumor Immunity. *Front Cell Dev Biol* **9**. doi:10.3389/FCELL.2021.660969

Michelle D Peñaranda M, Jensen I, Tollersrud LG, Bruun JA, Jørgensen JB. 2019. Profiling the Atlantic salmon IgM+ B cell surface proteome: Novel information on teleost fish B cell protein repertoire and identification of potential B cell markers. *Front Immunol* **10**:37. doi:10.3389/FIMMU.2019.00037/FULL

Mitra S, Alnabulsi A, Secombes CJ, Bird S. 2010. Identification and characterization of the transcription factors involved in T-cell development, t-bet, stat6 and foxp3, within the zebrafish, Danio rerio. *FEBS J* **277**:128–147. doi:10.1111/J.1742-4658.2009.07460.X

Molmeret M, Bitar DM, Han L, Kwaik YA. 2004. Cell biology of the intracellular infection by Legionella pneumophila. *Microbes Infect* **6**:129–139. doi:10.1016/J.MICINF.2003.11.004

Monte MM, Wang T, Costa MM, Harun NO, Secombes CJ. 2012. Cloning and expression analysis of two ROR-γ homologues (ROR-γa1 and ROR-γa2) in rainbow trout Oncorhynchus mykiss. *Fish Shellfish Immunol* **33**:365–374. doi:10.1016/J.FSI.2012.05.023

Moreira RA, Guzman H V., Boopathi S, Baker JL, Poma AB. 2020. Characterization of Structural and Energetic Differences between Conformations of the SARS-CoV-2 Spike Protein. *Mater 2020, Vol 13, Page 5362* **13**:5362. doi:10.3390/MA13235362

Mosser DM, Edwards JP. 2008. Exploring the full spectrum of macrophage activation. *Nat Rev Immunol* **8**:958–969. doi:10.1038/NRI2448

Mueller T, Wullimann MF, Mueller T, Wullimann MF. 2016. Chapter 1 – Vertebrate Central Nervous System Development: Introduction, Atlas of Early Zebrafish Brain Development.

Muñoz-Sánchez S, van der Vaart M, Meijer AH. 2020a. Autophagy and Lc3-Associated Phagocytosis in Zebrafish Models of Bacterial Infections. *Cells 2020, Vol 9, Page 2372* **9**:2372. doi:10.3390/CELLS9112372

Muñoz-Sánchez S, van der Vaart M, Meijer AH. 2020b. Autophagy and Lc3-Associated Phagocytosis in Zebrafish Models of Bacterial Infections. *Cells* **9**. doi:10.3390/CELLS9112372

Murayama E, Kissa K, Zapata A, Mordelet E, Briolat V, Lin HF, Handin RI, Herbomel P. 2006. Tracing hematopoietic precursor migration to successive hematopoietic organs during zebrafish development. *Immunity* **25**:963–975. doi:10.1016/J.IMMUNI.2006.10.015

Nasevicius A, Ekker SC. 2000. Effective targeted gene 'knockdown' in zebrafish. *Nat Genet 2000 262* **26**:216–220. doi:10.1038/79951

Nathan C. 2006. Neutrophils and immunity: challenges and opportunities. *Nat Rev Immunol 2006 63* **6**:173–182. doi:10.1038/nri1785

Nguyen-Chi M, Laplace-Builhé B, Travnickova J, Luz-Crawford P, Tejedor G, Lutfalla G, Kissa K, Jorgensen C, Djouad F. 2017. TNF signaling and macrophages govern fin regeneration in zebrafish larvae. *Cell Death Dis 2017 88* **8**:e2979–e2979. doi:10.1038/cddis.2017.374

Nguyen-Chi M, Laplace-Builhe B, Travnickova J, Luz-Crawford P, Tejedor G, Phan QT, Duroux-Richard I, Levraud JP, Kissa K, Lutfalla G, Jorgensen C, Djouad F. 2015a. Identification of polarized macrophage subsets in zebrafish. *Elife* **4**. doi:10.7554/ELIFE.07288

Nguyen-Chi M, Laplace-Builhe B, Travnickova J, Luz-Crawford P, Tejedor G, Phan QT, Duroux-Richard I, Levraud JP, Kissa K, Lutfalla G, Jorgensen C, Djouad F. 2015b. Identification of polarized macrophage subsets in zebrafish. *Elife* **4**. doi:10.7554/ELIFE.07288

Nie L, Xiong R, Zhang YS, Zhu L yun, Shao JZ, Xiang LX. 2014. Conserved inhibitory role of teleost SOCS-1s in IFN signaling pathways. *Dev Comp Immunol* **43**:23–29. doi:10.1016/J.DCI.2013.10.007

Nintasen R, … FU-M and, 2007 undefined. 2007. Enhancement of Legionella pneumophila Culture Isolation from Microenvironments by Macrophage Infectivity Potentiator (mip) Gene-Specific Nested Polymerase. *Wiley Online Libr Nintasen, F Utrarachkij, K Siripanichgon, A Bhumiratana, Y Suzuki, O SuthienkulMicrobiology Immunol 2007•Wiley Online Libr* **51**:777–785. doi:10.1111/j.1348-0421.2007.tb03967.x

Novais FO, Santiago RC, Báfica A, Khouri R, Afonso L, Borges VM, Brodskyn C, Barral-Netto

M, Barral A, de Oliveira CI. 2009. Neutrophils and Macrophages Cooperate in Host Resistance against Leishmania braziliensis Infection. *J Immunol* **183**:8088–8098. doi:10.4049/JIMMUNOL.0803720

Novoa B, Figueras A. 2012. Zebrafish: model for the study of inflammation and the innate immune response to infectious diseases. *Adv Exp Med Biol* **946**:253–275. doi:10.1007/978-1-4614-0106-3_15

Nüsslein-Volhard C. 2012. The zebrafish issue of Development. *Development* **139**:4099–4103. doi:10.1242/DEV.085217

Oehlers SHB, Flores MV, Hall CJ, O'Toole R, Swift S, Crosier KE, Crosier PS. 2010. Expression of zebrafish cxcl8 (interleukin-8) and its receptors during development and in response to immune stimulation. *Dev Comp Immunol* **34**:352–359. doi:10.1016/J.DCI.2009.11.007

Oosterhof N, Holtman IR, Kuil LE, van der Linde HC, Boddeke EWGM, Eggen BJL, van Ham TJ. 2017. Identification of a conserved and acute neurodegeneration-specific microglial transcriptome in the zebrafish. *Glia* **65**:138–149. doi:10.1002/GLIA.23083

Oosterhof N, Kuil LE, van der Linde HC, Burm SM, Berdowski W, van Ijcken WFJ, van Swieten JC, Hol EM, Verheijen MHG, van Ham TJ. 2018. Colony-Stimulating Factor 1 Receptor (CSF1R) Regulates Microglia Density and Distribution, but Not Microglia Differentiation In Vivo. *Cell Rep* **24**:1203-1217.e6. doi:10.1016/J.CELREP.2018.06.113

Oswald ME, Drew RE, Racine M, Murdoch GK, Robison BD. 2012. Is Behavioral Variation along the Bold-Shy Continuum Associated with Variation in the Stress Axis in Zebrafish?*. *https://doi.org/101086/668203* **85**:717–728. doi:10.1086/668203

Page DM, Wittamer V, Bertrand JY, Lewis KL, Pratt DN, Delgado N, Schale SE, McGue C, Jacobsen BH, Doty A, Pao Y, Yang H, Chi NC, Magor BG, Traver D. 2013. An evolutionarily conserved program of B-cell development and activation in zebrafish. *Blood* **122**:e1. doi:10.1182/BLOOD-2012-12-471029

Palha N, Guivel-Benhassine F, Briolat V, Lutfalla G, Sourisseau M, Ellett F, Wang CH, Lieschke GJ, Herbomel P, Schwartz O, Levraud JP. 2013. Real-Time Whole-Body Visualization of Chikungunya Virus Infection and Host Interferon Response in Zebrafish. *PLoS Pathog*

9:e1003619. doi:10.1371/journal.ppat.1003619

Papian S, Mohabati Mobarez A, khoramabadi N, Mehdi Abdol M, Talebi Bezmin Abadi A. 2020. Investigating the role of L. pnuemophila LPS derivatives in formation of specific cell-mediated immune responses against the pathogen. *Microb Pathog* **147**. doi:10.1016/J.MICPATH.2020.104396

Parichy DM. 2015a. The natural history of model organisms: Advancing biology through a deeper understanding of zebrafish ecology and evolution. *Elife* **2015**. doi:10.7554/eLife.05635.001

Parichy DM. 2015b. The natural history of model organisms: Advancing biology through a deeper understanding of zebrafish ecology and evolution. *Elife* **2015**.

Passoni G, Langevin C, Palha N, Mounce BC, Briolat V, Affaticati P, De Job E, Joly J-S, Vignuzzi M, Saleh M-C, Herbomel P, Boudinot P, Levraud J-P. 2017. Imaging of viral neuroinvasion in the zebrafish reveals that Sindbis and chikungunya viruses favour different entry routes. *DMM Dis Model Mech* **10**:847–857. doi:10.1242/dmm.029231

Paull GC, Filby AL, Giddins HG, Coe TS, Hamilton PB, Tyler CR. 2010. Dominance Hierarchies in Zebrafish (Danio rerio) and Their Relationship with Reproductive Success. *https://home.liebertpub.com/zeb* **7**:109–117. doi:10.1089/ZEB.2009.0618

Pedroni A, Ampatzis K. 2019. Large-Scale Analysis of the Diversity and Complexity of the Adult Spinal Cord Neurotransmitter Typology. *iScience* **19**:1189–1201. doi:10.1016/J.ISCI.2019.09.010

Peichel CL. 2004. Social behavior: How do fish find their shoal mate? *Curr Biol* **14**. doi:10.1016/j.cub.2004.06.037

Perlman S, Netland J. 2009. Coronaviruses post-SARS: update on replication and pathogenesis. *Nat Rev Microbiol 2009 76* **7**:439–450. doi:10.1038/nrmicro2147

Petermann N, Hansen G, Schmidt CL, Hilgenfeld R. 2010. Structure of the GTPase and GDI domains of FeoB, the ferrous iron transporter of Legionella pneumophila. *FEBS Lett* **584**:733–738. doi:10.1016/J.FEBSLET.2009.12.045

Petrovski G, Zahuczky G, Májai G, Fésüs L. 2007. Phagocytosis of Cells Dying through

Autophagy Evokes a Pro-Inflammatory Response in Macrophages. *https://doi.org/104161/auto4731* **3**:508–510. doi:10.4161/AUTO.4731

Piano M Del, Palombara P La, … RN-BD, 1984 U. 1984. The legionellosis. *Boll Ist Sieroter Milan*.

Picchietti S, Guerra L, Bertoni F, Randelli E, Belardinelli MC, Buonocore F, Fausto AM, Rombout JH, Scapigliati G, Abelli L. 2011. Intestinal T cells of Dicentrarchus labrax (L.): gene expression and functional studies. *Fish Shellfish Immunol* **30**:609–617. doi:10.1016/J.FSI.2010.12.006

Pijanowski L, Golbach L, Kolaczkowska E, Scheer M, Verburg-van Kemenade BML, Chadzinska M. 2013. Carp neutrophilic granulocytes form extracellular traps via ROS-dependent and independent pathways. *Fish Shellfish Immunol* **34**:1244–1252. doi:10.1016/J.FSI.2013.02.010

Poirier EZ, Mounce BC, Rozen-Gagnon K, Hooikaas PJ, Stapleford KA, Moratorio G, Vignuzzi M. 2015. Low-Fidelity Polymerases of Alphaviruses Recombine at Higher Rates To Overproduce Defective Interfering Particles. *J Virol* **90**:2446–2454. doi:10.1128/JVI.02921-15

Powell D, Lou M, Barros Becker F, Huttenlocher A. 2018. Cxcr1 mediates recruitment of neutrophils and supports proliferation of tumor-initiating astrocytes in vivo. *Sci Reports 2018 81* **8**:1–12. doi:10.1038/s41598-018-31675-0

Propper DJ, Balkwill FR. 2022. Harnessing cytokines and chemokines for cancer therapy. *Nat Rev Clin Oncol 2022 194* **19**:237–253. doi:10.1038/s41571-021-00588-9

Qin T, Zhou H, Ren H, Liu W. 2017. Distribution of secretion systems in the genus Legionella and its correlation with pathogenicity. *Front Microbiol* **8**. doi:10.3389/FMICB.2017.00388/FULL

Qualitative and Quantitative Evaluation of Two New Histogram Limiting Binarization Algorithms. n.d. https://www.cscjournals.org/library/manuscriptinfo.php?mc=IJIP-829

Quiñonez-Silvero C, Hübner K, Herzog W. 2020. Development of the brain vasculature and the blood-brain barrier in zebrafish. *Dev Biol* **457**:181–190. doi:10.1016/J.YDBIO.2019.03.005

Quintana FJ, Iglesias AH, Farez MF, Caccamo M, Burns EJ, Kassam N, Oukka M, Weiner HL. 2010. Adaptive Autoimmunity and Foxp3-Based Immunoregulation in Zebrafish. *PLoS One* **5**. doi:10.1371/JOURNAL.PONE.0009478

Raghuvamsi P V., Tulsian NK, Samsudin F, Qian X, Purushotorman K, Yue G, Kozma MM, Hwa WY, Lescar J, Bond PJ, Macary PA, Anand GS. 2021. Sars-cov-2 s protein:Ace2 interaction reveals novel allosteric targets. *Elife* **10**:1–47. doi:10.7554/ELIFE.63646

Ramakrishnan L. 2013. The Zebrafish Guide to Tuberculosis Immunity and Treatment. *Cold Spring Harb Symp Quant Biol* **78**:179–192. doi:10.1101/SQB.2013.78.023283

Ramsay JM, Watral V, Schreck CB, Kent ML. 2009. Husbandry stress exacerbates mycobacterial infections in adult zebrafish, Danio rerio (Hamilton). *J Fish Dis* **32**:931–941. doi:10.1111/J.1365-2761.2009.01074.X

Rasighaemi P, Basheer F, Liongue C, Ward AC. 2015. Zebrafish as a model for leukemia and other hematopoietic disorders. *J Hematol Oncol* **8**. doi:10.1186/S13045-015-0126-4

Ray K, Marteyn B, Sansonetti PJ, Tang CM. 2009. Life on the inside: the intracellular lifestyle of cytosolic bacteria. *Nat Rev Microbiol 2009 75* **7**:333–340. doi:10.1038/nrmicro2112

Renshaw SA, Trede NS. 2012. A model 450 million years in the making: zebrafish and vertebrate immunity. *Dis Model Mech* **5**:38–47. doi:10.1242/DMM.007138

Richard AS, Shim BS, Kwon YC, Zhang R, Otsuka Y, Schmitt K, Berri F, Diamond MS, Choe H. 2017. AXL-dependent infection of human fetal endothelial cells distinguishes Zika virus from other pathogenic flaviviruses. *Proc Natl Acad Sci U S A* **114**:2024–2029. doi:10.1073/PNAS.1620558114

Robison BD, Rowland W. 2011. A potential model system for studying the genetics of domestication: behavioral variation among wild and domesticated strains of zebra danio (Danio rerio). *https://doi.org/101139/f05-118* **62**:2046–2054. doi:10.1139/F05-118

Roca FJ, Mulero I, López-Muñoz A, Sepulcre MP, Renshaw SA, Meseguer J, Mulero V. 2008. Evolution of the Inflammatory Response in Vertebrates: Fish TNF-α Is a Powerful Activator of Endothelial Cells but Hardly Activates Phagocytes. *J Immunol* **181**:5071–5081. doi:10.4049/JIMMUNOL.181.7.5071

Rose PP, Hanna SL, Spiridigliozzi A, Wannissorn N, Beiting DP, Ross SR, Hardy RW, Bambina SA, Heise MT, Cherry S. 2011. Natural resistance-associated macrophage protein is a cellular receptor for Sindbis virus in both insect and mammalian hosts. *Cell Host Microbe* **10**:97–104. doi:10.1016/j.chom.2011.06.009

Rosowski EE, Raffa N, Knox BP, Golenberg N, Keller NP, Huttenlocher A. 2018. Macrophages inhibit Aspergillus fumigatus germination and neutrophil-mediated fungal killing. *PLOS Pathog* **14**:e1007229. doi:10.1371/JOURNAL.PPAT.1007229

Rougeot J, Torraca V, Zakrzewska A, Kanwal Z, Jansen HJ, Sommer F, Spaink HP, Meijer AH. 2019. RNAseq profiling of leukocyte populations in zebrafish larvae reveals a cxcl11 chemokine gene as a marker of macrophage polarization during mycobacterial infection. *Front Immunol* **10**:443723. doi:10.3389/FIMMU.2019.00832/BIBTEX

Ruzicka L, Bradford YM, Frazer K, Howe DG, Paddock H, Ramachandran S, Singer A, Toro S, Van Slyke CE, Eagle AE, Fashena D, Kalita P, Knight J, Mani P, Martin R, Moxon SAT, Pich C, Schaper K, Shao X, Westerfield M. 2015. ZFIN, The zebrafish model organism database: Updates and new directions. *genesis* **53**:498–509. doi:10.1002/DVG.22868

Sakai C, Ijaz S, Hoffman EJ. 2018. Zebrafish Models of Neurodevelopmental Disorders: Past, Present, and Future. *Front Mol Neurosci* **11**:396075. doi:10.3389/FNMOL.2018.00294/BIBTEX

Saleem S, Kannan RR. 2018. Zebrafish: an emerging real-time model system to study Alzheimer's disease and neurospecific drug discovery. *Cell Death Discov 2018 41* **4**:1–13. doi:10.1038/s41420-018-0109-7

Sane J, Guedes S, Ollgren J, Kurkela S, Klemets P, Vapalahti O, Kela E, Lyytikäinen O, Nuorti JP. 2011. Epidemic Sindbis Virus Infection in Finland: A Population-Based Case-Control Study of Risk Factors. *J Infect Dis* **204**:459–466. doi:10.1093/INFDIS/JIR267

Sane J, Kurkela S, Desdouits M, Kalimo H, Mazalrey S, Lokki ML, Vaheri A, Helve T, Törnwall J, Huerre M, Butler-Browne G, Ceccaldi PE, Gessain A, Vapalahti O. 2012. Prolonged Myalgia in Sindbis Virus Infection: Case Description and In Vitro Infection of Myotubes and Myoblasts. *J Infect Dis* **206**:407–414. doi:10.1093/INFDIS/JIS358

Sanford JP. 1979. Legionnaires' Disease — The First Thousand Days. *N Engl J Med* **300**:654–656. doi:10.1056/NEJM197903223001205

Sanz-Morejón A, García-Redondo AB, Reuter H, Marques IJ, Bates T, Galardi-Castilla M, Große A, Manig S, Langa X, Ernst A, Piragyte I, Botos MA, González-Rosa JM, Ruiz-Ortega M, Briones AM, Salaices M, Englert C, Mercader N. 2019. Wilms Tumor 1b Expression Defines a Pro-regenerative Macrophage Subtype and Is Required for Organ Regeneration in the Zebrafish. *Cell Rep* **28**:1296-1306.e6. doi:10.1016/J.CELREP.2019.06.091

Sawicki SG, Sawicki DL. 1995. Coronaviruses use discontinuous extension for synthesis of subgenome-length negative strands. *Adv Exp Med Biol* **380**:499–506. doi:10.1007/978-1-4615-1899-0_79

Scherwitzl I, Opp S, Hurtado AM, Pampeno C, Loomis C, Kannan K, Yu M, Meruelo D. 2020. Sindbis Virus with Anti-OX40 Overcomes the Immunosuppressive Tumor Microenvironment of Low-Immunogenic Tumors. *Mol Ther - Oncolytics* **17**:431–447. doi:10.1016/j.omto.2020.04.012

Schild Y, Mohamed A, Wootton EJ, Lewis A, Elks PM. 2020. Hif-1alpha stabilisation is protective against infection in zebrafish comorbid models. *FEBS J* **287**:3925–3943. doi:10.1111/FEBS.15433

Schindelin J, Arganda-Carreras I, Frise E, Kaynig V, Longair M, Pietzsch T, Preibisch S, Rueden C, Saalfeld S, Schmid B, Tinevez J-Y, White DJ, Hartenstein V, Eliceiri K, Tomancak P, Cardona A. 2012. Fiji: an open-source platform for biological-image analysis. *Nat Methods* **9**:676–682. doi:10.1038/nmeth.2019

Schoggins JW, Rice CM. 2011. Interferon-stimulated genes and their antiviral effector functions. *Curr Opin Virol* **1**:519–525. doi:10.1016/J.COVIRO.2011.10.008

Schubert K, Karousis ED, Jomaa A, Scaiola A, Echeverria B, Gurzeler LA, Leibundgut M, Thiel V, Mühlemann O, Ban N. 2020. SARS-CoV-2 Nsp1 binds the ribosomal mRNA channel to inhibit translation. *Nat Struct Mol Biol 2020 2710* **27**:959–966. doi:10.1038/s41594-020-0511-8

Seelye SL, Chen PL, Deiss TC, Criscitiello MF. 2016. Genomic organization of the zebrafish

(Danio rerio) T cell receptor alpha/delta locus and analysis of expressed products. *Immunogenetics* **68**:365–379. doi:10.1007/S00251-016-0904-3

Shen Y, Xu J, Zhi S, Wu W, Chen Y, Zhang Q, Zhou Y, Deng Z, Li W. 2022. MIP From Legionella pneumophila Influences the Phagocytosis and Chemotaxis of RAW264.7 Macrophages by Regulating the lncRNA GAS5/miR-21/SOCS6 Axis. *Front Cell Infect Microbiol* **12**. doi:10.3389/FCIMB.2022.810865/FULL

Sherman' And LA, Griffin' DE. 1990. Pathogenesis of encephalitis induced in newborn mice by virulent and avirulent strains of Sindbis virus. *J Virol* **64**:2041–2046. doi:10.1128/JVI.64.5.2041-2046.1990

Shevchuk O, Jäger J, Steinert M. 2011. Virulence properties of the Legionella pneumophila cell envelope. *Front Microbiol* **2**. doi:10.3389/FMICB.2011.00074/FULL

Shilts J, Crozier T, Greenwood E, reports PL-S, 2021 undefined. n.d. No evidence for basigin/CD147 as a direct SARS-CoV-2 spike binding receptor. *nature.comJ Shilts, TWM Crozier, EJD Greenwood, PJ Lehner, GJ WrightScientific reports, 2021•nature.com*.

Sieger D, Stein C, Neifer D, Van Der Sar AM, Leptin M. 2009. The role of gamma interferon in innate immunity in the zebrafish embryo. *Dis Model Mech* **2**:571–581. doi:10.1242/DMM.003509

Silva MT. 2010. Neutrophils and macrophages work in concert as inducers and effectors of adaptive immunity against extracellular and intracellular microbial pathogens. *J Leukoc Biol* **87**:805–813. doi:10.1189/JLB.1109767

Silva MT, Correia-Neves M. 2012. Neutrophils and macrophages: The main partners of phagocyte cell systems. *Front Immunol* **3**:24656. doi:10.3389/FIMMU.2012.00174/BIBTEX

Silva NJ, Dorman LC, Vainchtein ID, Horneck NC, Molofsky A V. 2021. In situ and transcriptomic identification of microglia in synapse-rich regions of the developing zebrafish brain. *Nat Commun 2021 121* **12**:1–12. doi:10.1038/s41467-021-26206-x

Slauch JM. 2011. How does the oxidative burst of macrophages kill bacteria? Still an open question. *Mol Microbiol* **80**:580–583. doi:10.1111/J.1365-2958.2011.07612.X

Sola I, Almazán F, Zúñiga S, Enjuanes L. 2015. Continuous and Discontinuous RNA Synthesis in Coronaviruses. *Annu Rev Virol* **2**:265–288. doi:10.1146/ANNUREV-VIROLOGY-100114-055218

Sollberger G, Choidas A, Burn GL, Habenberger P, Lucrezia R Di, Kordes S, Menninger S, Eickhoff J, Nussbaumer P, Klebl B, Krüger R, Herzig A, Zychlinsky A. 2018. Gasdermin D plays a vital role in the generation of neutrophil extracellular traps. *Sci Immunol* **3**:6689. doi:10.1126/SCIIMMUNOL.AAR6689/SUPPL_FILE/AAR6689_TABLE_S1.XLSX

Somamoto T, Koppang EO, Fischer U. 2014. Antiviral functions of CD8+ cytotoxic T cells in teleost fish. *Dev Comp Immunol* **43**:197–204. doi:10.1016/j.dci.2013.07.014

Sommer F, Ortiz Zacarías N V., Heitman LH, Meijer AH. 2021. Inhibition of macrophage migration in zebrafish larvae demonstrates in vivo efficacy of human CCR2 inhibitors. *Dev Comp Immunol* **116**:103932. doi:10.1016/J.DCI.2020.103932

Sommer F, Torraca V, Kamel SM, Lombardi A, Meijer AH. 2020. Frontline Science: Antagonism between regular and atypical Cxcr3 receptors regulates macrophage migration during infection and injury in zebrafish. *J Leukoc Biol* **107**:185–203. doi:10.1002/JLB.2HI0119-006R

Spence R, Ashton R, Smith C. 2007. Oviposition decisions are mediated by spawning site quality in wild and domesticated zebrafish, Danio rerio. *Behaviour* **144**:953–966. doi:10.1163/156853907781492726

Spence R, Fatema MK, Reichard M, Huq KA, Wahab MA, Ahmed ZF, Smith C. 2006. The distribution and habitat preferences of the zebrafish in Bangladesh. *J Fish Biol* **69**:1435–1448. doi:10.1111/J.1095-8649.2006.01206.X

Spinner JL, Hasenkrug AM, Shannon JG, Kobayashi SD, Hinnebusch BJ. 2016. Role of the Yersinia YopJ protein in suppressing interleukin-8 secretion by human polymorphonuclear leukocytes. *Microbes Infect* **18**:21–29. doi:10.1016/J.MICINF.2015.08.015

Spitz O, Erenburg IN, Beer T, Kanonenberg K, Holland IB, Schmitt L. 2019. Type I Secretion Systems—One Mechanism for All? *Microbiol Spectr* **7**. doi:10.1128/MICROBIOLSPEC.PSIB-0003-2018

Stein C, Caccamo M, Laird G, Leptin M. 2007. Conservation and divergence of gene families encoding components of innate immune response systems in zebrafish. *Genome Biol* **8**:1–23. doi:10.1186/GB-2007-8-11-R251/FIGURES/16

Stout RD, Suttles J. 2004. Functional plasticity of macrophages: reversible adaptation to changing microenvironments. *J Leukoc Biol* **76**:509. doi:10.1189/JLB.0504272

Strauss EG, Rice CM, Strauss JH. 1984. Complete nucleotide sequence of the genomic RNA of Sindbis virus. *Virology* **133**:92–110. doi:10.1016/0042-6822(84)90428-8

Strauss James H, Strauss EG. 1994. The alphaviruses: gene expression, replication, and evolution. *Microbiol Rev* **58**:491–562. doi:10.1128/MR.58.3.491-562.1994

Strauss J H, Strauss EG. 1994a. The alphaviruses: gene expression, replication, and evolution. *Microbiol Rev* **58**:491–562.

Strauss J H, Strauss EG. 1994b. The alphaviruses: gene expression, replication, and evolution. *Microbiol Rev* **58**:491–562. doi:10.1128/mr.58.3.491-562.1994

Streisinger G, Walker C, Dower N, Knauber D, Singer F. 1981. Production of clones of homozygous diploid zebra fish (Brachydanio rerio). *Nat 1981 2915813* **291**:293–296. doi:10.1038/291293a0

Sullivan C, Soos BL, Millard PJ, Kim CH, King BL. 2021. Modeling Virus-Induced Inflammation in Zebrafish: A Balance Between Infection Control and Excessive Inflammation. *Front Immunol* **12**:636623. doi:10.3389/FIMMU.2021.636623/BIBTEX

Swanson PA, McGavern DB. 2015. Viral diseases of the central nervous system. *Curr Opin Virol* **11**:44–54. doi:10.1016/j.coviro.2014.12.009

Swinburne IA, Mosaliganti KR, Green AA, Megason SG. 2015. Improved Long-Term Imaging of Embryos with Genetically Encoded α-Bungarotoxin. *PLoS One* **10**:e0134005. doi:10.1371/journal.pone.0134005

Takizawa F, Dijkstra JM, Kotterba P, Korytář T, Kock H, Köllner B, Jaureguiberry B, Nakanishi T, Fischer U. 2011. The expression of CD8α discriminates distinct T cell subsets in teleost fish. *Dev Comp Immunol* **35**:752–763. doi:10.1016/J.DCI.2011.02.008

Takizawa F, Magadan S, Parra D, Xu Z, Korytář T, Boudinot P, Sunyer JO. 2016. Novel Teleost CD4-Bearing Cell Populations Provide Insights into the Evolutionary Origins and Primordial Roles of CD4+ Lymphocytes and CD4+ Macrophages. *J Immunol* **196**:4522–4535. doi:10.4049/JIMMUNOL.1600222

Tauzin S, Starnes TW, Becker FB, Lam P ying, Huttenlocher A. 2014. Redox and Src family kinase signaling control leukocyte wound attraction and neutrophil reverse migration. *J Cell Biol* **207**:589–598. doi:10.1083/JCB.201408090/VIDEO-8

Teame T, Zhang Z, Ran C, Zhang H, Yang Y, Ding Q, Xie M, Gao C, Ye Y, Duan M, Zhou Z. 2019. The use of zebrafish (Danio rerio) as biomedical models. *Anim Front Rev Mag Anim Agric* **9**:68. doi:10.1093/AF/VFZ020

Tenor JL, Oehlers SH, Yang JL, Tobin DM, Perfect JR. 2015. Live imaging of host-parasite interactions in a zebrafish infection model reveals cryptococcal determinants of virulence and central nervous system invasion. *MBio* **6**. doi:10.1128/MBIO.01425-15/ASSET/74CF9B49-9BBA-4434-9E00-FB20FA9B6865/ASSETS/GRAPHIC/MBO0051524760006.JPEG

Thoms M, Buschauer R, Ameismeier M, Koepke L, Denk T, Hirschenberger M, Kratzat H, Hayn M, MacKens-Kiani T, Cheng J, Straub JH, Stürzel CM, Fröhlich T, Berninghausen O, Becker T, Kirchhoff F, Sparrer KMJ, Beckmann R. 2020. Structural basis for translational shutdown and immune evasion by the Nsp1 protein of SARS-CoV-2. *Science (80-)* **369**:1249–1256. doi:10.1126/SCIENCE.ABC8665/SUPPL_FILE/ABC8665_THOMS_SM.PDF

Tobin David M., May RC, Wheeler RT. 2012. Zebrafish: A See-Through Host and a Fluorescent Toolbox to Probe Host–Pathogen Interaction. *PLOS Pathog* **8**:e1002349. doi:10.1371/JOURNAL.PPAT.1002349

Tobin David M, May RC, Wheeler RT. 2012. Zebrafish: a see-through host and a fluorescent toolbox to probe host-pathogen interaction. *PLoS Pathog* **8**:e1002349. doi:10.1371/journal.ppat.1002349

Tobin DM, Vary JC, Ray JP, Walsh GS, Dunstan SJ, Bang ND, Hagge DA, Khadge S, King MC, Hawn TR, Moens CB, Ramakrishnan L. 2010. The lta4h Locus Modulates Susceptibility to Mycobacterial Infection in Zebrafish and Humans. *Cell* **140**:717–730.

doi:10.1016/j.cell.2010.02.013

Toda H, Araki K, Moritomo T, Nakanishi T. 2011. Perforin-dependent cytotoxic mechanism in killing by CD8 positive T cells in ginbuna crucian carp, Carassius auratus langsdorfii. *Dev Comp Immunol* **35**:88–93. doi:10.1016/J.DCI.2010.08.010

Torraca V, Mostowy S. 2018. Zebrafish Infection: From Pathogenesis to Cell Biology. *Trends Cell Biol* **28**:143. doi:10.1016/J.TCB.2017.10.002

Traver D, Herbomel P, Patton EE, Murphey RD, Yoder JA, Litman GW, Catic A, Amemiya CT, Zon LI, Trede NS. 2003. The Zebrafish as a Model Organism to Study Development of the Immune System. *Adv Immunol* **81**:253–330. doi:10.1016/S0065-2776(03)81007-6

Tsang B, Gerlai RT, Ansari R. 2020. Maintenance and breeding of zebrafish, with some ethological and ecological considerations in mind. *Behav Neural Genet Zebrafish* 17–32. doi:10.1016/B978-0-12-817528-6.00002-4

Tsarouchas TM, Wehner D, Cavone L, Munir T, Keatinge M, Lambertus M, Underhill A, Barrett T, Kassapis E, Ogryzko N, Feng Y, van Ham TJ, Becker T, Becker CG. 2018. Dynamic control of proinflammatory cytokines Il-1β and Tnf-α by macrophages in zebrafish spinal cord regeneration. *Nat Commun* **9**:4670. doi:10.1038/s41467-018-07036-w

Tyson JY, Vargas P, Cianciotto NP. 2014. The novel Legionella pneumophila type II secretion substrate NttC contributes to infection of amoebae Hartmannella vermiformis and Willaertia magna. *Microbiol (United Kingdom)* **160**:2732–2744. doi:10.1099/MIC.0.082750-0

V'kovski P, Kratzel A, Steiner S, Stalder H, Thiel V. 2020. Coronavirus biology and replication: implications for SARS-CoV-2. *Nat Rev Microbiol 2020 193* **19**:155–170. doi:10.1038/s41579-020-00468-6

van der Aa LM, Chadzinska M, Tijhaar E, Boudinot P, Lidy verburg-Van kemenade BM. 2010. CXCL8 Chemokines in Teleost Fish: Two Lineages with Distinct Expression Profiles during Early Phases of Inflammation. *PLoS One* **5**:e12384. doi:10.1371/JOURNAL.PONE.0012384

Van Der Vaart M, Spaink HP, Meijer AH. 2012. Pathogen recognition and activation of the innate immune response in zebrafish. *Adv Hematol* **2012**. doi:10.1155/2012/159807

Varela M, Dios S, Novoa B, Figueras A. 2012. Characterisation, expression and ontogeny of interleukin-6 and its receptors in zebrafish (Danio rerio). *Dev Comp Immunol* **37**:97–106. doi:10.1016/J.DCI.2011.11.004

Vascotto SG, Beckham Y, Kelly GM. 2011. The zebrafish's swim to fame as an experimental model in biology. *https://doi.org/101139/o97-081* **75**:479–485. doi:10.1139/O97-081

Venkatesan A. 2015. Epidemiology and outcomes of acute encephalitis. *Curr Opin Neurol* **28**:277–282. doi:10.1097/WCO.0000000000000199

Viana F, Boucontet L, Laghi V, Schator D, Ibranosyan M, Jarraud S, Colucci-Guyon E, Buchrieser C. 2023. Hiding in the yolk: A unique feature of Legionella pneumophila infection of zebrafish. *PLoS Pathog* **19**:e1011375. doi:10.1371/journal.ppat.1011375

Viengkhou B, Hofer MJ. 2023. Breaking down the cellular responses to type I interferon neurotoxicity in the brain. *Front Immunol* **14**:1110593. doi:10.3389/fimmu.2023.1110593

Villalta SA, Nguyen HX, Deng B, Gotoh T, Tidball JG. 2008. Shifts in macrophage phenotypes and macrophage competition for arginine metabolism affect the severity of muscle pathology in muscular dystrophy. *Hum Mol Genet* **18**:482–496. doi:10.1093/hmg/ddn376

Virta VC, Cooper MS. 2011. Structural components and morphogenetic mechanics of the zebrafish yolk extension, a developmental module. *J Exp Zool Part B Mol Dev Evol* **316B**:76–92. doi:10.1002/JEZ.B.21381

Voleti V, Patel KB, Li W, Perez Campos C, Bharadwaj S, Yu H, Ford C, Casper MJ, Yan RW, Liang W, Wen C, Kimura KD, Targoff KL, Hillman EMC. 2019. Real-time volumetric microscopy of in vivo dynamics and large-scale samples with SCAPE 2.0. *Nat Methods 2019 1610* **16**:1054–1062. doi:10.1038/s41592-019-0579-4

Wan F, Hu C Bin, Ma JX, Gao K, Xiang LX, Shao JZ. 2017. Characterization of γδ T cells from zebrafish provides insights into their important role in adaptive humoral immunity. *Front Immunol* **7**:9. doi:10.3389/FIMMU.2016.00675/FULL

Wan T, Zhao Y, Fan F, Hu R, Jin X. 2017. Dexamethasone inhibits S. aureus-induced neutrophil extracellular pathogen-killing mechanism, possibly through toll-like receptor regulation. *Front Immunol* **8**:216336. doi:10.3389/FIMMU.2017.00060/BIBTEX

Wang Qihui, Zhang Y, Wu L, Niu S, Song C, Zhang Z, Lu G, Qiao C, Hu Y, Yuen KY, Wang Qisheng, Zhou H, Yan J, Qi J. 2020. Structural and Functional Basis of SARS-CoV-2 Entry by Using Human ACE2. *Cell* **181**:894-904.e9. doi:10.1016/J.CELL.2020.03.045

Wang X, Copmans D, de Witte PAM. 2021. Using Zebrafish as a Disease Model to Study Fibrotic Disease. *Int J Mol Sci 2021, Vol 22, Page 6404* **22**:6404. doi:10.3390/IJMS22126404

Wang Z, Ding Y, Satta S, Roustaei M, Fei P, Hsiai TK. 2021. A hybrid of light-field and light-sheet imaging to study myocardial function and intracardiac blood flow during zebrafish development. *PLOS Comput Biol* **17**:e1009175. doi:10.1371/JOURNAL.PCBI.1009175

White RM, Patton EE. 2023. Adult zebrafish as advanced models of human disease. *Dis Model Mech* **16**. doi:10.1242/DMM.050351/324979

Wickramaarachchi WDN, Wan Q, Lim BS, Jung HB, De Zoysa M, Park MA, Lee J, Whang I. 2014. Genomic characterization of interferon regulatory factor 5 from rock bream (Oplegnathus fasciatus) and its role in antiviral defense. *Fish Shellfish Immunol* **37**:256–267. doi:10.1016/J.FSI.2014.02.002

Wiegertjes GF, Wentzel AS, Spaink HP, Elks PM, Fink IR. 2016. Polarization of immune responses in fish: The 'macrophages first' point of view. *Mol Immunol* **69**:146–156. doi:10.1016/J.MOLIMM.2015.09.026

Wilkinson RN, Jopling C, Van Eeden FJM. 2014. Zebrafish as a Model of Cardiac Disease. *Prog Mol Biol Transl Sci* **124**:65–91. doi:10.1016/B978-0-12-386930-2.00004-5

Willett CE, Kawasaki H, Amemiya CT, Lin S, Steiner LA. 2001. Ikaros expression as a marker for lymphoid progenitors during zebrafish development. *Dev Dyn* **222**:694–698. doi:10.1002/DVDY.1223

Wu S, Nguyen LTM, Pan H, Hassan S, Dai Y, Xu J, Wen Z. 2020. Two phenotypically and functionally distinct microglial populations in adult zebrafish. *Sci Adv* **6**. doi:10.1126/SCIADV.ABD1160

Xiong C, Levis R, Shen P, Schlesinger S, Rice CM, Huang H V. 1989. Sindbis Virus: An Efficient, Broad Host Range Vector for Gene Expression in Animal Cells. *Science (80-)* **243**:1188–1191. doi:10.1126/SCIENCE.2922607

Xu J, Zhu L, He S, Wu Y, Jin W, Yu T, Qu JY, Wen Z. 2015. Temporal-Spatial Resolution Fate Mapping Reveals Distinct Origins for Embryonic and Adult Microglia in Zebrafish. *Dev Cell* **34**:632–641. doi:10.1016/j.devcel.2015.08.018

Xu X, Hu J, Ma J, Nie L, Shao T, Xiang L, Shao J. 2016. Essential Roles of TIM-1 and TIM-4 Homologs in Adaptive Humoral Immunity in a Zebrafish Model. *J Immunol* **196**:1686–1699. doi:10.4049/JIMMUNOL.1501736

Xue J, Schmidt S V., Sander J, Draffehn A, Krebs W, Quester I, DeNardo D, Gohel TD, Emde M, Schmidleithner L, Ganesan H, Nino-Castro A, Mallmann MR, Labzin L, Theis H, Kraut M, Beyer M, Latz E, Freeman TC, Ulas T, Schultze JL. 2014. Transcriptome-Based Network Analysis Reveals a Spectrum Model of Human Macrophage Activation. *Immunity* **40**:274. doi:10.1016/J.IMMUNI.2014.01.006

Yadav R, Chaudhary JK, Jain N, Chaudhary PK, Khanra S, Dhamija P, Sharma A, Kumar A, Handu S. 2021. Role of Structural and Non-Structural Proteins and Therapeutic Targets of SARS-CoV-2 for COVID-19. *Cells 2021, Vol 10, Page 821* **10**:821. doi:10.3390/CELLS10040821

Yamaguchi T, Takizawa F, Furihata M, Soto-Lampe V, Dijkstra JM, Fischer U. 2019. Teleost cytotoxic T cells. *Fish Shellfish Immunol* **95**:422–439. doi:10.1016/J.FSI.2019.10.041

Yang CT, Cambier CJ, Davis JM, Hall CJ, Crosier PS, Ramakrishnan L. 2012. Neutrophils exert protection in the early tuberculous granuloma by oxidative killing of mycobacteria phagocytosed from infected macrophages. *Cell Host Microbe* **12**:301–312. doi:10.1016/j.chom.2012.07.009

Yang Z-Y, Huang † Yue, Ganesh L, Leung † Kwanyee, Kong W-P, Schwartz O, Subbarao K, Nabel GJ. 2004. pH-dependent entry of severe acute respiratory syndrome coronavirus is mediated by the spike glycoprotein and enhanced by dendritic cell transfer through DC-SIGN. *Am Soc MicrobiolZY Yang, Y Huang, L Ganesh, K Leung, WP Kong, O Schwartz, K Subbarao, GJ NabelJournal Virol 2004•Am Soc Microbiol* **78**:5642–5650. doi:10.1128/JVI.78.11.5642-5650.2004

Yang Z, Chen Y, Zhang Q, Chen X, Deng Z. 2021. Research Article Major Outer Membrane

Protein from Legionella pneumophila Inhibits Phagocytosis but Enhances Chemotaxis of RAW 264.7 Macrophages by. *J Immunol Res* **2021**. doi:10.1155/2021/9409777

Yaniv K, Isogai S, Castranova D, Dye L, Hitomi J, Weinstein BM. 2006. Live imaging of lymphatic development in the zebrafish. *Nat Med 2006 126* **12**:711–716. doi:10.1038/nm1427

Yoder JA, Nielsen ME, Amemiya CT, Litman GW. 2002. Zebrafish as an immunological model system. *Microbes Infect* **4**:1469–1478. doi:10.1016/S1286-4579(02)00029-1

Yoon S, Mitra S, Wyse C, Alnabulsi A, Zou J, Weerdenburg EM, Van Der Sar AM, Wang D, Secombes CJ, Bird S. 2015. First Demonstration of Antigen Induced Cytokine Expression by CD4-1+ Lymphocytes in a Poikilotherm: Studies in Zebrafish (Danio rerio). *PLoS One* **10**:e0126378. doi:10.1371/JOURNAL.PONE.0126378

Yoshida N, Frickel EM, Mostowy S. 2017. Macrophage-microbe interactions: Lessons from the Zebrafish model. *Front Immunol* **8**:322709. doi:10.3389/FIMMU.2017.01703/BIBTEX

Yu T, Guo W, Tian Y, Xu J, Chen J, Li L, Wen Z. 2017. Distinct regulatory networks control the development of macrophages of different origins in zebrafish. *Blood* **129**:509–519. doi:10.1182/BLOOD-2016-07-727651

Zakrzewska A, Cui C, Stockhammer OW, Benard EL, Spaink HP, Meijer AH. 2010. Macrophage-specific gene functions in Spi1-directed innate immunity. *Blood* **116**:e1–e11. doi:10.1182/BLOOD-2010-01-262873

Zanandrea R, Bonan CD, Campos MM. 2020. Zebrafish as a model for inflammation and drug discovery. *Drug Discov Today* **25**:2201–2211. doi:10.1016/J.DRUDIS.2020.09.036

Zhang H, Fei C, Wu H, Yang M, Liu Q, Wang Q, Zhang Y. 2013. Transcriptome Profiling Reveals Th17-Like Immune Responses Induced in Zebrafish Bath-Vaccinated with a Live Attenuated Vibrio anguillarum. *PLoS One* **8**. doi:10.1371/JOURNAL.PONE.0073871

Zhang L, Chen WQ, Hu YW, Wu XM, Nie P, Chang MX. 2016. TBK1-like transcript negatively regulates the production of IFN and IFN-stimulated genes through RLRs-MAVS-TBK1 pathway. *Fish Shellfish Immunol* **54**:135–143. doi:10.1016/J.FSI.2016.04.002

Zhang Y, Liu H, Yao J, Huang Y, Qin S, Sun Z, Xu Y, Wan S, Cheng H, Li C, Zhang X, Ke Y. 2016. Manipulating the air-filled zebrafish swim bladder as a neutrophilic inflammation model for acute lung injury. *Cell Death Dis 2016 711* **7**:e2470–e2470. doi:10.1038/cddis.2016.365

Ziegler U, Fischer D, Eiden M, Reuschel M, Rinder M, Müller K, Schwehn R, Schmidt V, Groschup MH, Keller M. 2019. Sindbis virus- a wild bird associated zoonotic arbovirus circulates in Germany. *Vet Microbiol* **239**:108453. doi:10.1016/J.VETMIC.2019.108453

Zimmerman AM, Moustafa FM, Romanowski KE, Steiner LA. 2011. Zebrafish immunoglobulin IgD: unusual exon usage and quantitative expression profiles with IgM and IgZ/T heavy chain isotypes. *Mol Immunol* **48**:2220. doi:10.1016/J.MOLIMM.2011.06.441

ANNEXES

Annexe 1

diagnostics

MDPI

Article

A User-Friendly Approach for Routine Histopathological and Morphometric Analysis of Skeletal Muscle Using CellProfiler Software

Valerio Laghi [1], Valentina Ricci [2], Francesca De Santa [2] and Alessio Torcinaro [2,*]

[1] Unité Macrophages et Développement de l'Immunité, Institut Pasteur, CNRS UMR3738, 75015 Paris, France; valerio.laghi@pasteur.fr

[2] Institute of Biochemistry and Cell Biology (IBBC), National Research Council of Italy (CNR), Via Ercole Ramarini, 32, Monterotondo, 00015 Rome, Italy; valentina_ricci_@hotmail.it (V.R.); francesca.desanta@cnr.it (F.D.S.)

* Correspondence: alessio.torcinaro@ibbc.cnr.it; Tel.: +39-90091482

Abstract: Adult skeletal muscle is capable of active and efficient differentiation in the event of injury in both physiological and pathological conditions, such as in Duchenne muscular dystrophy (DMD). DMD is characterized by different features, such as continuous cycles of degeneration/regeneration, fiber heterogeneity, chronic inflammation and fibrosis. A well-defined and standardized approach for histological and morphometric analysis of muscle samples is necessary in order to measure and quantify specific regenerative parameters in myopathies. Indeed, non-automatic methods are time-consuming and prone to error. Here, we describe a simple automatized computational approach to quantify muscle parameters with specific pipelines to be run by CellProfiler software in an open-source and well-defined fashion. Our pipelines consist of running image-processing modules in CellProfiler with the aim of quantifying different histopathological muscle hallmarks in *mdx* mice compared to their wild-type littermates. Specifically, we quantified the minimum Feret diameter, centrally nucleated fibers and the number of macrophages, starting from multiple images. Finally, for extracellular matrix quantification, we used Sirius red staining. Collectively, we developed reliable and easy-to-use pipelines that automatically measure parameters of muscle histology, useful for research in myobiology. These findings should simplify and shorten the time needed for the quantification of muscle histological properties, avoiding challenging manual procedures.

Keywords: skeletal muscle; skeletal muscle differentiation; histology; quantitative analysis; myopathies; Duchenne muscular dystrophy; cell localization; histopathological analysis

Citation: Laghi, V.; Ricci, V.; De Santa, F.; Torcinaro, A. A User-Friendly Approach for Routine Histopathological and Morphometric Analysis of Skeletal Muscle Using CellProfiler Software. *Diagnostics* **2022**, *12*, 561. https://doi.org/10.3390/diagnostics12030561

Academic Editor: Massimiliano Leigheb

Received: 14 January 2022
Accepted: 21 February 2022
Published: 22 February 2022

1. Introduction

Skeletal muscle is a highly dynamic and plastic organ, able to respond to environmental changes and characterized by complete functional recovery upon perturbations such as endurance exercise, overload or muscle injury [1]. These exceptional adaptive features of adult skeletal muscle are reduced or even compromised in conditions such as aging and atrophy or in genetic myopathies, such as Duchenne muscular dystrophy (DMD) [1–3]. DMD is a lethal X-linked recessive disease that affects approximately 1/3500 boys and is caused by different mutations in the dystrophin gene, leading to the loss of the functional protein, which is crucial for the proper structure and stability of myofibers [4]. The dystrophin-deficient mouse (C57BL/10ScSn-*DMD*^{mdx}/J), referred to as *mdx* mouse, represents the most frequently used animal model to study DMD, although the pathology is less severe in this animal compared to DMD patients [5,6]. In both cases, this fatal myopathy leads to continuous cycles of degeneration and regeneration, resulting in high heterogeneity in fiber size and distribution as well as an increase in centrally nucleated fibers (CNFs) [7]. Another key feature of DMD is chronic inflammation, resulting in persistent inflammatory

cell infiltration, mainly macrophages, upon the degeneration of myofibers, accompanied by irreversible extracellular matrix deposition (ECM), leading to fibrosis [8,9].

The study of skeletal muscle physiology or pathologies mainly relies on histological analyses of muscle cross-sections. This analysis is commonly carried out by measuring the cross-sectional area (CSA) or minimum Feret diameter (MFD) of myofibers and the fiber size distribution in order to evaluate muscle fiber size and heterogeneity within the muscle [10]. Indeed, in physiological conditions, wild-type mice show a homogenous fiber size distribution and a constant CSA in the absence of perturbations. On the contrary, *mdx* mice usually show decreased CSA and an increase in fibers with a smaller caliber, together with high fiber heterogeneity, which becomes more evident with the progression of the disease. Notably, MFD quantification is usually preferable to CSA [11]. CSA and fiber size distribution measurements are usually performed by anti-laminin immunofluorescence with the goal of detecting fiber boundaries, whereas, for CNF quantification, nuclei detection is also necessary, which can be accomplished, for example, using 4′,6-diamidino-2-phenylindole (DAPI) [1]. This type of analysis can be performed by many software packages that can allow either manual or automated quantification, although both of these procedures have crucial pros and cons. Indeed, although manual quantification accounts for the critical assessment of the investigator concerning the biological problems under examination, this approach is undoubtedly time-consuming and highly subjective among users. On the contrary, automatized software packages are designed to save time and to standardize the procedure but often do not include a step of "manual revision" by the user, thus compromising the accuracy of the quantification. Moreover, some of these software platforms are not open-source, can be difficult to implement and require specific operating systems or a good knowledge of programming languages [10,12–18]. Additionally, automatized software is usually not designed for the quantification of a cell population or the extracellular matrix deposition within the muscle, two fundamental features in myobiology [1,17]. Different readily available software packages are often optimized towards one or more parameters, reducing the ability of the user to mine different data measurements and the versatility of the software [19].

CellProfiler represents a robust, user-friendly and open-access software platform with algorithms and features that facilitate high-throughput work in biological research [20]. Advanced algorithms for image analysis are organized in individual modules that can be inserted in a sequential order to generate a customizable pipeline to identify or measure biological elements, named "objects", or quantify positive areas in acquired images [20–22].

In the current manuscript, we propose a method to perform image analysis of muscle sections by using pipelines built with CellProfiler software, which have been recently implemented and updated to CellProfiler 4 [23]. Specifically, we present the data obtained by using a pipeline, which we named MyoProfiler, to measure MFD, CNF, PNF, cell localization and the number of macrophages in muscle sections from *mdx* mice compared with wild-type ones. We also developed another pipeline, which we named SiriusProfiler, for the precise quantification of extracellular matrix deposition. Moreover, with the goal of validating the performance of our method, we compared automatic quantification, performed using CellProfiler, with manual quantification, performed using Fiji software. The results show that these pipelines allow the automatic analysis of multiple images in a quick and reliable manner by using a single software package for multiple outputs, thus representing useful tools for the quantification of key muscle parameters in both physiological and non-physiological conditions.

2. Materials and Methods

2.1. Mice and Ethical Approval

Wild-type (C57BL/10J, The Jackson Laboratory, Bar Harbor, ME, USA) and dystrophic *mdx* mice (C57BL/10ScSn-*DMD*^{mdx}/J, The Jackson Laboratory, Bar Harbor, ME, USA) were purchased from Charles River. Five-month-old wild-type and *mdx* mice were used for experiments. All experimental protocols and procedures were conducted following the

National Ethical Guidelines (Italian Ministry of Health; D.L. 26, 4 March 2014), approved by the local ethics committee (protocol number 375/2019/PR). Animals were housed at controlled temperature (22 ± 1 °C) and humidity (60 ± 5%) and maintained under a 12 h/12 h light/dark cycle with ad libitum access to food and water.

Mice were euthanized and then dissected in order to carefully excise tibialis anterior (TA) muscles from the hind limbs. Collected TA muscles were mounted in Optimal Cutting Temperature (OCT, Tissue Tek®, Sakura Finetek, Alphen aan den Rijn, The Netherlands, Europe) compound and then frozen in liquid nitrogen-cooled isopentane (2-methylbutane; Sigma-Aldrich, Merck KGaA, Burlington, MA, USA). Embedded muscles were then cross-sectioned at a thickness of 8 µm using a Leica cryostat (Leica CM1850UV, Wetzlar, Germany) set at −25 °C, and sections were stored in a −80 °C freezer.

2.2. Immunofluorescence of Muscle Sections and Image Acquisition

The immunofluorescence of muscle sections was performed following a previously described procedure [3,24]. Primary antibodies used for this study were rabbit polyclonal antibody raised against laminin, α1 (Sigma-Aldrich, Merck KGaA, Burlington, MA, USA; Cat#: L9393, RRID:AB_477163, 1:500) and rat monoclonal antibody raised against F4/80 (Bio-Rad Laboratories, Hercules, CA, USA; Cat#: MCA497G, RRID:AB_872005, 1:300). Secondary antibodies for immunofluorescence were Alexa Fluor® 488 goat anti-rabbit IgG (H+L; Thermo Fisher Scientific, Waltham, MA, USA; Cat#: A11034, RRID:AB_2576217, 1:500) and Alexa Fluor® 594 goat anti-rat IgG (H+L; Molecular Probes, Eugene, OR, USA; Cat#: A11007, RRID:AB_141374, 1:500). Nuclei were counterstained with 4′,6-diamidino-2-phenylindole (DAPI; Thermo Fisher Scientific, Waltham, MA, USA; Cat#: D1306, RRID:AB_2629482).

Representative images of TA muscle immunofluorescences were acquired using an Olympus confocal microscope (Olympus FV1200, Olympus, Tokyo, Japan) with 40× magnification and visualized with FV10-ASW software (version 4.2; Olympus, Tokyo, Japan). Images for histological analysis were acquired using an Olympus BX53 microscope mounting an XM10 cam (Olympus, Tokyo, Japan) and using "cellSens Standard" software (version 1.17; Olympus, Tokyo, Japan). We acquired adjacent images at 10× magnification of the whole muscle section from both WT and *mdx* mice. A few fields with evident histological defects were removed before the analysis in order to avoid artifacts. Images were saved and exported as 16-bit images (grayscale images).

2.3. Staining for Extracellular Matrix Deposition and Image Acquisition

Sirius red staining is commonly used to detect extracellular matrix deposition and fibrosis within tissue sections. Briefly, muscle cryosections were thawed and then fixed with Bouin's solution (Sigma-Aldrich, Merk KGaA, Burlington, MA, USA; Cat#: HT10132) for 1 h, washed and then stained with Picrosirius red dye (Direct Red 80; Sigma-Aldrich, Merk KGaA, Burlington, MA, USA; Cat#: CI 35780) for 1 h, followed by sequential dehydration in 90%, 100% ethanol and xylene and then mounted with EUKITT (Sigma-Aldrich, Merk KGaA, Burlington, MA, USA; Cat#: 03989). Images were acquired using an Olympus BX-41 microscope (Olympus, Tokyo, Japan) with 10× magnification and visualized using "cellSens Entry" software (version 3.1.1, Olympus, Tokyo, Japan). Specifically, we acquired adjacent images at 10× magnification of entire muscle sections from both genotypes.

2.4. CellProfiler-Based Pipelines for Muscle Analysis

CellProfiler, developed by the Carpenter Lab at the Broad Institute of Harvard and MIT, is open-access software and available for Windows and macOS [20,21]. CellProfiler code was written using Python [22], and an updated, faster version of CellProfiler was recently released (CellProfiler 4) [23]. Java (www.java.com, accessed on 20 October 2018) installation and update are required prior to CellProfiler installation. Inexperienced users are encouraged to read the CellProfiler manual before using it. For the analysis of data described in this paper, we used the latest version (4.2.1) of CellProfiler downloaded from the official CellProfiler website (www.cellprofiler.org, accessed on 11 October 2021) and

installed it on a laptop computer (Intel® Core™ i7 4500 U CPU @1.80 GHz 2.40 GHz, 8.00 GB RAM, and 64 bit Windows 10 Home operating system). CellProfiler can process a wide range of image formats using the BioFormats library (complete list of formats permissible here https://docs.openmicroscopy.org/bio-formats/5.9.2/supported-formats.html, accessed on 20 February 2018).

To use a pipeline, the user has to run CellProfiler (version 4.2.1), go to "file", select "open project" and run the project corresponding to the pipeline of interest. Alternatively, .cpproj or .cppipe files can be run. Then, a list of images can be dropped into the Images module. Image processing and data extraction can be performed through Metadata, NamesAndTypes and Groups modules: for each module, a caption with detailed information is available. Together with these four standard modules, custom modules are displayed as soon as the pipeline/project is opened. We also added captions for each module of both pipelines that we designed. The shared workflow proceeds with data processing, including the pipeline of interest (composed of defined modules), and then with the test mode (Start Test Mode) in order to check the result of each module, followed by image analysis (Analyze Images). Test mode is particularly convenient when the user is designing a new pipeline or implementing an old one in order to check how the pipeline itself works with different image sets. Before running these commands, modules can also be selected/deselected (checkmark) or hidden, depending on the outputs that have to be displayed. The analysis ends with the generation of output data and a spreadsheet. It is important to define input and output folders before image processing. Pipelines developed in our lab are available in the Supplementary Materials section (Supplementary Files S1–S3). Additionally, in the Supplementary Materials section, we provide a troubleshooting guide (Troubleshooting_guide, Supplementary File S4).

2.5. Validation of CellProfiler-Based Pipelines by Fiji

Quantifications obtained with pipelines designed with CellProfiler were validated using Fiji software [25,26]. The quantification of the minimum Feret diameter (MFD) of muscle fibers began using anti-laminin, α1-labeled images. DAPI-labeled nuclei and anti-F480-stained macrophages were manually counted using the Cell Counter plugin. CNFs were quantified by combining anti-laminin, α1-labeled images and DAPI-labeled images. All numerical data were exported to Excel files and used for final quantifications. Sirius red quantifications with Fiji were performed using the Color Deconvolution plugin, and the red image was thresholded using the Otsu threshold method [27]. All analyzed images and samples used for quantifications in CellProfiler were used for the validation with Fiji.

2.6. Statistical Analysis

Data are presented as means plus/minus standard error of the mean (SEM). Output data were compared by 2-tailed unpaired Student's *t*-test. Results with p value < 0.05 were considered statistically significant. All "p values" are indicated on the graphs in the figures. All data analyses were performed using GraphPad Prism 9.3 (GraphPad Software, San Diego, CA, USA).

3. Results

3.1. Fully Automated Segmentation of Muscle Fibers by MyoProfiler Pipeline

Experiments concerning skeletal muscle regeneration usually require an overview of muscle architecture, which can be evaluated, for instance, by immunostaining muscle cross-sections with antibodies that recognize the sarcolemma (e.g., caveolin) or the basal lamina (e.g., laminin, α1) of muscle fibers [28]. In our study, we stained tibialis anterior (TA) muscle cryosections of both wild-type (WT) and *mdx* mice with anti-laminin, α1 (muscle fiber boundaries) and anti-F480 (macrophage surface marker), and nuclei were counterstained with 4′,6-diamidino-2-phenylindole (DAPI). We used 16-bit grayscale images as input. If the input images are RGB color images, it is necessary to add a ColorToGray module for each fluorophore.

For the quantification of minimum Feret diameter (MFD), we set up a pipeline primarily aimed at better defining the edges of myofibers. The workflow of the first part of the MyoProfiler pipeline is reported in Figure 1A and downloadable in the Supplementary Materials section (Supplementary File S1). The first module of the pipeline was RescaleIntensity, which stretches the intensity of the image to the full intensity range, which is particularly useful for 16-bit images (Figure 1B). The next steps aimed at making the boundaries of muscle fibers sharper, and to this end, we set up a custom "unsharp mask". Briefly, we used GaussianFilter to blur the input image and reduce its background noise (Figure 1C). We then used two ImageMath modules, which perform simple mathematical operations on image intensities, as follows: with the first one, we subtracted the blurred image, obtained with GaussianFilter, from the rescaled laminin image in order to sharpen the edges of muscle fibers; secondly, we added the sharpened laminin image to the original one (Figure 1C, ImageMath 1+2).

As the name implies, the EnhanceOrSuppressFeatures module is designed to enhance or suppress specific image features of interest. In this case, we enhanced "Line structures" from original rescaled images in order to recover and highlight low-intensity linear structures (Figure 1D, EnhanceFeatures 1). With another EnhanceOrSuppressFeatures module, we made muscle fiber boundaries sharper and clearer by enhancing the "Neurites" feature and using "Tubeness" as an enhancing method (Figure 1D, EnhanceFeatures 2). The signal of the output image was then enhanced using an ImageMath module. Afterwards, another ImageMath module took the average of the two enhanced laminin output images ("Enhance_Line_Laminin_09" and "Enhance_Laminin_11") to further reconstruct the laminin signal without increasing the background noise (Figure 1D, ImageMath 3+4). A subsequent Closing module, which applies a Dilate/Erode cycle, closed the intensity gaps between pixels with a disk-shaped structuring element of 2 pixels in order to connect interrupted fiber boundaries as much as possible (Figure 1E). We observed that increasing the size of the structuring element could lead to the formation of small oversegmented fibers. Afterwards, we used the MedianFilter module to reduce the salt-and-pepper noise in the image while still preserving the positive signal. (Figure 1F).

The Threshold module is necessary to detect the entire positive signal before the segmentation of muscle fibers. We selected a global threshold strategy and Otsu [27] with three classes as a thresholding method, since the percentage of the image covered by foreground varied from image to image, especially in *mdx* samples. Accordingly, we chose to assign the middle-intensity class to the background in order to exclusively select the true-positive signal. The output image is a binary image in which the negative signal is set to 0, while the positive signal is set to 1 (Figure 1G). In order to ensure the correct performance of the segmentation, we also added a Morph module, which further closed the gaps between muscle fibers and filled small holes, such as capillaries and nerve bundles (Figure 1H). We then inverted the pixel values of the binary input image by using an ImageMath module (with the "Invert" operation). This step is necessary to ensure that the muscle fibers are segmented correctly, as explained in the next step (Figure 1I, ImageMath 5).

The IdentifyPrimaryObjects module received the inverted thresholded image as input and identified muscle fibers as objects by using a global minimum cross-entropy threshold [29]. Objects touching borders were discarded. As a method to distinguish and segment clumped objects, we used "Intensity" (used for objects that are dimmer towards their edges and usually brighter in the middle) and "Shape" as the method to draw dividing lines between clumped objects. This approach follows the indentation of two touching objects, which is useful for dividing fused muscle fibers. Another fundamental parameter to be defined is the typical diameter range (in pixel units) of objects. We found that a range of 18–2000 pixels in diameter was suitable for our images (Figure 1J). However, it is possible to measure the diameter of objects from the Images module before processing the image set. Afterwards, we used the MeasureObjectSizeShape module to measure the area and shape features of identified muscle fibers. FilterObjects (followed by a MeasureObjectSizeShape module) is a very important module, since it allows the exclusion of objects that do not meet

the criteria for specific parameters determined by the user. For our pipeline, we decided to discard all objects below 40 pixels in area and objects with a minimum value of 0.32 for the form factor and a minimum of 0.75 for solidity (Figure 1J; magenta-colored arrows point to discarded objects). Nevertheless, we found that a minimal number of elongated muscle fibers (which is rarely present only in *mdx* mice or in poor histological sections) could be discarded. Overall, this setting was solid and successful in all image sets used for this paper. We also decided to add an optional module (EditObjectsManually #22, followed by a MeasureObjectSizeShape #23 module), which can be enabled and used in the analysis. Once the analysis of an image set reaches the EditObjectsManually module, an editing user interface allows objects to be created, removed and edited. The interface shows the current image overlaid with colored outlines of the selected objects. A number of operations are available: remove an object, restore a removed object, edit objects, finish editing an object and abandon changes to an object. Moreover, quick key commands for object editing are listed. Object editing includes deletion, manually drawing, joining and splitting, or removal of an object. Furthermore, it is necessary to replace the input "Muscle_Fibers_20" of modules 24, 25, 26, 33 and 38 with "Edited_Muscle_Fibers_22". In "Select measurement" and "data to export" options of the ExportToSpreadsheet module, it is necessary to select/indicate the correct modules accordingly. However, this semi-automatic step can be skipped if the overall detection and segmentation of muscle fibers have been performed well. However, we suggest always using the "Test Mode" and the "Show display" mode provided by CellProfiler before analyzing new image sets.

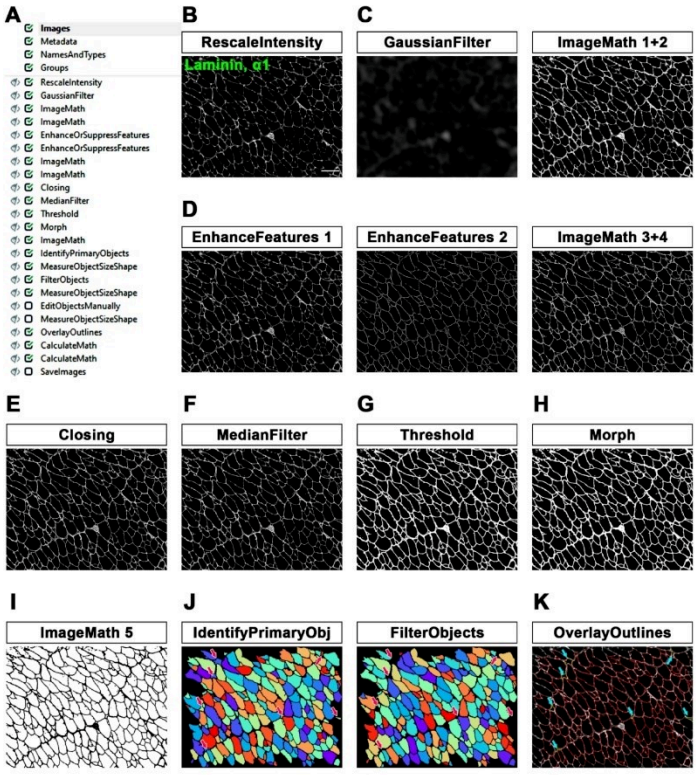

Figure 1. MyoProfiler: detection and segmentation of myofibers using anti-laminin, α1-stained muscle cross-sections. (**A**) Workflow of the first part of MyoProfiler pipeline. (**B**) RescaleIntensity

module for laminin signal. Scale bar = 100 µm. (**C**) Custom "unsharp mask" step (GaussianFilter and ImageMath 1+2) for sharpening myofiber boundaries. (**D**) Line structures and myofiber boundaries are further enhanced with 4 sequential modules (two EnhanceAndSuppressFeatures modules and two ImageMath modules). (**E**) Closing module closes the intensity gaps between pixels. (**F**) MedianFilter module reduces salt-and-pepper background noise. (**G**) Threshold module detects positive signal and produces a binary image. (**H**) Morph module closes the gaps between muscle fibers and fills small holes. (**I**) Inverted binary image (ImageMath 5). (**J**) Color map image of segmented myofibers with IdentifyPrimaryObjects module. FilterObjects module discards wrong muscle fibers (magenta arrows point to discarded fibers). (**K**) OverlayOutlined generated an output image in which both segmented (red) and discarded (yellow outlines and pointed by cyan arrows) myofibers are outlined.

The output of all of these steps can be visualized with the OverlayOutlines module, with which the boundaries of final muscle fibers (from FilterObjects module) are identified (red) and displayed on the original image. Discarded objects are outlined in yellow in Figure 1K and indicated with cyan-colored arrows. Finally, the two following CalculateMath modules were used to convert the calculated CSA of muscle fibers from pixel to μm^2 and the MFD from pixel to µm. Conversion factors for both modules were calculated starting from the pixel/µm ratio assigned to the immunofluorescence images used for this procedure. Finally, we also developed an alternative version of MyoProfiler (MyoProfiler_variant, Supplementary File S2), in which we selected an adaptive three-class Otsu threshold with an adaptive window set to 500 pixels. This could be useful for an input image if there is uneven intensity across the image.

3.2. Quantification of Nuclei, CNFs and PNFs in Muscle Sections

A well-known hallmark of skeletal muscle regeneration in physiological and pathological conditions (e.g., DMD) is the presence of centrally nucleated fibers (CNFs), corresponding to foci of regeneration in the injured muscle. This fact represents a reliable aspect of muscle condition, especially in *mdx* mice in which muscle fibers remain centrally nucleated even at the end of the regenerative process, whereas the nuclei of regenerated healthy muscles migrate towards the periphery of myofibers (i.e., peripherally nucleated fibers or PNFs) [17,30]. Therefore, we co-stained tibialis anterior (TA) muscle cryosections of both wild-type and *mdx* mice with laminin, α1 and with 4′,6-diamidino-2-phenylindole (DAPI).

The workflow of the second part of the MyoProfiler pipeline is shown in Figure 2A. First, we used RescaleIntensity on the DAPI signal (Figure 2B), similarly to what was previously performed with laminin. We then used the MedianFilter module to reduce the background noise, followed by the EnhanceOrSuppressFeatures module (Figure 2C, MedianFilt+Enhance). In this case, we were interested in enhancing the speckles of nuclei, since the DAPI signal is usually characterized by spots of enhanced intensity relative to the background. The module enhances speckles using a white tophat filter. The feature size was set to 10 pixels, which corresponds, in our images, to the typical nucleus diameter. Nuclei were segmented using IdentifyPrimaryObjects, setting a diameter range of 6–20 pixels and using the minimum cross-entropy threshold method [29] with an adaptive window of 20 pixels in size, corresponding to the maximum diameter set for nuclei. Objects touching borders were discarded. Intensity was used as a method to both distinguish clumped objects and to draw lines between them (Figure 2D, IdentifyPrimaryObj). The OverlayOutlines module outlines identified nuclei to the rescaled original DAPI image (yellow outlines; Figure 2E).

Once we had successfully identified and segmented both muscle fibers and nuclei, we focused on CNF and PNF detection. To this end, we used the ExpandOrShrinkObjects module to shrink identified muscle fibers by 5 pixels. This procedure is necessary to exclude all peripheral nuclei juxtaposed to myofiber boundaries (Figure 2F, ExpandOrShrinkObj). With another ExpandOrShrinkObjects module, this time, we shrank the nuclei to one point in order to clearly mask and detect nuclei of CNFs in the following steps. As previously

mentioned, we took advantage of the MaskObjects module to mask and remove all one-point nuclei outside shrunken muscle fibers, thus considering only nuclei inside myofibers (Figure 2G, Shrink+MaskObjects). Afterwards, the RelateObjects module assigned the relationship between previously identified objects. In this case, "child objects" are all objects (nuclei) inside "parent objects" (shrunken fibers). Shrunken fibers were then classified into CNFs and PNFs by the ClassifyObjects module. Interestingly, as output values, it is also possible to quantify the number of nuclei per CNF. Finally, we added an OverlayOutlines to highlight myofiber boundaries (red), nuclei (yellow), shrunken fibers (cyan) and nuclei of CNFs (outlined as pink dots; Figure 2G, RelateObj+Overlay).

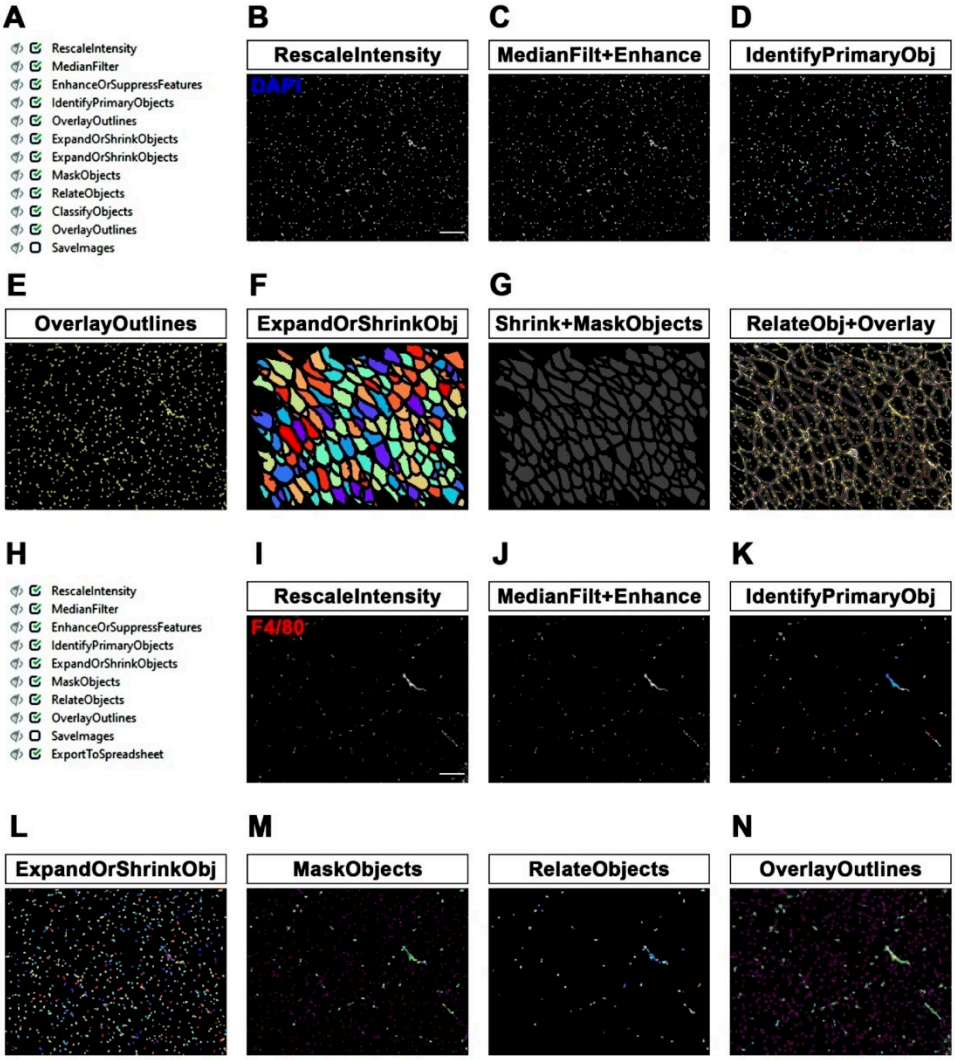

Figure 2. MyoProfiler: detection of centrally nucleated fibers (CNFs) and segmentation of nuclei and macrophages. (**A**) Workflow of the second part of MyoProfiler pipeline. (**B**) RescaleIntensity module for DAPI signal. Scale bar = 100 µm. (**C**) MedianFilter module reduces salt-and-pepper background

noise and EnhanceOrSuppressFeatures enhances the "speckles" signal of nuclei. (**D**) Color map image of segmented nuclei generated with IdentifyPrimaryObjects module. (**E**) OverlayOutlines generates an output image in which nuclei are outlined (yellow). (**F**) Color map image of shrunken myofibers generated with ExpandOrShrinkObjects module. (**G**) Output image generated from the shrinking of nuclei to one pixel and masking with shrunken myofibers (Shrink+MaskObjects) for the identification of CNFs. OverlayOutlines outlines segmented (red) and shrunken myofibers (cyan), as well as nuclei inside (dark pink dots) and outside (yellow) of shrunken fibers. (**H**) Workflow of the third part of MyoProfiler pipeline. (**I**) RescaleIntensity module for F4/80 (macrophage) signal. Scale bar = 100 µm. (**J**) MedianFilter module reduces salt-and-pepper background noise, and EnhanceOrSuppressFeatures enhances the "speckles" signal of macrophages. (**K**) Color map image of segmented macrophages generated with IdentifyPrimaryObjects module. (**L**) ExpandOrShrinkObjects module enlarges nuclei to improve detection of macrophages. (**M**) Color map image of nuclei belonging to macrophages (MaskObjects module); other nuclei are outlined in purple. RelateObjects module assigns the relationship between nuclei and macrophages. (**N**) OverlayOutlines outlines nuclei belonging (yellow) and not (purple) to macrophages. Macrophage boundaries are outlined in cyan.

3.3. Detection and Quantification of Macrophages in Skeletal Muscle

Cell localization is an important aspect in the field of cell biology and imaging; it is intended to locate and analyze specific cell populations within a tissue or organ. Usually, a specific cell population is identified by using cells expressing a reporter gene encoding for a fluorescent protein (e.g., GFP) or by using an antibody directed towards a protein specific for the cell population. For both methods, counterstaining with a nuclear dye (e.g., DAPI) is suggested [31]. In the context of skeletal muscle histology, cell localization is particularly important for the detection of muscle stem cells (i.e., satellite cells), interstitial cells (e.g., fibroadipogenic progenitors) and infiltrating immune cells, such as monocytes/macrophages [3,30].

In this study, we detected and quantified the number of macrophages in muscle sections by automatically counting the number of cells (DAPI) co-stained with an antibody raised against F4/80, a pan-macrophage surface marker. Specifically, in the third part of the MyoProfiler pipeline (Figure 2H), we applied the RescaleIntensity module to an original F4/80 image (Figure 2I), followed by MedianFilter for removing salt-and-pepper noise and the EnhanceOrSuppressFeatures module. This module enhances speckles using a white tophat filter. We chose a feature size of 100 pixels, since macrophages can assume different shapes, reflecting the position occupied by macrophages within the tissue in vivo with respect to an in vitro culture. Indeed, macrophages can also assume an elongated shape inside a tissue (Figure 2J, MedianFilt+Enhance).

We then took advantage of the IdentifyPrimaryObjects module to detect macrophages as F4/80-positive signals. We chose the minimum cross-entropy threshold method, with an adaptive window of 100 pixels in size; as the diameter range, we chose 8–100 pixels. Objects touching borders were discarded, as usual. We used intensity to distinguish clumped objects and shape to draw the dividing line between clumped objects, since the peak intensity of these objects is more variable than that of the nuclei. Moreover, we selected the "Log transform before thresholding" option, which helps to detect areas of staining that have a wide dynamic range, such as the F4/80 signal (Figure 2K, IdentifyPrimaryObj). Afterwards, we decided to use an ExpandOrShrinkObjects module to expand the area of the nuclei by 2 pixels in order to better detect macrophages. Indeed, F4/80 is a membrane marker, and this module prevents objects with the DAPI signal juxtaposed to the F4/80 signal from being discarded (Figure 2L, ExpandOrShrinkObj). With the MaskObjects module, we were able to mask (remove) objects or regions outside the region of interest. The objects that were partially masked were removed on the basis of the overlap fraction. Mask objects (macrophages) will keep an object (expanded nuclei generated by the previous module) only if the overlap is at least 0.1, meaning that 1/10 of an object must be in the

masking region (expanded nuclei are outlined in purple; Figure 2M, MaskObjects). Afterwards, the RelateObjects module assigned the relationship between previously identified objects (Figure 2M, RelateObjects). In this case, "child objects" are all objects (nuclei) inside "parent objects" (macrophages). Finally, we used the OverlayOutlines module to outline expanded nuclei (purple), masked macrophage nuclei (yellow) and macrophage boundaries (cyan; Figure 2N). Interestingly, the quantification of macrophages (F4/80-positive cells) is an approach that is potentially applicable to all quantification methods involving the co-localization or co-staining of DAPI with another fluorescent dye or antibody, which is useful for the detection of many cell populations residing in tissues and organs. Indeed, it can be applied to other cell populations of skeletal muscle, such as satellite cells and fibro-adipogenic progenitors (Appendix A.1), or to cell populations of other tissues and organs.

3.4. Comparison between CellProfiler-Based Fully Automatic Quantification and Non-Automatic Quantification

In order to validate the accuracy of the MyoProfiler pipeline developed in our lab, we decided to compare output data generated with CellProfiler with those generated with Fiji, a widely used software package for image analysis. To this end, we used images acquired from the immunofluorescence of TA muscle from wild-type (WT) and *mdx* mice stained for laminin, α1 (green), DAPI (blue) and F4/80 (red). Figure 3A shows a compact muscle architecture in WT and a heterogeneous myofiber composition in *mdx* muscle, together with a high increase in CNFs and massive macrophage infiltration (Figure 3A).

The first output data generated by the MyoProfiler analysis was the MFD of muscle fibers, a well-known parameter for quantifying fiber size. Our data showed that MFD values quantified with MyoProfiler were extremely similar to those obtained with Fiji (WT: $p = 0.8117$; *mdx*: $p = 0.8188$). Consistently, fiber size distributions were also almost equal when comparing the two approaches (Figure 3B). Moreover, the numbers of detected and segmented nuclei were also comparable between the two methods (WT: $p = 0.4880$; *mdx*: $p = 0.5724$; Figure 3C). Consistency in detecting nuclei and segmenting myofibers was also observed for the quantification of CNFs (WT: $p = 0.8906$; *mdx*: $p = 0.7162$) and PNFs (WT: $p = 0.9413$; *mdx*: $p = 0.6020$; Figure 3D). Interestingly, MyoProfiler also allowed the quantification of the number of nuclei per myofiber. As expected, we observed a significant increase in the number of nuclei per myofiber in *mdx* mice compared to their WT littermates (Figure 3E). Finally, we found that MyoProfiler was also proficient in segmenting macrophages in skeletal muscle, despite the irregular F4/80 signal (WT: $p = 0.6536$; *mdx*: $p = 0.8367$; Figure 3F). Collectively, these data demonstrated that the MyoProfiler pipeline efficiently and robustly quantified many fundamental parameters for routine muscle analysis.

We calculated an average processing time of 10 min for quantifying 10 image sets (each image set composed of laminin, α1, DAPI and F4/80 images) with MyoProfiler. Conversely, quantification performed with Fiji on the same image sets took several hours. Overall, our pipeline represents a robust, reliable and fast approach for quantifying many histological features starting from immunofluorescence images of muscle sections.

3.5. Quantification of Extracellular Matrix in Skeletal Muscle

Picrosirius red staining is a fast and reliable staining method that is largely used to identify and quantify the level of extracellular matrix (ECM) deposition in healthy and diseased muscle cross-sections. Direct Red 80 is a dye that stains the ECM red, whereas the cytoplasm and muscle fibers are yellow.

The pipeline that we created for ECM quantification (SiriusProfiler, Supplementary File S3) comprises fewer modules (Figure 4A) with respect to the previous one. Once we updated the image set corresponding to a muscle section, we assigned the name "Sirius" to all of the images of the uploaded image set. We used RGB colored images (Figure 4B), so we selected "Color image" from the drop-down menu. We decided to add two

optional sequential pre-processing modules designed to correct the background of the image when the illumination is not consistent. The illumination across the image is first calculated (CorrectIlluminationCalculate) and then fixed accordingly (CorrectIlluminationApply).

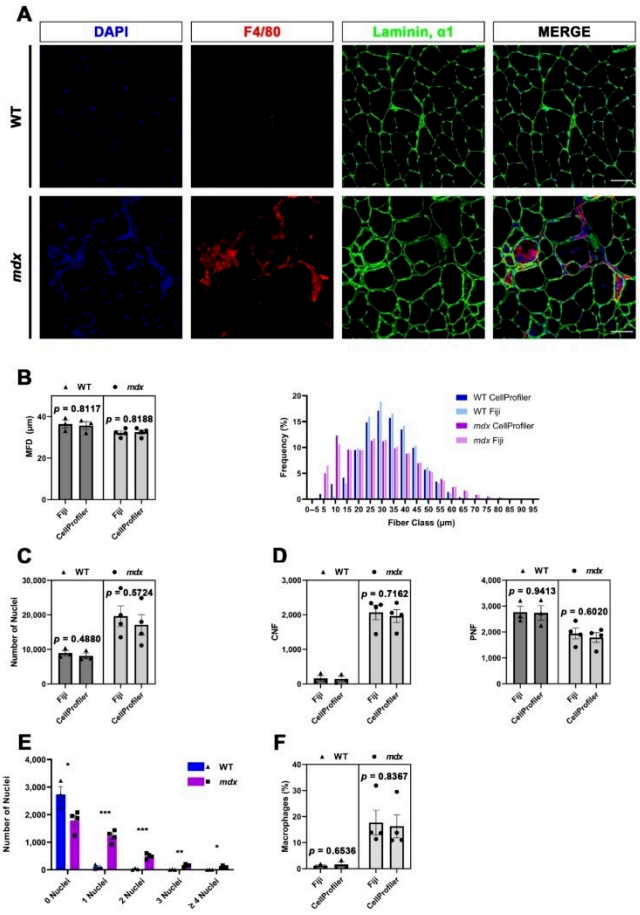

Figure 3. Quantitative measurements automatically performed with MyoProfiler and compared with Fiji software. (**A**) Representative immunofluorescence images of tibialis anterior sections from wild-type (WT) and *mdx* mice. Sections were stained with anti-laminin, α1 (green) and anti-F4/80 (red) antibodies and counterstained with DAPI (blue). Scale bar = 50 µm. (**B**) Minimum Feret diameter (MFD) quantification and fiber size distribution of myofibers. (**C**) Quantification of the number of nuclei. (**D**) Quantification of centrally nucleated (CNFs) and peripherally nucleated fibers (PNF). (**E**) Quantification of the number of nuclei per CNF performed by CellProfiler. (**F**) Quantification of the percentage of macrophages. Data are expressed as mean ± SEM, and unpaired *t*-test was used for comparison (N = 3 for WT and N = 4 for *mdx*; * = $p < 0.05$; ** = $p < 0.01$; *** = $p < 0.001$).

The UnmixColors module creates different grayscale images starting from the original colored one. The main goal is to select the best absorbance for Sirius red staining. Specifically, we split the image into blue, yellow and red by selecting Fast blue (blue), DAB (yellow) and Fast red (red). The reliability of this approach is clear, since the grayscale image resulting from the Fast red image perfectly corresponds to the red area of the original

image. Indeed, the grayscale Fast blue image is almost completely dark, while the greyscale DAB image highlights cytoplasm and muscle fibers (Figure 4C).

The following module, Threshold, is the most critical when dealing with the quantification of areas. We applied a global Otsu thresholding method since it allows the division of a grayscale input image into three classes. Indeed, the intensity of Sirius red appeared to be composed of high- and middle-intensity signals. Therefore, we assigned pixels in the middle-intensity class to the foreground (Figure 4D). We also added two optional modules to perform a quality check of the quantification. Briefly, the thresholded image is converted into objects (ConvertImageToObjects), and then this output image is used to display the outlines (in red) of the selected area in the original image.

The positive area is then quantified and multiplied by a conversion factor (0.2289), calculated starting from the pixel/µm ratio value, in order to convert the calculated area from pixel to μm^2. Output data are generated as a ".txt" file. Finally, we added another two optional modules, which allowed us to save the Fast red and thresholded image.

Representative images of whole tibialis anterior muscles from WT and *mdx* mice stained with Sirius red clearly show a massive increase in fibrotic scars in *mdx* mice, a typical hallmark of DMD (Figure 4E). We calculated an average processing time of 80 s for quantifying 10 images with SiriusProfiler. Conversely, manual quantification with Fiji took approximately 13 min for 10 input images. As expected, the quantification of the percentage of the positive area increased in *mdx* mice compared to their WT littermates. Notably, the quantification performed with CellProfiler was almost identical to the one performed with Fiji (WT: $p = 0.7361$; *mdx*: $p = 0.9591$; Figure 4F) in both genotypes, thus validating the robustness of our fully automatic pipeline for ECM quantification.

Among other applications, SiriusProfiler pipeline, allows also to quantify ECM, with appropriate modifications, by WGA-stained sections (Appendix A.2) or immunofluorescence of muscle sections for markers specific for ECM (e.g., anti-Collagen I; Appendix A.2). Finally, SiriusProfiler pipeline can quantify ECM also in Masson's Trichrome-stained muscle sections (Appendix A.3).

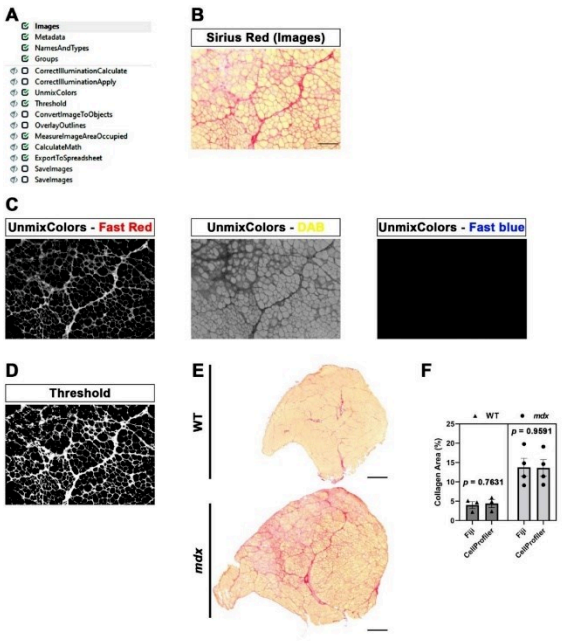

Figure 4. SiriusProfiler workflow and quantitative measurements. (**A**) Workflow of SiriusProfiler

pipeline. (**B**) Original input Sirius red image uploaded in Images module. Scale bar = 200 µm. (**C**) UnmixColors module for the split of input image into red (Fast red), yellow (DAB) and blue (Fast blue) components. (**D**) Threshold image of the red signal. (**E**) Representative images of Sirius red-stained whole muscle sections of tibialis anterior muscle from wild-type (WT) and *mdx* mice. Scale bar = 500 µm. (**F**) Percentage of collagen-positive area (Sirius red staining) in WT and *mdx* mice, quantified with CellProfiler (SiriusProfiler) and Fiji software. Data are expressed as mean ± SEM, and unpaired *t*-test was used for comparison (N = 3 for WT and N = 4 for *mdx*).

4. Discussion

Dystrophic muscles show high fiber heterogeneity, an elevated number of centrally nucleated fibers (CNFs) and heterogeneous cell populations and dynamics, especially in close proximity to injury sites. Moreover, due to massive extracellular matrix (ECM) deposition, significant interstitial spaces are detectable, especially at late stages of the disease [30]. For this reason, the full automation of fiber quantification can be tricky and inaccurate, and hence, a further step of manual adjustment and revision is required [15].

In the present study, by taking advantage of CellProfiler software, we developed two pipelines for the fully automated histological analysis of specific muscle hallmarks, starting from tibialis anterior (TA) sections of *mdx* mice, a widely used animal model for Duchenne muscular dystrophy (DMD), and their wild-type (WT) littermates. The quantifications performed with CellProfiler were then compared to those performed with Fiji in order to validate the robustness and efficiency of our method. It is therefore clear that this work did not aim to address differences between the two genotypes, which have been widely investigated in a multitude of previous works. We are interested in the validation of our CellProfiler-based pipelines. The first pipeline, named MyoProfiler, was designed for enhancing and redefining myofiber boundaries, starting from images of muscle cross-sections stained with laminin, α1 antibody; then, once the signal was satisfactorily identified, muscle sections were segmented, and their cross-sectional area (CSA) and minimum Feret diameter (MFD) were measured. The second part of MyoProfiler is aimed at identifying and segmenting DAPI-stained nuclei and at classifying segmented myofibers into CNFs and peripherally nucleated fibers (PNFs). The last part of the pipeline included the detection of macrophages, starting from the detection of F4/80, a pan-macrophage-specific surface marker. Finally, the SiriusProfiler pipeline was developed with the goal of identifying and quantifying ECM from Sirius red-stained muscle sections. To this end, we used the same samples used for the analysis by MyoProfiler. Concerning the time needed for analysis, Myoprofiler takes ~10 min to analyze 10 images, while an analysis performed with Fiji takes several hours for the user. Meanwhile, SiriusProfiler takes ~80 s to analyze 10 images, while manual quantification with Fiji takes ~13 min.

In the MyoProfiler pipeline, one of the most critical steps to deal with is the identification of muscle fibers and their appropriate segmentation. Muscle fiber integrity and laminin, α1 signals rely on the quality of muscle sections. Moreover, the laminin signal identifies not only myofiber boundaries but also nerve bundles, capillaries, veins, arteries and interstitial space (among fiber boundaries). It is therefore necessary to enhance the laminin signal, fix interrupted fibers where possible and reduce the background. All of the steps preceding the Threshold module resolve those problems. Moreover, we used the three-class Otsu method [27], in which we assigned the middle-class to the background in order to exclusively select the positive signal. Object segmentation (IdentifyPrimary-Objects module) was performed using the minimum-cross entropy threshold method [29]. Segmented fibers can be filtered out (FilterObjects module) if they do not achieve specified filter values (area, form factor and solidity). Finally, the automation of the procedure can be supported by a step of manual revision (EditObjects), necessary for an accurate evaluation of the quantification. Interestingly, the lack of this step was one of the limitations of the previously published MuscleAnalyzer pipeline [32].

Contrary to myofibers, the identification and segmentation of nuclei are easily affordable, as is nuclei segmentation from 2D cell culture images. This is possible since nuclei show a relatively uniform morphology, dimension and contrast due to the high contrast of the DAPI signal relative to the background. Once we reduced the salt-and-pepper background noise (MedianFilter) and increased the speckle features (EnhanceOrSuppressFeatures), we identified nuclei using an adaptive minimum-cross entropy threshold [29]. The quantification of nuclei worked appropriately, and the values obtained were comparable to those obtained with Fiji, although with Fiji, we detected slightly more nuclei. This is probably because in CellProfiler analysis, we excluded objects touching the borders. The identified nuclei were then shrunk to one point (ExpandOrShrinkObjects) and masked with 5-pixel-shrunken fibers (MaskObjects) in order to detect CNFs and PNFs with RelateObjects and ClassifyObjects modules. The strategy of identification and quantification of CNFs and PNFs, as with myofiber and nuclei, worked efficiently.

We also used the identified nuclei for the detection and quantification of resident (in WT mice) and infiltrating (in *mdx* mice) macrophages. Once the background noise had been reduced (MedianFilter) and the F4/80 signal had been enhanced (EnhanceOrSuppressFeatures), we once again used an adaptive minimum cross-entropy threshold for macrophage segmentation. Since F4/80 is a membrane surface marker, we chose to expand nuclei dimensions by 2 pixels and then expanded segmented nuclei with macrophages in order to better detect them. To finely select true macrophages, we decided to discard all objects that were partially masked (10% of masking region). Despite the challenge in detecting macrophages, especially in *mdx* cross-sections, we found overall comparable values in CellProfiler vs. Fiji analysis.

The SiriusProfiler pipeline, in contrast to MyoProfiler, works on brightfield images. This pipeline consists of a few crucial steps: the splitting of the input image into red, yellow and blue components and then the application of a Threshold module to the image corresponding to the red component. In this case, we used the three-class Otsu method [27], in which we assigned the middle-class intensity to the foreground, since Sirius red staining always shows a bright red signal and a less intense one. For Fiji analysis, we basically used the same approach, and we found no differences between the two methods, demonstrating the effectiveness of this method.

Occasionally, experimental errors can occur during the histological preparation of muscle samples, such as the wrong orientation of the sectioning angle (i.e., oblique sectioning), thus resulting in muscle fibers with a non-polygonal/non-circular aspect. This fact results in the incorrect measurement of muscle area by the CSA of myofibers, as has been previously demonstrated [33]. This inconvenient issue can be overcome using the minimal Feret diameter (MFD) as a parameter for the analysis of muscle fibers. Indeed, MFD is defined as the distance between the two parallel planes restricting the object perpendicular to that direction, so it is independent of the sectioning angle of the sample [33]. Using MyoProfiler, we quantified both CSA and MFD, but we present only the MFD quantification (Figure 3B). Moreover, isolated muscles can undergo poor inclusion or inappropriate storage before the sectioning. Finally, histological artifacts can occur during the sectioning of muscles, or they can have an uneven or irregular signal pattern due to errors occurring during the staining. Even one of these events can make the identification of objects and cellular components difficult, thus also affecting the quantification. This identification is allowed by CellProfiler thanks to the IdentifyPrimaryObjects module, which relies on a thresholding method that needs to be finely tuned in order to realize correct image segmentation. Fortunately, CellProfiler provides a test mode that makes it possible to test the pipeline on selected image sets and correct or change specific parameters once the output image has been generated. Of course, it is always better to test the pipeline, with a selected parameter, on a large set of images and on images of perfect or poorer quality, thus making the pipeline more robust. Finally, it is recommended to use appropriate conversion factors depending on camera properties and magnification, as well as parameters set in IdentifyPrimaryObjects, if necessary.

Undoubtedly, an automatic or semi-automatic approach should only be applied using good or average–good staining and images to avoid, for instance, the quantification of interstitial spaces or of other non-fiber structures. MyoProfiler proficiently quantifies muscle fibers with minimal error and ensures the possibility of an automated method to decrease the time required for quantification and, at the same time, offers a step of manual editing in order to maximize the efficiency and reliability of this approach, if needed.

In recent years, several other semi-automatic software packages or tools have been described [10,15,17,33]. Some of the issues with these approaches include the necessity of programming skills, the need for images of very high quality and the lack of implementation and of batch analysis. Moreover, Lau and colleagues proposed a method to detect and quantify muscle fibers and CNFs by using a previous version of CellProfiler. As also stated by the authors, their pipeline is not designed to identify specific cell populations and does not have a manual editing step [32]. Finally, Sanz and colleagues proposed a useful pipeline for the detection of fibers and the capillary-to-muscle fiber interface on muscle biopsies. Nevertheless, the pipeline has been designed using only muscles from healthy patients and images acquired with 20× magnification, thus reducing the reproducibility if input images are, for instance, 10× magnification-acquired images from dystrophic muscles [34]. Furthermore, the benefit of using CellProfiler for automated image analysis relies on its flexibility and the possibility of custom modifications that can also be applied by non-expert users. It can distinguish subtle changes and measure multiple properties at once. Moreover, it can perform batch analysis (thousands of images), and the latest version (CellProfiler 4) has been demonstrated to be faster and less tedious than previous ones [23]. Finally, the use of CellProfiler hints at the possibility to build user-friendly tools that are able to adapt and perform their tasks without needing to use long and more complex tools based on machine learning or deep learning.

The applicability of our pipelines relies on the possibility of also using them on images acquired from histological sections of human biopsies in order to obtain robust and valuable quantifications of histological parameters in both healthy and diseased patients (e.g., DMD patients). Indeed, as stated in Appendix A.4, our pipelines can be used also for quantifications on human muscle sections. Therefore, it would be possible, for instance, to histologically visualize the effect of corticosteroids, a widely used therapy in muscular dystrophies [35]. This should aid research and preclinical studies concerning muscle diseases.

To conclude, future directions starting from this work could include the development of novel CellProfiler-based pipelines aimed at quantifying other histological features of muscle histology as well as the detection and counting of other cell populations infiltrating or residing in skeletal muscle upon immunofluorescence for specific cell markers.

5. Conclusions

The CellProfiler-based pipelines designed in this study for the histopathological analysis of muscles allow the multi-parametric analysis of muscle sections in both physiological and pathological (DMD) conditions. These pipelines were designed in order to ensure automatic quantification of multiple images, starting from images acquired with non-automatic microscopes, and reduce the time usually spent on manual quantification. With this approach, it is possible to compare different experiments from different laboratories in a highly reproducible and easy-to-use interface. Finally, we developed a tool that should aid in the study and evaluation of pathologies affecting skeletal muscle by facilitating data generation and analysis, thus further improving the consistency of quantifications and the reliability of results.

Supplementary Materials: The following supporting information can be downloaded at: https://www.mdpi.com/2075-4418/12/3/561/s1, Supplementary File S1: MyoProfiler; Supplementary File S2: MyoProfiler_variant; Supplementary File S3: SiriusProfiler; Supplementary File S4: Troubleshooting_guide.

Author Contributions: Conceptualization, A.T. and V.L.; methodology, A.T., V.L. and V.R.; software, A.T., V.L. and V.R.; validation, A.T., V.L. and V.R.; formal analysis, A.T., V.L., F.D.S. and V.R.; investigation, A.T., V.L. and F.D.S.; resources, F.D.S.; data curation, A.T., V.L., F.D.S. and V.R.; writing—original draft preparation, A.T.; writing—review and editing, A.T., V.L., F.D.S. and V.R.; visualization, A.T., V.L., F.D.S. and V.R.; supervision, A.T.; project administration, A.T. and F.D.S.; funding acquisition, A.T. and F.D.S. All authors have read and agreed to the published version of the manuscript.

Funding: This research was funded by AFM-Téléthon, Fellowship #22613 to A.T, and by the Italian Ministry of Education, Universities and Research (MIUR) (Grant IRMI: CTN01_00177_888744) to F.D.S.

Institutional Review Board Statement: The study was conducted according to the guidelines of the Declaration of Helsinki and approved by the Institutional Review Board of the Institute of Biochemistry and Cell Biology (IBBC) of the National Council of Research (CNR). The protocol code is 375/2019, approved on 20 May 2019.

Informed Consent Statement: Not applicable.

Data Availability Statement: Not applicable.

Acknowledgments: We would like to thank Agnese Bonato and Sabrina Mattei for testing the pipelines presented in this paper. Moreover, we thank Silvia Middei for offering critical suggestions during paper preparation. Finally, we wish to thank Vittoria Nicolis di Robilant for providing valuable editorial work and revision.

Conflicts of Interest: The authors declare no conflict of interest. The funders had no role in the design of the study; in the collection, analyses or interpretation of data; in the writing of the manuscript; or in the decision to publish the results.

Appendix A. Additional Applications of MyoProfiler and SiriusProfiler Pipelines

Appendix A.1. Identification and Segmentation of Specific Cell Populations by MyoProfiler Pipeline

As stated in the manuscript, the identification and proper segmentation of cell populations rely on the correct segmentation of nuclei and the cell population-specific marker/antibody and its distribution in the cell. For instance, F4/80 is a surface marker, and we had to expand nuclei to properly mask F4/80 with a DAPI signal. Moreover, interstitial and infiltrating cells, such as macrophages, can assume elongated shapes within the muscle. The same issue could occur, for instance, with the detection and segmentation of fibro-adipogenic progenitors (FAPs), which are usually detected by immunofluorescence with an anti-PDGFRα antibody [36]. Since PDGFRα is a cell surface marker, we suggest using the same steps that we followed for macrophage segmentation. Of course, proper tuning of the Min and Max diameter and a threshold are needed before analyzing images. For the detection of satellite cells, we suggest the use of an anti-Pax7 antibody. Considering that Pax7 is expressed in the nuclei and that its signal is similar to the DAPI signal, we suggest using the same feature size in the EnhanceOrSuppressFeatures module (module #42 in MyoProfiler pipeline) that has been established for DAPI (module #30 in the MyoProfiler pipeline). Of course, the typical diameter of objects also has to be adjusted accordingly (IdentifyPrimaryObjects = module #43 in the MyoProfiler pipeline). Furthermore, the expansion of nuclei is not necessary because the Pax7 signal overlaps with the DAPI signal (ExpandOrShrinkObjects = module #44 in the MyoProfiler pipeline). Finally, concerning the MaskObjects module (module #45 in the MyoProfiler pipeline), we suggest using the option "Keep" for the handling of objects that are partially masked. Collectively, the proper identification and segmentation of a cell-population-specific marker require the following steps: measurement of the typical object size before image processing (Min and Max pixel values, to be used for EnhanceOrSuppressFeature and IdentifyPrimaryObjects modules) and adjustment of threshold parameters in IdentifyPrimaryObjects module. As for all types of measurements, "Test mode" helps the user in tuning the best setting before processing images.

Appendix A.2. Quantification of Extracellular Matrix by WGA Immunofluorescence

Fluorescently conjugated wheat germ agglutinin (WGA) can be potentially used to detect extracellular matrix accumulation [37]. CellProfiler offers the advantage of personalizing the modules with a low learning curve and providing a detailed explanation of every single module. Indeed, we have tested several images of WGA-stained muscle sections (which will be used for another project) using a modified version of the SiriusProfiler pipeline, and it worked correctly. Specifically, in the NamesAndTypes module, we selected "grayscale image" instead of "color image" and then replaced UnmixColors with the RescaleIntensity module. The detection and quantification of WGA-positive areas worked correctly with the threshold setting used in SiriusProfiler. However, a more appropriate alternative to picrosirius red would be an anti-collagen I antibody (e.g., Abcam, Cat# ab6308), since WGA detects not only the extracellular matrix but also cell membranes [38] and is thus not completely specific for extracellular matrix.

Appendix A.3. Analysis of Masson's Trichrome Staining by SiriusProfiler

We have found that Masson's trichrome staining is successfully detected and quantified using the same threshold parameters used for SiriusProfiler. However, since the blue component, corresponding to ECM/fibrosis, is present in this staining, we chose "Aniline blue" absorbance in the UnmixColors module for the detection of the signal. The best combination and results were obtained with the combination of "Aniline blue" for the blue component and "Fast red" for the red one.

Appendix A.4. Application of SiriusProfiler and MyoProfiler to Muscle Samples from Larger Mammals

A crucial aspect of myobiology is the need to translate methods established in mice to higher mammals, including human biopsies. Concerning SiriusProfiler and the quantification of ECM, the approach described for murine muscle sections can also be used for muscle sections obtained from larger mammals by loading and analyzing a larger number of fields. Indeed, the goal of the pipeline is to quantify the area positive for picrosirius red, so the approach can be used for muscle sections of larger mammals. In regard to MyoProfiler, it is necessary to test an image set (using "Test mode") before analyzing images. The overall setting used in our pipeline most likely works for immunofluorescence of muscle sections from different animals (if the quality of the section and staining is good). The only thing that needs to be adjusted before image analysis is the expected Min and Max diameter range, in pixel units, of muscle fibers. As is already known, the myofiber diameter can vary depending on the fiber type (Type IIB and IIX > Type IIA > Type I) or the muscle type and even from species to species. For instance, in relation to muscle cryosections of murine samples, we found a diameter range of 20–150 µm (considering TA muscles from both wild-type and mdx mice), whereas, for human samples, we found a diameter range of 30–250 µm (considering muscle biopsies from both DMD patients and healthy donors).

References

1. Liu, J.; Saul, D.; Böker, K.O.; Ernst, J.; Lehman, W.; Schilling, A.F. Current Methods for Skeletal Muscle Tissue Repair and Regeneration. *Biomed Res. Int.* **2018**, *2018*, 1984879. [CrossRef] [PubMed]
2. Bouché, M.; Muñoz-Cánoves, P.; Rossi, F.; Coletti, D. Inflammation in Muscle Repair, Aging, and Myopathies. *Biomed Res. Int.* **2014**, *2014*, 821950. [CrossRef] [PubMed]
3. Madaro, L.; Torcinaro, A.; De Bardi, M.; Contino, F.F.; Pelizzola, M.; Diaferia, G.R.; Imeneo, G.; Bouché, M.; Puri, P.L.; De Santa, F. Macrophages Fine Tune Satellite Cell Fate in Dystrophic Skeletal Muscle of Mdx Mice. *PLoS Genet.* **2019**, *15*, e1008408. [CrossRef]
4. Hoffman, E.P.; Brown, R.H.; Kunkel, L.M. Dystrophin: The Protein Product of the Duchenne Muscular Dystrophy Locus. *Cell* **1987**, *51*, 919–928. [CrossRef]
5. Bulfield, G.; Siller, W.G.; Wight, P.A.; Moore, K.J. X chromosome-linked muscular dystrophy (mdx) in the mouse. *Proc. Natl. Acad. Sci. USA* **1984**, *81*, 1189–1192. [CrossRef]
6. Gutpell, K.M.; Hrinivich, W.T.; Hoffman, L.M. Skeletal Muscle Fibrosis in the Mdx/Utrn +/− Mouse Validates Its Suitability as a Murine Model of Duchenne Muscular Dystrophy. *PLoS ONE* **2015**, *10*, e0117306. [CrossRef] [PubMed]

7. Mcdonald, A.A.; Hebert, S.L.; Kunz, M.D.; Ralles, S.J.; Mcloon, L.K. Disease Course in Mdx:Utrophin +/− Mice: Comparison of Three Mouse Models of Duchenne Muscular Dystrophy. *Physiol. Rep.* **2015**, *3*, e12391. [CrossRef]
8. Porter, J.D.; Khanna, S.; Kaminski, H.J.; Rao, J.S.; Merriam, A.P.; Richmonds, C.R.; Leahy, P.; Li, J.; Guo, W.; Andrade, F.H. A Chronic Inflammatory Response Dominates the Skeletal Muscle Molecular Signature in Dystrophin-Deficient Mdx Mice. *Hum. Mol. Genet.* **2002**, *11*, 263–272. [CrossRef]
9. Mann, C.J.; Perdiguero, E.; Kharraz, Y.; Aguilar, S.; Pessina, P. Aberrant Repair and Fibrosis Development in Skeletal Muscle. *Skelet. Muscle* **2011**, *1*, 21. [CrossRef]
10. Desgeorges, T.; Liot, S.; Lyon, S.; Bouvière, J.; Kemmel, A.; Trignol, A. Open-CSAM, a New Tool for Semi-Automated Analysis of Myofiber Cross-Sectional Area in Regenerating Adult Skeletal Muscle. *Skelet. Muscle* **2019**, *9*, 2. [CrossRef]
11. Henry, C.C.; Martin, K.S.; Ward, B.B.; Handsfield, G.G.; Peirce, M.; Blemker, S.S. Spatial and Age-Related Changes in the Microstructure of Dystrophic and Healthy Diaphragms. *PLoS ONE* **2017**, *12*, e0183853. [CrossRef]
12. Kim, Y.; Brox, T.; Feiden, W.; Weickert, J. Fully Automated Segmentation and Morphometrical Analysis of Muscle Fiber. *Cytometry* **2007**, *71*, 8–15. [CrossRef] [PubMed]
13. Kostrominova, T.Y.; Reiner, D.S.; Haas, R.H.; Ingermanson, R.; Mcdonough, P.M. Automated Methods for the Analysis of Skeletal Muscle Fiber Size and Metabolic Type. *Int. Rev. Cell Mol. Biol.* **2013**, *306*, 275–332.
14. Pertl, C.; Eblenkamp, M.; Pertl, A.; Pfeifer, S.; Wintermantel, E.; Lochmüller, H.; Walter, M.C.; Krause, S.; Thirion, C. A New Web-Based Method for Automated Analysis of Muscle Histology. *BMC Musculoskelet. Disord.* **2013**, *14*, 26. [CrossRef]
15. Smith, L.R.; Barton, E.R. SMASH—Semi-Automatic Muscle Analysis Using Segmentation of Histology: A MATLAB Application. *Skelet. Muscle* **2014**, *4*, 21. [CrossRef] [PubMed]
16. Miazaki, M.; Viana, M.P.; Yang, Z.; Comin, C.H.; Wang, Y.; Costa, L.F.; Xu, X. Automated high-content morphological analysis of muscle fiber histology. *Comput. Biol. Med.* **2015**, *63*, 28–35. [CrossRef]
17. Mayeuf-Louchart, A.; Hardy, D.; Thorel, Q.; Roux, P.; Gueniot, L.; Briand, D.; Mazeraud, A.; Bouglé, A.; Shorte, S.L.; Staels, B.; et al. MuscleJ: A High-Content Analysis Method to Study Skeletal Muscle with a New Fiji Tool. *Skelet. Muscle* **2018**, *8*, 25. [CrossRef] [PubMed]
18. Wen, X.Y.; Murach, K.A.; Vechetti, I.J.; Fry, C.S.; Vickery, C.; Peterson, C.A.; Mccarthy, J.J.; Campbell, X.K.S. MyoVision: Software for Automated High-Content Analysis of Skeletal Muscle Immunohistochemistry. *J. Appl. Physiol.* **2018**, *124*, 40–51. [CrossRef]
19. Stöter, M.; Niederlein, A.; Barsacchi, R.; Meyenhofer, F.; Brandl, H.; Bickle, M. CellProfiler and KNIME: Open Source Tools for High Content Screening. *Methods Mol. Biol.* **2013**, *986*, 105–122.
20. Carpenter, A.E.; Jones, T.R.; Lamprecht, M.R.; Clarke, C.; Kang, I.H.; Friman, O.; Guertin, D.A.; Chang, J.H.; Lindquist, R.A.; Moffat, J.; et al. CellProfiler: Image Analysis Software for Identifying and Quantifying Cell Phenotypes. *Genome Biol.* **2006**, *7*, 100. [CrossRef] [PubMed]
21. Kamentsky, L.; Jones, T.R.; Fraser, A.; Bray, M.; Logan, D.J.; Madden, K.L.; Ljosa, V.; Rueden, C.; Eliceiri, K.W.; Carpenter, A.E. Improved Structure, Function and Compatibility for CellProfiler: Modular High-Throughput Image Analysis Software. *Bioinformatics* **2011**, *27*, 1179–1180. [CrossRef] [PubMed]
22. Mcquin, C.; Goodman, A.; Chernyshev, V.; Kamentsky, L.; Cimini, A.; Karhohs, K.W.; Doan, M.; Ding, L.; Rafelski, S.M.; Thirstrup, D.; et al. CellProfiler 3.0: Next-generation image processing for biology. *PLoS Biol.* **2018**, *16*, e2005970. [CrossRef] [PubMed]
23. Stirling, D.R.; Bowden, M.J.S.; Lucas, A.M.; Carpenter, A.E.; Cimini, B.A.; Goodman, A. CellProfiler 4: Improvements in Speed, Utility and Usability. *BMC Bioinform.* **2021**, *22*, 433. [CrossRef] [PubMed]
24. Torcinaro, A.; Ricci, V.; Strimpakos, G.; De Santa, F.; Middei, S. Peripheral Nerve Impairment in a Mouse Model of Alzheimer's Disease. *Brain Sci.* **2021**, *11*, 1245. [CrossRef] [PubMed]
25. Abràmoff, M.D.; Hospitals, I.; Magalhães, P.J.; Abràmoff, M. Image Processing with ImageJ. *Biophotonics Int.* **2004**, *11*, 36–42.
26. Schindelin, J.; Arganda-Carreras, I.; Frise, E.; Kaynig, V.; Longair, M.; Pietzsch, T.; Preibisch, S.; Rueden, C.; Saalfeld, S.; Schmid, B.; et al. Fiji: An Open-Source Platform for Biological-Image Analysis. *Nat. Methods* **2012**, *9*, 676–682. [CrossRef] [PubMed]
27. Otsu, N. A Threshold Selection Method from Gray-Level Histograms. *IEEE Trans. Syst. Man Cybern.* **1979**, *9*, 62–66. [CrossRef]
28. Mula, J.; Lee, J.D.; Liu, F.; Yang, L.; Peterson, C.A. Automated Image Analysis of Skeletal Muscle Fiber Cross-Sectional Area. *J. Appl. Physiol.* **2013**, *114*, 148–155. [CrossRef]
29. Li, C.H.; Lee, C.K. Minimum Cross Entropy Thresholding. *Pattern Recognit.* **1993**, *26*, 617–625. [CrossRef]
30. De Santa, F.; Vitiello, L.; Torcinaro, A.; Ferraro, E. The Role of Metabolic Remodeling in Macrophage Polarization and Its Effect on Skeletal Muscle Regeneration. *Antioxid. Redox Signal.* **2019**, *30*, 1553–1598. [CrossRef]
31. Vacaru, A.M.; Vitale, J.; Nieves, J.; Baron, M.H. Generation of transgenic mouse fluorescent reporter lines for studying hematopoietic development. *Methods Mol. Biol.* **2014**, *1194*, 289–312.
32. Lau, Y.S.; Xu, L.; Gao, Y.; Han, R. Automated Muscle Histopathology Analysis Using CellProfiler. *Skelet. Muscle* **2018**, *8*, 32. [CrossRef] [PubMed]
33. Briguet, A.; Courdier-Fruh, I.; Foster, M.; Meier, T.; Magyar, J.P. Histological Parameters for the Quantitative Assessment of Muscular Dystrophy in the Mdx-Mouse. *Neuromuscul. Disord.* **2004**, *14*, 675–682. [CrossRef]

34. Sanz, X.G.; Martínez-Aranda, L.M.; Tesch, P.A.; Fernandez-Gonzalo, X.R.; Lundberg, X.T.R. Muscle2View, a CellProfiler Pipeline for Detection of the Capillary-to-Muscle Fiber Interface and High-Content Quantification of Fiber Type-Specific Histology. *J. Appl. Physiol.* **2019**, *127*, 1698–1709. [CrossRef]
35. Mcdonald, C.M.; Henricson, E.K.; Abresch, R.T.; Duong, T.; Joyce, N.C.; Hu, F.; Clemens, P.R.; Hoffman, E.P. Long-Term Effects of Glucocorticoids on Function, Quality of Life, and Survival in Patients with Duchenne Muscular Dystrophy: A Prospective Cohort Study. *Lancet* **1989**, *391*, 451–461. [CrossRef]
36. Reggio, A.; Rosina, M.; Krahmer, N.; Palma, A.; Petrilli, L.L.; Maiolatesi, G.; Massacci, G.; Salvatori, I.; Valle, C.; Testa, S.; et al. Metabolic reprogramming of fibro/adipogenic progenitors facilitates muscle regeneration. *Life Sci. Alliance* **2020**, *3*, e202000646. [CrossRef] [PubMed]
37. Emde, B.; Heinen, A.; Gödecke, A.; Bottermann, K.; Düsseldorf, H. Wheat Germ Agglutinin Staining as a Suitable Method for Detection and Quantification of Fibrosis in Cardiac Tissue after Myocardial Infarction. *Eur. J. Histochem.* **2014**, *58*, 315–319. [CrossRef] [PubMed]
38. Chazotte, B. Labeling Membrane Glycoproteins or Glycolipids with Fluorescent Wheat Germ Agglutinin. *Cold Spring Harb. Protoc.* **2011**, *5*, 570–573. [CrossRef] [PubMed]

Annexe 2

IFN-Stimulated Genes in Zebrafish and Humans Define an Ancient Arsenal of Antiviral Immunity

Jean-Pierre Levraud,* Luc Jouneau,† Valérie Briolat,* Valerio Laghi,* and Pierre Boudinot†

The evolution of the IFN system, the major innate antiviral mechanism of vertebrates, remains poorly understood. According to the detection of type I IFN genes in cartilaginous fish genomes, the system appeared 500 My ago. However, the IFN system integrates many other components, most of which are encoded by IFN-stimulated genes (ISGs). To shed light on its evolution, we have used deep RNA sequencing to generate a comprehensive list of ISGs of zebrafish, taking advantage of the high-quality genome annotation in this species. We analyzed larvae after inoculation of recombinant zebrafish type I IFN, or infection with chikungunya virus, a potent IFN inducer. We identified more than 400 zebrafish ISGs, defined as being either directly induced by IFN or induced by the virus in an IFNR-dependent manner. Their human orthologs were highly enriched in ISGs, particularly for highly inducible genes. We identified 72 orthology groups containing ISGs in both zebrafish and humans, revealing a core ancestral ISG repertoire that includes most of the known signaling components of the IFN system. Many downstream effectors were also already present 450 My ago in the common ancestor of tetrapods and bony fish and diversified as multigene families independently in the two lineages. A large proportion of the ISG repertoire is lineage specific; around 40% of protein-coding zebrafish ISGs had no human ortholog. We identified 14 fish-specific gene families containing multiple ISGs, including finTRIMs. This work illuminates the evolution of the IFN system and provides a rich resource to explore new antiviral mechanisms.
***The Journal of Immunology*, 2019, 203: 3361–3373.**

All living organisms are targeted by viruses, and evolution has given rise to various antiviral strategies. Vertebrates possess many unique immune features, including their principal innate antiviral system based on signaling by type I IFNs. Type I IFNs induce the expression of hundreds of proteins encoded by IFN-stimulated genes (ISGs), making cells refractory to viral infection (1). The origin of the IFN system, which seems to have replaced the RNA interference antiviral system still used by plants and most invertebrates (2, 3), is shrouded in mystery. Cartilaginous fish are the most basal clade with genomes containing recognizable type I IFN genes (4, 5), suggesting that this system appeared ∼500 My ago with jawed vertebrates. The IFN system integrates many components, most of which are encoded by ISGs, which can be traced back in genomes from distant clades. However, finding the ortholog(s) of a human ISG in another taxon does not imply that this gene is part of its IFN system. To understand the evolution of antiviral immunity, it is therefore desirable to establish how the repertoire of ISGs changed from early to modern vertebrates. This can be inferred by comparing the ISGs of current living representatives of distant vertebrate taxa.

Bony fishes (hereafter simply called fish) diverged from the tetrapod lineage ∼450 My ago, and because viral infections are a major problem in aquaculture, their IFN system has been the subject of many studies, as reviewed in Ref. 6–9. Teleost fish possess several subgroups of type I IFNs (but no type III genes), with strong variation in gene numbers among fish taxa (8). The zebrafish possess four type I IFN genes, named *ifnphi1-4*; only *ifnphi1* and *ifnphi3* are active at the larval stage (10). Their receptors have been identified (10). Even before fish IFNs were known, the first fish ISGs were identified by homology cloning from cells stimulated by poly(I:C) (11) or by differential transcript analysis of cells infected by viruses (12, 13). Because many virus-induced genes (*vig*) were homologous to well-known mammalian ISGs, they were hypothesized to be IFN inducible, which was often confirmed by later studies, as in the case of *vig-1*, the *rsad2/viperin* ortholog (12, 14). Similarly, upon cloning of fish IFNs, induction of *Mx* (11) was used as a readout for their activity (15–17), confirming it was an ISG. The list of fish homologs of known ISGs rapidly grew with the release of new fish genomes and expressed sequence tag (EST) collections, allowing the development of microarrays to study fish response to virus or recombinant type I IFNs (18, 19). Candidate gene approaches were also developed, testing orthologs of known mammalian ISGs in quantitative RT-PCR (qRT-PCR) assays in multiple fish infection models

*Macrophages et Développement de l'Immunité, Institut Pasteur, CNRS UMR3738, 75015 Paris, France; and †Institut National de la Recherche Agronomique, Virologie et Immunologie Moléculaires, Université Paris-Saclay, 78352 Jouy-en-Josas, France

ORCIDs: 0000-0001-6775-2416 (J.-P.L.); 0000-0003-0726-073X (V.L.).

Received for publication July 12, 2019. Accepted for publication October 8, 2019.

This work was supported by Agence Nationale de la Recherche Project Fish-RNAvax (Grants ANR-16-CE20-0002-02 and ANR-16-CE20-0002-03) and the European Union Horizon 2020 Research and Innovation Programme under Marie Sklodowska-Curie Grant Agreement 721537–ImageInLife.

The sequences presented in this article have been submitted to BioProject National Center for Biotechnology Information (https://www.ncbi.nlm.nih.gov/bioproject) under the Sequence Read Archive accession number PRJNA531581.

Address correspondence and reprint requests to Dr. Jean-Pierre Levraud or Dr. Pierre Boudinot, Macrophages et Développement de l'Immunité, Institut Pasteur, CNRS UMR3738, 25 Rue du Docteur Roux, 75015 Paris, France (J.-P.L.) or Institut National de la Recherche Agronomique, Virologie et Immunologie Moléculaires, Université Paris-Saclay, Allée de Vilvert, 78352 Jouy-en-Josas, France (P.B.). E-mail addresses: jean-pierre.levraud@pasteur.fr (J.-P.L.) or Pierre.Boudinot@inra.fr (P.B.)

The online version of this article contains supplemental material.

Abbreviations used in this article: ADAR, adenosine deaminase acting on dsRNA; *btr*, bloodthirsty-like TRIM; CHIKV, chikungunya virus; dpf, day postfertilization; FC, fold change; hpi, hour postinfection; ISG, IFN-stimulated gene; LCATT, last common ancestor of teleosts and tetrapods; PARP, poly (ADP-ribose) polymerase; PKR, protein kinase R; qRT-PCR, quantitative RT-PCR; RNAseq, RNA sequencing; *vig*, virus-induced gene.

www.jimmunol.org/cgi/doi/10.4049/jimmunol.1900804

(14, 20, 21). In parallel, approaches without a priori identified fish ISGs that had no ortholog in mammals, although they belonged to gene families involved in antiviral immunity. A large set of tripartite-motif protein–encoding genes, called *fintrims* (*ftr*), distantly related to *trim25* was identified in rainbow trout cells as a induced by virus infection (13) and later shown to form multigene families in teleosts, particularly extensive in zebrafish (22). Similarly, a family of IFN-induced ADP-ribosyltransferases named *gig2* was identified in crucian carp cells treated with UV-inactivated grass carp hemorrhage virus (23, 24). Some ISG were restricted to particular fish groups, such as the noncoding RNA *vig-2* that is found only in salmonids (25).

We previously established a list of zebrafish candidate ISGs using microarray analysis (26). For this, we compared the response to a poor IFN inducer, infectious hematopoietic necrosis virus (27) and a strong IFN inducer, chikungunya virus (CHIKV) (28). However, the array did not include the full complement of zebrafish genes, and the study identified *vig* that were not necessarily ISGs. In this study, to directly identify ISGs, we analyze the transcriptional response of zebrafish larvae injected with recombinant type I IFN. We rely on deep RNA sequencing (RNAseq), which is intrinsically quasi-exhaustive. Our approach is therefore limited mainly by the quality of genome assembly and annotation, which is excellent for the zebrafish (29). We complemented this analysis with a study of the response to CHIKV and its dependence to expression of the zebrafish IFNR chains *crfb1* and *crfb2* (10). We thus established a comprehensive list of ISGs of zebrafish larvae and performed a detailed comparison with the human ISG repertoire. Our comparative analysis was facilitated by a compilation of human ISGs made to perform a systematic screen (30) and by the specialized database Interferome (31). We identify ~70 orthology groups that include ISG in both species and thus approximate the ISG repertoire of the common ancestor of all Osteichthyes. As ISGs typically evolve fast, with frequent duplications and gene loss, we also identify many families of fish-specific ISGs that represent a rich resource for seeking new antiviral mechanisms. Our study provides a broad overview of the evolutionary patterns of genes belonging to the type I IFN pathway and identifies gene modules induced by a viral infection independently of IFN.

Materials and Methods

Zebrafish husbandry

Wild-type AB zebrafish, initially obtained from the Zebrafish International Resource Center (Eugene, OR), were raised in the Institut Pasteur facility. Animal experiments were performed according to European Union guidelines for handling of laboratory animals (http://ec.europa.eu/environment/chemicals/lab_animals/home_en.htm) and were approved by the Institut Pasteur Animal Care and Use Committee. Eggs were obtained by marble-induced spawning, cleaned by treatment with 0.003% bleach for 5 min, and then kept in petri dishes containing Volvic source water at 28°C. All timings in the text refer to the developmental stage at the reference temperature of 28.5°C. At 3 d postfertilization (dpf), shortly before injections, larvae that had not hatched spontaneously were manually dechorionated. Larvae were anesthetized with 200 μg/ml tricaine (A5040; Sigma-Aldrich) during the injection procedure.

IFN and virus inoculation

Recombinant zebrafish IFNφ1 (10), kindly provided by R. Hartmann (University of Aarhus, Aarhus, Denmark), was inoculated by i.v. injection in the caudal cardinal vein. One nanoliter of 1 mg/ml IFNφ1, or, as a control, BSA (New England Biolabs) in ×1 PBS/10% glycerol, was injected. CHIKV infections were performed as described (26, 28). Briefly, ~200 PFU of CHIKV115 was injected i.v. in a volume of 1 nl at 3 dpf.

IFNR knockdown

Morpholino antisense oligonucleotides (Gene Tools) were injected at the one-to-two cells stage as described (32). Two nanograms of *crfb1* splice morpholino (5′-CGCCAAGATCATACCTGTAAAGTAA-3′) was injected together with 2 ng of *crfb2* splice morpholino (5′-CTATGAATCCTCACCTAGGGTAAAC-3′), knocking down all type I IFNR (10). Control morphants were injected with 4 ng of control morpholino (5′-GAAAGCATGGCATCTGGATCATCGA-3′) with no known target.

RNA extraction

For RNAseq analysis, total RNA was extracted from replicate pools of 10 injected larvae (at 6 h postinjection for IFNφ1 treatment, or 24 h postinjection for CHIKV infections), using TRIzol (Invitrogen), following the manufacturer's protocol. The integrity of the RNA was confirmed by laboratory-on-chip analysis using the 2100 Bioanalyzer (Agilent Technologies), using only samples with an RNA integrity number of at least 8.

Illumina sequencing

Libraries were built using a TruSeq mRNA Library Preparation Kit (Illumina), according to the manufacturer's recommendations. Quality control was performed on an Agilent Bioanalyzer. Sequencing was performed on a HiSeq 2500 System (Illumina) and produced 65-base, single-end reads.

Mapping reads and gene expression counts

Sequences were trimmed using Cutadapt (v1.8.3). The reads quality was checked with FastQC. Reads were then spliced-aligned to the zebrafish genome (GRCz10, Ensembl release 88) using TopHat2 (v2.0.14). The average number of mapped read per sample was 16.5 million. Only fragments mapping coherently and unambiguously to genes have been considered for gene counts. Gene counts have been assigned using featureCounts v1.5.2 (33).

Identification of differentially expressed genes

Differentially expressed nuclear genes between larvae treated with IFNφ1 and controls, between larvae infected by CHIKV and controls, or between crfb1+2 and control morphants all infected by CHIKV were identified. Differentially expressed genes were identified using DESeq 1.18.0 (Bioconductor) (34) and R: 3–1-2 (35). Briefly, raw counts of genes were subjected to a minimal prefiltering step: genes for which the count sum, per group of samples, was equal or higher than 10, in at least one group, were kept. Raw counts were normalized for library size, and normalized data were fitted using a negative binomial general linear model. Data were adjusted for multiple testing using the Benjamini–Hochberg procedure (adjusted p value). Genes with an adjusted p value < 0.01 and an absolute fold change (FC) > 2 or FC < 0.5 were considered as differentially expressed genes.

Sequence data were registered in the BioProject National Center for Biotechnology Information database (https://www.ncbi.nlm.nih.gov/bioproject) with the Sequence Read Archive accession number: PRJNA531581.

Identification of human orthologs and ISGs

Orthology analysis was primarily based on data from the Ensembl database (www.ensembl.org), the zfin database (zfin.org), and the literature, notably, our previous analysis of zebrafish orthologs of human ISGs (26). Data were systematically curated manually and conflicts resolved using a combination of literature search, synteny analysis, and sequence homology analysis (two-way protein BLAST). When human genes were present on the list compiled by Schoggins et al. (30), they were labeled as ISGs. If absent from the list, gene names were further queried on the Interferome Web site (http://www.interferome.org/interferome/search/showSearch.jspx), which compiles the results of many transcriptomic studies on human and mouse samples after IFN stimulation (31). We postulated that human genes present in Interferome could be considered as ISG when being significantly induced at least 2-fold with a stimulation for no more than 12 h by type I IFN in at least four datasets.

qRT-PCR

RNA was extracted from individual larvae using RNeasy Mini Kit (QIAGEN). cDNA was obtained using Moloney Murine Leukemia Virus H Minus Reverse Transcriptase (Promega) with a dT17 primer. Quantitative PCR was then performed on an ABI 7300 thermocycler (Applied Biosystems) using Takyon ROX SYBR 2× MasterMix (Eurogentec) in a final volume of 25 μl. The following pairs of primers were used: *ef1a* (housekeeping gene used for normalization), 5′-GCTGATCGTTGGAGTCAACA-3′ and 5′-ACAGACTTGACCTCAGTGGT-3′; *mxa*, 5′-GACCGTCTCTGATGTGGTTA-3′ and 5′-GCATGCTTTAGACTCTGGCT-3′; *ddx58*, 5′-ACGCCGGAGAAAGAATTTTTC-3′ and 5′-TCGACAGACTCTCGATGTTG-3′;

and *aqp9a*, 5′-CTGTACTACGACGCCTTCAT-3′ and 5′-GAGAATACAG-AGCACCAGCA-3′.

Results

RNAseq analysis of IFNφ1-regulated genes

To make an inventory of zebrafish ISGs, we first injected 3-dpf larvae with recombinant zebrafish IFNφ1, the first type I IFN to be identified in zebrafish, or BSA as a negative control. Based on preliminary kinetic experiments, we chose 6 h postinjection as the early plateau phase of ISG expression (Supplemental Fig. 1A). RNA was extracted from multiple pools of 10 larvae and subjected to deep sequencing using an Illumina-based platform sequencing. Reads were mapped to zebrafish genome (zv10), and the differential analysis performed using the DESeq package.

Choosing as cutoff values adjusted p values $< 5\%$ and FC > 2, we identified 360 IFNφ1 upregulated genes (which are ISGs, by definition) and 75 downregulated genes (Supplemental Table I, Tab 1). As expected, genes with high basal expression levels tended to display lower FC (Fig. 1A). The top IFNφ1-upregulated genes (with FC > 100) comprised many well-known ISGs, many previously used as IFN signature genes in zebrafish, including several *mx* genes, *rsad2*, *cmpk2*, several *ifit* genes, the ubiquitin-like *isg15*, the helicase *dhx58* (also known as *lgp2*), the kinase *pkz*, the transcription factor *stat1b*, and the chemokine *ccl19a.2* (Fig. 1B). To our surprise, *ddx58* (encoding RIG-I), a well-known and conserved ISG (36), was not found in that list. In fact, the gene model is missing on the zebrafish reference genome, with only fragments of the sequence present in the assembly. Therefore, we performed qRT-PCR for *ddx58* and confirmed that it is induced by IFNϕ1 (Supplemental Fig. 1B). We searched the list of zebrafish orthologs of human ISGs (26) for more genes not annotated on the reference genome and found only one besides *ddx58*, *aqp9a*. By qRT-PCR, this gene appeared to be moderately (0.75-fold) downregulated by IFNφ1 (Supplemental Fig. 1B) and, thus, was not an ISG.

Among the 360 zebrafish ISGs identified by RNAseq, 23 corresponded to noncoding ISGs or transposons with no clear homologs in mammals and were excluded from further phylogenetic analyses.

Gene ontology analysis was performed using the Database for Annotation, Visualization and Integrated Discovery (DAVID) and the Gene Ontology Enrichment Analysis and Visualization tool (GOrilla), and showed, as expected, that IFNφ1-upregulated genes were strongly enriched in genes linked to antiviral response, type I IFN pathway, and Ag processing and presentation (data not shown). Similarly, enrichment analyses identified Kyoto Encyclopedia of Genes and Genomes (KEGG) pathways for influenza, measles, and herpes simplex infection as well as RIG-I signaling and cytosolic DNA–sensing pathways. The list of downregulated genes was not found associated with any particularly notable function in these analyses.

Human orthologs of zebrafish ISGs are enriched in ISGs

We then searched for the human orthologs of the 337 identified protein-coding zebrafish ISGs (Supplemental Table I, Tab 2). All types of orthology relationships between zebrafish and humans were observed from none to "many-to-many." One-to-one orthology was found for 77 genes (Fig. 1C). We identified one or several human orthologs for 200 zebrafish ISGs. This proportion (200/337, 59%) is significantly lower than the 71% reported for the whole genome (29) (Fisher exact test, $p < 0.0001$).

We then searched which of these human genes were themselves ISGs. We found 61 ISGs present in the list of 446 human ISGs compiled by Schoggins et al. (30); by querying the Interferome database (31), we identified 11 additional human ISGs (Supplemental Table I, Tab 2). In total, 97 zebrafish IFNϕ1–inducible genes were orthologous to at least one human ISG (Fig. 1C). In addition, we identified a handful of genes that were not true orthologs but shared ancestry with a human ISG at the vertebrate level, such as MHC class I genes (see comments on Supplemental Table I, Tab 2).

As expected, human orthologs of zebrafish ISGs were strongly enriched in ISGs; whereas there are 446 human ISGs out of 20,454 genes in the genome (i.e., 2%), we found 72 ISGs among the 196 human orthologs to zebrafish ISGs (i.e., 37%) (Fisher exact test, $p < 0.0001$). Interestingly, FC values of zebrafish ISGs were higher when they were orthologous to a human ISG than when their orthologs were not ISGs (red versus blue on Fig. 1C, 1D), whereas FCs of zebrafish ISGs without human orthologs (gray on Fig. 1C, 1D) were intermediate (mean values, 127.7, 10.6, and 46.9, respectively; all groups significantly different from each other, $p < 0.001$, Kruskal–Wallis test). Thus, inducibility by type I IFNs is often evolutionary conserved, making it possible to infer an ancestral set of ISGs.

Fish-specific ISG genes and families

Consistent with the expected high rate of duplication and divergence of ISGs, a significant proportion of zebrafish IFNφ1–upregulated protein-coding genes had no identifiable ortholog in the human genome (137/337; 41%). Interestingly, but not unlike genes with human orthologs, many of these genes belonged to multigenic families. We show on Fig. 2 the fish-specific gene families that contain several zebrafish ISGs, with domains identified by the SMART tool (37).

The genes listed on Fig. 2 included more than 20 *fintrim* (*ftr*) genes, a family identified first as virus-inducible genes in rainbow trout (13), highly diversified in zebrafish, and hypothesized to antagonize retroviruses (22). Of note, besides finTRIM, there are two other large TRIM gene expansions in zebrafish, each with a single human ortholog of unknown function (38). The bloodthirsty-like TRIMs (*btr*), related to human TRIM39, include several ISGs. By contrast, no member of the TRIM35-like family was upregulated by IFNφ1.

Another family had been described as virus-inducible in fish: *gig2* (23). *gig2* are distantly related to the poly (ADP-ribose) polymerase (PARP) family (24), which include several ISGs in humans and zebrafish. The zebrafish *gig2p* and *gig2o* are induced by IFNφ1.

To our knowledge, the genes in the remaining fish-specific families had not previously been described to be IFN or virus inducible. These families are diverse, encoding proteins expected to be membrane receptors and presumably secreted, nuclear, or cytosolic proteins (Fig. 2).

Eight members of the very large NLR family were ISGs. These genes belong to groups 1, 2, 3, and 4, as defined in Ref. 39, and two of them belong to a fish-specific subset defined by the presence of a C-terminal B30.2 (or PRY/SPRY) domain (40, 41), which is most similar to the corresponding domain of finTRIM genes (22). The specific function(s) of zebrafish NLR genes remain poorly understood, but this highly expanded family may be central for inflammatory mechanisms.

Additionally, three ISGs corresponded to membrane proteins with two Ig domains and a transmembrane region, but not ITAM or ITIM. These genes belong to a very large family with 140 members that we propose to name fish genes with two Ig domains (f2Ig).

RNAseq analysis of CHIKV-induced genes

Experimental infection of zebrafish larvae with CHIKV induces a strong type I IFN response (28). Our previous microarray-based analysis indicated that the response to CHIKV was dominated by

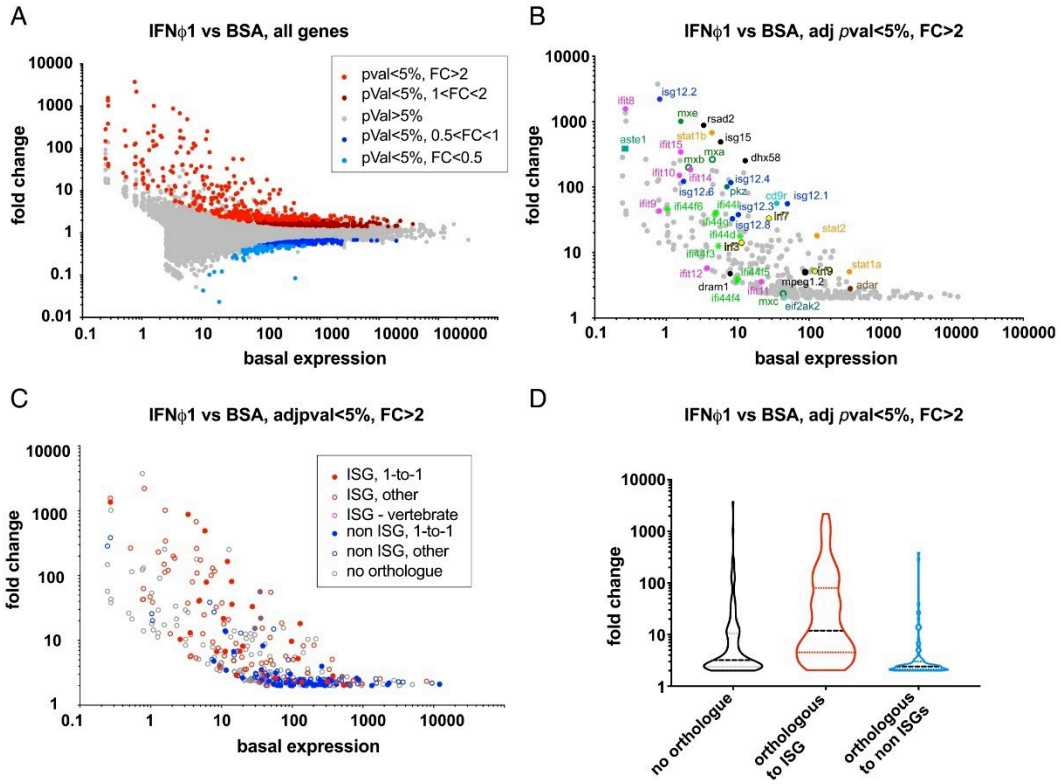

FIGURE 1. Zebrafish larva transcriptional response to type I IFN. (**A**) FC/basal expression representation with all genes detected in the analysis. Basal expression was the average of read numbers mapped onto a given gene in control (BSA-injected) larvae. FC is the ratio of reads numbers in IFNφ1-injected larvae divided by basal expression. (**B**) FC/basal expression representation, limited to ISGs identified in IFNφ1-injected larvae [e.g., red dots in (A)]; key genes commented in the text are indicated with gene families identified by different colors/symbols. (**C**) FC/basal expression representation for zebrafish ISGs represented according to the type of orthology with human genes and if human orthologs include at least one human ISG. One-to-one, single zebrafish gene orthologous to single human gene. Other, other orthology relationships between zebrafish and human genes (many-to-many, one-to-many, and many-to-one). Vertebrate, zebrafish gene sharing a common ancestor with a human ISG at the basal or jawed vertebrate level, but not orthologous. No ortholog, no orthology relationship with a human gene, and no known common ancestor with human ISG at vertebrate level. Non-ISG, orthologous human gene(s) do not include any ISG. (**D**) FC distribution for zebrafish ISG with different types of orthology relationship to human genes, using the same color code as in (C) but pooling genes with single and multiple human orthologs. Zebrafish ISGs with a human ISG within a vertebrate-level orthology groups were not included in this analysis. pVal, adjusted *p* value.

ISGs (26). However, to allow comparison with another virus with slower IFN induction kinetics, this analysis had been performed at 48 h postinfection (hpi), whereas the peak of the IFN and ISG response, as determined by qRT-PCR, is at 24 hpi (26). Therefore, we reanalyzed in this study the transcriptome of CHIKV-infected larvae at 24 hpi using deep RNAseq. Choosing the same cutoff values as for the IFNφ1 analysis, we identified 466 CHIKV upregulated genes and 26 downregulated genes (Supplemental Table I, Tab 3). Hundreds of new CHIKV-inducible genes were identified, either because they were absent from the microarray or because their induction were below the cutoff of the first analysis. Among the genes significantly upregulated in the microarray study, all those with a human ISG ortholog were also upregulated in this new dataset, and, as expected, typically much more (Supplemental Fig. 2).

About half of genes induced by IFNφ1 were also induced by the viral infection (181/360 Fig. 3A, Supplemental Table I, Tab 3, yellow), including almost all (84 out of 97) genes orthologous to a human ISG, such as *mxa*, *b*, and *e*, *stat1a* and *b*, *stat2*, *rasd2*, *isg15*, etc. There was a clear correlation of the FC values for genes induced by both IFNϕ1 and CHIKV (Fig. 3B). However, almost two thirds of the genes induced by CHIKV infection were not significantly modulated by IFNφ1 (285/466; Fig. 3A). We then asked whether this CHIKV-specific response could correspond essentially to genes for which there was weak induction by rIFNφ1, below our arbitrary cutoff. We therefore extracted from this list genes induced by IFNφ1 with FC $>$ 1.5 and with an adjusted *p* value $<$ 20%, and we found 66 genes matching these conditions (Supplemental Table I, Tab 3, green): 21 genes without annotation and 45 annotated genes, many of which were notoriously linked to the type I IFN system. These genes notably comprised *crfb1*, encoding a type I IFNR subunit, and two other cytokine receptors *il10Ra* and *il13Ra*; four chemokines (*ccl34*, *cxcl11.6*, *cxc18b*, and *cxc20*); 10 additional *fintrim* and three other members of the *gig2* family; and two *irf* transcription factors (*irf2*, *irf10*). It also includes the metalloreductase *steap3*, whose mammalian ortholog is not an ISG, but regulates type I IFN response, CXCL10 induction, and iron homeostasis in mouse macrophages (42).

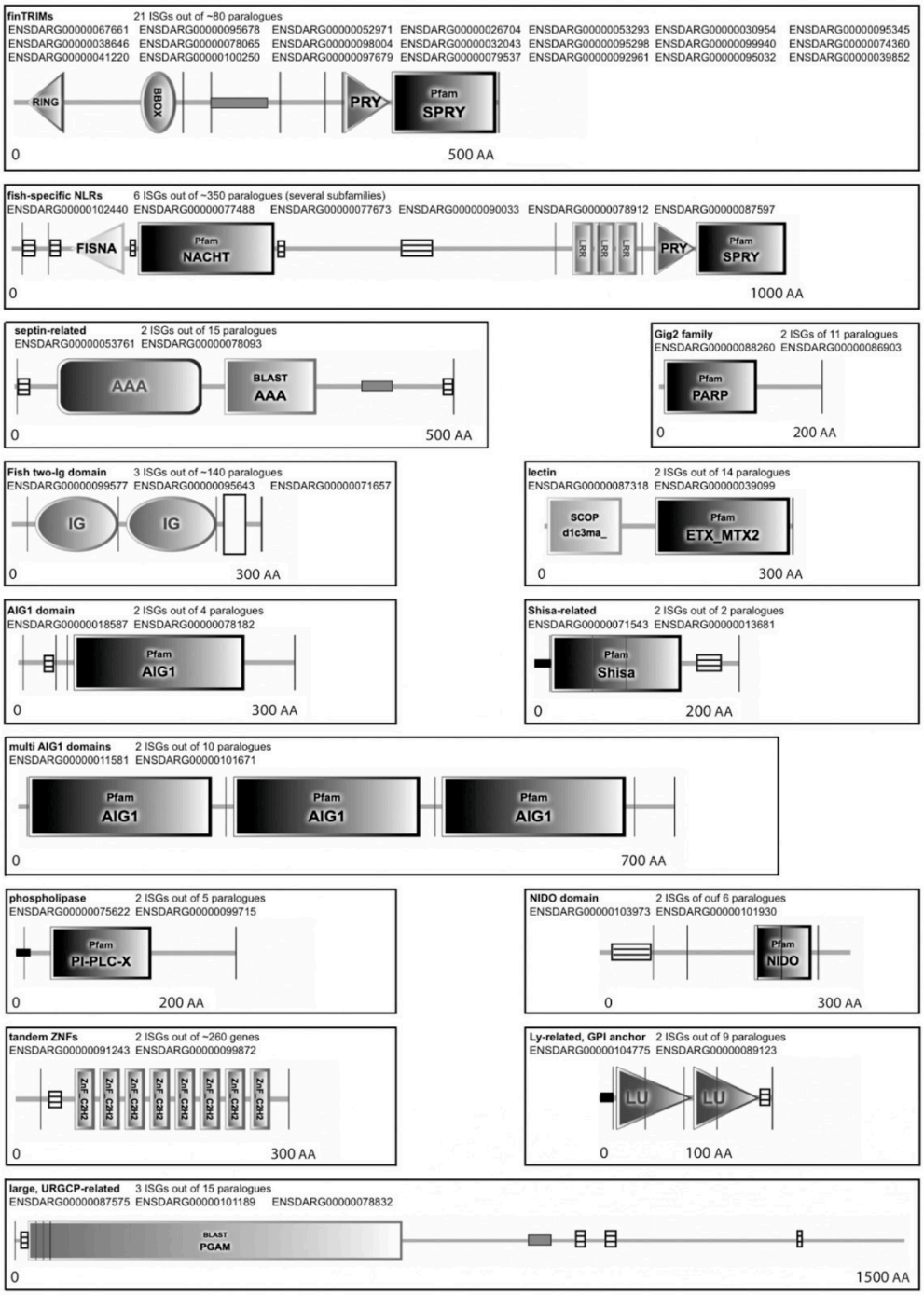

FIGURE 2. Main families of fish-specific ISG and their domain organization. Each panel show the typical domain organization of a family of fish-specific ISGs (e.g., with no human ortholog), as determined by SMART analysis (http://smart.embl-heidelberg.de/). The accession numbers of IFNφ1-induced genes (FC $>$ 2 and adjusted p value $<$ 5%) and the fraction they represent within the family are indicated. Vertical lines represent exon boundaries. Besides named domains, boxes represent coiled-coil regions (gray), low-complexity regions (striped), transmembrane domains (black), and leader peptides (white).

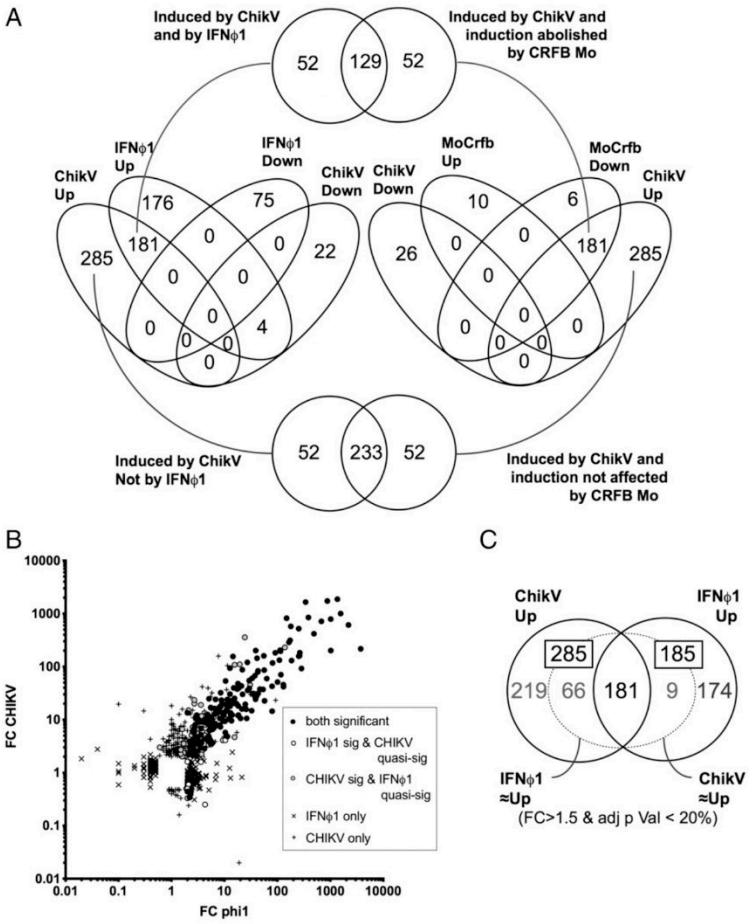

FIGURE 3. Comparison of ISG repertoires identified by IFNφ1 induction and by CHIKV infection (ChikV). (**A**) Venn analysis of genes up- or down-regulated in zebrafish larva by IFNφ1 treatment (IFNφ1), ChikV, and ChikV in the context of type I IFNR knockdown (MoCrfb). ISG are identified either by their responsiveness to IFNφ1 or by a CHIKV induction abolished in crfb1+2 morphants (Venn diagram at the top). Genes induced by ChikV in an IFNφ1-independent way are analyzed in the Venn diagram at the bottom of the panel. (**B**) FC/FC representation of transcriptome response to IFNφ1 and CHIKV. Symbol type identifies genes significantly induced by IFNφ1 and/or CHIKV and genes that are significantly induced in one condition (FC $>$ 2 and adjusted [adj] p value $<$ 0.05), whereas they are almost significantly induced in the other (quasi-significantly [quasi-Sig]; thresholds FC $>$ 1.5 and/or adjusted p value [adj p Val] $<$ 0.2). (**C**) Venn analysis of genes significantly induced by IFNφ1 and/or CHIKV. Gene subsets corresponding to genes induced quasi-Sig are represented within dotted lines.

Besides this intermediate gene set, a conservative list of 219 genes seems to be upregulated only by the virus (FC $>$ 2 and adjusted p value $<$ 5%) independently of IFNφ1 (FC $<$ 1.5 or adjusted p value $>$ 20%) (Fig. 3C; Supplemental Table I, Tab 3, blue). This list contains 105 genes without annotation, but also several functional modules, providing interesting insights on the virus/host interactions. Functional analysis using the Database for Annotation, Visualization and Integrated Discovery identified six enriched Kyoto Encyclopedia of Genes and Genomes pathways, namely cytokine/cytokine receptor interaction, cytosolic DNA sensing, TLR signaling, RIG-I–like receptor signaling, proteasome, and herpes simplex infection.

Importantly, type I IFNs were induced by the infection. Consistent with our previous report with another virus (10), *ifnphi1* and *ifnphi3* were clearly dominant at this larval stage, with 58 ± 3 and 47 ± 11 reads respectively, compared with 9 ± 4 reads for *ifnphi2*, and none detected for *ifnphi4*. Two proinflammatory cytokines *il1b* and *tnfb* were also upregulated. Among typical sensors, *tlr3*, *mb21d1* (encoding cGAS) and its downstream adaptor *tmem173* (encoding STING), and several kinases of the IFN signaling pathways (*ripk1* and *tbk1*) were present. Seven proteasome subunits are induced by the virus, suggesting activation of protein degradation and Ag presentation pathways. The complement pathway also stands out as an important module upregulated by CHIKV infection: 12 complement component genes (*c1*, *c2*, several *c3*, *c7*, *c9*, *cfB*, and *cfhl-1*,*-3*, and *-5*) were induced by CHIKV, suggesting that it is an important defense triggered in a type I IFN–independent manner. Additionally, this response comprises three metalloaminopeptidases (*anpepb* and *erap1b* and *2*); the myeloid markers *ncf1*, *mpx*, and *marco*; two guanylate binding proteins (*gbp1* and *2*) that have well-known orthologs in humans; the transcription factors *atf3* and *irf1b*; and, with a high level of expression, the enzyme *rnasel3* (an ortholog of human RNASE4, not of RNASEL, an ISG with no fish counterpart). Nine *fintrim* and three *btr* can also be noted, underscoring the importance of these TRIM with PRY/SPRY domains in virus/host interactions altogether.

Thus, CHIKV induces a typical IFN-stimulated response of high magnitude, but also a broader and less overt inflammatory response.

IFNR dependence of the response to CHIKV

To test the IFN-dependence of the response to CHIKV, we used morpholinos to knockdown in zebrafish larvae *crfb1* and *crfb2*, which encode specific chains of the two types of type I IFNR of zebrafish (10). We previously showed that such IFNR morphant

larvae are hypersusceptible to CHIKV infection, dying 2–3 d after virus injection (28). We analyzed by deep RNAseq their transcriptional response to CHIKV at 24 h postinoculation and compared it to that of control morphant larvae. Choosing as cutoff values adjusted p values $< 5\%$ and a ratio between IFN-R morphants and controls >2, we identified 187 genes for which induction was dampened by IFNR knockdown, and 10 genes that were upregulated in morphants (Supplemental Table I, Tab 4). Among CHIKV-induced genes (Supplemental Table I, Tab 3), 181 were IFNR dependent, representing a significant fraction (181/466; 39%) (Fig. 3A). Predictably, the list of genes upregulated by CHIKV in a IFNR-dependent manner largely, but not fully, overlapped with the gene set induced by rIFNφ1 (129/181; 71%, see Fig. 3A). This approach led us to classify 52 new zebrafish genes as ISGs, being induced by CHIKV in an IFNR-dependent manner, even if they were not significantly induced by rIFNφ1. As previously, we searched the human orthologs of these additional ISGs (Supplemental Table I, Tab 2, bottom), identifying a few more human ISGs in this list, such as cGAS, NLRC5, or IFI35.

Together, our results provide a near-exhaustive list of zebrafish ISGs at the larval stage, identified by two independent approaches, and a useful reference for future studies.

Ancestral ISGs

Assuming that the common ancestor of genes that are IFN inducible in both humans and zebrafish was itself an ISG in their last common ancestor ∼450 My ago, we can define a list of ancestral ISGs. We identified 66 orthology groups that included an ISG on both the human and the zebrafish sides (Table I, Supplemental Table I, Tab 5). A few more ancestral ISGs were also defined by pairs of ISGs with orthology relationships at the early vertebrate or gnathostome level, meaning that the zebrafish gene is not directly orthologous to a human ISG but is paralogous (with an ancestral taxonomy level labeled in Ensembl as vertebrates or jawed vertebrates) to another gene itself orthologous to a human ISG. In total, our list includes 72 ancestral genes (Fig. 4, Table I).

Based on our orthology analysis, we propose new, more explicit names for many of the zebrafish ISGs with known human orthologs (in red on Supplemental Table I, Tab 5). This ancestral ISG core includes most ISGs with known functions. The IFN system of 450 My ago seems fairly similar to the present one, particularly in its signaling components (Fig. 4). Many ancestral genes have been duplicated independently in one or both lineages (Supplemental Table I, Tab 5), in addition to multiple ISGs apparently gained by either group (Fig. 5).

IFN-downregulated genes

Two of the most strongly IFNφ1-downregulated genes (Supplemental Table I, Tab 1, bottom) were orthologous to human genes downregulated by type I IFNs, according to the Interferome database: perilipin 1 (*plin1*) and palmytoil acyl-CoA oxidase 1 (*acox1*). This suggests that downregulation of fatty acid oxidation pathway is an ancient feature of the IFN system.

Many IFNφ1-downregulated genes were orthologous to a human gene in a one-to-two manner, with the two zebrafish paralogues having arisen during the teleost-specific, whole-genome duplication (ohnologues). Systematically, only one of the two paralogues was downregulated.

Remarkably, no gene was downregulated by both IFNφ1 injection and CHIKV infection (Fig. 3B, Supplemental Table I, Tab 3).

Discussion

The zebrafish has become an important model to study host/pathogen interactions, particularly at its early life stages that are the most prone to live imaging and genetically tractable. Although its antiviral IFN genes and receptors are now well identified, knowledge of IFN-induced genes, or ISGs, was only partial. In this work, we used deep sequencing to characterize the transcriptomic response of the 3 dpf zebrafish larva to rIFNφ1, the first type I IFN identified in zebrafish and the most highly inducible one. We analyzed in parallel the response to an alphavirus inducing a strong type I IFN induction and the impact of IFNR knockdown on this response. From these different datasets, we established a comprehensive list of zebrafish ISGs. This list was compared with the human ISG repertoire, and a phylogenetic analysis was performed to approach the ancestral ISG repertoire of early vertebrates.

New insights and limitations of the work

A number of studies have identified genes induced by IFN or viral infections in fish (reviewed in Ref. 7). However, very few global descriptions after treatment with recombinant type I IFN have been reported using microarrays (19). Microarray analyses are limited by probe choice and are typically biased toward genes with known human homologs. RNAseq, by contrast, is mainly limited by the genome annotation quality and by the analysis method and can be reanalyzed; this approach is, thus, more complete. Because the early zebrafish larva constitutes a reference model for investigating innate immune response, drug screening as well as for modeling diseases, we undertook a comprehensive description of the repertoire of ISG upregulated at this developmental stage. Importantly, we previously reported a clear transcriptional response of zebrafish embryos to IFNφ1 as early as 24 h postfertilization (14); the responsiveness to type I IFNs is thus already well established at 3 dpf. We are aware that cells present in adult, but not yet in larvae, notably those of the adaptive immune system such as lymphocytes and dendritic cells, may express additional ISGs, which should be assessed in further work.

There are two groups of type I IFNs in teleost fish (43) with two different receptors (10). This study only addresses the ISG repertoire induced by IFNφ1 (a group 1 IFN), and it is possible that group 2 IFNs (IFNφ2 and IFNφ3) induce a different ISG subset. Determining this will require more studies; however, because CHIKV induces both IFNφ1 and IFNφ3, whereas *crfb1* and *2* morpholinos target receptors for both type I IFN groups, IFNφ3-only–induced ISGs should, therefore, be found among CHIKV-induced, IFNR-dependent, but non-IFNφ1–induced, genes. Such genes (listed on Supplemental Table I, Tab 2, bottom) constituted ∼30% of genes for which induction by CHIKV was impacted in morphants and only ∼15% if one also excludes genes for which induction by IFNφ1 is almost significant (Fig. 3A, 3C). A previous report by López-Muñoz et al. (20) suggests differences in ISG induction, notably in kinetics, by different IFNφs.

Comparative and phylogenetic analysis of zebrafish ISGs

Our comparative and phylogenetic approach led to a tentative reconstruction of the ISG repertoire of the last common ancestor of teleosts and tetrapods (LCATT) that lived ∼450 My ago and probably resembled the fossil osteichtyan *Ligulalepis* (44). To do so, we looked for human (co)ortholog(s) of all zebrafish ISGs identified in our analysis. Based on available data compilations (30, 31), we then determined which one(s) of these human orthologs were themselves induced by type I IFN. In such cases, we considered that they most likely originated from an "ancestral" ISG present in the LCATT. It is generally believed that the type I IFN system emerged during the early evolution of jawed vertebrates, because chondrichtyans (rays, sharks, and chimeras), but not agnathans (lampreys and hagfish), possess typical type I IFN genes (4, 45). Hence, it is important to note that the IFN system

Table I. Orthology groups defining ancestral ISGs

Ancestral Gene	Zebrafish	Human
Osteichtyan-Level Orthologs		
ADAR	*adar*	*ADAR*
AHNAK	*ahnak*	*AHNAK*
APOL	*apol*	*APOL1, 2, 3, 6*
B2M	*b2m,b2ml*	*B2M*
BATF2	*batf2*	*BATF2*
CASP1	*caspb*	*CASP1, CASP4*
CASP7	*casp7*	*CASP7*
CCL19	*ccl19a.1, a.2*	*CCL19*
CD40	*cd40*	*CD40*
cGAS	*cgas*	*CGAS*
CMPK2	*cmpk2*	*CMPK2*
CXCL11	*cxcl11.3*	*CXCL11*
DDX58 (RIG-I)	*ddx58*	*DDX58*
DHX58 (LGP2)	*dhx58*	*DHX58*
DTX3L	*dtx3lb1,2,3*	*DTX3L*
EPSTI1	*epsti1*	*EPSTI1*
FAM111	*fam111.1*	*FAM111A*
FAS	*fas*	*FAS*
FPR	*fpr*	*FPR2*
GIMAP	*gimapb1*	*GIMAP2*
HELZ2	*helz2a,b*	*HELZ2*
HERC5/6	*herc56.1, 2, 3, 4*	*HERC5, HERC6*
IFI35	*ifi35*	*IFI35*
IFI44	*ifi44a1, a5, c2, d, f3-6, g*	*IFI44, IFI44L*
IFIH1 (MDA-5)	*ifih1*	*IFIH1*
IFIT	*ifit8–12, 14–16*	*IFIT1-3, 5*
IL-4i1	*il4i1*	*IL4I1*
IRF7	*irf7*	*IRF7*
IRF9	*irf9*	*IRF9*
ISG12	*isg12.1–4, 6–7*	*IFI6, IFI27*
ISG15	*isg15*	*ISG15*
LGALS9	*lgals9l1, 3*	*LGALS9, 9C*
MOV10	*mov10a, b.1, b.2*	*MOV10*
MX	*mxa, b, c, e*	*MX1, MX2*
NAMPT	*nampta, namptb*	*NAMPT*
NCOA7	*ncoa7a*	*NCOA7*
NLRC5	*nlrc5*	*NLRC5*
OGFR	*ogfrl1,2*	*OGFR*
PARP12	*parp12a,b*	*PARP12*
PARP14	*parp14a,c*	*PARP14*
PARP9	*parp9*	*PARP9*
PHF11	*phf11*	*PHF11*
PKR	*pkz, eif2ak2*	*EIF2AK2*
PMAIP1	*pmaip1*	*PMAIP1*
PSMB8	*psmb8a*	*PSMB8*
PTMA	*ptmaa*	*PTMA*
PYCARD (ASC)	*pycard*	*PYCARD*
RARRES3	*rarres3*	*RARRES3*
RNF114	*rfn114*	*RNF114*
RNF213	*rnf213a,b*	*RNF213*
RSAD2	*rsad2*	*RSAD2*
SOCS1	*socs1a,b*	*SOCS1*
SP100	*sp100.1, sp100.3, sp100.4*	*SP100, 110, 140, 140L*
STAT1	*stat1a,b*	*STAT1*
STAT2	*stat2*	*STAT2*
TAP1	*tap1*	*TAP1*
TAP2	*tap2a,t*	*TAP2*
TDRD7	*tdrd7b*	*TDRD7*
TMEM173 (STING)	*tmem173*	*TMEM173*
TRAFD1	*trafd1*	*TRAFD1*
TREX	*trex3*	*TREX1*
TRIM25	*trim25*	*TRIM25*
UBA7	*uba7*	*UBA7*
USP18	*usp18*	*USP18*
XAF1	*xaf1*	*XAF1*
ZNFX1	*znfx1*	*ZNFX1*
Vertebrate-Level Orthologs		
CD9	*cd9r*	*CD9*
CDKN1	*cdkn1d*	*CDKN1A*
GJ	*cx30.3*	*GJA4*
MHC class I	*mhc1zba*	*HLA-A, -B, -C*
SAMD9	*samd9r*	*SAMD9*
TABPB	*tapbpr1, tapbpr2*	*TAPBP*

Orthology groups that include ISGs in both zebrafish and humans and therefore define an ancestral ISG in their common ancestor. Orthologous genes are produced by speciation (orthogenesis), by opposition to paralogous genes produced by duplication. Thus, an osteichtyan-level orthology group includes human and zebrafish genes with a direct ancestor in the LCATT. Vertebrate-level orthologs share this ancestral gene at the basal or jawed vertebrate level. This is a condensed version of Supplemental Table I, Tab5, which also include non-IFN–inducible genes that belong to the osteichtyan-level orthology groups and provide Ensembl Gene IDs.

had already evolved, expanded, and standardized for more than 50 My before our last common ancestor with zebrafish.

Approximately half of what we defined as ancestral ISGs are represented by one-to-one orthologs in zebrafish and humans (Supplemental Table I, Tab 5, top rows), a situation of practical interest, as the likelihood of conservation of gene function is highest in this case. These are either isolated genes (e.g., *RSAD2*, *ISG15*, or *cGAS*) or members of "old" families already stabilized in the LCATT (e.g., *IRF7* and *IRF9*) (26). The situation is relatively similar for a few ancestral genes, such as *STAT1* or *SOCS1*, with one human ortholog and two zebrafish co-orthologs that arose during the teleost-specific, whole-genome duplication and were retained. In contrast, many other "young" families have clearly been subjected to further duplication during later evolution of fish or tetrapods, leading to orthology groups containing multiple ISGs both in zebrafish and humans, the most spectacular examples being the *ISG12*, *IFIT*, and *IFI44* families.

The frequency of orthology with a human gene is lower for ISGs (59%) than for the entire genome (71%). This is probably a consequence of the stronger evolutionary pressure of genes involved in the arms race with pathogens, as postulated by the Red Queen hypothesis (46). Similar mechanisms also explain the frequent and extensive gene duplications, as well as gene losses if some virus disappears, removing the corresponding selective pressure on a given ISG. Possibly, a greater diversity of aquatic viruses could further favor ISG retention and divergence after duplication, but few direct evidences are available.

In addition to the ancestral genes with true zebrafish and human orthologs, we added to this list a few genes with a more complex history, with human and zebrafish ISGs that shared an ancestor at the basal vertebrate level (Table I, Supplemental Table I, Tab 5, bottom). These ancestral genes must have been duplicated in the LCATT genome; the teleost and tetrapod lineages then retained distinct paralogues. This comprises some genes whose evolutionary history is extremely difficult to trace because of multiple copies and extensive polymorphism, such as MHC class I genes. In this study, only *mhc1zba* was found to be a zebrafish ISG, but this does not necessarily imply that other zebrafish MHC class I genes are not ISGs, as they may have been missed because of mapping issues; the strain we used (AB) is not the same as the one of the reference genome (Tü), and strain-specific divergences are considerable between strains for MHC class I, with deep evolutionary roots (47). Importantly, we did not define ancestral ISGs for zebrafish/human ISG pairs that appeared to be related at first glance but, upon further analysis, were too distant; for example, zebrafish *vamp5* and human *VAMP8* are both ISGs but share their

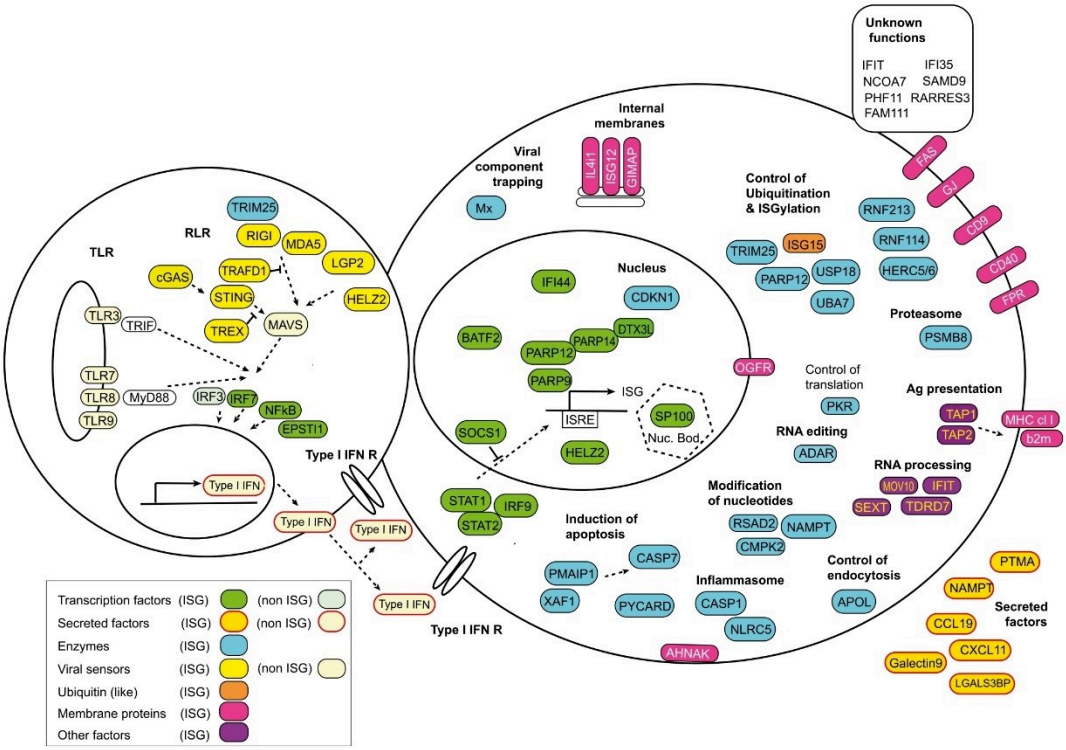

FIGURE 4. Graphic overview of the ancestral ISG repertoire, organized by functional modules.

last common ancestor at the Opistokontha level, before the split of fungi and animals, very long before the emergence of IFNs.

Nevertheless, the type I IFN system also includes very old genes that were already present in basal metazoans. The RNAseL/OAS module is a good example of such cases, being found across metazoans from mammals to sponges (48) but lost in the fish branch. Another striking example is the cGAS/STING module recently identified in cnidaria (49). The implication of these genes in the antiviral immunity of basal branches of animals is unknown but certainly worth investigating. The main models for invertebrate immunity are flies and mosquitoes, but they largely rely on RNA-interference mechanisms to contain viruses (3). Central signaling modules of the vertebrate IFN system, such as TLR/NF-κB and JAK/STAT, are also present in insects and in more distant metazoans, but they induce different set of genes with other functions (50).

Additionally, a few important genes do not meet our criteria for ancestral ISG, because they are not typically inducible either in zebrafish or in humans (Fig. 5). For example, *irf3* is an ISG in fish, but not in humans, whereas it is the reverse for *JAK2*. Hence, our list of ancestral ISG is likely not complete, but it provides a core repertoire pointing to most fundamental factors of the vertebrate innate antiviral arsenal.

A relatively large number of ISGs have no ortholog in the other lineage, such as human APOBEC3, RNASEL, OAS, and AIM2 (Fig. 5). Similarly, many fish-specific ISG likely have been co-opted by the IFN pathway during fish evolution. In this case, they do not have clear orthologs in humans and other tetrapods (as for finTRIMs and nlr-B30.2), or their ortholog(s) have no link with the type I IFN system. The finTRIM family contains the largest number of zebrafish ISGs of any family, ancestral or not. Interestingly, ISGs are found only among the recently diversified, species-specific finTRIMs; the most basal members (*ftr82–84*), well-conserved among fish, were not found in this study to be induced by IFNφ1 or by CHIKV, consistent with previous studies (51). Nevertheless, *ftr83* appears to mediate protection especially in the gill region by stimulating local *ifnphi1* expression (52). The diversity and evolution under positive selection of the IFN-inducible finTRIMs evoke viral recognition (22), yet their functions remain unclear.

The co-optation of new genes in the ISG repertoire may be operated quickly and in a group-specific manner, by introduction of sequence motifs in the regulatory sequences, for example, via retroviral insertion (53, 54). However, we cannot exclude that these branch-specific ISGs are, in fact, ancestral but lost in one of the two lineages; this is the case for *Gig2* genes, which are present in the coelacanth genome as well as in fish and, thus, were lost in tetrapods. Thus, our repertoire of ancestral ISGs is underestimated, because we cannot include the lineage-specific losses.

Do ancestral ISGs identified in this study define a minimal, but complete, set of response elements from recognition to elimination of invading viruses? Probably not, as this ancestral core group of ISGs was backed up by more ISGs is any species, including the LCATT. For example, the absence of the well-known OAS/RNAseL module genes in fish (and therefore in our list of conserved ancestral ISGs) is puzzling, and one could predict that other fish genes have taken over similar functions. Similarly, APOBEC3

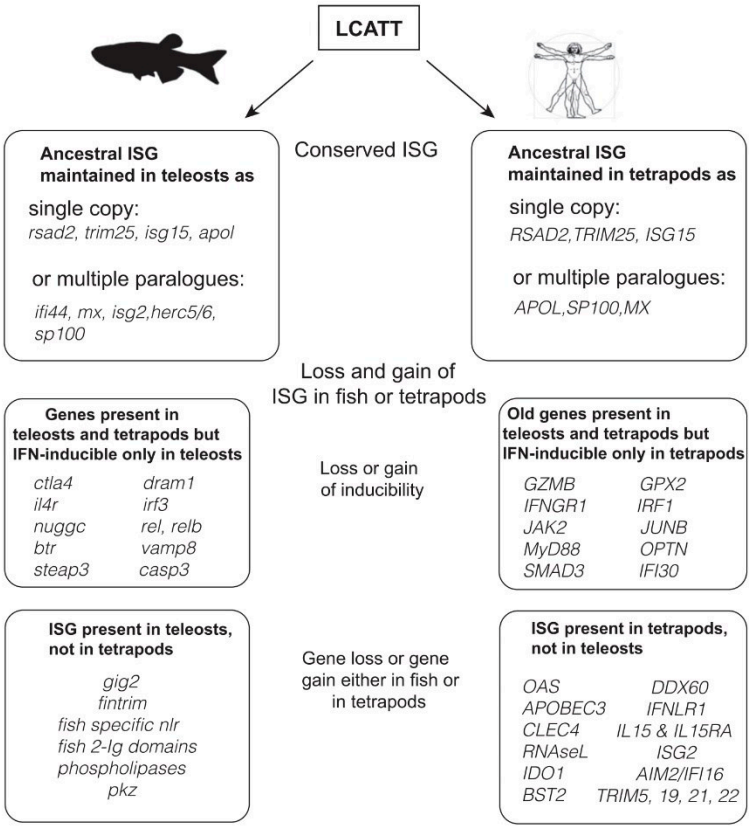

FIGURE 5. Evolution of the ISG repertoire since the LCATT. Genes names are given as examples, with no attempt to be exhaustive.

genes are absent in fish, and maybe their RNA-editing mechanisms are mediated by other genes, possibly by ADAR1.

Ancestral ISGs encode very diverse proteins in localization and function (Fig. 4). We provide an extended discussion of their classification below.

Characterization of the IFN-independent response to CHIKV infection

Knowing the repertoire of ISG also offers the possibility to identify genes that are induced by viral infection independently of the type I IFN pathway, whereas a subset of ISGs can be induced via IFN-dependent and -independent pathways in humans and fish, for example, *rsad2* (12). Thus, IRF3-dependent, type I IFN–independent induction of many ISG by particular viruses has been described (55).

However, about half of the genes upregulated by CHIKV were not induced by IFNϕ1 injection, and most were not affected by IFNR knockdown. Notably, three gene sets stand out in this list: 1) components of the complement cascade that are known to play a role in antiviral defense; 2) cytokines, including some CC and CXC chemokines, as well as the type I IFN themselves, which do not appear to be strongly auto/cross-inducible; and 3) many *btr* and *ftr* TRIM E3 ligases as well as multiple proteasome components. Interestingly too, *irf1b*, the zebrafish ortholog of IRF1 (a human ISG), is CHIKV inducible, but not in a IFNR-dependent manner, consistent with previous work (26), and was not induced by IFNϕ1. Many other genes of unknown function also share the same induction pattern and would certainly be worth investigating. A strong redundancy of antiviral pathways has certainly been selected during evolution, because viruses have developed multiple strategies of immune subversion.

Contrary to what was observed with upregulated genes, there was no overlap between gene sets downregulated by IFNϕ1 and by CHIKV. This remarkable difference could be due to the alternative inflammatory response induced by the virus besides type I IFNs or to kinetic differences.

Classification of ancestral ISGs

The ancestral ISG presented in Table I can be classified based on molecular functions: sensors, transcription factors and other signal transduction factors, secreted factors, enzymes including ubiquitination factors, and membrane receptors, which we discuss below. The antiviral mechanisms described in humans or in other mammalian systems also provide hints about the likely conserved mode of action of these factors.

Transcription factors. Many members of the list appear to have DNA binding capacity and may be classified as transcription factors.

Three IRF (3, 7, and 9) and two STAT (1 and 2) constitute fundamental components of the type I pathway signaling and were already present in the LCATT.

BATF2 is a member of the AP-1/ATF family transcription factors that controls the differentiation of immune cells and plays key regulatory roles in immune responses. BATF2 promotes TLR7-induced Th1 responses (56).

SP100 is a tumor suppressor and a major constituent of the PML bodies controlling transcription and/or chromatin conformation.

HELZ2 is a helicase that acts as a transcriptional coactivator for a number of nuclear receptors, including AHR, a nuclear receptor regulating lipid metabolism and the susceptibility to dengue virus (57).

Transcription coactivators. PARPs can act as transcriptional coactivators and potentiate induction of many ISG (58). The multiple ifi44 zebrafish genes counts seven ISG among 19 members, but their two human co-orthologs are induced by type I IFN. Located in the nucleus, IFI44 binds and blocks the HIV1 LTR promoter (59). However, the numerous zebrafish ifi44 probably have subfunctionalized and mediate multiple antiviral mechanisms.

Sensors and related genes. The helicases RIG-I, LPGP2, and IFIH1 (i.e., MDA5) stand as primary ISGs encoding viral sensors. Besides, as a cytoplasmic helicase, HELZ2 might also play a sensor role. In keeping with this, TREX proteins have a 3′-to-5′ DNA exonuclease activity that is important to block the sting-dependent initiation of IFN responses by DNA fragments from endogenous retroviruses and elements (60).

Enzymes. Besides transcription factors, enzymes are the most important category of ancestral ISG. They may play a role in signaling or have a direct antiviral activity.

PARP are involved in many cellular processes, from regulation of chromatin conformation to transcription control, and several PARP also are induced by infection and inflammation. PARP are represented by *parp9*, *parp*12, and *parp*14 among ancestral ISG. Strikingly, these three PARP are part of a nuclear complex, with the E3 ubiquitin ligase encoded by *dtx3l* that is also an ancestral ISG that promotes RNA polymerase II recruitment at IRF3-dependent promoters (58). Our data showing that key components of this complex are part of the essential type I IFN system underscore its importance in the core antiviral response. Besides, other activities of PARP may be involved in antiviral mechanisms; for example, PARP12 mediates ADP-ribosylation of Zika virus NS1 and NS3, leading to their degradation by the proteasome (61). The ADP-ribose-hydrolase encoded by the CHIKV, which is required for its virulence, is another hint of the central importance of these enzymes in antiviral defense (62).

Several E3 ubiquitin ligases were found among ancestral ISG, including tri*m25*, *usp18*, *rnf114*, and *dtx3l*. The mechanisms through which they exert antiviral activity or regulate the response are not fully resolved. The critical role of tri*m25* in RIG-I activation and its capacity of ISGylation (63) have been well documented in fish and mammals. *isg15*, a ubiquitin-like protein, is also an ancestral ISG playing a central role in the type I IFN pathway in fish and mammals (7, 63) via multiple mechanisms.

The proapoptotic caspase *casp7* possesses type I IFN–induced orthologs in zebrafish and humans. Interestingly, ancestral ISGs also comprise *pmaip1*, which promotes caspase activation and apoptosis via modifications of the mitochondrial membrane and *xiaf1*, a negative regulator of members of inhibitor of apoptosis proteins. Taken together, these observations indicate that the ancestral type I IFN system comprised a proapoptotic module.

The proinflammatory caspase *casp1* is also an ancestral ISG, as is *pycard*, which encodes ASC, the major scaffold protein of the canonical inflammasome. Induction of the inflammasome is thus an ancestral property of the IFN response. Many upstream sensors of the inflammasome are IFN inducible, but they are generally divergent in the two lineages, *nlrc5* being the only ancestral ISG.

Rsad2 (also known as *viperin*) is an enzyme with a direct antiviral function that catalyzes the conversion of CTP to a completely new ribonucleoside, the 3′-deoxy-3′,4′-didehydro-CTP acting as a terminator of RNA synthesis (64). Interestingly, both ancestral ISG *rsad2* and the nucleotide modifier *cpmk2* are located very close to each other in the genome in fish as well as in mammals, likely forming a conserved functional antiviral unit.

Adenosine deaminases acting on dsRNA (ADARs) deaminate adenosine to produce inosine in dsRNA structures, regulating the inflammation induced by such molecules (65). Accordingly, loss of function of *adar* in zebrafish larvae leads to brain inflammation in a model of Aicardi–Goutières syndrome, suggesting a key regulatory role of this gene during type I IFN response (66).

Protein kinase R (PKR; encoded by *eif2ak2*) is activated by dsRNA (and thus could have been listed above as a sensor), leading to phosphorylation of EIF2α and to inhibition of protein synthesis and viral replication. Many viruses encode PKR inhibitors of this cornerstone antiviral factor that also affects transcription factors like IRF1, STATs, and NF-κB and upregulates many genes including *β2microglobulin* and *isg15* (67). Interestingly, the other ancestral ISG *epsti1* can activate PKR promoters and induce PKR-dependent genes in humans (68), questioning whether *pkr* and *epsti1* may have been functionally coupled from the LCATT. Fish possess a lineage-specific paralogue of PKR called PKZ, which detects Z-DNA (69).

Secreted factors. In humans and mice, ccl19 is implicated in lymphocyte migration and is important to define compartments within lymphoid tissues. In rainbow trout, one of the six ccl19 paralogues present in the genome participate to antiviral immunity through promotion of mucosal and central $CD8^+$ T cell response (70).

Some of the fish homologs of murine and human IFN–inducible CXC chemokines (i.e., CXCL9–11, which bind CXCR3, a receptor expressed by various leukocyte, including some T cells, macrophages, and dendritic cell subsets) are also upregulated by IFNφ in zebrafish larvae. These genes have been largely expanded in fish, and two lineages of CXCL11 have been recently distinguished, both closely related to the mammalian CXCL9–11 (71, 72). The upregulated *cxcl11.3* (i.e., *cxc66* or *cxcl11ac*) identified in this work belongs to the lineage 1. The zebrafish has three *cxcr3* paralogues, and receptor/ligand binding, tested for three other zebrafish cxcl11 ligands, does not follow ligand lineage (73), so the receptor(s) of this ISG remains to be identified experimentally.

Another soluble factor upregulated by type I IFN and viral infection in fish is galectin-9 [this work and (13)]. In mammals, Galectin-9 is involved in multiple mechanisms of antiviral immunity. For example, it is a potent factor against human CMV because it blocks the entry of the virus in target cells (74). Galectin-9 can also regulate HIV transcription and induces the expression of the deaminase APOBEC3G, a potent antiviral factor (75). Besides, the galectin-9 receptor TIM3 is implicated in the control of Th1 cells (76).

Membrane proteins. Whereas zebrafish and human *mhc class I* are not direct orthologs, *mhc class I* genes are in the list, with *β2microglobulin* and the peptide transporters *tap-1* and *tap-2*, as well as homologs of TAPBP and proteasome subunits, indicating that this pathway is a fundamental component of the type I IFN system.

Other important membrane proteins in the list are tetraspanins of the CD9 family that regulate degranulation of myeloid subsets and secretion of cytokines and, hence, constitute key players in inflammation (77).

Zebrafish possess eight *isg12* genes located in tandem, of which six were highly inducible by IFNφ1 and by CHIKV. Their human ISG orthologs IFI6 and IFI27 (i.e., ISG12A) are internal membrane proteins stabilizing endoplasmic reticulum membrane and preventing the formation of flavivirus-induced endoplasmic reticulum

membrane invaginations (78) or destabilize mitochondrial membrane and promote apoptosis (79). In fact, IFI27 can also recruit a E3 ubiquitin ligase and targets HCV NS5 protein to degradation (80), illustrating the potential diversity of antiviral mechanisms mediated by members of this family.

APOL1 affects endocytosis and promotes an expansion of the lysosomal compartment, favoring, for example, the degradation of the HIV-1 protein Vif (81).

ISG with unknown functions or unknown antiviral mechanisms. Even in humans and mice, the basis of antiviral activity of certain ISGs remains completely unknown. For example, the effects of PHF11, RNF114, or SAMD9 are elusive. In the latter, a DNA/RNA-binding AlbA, a nucleoside triphosphatase, and a OB domain with predicted RNA-binding properties suggest a link with nucleic acid metabolism or sensing (82). These very old ISG with counterparts found across Metazoa and even in procaryotes are key restriction factors of poxviruses (83).

In conclusion, antiviral genes are well known to evolve very fast, as postulated by the Red Queen hypothesis, under strong pressure from pathogens. This is indeed illustrated by the large number of ISGs that are either fish or mammal specific. Nevertheless, our data define a surprisingly stable set of core ISGs that were apparently coopted into the new IFN system of early vertebrates ~500 My ago and have been maintained for the last 450 My both in fish and tetrapods. The full list of zebrafish ISG provides a powerful reference to characterize the subtle interactions between viruses and the host response, including redundancy of immune pathways and viral subversion mechanisms. It also constitutes a valuable resource for the study of autoinflammatory disease using the emerging zebrafish model.

Acknowledgments

We thank Jean-Yves Coppee and Caroline Proux (Transcriptomics Platform, Institut Pasteur) for generation and sequencing of RNA libraries. We are indebted to Rune Hartmann (Aarhus University) for recombinant zebrafish IFN and stimulating discussion. We thank Emma Colucci and Pedro Hernandez-Cerda for critical reading of the manuscript.

Disclosures

The authors have no financial conflicts of interest.

References

1. Schoggins, J. W., and C. M. Rice. 2011. Interferon-stimulated genes and their antiviral effector functions. *Curr. Opin. Virol.* 1: 519–525.
2. Backes, S., R. A. Langlois, S. Schmid, A. Varble, J. V. Shim, D. Sachs, and B. R. tenOever. 2014. The mammalian response to virus infection is independent of small RNA silencing. *Cell Rep.* 8: 114–125.
3. Guo, Z., Y. Li, and S. W. Ding. 2019. Small RNA-based antimicrobial immunity. *Nat. Rev. Immunol.* 19: 31–44.
4. Secombes, C. J., and J. Zou. 2017. Evolution of interferons and interferon receptors. *Front. Immunol.* 8: 209.
5. Redmond, A. K., J. Zou, C. J. Secombes, D. J. Macqueen, and H. Dooley. 2019. Discovery of all three types in cartilaginous fishes enables phylogenetic resolution of the origins and evolution of interferons. *Front. Immunol.* 10: 1558.
6. Zou, J., and C. J. Secombes. 2011. Teleost fish interferons and their role in immunity. *Dev. Comp. Immunol.* 35: 1376–1387.
7. Langevin, C., E. Aleksejeva, G. Passoni, N. Palha, J. P. Levraud, and P. Boudinot. 2013. The antiviral innate immune response in fish: evolution and conservation of the IFN system. *J. Mol. Biol.* 425: 4904–4920.
8. Boudinot, P., C. Langevin, C. J. Secombes, and J.-P. Levraud. 2016. The peculiar characteristics of fish type I interferons. *Viruses* 8: e298.
9. Robertsen, B. 2018. The role of type I interferons in innate and adaptive immunity against viruses in Atlantic salmon. *Dev. Comp. Immunol.* 80: 41–52.
10. Aggad, D., M. Mazel, P. Boudinot, K. E. Mogensen, O. J. Hamming, R. Hartmann, S. Kotenko, P. Herbomel, G. Lutfalla, and J.-P. Levraud. 2009. The two groups of zebrafish virus-induced interferons signal via distinct receptors with specific and shared chains. *J. Immunol.* 183: 3924–3931.
11. Stacheli, P., Y. X. Yu, R. Grob, and O. Haller. 1989. A double-stranded RNA-inducible fish gene homologous to the murine influenza virus resistance gene Mx. *Mol. Cell. Biol.* 9: 3117–3121.
12. Boudinot, P., P. Massin, M. Blanco, S. Riffault, and A. Benmansour. 1999. Vig-1, a new fish gene induced by the rhabdovirus glycoprotein, has a virus-induced homologue in humans and shares conserved motifs with the MoaA family. *J. Virol.* 73: 1846–1852.
13. O'Farrell, C., N. Vaghefi, M. Cantonnet, B. Buteau, P. Boudinot, and A. Benmansour. 2002. Survey of transcript expression in rainbow trout leukocytes reveals a major contribution of interferon-responsive genes in the early response to a rhabdovirus infection. *J. Virol.* 76: 8040–8049.
14. Levraud, J.-P., P. Boudinot, I. Colin, A. Benmansour, N. Peyrieras, P. Herbomel, and G. Lutfalla. 2007. Identification of the zebrafish IFN receptor: implications for the origin of the vertebrate IFN system. *J. Immunol.* 178: 4385–4394.
15. Lutfalla, G., H. Roest Crollius, N. Stange-Thomann, O. Jaillon, K. Mogensen, and D. Monneron. 2003. Comparative genomic analysis reveals independent expansion of a lineage-specific gene family in vertebrates: the class II cytokine receptors and their ligands in mammals and fish. *BMC Genomics* 4: 29.
16. Altmann, S. M., M. T. Mellon, D. L. Distel, and C. H. Kim. 2003. Molecular and functional analysis of an interferon gene from the zebrafish, *Danio rerio*. *J. Virol.* 77: 1992–2002.
17. Robertsen, B., V. Bergan, T. Røkenes, R. Larsen, and A. Albuquerque. 2003. Atlantic salmon interferon genes: cloning, sequence analysis, expression, and biological activity. *J. Interferon Cytokine Res.* 23: 601–612.
18. Purcell, M. K., K. M. Nichols, J. R. Winton, G. Kurath, G. H. Thorgaard, P. Wheeler, J. D. Hansen, R. P. Herwig, and L. K. Park. 2006. Comprehensive gene expression profiling following DNA vaccination of rainbow trout against infectious hematopoietic necrosis virus. *Mol. Immunol.* 43: 2089–2106.
19. Martin, S. A. M., J. B. Taggart, P. Seear, J. E. Bron, R. Talbot, A. J. Teale, G. E. Sweeney, B. Høyheim, D. F. Houlihan, D. R. Tocher, et al. 2007. Interferon type I and type II responses in an Atlantic salmon (Salmo salar) SHK-1 cell line by the salmon TRAITS/SGP microarray. *Physiol. Genomics* 32: 33–44.
20. López-Muñoz, A., F. J. Roca, J. Meseguer, and V. Mulero. 2009. New insights into the evolution of IFNs: zebrafish group II IFNs induce a rapid and transient expression of IFN-dependent genes and display powerful antiviral activities. *J. Immunol.* 182: 3440–3449.
21. Rothenburg, S., N. Deigendesch, M. Dey, T. E. Dever, and L. Tazi. 2008. Double-stranded RNA-activated protein kinase PKR of fishes and amphibians: varying the number of double-stranded RNA binding domains and lineage-specific duplications. *BMC Biol.* 6: 12.
22. van der Aa, L. M., J.-P. Levraud, M. Yahmi, E. Lauret, V. Briolat, P. Herbomel, A. Benmansour, and P. Boudinot. 2009. A large new subset of TRIM genes highly diversified by duplication and positive selection in teleost fish. *BMC Biol.* 7: 7.
23. Zhang, Y. B., and J. F. Gui. 2004. Identification and expression analysis of two IFN-inducible genes in crucian carp (*Carassius auratus* L.). *Gene* 325: 43–51.
24. Zhang, Y. B., T. K. Liu, J. Jiang, J. Shi, Y. Liu, S. Li, and J. F. Gui. 2013. Identification of a novel Gig2 gene family specific to non-amniote vertebrates. *PLoS One* 8: e60588.
25. Boudinot, P., S. Salhi, M. Blanco, and A. Benmansour. 2001. Viral haemorrhagic septicaemia virus induces vig-2, a new interferon-responsive gene in rainbow trout. *Fish Shellfish Immunol.* 11: 383–397.
26. Briolat, V., L. Jouneau, R. Carvalho, N. Palha, C. Langevin, P. Herbomel, O. Schwartz, H. P. Spaink, J.-P. Levraud, and P. Boudinot. 2014. Contrasted innate responses to two viruses in zebrafish: insights into the ancestral repertoire of vertebrate IFN-stimulated genes. *J. Immunol.* 192: 4328–4341.
27. Ludwig, M., N. Palha, C. Torhy, V. Briolat, E. Colucci-Guyon, M. Brémont, P. Herbomel, P. Boudinot, and J. P. Levraud. 2011. Whole-body analysis of a viral infection: vascular endothelium is a primary target of infectious hematopoietic necrosis virus in zebrafish larvae. *PLoS Pathog.* 7: e1001269.
28. Palha, N., F. Guivel-Benhassine, V. Briolat, G. Lutfalla, M. Sourisseau, F. Ellett, C. H. Wang, G. J. Lieschke, P. Herbomel, O. Schwartz, and J. P. Levraud. 2013. Real-time whole-body visualization of Chikungunya virus infection and host interferon response in zebrafish. *PLoS Pathog.* 9: e1003619.
29. Howe, K., M. D. Clark, C. F. Torroja, J. Torrance, C. Berthelot, M. Muffato, J. E. Collins, S. Humphray, K. McLaren, L. Matthews, et al. 2013. The zebrafish reference genome sequence and its relationship to the human genome. [Published erratum appears in 2014 *Nature* 505: 248.] *Nature* 496: 498–503.
30. Schoggins, J. W., S. J. Wilson, M. Panis, M. Y. Murphy, C. T. Jones, P. Bieniasz, and C. M. Rice. 2011. A diverse range of gene products are effectors of the type I interferon antiviral response. [Published erratum appears in 2015 *Nature* 525: 144.] *Nature* 472: 481–485.
31. Rusinova, I., S. Forster, S. Yu, A. Kannan, M. Masse, H. Cumming, R. Chapman, and P. J. Hertzog. 2013. Interferome v2.0: an updated database of annotated interferon-regulated genes. *Nucleic Acids Res.* 41: D1040–D1046.
32. Levraud, J.-P., E. Colucci-Guyon, M. J. Redd, G. Lutfalla, and P. Herbomel. 2008. In vivo analysis of zebrafish innate immunity. *Methods Mol. Biol.* 415: 337–363.
33. Liao, Y., G. K. Smyth, and W. Shi. 2014. featureCounts: an efficient general purpose program for assigning sequence reads to genomic features. *Bioinformatics* 30: 923–930.
34. Love, M. I., W. Huber, and S. Anders. 2014. Moderated estimation of fold change and dispersion for RNA-seq data with DESeq2. *Genome Biol.* 15: 550.
35. R Core Team. 2017. R: a language and environment for statistical computing. R Foundation for Statistical Computing, Vienna, Austria. Available at: https://www.R-project.org/.
36. Biacchesi, S., M. LeBerre, A. Lamoureux, Y. Louise, E. Lauret, P. Boudinot, and M. Brémont. 2009. Mitochondrial antiviral signaling protein plays a major role in induction of the fish innate immune response against RNA and DNA viruses. *J. Virol.* 83: 7815–7827.

37. Letunic, I., and P. Bork. 2018. 20 years of the SMART protein domain annotation resource. *Nucleic Acids Res.* 46: D493–D496.
38. Boudinot, P., L. M. van der Aa, L. Jouneau, L. Du Pasquier, P. Pontarotti, V. Briolat, A. Benmansour, and J. P. Levraud. 2011. Origin and evolution of TRIM proteins: new insights from the complete TRIM repertoire of zebrafish and pufferfish. *PLoS One* 6: e22022.
39. Howe, K., P. H. Schiffer, J. Zielinski, T. Wiehe, G. K. Laird, J. C. Marioni, O. Soylemez, F. Kondrashov, and M. Leptin. 2016. Structure and evolutionary history of a large family of NLR proteins in the zebrafish. *Open Biol.* 6: 160009.
40. Stein, C., M. Caccamo, G. Laird, and M. Leptin. 2007. Conservation and divergence of gene families encoding components of innate immune response systems in zebrafish. *Genome Biol.* 8: R251.
41. Laing, K. J., M. K. Purcell, J. R. Winton, and J. D. Hansen. 2008. A genomic view of the NOD-like receptor family in teleost fish: identification of a novel NLR subfamily in zebrafish. *BMC Evol. Biol.* 8: 42.
42. Zhang, F., Y. Tao, Z. Zhang, X. Guo, P. An, Y. Shen, Q. Wu, Y. Yu, and F. Wang. 2012. Metalloreductase Steap3 coordinates the regulation of iron homeostasis and inflammatory responses. *Haematologica* 97: 1826–1835.
43. Zou, J., C. Tafalla, J. Truckle, and C. J. Secombes. 2007. Identification of a second group of type I IFNs in fish sheds light on IFN evolution in vertebrates. *J. Immunol.* 179: 3859–3871.
44. Clement, A. M., B. King, S. Giles, B. Choo, P. E. Ahlberg, G. C. Young, and J. A. Long. 2018. Neurocranial anatomy of an enigmatic early devonian fish sheds light on early osteichthyan evolution. *eLife* 7: e34349.
45. Venkatesh, B., A. P. Lee, V. Ravi, A. K. Maurya, M. M. Lian, J. B. Swann, Y. Ohta, M. F. Flajnik, Y. Sutoh, M. Kasahara, et al. 2014. Elephant shark genome provides unique insights into gnathostome evolution. [Published erratum appears in 2014 *Nature* 513: 574.] *Nature* 505: 174–179.
46. tenOever, B. R. 2016. The evolution of antiviral defense systems. *Cell Host Microbe* 19: 142–149.
47. McConnell, S. C., K. M. Hernandez, D. J. Wcisel, R. N. Kettleborough, D. L. Stemple, J. A. Yoder, J. Andrade, and J. L. O. de Jong. 2016. Alternative haplotypes of antigen processing genes in zebrafish diverged early in vertebrate evolution. *Proc. Natl. Acad. Sci. USA* 113: E5014–E5023.
48. Päri, M., A. Kuusksalu, A. Lopp, T. Reintamm, J. Justesen, and M. Kelve. 2007. Expression and characterization of recombinant 2′,5′-oligoadenylate synthetase from the marine sponge Geodia cydonium. *FEBS J.* 274: 3462–3474.
49. Kranzusch, P. J., S. C. Wilson, A. S. Y. Lee, J. M. Berger, J. A. Doudna, and R. E. Vance. 2015. Ancient origin of cGAS-STING reveals mechanism of universal 2′,3′ cGAMP signaling. *Mol. Cell* 59: 891–903.
50. Liongue, C., R. Sertori, and A. C. Ward. 2016. Evolution of cytokine receptor signaling. *J. Immunol.* 197: 11–18.
51. Langevin, C., J. P. Levraud, and P. Boudinot. 2019. Fish antiviral tripartite motif (TRIM) proteins. *Fish Shellfish Immunol.* 86: 724–733.
52. Langevin, C., E. Aleksejeva, A. Houel, V. Briolat, C. Torhy, A. Lunazzi, J.-P. Levraud, and P. Boudinot. 2017. FTR83, a member of the large fish-specific finTRIM family, triggers IFN pathway and counters viral infection. *Front. Immunol.* 8: 617.
53. Chuong, E. B., N. C. Elde, and C. Feschotte. 2016. Regulatory evolution of innate immunity through co-option of endogenous retroviruses. *Science* 351: 1083–1087.
54. Arnold, M. L., and K. Kunte. 2017. Adaptive genetic exchange: a tangled history of admixture and evolutionary innovation. *Trends Ecol. Evol. (Amst.)* 32: 601–611.
55. Ashley, C. L., A. Abendroth, B. P. McSharry, and B. Slobedman. 2019. Interferon-independent upregulation of interferon-stimulated genes during human cytomegalovirus infection is dependent on IRF3 expression. *Viruses* 11: e246.
56. Kanemaru, H., F. Yamane, K. Fukushima, T. Matsuki, T. Kawasaki, I. Ebina, K. Kuniyoshi, H. Tanaka, K. Maruyama, K. Maeda, et al. 2017. Antitumor effect of *Batf2* through IL-12 p40 up-regulation in tumor-associated macrophages. *Proc. Natl. Acad. Sci. USA* 114: E7331–E7340.
57. Fusco, D. N., H. Pratt, S. Kandilas, S. S. Y. Cheon, W. Lin, D. A. Cronkite, M. Basavappa, K. L. Jeffrey, A. Anselmo, R. Sadreyev, et al. 2017. HELZ2 is an IFN effector mediating suppression of dengue virus. *Front. Microbiol.* 8: 240.
58. Caprara, G., E. Prosperini, V. Piccolo, G. Sigismondo, A. Melacarne, A. Cuomo, M. Boothby, M. Rescigno, T. Bonaldi, and G. Natoli. 2018. PARP14 controls the nuclear accumulation of a subset of type I IFN-inducible proteins. *J. Immunol.* 200: 2439–2454.
59. Power, D., N. Santoso, M. Dieringer, J. Yu, H. Huang, S. Simpson, I. Seth, H. Miao, and J. Zhu. 2015. IFI44 suppresses HIV-1 LTR promoter activity and facilitates its latency. *Virology* 481: 142–150.
60. Yan, N. 2017. Immune diseases associated with TREX1 and STING dysfunction. *J. Interferon Cytokine Res.* 37: 198–206.
61. Li, L., H. Zhao, P. Liu, C. Li, N. Quanquin, X. Ji, N. Sun, P. Du, C. F. Qin, N. Lu, and G. Cheng. 2018. PARP12 suppresses Zika virus infection through PARP-dependent degradation of NS1 and NS3 viral proteins. *Sci. Signal.* 11: eaa9332.
62. McPherson, R. L., R. Abraham, E. Sreekumar, S.-E. Ong, S.-J. Cheng, V. K. Baxter, H. A. V. Kistemaker, D. V. Filippov, D. E. Griffin, and A. K. L. Leung. 2017. ADP-ribosylhydrolase activity of Chikungunya virus macrodomain is critical for virus replication and virulence. *Proc. Natl. Acad. Sci. USA* 114: 1666–1671.
63. Langevin, C., L. M. van der Aa, A. Houel, C. Torhy, V. Briolat, A. Lunazzi, A. Harmache, M. Bremont, J. P. Levraud, and P. Boudinot. 2013. Zebrafish ISG15 exerts a strong antiviral activity against RNA and DNA viruses and regulates the interferon response. *J. Virol.* 87: 10025–10036.
64. Gizzi, A. S., T. L. Grove, J. J. Arnold, J. Jose, R. K. Jangra, S. J. Garforth, Q. Du, S. M. Cahill, N. G. Dulyaninova, J. D. Love, et al. 2018. A naturally occurring antiviral ribonucleotide encoded by the human genome. [Published erratum appears in 2018 *Nature* 562: E3.] *Nature* 558: 610–614.
65. Samuel, C. E. 2019. Adenosine deaminase acting on RNA (ADAR1), a suppressor of double-stranded RNA-triggered innate immune responses. *J. Biol. Chem.* 294: 1710–1720.
66. Kasher, P. R., E. M. Jenkinson, V. Briolat, D. Gent, C. Morrissey, L. A. H. Zeef, G. I. Rice, J.-P. Levraud, and Y. J. Crow. 2015. Characterization of samhd1 morphant zebrafish recapitulates features of the human type I interferonopathy Aicardi-Goutières syndrome. *J. Immunol.* 194: 2819–2825.
67. Guerra, S., L. A. López-Fernández, M. A. García, A. Zaballos, and M. Esteban. 2006. Human gene profiling in response to the active protein kinase, interferon-induced serine/threonine protein kinase (PKR), in infected cells. Involvement of the transcription factor ATF-3 IN PKR-induced apoptosis. *J. Biol. Chem.* 281: 18734–18745.
68. Meng, X., D. Yang, R. Yu, and H. Zhu. 2015. EPSTI1 is involved in IL-28A-mediated inhibition of HCV infection. *Mediators Inflamm.* 2015: 716315.
69. Rothenburg, S., N. Deigendesch, K. Dittmar, F. Koch-Nolte, F. Haag, K. Lowenhaupt, and A. Rich. 2005. A PKR-like eukaryotic initiation factor 2alpha kinase from zebrafish contains Z-DNA binding domains instead of dsRNA binding domains. *Proc. Natl. Acad. Sci. USA* 102: 1602–1607.
70. Sepahi, A., L. Tacchi, E. Casadei, F. Takizawa, S. E. LaPatra, and I. Salinas. 2017. CK12a, a CCL19-like chemokine that orchestrates both nasal and systemic antiviral immune responses in rainbow trout. *J. Immunol.* 199: 3900–3913.
71. Nomiyama, H., N. Osada, and O. Yoshie. 2013. Systematic classification of vertebrate chemokines based on conserved synteny and evolutionary history. *Genes Cells* 18: 1–16.
72. Chen, J., Q. Xu, T. Wang, B. Collet, Y. Corripio-Miyar, S. Bird, P. Xie, P. Nie, C. J. Secombes, and J. Zou. 2013. Phylogenetic analysis of vertebrate CXC chemokines reveals novel lineage specific groups in teleost fish. *Dev. Comp. Immunol.* 41: 137–152.
73. Torraca, V., C. Cui, R. Boland, J.-P. Bebelman, A. M. van der Sar, M. J. Smit, M. Siderius, H. P. Spaink, and A. H. Meijer. 2015. The CXCR3-CXCL11 signaling axis mediates macrophage recruitment and dissemination of mycobacterial infection. *Dis. Model. Mech.* 8: 253–269.
74. Machala, E. A., S. Avdic, L. Stern, D. M. Zajonc, C. A. Benedict, E. Blyth, D. J. Gottlieb, A. Abendroth, B. P. McSharry, and B. Slobedman. 2019. Restriction of human cytomegalovirus infection by galectin-9. *J. Virol.* 93: e01746-18.
75. Abdel-Mohsen, M., L. Chavez, R. Tandon, G. M. Chew, X. Deng, A. Danesh, S. Keating, M. Lanteri, M. L. Samuels, R. Hoh, et al. 2016. Human galectin-9 is a potent mediator of HIV transcription and reactivation. *PLoS Pathog.* 12: e1005677.
76. Zhu, C., A. C. Anderson, A. Schubart, H. Xiong, J. Imitola, S. J. Khoury, X. X. Zheng, T. B. Strom, and V. K. Kuchroo. 2005. The Tim-3 ligand galectin-9 negatively regulates T helper type 1 immunity. *Nat. Immunol.* 6: 1245–1252.
77. Brosseau, C., L. Colas, A. Magnan, and S. Brouard. 2018. CD9 tetraspanin: a new pathway for the regulation of inflammation? *Front. Immunol.* 9: 2316.
78. Richardson, R. B., M. B. Ohlson, J. L. Eitson, A. Kumar, M. B. McDougal, I. N. Boys, K. B. Mar, P. C. De La Cruz-Rivera, C. Douglas, G. Konopka, et al. 2018. A CRISPR screen identifies IFI6 as an ER-resident interferon effector that blocks flavivirus replication. *Nat. Microbiol.* 3: 1214–1223.
79. Cheriyath, V., D. W. Leaman, and E. C. Borden. 2011. Emerging roles of FAM14 family members (G1P3/ISG 6-16 and ISG12/IFI27) in innate immunity and cancer. *J. Interferon Cytokine Res.* 31: 173–181.
80. Xue, B., D. Yang, J. Wang, Y. Xu, X. Wang, Y. Qin, R. Tian, S. Chen, Q. Xie, N. Liu, and H. Zhu. 2016. ISG12a restricts hepatitis C virus infection through the ubiquitination-dependent degradation pathway. *J. Virol.* 90: 6832–6845.
81. Taylor, H. E., A. K. Khatua, and W. Popik. 2014. The innate immune factor apolipoprotein L1 restricts HIV-1 infection. *J. Virol.* 88: 592–603.
82. Mekhedov, S. L., K. S. Makarova, and E. V. Koonin. 2017. The complex domain architecture of SAMD9 family proteins, predicted STAND-like NTPases, suggests new links to inflammation and apoptosis. *Biol. Direct* 12: 13.
83. Meng, X., F. Zhang, B. Yan, C. Si, H. Honda, A. Nagamachi, L. Z. Sun, and Y. Xiang. 2018. A paralogous pair of mammalian host restriction factors form a critical host barrier against poxvirus infection. *PLoS Pathog.* 14: e1006884.

Annexe 3

Article

Current Biology

CSF-contacting neurons respond to *Streptococcus pneumoniae* and promote host survival during central nervous system infection

Graphical abstract

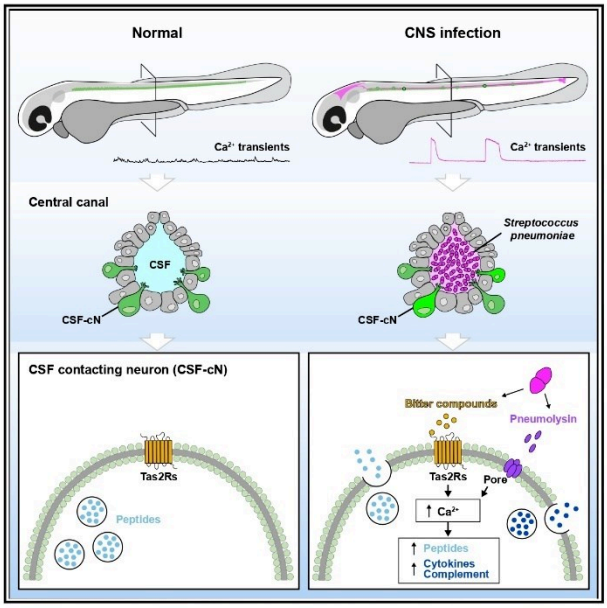

Authors

Andrew E. Prendergast, Kin Ki Jim, Hugo Marnas, ..., Diederik van de Beek, Christina M.J.E. Vandenbroucke-Grauls, Claire Wyart

Correspondence

vandenbrouckegrauls@amsterdamumc.nl (C.M.J.E.V.-G.), claire.wyart@icm-institute.org (C.W.)

In brief

Prendergast et al. discover that cerebrospinal fluid-contacting neurons (CSF-cNs), which are known to detect spinal curvature and control posture, also respond to bacterial metabolites, and during infections of the central nervous system, they secrete compounds that promote host survival.

Highlights

- Infection of zebrafish with *S. pneumoniae* elicits pathognomonic signs of meningitis
- CSF-cNs show massive activation when *S. pneumoniae* invade the CSF
- Metabolites secreted by *S. pneumoniae* induce similar activation of CSF-cNs
- CSF-cN secretion increases host survival upon *S. pneumoniae* infection

Prendergast et al., 2023, Current Biology *33*, 940–956
March 13, 2023
https://doi.org/10.1016/j.cub.2023.01.039

CellPress

CellPress
OPEN ACCESS

Current Biology

Article

CSF-contacting neurons respond to *Streptococcus pneumoniae* and promote host survival during central nervous system infection

Andrew E. Prendergast,[1,9,10] Kin Ki Jim,[2,3,4,5,10] Hugo Marnas,[1,10] Laura Desban,[1] Feng B. Quan,[1] Lydia Djenoune,[1] Valerio Laghi,[6] Agnès Hocquemiller,[1] Elias T. Lunsford,[1] Julian Roussel,[1] Ludovic Keiser,[7] Francois-Xavier Lejeune,[1] Mahalakshmi Dhanasekar,[1] Pierre-Luc Bardet,[1] Jean-Pierre Levraud,[6,8] Diederik van de Beek,[2,3] Christina M.J.E. Vandenbroucke-Grauls,[4,5,*] and Claire Wyart[1,11,*]

[1]Institut du Cerveau (ICM), Sorbonne Université, UPMC Univ Paris 06, Inserm, CNRS, AP-HP, Hôpital Pitié-Salpêtrière, 47 Boulevard de l'Hôpital, 75013 Paris, France
[2]Amsterdam UMC location University of Amsterdam, Department of Neurology, Meibergdreef 9, 1105 AZ Amsterdam, the Netherlands
[3]Amsterdam Neuroscience, 1081 HV Amsterdam, the Netherlands
[4]Amsterdam UMC location Vrije Universiteit Amsterdam, Department of Medical Microbiology and Infection Prevention, De Boelelaan 1117, 1081 HV Amsterdam, the Netherlands
[5]Amsterdam Institute for Infection and Immunity, 1081 HV Amsterdam, the Netherlands
[6]Institut Pasteur, Unité Macrophages et Développement, Centre National de la Recherche Scientifique (CNRS), Université Paris-Cité, 75015 Paris, France
[7]Ecole Polytechnique Fédérale de Lausanne (EPFL), Station 18, 1015 Lausanne, Switzerland
[8]Université Paris-Saclay, CNRS, Institut Pasteur, Université Paris-Cité, Institut des Neurosciences Paris-Saclay, 91400 Saclay, France
[9]Present address: Yale Zebrafish Research Core, Yale University, New Haven, CT 06511, USA
[10]These authors contributed equally
[11]Lead contact
*Correspondence: vandenbrouckegrauls@amsterdamumc.nl (C.M.J.E.V.-G.), claire.wyart@icm-institute.org (C.W.)
https://doi.org/10.1016/j.cub.2023.01.039

SUMMARY

The pathogenic bacterium *Streptococcus pneumoniae* (*S. pneumoniae*) can invade the cerebrospinal fluid (CSF) and cause meningitis with devastating consequences. Whether and how sensory cells in the central nervous system (CNS) become activated during bacterial infection, as recently reported for the peripheral nervous system, is not known. We find that CSF infection by *S. pneumoniae* in larval zebrafish leads to changes in posture and behavior that are reminiscent of pneumococcal meningitis, including dorsal arching and epileptic-like seizures. We show that during infection, invasion of the CSF by *S. pneumoniae* massively activates *in vivo* sensory neurons contacting the CSF, referred to as "CSF-cNs" and previously shown to detect spinal curvature and to control posture, locomotion, and spine morphogenesis. We find that CSF-cNs express orphan bitter taste receptors and respond *in vitro* to bacterial supernatant and metabolites via massive calcium transients, similar to the ones observed *in vivo* during infection. Upon infection, CSF-cNs also upregulate the expression of numerous cytokines and complement components involved in innate immunity. Accordingly, we demonstrate, using cell-specific ablation and blockade of neurotransmission, that CSF-cN neurosecretion enhances survival of the host during *S. pneumoniae* infection. Finally, we show that CSF-cNs respond to various pathogenic bacteria causing meningitis in humans, as well as to the supernatant of cells infected by a neurotropic virus. Altogether, our work uncovers that central sensory neurons in the spinal cord, previously involved in postural control and morphogenesis, contribute as well to host survival by responding to the invasion of the CSF by pathogenic bacteria during meningitis.

INTRODUCTION

During a bacterial infection of the skin, bacteria invading the subcutaneous tissues can directly activate nociceptor sensory neurons through N-formyl peptides and pore-forming toxins, contributing to inflammation and innate immunity by releasing regulatory neuropeptides.[1] A similar phenomenon occurs in the respiratory epithelium where ciliated epithelial cells detect bacterial metabolites and induce an inflammatory response.[2] During bacterial infection of the central nervous system (CNS), bacteria invade the cerebrospinal fluid (CSF) that circulates from the brain ventricles down to the central canal of the spinal cord. We hypothesized that bacteria in the CNS could similarly induce activation of sensory neurons in contact with the CSF.

Along the walls of the central canal in the spinal cord, sensory cells—referred to as CSF-contacting neurons (CSF-cNs)—are numerous across vertebrate species.[3,4] Our group and others have shown over the last decade that these cells are

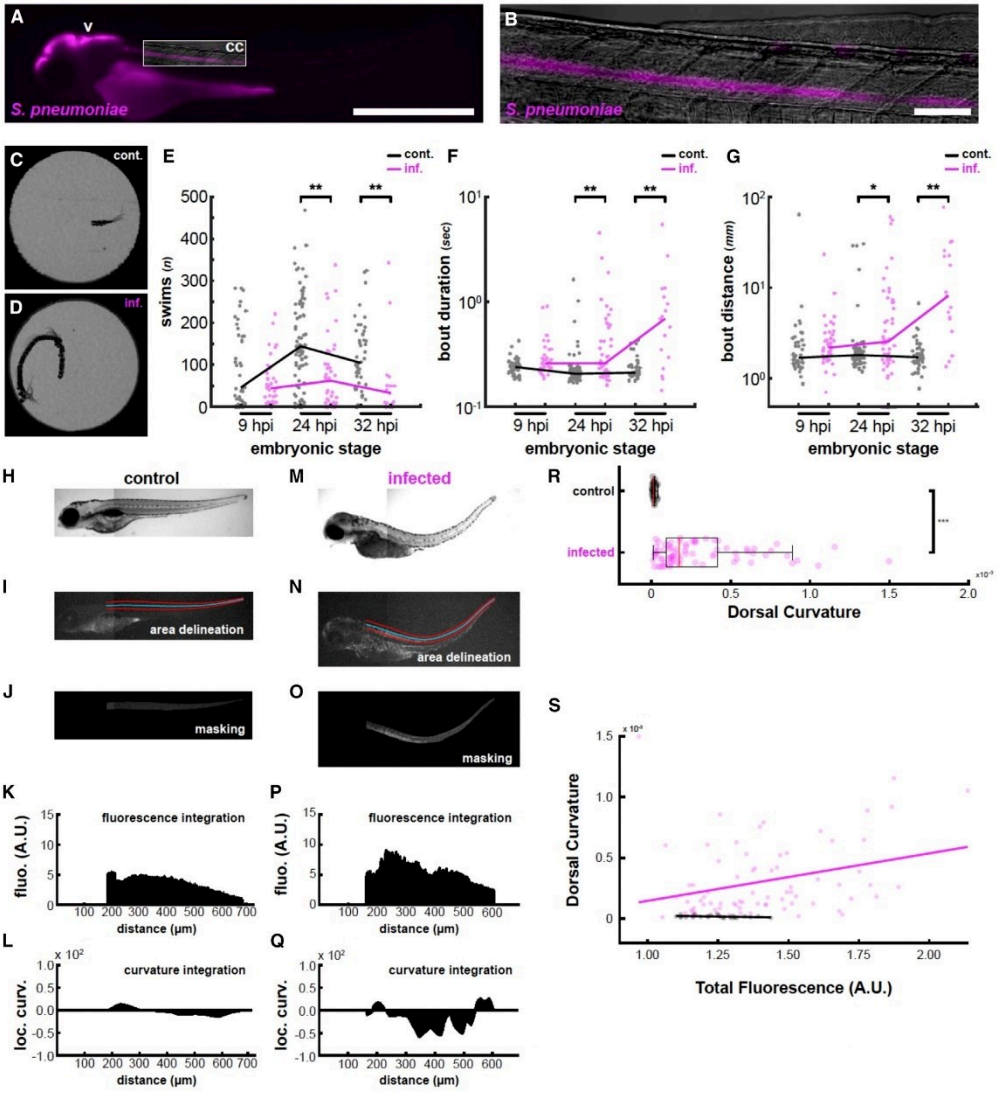

Figure 1. Infection induces behavioral changes and spinal curvature reminiscent of clinical symptoms of pneumococcal meningitis

(A) Fluorescence image of a larva infected with mCherry-labeled *S. pneumoniae* at 2 dpf and imaged at 24 hpi showing colonization of the brain ventricle (v) and central canal (cc). Box indicates field of view for (B). Scale bars, 500 μm.

(B) Higher magnification image of the central canal colonized with mCherry-labeled *S. pneumoniae*. Scale bars, 50 μm.

(C) Representative motion overlay of a detected swim bout from a larva injected with vehicle. Most bouts are short forward swims.

(D) Representative motion overlay of a detected swim bout from a larva infected with *S. pneumoniae*. These swim bouts tend to be much longer in duration and distance.

(E) Quantification of the overall number of bouts in PBS-injected (gray) and *S. pneumoniae*-infected (magenta) fish at three different time points post infection. At later infection time points, infected fish swim substantially less often (**$p < 0.01$).

(legend continued on next page)

interoceptive ciliated mechanosensory neurons that detect spinal curvature[5–8] and in turn release GABA to optimize the kinematics of locomotion[9] and active posture[10,11] in the short timescale as well as morphogenesis throughout life.[12,13] In particular, the release of peptides from the urotensin family by ventral CSF-cNs elicits dorsalward arching via contraction of the dorsal musculature.[12,14–19] CSF-cNs express the transient receptor channel PKD2L1[20,21] that enables them to detect changes in pH and osmolarity.[20–22] We hypothesize that these CSF-cNs could be recruited due to changes in CSF content during CNS infection, in order to modulate the inflammatory and immune response, and possibly contribute to changes in neck stiffness and posture seen in meningitis patients.[23] To investigate this hypothesis, we took advantage of a model of pneumococcal meningitis developed in larval zebrafish.[24] We used *Streptococcus pneumoniae* (*S. pneumoniae*) as it is the most common cause of community-acquired bacterial meningitis worldwide[25–28] and is associated with high mortality and morbidity rates despite the introduction of conjugate vaccines.[25] We therefore injected *S. pneumoniae* in the hindbrain ventricles (HBVs) of transgenic larval zebrafish expressing the fluorescent genetically encoded calcium sensor GCaMP under the *pkd2l1* promoter.

Supporting our hypothesis, we observed that CNS infection by *S. pneumoniae* in zebrafish larvae led to phenotypes reminiscent of pneumococcal meningitis in humans, including dorsal arching and epileptic-like seizures. In this model, we established a live calcium imaging approach to monitor the activation of CSF-cNs upon injection of *S. pneumoniae* in the brain ventricles. We discovered that CSF-cNs are activated when pathogenic bacteria invade the CSF, as shown by large and long-lasting calcium transients. We show that similarly large calcium transients in CSF-cNs can be elicited *in vitro* by exposure to microbial metabolites acting as bitter compounds. Accordingly, we find that CSF-cNs specifically express orphan bitter taste receptors along with neuropeptides with antimicrobial or immunomodulatory functions. Upon infection, CSF-cNs upregulate the expression of numerous cytokines and complement components. Finally, blocking the neurosecretion of CSF-cNs or ablating these cells reduces host survival upon infection. The massive activation of CSF-cNs in response to *S. pneumoniae* occurs for other bacterial and viral pathogens as well, suggesting their function as tasters of the CSF in the context of infection is widespread. Our study demonstrates that central sensory neurons respond to products of pathogenic bacteria, are recruited during pneumococcal infection of the CNS, and furthermore confer a survival benefit. We conclude that CSF-cNs are not only mechanosensory cells detecting spinal curvature to modulate locomotion, posture, and morphogenesis, but they also act akin to taste receptor cells and contribute to innate immunity during CNS infection.

RESULTS

Zebrafish larvae infected with *S. pneumoniae* exhibit phenotypes reminiscent of clinical symptoms of pneumococcal meningitis

Clinical features of pneumococcal meningitis include headache, fever, neck stiffness, and altered mental status.[29] Seizures occur in one out of five patients.[30] If left untreated by antibiotics, an extreme form of neck stiffness called opisthotonos, an abnormal posture where the back becomes extremely arched,[23] is exhibited. To validate our zebrafish model, we monitored the behavior and posture of larval zebrafish after injection of the mCherry-labeled *S. pneumoniae* D39 HlpA-mCherry strain in the HBV (Figure 1; STAR Methods). We observed that mCherry-positive pneumococci proliferate and migrate to colonize the brain ventricles and central canal over 24 h post injection (hpi) (Figures 1A and 1B). Freely swimming, vehicle-injected control larvae at 5 and 6 days post fertilization (dpf) typically explored their environment via slow locomotor bouts (Figures 1C–1G) typically occurring once a second.[31] By contrast, infected larvae swam less often (Figure 1E) as a possible reflection of sickness behavior and neuroinflammation.[32] When infected larval zebrafish swam, however, they exhibited locomotor bouts that lasted longer (Figure 1F) and covered a much larger distance traveled (Figures 1D and 1G), consistent with epileptic-like seizures occurring in ~25% of

(F) Quantification of bout duration in control versus infected fish. As infection progresses, swim bouts become substantially and progressively longer in infected fish while generally remaining stable in controls.
(G) Quantification of bout distance in control versus infected fish. Similarly to (E), infected fish swim substantially farther in a given bout than control fish (*$p < 0.05$).
(H) Bright-field image of a PBS-injected larva at 3 dpf.
(I) Spinal cord area (here in the control larva of H) was defined by manual tracing (red lines), from which a smoothing spline curve was fit (blue line).
(J) The resulting boundaries were used to isolate a masked portion of the red channel. Since this larva was not injected with fluorophores, this represents autofluorescence.
(K) The resulting image patch was summed along the x axis to derive a fluorescence plot.
(L) Curvature was locally determined along the x axis and plotted. Positive values indicate downward curvature, and negative values indicate upward curvature.
(M) Bright-field image of a larva injected with *S. pneumoniae* at 2 dpf and imaged at 32 hpi. Note the strong upward tail curvature.
(N) Similar spinal cord delineation as in (M) but applied to the larva in (K).
(O) Red channel fluorescence from the masked spinal cord of the infected larvae. Since this embryo was injected with mCherry-labeled *S. pneumoniae*, this plot provides a visual assessment of infection progression.
(P) Similar fluorescence plot as in (K). Note that fluorescence is overall higher than in (K).
(Q) Similar curvature plot as in (L). The larva's strong upward spinal curvature is reflected in the large downward deflection of the curvature plot midway along the anterior/posterior axis.
(R) Quantification of the absolute value of the curvature along the spinal cord in control (PBS) and infected fish. Infected fish exhibit significant greater spinal curvature ($p < 10^{-16}$). Red bars represent the medians. Boxplot represents IQR ± minimum/maximum sans outliers.
(S) Fluorescence was quantified along the spinal cord for all fish and plotted against overall curvature. In infected fish (in purple), there is a positive correlation between spinal fluorescence (i.e., implied infection progression) and spinal curvature ($R^2 = 0.0900$, $p = 0.0089$), while control fish (in black) do not show positive correlation ($R^2 = 0.0892$, $p = 0.1230$). n = 29 PBS-injected larvae; n = 75 *S. pneumoniae*-injected larvae.
See also Table S1.

infected fish.[33] Furthermore, the posture of infected larvae also became affected. While the body axis of vehicle-injected control larvae was reliably straight (Figures 1H–1L), infected larvae developed 24 h after the injection with *S. pneumoniae* pronounced dorsal arching (Figures 1M–1Q). The dorsal curvature remarkably scaled with the degree of bacterial invasion estimated by the fluorescence of the larvae injected with *S. pneumoniae* D39 fluorescent bacteria (observed both in red for HlpA-mCherry and green for HlpA-GFP; Figures 1R and 1S). Taken together, the reduced activity and abnormal posture in larval zebrafish whose CSF is invaded by bacteria are reminiscent of clinical features of pneumococcal meningitis.

Sensory neurons contacting the CSF respond *in vivo* to live *S. pneumoniae* invading the CSF

We know that overexpression of urotensin-related peptides (*urp1* and *urp2*) that are highly expressed by CSF-cNs[14] induces dorsal arching in zebrafish embryos and larvae.[12,14–19] We therefore hypothesize that CSF-cNs could be activated upon pneumococcal infection of the CSF. We investigated whether upon CSF pneumococcal infection, an activation of CSF-cNs could precede the occurrence of late symptom of dorsal arching (i.e., after 24 hpi). After *S. pneumoniae* injection in 2 dpf transgenic *Tg(pkd2l1:GCaMP5G)* larvae expressing GCaMP5G in CSF-cNs (STAR Methods), we monitored the activity of CSF-cNs for 24 h (Figures 2A–2D). In larvae injected with vehicle, CSF-cNs spontaneously exhibited baseline activity as small calcium transients (rarely rising above 50% ΔF/F; Figures 2C and 2E). By contrast, in infected larvae, a subset of CSF-cNs produced large and sustained calcium transients (mean maximum ΔF/F of 240%, mean duration of 13 s) (Figures 2D and 2F; Video S1). These massive calcium transients began as early as 12 hpi and continued within the same cells for several hours (Figures 2D, 2F, and 2G). Concomitant with the unusual activation of CSF-cNs in infected larvae, we observed an overall decline in baseline calcium activity relative to controls (Figure 2H). Note that under the same conditions, we did not observe recruitment of neutrophils in the CSF at the level of the central canal before 24 hpi (Figure S1), suggesting the response of CSF-cNs is due to bacteria or their products secreted in the CSF.

Determining whether active pathogenic bacteria are required to generate the observed neuronal activation during infection, we injected different bacterial preparations into the central canal. As before, the injection of vehicle did not trigger substantial CSF-cN activity and neither did the injection of non-pathogenic *E. coli* nor heat-killed *S. pneumoniae* (Figure 2I). In this series of experiments, only infection with live pathogenic pneumococci generated large CSF-cN transients ($p = 6.28E-16$) (Figures 2I and 2J). Taken together, these results suggest that the observed effect in CSF-cNs is specific to infection by live pneumococci.

CSF-cNs respond *in vitro* to cytolysins and microbial metabolites secreted by *S. pneumoniae*

Several meningeal pathogens produce pore-forming toxins that are major virulence factors; an example of this is the production of pneumolysin by *S. pneumoniae*.[34] Initially, we attempted to access the central canal directly via a pipette to test the response to pneumolysin *in vivo*; however, the small size of the central canal and the fact that CSF-cNs respond to mechanical stimulation[5] impeded this experiment. We therefore decided instead to test the effects of pneumolysin on a primary culture of CSF-cNs expressing the genetically encoded calcium indicator GCaMP5G together with tagRFP in the double-transgenic larvae *Tg(pkd2l1:tagRFP; pkd2l1:GCaMP5G)*.[5] By numerical simulations based on tests with pressure applications of fluorescent dyes, we estimated that during a 1-s pressure application, a CSF-cN *in vitro* is typically exposed to at most 50% of the initial concentration in the stimulation pipette, independent of the molecule's coefficient of diffusion that will only impact the decay of the chemical pulse (Figure 3A; STAR Methods). Thus, an initial concentration of 0.1 mg/mL pneumolysin diluted in artificial CSF (aCSF) leads to a transient chemical pulse of 0.05 mg/mL onto the cultured neurons (Figure 3A; rationales for doses of all applied compounds are provided in STAR Methods). In primary cultures, the focal pressure application of aCSF alone did not induce a response in CSF-cNs (Figures 3B, 3C, middle panel, and 3D; Video S2), showing that this pressure application was not sufficient to mechanically activate CSF-cNs. By contrast, exposure to 0.05 mg/mL pneumolysin led to a small and brief stimulus-locked calcium increase in CSF-cNs (median = 17.49% ± 14.51%; Figures 3B, right panel, and 3D; Video S2).

We next tested whether CSF-cNs respond to microbial metabolites secreted by *S. pneumoniae* during growth[35]—which could act as bitter compounds on taste receptor cells—similarly to what was previously shown for ciliated sensory cells in the mammalian airway epithelium.[2,36–39] Microbial metabolites secreted by *S. pneumoniae* include a number of microbial volatile organic compounds (mVOCs) that act indeed as bitter compounds, such as acetone, 2-butanone, 2-pentanone, 2-methylpropanal, dimethyl disulfide (DMDS), methylmercaptan, γ-butyrolactone, isopentanol, formaldehyde, and trimethylamine.[40,41] Exposure to a mixture of 50 mM bitter compounds, including acetone, 2-butanone, 2-pentanone, 2-methylpropanal, and DMDS, elicited large calcium transients in CSF-cNs (median ΔF/F = 101.25% ± 61%; Figures 3C and 3E–3G; Video S2; STAR Methods), an effect not observed with aCSF only (Figures 3C–3E). CSF-cN responses were larger for bitter compounds than for pneumolysin and mimicked more closely the response to live bacteria observed *in vivo*. When bitter compounds were tested individually, 2-pentanone and DMDS both induced responses (Figures 3H–3J and S2; Video S2), but only DMDS recapitulated in a dose-dependent manner the large responses observed with the mixture of compounds. This suggests that DMDS is a major bitter, metabolite-activating CSF-cN (Figure 3H). Taken together, these results show that CSF-cNs exhibited calcium responses to at least two different bacterial products: pneumolysin, a pore-forming cytolysin, and also mVOCs, classified as bitter compounds. The latter are especially effective in triggering massive calcium transients. These observations show that bacterial metabolites can activate CSF-cNs, indicating that they may contribute to the response of sensory neurons we observed *in vivo*.

CSF-cNs selectively express taste receptors and numerous peptides involved in innate immunity

To determine how CSF-cNs could respond to pneumococci, we analyzed CSF-cN-enriched transcripts (Figure 4). The spinal cord of 3 dpf larvae contains approximately 150 CSF-cNs (see cell counts in the transgenic line *Tg(pkd2l1:GFP)* that are all

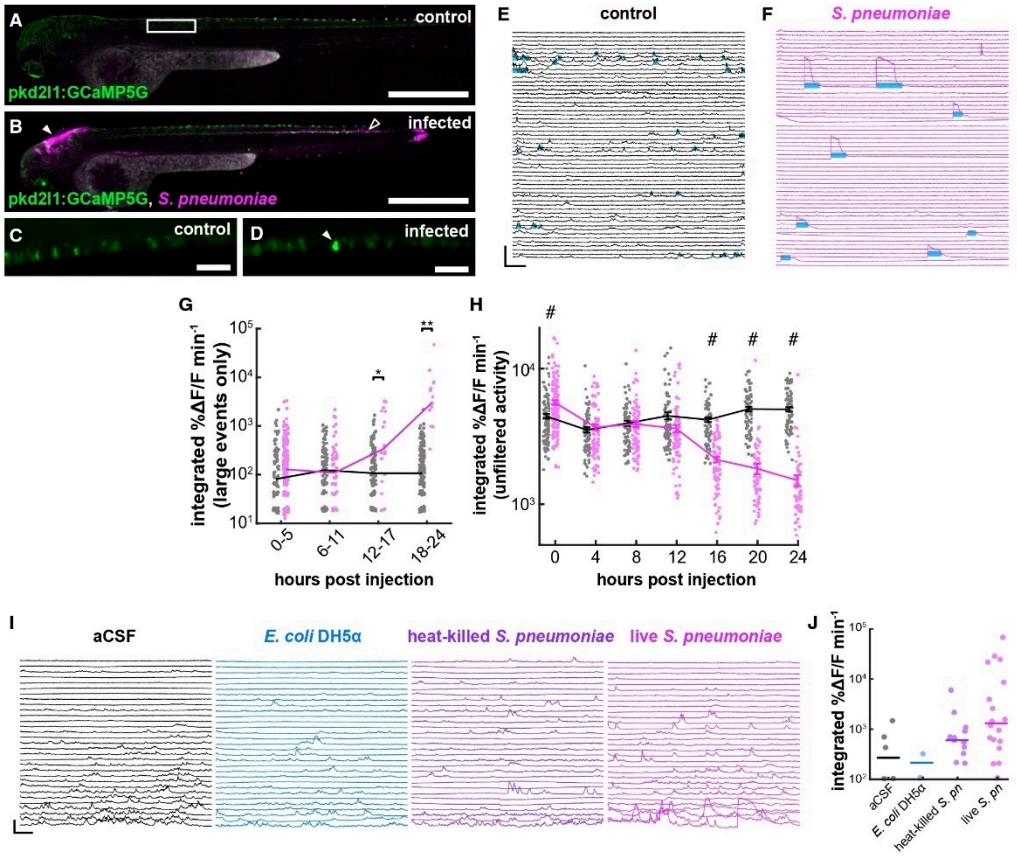

Figure 2. Activity of CSF-cNs drastically changes in response to the invasion of *Streptococcus pneumoniae* into the CSF

(A) Untreated 3 dpf *Tg(pkd2l1:GCaMP5G)* larva. Box indicates field of view for (C) and (D). Scale bars, 500 μm.

(B) Sibling larva, 24 hpi of fluorescently labeled *S. pneumoniae* into the hindbrain ventricle (HBV, indicated by filled arrowhead); empty arrowhead indicates extent of bacterial proliferation.

(C) Higher magnification image of control CSF-cN calcium imaging. Scale bars, 50 μm.

(D) Comparable image from an infected larva with *S. pneumoniae*. Arrowhead indicates a CSF-cN undergoing a high-amplitude transient.

(E) Ca^{2+} activity plots of uninfected CSF-cNs 21 h after the beginning of the experiment. Cyan bars indicate detected long-lasting high-amplitude events. Vertical scale, 500% ΔF/F; horizontal scale, 20 s. These events precede the arrival of neutrophils (Figure S1).

(F) Similar plots from CSF-cNs of infected larvae showing high-amplitude transients.

(G) Quantification of software-detected high-amplitude transients in control (gray) and *S. pneumoniae*-infected (magenta) larvae. Large transients appear 12 hpi (lines represent median values, Wilcoxon signed-rank test, *p < 0.0125, **p < 0.0063).

(H) Integrated Ca^{2+} activity in CSF-cNs in control (gray) and infected (magenta) larvae over 24 h of infection. Overall activity undergoes a decline over the course of infection (two-factor ANOVA, injection factor F = 124.36, $p = 1.61 \times 10^{-27}$, Scheffé post hoc testing, #p < 0.05, data are represented as mean ± SEM).

(I) Individual CSF-cN Ca^{2+} traces from 2 dpf zebrafish injected with aCSF, DH5α *Escherichia coli*, heat-killed *S. pneumoniae*, and live *S. pneumoniae*. Injection with live *S. pneumoniae* elicits by far the largest transients. Vertical scale, 200% ΔF/F; horizontal scale, 25 s.

(J) Quantification of software-detected large transients from the four conditions in (M); lines represent median values. More transients are observed in live infected fish than the other three conditions (chi-square test, p = 6.28E−16).

See also Figure S1, Table S1, and Video S1.

GFP positive; Figure S3). We therefore used fluorescence-activated cell sorting (FACS) to isolate GFP-positive CSF-cNs from guillotined 3 dpf *Tg(pkd2l1:GAL4; UAS:GFP)* larvae[9] (Figures 4A–4C; STAR Methods). Relative to the GFP-negative fraction, the GFP-positive fraction displayed elevated expression of known CSF-cN markers, such as *pkd2l1*,[20,21]

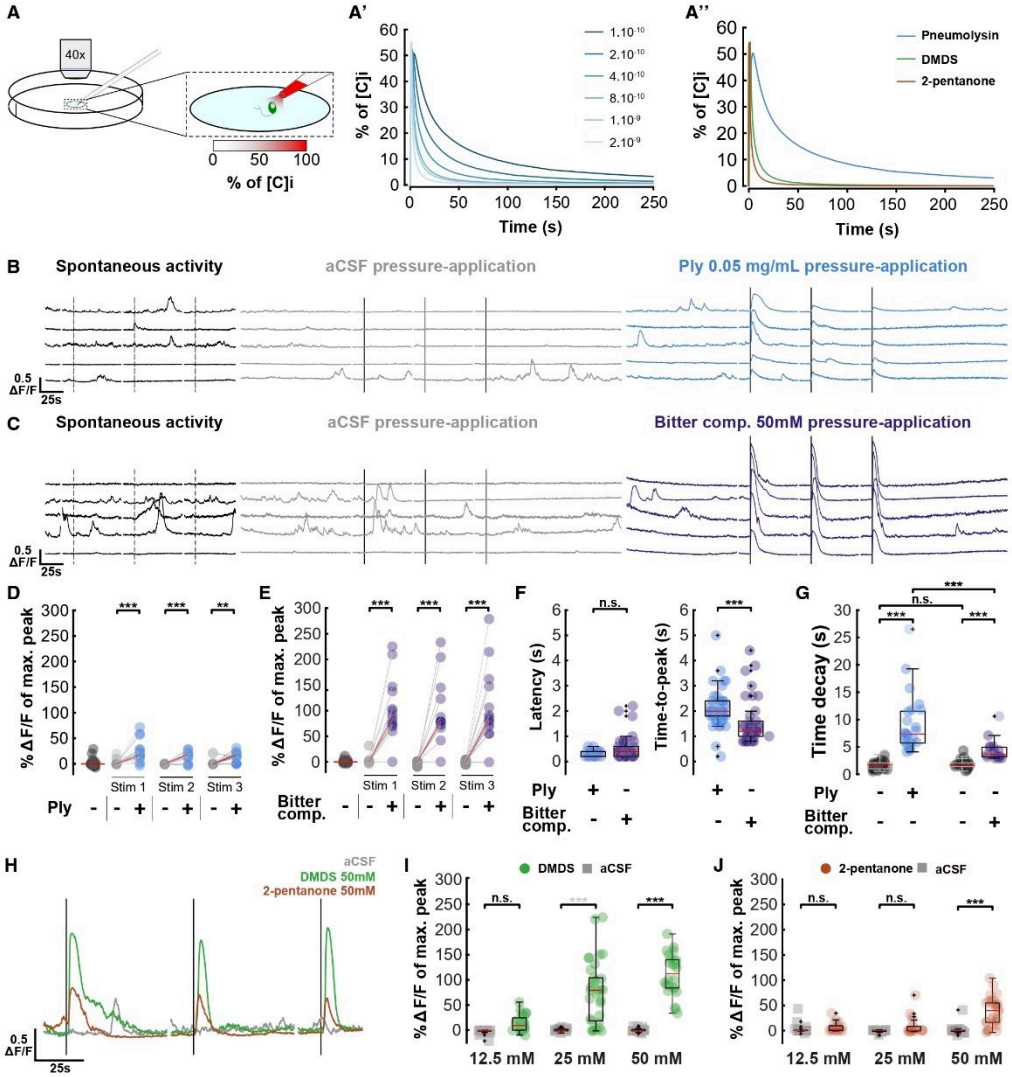

Figure 3. CSF-cNs respond *in vitro* to pneumolysin and bitter compounds

(A) Simulations of *in vitro* CSF-cN stimulation. (A) Schematic view of the *in vitro* stimulation experimental setup combining calcium imaging at 40×, 5 Hz and stimulation of CSF-cN with a gradient of molecule. (A') Simulation of the concentration of molecule sensed by CSF-cN for a range of coefficients of diffusion (from 1×10^{-10} to 2×10^{-9} m^2/s); [C]i corresponds to initial concentration in the stimulation pipette. (A'') Simulation of the concentration of pneumolysin (Ply), dimethyl disulfide (DMDS), and 2-pentanone; coefficients of diffusion: 1×10^{-10}, 1×10^{-9}, and 2×10^{-9} m^2/s, respectively; [C]i corresponds to initial concentration within the stimulation pipette.

(B) Representative individual *in vitro* CSF-cN Ca^{2+} traces from no stimulation control (left, dark), 3 successive 1-s stimulations of aCSF (middle, gray), and 3 successive 1-s stimulations of 0.05 mg/mL pneumolysin (Ply) (right, blue). Dark lines correspond to 1-s stimulations, and dashed lines correspond to putative 1-s stimulations during spontaneous activity. Vertical scale, 0.5 ΔF/F; horizontal scale, 25 s.

(C) Representative individual *in vitro* CSF-cN Ca^{2+} traces from no stimulation control (left, dark), 3 successive 1-s stimulations of aCSF (middle, gray), and 3 successive 1-s stimulations of 50 mM bitter compounds mix (right, purple). Bitter compound mix: acetone, 2-butanone, 2-pentanone, 2-methylpropanal, and

(legend continued on next page)

pkd1l2,[42,43] and the GABAergic neuronal marker *gad67*, but as expected, no hindbrain-specific markers (*raraa* and *rarab*) (Figure S4).

We then performed RNA-seq on 5 biological replicates and identified 202 transcripts that were enriched in GFP-positive CSF-cNs relative to GFP-negative cells (Figures 4D and 4E; Data S1; STAR Methods). This set contained all previously identified CSF-cN-specific transcription factors for differentiation (members of the *nkx* and *gata* family, *tal2*, and *olig2*),[43–47] enzymes involved in GABA synthesis (*gad65/67*),[20] the transient receptor potential channel *pkd2l1* and associated protein *pkd1l2*,[20,21,42,43] the secreted peptides involved in dorsal arching of the spine (*urp1* and *urp2*),[12,14,15] and the somatostatin *sst1.1*.[48–50]

To validate our CSF-cN transcriptome, we combined fluorescence *in situ* hybridization (FISH) with GFP antibody staining in 1 and 3 dpf *Tg(pkd2l1:GCaMP5G)* transgenic larvae for 47 of the enriched transcripts and found 40 (85%) where gene expression was confirmed and selective to CSF-cNs (Figures 4F–4J″ and S5). The 7 out of 47 genes whose expression was not confirmed corresponded to genes expressed at low level or to contamination from floor plate or motor neurons (the close disposition of the latter can be seen in Figure 4G). In agreement with CSF-cN responses to mVOCs *in vitro* (Figures 3C–3E), orphan taste receptors from the type 2 taste receptor family responding to bitter compounds, *tas2r3a* and *tas2r3b*, were the most enriched transcripts in CSF-cNs (Figures 4D and 4E). We generated a double-knockout zebrafish mutant for the taste 2 receptors *tas2r3a* and *tas2r3b* (Figures S6A–S6C). The calcium response of CSF-cNs to the bitter compound DMDS in these double-knockout mutants was not abolished (Figure S6D), possibly due to compensation by other taste receptors expressed in CSF-cNs that may occur.

The entry of *S. pneumoniae* in the brain triggers host cells to secrete proinflammatory cytokines (such as TNF-α, IL-1, and IL-6) and chemokines (such as monocyte chemoattractant protein-1, macrophage inflammatory protein-1α, and IL-8). Interestingly, we found that CSF-cNs express several immune-related receptors, including the TNF-α receptor (*tnfrsf1a*), IL-13 receptor, and IL-17 receptor (Figure 4E), and several inflammasome components (*asc*, *caspa/b*, and *nod1/2*).

In the category of secreted peptides and proteins, CSF-cNs expressed, in addition to the well-known somatostatin 1.1[49] and urotensin-related peptides,[14] numerous secreted factors implicated in immune responses: *esm1*, *nppc*, *msmp2*, *scg2a*, *sst3*, *ntn1b*, and *txn* (Figures 4G and 4H), some of which were expressed into adulthood (Figures 4I and 4J″).

CSF-cNs upregulate transcripts for secreted factors involved in innate immunity during pneumococcal infection

To investigate changes in CSF-cN expression upon infection, we used FACS again to isolate GFP-positive CSF-cNs from *Tg(pkd2l1:GAL4; UAS:GFP)* larvae and performed RNA-seq on sorted CSF-cNs at 24 hpi of either vehicle or *S. pneumoniae* (Figure 5; STAR Methods). We validated that transcripts (*pkd2l1* and *pkd1l2*) previously found to be CSF-cN specific were again

dimethyl disulfide (DMDS). Dark lines correspond to 1-s stimulations, and dashed lines correspond to putative 1-s stimulations during spontaneous activity. Vertical scale, 0.5 ΔF/F; horizontal scale, 25 s.

(D) Quantification of calcium transients' amplitude elicited by pneumolysin pressure application. Paired line plots showing responses of individual cells to absence of stimulation (corresponding to spontaneous activity, on the left in black circle) or 3 successive 1-s stimuli of aCSF (gray circle) versus 0.05 mg/mL pneumolysin (Ply, blue circle). Two-factor ANOVA, treatment factor $F = 66.185$, $p = 1.47 \times 10^{-12}$, Tukey HSD post hoc testing, ***$p < 0.001$. Red bar: median ΔF/F (median spontaneous activity = 0.03%; median Ply = 17.49% and median aCSF = 0.19% for stimulation 1; median Ply = 18.78% and median aCSF = 0.03% for stimulation 2; median Ply = 17.20% and median aCSF = −0.20% for stimulation 3), 16 responding cells out of 17.

(E) Quantification of the amplitude and kinematics of calcium transients elicited by pressure application of bitter compounds. Paired line plots showing responses of individual cells to absence of stimulation (corresponding to spontaneous activity, on the left in black circle) or 3 successive 1-s stimuli of aCSF (gray circle) versus 50 mM bitter compounds mix (purple circle). Two-factor ANOVA, treatment factor $F = 116.762$, $p < 2.0 \times 10^{-16}$, Tukey HSD post hoc testing, ***$p < 0.001$. Red bar: median ΔF/F (median spontaneous activity = 0.10%; median bitter compounds = 87.26% and median aCSF = 0.05% for stimulation 1; median bitter compounds = 78.85% and median aCSF = −0.13% for stimulation 2; median bitter compounds = 83.64% and median aCSF = −0.50% for stimulation 3), 15 responding cells out of 15.

(F) Quantification of latency and time-to-peak after pneumolysin (blue circle) or bitter compounds in mix (purple circle) stimuli. Red bar: median (for latency, median Ply = 0.2 s and median bitter compounds = 0.4 s, $p > 0.05$; for time-to-peak, median Ply = 2 s and median bitter compounds = 1.2 s, $p < 1 \times 10^{-6}$; Kolmogorov-Smirnov test). Boxplot represents IQR ± minimum/maximum sans outliers.

(G) Quantification of time decay for spontaneous activity (black circle) or after pneumolysin (blue circle) or bitter compounds in mix (purple circle) stimuli. Red bar: median (on the left, median Ply = 7.36 s and median spontaneous activity = 1.71 s, $p < 1 \times 10^{-11}$; on the right, median bitter compounds = 3.59 s and median spontaneous activity = 1.69 s, $p < 1 \times 10^{-6}$, Ply and bitter compounds decays are different, $p < 1 \times 10^{-4}$; Kolmogorov-Smirnov test). Boxplot represents IQR ± minimum/maximum sans outliers. Longer time decay for Ply compared with bitter compounds in mix is probably due to a smaller coefficient of diffusion as shown in (A″).

(H) Illustration of calcium transients after pressure application of DMDS and 2-pentanone. Representative individual *in vitro* CSF-cN Ca^{2+} traces from 3 successive 1-s stimulations with either aCSF (gray), DMDS 50 mM (green), or 2-pentanone 50 mM (brown). Dark lines correspond to 1-s stimulations. Vertical scale, 0.5 ΔF/F; horizontal scale, 25 s.

(I) Quantification of calcium transients after aCSF (gray circle) or DMDS (green circle) stimuli. Two-factor ANOVA, treatment factor $F = 170.58$, $p \leq 2.0 \times 10^{-16}$, concentration factor $F = 29.43$, $p = 1.66 \times 10^{-11}$, Tukey HSD post hoc testing, ***$p < 0.001$, n.s., not significant. Red bar: median ΔF/F (median 12.5 mM DMDS = 9.44% and median aCSF = −1.20%, 6 responding cells out of 8; median 25 mM DMDS = 78.96% and median aCSF = −0.26%, 8 responding cells out of 10; median 50 mM DMDS = 112.09% and median aCSF = −0.54%, 8 responding cells out of 8). Boxplot represents IQR ± minimum/maximum sans outliers.

(J) Quantification of calcium transients after aCSF (gray circle) or 2-pentanone (brown circle) stimuli. Two-factor ANOVA, treatment factor $F = 53.48$, $p = 2.67 \times 10^{-11}$, concentration factor $F = 13.89$, $p = 3.53 \times 10^{-6}$, Tukey HSD post hoc testing, ***$p < 0.001$, n.s., not significant. Red bar: median ΔF/F (median 12.5 mM 2-pentanone = 2.19% and median aCSF = 0.14%, 4 responding cells out of 6; median 25 mM DMDS = 0.63% and median aCSF = 0.04%, 3 responding cells out of 6; median 50 mM DMDS = 39.72% and median aCSF = −0.39%, 9 responding cells out of 10). Boxplot represents IQR ± minimum/maximum sans outliers. Figure S2 shows similar results for bitter compounds that do not activate CSF-cNs, suggesting some specificity.

See also Figure S2 and Video S2.

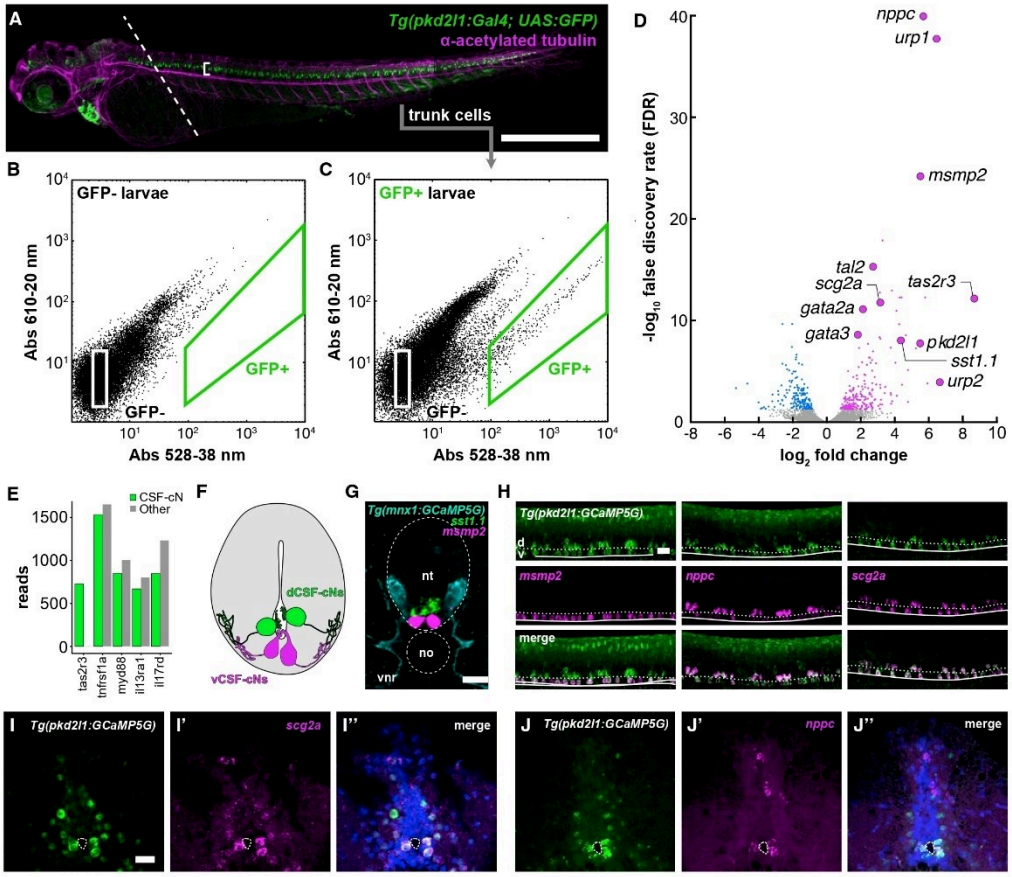

Figure 4. The CSF-cN transcriptome reveals the expression of taste receptors and immune-related secreted factors

(A) 3 dpf zebrafish *Tg(pkd2l1:GAL4; UAS:GFP)* larva immunostained for GFP (green) and acetylated tubulin (magenta). Dashed line indicates plane of decapitation prior to dissociation (anterior tissues were discarded to exclude labeled cells in brain and heart); bracket indicates CSF-cN domain. Scale bars, 500 μm.

(B) Calibration FACS plot from non-transgenic siblings.

(C) FACS plot from a typical dissociation of cells from transgenic larvae. A small fraction (~0.2% of input) of cells is green-shifted. Figure S3 quantifies the upper bound of cells/larvae we could reasonably expect to obtain. In Figure S4A, we use qPCR to show that this fraction appeared to be CSF-cNs.

(D) Volcano plot of all RNA-seq replicates: 202 transcripts were enriched in CSF-cNs. Figure S4B provides more categorical information on these hits. Figure S6 shows that knocking out individual CSF-cN-enriched taste receptors identified by this approach did not impair CSF-cNs' ability to detect bitter compounds.

(E) Quantification of reads for selected immune-related receptors in both GFP$^+$ CSF-cNs and GFP$^-$ (i.e., all other) cells.

(F) Schematic representation of a transverse section of the spinal cord and central canal showing the disposition of dorsolateral CSF-cNs (dCSF-cNs, green) and ventromedial CSF-cNs (vCSF-cNs, magenta).

(G) A mixed fluorescence *in situ* hybridization/immunofluorescent stain showing the disposition of motor neurons (cyan, *Tg(mnx1:GCaMP5)*), dCSF-cNs (green, *sst1.1*), and vCSF-cNs (magenta, *msmp2*). The section here is a frontal section, e.g., a cross-section of the spinal cord. Scale bars, 50 μm.

(H) Fluorescence *in situ* hybridization reveals that the putative immune-related secreted factors *msmp2*, *nppc*, and *scg2a* are expressed in CSF-cNs. These confocal stacks are lateral stacks, so at 90° orientation to the image in (G). Scale bars, 50 μm. Figure S5 shows additional *in situ* hybridization results from some of these RNA-seq hits; most hits we assessed were verified histologically.

(I) Transverse section of adult *Tg(pkd2l1:GCaMP5G)* spinal cord; expression of *scg2a* is specific to CSF-cNs. Scale bars, 50 μm.

(J) Adults continue to express *nppc* and *scg2a* in CSF-cNs.

See also Figures S3–S6, Table S1, and Data S1.

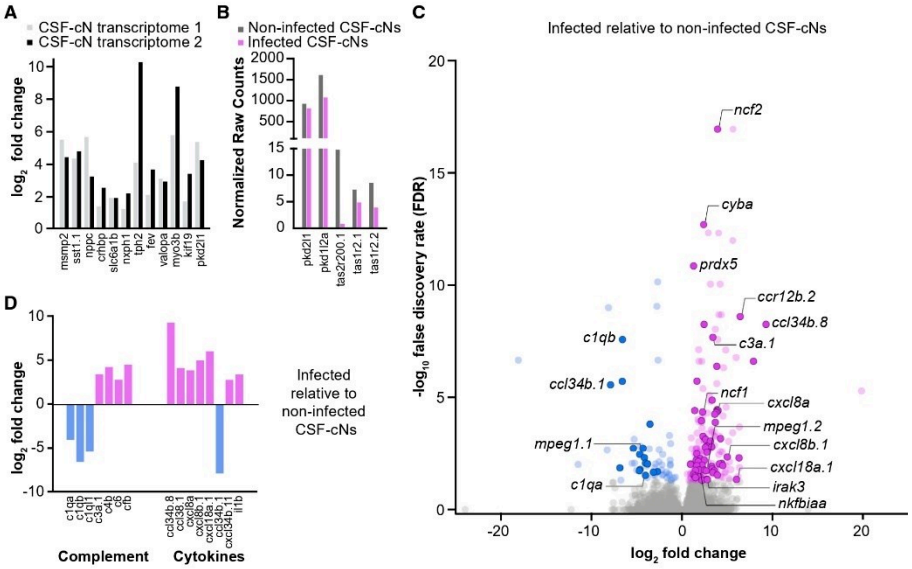

Figure 5. RNA-seq shows upregulation of complement system of the alternative and terminal pathway as well as cytokines in CSF-cNs during *S. pneumoniae* infection

(A) Log fold change bar plot comparing enrichment of known CSF-cN transcripts in the GFP$^+$ fraction with control GFP$^-$ cells in the original differential transcriptome 1 (gray bars; see Figure 4 and Table S1) and subsequent transcriptome 2 for non-infected larvae (black bars; see Table S1).

(B) A plot of raw reads comparing selected receptors in non-infected (gray bars) and infected (pink bars) CSF-cNs, showing that the expression of receptors that are specifically enriched in CSF-cNs (*pkd2l1*, *pkd1l2*, and taste receptors) remains stable.

(C) Volcano plot comparing the expression of transcripts in infected CSF-cNs relative to uninfected CSF-cNs. Transcripts for several immune-related secretory compounds are differentially expressed.

(D) Log fold change bar plot of selected immune-related transcripts corresponding to complement system and cytokines from the same data as in (B). We observe significant upregulation of complement system of the alternative (C3), classical (C4), and terminal (C6) pathway (left side) as well as cytokines (right side).

See also Table S1 and Data S1.

enriched in this dataset, and we found numerous taste 1 and 2 receptor families such as *tas2r200.1*, *tas1r2.2*, and *tas1r2.1* (Figure 5A; Data S1), while transcripts for receptors (*pkd2l1*, *pkd1l2*, *tas1r2.1*, *tas2r200.1*, and *tas1r2.2*) did not increase upon infection in CSF-cNs (Figure 5B). By contrast, numerous transcripts encoding immune-related secretory compounds were upregulated in CSF-cNs upon infection (76 out of 231, 33%; Figures 5C and 5D; Data S1): multiple cytokines including IL-1β and IL-8/CXCL8 (Figure 5D, right), and complement factors C3 (alternative pathway), C4 (classical and lectin pathway), and C6 (terminal pathway) (Figure 5D, left).

Secretion from CSF-cNs contributes to host defense during pneumococcal infection

To test the role of CSF-cNs in host defense, we ablated CSF-cNs at 2 dpf using the nitroreductase/metronidazole (MTZ) chemogenetic system (Figures 6A, 6B, 6D, and S3)[51] or selectively blocked their secretion using the botulinum toxin B light chain fused to GFP (BoTxBLC-GFP; Figures 6C, 6E, and 6F).[52] After MTZ treatment (Figures 6A and 6B), nitroreductase-expressing and non-expressing larvae were infected the following day and scored for survival every 12 h. We observed that MTZ itself conferred a survival benefit in control fish (38% survival 96 hpi; Figure 6D). Larvae in which CSF-cNs were ablated, however, exhibited a nearly 3-fold decrease in survival (13% survival 96 hpi; Figure 6D).

As large and sustained calcium transients, observed in CSF-cNs during pneumococcal infection (Figure 2), enable the SNARE-dependent docking and releasing of dense core vesicles containing peptides,[53–56] we next tested the role of SNARE-dependent neurosecretion from CSF-cNs during infection. By cleaving VAMP2,[57] we previously showed that the expression of BoTxBLC effectively prevents vesicular fusion and release in CSF-cNs.[52] In *Tg(pkd2l1:GAL4; UAS:BoTxBLC-GFP)* transgenic larvae in which BoTxBLC was selectively expressed in CSF-cNs (Figure 6C),[52] the survival following infection at 2 dpf was reduced by 2-fold, compared with their control siblings (15% compared with 32% survival at 96 hpi; Figure 6E). Accordingly, more live bacteria were observed 24 h after infection in transgenic larvae in which CSF-cN neurosecretion was altered, compared with control siblings (Figure 6F). In order to test whether individual CSF-cN peptides were involved in this effect, we generated zebrafish knockout mutants for the peptides *scg2a*, *nppc*, and *esm1* found specifically in CSF-cNs in the trunk. None of the individual homozygous

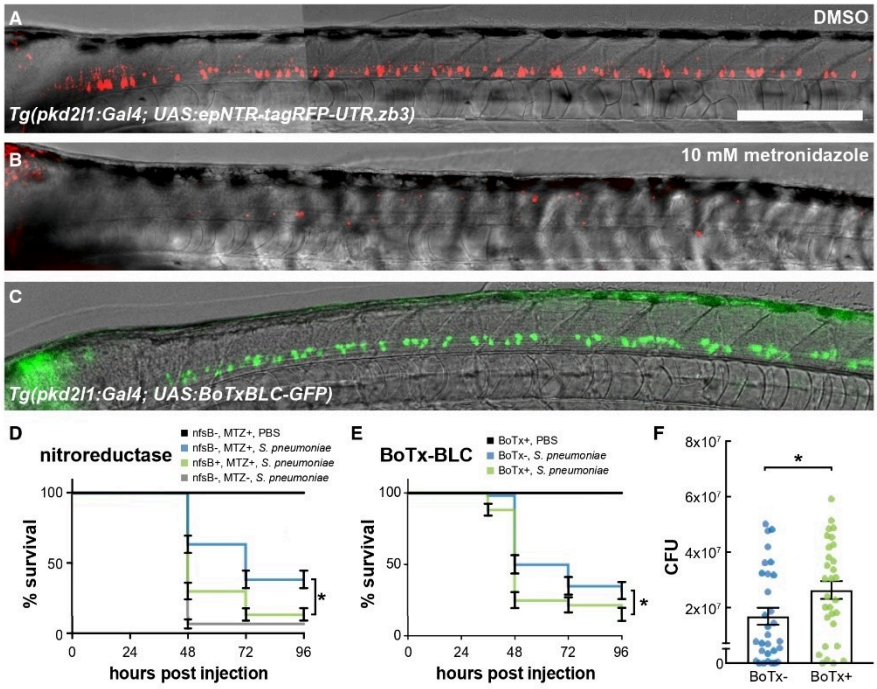

Figure 6. Secretory activity of CSF-cNs confers a survival benefit during pneumococcal meningitis

(A) *Tg(pkd2l1:GAL4; UAS:epNTR-tagRFPT-UTR.zb3)* larva at 3 dpf following 24 h of incubation in 0.1% DMSO. Scale bars, 500 μm. Figure S3 addresses how complete NTR expression is in the full complement of CSF-cNs.

(B) Sibling larva incubated for the same time period in 10 mM metronidazole (MTZ). All tagRFP$^+$ CSF-cNs are lost.

(C) Expression of BoTxBLC-GFP in the *Tg(pkd2l1:GAL4; UAS:BoTxBLC-GFP)* larva at 3 dpf.

(D) Survival curves of *Tg(pkd2l1:GAL4; UAS:epNTR-tagRFPT-UTR.zb3)*(nfsB) larvae and their siblings when exposed to metronidazole or DMSO from 1 to 2 dpf, washed with fish facility water, and subsequently infected with 4,000 CFU *S. pneumoniae*. Metronidazole alone slightly protects larvae against infection by *S. pneumoniae* (compare blue and gray lines, log-rank test, $p < 0.0001$). However, metronidazole-mediated ablation of CSF-cNs confers a large survival deficit (compare blue and green lines, log-rank test, $p = 0.0002$). The survival data represent the mean ± SEM of three individual experiments with n = 20 larvae per group (total n = 60 per group).

(E) Survival curves of *Tg(pkd2l1:GAL4; UAS:BoTxBLC-GFP)* ("BoTx") larvae (green line) and non-transgenic sibling controls (blue line) injected with ~300 CFU *S. pneumoniae* D39 wild-type strain into the hindbrain ventricle at 2 dpf reveal that BoTx-expressing larvae exhibit higher mortality rates (log-rank test, $p = 0.0065$). The survival data represent the mean ± SEM of three individual experiments with n = 20 larvae per group (total n = 60 per group). Figure S7 shows that knocking out individual secreted factors identified by the transcriptome does not impair larval survival in the meningitis model.

(F) *Tg(pkd2l1:GAL4; UAS:BoTxBLC-GFP)* (referred to as "BoTx") larvae (green line) exhibit higher bacterial loads at 24 h post injection as compared with non-transgenic sibling controls (unpaired t test, $p = 0.0368$). Each dot represents a single larva. Error bars = mean ± SEM of three individual experiments with n = 10 larvae per group (total n = 30 per group).

See also Figures S3 and S7 and Table S1.

mutants statistically differed in terms of survival, compared with their control siblings (Figure S7), suggesting that multiple secretory compounds act in concert. Altogether, our results indicate that CSF-cNs contribute to host survival in response to pneumococcal meningitis via VAMP2-dependant extracellular secretion, likely via the release of multiple secreted factors.

CSF-cNs respond to multiple types of pathogens

To test whether CSF-cNs respond to other pathogen-related cues, we tested CSF-cN response to supernatant of *S. pneumoniae*, to culture medium from cells infected with a neurotropic virus (Sindbis virus; SINV), as well as to another Gram-positive bacterium that is known to cause meningitis, *Listeria monocytogenes* (Figure 7). *S. pneumoniae* supernatant elicited large calcium responses in CSF-cNs *in vitro* (73.35% on average observed in all cells tested, n = 6; Figures 7A and 7B). Similarly, the UV-inactivated supernatant of cells infected with SINV elicited large calcium transients in CSF-cNs *in vitro* that were not observed in the control supernatant (45.63% on average observed in all cells tested, n = 7; Figures 7C and 7D). Finally, we tested the response of CSF-cNs to *L. monocytogenes in vivo* using the same injection paradigm

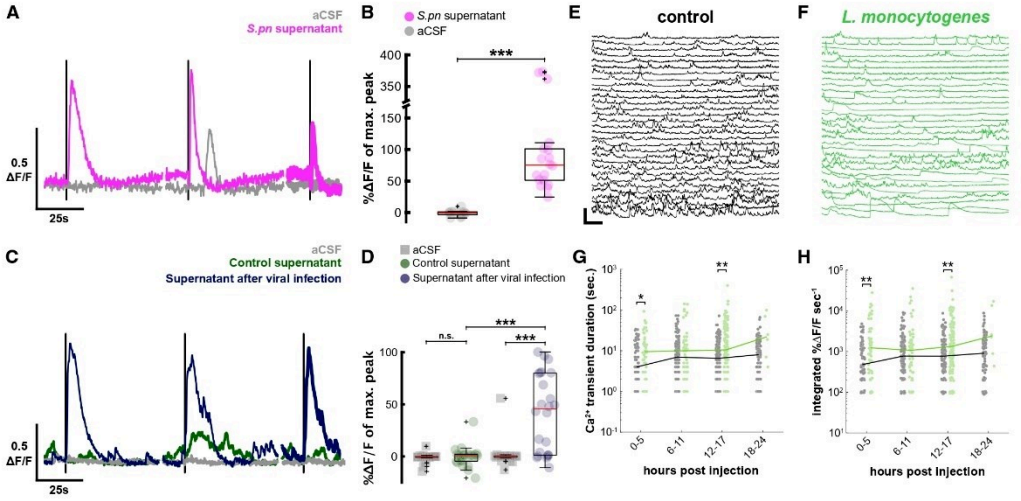

Figure 7. *Streptococcus pneumoniae* supernatant, virus culture supernatant, and *Listeria monocytogenes* infection also activate CSF-cNs

(A) Representative individual *in vitro* CSF-cN Ca^{2+} traces from 3 successive 1-s stimulations of aCSF (gray) and supernatant (purple). Dark lines correspond to 1-s stimulations. Vertical scale, 0.5 ΔF/F; horizontal scale, 25 s.

(B) Quantification of calcium transients after aCSF (gray circle) or *S. pneumoniae* supernatant (purple circle) stimuli. Paired t test, $p = 5.0 \times 10^{-4}$, ***$p < 0.001$. Red bar: median ΔF/F (median *S. pneumoniae* supernatant = +75.35% versus median aCSF = −0.73%, n = 6 cells). Boxplot represents IQR + minimum/maximum sans outliers.

(C) Representative individual *in vitro* CSF-cN Ca^{2+} traces from 3 successive 1-s stimulations of aCSF (gray), UV-inactivated supernatant of BHK cells infected with Sindbis virus (blue), and control BHK supernatant (green). Dark lines correspond to 1-s stimulations. Vertical scale, 0.5 ΔF/F; horizontal scale, 25 s.

(D) Quantification of calcium transients after aCSF (gray circle), control supernatant (green circle), or supernatant after viral infection (blue) stimuli. Two-factor ANOVA, treatment factor F = 24.52, $p = 3.32 \times 10^{-6}$, Tukey HSD post hoc testing, ***$p < 0.001$. Red bar: median ΔF/F (median control supernatant = +0.82% versus median aCSF = −0.26%, n = 8 cells; median supernatant after virus infection = 45.63% versus median SF = −0.22%, n = 7 cells; median 100 mM DMDS = 112.09% versus median aCSF = −0.54%, n = 8 cells.

(E) *In vivo* Ca^{2+} activity of CSF-cNs in uninfected larvae 8 h after injection in the brain ventricle. Vertical scale, 250% ΔF/F; horizontal scale, 20 s.

(F) Long-lasting and large calcium transients from larvae infected with *L. monocytogenes* occur in a similar manner as with *S. pneumoniae*.

(G) Quantification of duration of software-detected high-amplitude transients in control (gray) and *L. monocytogenes*-infected (green) larvae (Wilcoxon signed-rank test, *$p < 0.0125$, **$p < 0.0063$). Lines indicate median values.

(H) Similar quantification of integrated signal of large transients during *L. monocytogenes* infection.

See also Table S1.

as with *S. pneumoniae* (Figures 7E–7H). Our results suggest that CSF-cNs not only respond to live *S. pneumoniae* but also to their by-products secreted upon infection, as well as other bacteria and viruses.

DISCUSSION

Pathogenetic steps of pneumococcal meningitis involve mucosal colonization and invasion, survival, and replication in the bloodstream, followed by traversal of the blood brain/CSF barrier.[26] How the initial host immune response is orchestrated in the phase of bacterial penetration in the CSF remains incompletely understood. In a meningitis model in larval zebrafish, we show here that central sensory neurons respond to the invasion of *S. pneumoniae* dividing in the CSF and that neurosecretion from these neurons contributes to host survival. The timing of this response suggests that the phenomena we report on in the spinal cord do not likely relate to the earliest steps of detection of pathogens in the CNS but to later stages that nonetheless precede changes in muscle tonus. Owing to the role of CSF-cN peptides in triggering dorsal arching, we emphasize as well that CSF-cN activation may instead explain the evolution of symptoms at the advanced stage of meningitis, including the hallmark stiffness of the neck and opisthotonos.

Response to pathogenic bacteria proliferating in the CSF

We tested whether CSF-cNs could be directly or indirectly activated by chemical cues secreted by pathogenic bacteria during growth. As we did not observe an activation of ependymal radial glial cells—the most prominent CSF-contacting cell type along the central canal—during the *S. pneumoniae* infection, we hypothesized that bacterial products could trigger a response in CSF-cNs. To support this hypothesis, we found that CSF-cNs selectively express orphan taste 2 receptors for bitter compounds. We further demonstrated *in vitro* that CSF-cNs exhibit calcium transients in response to microbial metabolites acting as bitter compounds and to pneumolysin, a cytolysin and major

virulence factor released by pneumococci during growth. The CSF-cN response to bitter compounds was stronger than that to pneumolysin. These observations suggest that bacterial metabolites could directly trigger the response of sensory neurons we observed *in vivo*. Remarkably, the response to pathogenic bacteria as long and massive calcium transients occurs in a subset of CSF-cNs, possibly due to local changes in the growth and structures formed by bacteria. While dorsal arching appears at least 24 hpi, these transients occur in fully paralyzed, agarose immobilized fish well before 24 hpi, indicating that CSF-cN activation precedes the start of spinal curvature. CSF-cN calcium transients do not originate from pre-apoptotic calcium phenomenon, as they recur in individual cells over many hours without apparent cell death. *In vivo*, heat-killed bacteria and non-virulent bacteria failed to elicit as strong a response as we observed during live infection, suggesting that metabolites released by live bacteria proliferating in the CSF, or proinflammatory cues from host cells infected by the pathogenic bacteria, are necessary to activate CSF-cNs. Secretion of bitter compounds by bacteria has been shown to activate chemosensory neurons in the lung epithelium via type 2 taste receptors.[35–37,39,40,58,59] We show here that similarly at least two of these bitter compounds, DMDS and 2-pentanone, known to be secreted by *S. pneumoniae*,[40,41] strongly activate CSF-cNs in primary cultures. DMDS is also known to be secreted by *Neisseria meningitidis*, *Haemophilus influenzae*, and *L. monocytogenes*, after *S. pneumoniae*—the most common causative pathogens of bacterial meningitis.[26,35,58,60]

This initial study begins to address the diversity of pathogens that can cause CNS infection. In addition to responding to pneumococcal infection, we have evidence that CSF-cNs also respond to *L. monocytogenes*, the third most common cause of community-acquired bacterial meningitis.[27] We found that CSF-cNs also responded to the supernatant of cells infected by SINV, a neurotropic virus in zebrafish.[61] Future studies should address mechanisms by which CSF-cNs can respond to such diverse pathogens and further characterize the diversity of pathogens that can activate CSF-cNs.

Promotion of host survival during a bacterial infection of the CNS

During an infection with *S. pneumoniae*, when comparing survival of zebrafish larvae without CSF-cNs with that of their control siblings, CSF-cNs confer a 3-fold survival benefit to the host. We found that the selective blockage of neurosecretion in CSF-cNs led alone to a 2-fold reduction of survival in infected larvae. Accordingly, we found an elevated bacterial load in larvae where neurosecretion had been impaired. Although we did not monitor *in vivo* exocytosis at the CSF-cN membrane in the context of infection, our results from calcium imaging, transcriptome during infection, and survival upon silencing of CSF-cN release are all consistent with a model in which, upon activation, CSF-cNs release compounds that improve survival of the host (see graphical abstract). CSF-cNs can secrete multiple neuropeptides (*somatostatin 1.1*, *secretogranin 2a*, and *nppc*, among others; Figure 4) that they highly express at baseline together with the secreted compounds whose expression we found unregulated during an infection (Data S1), including cytokines and complement factors (Figures 5C and 5D). The mechanisms by which CSF-cNs promote host survival likely involve the secretion of multiple factors, including antimicrobial peptides such as secretogranin 2a[62] or the release of factors modulating inflammatory signaling (*msmp2*, *esm1*, *txn*, *nppc*, *sst3*, and *ntn1b*).[63–70] Knocking out single peptides did not lead to a decrease in survival in our infection model, possibly due to redundancy.[71] Combining knockouts of multiple peptides may be needed to observe an effect on survival rates. Since large calcium transients such as those observed in CSF-cNs during pneumococcal infection are typically necessary for neurosecretory cells to release the content of dense core vesicles in which peptides and secreted proteins are loaded,[53] we speculate that the large transients observed in CSF-cNs during the infection induce secretion. The reduced survival that we observed for zebrafish larvae with impaired CSF-cN secretion supports this hypothesis. Interestingly, an activation of broad neurosecretion in CSF-cNs would lead to an increase in the circulation of peptides of the urotensin family, which recently have been shown to precisely elicit dorsal arching in *Xenopus* and zebrafish embryos and larvae.[12,14–19] By this means, CSF-cN activation during bacterial infection could directly lead to the postural defects referred to as stiffness of the neck and opisthotonos, which are pathognomonic signs for meningeal infection in patients of unknown origin.

Taken together, our data reveal that CSF-cNs can play an important role in CNS defense by tasting the CSF to detect the presence of multiple bacterial and viral pathogens and by secreting factors that enhance the innate immune response. It does, however, have some limitations. First, our observations that pneumolysin and bacterial metabolites elicit calcium transients in CSF-cNs *in vitro* only suggest that these molecules may be involved *in vivo*. Accordingly, CSF-cNs express multiple orphan bitter taste receptors that could mediate the response to bacterial metabolites, but CSF-cN response to bitter compounds was not abolished in double bitter taste receptor mutants for *tas2r3a/b*. Further studies are needed to decipher the contribution of these pathways to CSF-cN response during pneumococcal infection as well as the chemical cues secreted by bacteria *in vivo*. The redundancy of taste receptor expression in CSF-cNs suggests that loss of function of a subset only may not be sufficient to ablate the calcium response to pathogens. Furthermore, we serendipitously identified two likely *tas2r3* paralogs in our fish, but there could be more due to incomplete annotation of the genome.

Second, consistent with an induction of CSF-cN neurosecretion during infection, larval zebrafish exhibited a dorsal arching posture, in a similar manner to that described upon injection of CSF-cN-specific peptides from the urotensin family.[12,14–19] Upon pneumococcal infection of the CNS, we showed that CSF-cNs upregulated the expression of secreted factors (cytokines and complement factors). Together with the evidence that blocking secretion from CSF-cNs reduced host survival and increased bacterial loads, our results point toward an activation of secretion of CSF-cNs during infection to promote innate immunity. We were unable to affect post-infection survival by knocking out any of the expressed secreted factors individually. However, again, any individual loss of function may be insufficiently deleterious as peptides may exhibit redundancy. Future studies will be needed to monitor vesicular fusion associated

with CSF-cN neurosecretion *in vivo*. Third, our results indicate that ciliated sensory neurons in contact with the CSF exhibit categorically different calcium responses to pathogenic bacteria *in vivo*, although they homogeneously responded to pneumolysin and bitter compounds *in vitro*. This discrepancy suggests that the CSF in the central canal is a heterogeneous medium, where pneumococci may differ locally in terms of density or state during an infection. Although estimating the density and movements of bacteria is theoretically possible *in vivo* by using confocal microscopy with mCherry-positive bacteria, monitoring two channels to collect the information of CSF-cN activation does lead to phototoxicity and subsequent silencing of activity in CSF-cNs. This experiment could therefore not be achieved with the fluorescent sensors available for monitoring calcium and bacteria simultaneously *in vivo*. It is critical to note here that the observed calcium transients may not correspond to the earliest steps of detection of pathogens as they occur more than 10 h into infection. CSF-cNs may therefore contribute more to later symptoms (such as opisthotonos and seizures) rather than to initial pathogen detection. We effectively did correlate the loss of CSF-cN function with reduced survival. However, our study did not show the causal link between CSF-cN activation via massive calcium transients and larval survival. As it is well known for other neurosecretory systems, massive calcium transients are associated with exocytosis of dense core vesicles containing peptides. Since blocking neurosecretion specifically in CSF-cNs reduced survival, we propose that CSF-cNs are activated by the presence of bacteria in the CSF and respond by secretion to boost innate immunity. Whether CSF-cN calcium events are necessary to improve survival will be the subject of subsequent studies.

Similarity with peripheral sensory neurons involved in proprioception and pain

CSF-cNs are located in an ideal position to respond to pathogenic bacteria invading the CSF, as well as to modulate immunity in the CNS by interacting with resident microglia and circulating leukocytes recruited in the ventricular space. Our discovery that *in vivo*, central sensory neurons are activated by live pathogens in the CSF and that they confer a survival benefit to the host recalls recent *in vitro* results on peripheral nociceptive sensory neurons activated by bacteria[1,72] or nodose ganglia.[73] Dorsal root ganglia (DRG) are anatomically positioned to detect pathogens entering the body following injury. The similarity in sensory and secretory properties between nociceptive peripheral neurons and interoceptive CSF-cNs is important: (1) DRG, like CSF-cNs, are activated by bacterial toxins as well as other bacterial products,[1] and (2) upon activation, both DRG and CSF-cNs secrete immunomodulatory neuropeptides.[1,72–74] Our results therefore emphasize that sensory neurons are tuned throughout the nervous system (peripheral and central) to respond to intruding pathogens and to promote host survival. We find here that CSF-cNs carry polymodal sensory functions in different physiological contexts. We and others have shown that these neurons are mechanosensory cells activated by spinal compression,[5,8] influencing posture[10,11] and leading to dorsal arching by release of urotensin-related peptides.[12,14,15,52] We show here that CSF-cNs' sensory role can be expanded to tasting chemical compounds in the CSF associated with the intrusion of bacteria, and it provides a potential mechanism by which CSF-cN activation could lead to postural defects that are pathognomonic for meningeal infection.

STAR★METHODS

Detailed methods are provided in the online version of this paper and include the following:

- KEY RESOURCES TABLE
- RESOURCE AVAILABILITY
  - Lead contact
  - Materials availability
  - Data and code availability
- EXPERIMENTAL MODEL AND SUBJECT DETAILS
  - Zebrafish handling and husbandry
  - Bacterial strains and growth conditions
  - Primary cell culture of CSF-cNs
- METHOD DETAILS
  - Confocal imaging
  - Bacterial load
  - Simulations of *in vitro* CSF-cN stimulation
  - Fluorescence activated cell sorting of CSF-cNs and validation
  - Library preparation and RNAseq (differential CSF-cN RNAseq)
  - Fluorescent *in situ* hybridization and immunohistochemistry
  - Generation of transgenic zebrafish lines
  - Generation of *tas2r3* mutants
  - Generation of mutants in genes encoding CSF-cN neuropeptides
  - Calcium imaging of zebrafish larvae after injections in the hindbrain ventricle
  - Calcium imaging in primary cell culture
  - FACS sorting of infected larvae
  - Library preparation and RNAseq (uninfected vs. infected CSF-cNs)
  - RNAseq (uninfected vs. infected CSF-cNs) analysis using DESeq2
  - Larval zebrafish survival assays
  - Survival experiments in CSF-cN compromised transgenic larvae
  - Survival experiments in mutant larvae
  - Analysis of calcium transients *in vivo*
  - Analysis of calcium transients *in vitro*
  - Production of virus-containing supernatant
  - Analysis of neutrophil infiltration to the central canal after infection
  - Behavioral analysis
- QUANTIFICATION AND STATISTICAL ANALYSIS
  - Behavioral analysis
  - Quantification and analysis of axial curvature and fluorescence
  - In vivo calcium imaging
  - RNAseq
  - In vitro calcium imaging
  - Survival analysis

SUPPLEMENTAL INFORMATION

Supplemental information can be found online at https://doi.org/10.1016/j.cub.2023.01.039.

ACKNOWLEDGMENTS

We wish to thank Sophie Nunes-Figueiredo, Antoine Arneau, Monica Dicu, and Bénédicte Daboval for keeping fish in excellent housing conditions in the PhenoZfish facility of the Paris Brain Institute. We thank Prof. Hitoshi Okamoto and Prof. Wilbert Bitter for fruitful discussions; Bethany Berry for her generous gift of *gfap* promoter construct (originally cloned by Brooke Gaynes); Prof. Jan-Willem Veening for providing the *S. pneumoniae* D39 HlpA-mCherry and *S. pneumoniae* D39 HlpA-GFP strains; Dr. Taurai Tasara for providing the *L. monocytogenes* LL195 strain; Yannick Marie, Romain Daveau, and Justine Guégan for their critical assistance in completing the transcriptomic analysis; Dr. Giovanna Barba-Spaeth for her help with UV-inactivation; as well as Cora Chadick, Jeroen Kole, Coen Kuijl, and Theo Verboom for technical assistance. C.W. was a New York Stem Cell Foundation (NYSCF) Robertson Investigator (grant no. NYSCF-R-NI39). This work was supported by the Fondation Schlumberger pour l'Education et la Recherche (FSER/2017), the Fondation pour la Recherche Médicale (FRM no. Equation 202003010612), the ERC Starting Grant "Optoloco" no. 311673, ERC PoC "ZebraZoom" no. 825273, and ERC Consolidator Grant "Exploratome" no. 101002870 (to C.W.). We acknowledge support from "MeninGene" no. 281156 and the HFSP Program grant nos. RGP0063/2014 and RGP0063/2017 and grants from the Agence Nationale de la Recherche (ANR) ASCENTS no. ANR-21-CE13-0008, MOTOMYO no. ANR-21-CE14-0042, and ANR LOCOCONNECT no. ANR-22-CE37-0023 et la Fondation Bettencourt-Schueller don 0031. D.v.d.B. was supported by a ZonMw VICI grant no. 391819627. A.E.P. was supported by an EMBO long-term fellowship (ALTF-549-2013) and a Research in Paris grant from the Marie de Paris. L. Desban was supported by the French Ministry of Higher Education and Research doctoral fellowship. M.D. was supported by a PhD fellowship from the Sorbonne Université Ecole Doctorale ED3C.

AUTHOR CONTRIBUTIONS

The project was conceived by C.W., C.M.J.E.V.-G., A.E.P., K.K.J., and D.v.d.B. A.E.P., L. Desban, and K.K.J. performed FACS and transcriptome analysis with the help of F.-X.L. for statistical analysis. A.E.P., K.K.J., and C.W. combined bacterial infections with calcium imaging. H.M. performed primary culture experiments and collected all calcium imaging data *in vitro*. A.E.P., K.K.J., H.M., A.H., F.B.Q., and C.W. performed the behavioral experiments and postural analysis. A.E.P., H.M., F.B.Q., L. Desban, and L. Djenoune performed histochemistry and provided *in situ* gene expression data. V.L. and J.-P.L. produced the SINV supernatants. M.D. counted CSF-cNs for supplemental figure. J.-P.L. and P.-L.B. provided advice on the transcriptome analysis. J.R. helped with Tol-mediated transgenesis for one fish transgenic line. A.E.P., K.K.J., and F.B.Q. performed survival analysis. C.W., A.E.P., K.K.J., H.M., and F.B.Q. generated figures. C.W., A.E.P., K.K.J., C.M.J.E.V.-G., and D.v.d.B. wrote the manuscript with input from all authors.

DECLARATION OF INTERESTS

The authors declare no competing interests.

INCLUSION AND DIVERSITY

We support inclusive, diverse, and equitable conduct of research.

Received: July 25, 2022
Revised: December 8, 2022
Accepted: January 19, 2023
Published: February 14, 2023

REFERENCES

1. Chiu, I.M., Heesters, B.A., Ghasemlou, N., Hehn, C.A.v., Zhao, F., Tran, J., Wainger, B., Strominger, A., Muralidharan, S., Horswill, A.R., et al. (2013). Bacteria activate sensory neurons that modulate pain and inflammation. Nature *501*, 52–57. https://doi.org/10.1038/nature12479.
2. Shah, A.S., Ben-Shahar, Y., Moninger, T.O., Kline, J.N., and Welsh, M.J. (2009). Motile cilia of human airway epithelia are chemosensory. Science *325*, 1131–1134. https://doi.org/10.1126/science.1173869.
3. Agduhr, E. (1922). Über ein zentrales Sinnesorgan (?) bei den Vertebraten. Z. Anat. Entwicklungsgesch. *66*, 223–360. https://doi.org/10.1007/BF02593586.
4. Kolmer, W. (1921). Das 'Sagitallorgan' der Wirbeltiere. Z. Anat. Entwickl. Gesch. *60*, 652–717.
5. Böhm, U.L., Prendergast, A., Djenoune, L., Nunes Figueiredo, S., Gomez, J., Stokes, C., Kaiser, S., Suster, M., Kawakami, K., Charpentier, M., et al. (2016). CSF-contacting neurons regulate locomotion by relaying mechanical stimuli to spinal circuits. Nat. Commun. *7*, 10866. https://doi.org/10.1038/ncomms10866.
6. Jalalvand, E., Robertson, B., Wallén, P., and Grillner, S. (2016). Ciliated neurons lining the central canal sense both fluid movement and pH through ASIC3. Nat. Commun. *7*, 10002. https://doi.org/10.1038/ncomms10002.
7. Orts-Del'Immagine, A., Cantaut-Belarif, Y., Thouvenin, O., Roussel, J., Baskaran, A., Langui, D., Koëth, F., Bivas, P., Lejeune, F.X., Bardet, P.L., and Wyart, C. (2020). Sensory neurons contacting the cerebrospinal fluid require the reissner fiber to detect spinal curvature in vivo. Curr. Biol. *30*, 827–839.e4.
8. Sternberg, J.R., Prendergast, A.E., Brosse, L., Cantaut-Belarif, Y., Thouvenin, O., Orts-Del'Immagine, A., Castillo, L., Djenoune, L., Kurisu, S., McDearmid, J.R., et al. (2018). Pkd2l1 is required for mechanoception in cerebrospinal fluid-contacting neurons and maintenance of spine curvature. Nat. Commun. *9*, 3804. https://doi.org/10.1038/s41467-018-06225-x.
9. Fidelin, K., Djenoune, L., Stokes, C., Prendergast, A., Gomez, J., Baradel, A., Del Bene, F., and Wyart, C. (2015). State-dependent modulation of locomotion by GABAergic spinal sensory neurons. Curr. Biol. *25*, 3035–3047. https://doi.org/10.1016/j.cub.2015.09.070.
10. Hubbard, J.M., Böhm, U.L., Prendergast, A., Tseng, P.B., Newman, M., Stokes, C., and Wyart, C. (2016). Intraspinal sensory neurons provide powerful inhibition to motor circuits ensuring postural control during locomotion. Curr. Biol. *26*, 2841–2853. https://doi.org/10.1016/j.cub.2016.08.026.
11. Wu, M.Y., Carbo-Tano, M., Mirat, O., Lejeune, F.X., Roussel, J., Quan, F.B., Fidelin, K., and Wyart, C. (2021). Spinal sensory neurons project onto the hindbrain to stabilize posture and enhance locomotor speed. Curr. Biol. *31*, 3315–3329.e5. https://doi.org/10.1016/j.cub.2021.05.042.
12. Cantaut-Belarif, Y., Orts Del'Immagine, A., Penru, M., Pézeron, G., Wyart, C., and Bardet, P.L. (2020). Adrenergic activation modulates the signal from the Reissner fiber to cerebrospinal fluid-contacting neurons during development. eLife *9*, e59469. https://doi.org/10.7554/eLife.59469.
13. Cantaut-Belarif, Y., Sternberg, J.R., Thouvenin, O., Wyart, C., and Bardet, P.L. (2018). The reissner fiber in the cerebrospinal fluid controls morphogenesis of the body axis. Curr. Biol. *28*, 2479–2486.e4. https://doi.org/10.1016/j.cub.2018.05.079.
14. Quan, F.B., Dubessy, C., Galant, S., Kenigfest, N.B., Djenoune, L., Leprince, J., Wyart, C., Lihrmann, I., and Tostivint, H. (2015). Comparative distribution and in vitro activities of the urotensin II-related peptides URP1 and URP2 in zebrafish: evidence for their colocalization in spinal cerebrospinal fluid-contacting neurons. PLoS One *10*, e0119290. https://doi.org/10.1371/journal.pone.0119290.
15. Zhang, X., Jia, S., Chen, Z., Chong, Y.L., Xie, H., Feng, D., Wu, X., Song, D.Z., Roy, S., and Zhao, C. (2018). Cilia-driven cerebrospinal fluid flow directs expression of urotensin neuropeptides to straighten the vertebrate body axis. Nat. Genet. *50*, 1666–1673. https://doi.org/10.1038/s41588-018-0260-3.

16. Lu, H., Shagirova, A., Goggi, J.L., Yeo, H.L., and Roy, S. (2020). Reissner fibre-induced urotensin signalling from cerebrospinal fluid-contacting neurons prevents scoliosis of the vertebrate spine. Biol. Open *9*, bio052027. https://doi.org/10.1242/bio.052027.

17. Alejevski, F., Leemans, M., Gaillard, A.L., Leistenschneider, D., de Flori, C., Bougerol, M., Le Mével, S., Herrel, A., Fini, J.B., Pézeron, G., et al. (2021). Conserved role of the urotensin II receptor 4 signalling pathway to control body straightness in a tetrapod. Open Biol. *11*, 210065. https://doi.org/10.1098/rsob.210065.

18. Bearce, E.A., Irons, Z.H., O'Hara-Smith, J.R., Kuhns, C.J., Fisher, S.I., Crow, W.E., and Grimes, D.T. (2022). Urotensin II-related peptides, Urp1 and Urp2, control zebrafish spine morphology. eLife *11*, e83883. https://doi.org/10.7554/eLife.83883.

19. Gaillard, A.-L., Mohamad, T., Quan, F.B., de Cian, A., Mosiman, C., Tostivint, H., and Pézeron, G. (2022). Urp1 and Urp2 act redundantly to maintain spine shape in zebrafish larvae. https://doi.org/10.1101/2022.08.09.503396.

20. Djenoune, L., Khabou, H., Joubert, F., Quan, F.B., Nunes Figueiredo, S., Bodineau, L., Del Bene, F., Burcklé, C., Tostivint, H., and Wyart, C. (2014). Investigation of spinal cerebrospinal fluid-contacting neurons expressing PKD2L1: evidence for a conserved system from fish to primates. Front. Neuroanat. *8*, 26. https://doi.org/10.3389/fnana.2014.00026.

21. Huang, A.L., Chen, X., Hoon, M.A., Chandrashekar, J., Guo, W., Tränkner, D., Ryba, N.J., and Zuker, C.S. (2006). The cells and logic for mammalian sour taste detection. Nature *442*, 934–938. https://doi.org/10.1038/nature05084.

22. Orts-Del'immagine, A., Wanaverbecq, N., Tardivel, C., Tillement, V., Dallaporta, M., and Trouslard, J. (2012). Properties of subependymal cerebrospinal fluid contacting neurones in the dorsal vagal complex of the mouse brainstem. J. Physiol. *590*, 3719–3741. https://doi.org/10.1113/jphysiol.2012.227959.

23. Hull, M., Parnes, M., and Jankovic, J. (2021). Botulinum neurotoxin injections in childhood opisthotonus. Toxins (Basel) *13*, 137. https://doi.org/10.3390/toxins13020137.

24. Jim, K.K., Engelen-Lee, J., van der Sar, A.M., Bitter, W., Brouwer, M.C., van der Ende, A., Veening, J.W., van de Beek, D., and Vandenbroucke-Grauls, C.M. (2016). Infection of zebrafish embryos with live fluorescent Streptococcus pneumoniae as a real-time pneumococcal meningitis model. J. Neuroinflammation *13*, 188. https://doi.org/10.1186/s12974-016-0655-y.

25. Zunt, J.R., Kassebaum, N.J., Blake, N., Glennie, L., Wright, C., Nichols, E., Abd-Allah, F., Abdela, J., Abdelalim, A., Adamu, A.A., et al. (2018). Global, regional, and national burden of meningitis, 1990–2016: a systematic analysis for the Global Burden of Disease Study 2016. Lancet Neurol. *17*, 1061–1082. https://doi.org/10.1016/S1474-4422(18)30387-9.

26. van de Beek, D., Brouwer, M., Hasbun, R., Koedel, U., Whitney, C.G., and Wijdicks, E. (2016). Community-acquired bacterial meningitis. Nat. Rev. Dis. Primers *2*, 16074. https://doi.org/10.1038/nrdp.2016.74.

27. van de Beek, D., Brouwer, M.C., Koedel, U., and Wall, E.C. (2021). Community-acquired bacterial meningitis. Lancet *398*, 1171–1183. https://doi.org/10.1016/S0140-6736(21)00883-7.

28. van de Beek, D., de Gans, J., Tunkel, A.R., and Wijdicks, E.F. (2006). Community-acquired bacterial meningitis in adults. N. Engl. J. Med. *354*, 44–53. https://doi.org/10.1056/NEJMra052116.

29. van de Beek, D., de Gans, J., Spanjaard, L., Weisfelt, M., Reitsma, J.B., and Vermeulen, M. (2004). Clinical features and prognostic factors in adults with bacterial meningitis. N. Engl. J. Med. *351*, 1849–1859. https://doi.org/10.1056/NEJMoa040845.

30. Zoons, E., Weisfelt, M., de Gans, J., Spanjaard, L., Koelman, J.H., Reitsma, J.B., and van de Beek, D. (2008). Seizures in adults with bacterial meningitis. Neurology *70*, 2109–2115. https://doi.org/10.1212/01.wnl.0000288178.91614.5d.

31. Budick, S.A., and O'Malley, D.M. (2000). Locomotor repertoire of the larval zebrafish: swimming, turning and prey capture. J. Exp. Biol. *203*, 2565–2579. https://doi.org/10.1242/jeb.203.17.2565.

32. Omdal, R. (2020). The biological basis of chronic fatigue: neuroinflammation and innate immunity. Curr. Opin. Neurol. *33*, 391–396. https://doi.org/10.1097/WCO.0000000000000817.

33. Gawel, K., Langlois, M., Martins, T., van der Ent, W., Tiraboschi, E., Jacmin, M., Crawford, A.D., and Esguerra, C.V. (2020). Seizing the moment: zebrafish epilepsy models. Neurosci. Biobehav. Rev. *116*, 1–20. https://doi.org/10.1016/j.neubiorev.2020.06.010.

34. Kadioglu, A., Weiser, J.N., Paton, J.C., and Andrew, P.W. (2008). The role of Streptococcus pneumoniae virulence factors in host respiratory colonization and disease. Nat. Rev. Microbiol. *6*, 288–301. https://doi.org/10.1038/nrmicro1871.

35. Filipiak, W., Sponring, A., Baur, M.M., Ager, C., Filipiak, A., Wiesenhofer, H., Nagl, M., Troppmair, J., and Amann, A. (2012). Characterization of volatile metabolites taken up by or released from Streptococcus pneumoniae and Haemophilus influenzae by using GC-MS. Microbiology (Reading) *158*, 3044–3053. https://doi.org/10.1099/mic.0.062687-0.

36. Freund, J.R., Mansfield, C.J., Doghramji, L.J., Adappa, N.D., Palmer, J.N., Kennedy, D.W., Reed, D.R., Jiang, P., and Lee, R.J. (2018). Activation of airway epithelial bitter taste receptors by Pseudomonas aeruginosa quinolones modulates calcium, cyclic-AMP, and nitric oxide signaling. J. Biol. Chem. *293*, 9824–9840. https://doi.org/10.1074/jbc.RA117.001005.

37. Lee, R.J., Chen, B., Redding, K.M., Margolskee, R.F., and Cohen, N.A. (2014). Mouse nasal epithelial innate immune responses to Pseudomonas aeruginosa quorum-sensing molecules require taste signaling components. Innate Immun. *20*, 606–617. https://doi.org/10.1177/1753425913503386.

38. Saunders, C.J., Christensen, M., Finger, T.E., and Tizzano, M. (2014). Cholinergic neurotransmission links solitary chemosensory cells to nasal inflammation. Proc. Natl. Acad. Sci. USA *111*, 6075–6080. https://doi.org/10.1073/pnas.1402251111.

39. Tizzano, M., Gulbransen, B.D., Vandenbeuch, A., Clapp, T.R., Herman, J.P., Sibhatu, H.M., Churchill, M.E., Silver, W.L., Kinnamon, S.C., and Finger, T.E. (2010). Nasal chemosensory cells use bitter taste signaling to detect irritants and bacterial signals. Proc. Natl. Acad. Sci. USA *107*, 3210–3215. https://doi.org/10.1073/pnas.0911934107.

40. Verbeurgt, C., Veithen, A., Carlot, S., Tarabichi, M., Dumont, J.E., Hassid, S., and Chatelain, P. (2017). The human bitter taste receptor T2R38 is broadly tuned for bacterial compounds. PLoS One *12*, e0181302. https://doi.org/10.1371/journal.pone.0181302.

41. Bos, L.D., Sterk, P.J., and Schultz, M.J. (2013). Volatile metabolites of pathogens: a systematic review. PLoS Pathog. *9*, e1003311. https://doi.org/10.1371/journal.ppat.1003311.

42. England, S.J., Campbell, P.C., Banerjee, S., Swanson, A.J., and Lewis, K.E. (2017). Identification and expression analysis of the complete family of zebrafish pkd genes. Front. Cell Dev. Biol. *5*, 5. https://doi.org/10.3389/fcell.2017.00005.

43. Petracca, Y.L., Sartoretti, M.M., Di Bella, D.J., Marin-Burgin, A., Carcagno, A.L., Schinder, A.F., and Lanuza, G.M. (2016). The late and dual origin of cerebrospinal fluid-contacting neurons in the mouse spinal cord. Development *143*, 880–891. https://doi.org/10.1242/dev.129254.

44. Andrzejczuk, L.A., Banerjee, S., England, S.J., Voufo, C., Kamara, K., and Lewis, K.E. (2018). Tal1, Gata2a, and Gata3 have distinct functions in the development of V2b and cerebrospinal fluid-contacting KA spinal neurons. Front. Neurosci. *12*, 170. https://doi.org/10.3389/fnins.2018.00170.

45. Shin, J., Poling, J., Park, H.C., and Appel, B. (2007). Notch signaling regulates neural precursor allocation and binary neuronal fate decisions in zebrafish. Development *134*, 1911–1920.

46. Yang, L., Rastegar, S., and Strähle, U. (2010). Regulatory interactions specifying Kolmer-Agduhr interneurons. Development *137*, 2713–2722. https://doi.org/10.1242/dev.048470.

47. Desban, L., Prendergast, A., Roussel, J., Rosello, M., Geny, D., Wyart, C., and Bardet, P.L. (2019). Regulation of the apical extension morphogenesis tunes the mechanosensory response of microvilliated neurons. PLoS Biol. *17*, e3000235. https://doi.org/10.1371/journal.pbio.3000235.

48. Christenson, J., Alford, S., Grillner, S., and Hökfelt, T. (1991). Co-localized GABA and somatostatin use different ionic mechanisms to hyperpolarize target neurons in the lamprey spinal cord. Neurosci. Lett. *134*, 93–97. https://doi.org/10.1016/0304-3940(91)90516-v.

49. Djenoune, L., Desban, L., Gomez, J., Sternberg, J.R., Prendergast, A., Langui, D., Quan, F.B., Marnas, H., Auer, T.O., Rio, J.P., et al. (2017). The dual developmental origin of spinal cerebrospinal fluid-contacting neurons gives rise to distinct functional subtypes. Sci. Rep. *7*, 719. https://doi.org/10.1038/s41598-017-00350-1.

50. Schotland, J.L., Shupliakov, O., Grillner, S., and Brodin, L. (1996). Synaptic and nonsynaptic monoaminergic neuron systems in the lamprey spinal cord. J. Comp. Neurol. *372*, 229–244. https://doi.org/10.1002/(SICI)1096-9861(19960819)372:2<229::AID-CNE6>3.0.CO;2-5.

51. Marquart, G.D., Tabor, K.M., Brown, M., Strykowski, J.L., Varshney, G.K., LaFave, M.C., Mueller, T., Burgess, S.M., Higashijima, S., and Burgess, H.A. (2015). A 3D searchable database of transgenic zebrafish Gal4 and Cre lines for functional neuroanatomy studies. Front. Neural Circuits *9*, 78. https://doi.org/10.3389/fncir.2015.00078.

52. Sternberg, J.R., Severi, K.E., Fidelin, K., Gomez, J., Ihara, H., Alcheikh, Y., Hubbard, J.M., Kawakami, K., Suster, M., and Wyart, C. (2016). Optimization of a neurotoxin to investigate the contribution of excitatory interneurons to speed modulation in vivo. Curr. Biol. *26*, 2319–2328. https://doi.org/10.1016/j.cub.2016.06.037.

53. Cropper, E.C., Jing, J., Vilim, F.S., and Weiss, K.R. (2018). Peptide co-transmitters as dynamic, intrinsic modulators of network activity. Front. Neural Circuits *12*, 78. https://doi.org/10.3389/fncir.2018.00078.

54. de Jong, E.K., Vinet, J., Stanulovic, V.S., Meijer, M., Wesseling, E., Sjollema, K., Boddeke, H.W., and Biber, K. (2008). Expression, transport, and axonal sorting of neuronal CCL21 in large dense-core vesicles. FASEB J. *22*, 4136–4145. https://doi.org/10.1096/fj.07-101907.

55. Moqbel, R., and Coughlin, J.J. (2006). Differential secretion of cytokines. Sci. STKE *2006*, pe26. https://doi.org/10.1126/stke.3382006pe26.

56. Murray, P.J., and Wynn, T.A. (2011). Protective and pathogenic functions of macrophage subsets. Nat. Rev. Immunol. *11*, 723–737. https://doi.org/10.1038/nri3073.

57. Brunger, A.T., Jin, R., and Breidenbach, M.A. (2008). Highly specific interactions between botulinum neurotoxins and synaptic vesicle proteins. Cell. Mol. Life Sci. *65*, 2296–2306. https://doi.org/10.1007/s00018-008-8088-0.

58. Allardyce, R.A., Langford, V.S., Hill, A.L., and Murdoch, D.R. (2006). Detection of volatile metabolites produced by bacterial growth in blood culture media by selected ion flow tube mass spectrometry (SIFT-MS). J. Microbiol. Methods *65*, 361–365. https://doi.org/10.1016/j.mimet.2005.09.003.

59. Lee, R.J., and Cohen, N.A. (2014). Sinonasal solitary chemosensory cells "taste" the upper respiratory environment to regulate innate immunity. Am. J. Rhinol. Allergy *28*, 366–373. https://doi.org/10.2500/ajra.2014.28.4077.

60. Yu, Y.X., Sun, X.H., Liu, Y., Pan, Y.J., and Zhao, Y. (2015). Odor fingerprinting of Listeria monocytogenes recognized by SPME-GC-MS and E-nose. Can. J. Microbiol. *61*, 367–372. https://doi.org/10.1139/cjm-2014-0652.

61. Passoni, G., Langevin, C., Palha, N., Mounce, B.C., Briolat, V., Affaticati, P., Job, E.D., Joly, J.S., Vignuzzi, M., Saleh, M.C., et al. (2017). Imaging of viral neuroinvasion in the zebrafish reveals that Sindbis and chikungunya viruses favour different entry routes. Dis. Model. Mech. *10*, 847–857. https://doi.org/10.1242/dmm.029231.

62. Shooshtarizadeh, P., Zhang, D., Chich, J.F., Gasnier, C., Schneider, F., Haïkel, Y., Aunis, D., and Metz-Boutigue, M.H. (2010). The antimicrobial peptides derived from chromogranin/secretogranin family, new actors of innate immunity. Regul. Pept. *165*, 102–110. https://doi.org/10.1016/j.regpep.2009.11.014.

63. Bertini, R., Howard, O.M., Dong, H.F., Oppenheim, J.J., Bizzarri, C., Sergi, R., Caselli, G., Pagliei, S., Romines, B., Wilshire, J.A., et al. (1999). Thioredoxin, a redox enzyme released in infection and inflammation, is a unique chemoattractant for neutrophils, monocytes, and T cells. J. Exp. Med. *189*, 1783–1789. https://doi.org/10.1084/jem.189.11.1783.

64. Chen, G., Zhao, J., Yin, Y., Wang, B., Liu, Q., Li, P., Zhao, L., and Zhou, H. (2014). C-type natriuretic peptide attenuates LPS-induced endothelial activation: involvement of p38, Akt, and NF-kappaB pathways. Amino Acids *46*, 2653–2663. https://doi.org/10.1007/s00726-014-1816-x.

65. Dalm, V.A., van Hagen, P.M., van Koetsveld, P.M., Achilefu, S., Houtsmuller, A.B., Pols, D.H., van der Lely, A.J., Lamberts, S.W., and Hofland, L.J. (2003). Expression of somatostatin, cortistatin, and somatostatin receptors in human monocytes, macrophages, and dendritic cells. Am. J. Physiol. Endocrinol. Metab. *285*, E344–E353. https://doi.org/10.1152/ajpendo.00048.2003.

66. Krantic, S. (2000). Peptides as regulators of the immune system: emphasis on somatostatin. Peptides *21*, 1941–1964.

67. Lee, R.J., Kofonow, J.M., Rosen, P.L., Siebert, A.P., Chen, B., Doghramji, L., Xiong, G., Adappa, N.D., Palmer, J.N., Kennedy, D.W., et al. (2014). Bitter and sweet taste receptors regulate human upper respiratory innate immunity. J. Clin. Invest. *124*, 1393–1405. https://doi.org/10.1172/JCI72094.

68. Ly, N.P., Komatsuzaki, K., Fraser, I.P., Tseng, A.A., Prodhan, P., Moore, K.J., and Kinane, T.B. (2005). Netrin-1 inhibits leukocyte migration in vitro and in vivo. Proc. Natl. Acad. Sci. USA *102*, 14729–14734. https://doi.org/10.1073/pnas.0506233102.

69. Pei, X., Sun, Q., Zhang, Y., Wang, P., Peng, X., Guo, C., Xu, E., Zheng, Y., Mo, X., Ma, J., et al. (2014). PC3-secreted microprotein is a novel chemoattractant protein and functions as a high-affinity ligand for CC chemokine receptor 2. J. Immunol. *192*, 1878–1886. https://doi.org/10.4049/jimmunol.1300758.

70. Tomasiuk, R., Lipowski, D., Szlufik, S., Peplinska, K., and Mikaszewska-Sokolewicz, M. (2016). Higher level of NT-proCNP in cerebrospinal fluid of patients with meningitis. Neurosci. Lett. *614*, 29–32. https://doi.org/10.1016/j.neulet.2015.12.053.

71. Jakutis, G., and Stainier, D.Y.R. (2021). Genotype-phenotype relationships in the context of transcriptional adaptation and genetic robustness. Annu. Rev. Genet. *55*, 71–91. https://doi.org/10.1146/annurev-genet-071719-020342.

72. Kashem, S.W., Riedl, M.S., Yao, C., Honda, C.N., Vulchanova, L., and Kaplan, D.H. (2015). Nociceptive sensory fibers drive interleukin-23 production from CD301b+ dermal dendritic cells and drive protective cutaneous immunity. Immunity *43*, 515–526. https://doi.org/10.1016/j.immuni.2015.08.016.

73. Talbot, S., Abdulnour, R.E., Burkett, P.R., Lee, S., Cronin, S.J., Pascal, M.A., Laedermann, C., Foster, S.L., Tran, J.V., Lai, N., et al. (2015). Silencing nociceptor neurons reduces allergic airway inflammation. Neuron *87*, 341–354. https://doi.org/10.1016/j.neuron.2015.06.007.

74. Foster, S.L., Seehus, C.R., Woolf, C.J., and Talbot, S. (2017). Sense and immunity: context-dependent neuro-immune interplay. Front. Immunol. *8*, 1463. https://doi.org/10.3389/fimmu.2017.01463.

75. Weinmaier, T., Riesing, M., Rattei, T., Bille, J., Arguedas-Villa, C., Stephan, R., and Tasara, T. (2013). Complete genome sequence of Listeria monocytogenes LL195, a serotype 4b strain from the 1983–1987 Listeriosis epidemic in Switzerland. Genome Announc. *1*. 16–12. https://doi.org/10.1128/genomeA.00152-12.

76. Hernandez, R., Sinodis, C., and Brown, D.T. (2010). Sindbis virus: propagation, quantification, and storage. Curr. Protoc. Microbiol. *Chapter 15*, Unit15B1. https://doi.org/10.1002/9780471729259.mc15b01s16.

77. Avery, O.T., Macleod, C.M., and McCarty, M. (1944). Studies on the chemical nature of the substance inducing transformation of pneumococcal types: induction of transformation by a desoxyribonucleic acid fraction isolated from pneumococcus type Iii. J. Exp. Med. *79*, 137–158. https://doi.org/10.1084/jem.79.2.137.

78. Slager, J., Aprianto, R., and Veening, J.W. (2018). Deep genome annotation of the opportunistic human pathogen Streptococcus pneumoniae D39. Nucleic Acids Res. *46*, 9971–9989. https://doi.org/10.1093/nar/gky725.

79. Kjos, M., Aprianto, R., Fernandes, V.E., Andrew, P.W., van Strijp, J.A., Nijland, R., and Veening, J.W. (2015). Bright fluorescent Streptococcus pneumoniae for live-cell imaging of host-pathogen interactions. J. Bacteriol. *197*, 807–818. https://doi.org/10.1128/JB.02221-14.

80. Beilharz, K., van Raaphorst, R., Kjos, M., and Veening, J.W. (2015). Red fluorescent proteins for gene expression and protein localization studies in Streptococcus pneumoniae and efficient transformation with DNA assembled via the Gibson assembly method. Appl. Environ. Microbiol. *81*, 7244–7252. https://doi.org/10.1128/AEM.02033-15.

81. Martin, B., García, P., Castanié, M.P., and Claverys, J.P. (1995). The recA gene of Streptococcus pneumoniae is part of a competence-induced operon and controls lysogenic induction. Mol. Microbiol. *15*, 367–379.

82. Scheer, N., Groth, A., Hans, S., and Campos-Ortega, J.A. (2001). An instructive function for Notch in promoting gliogenesis in the zebrafish retina. Development *128*, 1099–1107. https://doi.org/10.1242/dev.128.7.1099.

83. Renshaw, S.A., Loynes, C.A., Trushell, D.M., Elworthy, S., Ingham, P.W., and Whyte, M.K. (2006). A transgenic zebrafish model of neutrophilic inflammation. Blood *108*, 3976–3978. https://doi.org/10.1182/blood-2006-05-024075.

84. Schneider, C.A., Rasband, W.S., and Eliceiri, K.W. (2012). NIH Image to ImageJ: 25 years of image analysis. Nat. Methods *9*, 671–675. https://doi.org/10.1038/nmeth.2089.

85. Lawrence, C. (2011). Advances in zebrafish husbandry and management. Methods Cell Biol. *104*, 429–451. https://doi.org/10.1016/B978-0-12-374814-0.00023-9.

86. Lawrence, C. (2016). New frontiers for zebrafish management. Methods Cell Biol. *135*, 483–508. https://doi.org/10.1016/bs.mcb.2016.04.015.

87. Avery, O.T., Macleod, C.M., and McCarty, M. (1979). Studies on the chemical nature of the substance inducing transformation of pneumococcal types. Inductions of transformation by a desoxyribonucleic acid fraction isolated from pneumococcus type III. J. Exp. Med. *149*, 297–326. https://doi.org/10.1084/jem.149.2.297.

88. Manoli, M., and Driever, W. (2012). Fluorescence-activated cell sorting (FACS) of fluorescently tagged cells from zebrafish larvae for RNA isolation. Cold Spring Harb. Protoc. *2012*. pdb.prot069633. https://doi.org/10.1101/pdb.prot069633.

89. Morris, C.A., Benson, E., and White-Cooper, H. (2009). Determination of gene expression patterns using in situ hybridization to Drosophila testes. Nat. Protoc. *4*, 1807–1819. https://doi.org/10.1038/nprot.2009.192.

90. Thisse, C., and Thisse, B. (2008). High-resolution in situ hybridization to whole-mount zebrafish embryos. Nat. Protoc. *3*, 59–69. https://doi.org/10.1038/nprot.2007.514.

91. Vize, P.D., McCoy, K.E., and Zhou, X. (2009). Multichannel wholemount fluorescent and fluorescent/chromogenic in situ hybridization in Xenopus embryos. Nat. Protoc. *4*, 975–983. https://doi.org/10.1038/nprot.2009.69.

92. Bernardos, R.L., and Raymond, P.A. (2006). GFAP transgenic zebrafish. Gene Expr. Patterns *6*, 1007–1013. https://doi.org/10.1016/j.modgep.2006.04.006.

93. Johnson, K., Barragan, J., Bashiruddin, S., Smith, C.J., Tyrrell, C., Parsons, M.J., Doris, R., Kucenas, S., Downes, G.B., Velez, C.M., et al. (2016). Gfap-positive radial glial cells are an essential progenitor population for later-born neurons and glia in the zebrafish spinal cord. Glia *64*, 1170–1189. https://doi.org/10.1002/glia.22990.

94. Fisher, S., Grice, E.A., Vinton, R.M., Bessling, S.L., Urasaki, A., Kawakami, K., and McCallion, A.S. (2006). Evaluating the biological relevance of putative enhancers using Tol2 transposon-mediated transgenesis in zebrafish. Nat. Protoc. *1*, 1297–1305. https://doi.org/10.1038/nprot.2006.230.

95. Kwan, K.M., Fujimoto, E., Grabher, C., Mangum, B.D., Hardy, M.E., Campbell, D.S., Parant, J.M., Yost, H.J., Kanki, J.P., and Chien, C.B. (2007). The Tol2kit: a multisite gateway-based construction kit for Tol2 transposon transgenesis constructs. Dev. Dyn. *236*, 3088–3099. https://doi.org/10.1002/dvdy.21343.

96. Concordet, J.P., and Haeussler, M. (2018). CRISPOR: intuitive guide selection for CRISPR/Cas9 genome editing experiments and screens. Nucleic Acids Res. *46*, W242–W245. https://doi.org/10.1093/nar/gky354.

97. Auer, T.O., Xiao, T., Bercier, V., Gebhardt, C., Duroure, K., Concordet, J.P., Wyart, C., Suster, M., Kawakami, K., Wittbrodt, J., et al. (2015). Deletion of a kinesin I motor unmasks a mechanism of homeostatic branching control by neurotrophin-3. eLife *4*, 418. https://doi.org/10.7554/eLife.05061.

98. Boucontet, L., Passoni, G., Thiry, V., Maggi, L., Herbomel, P., Levraud, J.P., and Colucci-Guyon, E. (2018). A model of superinfection of virus-infected zebrafish larvae: increased susceptibility to bacteria associated with neutrophil death. Front. Immunol. *9*, 1084. https://doi.org/10.3389/fimmu.2018.01084.

99. Mirat, O., Sternberg, J.R., Severi, K.E., and Wyart, C. (2013). ZebraZoom: an automated program for high-throughput behavioral analysis and categorization. Front. Neural Circuits *7*, 107. https://doi.org/10.3389/fncir.2013.00107.

STAR★METHODS

KEY RESOURCES TABLE

REAGENT or RESOURCE	SOURCE	IDENTIFIER
Bacterial and virus strains		
Escherichia coli DH5α	ATCC	N/A
Listeria monocytogenes LL195	Weinmaier et al.[75]	N/A
Sindbis virus	Hernandez et al.[76]	N/A
Streptococcus pneumoniae D39V: serotype 2	Avery et al.[77] and Slager et al.[78]	N/A
Streptococcus pneumoniae D39V *hlpA*-GFP cam^r	Kjos et al.[79]	N/A
Streptococcus pneumoniae D39V *hlpA_hlpA*-mCherry cam^r	Beilharz et al.[80]	N/A
Chemicals, peptides, and recombinant proteins		
2-butanone	Sigma-Aldrich	Cat#W217012
2-methylpropanal	Sigma-Aldrich	Cat#W222003
2-pentanone	Sigma-Aldrich	Cat#W284220
α-bungarotoxin	Tocris Biosciences	Cat#2133
μ-Slide 8 Well	ibidi	Cat#80826
Acetone	Sigma-Aldrich	Cat#534064
B27 Supplement	Thermo Fisher Scientific	Cat#17504044
Bacto Brain Heart Infusion	Becton, Dickinson and Company	Cat#237500
C+Y medium	Martin et al.[81]	N/A
$CaCl_2$	Sigma-Aldrich	Cat#C3306
$CaCl_2$	Sigma-Aldrich	Cat#223506
Columbia agar, 5% v/v defibrinated sheep blood	bioMérieux	Cat#43049
Columbia Agar Base	Thermo Fisher Scientific	Cat# R452954
FBS	Thermo Fisher Scientific	Cat#10270106
Defibrinated Sheep Blood	bioTRADING	Cat#BTSG100
Dextran, Alexa Fluor 647; 10,000 MW, Anionic, Fixable	Invitrogen	Cat#D22914
Dimethyl disulfide (DMDS)	Sigma-Aldrich	Cat#W353604
DMEM	Thermo Fisher Scientific	Cat#10938025
DMSO	Sigma-Aldrich	Cat#D8418
Ethyl 3-aminobenzoate methanesulfonate	Sigma-Aldrich	Cat#A5040
Ethylenediaminetetraacetic acid disodium salt dihydrate (EDTA)	Sigma-Aldrich	Cat#E5134
FACSMax Buffer	AMC Biotechnology	Cat#T200100
Gibco Human GDNF Recombinant Protein	Fisher Scientific	Cat#10679963
Glass beads 1.0mm	Sigma-Aldrich	Cat#Z250473
D-(+)-Glucose	Sigma-Aldrich	Cat#G8769
D-(+)-Glucose	Sigma-Aldrich	Cat#G8270
HBSS	Fisher Scientific	Cat#14170088
HEPES	Sigma-Aldrich	Cat#H3375
KCl	Sigma-Aldrich	Cat#P9333
L-cysteine	Sigma-Aldrich	Cat#30089
L-glutamine	Thermo Fisher Scientific	Cat#25030024
Metronidazole	Sigma-Aldrich	Cat#M3761
$MgCl_2$	Sigma-Aldrich	Cat#M2670
N2 Supplement	Thermo Fisher Scientific	Cat#17502048
Na2HPO4	Sigma-Aldrich	Cat#5136
NaCl	Sigma-Aldrich	Cat#S7653
NaH2PO4	Sigma-Aldrich	Cat#4269

(*Continued on next page*)

Continued

REAGENT or RESOURCE	SOURCE	IDENTIFIER
NaOH	Sigma-Aldrich	Cat#71687
Neurobasal Medium	Thermo Fisher Scientific	Cat#10888022
NGF	Merck Millipore	Cat#01-125
Papain	Serlabo Technologies	Cat#WOLK03176-1
Paraformaldehyde	Sigma-Aldrich	Cat#158127
Penicillin/Streptomycin	Thermo Fisher Scientific	Cat#15140122
Phenol red solution	Sigma-Aldrich	Cat#P0290
Recombinant serotype 4 pneumolysin	MyBioSource	Cat#MBS1141054
Sea salts	Sigma-Aldrich	Cat#S9883
Sheep blood defibrinated	bioTRADING	Cat#BTSG10
Sodium pyruvate	Thermo Fisher Scientific	Cat#11360039
Streptococcus selective supplement (COBA)	Oxoid	Cat#SR0126
Sucrose	Sigma-Aldrich	Cat#S7903
Tricaine	Sigma-Aldrich	Cat#A5040
Critical commercial assays		
Clontech SMART-Seq v4 Kit	Clontech	Cat#634888
Gateway LR Clonase	Thermo Fisher Scientific	Cat#11791020
Illumina NextSeq 500	Illumina	Cat#SY-415-1001
Luminaris HiGreen qPCR Master Mix	Thermo Fisher Scientific	Cat#K0991
Nextera DNA Library Preparation Kit	Illumina	Cat#FC-131-1024
RNAeasy Micro Kit	Qiagen	Cat#74004
RNAeasy Mini Kit	Qiagen	Cat#74104
SMART-Seq v4 PLUS kit	Takara Bio	Cat#R400752
SuperScript IV First-Strand Synthesis System	Thermo Fisher Scientific	Cat#18091050
SuperScript IV VILO	Invitrogen	Cat#11756050
TOPO-TA for subcloning	Thermo Fisher Scientific	Cat#451641
Experimental models: Cell lines		
BHK-21 cells	ATCC	Cat#CCL-10; RRID:CVCL_1915
Experimental models: Organisms/strains		
Zebrafish: *AB* wild-type	N/A	ZFIN: ZDB-GENO-960809-7
Zebrafish: *pkd2l1*^{icm02}	Böhm et al.[5]	ZFIN: ZDB-ALT-160119-6
Zebrafish: *scg2a* mutant allele	This paper	*scg2a*^{icm71}
Zebrafish: *nppc* mutant allele	This paper	*nppc*^{icm36}
Zebrafish: *esm1* mutant allele	This paper	*esm1*^{icm34}
Zebrafish: *tas2r3a* mutant allele	This paper	*tas2r3a*^{icm64}
Zebrafish: *tas2r3b* mutant allele	This paper	*tas2r3b*^{icm65}
Zebrafish: *Tg(pkd2l1:GCaMP5G)*^{icm07}	Böhm et al.[5]	ZFIN: ZDB-ALT-160119-4
Zebrafish: *Tg(UAS:GCaMP5G)*^{icm08}	Fidelin et al.[9]	ZFIN: ZDB-ALT-150417-4
Zebrafish: *Tg(pkd2l1:Gal4)*^{icm10}	Fidelin et al.[9]	ZFIN: ZDB-ALT-150324-1
Zebrafish: *Tg(UAS:BoTxBLC-GFP)*^{icm21}	Sternberg et al.[52]	ZFIN: ZDB-ALT-160119-9
Zebrafish: *Tg(mnx1:Gal4)*^{icm23}	Böhm et al.[5]	ZFIN: ZDB-ALT-160120-1
Zebrafish: *Tg(GFAP:Gal4)*^{icm47}	This paper	ZFIN: ZDB-ALT-190115-1
Zebrafish: *Tg(UAS:epNTR-tagRFP-UTR.zb3)*^{y362}	Marquart et al.[51]	ZFIN: ZDB-ALT-160830-1
Zebrafish: *Tg(UAS:GFP)*^{kca33}	Scheer et al.[82]	ZFIN: ZDB-ALT-030716-2
Zebrafish: *Tg(UAS:tagRFP)*	Böhm et al.[5]	N/A
Zebrafish: *Tg(mpx:GFP)*^{i114}	Renshaw et al.[83]	ZFIN: ZDB-FISH-161202-8
Oligonucleotides		
scg2a F1 - TTTTTCTCTCTCATGTAAATCTGTCTG	This paper	N/A
scg2a R1 - GAGATGCCATTTTAAGCACTGAAC	This paper	N/A

(*Continued on next page*)

Continued

REAGENT or RESOURCE	SOURCE	IDENTIFIER
scg2a F2 - AAATTTATCCGGATTAGTGTAGACATG	This paper	N/A
scg2a R2 - ATAAGAAACGGGTTCAGTTCCACTAAG	This paper	N/A
nppc F1 - TGTTGATTTTAAGTCATAGGCTACATG	This paper	N/A
nppc R1 - TTAAAGCAGCTTTTCTTTTTAACACTG	This paper	N/A
nppc F2 - GAGAGGTTGTTAATGGAGTGGTAG	This paper	N/A
nppc R2 - TAGAGTGAATCCAGAGTCATTATGAAG	This paper	N/A
esm1 F1 - ATAATCATCCTCATCCTTGTAGAAGTC	This paper	N/A
esm1 R1 - CTTCATTCACTGTCACATCCAAGGAG	This paper	N/A
tas2r3 F1 - TAATGTTTTACTGTGGTCACTTATTGG	This paper	N/A
tas2r3 R1 - AAACACAACCTCGAATAGACATATATG	This paper	N/A
scg2a crRNA1 - GCTGGGAGGAGGGCGCAATT	This paper	N/A
scg2a crRNA2 - TCATCTCGATGCTGCGCAGC	This paper	N/A
nppc crRNA1 - CAGCAAATGCGAGATGATCA	This paper	N/A
nppc crRNA2 - ACACTCGGGCACGGGGCCCC	This paper	N/A
esm1 crRNA1 - GACTGAGGCGTGGGGTCCCG	This paper	N/A
esm1 crRNA2 - GCAGTGCTCACCCCGTCCCG	This paper	N/A
tas2r3 crRNA1 - ATGACTGAAATTCCTGCAGC	This paper	N/A
tas2r3 crRNA2 - TCCAGACCAAAAACGGCCAC	This paper	N/A
Software and algorithms		
Illustrator	Adobe	https://www.adobe.com/
ImageJ	Schneider et al.[84]	https://imagej.nih.gov/ij
MATLAB	Mathworks	N/A
Prism 7.0	GraphPad	https://www.graphpad.com/
Other		
Gemma Micro 500	Skretting	N/A

RESOURCE AVAILABILITY

Lead contact

Further information and requests for resources and reagents should be directed to and will be fulfilled by the lead contact, Claire Wyart (claire.wyart@icm-institute.org).

Materials availability

- Plasmids used in this study are available on request.
- Zebrafish lines generated in this study are available on request.
- This study did not generate new reagents.

Data and code availability

- All tabulated RNAseq results are provided as Data S1; the raw data are available from the lead contact upon request.
- all MATLAB code used for analysis can be obtained at https://github.com/wyartlab
- Any additional information required to reanalyze the data reported in this paper is available from the lead contact upon request.

EXPERIMENTAL MODEL AND SUBJECT DETAILS

Zebrafish handling and husbandry

Zebrafish adults were maintained on a 14h/10h light/dark cycle and fed using a combination of Gemma Micro 500 diet and cultured rotifers.[85,86] All embryos and larvae described in this study were obtained by natural mating procedures. Animals were used for experiments until no later than 6 days post fertilization. All experimental procedures comply with European animal welfare regulations.

Bacterial strains and growth conditions

Streptococcus pneumoniae D39 serotype 2 wild-type strain, the isogenic red fluorescent *S. pneumoniae* D39 HlpA-mCherry mutant strain, or green fluorescent *S. pneumoniae* D39 HlpA-GFP mutant strain, in which the fluorescent proteins are fused to the histone-like protein, was grown on Columbia agar supplemented with 5% (v/v) defibrinated sheep blood (Biomerieux; 43049) at 37°C in a humidified atmosphere with 5% CO_2.[78,80,87] The *Listeria monocytogenes* LL195 wild-type strain was grown on Columbia agar supplemented with 5% (v/v) defibrinated sheep blood at 37°C.[75] Before injection, *S. pneumoniae* or *L. monocytogenes* was grown to mid log phase in C+Y medium[81] or BHI medium respectively at 37°C. Bacteria were subsequently harvested by centrifugation (6000 rpm, 10 min for *S. pneumoniae*, 4000 RPM for 5 min for *L. monocytogenes*) and suspended in sterile 0.5% (w/v) phenol red solution in PBS (Sigma-Aldrich, P0290) to aid visualization of the injection process.[24] Note that at this concentration, the use of phenol red for injections did not affect bacterial growth during the pre-injection interval.

Primary cell culture of CSF-cNs

We adapted a two-step culture protocol previously published comprising an initial feeder layer of cells on which were plated a second layer of fluorescent positives CSF-cNs cells.[8] Briefly, all embryos were bleached prior to dissociation in 0.003% bleach in reverse osmosis water in order to avoid contaminations. To perform the initial feeder layer of cells, we dissociated 2 dpf AB WT embryos using papain at 20U/mL (Serlabo Technologies, WOLK03176-1) in HBSS 1X solution (Fisher Scientific, 14170088) complemented with 0.2 mg/mL cysteine (Sigma-Aldrich, 30089), 1.25 μM $CaCl_2$ (Sigma, C3306), 0.5 μM EDTA (Sigma-Aldrich, E5134), and 2 μM NaOH at 37° for 20 minutes. Dissociated cells were rinsed using HBSS 1X and plated overnight at a concentration of 1.10^6 cells/well in DMEM medium (ThermoFisher, 10938025) complemented with 2mM L-Glutamine (Thermo Fisher Scientific, 25030024), 50U/mL penicillin/streptomycin (Thermo Fisher Scientific, 15140122), 25ng/mL NGF (Merckmillipore, 01-125), 4ng/mL GDNF (Fisher Scientific, 10679963), 25mM glucose (Sigma-Aldrich, G8769-100ML), and 10% FBS (Thermo Fisher Scientific, 10270106). 24 hours after the initial feeder layer plating, we dissociated 3 dpf *Tg(pkd2l1:tagRFP, pkd2l1:GCaMP5G)* double transgenic embryos using the same 20u/mL papain complemented solution used for the initial layer. Dissociated cells were rinsed using HBSS 1X and plated overnight at a concentration of 5.10^5 cells/well in Neurobasal medium (Thermo Fisher Scientific, 10888022), complemented with 1X B27 supplement (Thermo Fisher Scientific, 17504044), 1X N2 supplement (Thermo Fisher Scientific, 17502048), 2 mM L-glutamine (Thermo Fisher Scientific, 25030024), 10 U/mL penicillin/streptomycin (Thermo Fisher Scientific, 15140122), decomplemented FBS (Thermo Fisher Scientific, 10270106), and 1 mM sodium pyruvate (Thermo Fisher Scientific, 11360039). Cells were used 48 hours after the plating of the second layer.

METHOD DETAILS

Confocal imaging

All widefield confocal imaging was either performed live or mounted in 1.5% agarose on a Nikon ECLIPSE Ti2 inverted microscope (Figure 1), a Nikon AIR confocal microscope system (Figure 2), a 3i VIVO spinning disk microscope (Figure 6), or fixed and mounted in 50% glycerol on a Zeiss LSM5 Pascal confocal microscope (Figure 4).

Bacterial load

We injected zebrafish larvae with *S. pneumoniae* D39 wild-type strain into the hindbrain ventricle (see Table S1 for a summary of all conditions used in imaging and survival experiments) and determined the bacterial load in whole infected zebrafish larvae homogenates at 24 hours post injection (hpi). At 24 hpi, infected zebrafish larvae were anesthetized in 0.02 % Tricaine (Sigma-Aldrich A5040), transferred to a 1.5 ml screwcap tube (1 larva per tube) filled with 1.0 mm glass beads (Sigma-Aldrich Z250473) to ~25% capacity of the tubes volume, placed in a microvial rack, and violently shaken (3 times 10 sec, 10 sec interval) in a bead beater (Biospec Products; Mini Beadbeater) to disrupt the cells and tissues. Subsequently, serial dilution plating of the homogenates was performed on Columbia Blood Agar (Thermo Fisher, R452954) plates supplemented with 5% defibrinated sheep blood (bioTRADING, BTSG10), 10 mg/ml colistin sulphate and 5 mg/ml oxolinic acid (COBA, Oxoid), to inhibit growth of commensal bacteria in zebrafish. The plates were incubated O/N at 37°C and quantified the next day. All experiments were performed in duplicate.

Simulations of *in vitro* CSF-cN stimulation

In order to estimate the concentration of molecules at the surface of the CSF-cN during and after the 1-second stimulus, we carried out numerical simulations applying finite-element method (Comsol Multiphysics, Transport of Diluted Species & Laminar Flow modules). We here describe the model in more details. The concentration of molecules c obeys the advection-diffusion law:

$$\frac{\partial c}{\partial t} + v \cdot \nabla c - D\Delta c = 0$$

where D is the diffusion coefficient of the molecule, ∇ is the differential operator and Δ is the Laplacian operator. Here v is the fluid velocity vector obeying the incompressible Navier-Stokes equations:

$$\rho \nabla \cdot (v) = 0$$

$$\rho\frac{\partial v}{\partial t}+\rho(v\cdot\nabla)v=-\nabla.\sigma+\mu\Delta v$$

where $\rho = 10^3$ kg/m is the water density and $\sigma = -pI+\mu\nabla u+\mu(\nabla u)^T$ is the total stress tensor, with $\mu = 10^{-3}$ Pa.s the water viscosity and I the identity matrix. Bold terms represent three dimensional vectors or tensors.

The flow is simulated in a cylindrical container of height 0.45 mm and diameter 2 mm. Note that the concentration distribution around the cell was found not to depend on the size of the container when the diameter exceeds 1.2 mm, which is smaller than the selected value. Inside this container, the initial concentration c_0 is set to 0. A flow of concentration c_{puff} passes through a spherical opening of diameter 3 μm, representing the stimulation pipette, with a flow rate of 3.6 nL/s during 1s, in the direction of the cell. The cell is represented by a portion of sphere of diameter 10 μm and of height above the floor plate 8 μm. The cell is located at a distance of 100 μm from the stimulation pipette.

Concerning the boundary conditions for the flow and the concentration, a no slip is imposed at the bottom wall and on the cell ($v = 0$), and a complete impermeability is imposed against the passage of molecules ($n\cdot(D\nabla c+cv) = 0$). The lateral walls as well as the upper wall of the cylindrical container are at imposed constant pressure p_0, and we impose the absence of concentration gradients $n\cdot\nabla c = 0$.

Numerically, the transition between the stimulus process (which lasts 1s) and the post-stimulus phase (t > 1s) is achieved via a smoothing function:

$$f(t) = \exp\left(-\left(\frac{t-1}{\tau}\right)^2\right), \text{with } \tau = 17 \text{ ms}$$

The number of tetrahedral mesh elements varies between 685000 and 850000 in the simulations presented in this manuscript. All the simulations converged, and doubling the number of mesh elements led to similar results.

Fluorescence activated cell sorting of CSF-cNs and validation

50 to 300 *Tg(pkd2l1:GAL4, UAS:GFP)* zebrafish larvae expressing green fluorescent protein (GFP) in cerebrospinal fluid-contacting neurons (CSF-cNs) were collected at 3 days post fertilization (dpf), anaesthetized in 0.02 % (w/v) buffered 3-aminobenzoic acid methyl ester (pH 7.0) (Tricaine; Sigma-Aldrich, A5040) and decapitated at the level of the hindbrain. The remaining trunk tissue was immediately de-yolked (in de-yolking buffer: 55 mM NaCl, 1.8 mM KCl, 1.25 mM $NaHCO_3$) and manually dissociated in FACSMax buffer (AMS Biotechnology, T200100) through a 30 μm sterile filter as described previously.[88] The resulting suspension was re-filtered and then sorted on a BD Biosciences FACS Jazz sorter to isolate CSF-cNs (between 3000-15000 cells/run, ~0.2% of total input). Cells were sorted directly into lysis buffer (Qiagen, 74004; Clontech, 634894) for both qRT-PCR validation and RNAseq library preparation; sorting runs were either entirely diverted to validation or library preparation as cell yield was insufficient to perform both analyses on the same sample. In each sorting run, we isolated separate populations of putative CSF-cNs and an assortment of other, GFP- cell types as a reference population (referred to as "green" and "dark" cells, respectively throughout this manuscript). To verify that a highly enriched population of CSF-cNs was being isolated prior to library preparation, several sorting runs were diverted to qRT-PCR analysis. These cells were converted to cDNA using the RNeasy Micro kit (Qiagen, 74004) followed by the VILO RT kit (Thermo Fisher, 11756500). qRT-PCR was performed comparing the relative expression of a panel of diagnostic transcripts including known CSF-cN-specific genes between "green" and "dark" cDNA pools using SYBR Green chemistry (Thermo Fisher, K0991). Previously known CSF-cN markers, such as *pkd2l1*[20,21] and *pkd1l2*,[42,43] were massively upregulated while markers of hindbrain cells (*raraa*, *rarab*) were not.

Library preparation and RNAseq (differential CSF-cN RNAseq)

Following validation by qPCR, five additional RNA pools were generated from both "dark" and "green" cells isolated by sorting on five different experimental days (since RNA yield was too low to split the pool for validation and sequencing). The SMART-Seq v4 Ultra Low Input kit (Qiagen, 74004) was used to generate double-stranded cDNA from each sorting replicate; these pools were fragmented and tagged for sequencing using the Nextera DNA Library Preparation Kit (Illumina). Finally, the prepared library was sequenced on an Illumina NextSeq 500 (SY-415-1001).

Fluorescent *in situ* hybridization and immunohistochemistry

cDNA was generated from 3 dpf AB larvae using the RNeasy Mini Kit (Qiagen, 74104) and SuperScript IV reverse transcriptase (Thermo Fisher, 18091050). DNA fragments from a subset of ~40 candidate genes derived from the RNAseq hitlist were amplified from this cDNA by PCR and cloned into TOPO vectors (Thermo Fisher, 451641). Antisense digoxigenin-incorporating probes were transcribed from these clones and hydrolyzed to ~300 bp as previously described.[89–91] To verify that these transcripts were enriched in CSF-cNs, we combined fluorescent *in situ* hybridization and immunohistochemistry for GFP in *Tg(pkd2l1:GCaMP5G)* or *Tg(mnx1:GCaMP5)* transgenic animals at 24 hours post fertilization (hpf) and adult stages as previously described.[20,49,90,91]

Generation of transgenic zebrafish lines

To generate a Tol2 vector driving GAL4 under the control of GFAP regulatory elements, we used Gateway recombination-based cloning (Thermo Fisher, 11791020) using p5E-GFAP, which contains 7.4 Kb of GFAP intron 1 and exon 1,[92,93] pME-GAL4, and

p3E-poly(A) into pDestpA2. The resulting vector was injected into *Tg(UAS:RFP; cryAA:Venus)* at 30 ng/μL with 35 ng/μL Tol2 transposase to generate germline transgenics as previously described.[94,95]

Generation of *tas2r3* mutants

Site-specific crRNAs were designed targeting the *tas2r3* coding sequence using the CRISPOR web tool[96] (IDT). These were then annealed to a common tracRNA component to form an RNA duplex stock (33 μM) which was then complexed with 10 μg/μL Alt-R-S.p. Cas9 Nuclease V3 (IDT) in Cas9 buffer (20 mM HEPES, 150 mM KCl, pH 7.5) at a 1:1 molar ratio according to the manufacturer's instructions. Zebrafish embryos were obtained at the 1-2 cell stage and 1 nL of the described mixture was injected into each embryo. Embryos were allowed to recover in E3 medium. ~10 embryos were collected at 1-3 days post fertilization (dpf) and their DNA was harvested by proteinase K digest and gRNAs were validated using an EaeI restriction cleavage site present in the crRNA binding region that would be disrupted by indel mutations caused by CRISPR/Cas9 modification. As noted in Figure S6, we would later find that *tas2r3* is present in our wild type background as at least two different paralogous alleles, which we were able to independently mutate and segregate in genotyping assays using paralog-specific PCR.

Generation of mutants in genes encoding CSF-cN neuropeptides

To generate *scg2a, nppc, esm1* null mutant line, we used the CRISPR/Cas9-mediated genome editing method. crRNA were designed by using online CRISPOR program (crispor.tefor.net/). crRNA and tracRNA were ordered from Integrated DNA Technology. The guiding RNA (key resources table) complex is prepared by duplex buffer, and mixed with Cas9 protein provided by Dr. Jean-Paul Concordet (MNHN, Paris, France). The mixed complex was injected into one-cell stage wild type eggs. The editing efficiency was tested after injection at 2 dpf by performing genotyping on 3 pools of 20 embryos. Genomic DNA was extracted in lysis buffer (10 mM Tris pH 8.2 mM EDTA, 0.2% Triton X-100, 200 μg/mL Proteinase K) at 55°C for 2 h followed by 10 min of deactivation at 99°C. Then the target region was amplified by performing PCR with specific primers (key resources table). The F0 generation which contains high efficiency mutations was raised to sexual maturity. The best transmitters were selected by screening the rate of mutation in F1 embryos. The mutations of F1 adult fish have been analyzed by sequencing the subcloned PCR product. The F1 fish that carried the best type of the mutation has been chosen and raised by crossing with AB wild type fish to generate the F2 fish. Analyzing enzymatic restriction digest in the targeted site was used to screen the homozygote, heterozygote, and wild type F2 fish.

scg2a encodes a precursor of 540 amino acids in a single exon. The beginning of this exon was targeted by two gRNAs. To generate the *scg2a*^{icm42} mutant allele, sequence analysis revealed that 10 nucleotides were deleted by the gRNA1/Cas9 complex, leading to a frameshift and a premature STOP codon leading to a truncated amino acid sequence deprived of the mature peptide precursor sequence. The Nppc precursor is encoded by 3 exons and the mature peptide sequence is contained in the second exon. To generate the *nppc*^{icm36} mutant allele, we targeted the beginning of the first exon in order to disrupt the signal peptide sequence. The gRNA/Cas9 complex we used mediated a 3 nucleotide deletion that led to a mutation on the start codon (from ATG to ATT), hindering the translation of first exon. The *esm1* gene is composed of 3 exons and encodes a 139 amino acids protein whose binding domain is encoded by exon1. The gRNA1/Cas9 complex we used induced an insertion of 13 nucleotides, which led to frame shift and premature STOP codon forming a truncated protein of 29 amino acids devoid of the binding domain in the *esm1*^{icm34} mutant allele.

Calcium imaging of zebrafish larvae after injections in the hindbrain ventricle

Transgenic zebrafish larvae expressing GCaMP in a cell-type specific manner—*Tg(pkd2l1:GCaMP5)* transgenic larvae for CSF-cNs and *Tg(GFAP:GAL4, UAS:GCaMP5G)* for ependymal radial glia—were anesthetized in tricaine and paralyzed with α-bungarotoxin (1mM, 1nL, Tocris Biosciences, 2133) i.m. or i.v. for imaging. Subsequently, the larvae were embedded in 1.5% low-melting point agarose dissolved in egg water (60 μg/mL sea salts, Sigma-Aldrich, S9883) in MilliQ) in an open uncoated 8-well chamber slide (ibidi, 80826) and kept at 28°C in a temperature-controlled chamber (Okolab). Larvae were imaged on a Nikon AIR confocal microscope system. FIJI/MATLAB was used for image analysis. Imaging involved several experimental conditions, unless otherwise noted, all solutions were injected into the hindbrain ventricle of 2 dpf larvae.

Pneumococcal meningitis

2000 colony forming units (CFU) of red fluorescent *S. pneumoniae* D39 HlpA-HlpA-mCherry or vehicle-injected with sterile 0.5% (w/v) phenol red solution in PBS were injected into the hindbrain ventricle after anesthesia of zebrafish larvae with tricaine followed by paralysis with α-bungarotoxin injection, before being embedded in low-melting point agarose as described previously.[24,80]

Heat-killed S. pneumoniae

Bacteria were prepared as above, except the culture was incubated for 20 minutes at 80° C prior to injection.

E. coli

A culture of DH5α *E. coli* (ATCC) was grown to OD_{600} 0.6. 1 nL of this culture was injected into the hindbrain ventricle as above.

Listerial meningitis

6000 CFU of *L. monocytogenes* LL195 or vehicle-injected with sterile 0.5% (w/v) phenol red solution in PBS were injected into the hindbrain ventricle after anesthesia of zebrafish larvae with tricaine followed by paralysis with α-bungarotoxin injection, before being embedded in low-melting point agarose.

Calcium imaging in primary cell culture

Calcium imaging on GCaMP5G-expressing neurons from the *Tg(pkd2l1:GCaMP5G)* transgenic line was performed on an epifluorescence microscope equipped with a Lumen Dynamics XT600 Xenon lamp and a GFP filter cube. Acquisition was performed at 5 Hz using an EM-CCD Camera from Hamamatsu. Puffs stimuli were delivered using a 1 s long TTL pulse from a Digidata acquisition system (Axon Instruments) and repeated 3 times with an inter trial interval of 64 seconds.

aCSF

Artificial CSF (aCSF) was composed of NaCl 140mM (Sigma-Aldrich, S7653), KCl 1mM (Sigma-Aldrich, P9333), $CaCl_2$ 2.5mM (Sigma-Aldrich, 223506), $MgCl_2$ 1mM (Sigma-Aldrich, M2670), HEPES 10mM (Sigma-Aldrich, H3375), D-(+)-Glucose 10mM (Sigma-Aldrich, G8270), diluted in MilliQ water; pH was adjusted at 7.4.

Pneumolysin

Recombinant serotype 4 pneumolysin purified from *E. coli* (MyBioSource, MBS1141054) was reconstituted in aCSF at a concentration of 0.1 mg/mL. In our *in vitro* experiments, the concentration of pneumolysin applied onto the cultured CSF-cNs was 50 μg/mL, which exceeds the threshold for 100% hemolytic activity more than threefold.

Mix of bitter compounds

Acetone (Sigma, 534064), 2-butanone (Sigma, W217012), 2-pentanone (Sigma, W284220), dimethyl disulfide (Sigma, W353604), 2-methylpropanal (Sigma, W222003) were diluted as a mix of bitter compounds in aCSF at a concentration of 100mM each. In our *in vitro* experiments, the concentration of each bitter compound applied onto the cultured CSF-cNs was 50 mM according to *in silico* simulations (Figure 3).

Dimethyl disulfide (DMDS) and 2-pentanone

DMDS (Sigma-Aldrich, W353604) and 2-pentanone (Sigma-Aldrich, W284220) were diluted in aCSF at 25, 50 and 100mM concentrations. In our *in vitro* experiments, the concentrations of DMDS and 2-pentanone applied onto the cultured CSF-cNs were 12.5, 25 and 50 mM according to *in silico* simulations (Figure 3).

Acetone, 2-butanone and 2-methylpropanal

Acetone (Sigma-Aldrich, 534064), 2-butanone (Sigma-Aldrich, W217012) and 2-methylpropanal (Sigma-Aldrich, W222003) were diluted in aCSF at 100 mM concentration. In our *in vitro* experiments, the concentration of acetone, 2-butanone and 2-methylpropanal applied onto the cultured CSF-cNs was 50 mM according to *in silico* simulations (Figures 3 and S2).

Supernatant after viral infection

Baby hamster kidney (BHK) cells were infected *in vitro* for 48 hours with Sindbis virus expressing the fluorescent protein mCherry. Uninfected cells were used as control group. After 48 hours, infected BHK cells showed red fluorescence and were detaching from their support, signs of infection of the cells by Sindbis virus – while control unifected cells did not show adhesion problem. Supernatants of control and infected cells were collected and inactivated by UV irradiation before pressure-applications.

S. pneumoniae *supernatant*

Cell-free culture supernatant produced by *S. pneumoniae* was obtained by growing *S. pneumoniae* D39 wild-type bacteria until the end of the mid-log growth phase in C+Y medium, supplemented with 0.8% yeast extract instead of 2.5% yeast extract to minimize autofluorescence of the medium while retaining optimal growth conditions for the bacteria. The culture was then centrifuged for 15 minutes at 5000 x *g*, and subsequently the supernatant was collected and filtered through a 0.22μM filter to remove residual bacterial cells before pressure-applications.

FACS sorting of infected larvae

Larvae were injected with 2000 CFU *S. pneumoniae* D39 wild-type strain as described above, collected at 24 hours post infection, and a single-cell suspension was generated using the same protocol as for prior rounds of FACS. Analysis and isolation were performed using a BD InFlux cell sorter controlled by BD FACS Sortware v1.2.0.142 software. Infected neurons were identified by eGFP reporter protein which was excited by a 488nm, 200mW laser and detected through a 530/40 bp filter. Cell auto-fluorescence was also excited by the 488nm laser and detected through a 692/40 bp filter. Live and intact cells were identified by DAPI staining and excited by a 405nm, 100mW laser. For gating and trigger thresholds, background particulate was identified by running cell suspension buffer alone and standard FSC vs SSC gating was applied to select whole, intact events of similar scatter properties. Live cells were then gated according to low DAPI signal events withing a distinct event cluster and, from there, 2 separate auto-fluorescent populations were sorted from the eGFP positive events. eGFP gating edges were set with no-color and eGFP FMO controls. Compensation was not applied to any parameters.

Library preparation and RNAseq (uninfected vs. infected CSF-cNs)

Three RNA pools were generated from both "dark" and "green" cells isolated in control and infected conditions by sorting. The SMART-Seq v4 Ultra Low Input kit (Clontech, 634888) was used to generate double-stranded cDNA from each sorting replicate; these pools were fragmented and tagged for sequencing using the Nextera XT DNA Library Preparation Kit (Illumina). Finally, the prepared library was sequenced on an Illumina NovaSeq 6000 SP (200 cycles, up to 800 million reads, Illumina).

RNAseq (uninfected vs. infected CSF-cNs) analysis using DESeq2

Differential expression (DE) analysis of uninfected vs. infected CSF-cNs RNAseq data was conducted in R version 3.6.1 (R Development Core Team, 2019) using the DESeq2 Bioconductor package (v1.26.0). From the raw count data, the DESEeq function performs

all the processing steps from the normalization of the counts with the calculation of size factors (accounting for differences in library sizes) and dispersion factors to the differential analysis itself. DE genes between infected and control cells were explored separately within each population of green and dark cells, and also for the difference of variation observed in the two populations (testing the "ratio of ratios": i.e. the Infected/Control ratio in the green cells divided by the Infected/Control ratio in the dark cells). Significant DE genes were determined by fitting Negative Binomial Generalized Linear Models (one model per gene), followed by a Wald test on the model coefficients for significance testing. To control for the false discovery rate (FDR), all p-values were adjusted using the Benjamini-Hochberg (BH) procedure, and all DE genes with a BH-adjusted p-value < 0.05 were considered statistically significant. Within each population of green and dark cells, the directional change of the DE gene expression level was indicated by the sign of the log fold: either positive when the average expression level in the infected cells was significantly higher than that in the control cells ("up in infected"); or negative when expression level was decreased in the infected cells ("down in infected").

Larval zebrafish survival assays

Survival (death here is defined as larvae that do not respond to tail touches nor have a beating heart) was assessed every 24 hours. Curves were generated with GraphPad Prism 7.0 and survival data were analyzed with the log rank (Mantel-Cox) test.

Survival experiments in CSF-cN compromised transgenic larvae

Zebrafish larvae were infected as described previously by injecting 2000 colony forming units (CFU) wild-type *S. pneumoniae* D39 into the hindbrain ventricle and kept in 6-well plates at 28°C with 20 larvae in each group per well.[24] The mortality rate was scored by monitoring live and dead embryos at 24 hours intervals post-injection; mortality was determined by heartbeat and response mechanical stimuli. All experiments were performed in triplicate. Survival analyses were performed and involved the following experimental conditions:

Nitroreductase

Tg(pkd2l1:GAL4, UAS:epNTR-tagRFPT-UTR.zb3) zebrafish embryos[51] and control sibling embryos were treated with 10 mM metronidazole (Sigma-Aldrich, M3761) in 0.1% DMSO (Sigma-Aldrich, D8418) for at least 16 hours to induce nitroreductase-mediated ablation of *pkd2l1*+ cells after mechanical dechorionation. At 2 dpf the larvae were washed 3 times with egg water and subsequently infected.

Botulinum toxin B Light Chain

Tg(pkd2l1:GAL4, UAS:BoTxBLC-GFP) zebrafish embryos[5,52,97] and control wild-type embryos were infected at 2 dpf.

Survival experiments in mutant larvae

Adult heterozygous zebrafish mutants (*pkd2l1*^{icm02}, *sgc2a*^{icm42}, *esm1*^{icm34}, *nppc*^{icm36}) were incrossed in order to compare survival between homozygous mutants and control siblings within the same clutches. Injection of *S. pneumoniae* targeted the hindbrain ventricle of 2 dpf zebrafish mutants and their control siblings (Figure S7) at different doses (1000 CFU or 2000 CFU per larva). We typically injected ~25 larvae for each CFU for each group in each experiment. The survival rate was evaluated every 12h until 72 hours post-infection (hpi) prior to genotyping after euthanasia of all larvae.

Analysis of calcium transients *in vivo*

To determine the overall activity of a given cell of interest defined within a region of interest (ROI), the ΔF/F integrated over time was calculated as it more reliable and less sensitive to fluctuations in the level of expression of the fluorescent calcium sensor; comparisons across conditions were made using multifactorial ANOVAs with Scheffé post-hoc tests. To compare isolated large-amplitude calcium transients (as in Figures 2E–2G and 2N), a MATLAB script was written to identify features of the Ca^{2+} trace where a sustained high-amplitude calcium transient (i.e. > 100% ΔF/F) was associated with a sharp onset (i.e. differential of ΔF/F trace > 30). Statistical testing was performed on these isolated events using the Wilcoxon rank sum test with Bonferroni correction for multiple comparisons.

Analysis of calcium transients *in vitro*

Slow translational drifts of the image due to cell movements were corrected using image registration by taking as a reference image a frame of the original position of the CSF-cN. We identified CSF-cN calcium transients in response to 1-second stimulus by using a 100 ms-long flash of green light performed 12.74s before the stimulus. Frames corresponding to flashes stimuli were removed from the representative traces (see Figures 3B and 3C). To determine the response of a given cell (ROI) to a 1-second stimulus (as in Figures 3D and 3E), the ΔF/F amplitude of each peak calcium response after stimulus was calculated using a home-made MATLAB script available on the Wyart lab github: the ΔF/F average of over six time points around the maximum ΔF/F of the peak was calculated, and was subtracted to this the ΔF/F average of six points before the stimulus. A cell was considered as a responding cell when we observed a response for at least one of the 3 1-second stimuli. Latency was calculated as time between the 1s-stimulus and the beginning of the peak response. Time-to-peak was calculated as the time between the beginning of the peak response and the maximum of the peak. Time decay was calculated by applying an exponential fit of model 'a*exp(-b*x)+c' and extracting the time decay as follow: decay = 1/b. As control for no-stimulus (see Figure 3G, black circles), we measured the time decay of transients corresponding to spontaneous activity with no stimulus (see Figures 3B and 3C, left). Comparisons across conditions (as in

Figures 3D and 3E) were made using 2-factor ANOVAs with Turkey HSD post-hoc tests on R. Comparisons for latency, time-to-peak and time decay were made using two-sample Kolmogorov-Smirnov non-parametric test on MATLAB.

Production of virus-containing supernatant

Sindbis virus (SINV)[76] was used to infect BHK cells. BHK-21 cells (ATCC #CCL-10) were cultured at 37°C and 5% CO2 in DMEM/F-12 containing phenol red (Gibco) supplemented with 5% heat-inactivated fetal bovine serum (Gibco) and penicillin-streptomycin (Life Technologies). To produce the supernatant, DMEM without phenol red was used instead. A near-confluent layer of cells in a 75cm^2 flask in 20 ml of culture medium was seeded with ~10^3 PFU of SINV-mCherry/2A virus, isogenic with the SINV-eGFP/2A virus whose construction is described in Boucontet et al.[98] and generated in the same way but replacing eGFP with mCherry. A control flask of BHK cells without virus was cultured in parallel. Two days later, supernatants were harvested and cell debris removed by centrifugation (5000 rpm, 10 min, 4°C). These supernatants were UV-inactivated by delivering 30mJ/cm^2 of 254 nm UV light using a CL-508 crosslinker (Uvitek). Titration on BHK cells ascertained that infective SINV particles fell from ~10^7 PFU/ml to zero after UV inactivation. Supernatants were frozen until use.

Analysis of neutrophil infiltration to the central canal after infection

Tg(mpo:GFP) transgenic larvae[83] expressing green fluorescent neutrophils were anesthetized and infected with 2000 CFU mCherry+ *S. pneumoniae* as described above or injected with 1 nl Alexa 647 Dextran (Thermo Scientific, D22914) in the hindbrain ventricle. After embedding the larvae in low-melting point agarose, time-lapse imaging was performed at 28°C on a Nikon AIR confocal microscope system equipped with a temperature-controlled chamber. Images were obtained at 20 min. intervals for 12-24 hours.

Behavioral analysis

Zebrafish larvae were either infected with 6000 CFU *S. pneumoniae* or injected with PBS at 5 dpf as above. Larvae were rested until 9, 24, or 32 hours post injection and plated individually in a 32 well (80 mm x 140 mm) made from 3 mm acrylic sheets (plexiglass) plate (BFP CINDAR, Champigny-sur-Marne, France) cut by a laser cutter into 1.5 cm diameter wells holding a volume of 500 μL. Larvae were then recorded freely for 5 minutes at 160 fps after 10 min of acclimation. Behavioral parameters were extracted using ZebraZoom.[99]

QUANTIFICATION AND STATISTICAL ANALYSIS

Behavioral analysis

Behavioral parameters were extracted from tracking videos as previously described.[99] These were tested across time points and conditions using a 2-factor ANOVA followed by Scheffé post-hoc testing.

Quantification and analysis of axial curvature and fluorescence

Following injection and imaging, the spinal cord was manually delineated using MATLAB (*curvature.m*, *linecurvature2D.m*).[8] This produced an imaging area from which curvature was calculated from a smoothing spline curve fit to the x-axis boundaries and total 568 nm fluorescence was integrated across the x-axis. We therefore obtained both a total fluorescence and local curvature for each spinal cord; curvature was compared via a Student's t-test (Figure 1R) while curvature and fluorescence were correlated by simple linear regression (Figure 1S).

In vivo calcium imaging

Large ΔF/F events were detected using a MATLAB algorithm. These large events were effectively filtered for those where—

- Amplitude > 100% ΔF/F
- Initial first differential of ΔF/F > 30%/frame

These criteria were effectively used to threshold a series of time points where ΔF/F rose very rapidly to high levels; *strel()* and *imclose()* functions were then used to smooth those thresholded points into continuous intervals (for further details, see *super.m* in the referenced GitHub repository).

After filtering, these events were tabulated by time point and condition and evaluated for each experiment by 2-factor ANOVA followed by Scheffé post-hoc testing to find time-point-specific differences. The exception to this was in Figures 2I and 2J, where large events for most conditions were so infrequent as to not be statistically comparable; we therefore used chi-square analysis here to show that large events were more common in the live *S. pn.* condition than other conditions.

RNAseq

For the initial transcriptome (Figure 4) RNAseq reads were mapped to the zebrafish GRCz10 genome draft and evaluated for enrichment by evaluating false discovery rate of log fold change for fragments per kilobase of transcript per million fragments mapped (FPKM).

In vitro calcium imaging

Image registration was carried out using as image of reference a frame of the original position of the CSF-cN; this was used to correct small cell movements occurring during calcium imaging *in vitro*. To synchronize the 1-second stimulus on the cell with the calcium imaging movie recording, we used a 100 ms-long flash of green light (detectable on the calcium imaging movie) performed exactly 12.74 seconds before the stimulus. We removed frames corresponding to flash stimuli from the representative traces.

Quantification of the amplitude of CSF-cN calcium responses to 1-second stimuli was performed by calculating the ΔF/F amplitude of each peak calcium response after each stimulus using a home-made MATLAB script (see *Analyse_amplitudesV5.m* available on the Wyart lab GitHub repository). This script calculated the ΔF/F average of over six time points around the maximum ΔF/F of the peak, and subtracted to this the ΔF/F average of six points before the stimulus. We considered a cell responding to at least one of the three 1-second stimuli as a responding cell.

Quantification of latency was performed by calculating the time between the 1-second stimulus and the beginning of a peak response.

Quantification of time-to-peak was performed by calculating the time between the beginning of the peak response and the maximum of the peak.

Quantification of time decay was performed using a home-made MATLAB script (see *Analyse_kinematicsV3.m* available on the Wyart lab GitHub repository) applying an exponential fit of model 'a*exp(-b*x)+c' and extracting the time decay as follow: decay = 1/b. No-stimulus control (see Figure 3G, black circles) time decay was measured using the time decay of transients corresponding to spontaneous activity with no stimulus (see Figures 3B and 3C, left).

Statistics of comparisons across conditions (as in Figures 3D and 3E) were performed using 2-factor ANOVAs with Turkey HSD post-hoc tests on R, with the exception of *S. pneumoniae* supernatant experiment *in vitro* (Figures 7A and 7B) which was analyzed using paired t-test. Statistics of comparisons for latency, time-to-peak and time decay were made using two-sample Kolmogorov-Smirnov non-parametric test in MATLAB (see GitHub repository).

Survival analysis

All survival data were analyzed by log-rank test (Mantel-Cox). All data were analyzed by Student's t-test for comparison of two groups or two-way ANOVA followed by Sidak's or Tukey's post hoc test. Bacterial load and competitive index data were analyzed by unpaired t-test or one sample t-test respectively. The number of subjects and biological replicates is indicated in the figure legends. All data including error bars are presented as mean ± SD or mean ± SEM. *P value*s <0.05 were considered statistically significant, unless stated otherwise. All statistical analyses were performed using MATLAB or GraphPad Prism 7.0.